Journal of Experimental and Theoretical Physics, Vol. 92, No. 3, 2001, pp. 361–373.
Translated from Zhurnal Éksperimental'noĭ i Teoreticheskoĭ Fiziki, Vol. 119, No. 3, 2001, pp. 419–433.
Original Russian Text Copyright © 2001 by Sazonov.

ATOMS, SPECTRA, RADIATION

Extremely Short and Quasi-Monochromatic Electromagnetic Solitons in a Two-Component Medium

S. V. Sazonov*
Kaliningrad State Technical University, Kaliningrad, Russia
**e-mail: nst@alg.kaliningrad.ru*

Received May 3, 2000

Abstract—The propagation of extremely short (without high-frequency filling) pulses and nonresonant envelope solitons in a two-component medium comprising two-level atoms with substantially different quantum transition frequencies was studied. The dynamics of a pulse whose reciprocal time scale lay between these frequencies was shown to be described by the Kosevich–Kovalev equation, the one-way variant of which was the Konno–Kameyama–Sanuki equation. If the transition dipole moments of medium components were equal, the one-way equation became integrable. Soliton and soliton-like solutions to these equations were used to analyze pulse propagation regimes at various two-component medium initial states. The stability of these localized wave formations was analyzed. The possible existence of stable soliton-like pulses propagating in a nonequilibrium medium at group velocities exceeding the velocity of light in vacuum was discussed. *© 2001 MAIK “Nauka/Interperiodica”.*

1. INTRODUCTION

The progress in laser physics made during the past decade has, amongst other things, led to an improvement in the methods for creating nonequilibrium states of various media. This aroused interest of researchers in the formation and recording of electromagnetic pulses propagating in such media at velocities exceeding the speed of light, c, in vacuum [1]. It is common knowledge that superluminal regimes do inevitably exist in media that is unstable with respect to the transition to the equilibrium state [2].

At the same time, the generation of laser pulses of a width (τ_p) to one electromagnetic oscillation period [extremely short pulses (ESPs)] in laboratory conditions [3, 4] gave strong impetus to theoretical studies on interactions between such pulses and matter. The range of τ_p values for ESPs is at present several hundred to several femtoseconds. For obvious reasons, the approximation of slowly varying amplitudes and phases, which works well with pico- and nanosecond pulses having well defined carrier frequencies ω [5, 6], ceases to be valid when interaction between ESPs and matter are studied. Below, such pulses will be called quasi-monochromatic. A quantitative criterion of quasi-monochromatic pulses can be written as $\Delta\omega/\omega \ll 1$, where $\Delta\omega$ is the pulse spectral width, which is nonzero because of its finite duration.

Since the discovery of the self-induced transparency effect and its theoretical description [7] based on the approximation of slowly varying amplitudes and phases, alternative mathematical methods for studying this phenomenon have been continuously sought [8–13]. For instance, in [8, 9], a small parameter was found ($\epsilon = 8\pi d^2N/\hbar\omega_0$, where N is the concentration of two-level atoms interacting with the pulse field, ω_0 is the frequency, and d are the matrix elements of the quantum transition dipole moment) that allowed the order of the derivatives in the Maxwell equations to be decreased (the reduced Maxwell–Bloch system). The mathematical structure of the reduced equations is identical (except for notation) with the structure of the Maxwell–Bloch equations obtained using the approximation of slowly varying amplitudes and phases [8]. Both Maxwell–Bloch and reduced Maxwell–Bloch equations are integrated by the inverse scattering problem method. Abandoning the approximation of slowly varying amplitudes and phases [8, 9] was an important step in developing the theory of interactions between laser pulses and matter from the point of view of the modern trends in coherent optics.

The authors of [14, 15] did not use the approximation of a low-density medium ($\epsilon \ll 1$) but, in turn, suggested the approximations of pulses very short,

$$(\omega_1\tau_*)^2 \ll 1, \tag{1}$$

and very wide,

$$(\omega_2\tau_*)^2 \gg 1, \tag{2}$$

compared with interatomic times ω_1^{-1} and ω_2^{-1} (τ_* is the characteristic time scale of the propagating signal). In the limit given by Eq. (1), the dynamics of ESPs satisfies the sine-Gordon equation for the “area” of the electromagnetic pulse [14, 15], and in the limit given by Eq. (2), it obeys the modified Korteveg–de Vries equation for the ESP electric field [14–17].

Clearly, condition (1) can only be met for frequencies ω_1 in the infrared region, which corresponds with the vibrational spectra of molecules [14]; that is, with the motion of molecular ions. In gaseous media, this can be tunnel-inversion transitions of some molecules, for instance, ammonia. If it is, however, assumed that condition (1) can be satisfied for frequencies ω_1 in the visible region, ionization processes (transitions to the continuous spectrum) should be taken into account, which can considerably complicate the problem.

Within the framework of our approach, condition (2) can easily be satisfied by visible region ω_2 frequencies corresponding to electronic transitions. Recent years witnessed an increased interest in resonance interaction between laser pulses and two-component media. For instance, various propagation regimes of resonance quasi-monochromatic pulses in a system of two-level atoms of two kinds were considered in [18–20]. The transition frequencies for atoms of two kinds coincided, but the transition dipole moments were different. At the same time, when a nonmonochromatic pulse propagates in a medium, the process involves interactions with a large number of quantum transitions of different natures, both covered by the ESP spectrum and lying outside it. The simplest theoretical model is then a two-component medium comprising transitions satisfying conditions (1) (1-component or 1-atoms) and (2) (2-component or 2-atoms).

This work is concerned with a theoretical study of the propagation of ESPs and nonresonant quasi-monochromatic signals in a nonlinear medium comprising 1- and 2-components, which will be treated as sets of two-level atoms with frequencies ω_1 and ω_2 and transition dipole moments d_1 and d_2, respectively. Note that this model can more or less satisfactorily describe ESP interactions with gaseous media or some liquids like an absorbing dye [21]. The matter is that, in the transparency region, it unambiguously follows from the two-level medium model that the nonlinear refractive index, n_2, is negative [22, 23], whereas $n_2 > 0$ in dielectric solids [24]. It was shown in [25] that $n_2 > 0$ can only be obtained in the approximation of an at least three-level medium, the consideration of which is outside the scope of this work.

The paper is organized as follows. Equations (1) and (2) are used in Section 2 to derive nonlinear wave equations for the area of an electromagnetic pulse propagating in a two-component medium comprising two-level atoms. Section 3 contains a comprehensive analysis of some soliton-like solutions to these equations (from ESPs to envelope pulses, or quasi-monochromatic solitons). Generally, solitons considered in this work are not solutions to completely integrable equations. Where necessary, the distinction between true solitons and solutions to nonintegrable equations in the form of solitary traveling waves will be stressed. The "averaged Lagrangian" method used in Section 3 allowed us to study the problem of the stability of the solutions under consideration. In Section 4, we analyze stable ESP and envelope pulse propagation regimes in a two-component medium prepared in various initial states. Attention is paid to solitons propagating in nonequilibrium media at group velocities exceeding the velocity of light in the vacuum. In the Conclusion (Section 5), we formulate the most important results of this work and consider some unsolved problems, which would, in this author's opinion, be interesting to solve in the future.

2. THE KOSEVICH–KOVALEV AND KONNO–KEMEYAMA–SANUKI EQUATIONS

Consider a gas comprising two-level 1- and 2-components with quantum transitions satisfying conditions (1) and (2), respectively.

The system of material Bloch equations for such a medium has the form

$$\frac{\partial U_j}{\partial t} = -\omega_j V_j, \tag{3}$$

$$\frac{\partial V_j}{\partial t} = \omega_j U_j + \Omega_j W_j, \tag{4}$$

$$\frac{\partial W_j}{\partial t} = -\Omega_j V_j, \tag{5}$$

where index j ($j = 1, 2$) is the number of the medium component, $\Omega_j = 2d_jE/\hbar$, W_j is the inversion of transition populations of the jth component ($-1/2 \le W_j \le 1/2$), and dynamic variable U_j determines the polarization P of the medium,

$$P = 2\sum_{j=1}^{2} d_j N_j U_j, \tag{6}$$

where N_j is the concentration of atoms of the jth component.

Excluding V_j, which has no real physical meaning, from Eqs. (3)–(5) yields

$$\begin{gathered}\frac{\partial^2 U_j}{\partial t^2} = -\omega_j^2 U_j - \omega_j \Omega_j W_j,\\ \frac{\partial W_j}{\partial t} = \frac{\Omega_j}{\omega_j}\frac{\partial U_j}{\partial t}.\end{gathered} \tag{7}$$

Note that U_j and V_j are not the envelopes of the synphase and quadrature dipole moment components, but are the initial atomic variables related to the density matrix $\hat{\rho}$ elements as follows:

$$U = \frac{\rho_{21} + \rho_{12}}{2}, \quad V = \frac{\rho_{21} - \rho_{12}}{2i}.$$

Let us complement system (6), (7) by the Maxwell equation

$$\Delta E - \frac{1}{c^2}\frac{\partial^2 E}{\partial t^2} = \frac{4\pi}{c^2}\frac{\partial^2 P}{\partial t^2}. \tag{8}$$

By virtue of Eq. (1), the $\omega_1^2 U_1$ term in the right-hand side of the first equation in (7) can be neglected for the 1-component. The solution to Eq. (7) for $j = 1$ is then given by [14, 15]

$$W_1 = W_{1\infty}\cos\theta, \quad \frac{\partial U_1}{\partial t} = -\omega_1 W_{1\infty}\sin\theta, \tag{9}$$

where

$$\theta = \int_{-\infty}^{t}\Omega_1 dt'$$

and $W_{1\infty}$ is the inversion of 1-component atoms before the action of an ESP.

Let us rewrite the first equation in (7) for the 2-component in the form

$$U_2 = -\frac{\Omega_2}{\omega_2}W_2 - \frac{1}{\omega_2^3}\frac{\partial^2 U_2}{\partial t^2}. \tag{10}$$

In a zero-order approximation with respect to the small $(\omega_2\tau_p)^{-2}$ parameter [see Eq. (2)], we obtain $U_2 \approx -\Omega_2 W_2/\omega_2$. Substituting this result into the second term in the right-hand side of Eq. (10) and assuming $W_2 \approx W_{2\infty}$ in this equation (by virtue of a weak transition excitation, $W_{2\infty}$ is the initial inversion of 2-component atoms) yields

$$U_2 = -\frac{\Omega_2}{\omega_2}W_2 + \frac{W_{2\infty}}{\omega_2^3}\frac{\partial^2\Omega_2}{\partial t^2}. \tag{11}$$

The substitution of $U_2 \approx -\Omega_2 W_{2\infty}/\omega_2$ in the second equation in Eq. (7) followed by the integration of this equation gives

$$W_2 = W_{2\infty}\left(1 - \frac{\Omega_2^2}{2\omega_2^2}\right). \tag{12}$$

It follows from Eqs. (11) and (12) that

$$U_2 = -W_{2\infty}\frac{\Omega_2}{\omega_2} + W_{2\infty}\frac{\Omega_2^3}{2\omega_2^3} + \frac{W_{2\infty}}{\omega_2^3}\frac{\partial^2\Omega_2}{\partial t^2}. \tag{13}$$

Equations (8), (6), (9), and (13) give

$$\Delta\theta - \frac{n_0^2}{c^2}\frac{\partial^2\theta}{\partial t^2} = \alpha\sin\theta - \beta\left(\frac{\partial\theta}{\partial t}\right)^2\frac{\partial^2\theta}{\partial t^2} - \nu\frac{\partial^4\theta}{\partial t^4}, \tag{14}$$

where n_0 is the low-frequency refractive index corresponding to 2-component quantum transitions,

$$n_0^2 = 1 - \frac{16\pi d_2^2 N_2 W_{2\infty}}{\hbar\omega_2},$$

$$\alpha = -\frac{16\pi d_1^2 N_1 \omega_1 W_{1\infty}}{\hbar c^2}, \tag{15}$$

$$\nu = -\frac{16\pi d_2^2 N_2 W_{2\infty}}{\hbar c^2 \omega_2^3}, \quad \beta = \frac{3 d_2^2 \nu}{2 d_1^2}.$$

In the spatially one-dimensional case ($\Delta = \partial^2/\partial z^2$) and at $d_1 = d_2$ ($\beta = 3\nu/2$), Eq. (14) coincides with the Kosevich–Kovalev equation, which generalizes the Frenkel'–Kontorova model for dynamic dislocations in crystals to problems with lattice anharmonicity and spatial dispersion of the acoustic regime [26]. Precisely at $\beta = 3\nu/2$, Eq. (14) has an exact solution in the form of a solitary soliton-like pulse [26]. Equation (14) is not an integrable model, and its solution in the form of a solitary traveling wave therefore does not possess the soliton property of elastic interaction with its like. As in [27], solitary stationary waves will sometimes be called solitrons to distinguish them from true solitons. As far as true soliton solutions are concerned, of interest is the "one-way" variant of Eq. (14). To obtain the one-way equation from (14), we apply the approximation of one-way propagation [15] along axis z at a velocity close to c/n_0. This is justified if, by virtue of Eqs. (1) and (2), each term in the right-hand side of Eq. (14) is related to both left-hand side terms as $(\omega_1\tau_p)^2 \sim (\omega_2\tau_p)^{-2} \ll 1$ to one. As is seen from the equation for n_0^2, N_2 is formally bounded from above in the nonequilibrium case $W_{2\infty} > 0$. For $W_{2\infty} = 1/2$, this restriction has the form (see Eq. (12))

$$\epsilon_2 < 1, \tag{16}$$

where $\epsilon_j = 8\pi d_j^2 N_j/\hbar\omega_j$ ($j = 1, 2$). This is a weaker restriction than that imposed by the reduced Maxwell–Bloch system ($\epsilon \ll 1$) [8, 9]. At $\epsilon_2 > 1$, n_0 becomes imaginary, which corresponds to the effect of total reflection of nonresonant ESPs from a nonequilibrium medium. In contrast, no restriction is imposed on n_2 in an equilibrium medium ($W_\infty < 0$). A comparison of the first term in the right-hand side of Eq. (14) with an arbitrary left-hand side term of Eq. (14) yields one more condition for the applicability of the one-way propagation approximation, namely,

$$\epsilon_1(\omega_1\tau_p/n_0)^2 \ll 1. \tag{17}$$

By virtue of Eq. (1), Eq. (17) is also [like Eq. (16)] a much weaker restriction than that imposed by the reduced Maxwell–Bloch system ($\epsilon_1 \ll 1$).

Performing the standard procedure of the transition to the comoving reference frame [28, 29] and taking into account Eqs. (2) and (17), we obtain

$$\frac{\partial^2\theta}{\partial z\partial\tau} + a\sin\theta - b\left(\frac{\partial\theta}{\partial\tau}\right)^2\frac{\partial^2\theta}{\partial\tau^2} - g\frac{\partial^4\theta}{\partial\tau^4} = \frac{c}{2n_0}\Delta_\perp\theta, \qquad (18)$$

where $\Delta_\perp$ is the transverse Laplacian, $\tau = t - n_0z/c$ is the local time,

$$a = \frac{c\alpha}{2n_0}, \quad b = \frac{c\beta}{2n_0}, \quad g = \frac{c\nu}{2n_0}.$$

Leaving aside the transverse dynamics ($\Delta_\perp\theta = 0$), Eq. (18) includes the sine-Gordon equation for θ ($b = g = 0$ in the absence of the 2-component) and the modified Korteveg–de Vries equation for $E = (\hbar/2d)\partial\theta/\partial\tau$ ($a = 0$ in the absence of the 1-component) as particular cases. Both equations belong to the class of models integrable by the inverse scattering problem method [30]. Assuming $b = 3g/2$ in Eq. (18) at $\Delta_\perp\theta = 0$, which is equivalent to $d_1 = d_2$ [see Eq. (15)], leads to the Konno–Kameyama–Sanuki equation [29]. Precisely at this ratio between the b and g coefficients, Eq. (18) is integrable by the inverse scattering problem method [31]. This implies that its solutions in the ESP form are, unlike the corresponding solutions to Eq. (14), true solitons, which elastically interact with each other. In [26, 31], the relation $b = 3g/2$ was introduced artificially. Here, this relation follows from the assumption that the dipole moments of the two system components are equal. Note that the values in point are precisely dipole moments rather than "oscillator strengths," as for the system of three-level molecules with a V scheme of quantum transitions [32]. In our case, the ratio between the $f_j = d_j^2\,\omega_j$ ($j = 1, 2$) oscillator strengths of the transitions under consideration is, at $d_1 = d_2$, such that

$$\frac{f_2}{f_1} = \frac{d_2^2\omega_2}{d_1^2\omega_1} = \frac{\omega_2}{\omega_1} \gg 1.$$

Nevertheless, although $f_1 \ll f_2$, strong excitation of the 1-component compared with 2-component excitation can result from the presence in the ESP spectrum of the Fourier components in resonance with the corresponding transitions [see Eq. (1)].

The $d_1 = d_2$ condition is a fairly strong restriction of the model under consideration and can be regarded an exceptional case, when Eq. (14) has an exact solution in the form of a solitary pulse and, in addition, Eq. (18) at $\Delta_\perp\theta = 0$ is integrable and therefore has multisoliton solutions. Hereafter, it is, as a rule, implied that $d_1 \neq d_2$; the transition dipole moments will be assumed to equal each other only in analyzing exact solutions to Eq. (14) and Eq. (18), which will largely be considered for illustrative purposes. For ESPs, the difference of d_1 and d_2 will be taken to be small (more details are given below).

3. EXTREMELY SHORT SOLITON-LIKE PULSES, BREATHERS, AND ENVELOPE SOLITONS

In this section, we consider various approximate and exact solutions to Eqs. (14) and (18). Approximate solutions in the ESP form will be found using an averaged variational principle of the Ritz–Whitham type [33, 34]. This approach enables us not only to obtain solutions of the specified type but also to study the problem of their stability.

Equations (14) and (18) can be written as Euler–Lagrange equations using the Lagrangian densities

$$\mathcal{L}_1 = -\frac{1}{2}(\nabla\theta)^2 + \frac{n_0^2}{2c^2}\left(\frac{\partial\theta}{\partial t}\right)^2 - \alpha(1-\cos\theta) - \frac{\beta}{12}\left(\frac{\partial\theta}{\partial t}\right)^4 + \frac{\nu}{2}\left(\frac{\partial^2\theta}{\partial t^2}\right)^2 \qquad (19)$$

and

$$\mathcal{L}_2 = \frac{1}{2}\frac{\partial\theta}{\partial z}\frac{\partial\theta}{\partial\tau} - a(1-\cos\theta) - \frac{b}{12}\left(\frac{\partial\theta}{\partial\tau}\right)^4 + \frac{g}{2}\left(\frac{\partial^2\theta}{\partial\tau^2}\right)^2 - \frac{c}{4N_{20}}\left(\frac{\partial^2\theta}{\partial t^2}\right)^2. \qquad (20)$$

After the passage of an ESP, the medium should return to the initial state corresponding to $t \longrightarrow -\infty$. The complete pulse area is then

$$\theta_\infty \equiv \int_{-\infty}^{+\infty}\Omega_1 dt' = 2\pi$$

[see Eq. (9)]. Accordingly, the trial solution can be

$$\theta = 4\arctan\left\{\exp\left[\rho(\mathbf{r})\left(t - \frac{\Phi(\mathbf{r})}{c}\right)\right]\right\}, \qquad (21)$$

where $\Phi(\mathbf{r})$ and $\rho(\mathbf{r})$ are, in terms of [33], the "fast" and "slow" functions of coordinates. The profile of the electric field of the ESP is given by

$$E = \frac{\hbar}{2d_1}\frac{\partial\theta}{\partial t} = \frac{\hbar}{d_1}\rho(\mathbf{r})\,\mathrm{sech}\left[\rho(\mathbf{r})\left(t - \frac{\Phi(\mathbf{r})}{c}\right)\right]. \qquad (22)$$

Equations (14) and (18) have exact solutions in the form of traveling ESPs at $d_1 = d_2$ ($\beta = 3\nu/2$) and $\Delta_\perp\theta = 0$. Using Eq. (21) as the corresponding trial solution, it is therefore reasonable to assume that d_1 and d_2 insignificantly differ from each other (a more rigorous criterion will be found below). Otherwise, there is no guarantee that a solution of precisely this form can be found.

Substituting Eq. (21) into Eqs. (19) and (20), ignoring the derivatives of $\rho(\mathbf{r})$ [33], integrating the resulting equations with respect to t (or τ), and taking into account Eq. (15), we obtain the "averaged Lagrangians"

$$L_1 \equiv \frac{1}{4}\int_{-\infty}^{\infty} \mathscr{L}_1 dt = \frac{\rho}{c^2}[n_0^2 - (\nabla\Phi)^2] - \frac{\alpha}{\rho} - \frac{1}{3}(1+\delta)\nu\rho^3, \tag{23}$$

$$L_2 \equiv \frac{1}{2}\int_{-\infty}^{\infty} \mathscr{L}_2 d\tau = -\rho\frac{\partial\Phi}{\partial z} - \frac{a}{\rho} - \frac{1}{3}(1+\delta)g\rho^3 - \frac{c}{2n_0}\rho(\nabla_\perp\Phi)^2, \tag{24}$$

where $\Delta_\perp$ is the transverse gradient and $\delta = 2(d_2^2/d_1^2 - 1)$.

The δ parameter characterizes the relative detuning of the d_1 and d_2 quantum transition dipole moments from each other. Confidence in the correctness of the selected trial function of form Eq. (21) depends on the fulfillment of the condition $|\delta| < 1$ [see Eqs. (23) and (24)]. It follows from this condition and the equation for δ that the relative difference of d_1 and d_2 should not exceed 20%. Below, we assume that $\delta \ll 1$ for ESPs. Condition (1) can be satisfied by quantum transitions in a system of vibrational sublevels [14] or in a system of tunnel-inversion transitions, and condition (2) is met by electron-optical transitions. Then

$$d_1 \sim er_i, \quad d_2 \sim ea_B,$$

where e is the charge of the electron, $r_i \sim \sqrt{\hbar/m_i\omega_1}$ is the amplitude of mixing of molecular ions, m_i is the characteristic mass of ions, $a_B = \hbar^2/m_e e^2$ is the Bohr radius, and m_e is the mass of the electron. This gives

$$\frac{d_1}{d_2} \sim \hbar^{3/2}\frac{\sqrt{m_i\omega_1}}{m_e e^2}.$$

Putting $m_i \sim 10^4 m_e$ and $\omega_1 \sim 10^{13}$ s^{-1} yields $d_2/d_1 \sim 1$. It follows that closeness of the d_1 and d_2 values can correspond to real conditions.

Writing the Euler–Largange equations with L_1 for Φ and ρ, we obtain

$$(\nabla\Phi)^2 = n_0^2 + c^2\left[\frac{\alpha}{\rho^2} - (1+\delta)\nu\rho^2\right], \tag{25}$$

$$\nabla(\rho\nabla\Phi) = 0. \tag{26}$$

System (25), (26) can be treated as geometrical optics equations for solitrons [33]. The Φ value then has the meaning of the solitron eikonal, and Eq. (25) is the solitron eikonal equation, which determines the v_n velocity of solitron wave front propagation at each point in the direction normal to the front. Indeed, differentiating the solitron front equation

$$\rho\left(t - \frac{\Phi}{c}\right) = \text{const}$$

and ignoring slow variable ρ variations, we obtain

$$dt = \frac{d\Phi}{c} = \frac{|\nabla\Phi| dl_n}{c},$$

where dl_n is the displacement of the ESP front in the direction normal to it. Therefore,

$$v_n = \frac{dl_n}{dt} = \frac{c}{|\nabla\Phi|}. \tag{27}$$

Additionally using Eq. (25) yields

$$\frac{1}{v_n^2} = \frac{n_0^2}{c^2} + \frac{\alpha}{\rho^2} - (1+\delta)\nu\rho^2. \tag{28}$$

Equation (26) can be rewritten in the form

$$\frac{\partial(\rho\partial\Phi/\partial l_n)}{\partial l_n} = 0.$$

As $\partial\Phi/\partial l_n = |\nabla\Phi|$, taking Eq. (27) into account leads us to conclude that, along local normals to wave fronts,

$$\rho/v_n = \text{const}. \tag{29}$$

Based on these results, wave front profiles at each subsequent time moment can be obtained by applying Huygens-type constructions corresponding to the numerical solution to system (25), (26).

Prior to discussing these constructions, let us find a one-way soliton-like solution for pulse propagation along z. The ρ and Φ values then only depend on z. The wave fronts of such a pulse are planes normal to the z axis. Equations (27)–(29) yield

$$\rho = \tau_p^{-1} = \text{const}, \quad v_n = v = \text{const}, \quad \Phi = cz/v$$

and

$$\frac{1}{v} = \sqrt{\frac{n_0^2}{c^2} + \alpha\tau_p^2 - \frac{(1+\delta)\nu}{\tau_p^2}}. \tag{30}$$

According to Eq. (22), the ESP profile is given by

$$E = \frac{\hbar}{d_1\tau_p}\operatorname{sech}\frac{t - z/v}{\tau_p}. \tag{31}$$

Because Eq. (14) is not an integrable equation, ESPs of form Eqs. (30) and (31) do not possess the property of elastic interaction with their like.

Clearly, the τ_p and v values mean the ESP width and the velocity of ESP propagation along the z axis, respectively. We select the pulse width as a free parameter.

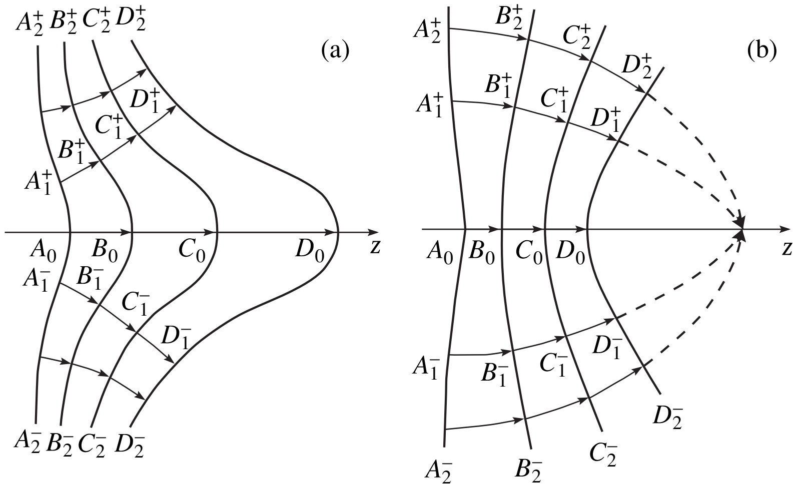

Fig. 1. Soliton wave fronts at equal time intervals obtained with the use of Huygens-type constructions corresponding to the numerical solution to Eqs. (25) and (26): (a) defocusing medium and (b) focusing medium. For simplicity, secondary spherical waves are shown by arrows normal to the soliton wave front: $A_j^{\pm}B_j^{\pm} = B_j^{\pm}C_j^{\pm} = C_j^{\pm}D_j^{\pm} = \ldots$.

Note that, at $d_1 = d_2$ ($\delta = 0$), Eqs. (30) and (31) correspond to the exact solution of Eq. (14) at $\Delta_\perp\theta = 0$ found in [26].

Equations (21), (31), (9), and (12) give the laws that determine how population inversions of both components vary when a pulse of form Eq. (31) passes through the medium:

$$\begin{aligned} W_1 &= W_{1\infty}\left(1 - 2\,\mathrm{sech}^2\,\frac{t - z/v}{\tau_p}\right), \\ W_2 &= W_{2\infty}\left(1 - \frac{2}{(\omega_2\tau_p)^2}\,\mathrm{sech}^2\,\frac{t - z/v}{\tau_p}\right). \end{aligned} \qquad (32)$$

It follows from Eq. (32) that the pseudospin corresponding to the 1-component makes a complete revolution over the Bloch sphere during the passage of a pulse (31), whereas the state of the 2-component changes insignificantly. Indeed, the ESP Eq. (31) spectrum contains Fourier components resonant to the 1-component [see Eq. (1)] and does not contain components resonant to the 2-component [see Eq. (2)].

In reality, a pulse should have finite dimensions in the plane normal to the z axis, and its amplitude is larger in the center of its cross section than at the periphery. In view of this observation, let us return to the non-one-dimensional variant of system (25), (26) [see also Eqs. (28) and (29)]. It follows from Eq. (22) that ρ is proportional to the pulse amplitude. Equation (28) then determines the amplitude dependence of velocity v_n normal to the soliton wave front at each front point. The wave front transformations shown in Fig. 1 correspond to v_n monotonically increasing ($dv_n/d\rho > 0$) and decreasing ($dv_n/d\rho > 0$) as the local ESP amplitude increases. In the first case, the center of the signal cross section moves faster than peripheral regions. The soliton wave front profile becomes convex forward, which, at long times, favors the formation of an "electromagnetic projectile" ("bullet") [35, 36]. Importantly, the pulse then remains stable; that is, it can propagate in the medium for large distances. In the second case, the cross section center lags behind ESP peripheral regions, which eventually results in their self-focusing (Fig. 1b). This effect causes instability of pulses Eq. (31) with respect to transverse perturbations. Note, however, that electromagnetic projectile formation and self-focusing occur when wave fronts are strongly curved. The condition of slow $\rho(\mathbf{r})$ function variations is then violated. Strictly speaking, the approach suggested in this work is inapplicable at final wave front evolution stages. Particular situations with stable pulse propagation (defocusing) and pulse self-focusing will be analyzed in the next section. Here, it is useful to consider one more approach to analyzing stable solutions of type (30), (31). Note that system (25), (26) can be written in the form of the Bernoulli integral and the continuity equation for a stationary potential flow of an ideal liquid,

$$\frac{\mathbf{V}^2}{2} + \int\frac{dp}{\rho} = \text{const}, \quad \nabla(\rho\mathbf{V}) = 0, \qquad (33)$$

where "velocity" $\mathbf{V}$ of liquid flow is defined as $\mathbf{V} = (c/n_0)\nabla\Phi$, and "pressure" p is related to "density" ρ as

$$\frac{dp}{d\rho} = \frac{c^4}{n_0^2}\left[\frac{\alpha}{\rho^2} + (1 + \delta)\nu\rho^2\right]. \qquad (34)$$

Clearly, the stability condition for an ESP described by Eqs. (30) and (31) takes the form of the criterion for a stable ideal liquid flow Eq. (33); that is, $dp/d\rho > 0$. Performing the $\rho = \tau_p^{-1}$ substitution in Eq. (34) then gives

$$\alpha\tau_p^4 + (1 + \delta)\nu > 0. \qquad (35)$$

Clearly, stability condition (35) is in agreement with the $dv_n/d\rho > 0$ criterion found above with the use of Huygens-type constructions.

The stability of soliton solutions to Eq. (18), which is a one-way variant of Eq. (14), is analyzed quite similarly. The use of the "averaged Lagrangian" L_2 [see Eq. (24)] and trial solution (21) for this purpose yields the system of variational parameter equations

$$\begin{gathered}\frac{\partial \mathbf{V}_\perp}{\partial z} + (\mathbf{V}_\perp \nabla_\perp)\mathbf{V}_\perp = -\frac{1}{\rho}\nabla_\perp p,\\ \frac{\partial \rho}{\partial z} + \nabla_\perp(\rho \mathbf{V}_\perp) = 0,\end{gathered} \tag{36}$$

where $\mathbf{V}_\perp = (c/n_0)\nabla_\perp\Phi$, and the $p(\rho)$ dependence is determined by Eq. (34) taking into account the relations between the a, b, and g coefficients of Eq. (18) and the corresponding α, β, and ν coefficients of Eq. (14).

System (36) includes the Euler equations of motion and the nonstationary continuity equation for a two-dimensional ideal liquid flow. In these equations, the role of time is played by the longitudinal coordinate z.

Curiously, ESPs of the complete (two-sided) Eq. (14) generate a system of variational parameter equations in the form of equations for a stationary potential ideal liquid flow in the three-dimensional space, and solutions to the reduced (one-way) Eq. (18) generate a system of equations of motion for a two-dimensional ideal liquid flow in two directions normal to the z axis, that is, to the pulse propagation axis.

An important circumstance is that the $p(\rho)$ "equations of state" coincide for ESPs of both equations. This allows us to formulate a unified stability criterion in the form of Eq. (35) for ESPs of type Eq. (22) obtained as solutions to Eqs. (14) and (18) [for solutions to Eq. (18), we must perform the substitutions $\alpha \longrightarrow a$, $\beta \longrightarrow b$, and $\nu \longrightarrow g$ in Eq. (35); as $(a, b, g) = (c/2n_0)(\alpha, \beta, \nu)$, these substitutions are inessential].

Note that the one-dimensional ($\Delta_\perp\theta = 0$) soliton-like solution to Eq. (18) has form Eq. (31), and the equation for the velocity v of the corresponding pulse is found by expanding Eq. (30) in powers of the small parameter

$$\left(\frac{c}{n_0}\right)^2\left[\alpha\tau_p^2 - \frac{(1+\delta)\nu}{\tau_p^2}\right]$$

with retention of the first two terms,

$$\frac{1}{v} = \frac{n_0}{c} + a\tau_p^2 - \frac{(1+\delta)g}{\tau_p^2}. \tag{37}$$

This expansion corresponds to the closeness of pulse velocity v to c/n_0. The populations of both components then change according to Eq. (32).

At $d_1 = d_2$ ($\delta = 0$), Eq. (18) becomes an integrable equation, and a solution of form (31), (37) is then an exact one-soliton solution to Eq. (18). Pulse (31) becomes a soliton in the strict sense; that is, it elastically interacts with its like. True, Eq. (18) only describes the interaction of solitons moving in one direction.

A two-soliton solution to Eq. (18) at $d_1 = d_2$ ($b = 3g/2$) has the form [29]

$$\begin{aligned}E &= \frac{\hbar}{2d_1}\frac{\partial\theta}{\partial t}\\ &= \frac{2\hbar}{d_1}\frac{\partial}{\partial t}\arctan\left[\frac{\exp s_1 + \exp s_2}{1 - \left(\frac{\tau_1-\tau_2}{\tau_1+\tau_2}\right)^2\exp(s_1+s_2)}\right],\end{aligned} \tag{38}$$

where

$$s_j = \frac{t - z/v}{\tau_j}, \quad \frac{1}{v_j} = \frac{n_0}{c} + a\tau_j^2 - \frac{g}{\tau_j^2} \quad (j = 1, 2);$$

τ_j and v_j are the width and velocity of the jth soliton, respectively, at a large soliton spacing.

Equation (38) can be used to obtain a breather solution to Eq. (18) by taking its free parameters τ_1 and τ_2 to be complex conjugate to each other [11]. With $\tau_{1,2} = \tau_p/(1 \pm i\omega\tau_p)$, we obtain

$$\begin{aligned}E &= \frac{2\hbar}{d_1}\\ &\times\frac{\partial}{\partial t}\arctan\left\{\frac{1}{\omega\tau_p}\operatorname{sech}\left(\frac{t-z/v}{\tau_p}\right)\sin\left[\omega\left(t - \frac{z}{v_{ph}}\right)\right]\right\}.\end{aligned} \tag{39}$$

The group v and phase v_{ph} breather velocities are expressed through the breather width τ_p and frequency ω as follows:

$$\frac{1}{v} = \frac{n_0}{c} + \frac{a}{\omega^2 + \tau_p^{-2}} + g(3\omega^2 - \tau_p^{-2}), \tag{40}$$

$$\frac{1}{v_{ph}} = \frac{n_0}{c} - \frac{a}{\omega^2 + \tau_p^{-2}} + g(\omega^2 - 3\tau_p^{-2}). \tag{41}$$

At $\omega\tau_p < 1$, the solution to Eqs. (39)–(41) corresponds to ESPs each including about one electromagnetic oscillation period, whereas if $\omega\tau_p \gg 1$, Eq. (39) gives the quasi-monochromatic soliton

$$E = E_m \operatorname{sech}\left(\frac{t-z/v}{\tau_p}\right)\cos\left[\omega\left(t - \frac{z}{v_{ph}}\right)\right], \tag{42}$$

where $E_m = 2\hbar/d_1\tau_p$ and the group v and phase v_{ph} velocities are determined by the equations

$$\frac{1}{v} = \frac{n_0}{c} + \frac{a}{\omega^2} + 3g\omega^2, \quad \frac{1}{v_{ph}} = \frac{n_0}{c} - \frac{a}{\omega^2} + g\omega^2. \tag{43}$$

respectively [see Eqs. (40) and (41) at $\omega^2 \gg \tau_p^{-2}$].

Note that Eqs. (40) and (41) can be obtained by analytically continuing the dispersion parameters to the complex plane. This technique, which has a visual quasi-particle interpretation [29], was suggested for one-parametric solitons and solitrons in [37, 38] and generalized and extended to two-parametric solutions in [23, 29]. The method is based on the assumption that there exists a solution to the nonlinear system under consideration in the form of an exponentially localized traveling pulse. The linearized variant of the system generates the $F(\omega, k) = 0$ dispersion relation, where k is the wave number in the laboratory frame of reference. Performing the substitutions $\omega \longrightarrow \omega + i\rho$ and $k \longrightarrow k + i\kappa$ in the dispersion equation and separating the real and imaginary parts, we obtain

$$F_1(\omega, \rho, k, \kappa) = 0, \quad F_2(\omega, \rho, k, \kappa) = 0.$$

These equations establish relations between the localized solution parameters, two of which can be selected as free. In addition,

$$\rho = \tau_p^{-1}, \quad v_{ph} = \frac{\omega}{k}, \quad v = \frac{\rho}{\kappa}.$$

The latter expression for the group velocity can be illustrated invoking the concept of quasi-particles. Clearly, the $\rho = \tau_p^{-1}$ value present in the imaginary addend to the frequency in the substitutions specified above is the reciprocal lifetime of quasi-particles (in our case, photons in a medium or polaritons [21]) in the state with the $\hbar\omega$ energy and the $\hbar k$ momentum; $l = \kappa^{-1}$ is then the mean free path of quasi-particles. The finiteness of τ_p and l resulting from the interaction between quasi-particles caused by nonlinearity leads to finite widths $\Delta\omega$ and Δk of the spectrum of quasi-particles, which generate a soliton-like formation. We have

$$\rho = \tau_p^{-1} = \Delta\omega, \quad \kappa = l^{-1} = \Delta k, \quad v = \frac{\rho}{\kappa} = \frac{\Delta\omega}{\Delta k}.$$

The linearization of Eq. (18) at $\Delta_\perp\theta = 0$ gives

$$\frac{\partial^2\theta}{\partial z\partial\tau} + a\theta - \frac{\partial^4\theta}{\partial\tau^4} = 0.$$

Substituting $\theta \sim \exp[i(\omega\tau - qz)]$ (q is the wave number in the comoving reference frame related to k by the equation $k = \omega n_0/c + q$) into this expression), we obtain the dispersion equation

$$k = \frac{n_0\omega}{c} + g\omega^3 - \frac{a}{\omega}.$$

Performing the substitutions $\omega \longrightarrow \omega + i\rho$ and $k \longrightarrow k + i\kappa$ and the procedure described above leads to Eqs. (40) and (41). Setting $\omega = k = 0$ at $\rho, \kappa \neq 0$, we obtain a one-parametric soliton-like solution. Note that, at $\omega = 0$, Eq. (40) transforms into Eq. (37) if $\delta = 0$. On the other hand, if $\omega < \rho$ and $k < \kappa$, we can hardly use the concept of separate quasi-particles. We then deal with a conglomerate of strongly interacting polaritons, which lose their identity. In the $\omega, k \longrightarrow 0$ limit, a polariton condensate is formed in the zero regime. Because of strong internal interactions in this condensate (interactions responsible for its formation), its spectrum has finite widths $\Delta\omega \sim \tau_p^{-1}$ and $\Delta k = l^{-1} = (v\tau_p)^{-1}$. As a result, the polariton condensate propagates in a medium in the form of ESP Eq. (31).

Since at $b = 3g/2$ and $\Delta_\perp\theta = 0$, Eq. (18) has solutions of the quasi-monochromatic pulse type, we can use Eq. (18) in the $\omega\tau_p \gg 1$ limit to directly obtain an approximate differential equation for the pulse envelope. Let quasi-monochromatic pulses propagate in the two-component medium under consideration. Clearly, the approximation of slowly varying amplitudes and phases is then applicable. We will write the electric field of the pulse in the form

$$E = \frac{1}{2}\mathcal{E}(z, \tau)\exp[i(\omega\tau - qz)] + \text{c.c.}, \tag{44}$$

where $\mathcal{E}(z, \tau)$ is the slowly varying pulse envelope. We have

$$\left|\frac{\partial\mathcal{E}}{\partial\tau}\right| \ll \omega|\mathcal{E}|, \quad \left|\frac{\partial\mathcal{E}}{\partial z}\right| \ll q|\mathcal{E}| \tag{45}$$

or $\omega\tau_p \gg 1$. Multiple integration by parts yields the expansion

$$\begin{aligned}\theta &= \int_{-\infty}^{\tau}\Omega_1 d\tau' \\ &= \frac{2d_1}{\hbar}\left(\frac{\mathcal{E}}{i\omega} + \frac{1}{\omega^2}\frac{\partial\mathcal{E}}{\partial\tau} + \frac{i}{\omega^3}\frac{\partial^2\mathcal{E}}{\partial\tau^2} + \ldots\right) + \text{c.c.}\end{aligned} \tag{46}$$

Here, the role of the characteristic time scale is played by the reciprocal frequency, ω^{-1}. It then follows from Eqs. (1) and (2) that

$$\omega_1^2 \ll \omega^2 \ll \omega_2^2. \tag{47}$$

Because the pulse is quasi-monochromatic, its spectral width satisfies the inequality $\Delta\omega \ll \omega$. For this reason, the spectrum of the signal does not contain resonance Fourier components, see Eq. (47). It follows that excitation of atoms can be considered insignificant. This allows the representation $\sin\theta \approx \theta - \theta^3/6$ to be used. Substituting Eq. (44) into Eq. (18) and using Eqs. (45) and (46) yields the nonlinear Schrödinger equation

$$i\frac{\partial\mathcal{E}}{\partial z} + \mu\frac{\partial^2\mathcal{E}}{\partial T^2} + \eta|\mathcal{E}|^2\mathcal{E} = \frac{c}{2n_0\omega}\Delta_\perp\mathcal{E}. \tag{48}$$

Here,

$$T = \tau - \left(\frac{a}{\omega^2} + 3g\omega^2\right)z, \quad \mu = 3g\omega - \frac{a}{\omega^3},$$

$$\eta = \left(\frac{d_1}{\hbar}\right)^2\left(b\omega - \frac{a}{2\omega^3}\right)$$

and the q parameter is related to the pulse frequency as $q = g\omega^3 - a/\omega$. At $\Delta_\perp\mathcal{E} = 0$, the soliton of the envelope of Eq. (48) in the laboratory frame of reference obtained taking into account Eq. (44) has form Eq. (42), where $E_m = \tau_p^{-1}\sqrt{2\mu/\eta}$, and the expressions for v and $v_{ph} = \omega/k$ coincide with Eq. (43). Note that we obtained Eq. (48) without using the condition of the equality or closeness of d_1 and d_2. It follows that, in contrast to ESPs, the existence of envelope pulses does not require imposing special restrictions on the d_1 and d_2 parameters. Note that Eq. (48) is integrable at $\Delta_\perp\mathcal{E} = 0$. Its solutions for the pulse envelope are therefore solitons in the strict sense. Below, these solutions are called envelope solitons.

It follows from the equation for v that the velocity of an envelope soliton in an equilibrium medium ($a > 0$, $b > 0$ or $W_{1\infty} < 0$, $W_{2\infty} < 0$) is smaller than c/n_0.

Note that the μ and η parameters in Eq. (48) can be written in the form [39]

$$\mu = \frac{k_2}{2}, \quad \eta = -\frac{\omega n_2}{c}, \tag{49}$$

where $k_2 = \partial^2 k/\partial\omega^2$ is the dispersion index of the group velocity, n_2 is the nonlinear index of refraction determined by the equation

$$n(\omega) = n_l(\omega) + n_2|\mathcal{E}|^2, \tag{50}$$

$n(\omega)$ is the total refractive index, and $n_l(\omega)$ is its linear part.

It follows from the equation for $\mathcal{E}_m$ that the formation of solitons of type Eq. (42) (we exclude "dark" solitons [39] from consideration) is possible if [39]

$$k_2 n_2 < 0. \tag{51}$$

Putting $b = 3g/2$ ($d_1 = d_2$) in the expressions for μ and η, we find that, if $\Delta_\perp\mathcal{E} = 0$, the envelope soliton for the nonlinear Schrödinger equation (47) coincides with breather Eqs. (39)–(41) at $\omega\tau_p \gg 1$. A similar conclusion on breathers of the modified Korteveg–de Vries equation and the sine-Gordon equation was made in [39, 40]. Note also that, if $b = 3g/2$, then $\eta = (1/2)(d_1/\hbar)^2\mu$. Condition (51) is then fulfilled automatically, which results in possible formation of one-dimensional envelope solitons no matter what the initial state of the medium. The example with $d_1 = d_2$ is yet again evidence that an envelope soliton is a limiting case of a breather at $\omega\tau_p \gg 1$. Further, we will be interested in not only ESPs but also in envelope solitons. These solitons are stable with respect to self-focusing if the nonlinear refractive index n_2 determined by Eqs. (49) and (50) is negative [6]. Otherwise, there occurs self-focusing or collapse [6, 33, 41]. According to Eq. (51), condition (52) can be satisfied in the region of normal group dispersion ($k_2 > 0$). From this and the equations for n_2 and k_2, we obtain the stability condition for a quasi-monochromatic soliton,

$$\max(\alpha/\omega^4 - 2\beta, \alpha/\omega^4 - 3\nu) < 0. \tag{52}$$

It is pertinent to mention here that Eqs. (35) and (52) are valid for spatially uniform media.

4. AN ANALYSIS OF PARTICULAR SITUATIONS

Below, we consider the possibility of the propagation of extremely short and quasi-monochromatic solitons at various initial states of a two-component medium. Inequalities (35) and (52) can conveniently be rewritten directly in terms of the macroscopic parameters of media with the use of the corresponding expressions for α, β, and ν [see Eq. (15)]. The stability condition for ESPs then takes the form

$$-W_{1\infty}(\omega_1\tau_p)(\omega_2\tau_p)^3 - W_{2\infty}\left(1 + \frac{3}{2}\delta\right)\frac{N_2}{N_1} > 0 \tag{53}$$

(hereafter, we neglect powers of δ higher than one because it is assumed that $\delta \ll 1$). The stability criteria for an envelope soliton can be written as

$$\max\left[-W_{1\infty}\frac{\omega_1}{\omega}\left(\frac{\omega_2}{\omega}\right)^3 + 3W_{2\infty}\left(\frac{d_2}{d_1}\right)^4\frac{N_2}{N_1},\right.$$
$$\left.-W_{1\infty}\frac{\omega_1}{\omega}\left(\frac{\omega_2}{\omega}\right) + 3W_{2\infty}\left(\frac{d_2}{d_1}\right)^2\frac{N_2}{N_1}\right] < 0. \tag{54}$$

To make the further discussion less cumbersome, the envelope soliton will be analyzed on the assumption $d_2 > d_1$. A similar analysis for $d_2 < d_1$ creates no difficulties and does not lead to basically new conclusions.

(a) An absorbing medium. In such a medium, $W_{1\infty} = W_{2\infty} = -1/2$, and therefore $a > 0$ and $g > 0$. According to Eq. (53), an ESP is absolutely stable, and its velocity decreases as its width increases [see Eqs. (30) and (37), and Fig. 2]. In addition, $v > c/n_0$ ($n_0 > 1$) if

$$\tau_p < \tau_m \equiv \left[\left(1 + \frac{3\delta}{2}\right)\frac{N_2}{N_1\omega_1\omega_2^3}\right]^{1/4}.$$

It is, however, easy to see that v cannot exceed c, because otherwise, inequality (2) would not hold. Envelope soliton Eq. (42) is stable if its frequency satisfies the conditions $\omega_m^2 < \omega^2 \ll \omega_2^2$ [see Eq. (54) and Fig. 3], where

$$\omega_m \equiv \left(\frac{a}{3g}\right)^{1/4} = \left(\frac{d_1^2 N_1}{3d_2^2 N_2}\omega_1\omega_2^3\right)^{1/4}.$$

The specified conditions can be met if $\omega_m^2 \ll \omega_2^2$. This gives

$$\frac{3N_2}{N_1} \gg \frac{\omega_1}{\omega_2}.$$

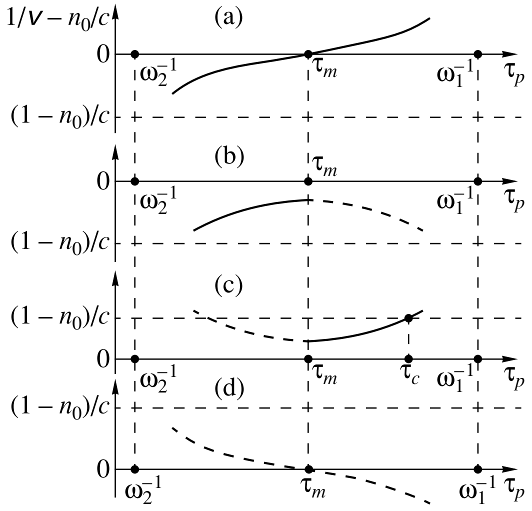

Fig. 2. Dependence of the velocity of a soliton-like ESP on its width: (a) absorbing medium, (b) amplifying-absorbing medium, (c) absorbing-amplifying medium, and (d) amplifying medium. Solid and dashed curves correspond to stable and unstable solitons, respectively. The part of the solid curve that lies below $(1 - n_0)/c$ at $n_0 < 1$ corresponds to $v > c$ (medium (c)).

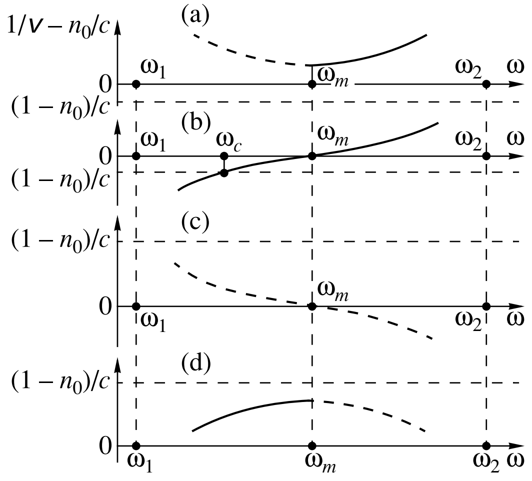

Fig. 3. Dependence of the group velocity of a quasi-monochromatic soliton on its carrying frequency. See Fig. 2 for notation.

As $\omega_1 \ll \omega_2$, this inequality can be satisfied, for instance, if $d_2 \sim d_1$ and $N_2 = N_1$. According to Eqs. (48) and (2), the group velocity of the envelope soliton also does not exceed c.

In what follows, a medium with the inverted 1-component ($W_{1\infty} = 1/2$) and the 2-component in the ground state ($W_{2\infty} = 1/2$) will be called amplifying-absorbing, otherwise ($W_{1\infty} = -1/2$, $W_{2\infty} = 1/2$) the medium is referred to as the absorbing-amplifying. The relaxation time from an excited to the ground state is known to be inversely proportional to the cube of the corresponding quantum transition frequency [5]. For this reason, the 1-component can exist in the inverse population state much longer than the 2-component. If $d_1 \approx d_2$, the estimate

$$\frac{T_{R_1}}{T_{R_2}} \sim \left(\frac{\omega_2}{\omega_1}\right)^3 \gg 1$$

is valid; here, $T_{R_1}(T_{R_2})$ is the lifetime of atom 1 (2) in the inverted state. A medium for which $W_{1\infty} = W_{2\infty} = 1/2$ will be called amplifying.

(b) An amplifying-absorbing medium ($W_{1\infty} = 1/2$ and $W_{2\infty} = -1/2$, or $a < 0$ and $g > 0$). According to Eq. (53), an ESP is then stable if $\omega_2^{-1} \ll \tau_p < \tau_m$ (Fig. 2), and its velocity cannot exceed c. Let us prove this. The condition $v > c$ for ESP (37) can be written as

$$\frac{n_0 - 1}{c} + a\tau_p^2 - \frac{(1+\delta)g}{\tau_p^2} < 0. \tag{55}$$

According to Eq. (43), a similar condition for an envelope soliton has the form

$$\frac{n_0 - 1}{c} + \frac{a}{\omega^2} + 3g\omega^2 < 0. \tag{56}$$

For simplicity, it will be assumed throughout that n_0 differs from one insignificantly; that is, $8\pi d^2 N_2/\hbar\omega_2 \ll 1$ [see Eq. (15)], and $n_0 \approx 1 - 8\pi d_2^2 N_2 W_{2\infty}/\hbar\omega_2$. Conditions (55) and (53) for an ESP in an amplifying-absorbing medium are written as

$$(\omega_2\tau_p)^2 > \left(1 + \frac{\delta}{2}\right)\frac{N_2\omega_2}{N_1\omega_1},$$

and

$$(\omega_2\tau_p)^4 < \left(1 + \frac{3\delta}{2}\right)\frac{N_2\omega_2}{N_1\omega_1},$$

respectively. By virtue of Eq. (2), these inequalities cannot be consistent. It follows that the velocity of an ESP is lower than that of light, $v < c$. Note that, in the absence of a 2-component ($N_2 = 0$), condition (53) determines the stability of solitons of the sine-Gordon equation. It follows from Eq. (53) that these solitons are unstable at $W_{1\infty} > 0$, which agrees with the numerical experiment data [1].

The situation with the group velocity of an envelope soliton is different. According to Eq. (54), this soliton is absolutely stable in an amplifying-absorbing medium (Fig. 3). Taking Eq. (2) into account, we easily obtain from Eq. (56) that $v > c$ if

$$\omega^2 < \frac{3\omega_m^4}{\omega_2^2} = \frac{d_1^2 N_1}{d_2^2 N_2}\omega_1\omega_2 \equiv \omega_c^2.$$

According to Eq. (1), $\omega^2 \gg \omega_1^2$, and therefore $d_1^2 N_1/d_2^2 N_2 \gg \omega_1/\omega_2$. The latter inequality can easily be satisfied if $d_1 \sim d_2$ and $N_1 = N_2$.

(c) An absorbing-amplifying medium ($W_{1\infty} = -1/2$ and $W_{2\infty} = 1/2$, or $a > 0$ and $g < 0$). An envelope soliton is then absolutely unstable [see Eq. (54)]. At the same time, ESPs are stable if $\tau_m < \tau_p \ll \omega_1^{-1}$ [see Eqs. (53) and (2)]. If, in addition,

$$\tau_m < \tau_p < \tau_c = \tau_m(\sqrt{Q} + \sqrt{Q-1})^{1/2}, \qquad (57)$$

where $Q = (1 - \delta/2)N_2\omega_2/4N_1\omega_1$, then $v > c$. It follows from Eq. (37) that τ_m is the pulse width at which the pulse velocity is maximum,

$$v_{\max} = \frac{c}{1-\sigma}, \quad \sigma = \frac{4\pi d_2^2 N_2}{\hbar\omega_2}\left(1 - \frac{1}{\sqrt{Q}}\right).$$

The necessary condition $Q > 1$ can be combined with the inequality $\tau_p > \tau_m$ as follows:

$$4\left(1 + \frac{\delta}{2}\right)\frac{\omega_1}{\omega_2} < \frac{N_2}{N_1} < \left(1 - \frac{3\delta}{2}\right)(\omega_1\tau_p)(\omega_2\tau_p)^3.$$

For instance, putting $\delta = 0$, $\omega_1\tau_p = 0.2$, and $\omega_2\tau_p = 5$ [see Eqs. (1) and (2)] yields

$$0.16 < N_2/N_1 < 25.$$

It follows that, if the 2-component is inverted and the 1-component is in the ground state, the condition $v > c$ does not contradict the initial assumptions (1) and (2). The corresponding pulse width dependence of soliton velocity is shown in Fig. 2c. The region $\tau_m < \tau_p < \tau_c$ corresponds to a stable superluminal soliton.

(d) An amplifying medium ($W_{1\infty} = W_{2\infty} = 1/2$, or $a < 0$ and $g < 0$). According to Eq. (53), an ESP is absolutely unstable. The region of envelope soliton stability is determined by the double inequality $\omega_1^2 \ll \omega^2 < (d_1/d_2)\omega_m^2$, see Eqs. (54) and (1) (Fig. 3). The group velocity of the envelope soliton given by Eq. (43) then exceeds the velocity of light in the vacuum. Let us rewrite the condition $(d_1/d_2)\omega_m^2 \gg \omega_1^2$, which is the necessary condition of the formation of an envelope soliton in an amplifying two-component nonresonant medium, in the form

$$\frac{3d_2^2N_2}{d_1^2N_1} \ll (\omega_2/\omega_1)^3.$$

(see the expression for ω_m). This inequality can easily be satisfied, for instance, if $d_2 \sim d_1$ and $N_2 \approx N_1$, because $\omega_2 \gg \omega_1$ according to Eqs. (1) and (2). Importantly, in the presence of only the second component ($N_1 = 0$), no stable ESPs can exist in an amplifying medium. It should be stressed that our conclusions refer to nonresonant pulses and are therefore somewhat different from those on pulses that propagate in resonance-amplifying media [18–20, 30]. Note also that the group velocity of stable envelope solitons increases as their width decreases (Fig. 2), which is in agreement with the general views on the properties of solitons. At the same time, the group velocity of stable envelope solitons decreases with the increase their filling frequency. The observation that solitons of the nonlinear Schrödinger equation are stable in homogeneous media with a normal group dispersion lends support to this conclusion.

Let us discuss localized solutions that correspond to superluminal group velocities in more detail.

The possibility of superluminal propagation of optical resonance signals in amplifying media was considered in several works [42–46]. It should be stressed that we discuss precisely the group velocity.

Superluminal propagation is caused by the impossibility of the spatial localization of the moving object [2]. The exponentially increasing pulse forefront, which is situated far from its center, induces radiation of inverted medium atoms. As a result, the energy of the center becomes converted into the energy of the forefront, and a new center is formed. The former center is absorbed by atoms that underwent the transition to the ground state. As a result, these atoms return into the excited state. In [45], this mechanism of superluminal propagation was called reshaping, and in [1], it is discussed visually and in much detail. To summarize, the profile of the pulse changes at the expense of energy stored in the medium, and precisely this profile moves at a superluminal speed [1, 42, 43, 45]. There is therefore no violation of the causality principle.

In our case, local pulse profile changes involve the participation of a large number of particles and are therefore a collective process. Photons themselves move in interatomic gaps at the velocity c. However, local amplification (an increase in the concentration of photons), which is more manifest in the front region of an exponential-localized pulse, results in a higher velocity of pulse profile propagation compared with photons that form this profile. The conclusion that a bunch of a large number of particles can move at superluminal speed without violating the causality principle was also made in [47].

It must be noted that, related to the profile of a pulse is such its important physical characteristic as the electric field, which excites the medium [see Eq. (32)] and induces its polarization. For this reason, medium excitations also propagate at superluminal speeds. The role of collective excitations is played by polaritons in our case. It can therefore be said that a superluminal soliton (or solitron) is a bunch of interacting polaritons (or, with an ESP, a polariton condensate, see Section 4) whose group velocity in a nonequilibrium medium exceeds the velocity of light in vacuum.

Because nonequilibrium medium states are unstable (that is, have finite lifetimes), superluminal pulses can only conventionally be called stable. They can be considered stable as far as the time of their propagation, τ_{prop}, through a medium much shorter than the relaxation times (T_{R_1} and T_{R_2}) of both system components to the equilibrium state. It has been mentioned above that $T_{R_1} \gg T_{R_2}$ because $\omega_1 \ll \omega_2$. The condition $\tau_{\mathrm{prop}} \ll T_{R_2}$ should therefore be fulfilled in media (c) (see Section 4). At the same time, $\tau_{\mathrm{prop}} \le l_m/c$ (l_m is the size of a medium sample along the direction of pulse propagation). Hence, $l_m \ll cT_{R_2}$. Putting $T_{R_1} \sim 10^{-8}$ s for an absorbing-amplifying medium, we find that a superluminal ESP can be observed in a medium with $l_m \ll 3$ m. With $\omega_1 \sim 10^{13}$ s^{-1} and $\omega_2 \sim 10^{15}$ s^{-1}, conditions (1) and (2) can be satisfied if $\tau_p \sim 10^{-14}$ s. The situation with superluminal envelope solitons is at first sight more impressive. As mentioned above, $T_{R_1}/T_{R_2} \sim (\omega_2/\omega_1)^3$ at $d_1 \approx d_2$, and, if $\omega_2/\omega_1 \sim 10^2$ and $T_{R_2} \sim 10^{-9}$–10^{-8} s, we have $T_{R_1} \sim 10^{-3}$ s. If the medium is amplifying-absorbing in the initial state [see Section 4, (b)], l_m can amount to several kilometers. In addition, envelope solitons have a fairly wide frequency range, $\omega_1^2 \ll \omega^2 \ll \omega_2^2$. However, there arises the problem of simultaneously creating the inverted state of the 1-component throughout the medium. Note also that the superluminal objects considered in this work should be formed in a medium, which takes time.

5. CONCLUSION

The analysis performed in this work leads us to conclude that the two-component character of the medium is a key factor determining the possibility of the propagation in it of wide-band extremely short pulses and nonresonant envelope solitons. The Konno–Kameyama–Sanuki equation obtained in this work [Eq. (18)] is one more example of integrable (at $\Delta_\perp\theta = 0$) models constructed based on the initial Maxwell–Bloch-type system. The Konno–Kameyama–Sanuki equation is integrable if the transition dipole moments of two atomic components are equal. Note that the integrability of the reduced Maxwell–Bloch system in the presence of an inhomogeneous broadening was proved in [9]. This broadening was also taken into account on the assumption of equal dipole moments for all frequencies of inhomogeneously broadened line contour transitions. Two transitions with substantially different eigenfrequencies considered in this work can, leaving aside their different physical natures, be treated as two components from the opposite wings of the contour of inhomogeneous broadening. The problem then seemingly reduces to that already solved in [9]. It should, however, be borne in mind that, in contrast to the reduced Maxwell–Bloch system, Eq. (18) was derived without anywhere using the approximation of low atomic concentrations. From this point of view, conditions (16) and (17) are much weaker than the corresponding conditions necessary for obtaining the reduced system from the complete Maxwell–Bloch system. Most likely, another suggestion advanced in [48] holds true; according to [48], equations obtained from an initial generally nonintegrable system with the use of limiting procedures are in a certain sense integrable. In the derivation of Eq. (18) from the initial (nonintegrable) system (3)–(5), (6), (8), we indeed used limiting procedures consistent with conditions (1) and (2) and the one-way propagation approximation.

The variational procedure used in this work to determine an ESP stability criterion allows equations for variable pulse parameters to be reduced to a system of equations of ideal liquid motion. An equally elegant procedure was effectively used with envelope solitons [33]. Extending this method to breather-like solutions embedding one or several electromagnetic oscillations encounters mathematical difficulties. This problem should probably be solved using alternative approaches to determining the stability of such breather solutions. Apart from being of purely scientific interest, such a study would be of interest for practical applications in view of the possible use of pulses comprising several oscillation periods in fiber optics [23].

Spontaneous emission with transition of atoms into the ground state is an irreversible process. Our analysis of the instability of nonequilibrium medium states and the possibility of the propagation of electromagnetic pulses at group velocities $v > c$ does not answer question of the relation between irreversibility of relaxation processes and the existence of superluminal objects [49, 50], a question that casts no doubt on the fundamental causality principle.

ACKNOWLEDGMENTS

This work was financially supported by the Russian Foundation for Basic Research (project no. 00-02-17436a) and by CDRF (grant 6104).

REFERENCES

1. A. N. Oraevskiĭ, Usp. Fiz. Nauk **168**, 1311 (1998) [Phys. Usp. **41**, 1199 (1998)].
2. A. Yu. Andreev and D. A. Kirzhnits, Usp. Fiz. Nauk **166**, 1135 (1996) [Phys. Usp. **39**, 1071 (1996)].
3. P. C. Becker, H. L. Fragnito, J. Y. Bigot, *et al.*, Phys. Rev. Lett. **63**, 505 (1989).
4. J. T. Darrow, B. B. Hu, X. C. Chang, and D. H. Auston, Opt. Lett. **15**, 323 (1990).
5. A. Allen and J. H. Eberly, *Optical Resonance and Two-Level Atoms* (Wiley, New York, 1975; Mir, Moscow, 1978).
6. G. Agrawal, *Nonlinear Fiber Optics* (Academic, San Diego, 1995; Mir, Moscow, 1996).
7. S. L. Mc Call and E. L. Hahn, Phys. Rev. Lett. **18**, 908 (1967).
8. P. J. Caudrey, J. C. Eilbeck, J. D. Gibbon, and R. K. Bullough, J. Phys. A **6**, L53 (1973).

9. J. C. Eilbeck, J. D. Gibbon, P. J. Caudrey, and R. K. Bullough, J. Phys. A **6**, 1337 (1973).
10. A. I. Maimistov, A. M. Basharov, S. O. Elyutin, and Yu. M. Sklyarov, Phys. Rep. **191**, 1 (1990).
11. A. Kujawski, Z. Phys. B **85**, 129 (1991).
12. A. V. Andreev, Zh. Éksp. Teor. Fiz. **108**, 796 (1995) [JETP **81**, 434 (1995)].
13. A. I. Maimistov and S. O. Elyutin, Chaos, Solitons and Fractals **8**, 369 (1997).
14. É. M. Belenov and A. V. Nazarkin, Pis'ma Zh. Éksp. Teor. Fiz. **51**, 252 (1990) [JETP Lett. **51**, 288 (1990)].
15. É. M. Belenov, A. V. Nazarkin, and V. A. Ushchapovskiĭ, Zh. Éksp. Teor. Fiz. **100**, 762 (1991) [Sov. Phys. JETP **73**, 422 (1991)].
16. A. I. Maimistov and S. O. Elyutin, J. Mod. Opt. **39**, 2201 (1992).
17. A. I. Maĭmistov, Opt. Spektrosk. **76**, 636 (1994) [Opt. Spectrosc. **76**, 569 (1994)].
18. A. V. Andreev and P. V. Polevoĭ, Zh. Éksp. Teor. Fiz. **106**, 1343 (1994) [JETP **79**, 727 (1994)].
19. A. V. Andreev and P. V. Polevoy, Proc. SPIE **3239**, 105 (1997).
20. Yu. V. Kistenev, Yu. N. Ponomarev, and A. V. Shapovalov, Kvantovaya Élektron. (Moscow) **29**, 56 (1999).
21. D. N. Klyshko, *Physical Principles of Quantum Electronics* (Nauka, Moscow, 1986).
22. S. A. Kozlov, Opt. Spektrosk. **79**, 290 (1995) [Opt. Spectrosc. **79**, 267 (1995)].
23. S. A. Kozlov and S. V. Sazonov, Zh. Éksp. Teor. Fiz. **111**, 404 (1997) [JETP **84**, 221 (1997)].
24. A. N. Azarenkov, G. B. Al'tshuler, N. R. Belashenkov, and S. A. Kozlov, Kvantovaya Élektron. (Moscow) **20**, 733 (1993).
25. N. Bloembergen, H. Lotem, and R. T. Linch, Indian J. Pure Appl. Phys. **16**, 151 (1978).
26. A. M. Kosevich and A. S. Kovalev, Solid State Commun. **12**, 763 (1973).
27. F. Calogero and A. Degasperis, *Spectral Transform and Solitons: Tools to Solve and Investigate Nonlinear Evolution Equations* (North-Holland, Amsterdam, 1982; Mir, Moscow, 1985).
28. M. B. Vinogradova, O. V. Rudenko, and A. P. Sukhorukov, *The Theory of Waves* (Nauka, Moscow, 1990).
29. S. V. Sazonov, Zh. Éksp. Teor. Fiz. **107**, 20 (1995) [JETP **80**, 10 (1995)].
30. G. L. Lamb, Jr., *Élements of Soliton Theory* (Wiley, New York, 1980; Mir, Moscow, 1983).
31. K. Konno, W. Kameyama, and H. Sanuki, J. Phys. Soc. Jpn. **37**, 171 (1974).
32. L. A. Bol'shov, T. K. Kirichenko, V. V. Likhanskiĭ, *et al.*, Zh. Éksp. Teor. Fiz. **86**, 1240 (1984) [Sov. Phys. JETP **59**, 724 (1984)].
33. Zh. K. Zhdanov and B. A. Trubnikov, *Quasi-Gaseous Unstable Media* (Nauka, Moscow, 1991).
34. D. Anderson, Phys. Rev. A **27**, 3135 (1983).
35. V. A. Mironov, Zh. Éksp. Teor. Fiz. **116**, 35 (1999) [JETP **89**, 18 (1999)].
36. A. S. Desyatnikov and A. I. Maimistov, Proc. SPIE **4061**, 193 (2000).
37. E. Schloman, Appl. Phys. Lett. **19**, 274 (1971).
38. V. G. Bar'yakhtar, B. A. Ivanov, and A. L. Sukstanskiĭ, Pis'ma Zh. Éksp. Teor. Fiz. **27**, 226 (1978) [JETP Lett. **27**, 211 (1978)].
39. A. V. Vederko, O. B. Dubrovskaya, V. F. Marchenko, and A. P. Sukhorukov, Vestn. Mosk. Univ., Ser. 3: Fiz., Astron. **33**, 4 (1992).
40. R. K. Dodd, J. C. Eilbeck, J. Gibbon, and H. C. Morris, *Solitons and Nonlinear Wave Equations* (Academic, New York, 1982; Mir, Moscow, 1988).
41. V. S. L'vov, *Nonlinear Spin Waves* (Nauka, Moscow, 1987).
42. N. G. Basov, R. V. Ambartsumyan, V. S. Zuev, *et al.*, Zh. Éksp. Teor. Fiz. **50**, 23 (1966) [Sov. Phys. JETP **23**, 16 (1966)].
43. D. A. Kirzhnits and V. N. Sazonov, in *Éinsteinian Collection 1973*, Ed. by V. L. Ginzburg (Nauka, Moscow, 1974), p. 84.
44. S. A. Bladman and M. A. Ruderman, in *Éinsteinian Collection 1973*, Ed. by V. L. Ginzburg (Nauka, Moscow, 1974), p. 190.
45. R. Y. Chiao, A. E. Kozhekin, and G. Kurizki, Phys. Rev. Lett. **77**, 1254 (1996).
46. G. Kurizki, A. E. Kozhekin, A. G. Kofman, and M. Blaauboer, Opt. Spektrosk. **87**, 551 (1999) [Opt. Spectrosc. **87**, 505 (1999)].
47. B. M. Bolotovskiĭ and V. L. Ginzburg, in *Éinsteinian Collection 1972*, Ed. by V. L. Ginzburg and G. N. Naan (Nauka, Moscow, 1974), p. 212.
48. F. Calogero, in *Integrability and Kinetic Equations for Solitons*, Ed. by V. G. Bar'yakhtar, V. E. Zakharov, and V. M. Chernousenko (Naukova Dumka, Kiev, 1990), p. 65.
49. Ya. P. Terletskiĭ, *Paradoxes in the Theory of Relativity* (Nauka, Moscow, 1966; Plenum, New York, 1968).
50. B. B. Kadomtsev, *Dynamics and Information* (Redaktsiya Usp. Fiz. Nauk, Moscow, 1999).

Translated by V. Sipachev

Journal of Experimental and Theoretical Physics, Vol. 92, No. 3, 2001, pp. 374–380.
Translated from Zhurnal Éksperimental'noĭ i Teoreticheskoĭ Fiziki, Vol. 119, No. 3, 2001, pp. 434–441.
Original Russian Text Copyright © 2001 by Zabolotskiĭ.

ATOMS, SPECTRA, RADIATION

Dynamics of Solitons in Periodic Systems with Different Nonlinear Media

A. A. Zabolotskiĭ

Institute of Automatics and Electrometry, Siberian Division, Russian Academy of Sciences,
Universitetskiĭ pr. 1, Novosibirsk, 630090 Russia
**e-mail: zabolotskii@iae.nsk.su*

Received August 3, 2000

Abstract—To analyze pulse dynamics in an optical system consisting of a periodic sequence of nonlinear media, a composite model is used. It includes a model of the resonance interaction of an ultrashort light pulse with the energy transition of the medium with allowance made for an upper level pump and an almost integrable model that describes the propagation of the light field in the other medium with a cubic nonlinearity and dispersion. Additional allowance is made for losses and other kinds of interaction by introducing perturbation terms. On the bases of the inverse scattering transform and perturbation theory, a simple method for analyzing specific features of soliton evolution in periodic systems of this kind is developed. It is used to describe various modes of soliton evolution in such a system, including chaotic dynamics. *© 2001 MAIK "Nauka/Interperiodica".*

1. INTRODUCTION

Generation of solitons in nonlinear optics, has been the objective of much research (see, e.g., [1] and survey [2]). One of the lines of studies is based on the use of completely integrable models. As a rule, the use of such models requires a number of physical constraints; however, they provide the most detailed description of the evolution of ultrashort pulses in nonlinear media. In addition, exact solutions to these models are used to verify numerical results obtained when analyzing nonlinear evolutionary processes.

The technique used in optics to generate ultrashort pulses often includes various nonlinear and linear media. The pulse is generated and amplified in one medium, and other media are used to compress the pulse and shape it. A single-pass two-level laser amplifier with an additional nonlinear medium in the form of an optical fiber light guide is an example of such a system. Another example is a laser unit with a ring resonator.

An extensive body of literature is devoted to the analysis of pulse dynamics in such systems. Nevertheless, a number of nonlinear optical phenomena remain poorly studied partly because of the lack of sufficiently simple and effective theoretical methods.

In this paper, we suggest a method for analyzing soliton dynamics in a medium consisting of a sequence of media with different nonlinear optical properties. The method is based on robust properties of soliton modes and on perturbation theory developed for almost integrable systems of equations [3, 4]. We construct a model consisting of integrable models that describe the evolution of fields on nonoverlapping adjacent intervals and analyze its properties. Such models are called "composite" in contrast to models that combine integrable models on identical intervals. The latter group of models includes, in particular, a combination of the Maxwell–Bloch system of equations for a two-level medium and the nonlinear Schrödinger equation for an infinite medium [2, 5]. To our knowledge, specific features of the soliton evolution in composite models have not been studied theoretically.

The nonlinear Schrödinger equation is often used to analyze the effects of ultrashort-soliton propagation in fiber light guides [6]. In such media, stable field pulses appear as a result of a balance between the effects of dispersion and nonlinearity. To compensate for the losses that occur in the process of the soliton propagation in a light guide, various devices are used, including those based on an amplification of the pulses on finite intervals placed periodically along the light guide. For example, a soliton is amplified when it passes through a finite two-level medium with a transition frequency close to the carrier frequency of the soliton. If the upper level is externally pumped, the soliton amplitude increases due to the nonlinear interaction in the resonance medium. This process can be also described in the framework of the integrable Maxwell–Bloch system of equations with allowance made for the pump depending only on the spatial variable [7].

As an example of the application of our approach, the propagation of a soliton in a periodic medium consisting of an alternating sequence of resonance media and media with a cubic nonlinearity and dispersion is considered. A fiber light guide can be used as the latter medium. By way of this example, we demonstrate that the approach suggested makes it possible to analyze various modes of the soliton dynamics. It is assumed that the shape of the optical pulse is described by the soliton solution to the nonlinear Schrödinger equation. The variation of the soliton parameters in a light guide is described according to the perturbation theory for a model similar to the integrable one assuming that the evolutionary equation is close to the nonlinear Schrödinger equation. The evolution of the soliton in the amplifying resonance medium is described in the framework of the Maxwell–Bloch system of equations, which is solved by the inverse scattering transform method. In such a medium, a soliton is associated with the phenomenon of self-induced transparency [2]. The existence of a stable soliton (2π-pulse), which is both the soliton of self-induced transparency and the nonlinear Schrödinger equation, in the combined model of the Maxwell–Bloch and the nonlinear Schrödinger equations was theoretically and experimentally proved in [8, 9].

In Section 2, the general structure of the composite integrable model and the boundary conditions are described. The physical model and a method for solving it are given in Section 3. In Section 4, an analysis of the soliton dynamics in the framework of this model is given, which is reduced to analyzing a discrete mapping. Various modes of soliton propagation are described.

2. COMPOSITE INTEGRABLE MODELS

First, we describe the general structure of the integrable model consisting of N integrable models (some of which can be identical). Let the integrable model be the consistency condition of the linear systems of equations

$$\frac{\partial}{\partial\tau}\psi(\tau, z; \lambda) = L(\tau, z; \lambda)\psi(\tau, z; \lambda), \qquad (1)$$

$$\frac{\partial}{\partial z}\psi(\tau, z; \lambda)$$

$$= \sum_{i=1}^{N}\alpha_{i,\,i+1}(z)A_i(\tau, z; \lambda)\psi(\tau, z; \lambda) = \mathcal{A}\psi, \qquad (2)$$

$$\alpha_{i,\,i+1}(z) = \theta(z - z_i)\theta(-z + z_{i+1}), \quad z_{i+1} > z_i.$$

Here $\theta(z)$ is a piecewise constant function; $\theta(z) = 0$ for $z \le 0$; $\theta(z) = 1$ for $z > 0$; and $\alpha_{i,\,i+1}(z)$ are projectors, i.e., $\alpha^2_{i,\,i+1}(z) = \alpha_{i,\,i+1}(z)$.

The consistency condition for these linear systems has the form

$$\frac{\partial}{\partial z}L - \frac{\partial}{\partial\tau}\sum_{i=1}^{N}\alpha_{i,\,i+1}(z)A_i + \left[L, \sum_{i=1}^{N}\alpha_{i,\,i+1}(z)A_i\right] = 0. \qquad (3)$$

Multiply (3) by $\alpha_{i,\,i+1}(z)$ to obtain

$$\frac{\partial}{\partial z}L - \frac{\partial}{\partial\tau}A_i + [L, A_i] = 0, \quad z \in [z_i, z_{i+1}]. \qquad (4)$$

Thus, the evolution in the strip $[z_i, z_{i+1}]$ is described, for any $\forall\tau$, by a system of equations having the linear system $\partial_\tau\psi = L\psi$, $\partial_z\psi = A_i\psi$ as its Lax representation.

In this paper, we study composite models with the Lax representation (1), (2) for $-\infty < \tau < \infty$. The specific features of the inverse scattering transform as applied to composite models manifest themselves in finding the dependence of the scattering parameters on z.

We assume that the field vanishes at infinity (as $\tau \longrightarrow \pm\infty$). For the example below, this means that the asymptotics of the matrix L are

$$\lim_{\tau\to\pm\infty} L(\tau, z; \lambda) = -i\sigma_3\lambda. \qquad (5)$$

Any two solutions of Eqs. (1) and (2), ψ and ϕ are related by the scattering matrix $\mathcal{T}$:

$$\psi(\tau, z; \lambda) = \phi(\tau, z; \lambda)\mathcal{T}(z; \lambda). \qquad (6)$$

It follows from the symmetric properties of the concrete spectral problem described in Section 3 (see Eq. (18) below) that the scattering matrix has the form

$$\mathcal{T}(\lambda) = \begin{pmatrix} a(\lambda) & \bar{b}(\lambda) \\ -b(\lambda) & \bar{a}(\lambda) \end{pmatrix}. \qquad (7)$$

Let us determine how the coefficients a and $\bar{b}$ depend on z for conditions (5). Using Eq. (6), we find that

$$\frac{\partial}{\partial z}\mathcal{T}(z; \lambda) = \tilde{A}^{+}\mathcal{T}(z; \lambda) - \mathcal{T}(z; \lambda)\tilde{A}^{-}, \qquad (8)$$

where

$$\tilde{A}^{\pm}(z; \lambda) = \lim_{\tau\to\pm\infty} E^{-1}(\tau; \lambda)\mathcal{A}(\tau, z; \lambda)E(\tau, \lambda),$$

$$E = \exp(-i\sigma_3\lambda\tau).$$

Introduce the functions

$$\mathcal{B}(y, z) = \int_0^z E^{-1}(y; \lambda)\sum_{i=1}^{N}\alpha_i(z)A_i(y, \zeta; \lambda)E(y; \lambda)d\zeta,$$

$$\mathcal{B}_i(y, z) = \int_{z_i}^{z} E^{-1}(y; \lambda)A_i(y, \zeta; \lambda)E(y; \lambda)d\zeta,$$

$$z_i \le z < z_{i+1}.$$

Consider the matrix $\mathcal{T}_i = \theta(z - z_i)\theta(z_{i+1} - z)\mathcal{T}$, which is the projection of $\mathcal{T}$ onto the interval $[z_i, z_{i+1}]$. The formal solution to Eq. (8) on the interval $-\tau_f < \tau < \tau_f$ is

$$\mathcal{T}_{i+1}(z; \lambda) = \exp[\mathcal{B}(\tau_f, z)]\mathcal{T}_1(0; \lambda)\exp[-\mathcal{B}(-\tau_f, z)]$$

$$\begin{aligned} &= \exp[\mathcal{B}_i(\tau_f, z)]\mathcal{T}_i(z_i; \lambda)\exp[-\mathcal{B}_i(-\tau_f, z)] \\ &= \exp[\mathcal{B}_i(\tau_f, z)]\ldots\exp[\mathcal{B}_1(\tau_f, z)]\mathcal{T}_1(z_1; \lambda) \\ &\quad\times\exp[-\mathcal{B}_1(-\tau_f, z)]\ldots\exp[-\mathcal{B}_i(-\tau_f, z)]. \end{aligned} \tag{9}$$

It is seen from this solution that the evolution of $\mathcal{T}_i(z; \lambda)$ on the interval $[z_i, z_{i+1}]$ is determined by formula (9) with the boundary condition $\mathcal{T}(z_i, \lambda)$.

For conditions (5) and $\tau_f \longrightarrow \infty$, the solution to Eq. (8) has the form

$$\begin{gathered} \mathcal{T}(z) = \aleph_+\mathcal{T}_0\aleph_-, \\ \aleph_\pm = \exp\left[-i\sigma_3\int_0^z\sum_{i=1}^N\alpha_{i,\,i+1}(s)\lim_{\tau\to\pm\infty}(A_i)_{11}(\tau, s; \lambda)ds\right], \end{gathered} \tag{10}$$

where $\mathcal{T}_0$ is the value of the matrix $\mathcal{T}$ at $z = 0$, which is determined by solving the spectral problem (1). Hence, we find the dependence of the coefficient $C_0(z; \lambda_0) = \bar{b}(\lambda)/a'(\lambda)|_{\lambda = \lambda_0}$ on z, where λ_0 is an isolated pole in the upper half-plane of the complex plane λ:

$$\begin{aligned} C_0(z; \lambda_0) &= C_0(0; \lambda_0) \\ \times\exp&\left[-2i\int_0^z\sum_{i=1}^N\alpha_{i,\,i+1}(s)\lim_{\tau\to-\infty}(A_i)_{11}(\tau, s; \lambda_0)ds\right]. \end{aligned} \tag{11}$$

3. A PHYSICAL EXAMPLE OF THE COMPOSITE MODEL

Consider the self-induced transparency model in a two-level medium under the single-frequency resonance on the interval $[Z_1 = 0, Z_2)$, $Z_2 > 0$ and an optical fiber light guide located on the interval $[Z_2, Z_3)$, where Z is the spatial coordinate. The dynamics of the medium and the field in the first medium is described by the Maxwell–Bloch model with allowance made for the upper level pump. The field dynamics in the light guide is described by the nonlinear Schrödinger equation (see, e.g., [2]). For simplicity, we consider the case of the exact resonance; taking into account the nonuniform broadening does not change the results qualitatively. The composite model has the form

$$\begin{aligned} \frac{\partial E}{\partial T} + \frac{\partial E}{\partial Z} &+ \alpha_{23}(Z)iD\frac{\partial^2 E}{\partial T^2} + \alpha_{23}(Z)\times 2iB|E|^2E \\ &= -\alpha_{12}(Z)iGP + \alpha_{23}(Z)W, \end{aligned} \tag{12}$$

$$\alpha_{12}(Z)\frac{\partial P}{\partial T} = -\alpha_{12}(Z)i\frac{\mu_0}{\hbar}EN, \tag{13}$$

$$\alpha_{12}(Z)\frac{\partial N}{\partial T} = -\alpha_{12}(Z)\frac{i}{2\hbar}(EP^* - E^*P) + \tilde{C}, \tag{14}$$

where $N_0^2(z) = N^2 + |P|^2$, T is the time variable, the speed of light is set to unity, $G = 2\pi k_0$, k_0 is the carrier wave vector, N and P are the occupation of levels and the polarization of the medium, respectively, and N_0 is the total number of particles. The physical values of the coefficients B and D are given, e.g., in [2, 6], $\alpha_{ij}(Z) = \theta(Z - Z_i)\theta(-Z + Z_j)$, $Z_i < Z_j$, $\theta(Z) = 0$ for $Z \le 0$, and $\theta(Z) = 1$ for $Z > 0$. Here, $\alpha_{ij}(Z)$ is the projector; its presence as the coefficient means that the second and third terms on the left-hand side of Eq. (12) are nonzero on the interval $[Z_2, Z_3)$, the polarization on the right-hand side of Eq. (12) is nonzero, Eqs. (13) and (14) are valid on the interval $[Z_1, Z_2)$, $\tilde{C}(Z)$ characterizes the upper level pump of the medium, and $W = W(E, T, Z)$ is the perturbation, which can account for various effects, such as linear or nonlinear losses, dispersion, combination interaction, and others.

Let $W = 0$. We consider two cases.

(1) The completely integrable consistent model. This case requires that strict constraints be imposed on the physical constants.

(2) Equations (12)–(14) represent two different integrable models (the case $\beta \neq 1$ is considered below).

The perturbation ($W \neq 0$) will be considered in the adiabatic approximation when the effect of the perturbation is reduced to ordinary differential equations for the spectral parameter that characterizes the soliton solutions to model Eqs. (12)–(14).

The solution obtained for the first case provides a basis for the approximations used in considering the second case.

A specific feature of this composite model consists in the possibility of taking into account the pump (which is proportional to $\tilde{C}$) without losing the integrability of the Maxwell–Bloch model. This property makes it possible to analyze various modes of soliton propagation, including chaotic ones, using the exact soliton solution for an arbitrary $\tilde{C}$ as a robust nonlinear mode.

Let us change the frame of reference:

$$T \longrightarrow t = \alpha(T - Z) = \sqrt{\frac{D}{B}}(T - Z),$$

$$Z + T \longrightarrow z = \frac{Z}{G}.$$

In what follows, we consider the case of a periodic sequence of media obeying the Maxwell–Bloch equations and the nonlinear Schrödinger equation. Let the field $\mathcal{E}$ propagate through the periodic medium consisting of a resonance medium on the interval $[z_1 + nL, z_2 + nL)$ and a light guide located on the interval $[z_2 + nL, z_3 + nL)$, where $L = z_3 - z_1$ is the period of the medium.

System (12)–(14) is reduced to the form

$$\partial_\zeta \mathcal{Q} + G\alpha_{1,2}(z-nL)R_+ + i\alpha_{2,3}(z-nL)[\partial_\tau^2\mathcal{E} + 2|\mathcal{E}|^2\mathcal{E} - \mathcal{W}] = 0, \tag{15}$$

$$\alpha_{1,2}(z-nL)(\partial_\tau R_+ - R_3\mathcal{E}) = 0, \tag{16}$$

$$\alpha_{1,2}(z-nL)\left[\partial_\tau R_3 + \frac{1}{2}(R_+^*\mathcal{E} + R_+\mathcal{E}^*) - c\right] = 0, \tag{17}$$

$$\mathcal{Q} = \mathcal{E}, \quad \tau = t, \quad \zeta = z, \quad z \in [z_2 + nL, z_3 + nL),$$

$$\mathcal{Q} = \beta\mathcal{E}, \quad \tau = \beta t, \quad \zeta = z\beta, \quad z \in [z_1 + nL, z_2 + nL).$$

Here

$$\beta^2 = \frac{\mu_0 D^{1/2}}{\hbar B^{1/2}}; \quad c(z) = \frac{\tilde{C}(z)}{\beta}; \quad \mathcal{W} = \frac{W}{G};$$

$\alpha_{ij}(z) = \theta(z - z_i)\theta(-z + z_j)$; for $z_j > z_i$; $\theta(z) = 0$ for $z \le 0$; and $\theta(z) = 1$ for $z > 0$. The facts that the perturbation $\mathcal{W}$ acts on the interval $[z_2 + nL, z_3 + nL)$ and the pump (which is proportional to c) acts on the interval $[z_1 + nL, z_2 + nL)$ are taken into account.

If $\mathcal{W} = 0$ and $\beta = 1$, then system (15)–(17) can be represented as the consistency condition of two linear systems of equations

$$\partial_\tau\Phi = \begin{pmatrix} -i\lambda & \mathcal{Q} \\ \bar{\mathcal{Q}} & i\lambda \end{pmatrix}\Phi, \tag{18}$$

$$\partial_\zeta\Phi = \frac{iG\alpha_{1,2}(z-nL)}{4\lambda}\begin{pmatrix} R_3 & -R_+ \\ -\bar{R}_+ & -R_3 \end{pmatrix}\Phi + \alpha_{2,3}(z-nL)\begin{pmatrix} -iH_{11} & H_{12} \\ H_{21} & iH_{11} \end{pmatrix}\Phi. \tag{19}$$

Here λ is the spectral parameter satisfying the equation $\partial_z\lambda = -c/(4\lambda)$,

$$H_{11} = 2\lambda^2 - |\mathcal{E}|^2, \quad H_{12} = 2\lambda\mathcal{E} + i\partial_\tau\mathcal{E},$$

$$H_{21} = 2\lambda\bar{\mathcal{E}} - i\partial_\tau\bar{\mathcal{E}}.$$

For $\beta = 1$, this consistent system is completely integrable. However, the condition $\beta = 1$ leads to strict constraints on the physical parameters. If $c = 0$, the Lax representation for the unperturbed model (15)–(17); i.e., for $\mathcal{W} = 0$, it is similar to the well-known representation for the model that combines the Maxwell–Bloch and the nonlinear Schrödinger equations on the same interval (see [2, 5]). For $\beta \ne 1$, the Lax representation is valid for each of the Maxwell–Bloch and nonlinear Schrödinger equation models separately on the corresponding intervals; i.e., for $\beta \ne 1$, Eqs. (18) and (19) are two unrelated Lax representations, although these models are connected by the common field $\mathcal{E}$. For $\beta = 1$ (the integrable case), joining the boundary conditions for the parameters of the solitons λ_k is very simple: $\lambda_k(z_i - nL - 0) = \lambda_k(z_i - nL + 0)$, where z_i is the boundary between the media. However, for $\beta \ne 1$, the problem of joining the boundary conditions for these models arises when a soliton crosses the boundary between the media. This is due to the fact that these models use different scales of the coordinates and the field.

We show that the system of equations (15)–(17) makes it easy to join the boundary conditions for soliton solutions in the case $\beta \ne 1$ as well. Let a soliton of the field $\mathcal{E}$ on the interval $[z_2 + nL, z_3 + nL)$ have the form

$$\mathcal{E}(z, \tau; \lambda_n) = \frac{2\lambda_n \exp(i\phi_n)}{\cosh[2\lambda_n(\tau - zV_n^{-1})]}, \tag{20}$$

where λ_n is a real-valued scalar function of n. Then, the following change of scale must be performed when crossing the boundary between the light guide and the resonance medium:

$$\mathcal{E} \longrightarrow \mathcal{E}\beta, \quad \tau \longrightarrow \tau\beta, \quad z \longrightarrow z\beta. \tag{21}$$

For the soliton solutions (20), this transformation is equivalent to the change of variables

$$\lambda_n \longrightarrow \lambda_n\beta, \quad V_n \longrightarrow V_n. \tag{22}$$

When the boundary between the nonlinear media is crossed, the parameter of the soliton that determines its height and duration undergoes a jump, but its area and speed remain unchanged; i.e., no solitons are absorbed or born, and no radiation is generated. In the present study, we do not take into account the effects of reflection and refraction of the light beam as it crosses the boundary between the media; these effects can result in the deformation of the soliton, radiation loss, etc. (see Section 5).

Thus, we use the following scenario to describe the dynamics of the soliton in the periodic medium. Let a light field pulse shaped like the soliton $q_0(\tau) = 2\eta_0\operatorname{sech}(\eta_0\tau)$ be injected in the medium at the point $z = 0$. We consider the dynamics of the field in the resonance medium in the framework of the inverse scattering transform method with the variable spectral parameter [7]. In the process of evolution in the resonance medium, the soliton is amplified, which is described by the change of its parameter

$$\eta = \sqrt{\eta_0^2 + C},$$

where

$$C = \int_0^l c(x)dx$$

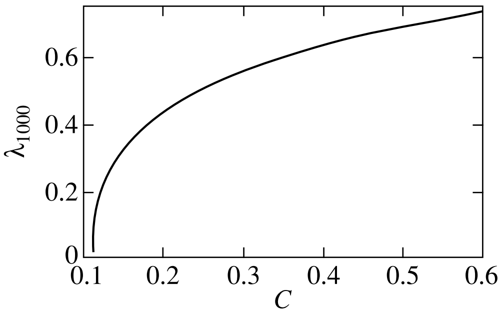

Fig. 1. Mapping (25). The dependence of λ_{1000} on C for $C > 0.111$, $a = 1$, and $\gamma = 0.1$.

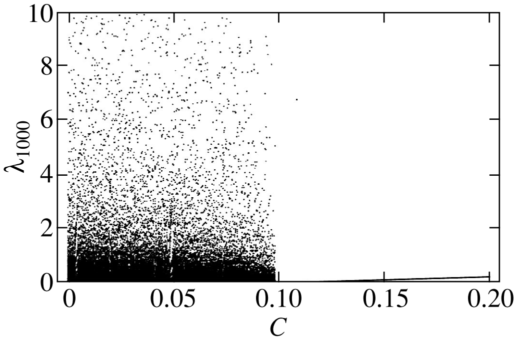

Fig. 2. The same as in Fig. 1 for $0.2 > C > 0$.

and $l = z_2 - z_1$ is the length of the resonance medium. We assume that C (an arbitrary real quantity) is independent of n, i.e., $C(z + nL) = C(z)$, $\forall z$.

The field evolution in the light guide is described in the framework of perturbation theory. The soliton solution (20) is used as a stable "robust" mode. The soliton is subject to the perturbation $\mathcal{W}$ on the interval $[z_2 + nL, z_3 + nL)$. The influence of the perturbation on the shape and parameters of the soliton is determined on the basis of the perturbation theory developed for nearly integrable models [3, 4], which is valid for sufficiently small coefficients.

Let the effect of the perturbation $\mathcal{W}$ in the nth medium be described (in the adiabatic approximation) by the equation

$$\partial_z \lambda_n = F(\lambda_n). \tag{23}$$

Then, the parameters of the soliton as it passes from the interval $[z_1 + (n - 1)L, z_3 + (n - 1)L)$ to the interval $[z_1 + nL, z_3 + nL]$ are changed as follows. We assume that the characteristics of the soliton in the light guide $z \in [z_2 + (n - 1)L, z_3 + (n - 1)L)$ at the point $z_3 + (n - 1)L - 0$ are determined by the spectral parameter $\lambda_{n-1}(z_3 + (n - 1)L - 0)$. As the soliton crosses the boundary, the parameter undergoes a jump: $\lambda_n(z_1 + nL + 0) = \beta\lambda_{n-1}(z_3 + (n - 1)L - 0)$. Then, the parameter increases due to the pump: $\lambda_n(z_2 + nL - 0) = [\lambda_n^2(z_1 + nL + 0) + C]^{1/2}$. Then, when the point $z_2 + nL - 0 \longrightarrow z_2 + nL + 0$ is passed, the parameter jumps back to the value $\lambda_n(z_2 + nL + 0) = \lambda_n(z_2 + nL - 0)/\beta$. In the light guide (for $z \in [z_2 + nL, z_3 + nL)$), the parameter varies according to Eq. (23). Then the cycle repeats. This approach makes it possible to analyze the values of C of order 1 and greater.

4. SOLITON PROPAGATION MODES IN THE PERIODIC SYSTEM

In this section, we analyze possible evolution modes of a soliton in the periodic system under study. Consider perturbations of the soliton evolution in the light guide due to dispersion, cubic nonlinearity, and friction; i.e., let $\mathcal{W} = -g_1\partial_\tau^2\mathcal{E} - g_2|\mathcal{E}|^2\mathcal{E} - g_3\mathcal{E}$. The contribution of these perturbations to the variation of the soliton parameters (20) is described (in the adiabatic approximation) by the following equation (cf. [4]):

$$\partial_\chi \lambda_n = -a\lambda_n^3 - \lambda_n. \tag{24}$$

Here

$$a = \left(-\frac{4}{3}g_1 + \frac{8}{3}g_2\right)\frac{1}{2g_3}, \quad \chi = 2g_3 z.$$

Following the procedure described above, we obtain the mapping

$$\lambda_{n+1} = \left[\frac{(\lambda_n^2 + C)(1 - a\gamma) - \gamma}{1 + a^2\gamma + a(\lambda_n^2 + C)(1 - a - a^2\gamma)}\right]^{1/2}, \tag{25}$$

where $\gamma = \exp[-4g_3(z_3 - z_2)] - 1 \ll 1$ is a small parameter characterizing the perturbation. The approach suggested makes it possible to analyze the domain of small values of γ and arbitrary C. The numerical analysis of mapping (25) shows that there exists an amplification limit. For example, let $\lambda_0 = 0.1$, $\gamma = 0.1$, and $a = 1$. Then, $\lambda_\infty \approx 0.099$ for $C = 0.113$; however, for $C = 0.114$, we have $\lambda_\infty \approx 1.2$.

The dependence of the asymptotic value λ_∞ on C in the domain $C \gtrsim 0.111$ is shown in Fig. 1. In the vicinity of $C \lesssim 0.111$, the dynamics becomes chaotic; i.e., the asymptotic value of the amplitude varies chaotically (see Fig. 2).

Let the perturbation have the form

$$\mathcal{W} = -\frac{f_0}{2\pi} - \frac{f_1}{4}\mathcal{E}(\tau)\int_{-\infty}^{\tau}|\mathcal{E}(\tau')|^2 d\tau'.$$

Then, $F(\lambda) = -f_0 - f_1\lambda^2$. By changing the scale of λ, the problem can be reduced to the condition $f_0 = f_1$. In this case, the mapping takes the form

$$\lambda_{n+1} = \tan[\arctan\sqrt{\lambda_n^2 + C} - \gamma_1], \tag{26}$$

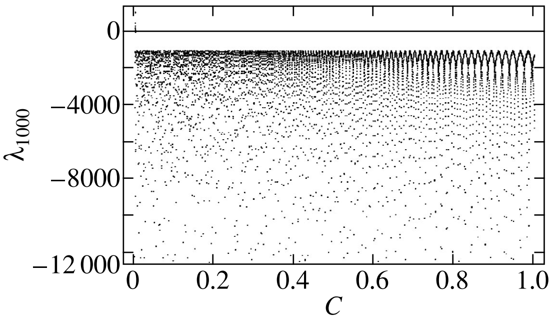

Fig. 3. Mapping (26). The dependence of λ_{1000} on C for $\gamma_1 = 0.01$.

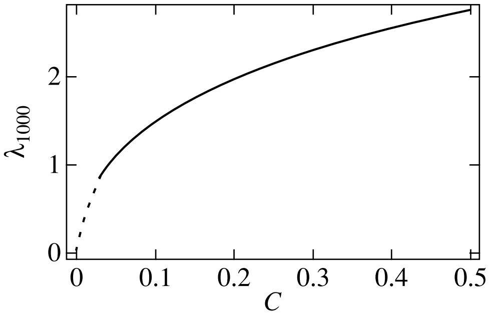

Fig. 4. The same as in Fig. 3 for $\gamma_1 = -0.01$.

$\gamma_1 = 1 - \exp[-f_0(z_3 - z_2)]$ and $|\gamma_1| \ll 1$. For $\gamma_1 < 0$, no chaotic behavior is observed. The dependence λ_n (n = 1000) on C is shown in Fig. 3. For $\gamma_1 > 0$, the chaotic behavior of the soliton in the periodic system is observed in the domain of small C. However, as C increases, the chaotic behavior disappears (Fig. 4).

If the external force is proportional to $\exp(ir_0\lambda^2 z)$, where r_0 is a real constant, then other, more complex scenarios of passing to the chaotic behavior are observed. A dependence of this type can be realized in a ring resonator [10–13]. The approach suggested in this paper can be directly used for analyzing the soliton dynamics with in a ring resonator with two or more different nonlinear media.

5. CONCLUSIONS

It is shown that the analysis of composite integrable models instead of combined ones or along with them makes it possible to analyze the evolution of light pulses in new physical conditions. The approach to the analysis of composite models suggested in the paper can be used to study the dynamics of solitons and other robust nonlinear structures.

For the case of the combined self-induced transparency model and the nonlinear Schrödinger equation, it was shown in [8, 9] (analytically and experimentally) that a stable 2π-pulse exists, which is similar to the self-induced transparency soliton. It was also shown in these papers that a pulse with an area of $2\pi N$ disintegrates into N isolated 2π-pulses. Similar effects can be expected in the composite model.

In the general case, the conditions of the existence of solitons in composite nonintegrable models can be weaker than for combined models. This is due to the fact that in the latter case, the existence of solitons can require a greater number of conditions than in the case of spatially separated media.

When passing from one optical medium into another, a reflected wave generally appears, which is not taken into account in this paper. Actually, the evolution of pulses in systems consisting of a sequence of linear and nonlinear optical media has been under study for several decades. For example, the laser with a ring resonator belongs to such systems. The reflective wave that appears when crossing the boundary between the media and the air is usually eliminated by positioning the medium surface at the Brewster angle to the direction of the wave propagation. Another way of eliminating the backward wave is the use of special plates or a lubricant of proper thickness (clarified optics), where the backward wave is eliminated due to the interference. These methods are effective for pulses with a duration up to several femtoseconds.

Another important circumstance in using composite models is the possible generation of additional following waves when the soliton crosses the boundary between the media. In the model under consideration, the shape of the soliton corresponds to one of the isolated poles. As the boundary between the media is crossed, a jump in the parameters of the soliton occurs, which is described by Eqs. (22). In the process, no additional solitons or radiation are generated in the framework of the approximation used. Indeed, since this jump results in a simultaneous change of the duration and height of the pulse, the area and the sech-shape of the soliton remain unchanged. Under these conditions, the solution to the general spectral problem (18) indicates that a unique pole in the upper half-plane exists both for the medium with self-induced transparency and for the medium obeying the nonlinear Schrödinger equation, despite the fact that the imaginary parts of the corresponding spectral parameters differ by a factor of $\beta \gg 1$. In practice, this manifests itself thus: in the resonance medium the self-induced transparency soliton is usually much shorter and higher (by a factor of $\beta \gg 1$) than the nonlinear Schrödinger equation soliton.

As a rule, the transformation and shaping of the soliton takes several soliton lengths. This implies another limitation of the applicability of the model studied in this paper: the z-size of the media must be much greater than the size of the soliton. For example, the resonance medium must be much longer than the nonlinear Schrödinger equation soliton, and so on.

In conclusion, we note that radiation effects that are related to the influence of perturbations are not taken into account in this paper. These effects usually manifest themselves in the next order of smallness and result in a deformation of the soliton shape.

ACKNOWLEDGMENTS

This work was supported by the Russian Foundation for Basic Research, project no. 98-02-17904.

The author is grateful to L.V. Il'ichev, K.P. Komarov, and V.P. Safonov for consultations and to the reviewer for references [8, 9].

REFERENCES

1. S. P. Novikov, S. V. Manakov, L. P. Pitaevskiĭ, and V. E. Zakharov, *Theory of Solitons: the Inverse Scattering Method* (Nauka, Moscow, 1980; Consultants Bureau, New York, 1984).
2. A. I. Maimistov and A. M. Basharov, *Nonlinear Optical Waves* (Kluwer, Dordrecht, 1999).
3. V. I. Karpman and E. M. Maslov, Zh. Éksp. Teor. Fiz. **73**, 537 (1977) [Sov. Phys. JETP **46**, 281 (1977)].
4. Yu. S. Kivshar and B. A. Malomed, Rev. Mod. Phys. **61**, 763 (1989).
5. E. A. Doktorov and R. A. Vlasov, Opt. Acta **30**, 2 (1983).
6. *Optical Solitons—Theory and Experiment*, Ed. by J. R. Taylor (Cambridge, 1992), Cambridge Studies in Modern Optics, Vol. 10; H. A. Haus, Proc. IEEE **81**, 970 (1993); A. Hasegawa and Y. Kodama, *Solitons in Optical Communications* (Clarendon Press, Oxford, 1995), Oxford Series in Optical and Imaging Sciences No. 7.
7. S. P. Burtsev, A. V. Mikhaĭlov, and V. E. Zakharov, Teor. Mat. Fiz. **70**, 323 (1987).
8. M. Nakazawa, E. Yamada, and H. Kubota, Phys. Rev. Lett. **66**, 2625 (1991).
9. M. Nakazawa, Y. Kimura, K. Kurokawa, and K. Suzuki, Phys. Rev. A **45**, 23 (1992).
10. D. W. McLaughlin, J. V. Moloney, and A. C. Newell, Phys. Rev. Lett. **54**, 681 (1985).
11. A. A. Zabolotskiĭ, Kvantovaya Élektron. (Moscow) **13**, 1682 (1986).
12. A. A. Zabolotskii, Phys. Lett. A **115**, 366 (1986).
13. H. Adashihara, D. W. McLaughlin, J. V. Moloney, and A. C. Newell, J. Math. Phys. **29**, 63 (1988).

Translated by A. Klimontovich

Journal of Experimental and Theoretical Physics, Vol. 92, No. 3, 2001, pp. 381–389.
Translated from Zhurnal Éksperimental'noĭ i Teoreticheskoĭ Fiziki, Vol. 119, No. 3, 2001, pp. 442–451.
Original Russian Text Copyright © 2001 by Miroshnichenko, Smirnov.

ATOMS, SPECTRA, RADIATION

A Quasi-Energy Operator in the Jaynes–Cummings Model in a Polychromatic Classical Field

G. P. Miroshnichenko and M. Z. Smirnov

St. Petersburg State Institute of Fine Mechanics and Optics (Technical University), St. Petersburg, 197101 Russia
e-mail: mirosh@mkk.ifmo.ru

Received August 10, 2000

Abstract—A perturbation theory is developed for constructing the quasi-energy operator Q of the Tavis–Cummings Hamiltonian, which includes the interaction of atoms with a classical quasi-monochromatic field. The operator Q of the first order in the interaction δ of an atom with a resonator mode has a form of the generalized Tavis–Cummings Hamiltonian (in the interaction representation) to which the oppositely rotating terms with a changed interaction constant are added. Such a Hamiltonian has a singularity in the dimensionless amplitude σ of a classical field. In the vicinity of this singularity, the Hamiltonian spectrum tends to a continuous one, while the degree of squeezing of field quadratures (in its eigenstates) increases infinitely. In the case of one atom and the biharmonic perturbation, the operator Q is obtained up to the third order of the perturbation theory. The spectral problem for Q is studied. The features of the dependence of the quasi-energy spectrum on σ are explained by the presence of an efficient barrier between the regions of the "coordinate" space. It is found that the above-mentioned singularity corresponds to the beginning of the parametric resonance zone. Analytic expressions for the top and bottom of this zone in the $\delta\sigma$ plane are presented. *© 2001 MAIK "Nauka/Interperiodica".*

1. INTRODUCTION

The known Jaynes–Cummings model (JCM), which describes the interaction of a quantized field mode with a two-level atom [1], has become especially important due to progress in the experimental possibilities in quantum optics. Thus, advances in resonator quantum electrodynamics resulted in the development of unique devices—micromasers and microlasers—in which calibrated, rarefied, and cooled atomic beams are used that are specially prepared by an external perturbation [1]. A number of quantum effects, which have been predicted in the JCM approximation, were experimentally observed. These are collapses and revivals of the atomic inversion [1], squeezed states of light [2], Schrödinger cat states [3], trapped states of a micromaser [4], Fock states of a quantum mode [5], etc. (a detailed review can be found, for example, in [1]).

In recent years, the model has found a new application in experiments on laser cooling of atomic beams and in the development of ion and atomic magnetooptical traps. Thus, it was shown in [6] that in the presence of a classical travelling or standing wave, the efficient interaction appears between the center-of-mass coordinate of an ion confined by a parabolic potential of the trap and the internal degrees of freedom of this ion. This interaction is described, under certain conditions (the Lamb–Dicke limit), by the JCM approximation. In this case, the center-of-mass coordinate plays the role of a boson variable, so that the quantum effects, which were found earlier for a field mode, acquire a new meaning. In particular, the nonclassical states of the ion motion such as Fock states, Schrödinger cat states, even and odd coherent states, etc. have been predicted and observed in experiments with traps (see [7] and references therein).

The above-mentioned quantum properties of the field and ions are used, for example, in nondestructive measurements [8]. The object of a new research field, which was called in [9] the engineering of quantum states and is based on the generalization of the JCM, is the development of methods for generating and controlling new nonclassical states of the field and atoms with specified properties. Thus, in [10, 11], a classical field was used in the JCM as a controlling system, whose parameters—the duration and shape of the pulse train [10] and the shape and rate of variation in the amplitude [11]—were appropriately chosen to obtain the desired effect.

In this paper, which is a continuation of papers [12], we propose another generalization of the JCM, based on the inclusion of a classical quasi-monochromatic field into the Hamiltonian, the carrier frequency of the field being almost resonant with an atomic transition frequency. Upon a certain choice of the periodically changing envelope, the quasi-energy operator of the JCM (in the first-order approximation of the perturbation theory) has a form of the generalized Jaynes–Cummings Hamiltonian, which differs from a usual operator (written in the interaction representation) by the addition of oppositely rotating terms with a changed interaction constant. This operator has a number of unusual properties, in particular, the field part of its eigenvectors represents squeezed states [13], whose degree of squeezing is determined by the amplitude and modulation frequency of a classical field.

2. PERTURBATION THEORY FOR THE QUASI-ENERGY OPERATOR

The method of quasi-energies is applied for the analysis of nonstationary quantum-mechanical problems with the periodic Hamiltonian

$$H(t) = H(t+T),$$

where T is the time period [14]. This method generalizes the concepts of papers devoted to parametric resonance, the interaction between "slow" and "fast" motions in linear and nonlinear systems of classical mechanics [15, 16].

Consider the Schrödinger equation for the evolution operator $U(t)$,

$$i\frac{d}{dt}U(t) = H(t)U(t), \quad U(0) = I, \tag{1}$$

where I is the unit operator (hereafter we assume that $\hbar = 1$). According to the Floquet–Lyapunov theory [15], because of its periodicity, the evolution operator can be written in the form

$$U(t) = u(t)\exp(-iQt). \tag{2}$$

Here, $u(t) = u(t+T)$ is a periodic operator and Q is a time-independent quasi-energy operator, which acts in the space of states of a quantum-mechanical system. The choice of Q is ambiguous because of the band structure of the spectrum [14]; all information on the spectrum is contained in the main Brillouin zone.

Let us assume that $H(t)$ has a small parameter and $H(t)$ can be divided into two terms—the zero-order Hamiltonian $H_0(t)$ and the perturbation $V(t)$:

$$H(t) = H_0(t) + V(t). \tag{3}$$

Assume further that the quasi-energy problem for $H_0(t)$ is solved, i.e., that we have found the decomposition of the unperturbed evolution operator $U_0(t)$, which satisfies the equation

$$H_0(t)U_0(t) = i\frac{d}{dt}U_0(t), \quad U_0(t) = I, \tag{4}$$

into two factors:

$$U_0(t) = u_0(t)\exp(-iQ_0t). \tag{5}$$

Here, $u_0(t)$ and Q_0 are the periodic evolution operator and quasi-energy operator in the zero-order approximation, respectively. Then, the solution of problems (1) and (2) can be derived using successive approximations by the Bogolyubov–Mitropolskii averaging method (its quantum-mechanical analogue) [16]. For this purpose, we rewrite Eqs. (1) and (2) in the form of equations determining $u(t)$ and Q (the periodic time representation):

$$H(t)u(t) = i\frac{d}{dt}u(t) + u(t)Q, \tag{6}$$

$$Q = M\left\{u^+(t)\left(H(t) - i\frac{d}{dt}\right)u(t)\right\}, \tag{7}$$

$$u(0) = I. \tag{8}$$

Here, we introduced the operator of averaging over the period

$$M\{\Phi(t)\} = \frac{1}{T}\int_0^T \Phi(t)dt.$$

Let us proceed in Eqs. (6)–(8) to a new time representation—the periodic interaction representation—with the help of the operator $u_0(t)$ (5):

$$\begin{aligned} u(t) &= u_0(t)W(t), \\ V_I(t) &= u_0^+(t)V(t)u_0(t). \end{aligned} \tag{9}$$

From Eqs. (4)–(8), we obtain equations for the periodic operator $W(t)$ and operator Q:

$$Q_0W(t) - W(t)Q + V_I(t)W(t) = i\frac{d}{dt}W(t), \tag{10}$$

$$Q = M\left\{W^+(t)\left(Q_0 + V_I(t) - i\frac{d}{dt}\right)W(t)\right\}. \tag{11}$$

To obtain the recurrence scheme of successive calculations, it is convenient to solve Eqs. (10) and (11) using the additional condition

$$M\{W(t)\} = I \tag{12}$$

instead of the conventional condition $W(0) = I$.

Let us introduce the notation of successive approximations for $W(t)$ and Q,

$$W(t) = I + W_1(t) + \dots, \quad Q = Q_0 + Q_1 + \dots, \tag{13}$$

substitute these series into Eqs. (10)–(12), and obtain the required recurrence formula

$$Q_n = M\{V_I(t)W_{n-1}(t)\}, \tag{14}$$

$$\begin{aligned} i\frac{d}{dt}W_n(t) - [Q_0, W_n(t)] &= Y_n(t) \\ &= V_I(t)W_{n-1}(t) - \sum_{j=0}^{n-1} W_j(t)Q_{n-j}, \end{aligned} \tag{15}$$

$$M\{W_n(t)\} = 0, \quad n = 1, 2, \dots. \tag{16}$$

Let us make some remarks concerning the above procedure. We denote the solutions of the system of Eqs. (14)–(16) with a tilde: $\tilde{W}(t)$ and $\tilde{Q}$. The scheme of successive calculations is closed because to determine $\tilde{Q}_n$, one should know $\tilde{W}_{n-1}(t)$, and the highest order of Q in Eq. (15) for the calculation of $\tilde{W}_n(t)$ is $\tilde{Q}_n$. The additional condition (12), Eq. (16) significantly simplifies the recurrence scheme; however, the solutions found in this case do not possess the unitary property $\tilde{W}(t)^{-1} \neq \tilde{W}(t)^+$ and the Hermitian property $\tilde{Q} \neq \tilde{Q}^+$. To obtain the operators Q and $W(t)$ in the final form, one should perform the transformations

$$Q = \tilde{W}(0)\tilde{Q}\tilde{W}^{-1}(0), \tag{17}$$

$$W(t) = \tilde{W}(t)\tilde{W}^{-1}(0). \tag{18}$$

These operators are the solutions of Eqs. (6)–(9) and possess the required properties.

We will seek a particular periodic solution of Eq. (15) in the following way. Let us denote the operator of the kth harmonic of the evolution operator $\tilde{W}_n(t)$ by $W_n^{(k)}$ and the operator of the kth harmonic of the right-hand side of Eq. (15) by $Y_n^{(k)}$:

$$\tilde{W}_n(t) = \sum_{\substack{k=-\infty \\ k \neq 0}}^{\infty} W_n^{(k)} \exp(ik\Omega t),$$

$$Y_n(t) = \sum_{\substack{k=-\infty \\ k \neq 0}}^{\infty} Y_n^{(k)} \exp(ik\Omega t).$$

Substitution of these series into Eq. (15) gives the steady-state operator equation for $W_n^{(k)}$

$$\begin{gathered} -\Omega k W_n^{(k)} - [Q_0, W_n^{(k)}] = Y_n^{(k)}, \\ k = \pm 1, \pm 2, \ldots. \end{gathered} \tag{19}$$

Assuming that the eigenvector and eigenvalue problem for the operator Q_0 ($Q_0|\phi_\alpha\rangle = E_\alpha|\phi_\alpha\rangle$) is solved, we obtain the solution of Eq. (19) in the form

$$\langle \phi_\alpha | W_n^{(k)} | \phi_\beta \rangle = \frac{\langle \phi_\alpha | Y_n^{(k)} | \phi_\beta \rangle}{E_{0\beta} - E_{0\alpha} - k\Omega}. \tag{20}$$

It follows from Eq. (20) that the difficulty encountered in this method can be related to the appearance of a small resonance denominator. For example, this always occurs when Q_0 has a continuous spectrum. If due to some approximations, Q_0 has only a discrete spectrum, the resonance can be avoided by changing Q_0 and retaining the decomposition $H(t)$ (3) (which is determined, as a rule, by the physical meaning of the problem) invariable. According to Eq. (5), Q_0 can be changed simultaneously with $u_0(t)$, so that $U_0(t)$ would remain invariable. Thus, we can add the operator

$$\sum_\alpha \Omega k(\alpha) |\phi_\alpha\rangle\langle\phi_\alpha|$$

to Q_0, where $k(\alpha)$ in an integer function of α. The spectrum of this operator is a multiple of the frequency Ω. Therefore, the spectrum of Q_0 can be located within the main Brillouin zone of width Ω. If, for example, the operator Q_0 contains two levels, we can choose the origin of the Brillouin zone so that the distance between these levels would be smaller than half the width Ω and the resonance denominator will not appear. We will call such a choice of Q_0 correct; in this case, the small ratio

$$|\langle \phi_\alpha | V_I(t) | \phi_\beta \rangle| / \Omega \ll 1$$

is a parameter of the theory.

3. THE QUASI-ENERGY OPERATOR OF THE "OPEN" TAVIS–CUMMINGS MODEL

Let us apply the method of quasi-energies to the problem of the interaction between N two-level atoms with a quantized field mode of the resonator and a classical quasi-monochromatic electromagnetic field. We assume that the conditions of the applicability of the Tavis–Cummings model (TCM) considered in [17] are satisfied. We will call this model the "open" model. The Hamiltonian $H_s(t)$ of the system under study has the form

$$\begin{aligned} H_s(t) = {} & \omega_0 S_3 + (g(t)\exp(-i\omega_c t)S_+ + \text{H.c.}) \\ & + \omega a^+ a + \kappa(S_+ a + S_- a^+). \end{aligned} \tag{21}$$

Here, ω_0, ω_c, and ω are the frequencies of the transition, the carrier harmonic, and the quantized mode, respectively; H.c. is the Hermitian conjugation; $g(t)$ is the complex "slow" envelope of the interaction of atoms with the classical field; κ is the interaction constant of an atom with the quantized mode; S_3, S_+, and S_- are collective atomic operators of the SU(2) algebra; and a and a^+ are the photon operators of the quantized mode. We assume that $g(t)$ is a periodic function of time:

$$g(t) = g(t+T).$$

Let us denote the evolution operator of the system by $U_s(t)$ and pass on in the Schrödinger equation to the coordinate system, which rotates at the carrier frequency ω_c, using the unitary operator $U_R(t)$:

$$U_R(t) = \exp\{-i\omega_c(S_3 + a^+ a)t\}.$$

The Hamiltonian $H(t)$ of the problem in the rotating coordinate system becomes periodical with the period T, which allows us to use the method of quasi-energies for obtaining the evolution operator

$$U(t) = U_R^+(t) U_s(t) \tag{22}$$

in the rotating coordinate system. Let us divide $H(t)$ into two terms:

$$H(t) = H_0(t) + V(t). \tag{23}$$

Here,

$$\begin{aligned} H_0(t) &= H_{0at}(t) + H_{0f}(t), \\ H_{0at}(t) &= (\omega_0 - \omega_c)S_3 + (g(t)S_+ + \text{H.c.}), \\ H_{0f} &= (\omega - \omega_c)a^+ a, \\ V(t) &= \kappa(a^+ S_- + \text{H.c.}). \end{aligned} \tag{24}$$

The interaction parameter κ is assumed small compared to the frequency $\Omega = 2\pi/T$. Then, by specifying the form of $g(t)$ and successively applying the formulas from the previous section, we can construct the operator Q and the periodic operator $u(t)$ of the atomic–field system in the form of a power series in the parameter $\delta = \kappa/\Omega$.

According to Eq. (24), the zero-order quasi-energy operator Q_0 (5) represents a sum of the atomic, Q_{0at}, and field, Q_{0f}, operators,

$$Q_0 = Q_{0at} + Q_{0f}, \tag{25}$$

while the zero-order periodic operator $u_0(t)$ (5) represents the product

$$u_0(t) = u_{0at}(t)u_{0f}(t). \tag{26}$$

The zero-order equations for $u_{0at}(t)$ and Q_{0at} have the form

$$\begin{aligned} H_{0at}(t)u_{0at}(t) &= i\frac{d}{dt}u_{0at}(t) + u_{0at}(t)Q_{0at}, \\ u_{0at}(0) &= I, \end{aligned} \tag{27}$$

$$Q_{0at} = M\left\{u^+_{0at}(t)\left(H_{0at}(t) - i\frac{d}{dt}\right)u_{0at}(t)\right\}. \tag{28}$$

The solution of this problem for the case of many atoms and an arbitrary function $g(t)$ is unknown. The zero-order problem for the field quasi-energy has the solution

$$\begin{aligned} &u_{0f}(t)\exp(-in\Omega a^+ at), \\ &Q_{0f} = (\omega - \omega_c - n\Omega)a^+ a. \end{aligned} \tag{29}$$

Here, we assume for generality that a sum of n quanta with the modulation frequency Ω of the envelope is approximately equal to one quantum $\omega - \omega_c$ of the quantized mode detuning from the carrier frequency. When seeking the zero-order solution, one should keep in mind, as noted at the end of the previous section, that the periodic operators $u_{0at}(t)$ and $u_{0f}(t)$ should be appropriately chosen.

The case of the exact resonance $\omega = \omega_c$ (a coincidence between the frequencies of the carrier harmonic and the quantized mode in the absence of any additional restrictions on the atomic transition frequency ω_0) is especially simple. In this case, the zero-order operator Q_1 represents a linear form in the operators a and a^+ of the general form

$$Q_1 = (a + a^+)\boldsymbol{\mu}\cdot\mathbf{S} + i(a - a^+)\boldsymbol{\nu}\cdot\mathbf{S}. \tag{30}$$

The parameters of the linear form, real vectors $\boldsymbol{\mu}$ and $\boldsymbol{\nu}$, are functions of the parameters of the Hamiltonian (21) and can have arbitrary lengths and directions; $\mathbf{S}$ is the vector atomic operator of the generalized spin with components S_x, S_y, and S_3.

The eigenfunction problem for Q_1 (30) is most simply solved in the case of the permutability of the atomic operators

$$[(\boldsymbol{\mu}\cdot\mathbf{S}), (\boldsymbol{\nu}\cdot\mathbf{S})] = i(\boldsymbol{\mu}\times\boldsymbol{\nu}\cdot\mathbf{S}) = 0. \tag{31}$$

The right-hand side of Eq. (31) is zero in three cases when

$$\boldsymbol{\mu} = 0, \quad \boldsymbol{\nu} = 0, \quad \boldsymbol{\mu} \parallel \boldsymbol{\nu}. \tag{32}$$

These are particular cases. The eigenvectors of Eq. (30) are factorized to atomic and field factors, and the problem has a continuous spectrum. The field eigenvectors represent the squeezed states for one of the field quadratures with the infinite degree of squeezing. If conditions (32) are not satisfied, another possibility exists: using the compression transformation [13], the operator (30) can be transformed to the Tavis–Cummings Hamiltonian form (in the interaction representation under conditions of the exact resonance). The unitary transformation operator has the form

$$G = \exp(-i\varphi a^+ a)\exp\{-\xi(aa - a^+ a^+)/2\}. \tag{33}$$

Here, φ and ξ are arbitrary real parameters. The operator Q_1 retains its form:

$$Q_1' = G^+ Q_1 G = (a + a^+)\boldsymbol{\mu}'\cdot\mathbf{S} + i(a - a^+)\boldsymbol{\nu}'\cdot\mathbf{S}.$$

The vectors $\boldsymbol{\mu}$ and $\boldsymbol{\nu}$ are replaced by new vectors $\boldsymbol{\mu}'$ and $\boldsymbol{\nu}'$:

$$\begin{aligned} \boldsymbol{\mu}' &= (\boldsymbol{\mu}\cos\varphi + \boldsymbol{\nu}\sin\varphi)\exp\xi, \\ \boldsymbol{\nu}' &= (\boldsymbol{\mu}\sin\varphi - \boldsymbol{\nu}\cos\varphi)\exp(-\xi). \end{aligned} \tag{34}$$

The operator Q_1' takes the form of the Tavis–Cummings Hamiltonian if the parameters φ and ξ are related in such a way that the two conditions

$$\boldsymbol{\mu}'\cdot\boldsymbol{\nu}' = 0, \quad |\boldsymbol{\mu}'| = |\boldsymbol{\nu}'| \tag{35}$$

are satisfied simultaneously.

Expressions (35) correspond to the following choice of the parameters φ and ξ:

$$\tan 2\varphi = \frac{2\boldsymbol{\mu}\cdot\boldsymbol{\nu}}{|\boldsymbol{\mu}|^2 - |\boldsymbol{\nu}|^2}, \tag{36}$$

$$\begin{aligned} &\exp(-4|\xi|) \\ &= \frac{|\boldsymbol{\mu}|^2 + |\boldsymbol{\nu}|^2 - \sqrt{(|\boldsymbol{\mu}|^2 - |\boldsymbol{\nu}|^2)^2 + 4(\boldsymbol{\mu}\cdot\boldsymbol{\nu})^2}}{|\boldsymbol{\mu}|^2 + |\boldsymbol{\nu}|^2 + \sqrt{(|\boldsymbol{\mu}|^2 - |\boldsymbol{\nu}|^2)^2 + 4(\boldsymbol{\mu}\cdot\boldsymbol{\nu})^2}}. \end{aligned} \tag{37}$$

We obtain from Eqs. (34), (36), and (37)

$$|\boldsymbol{\mu}'| = |\boldsymbol{\nu}'| = D = \sqrt{|\boldsymbol{\mu} \times \boldsymbol{\nu}|}. \tag{38}$$

By directing the coordinate axes along mutually orthogonal vectors $\boldsymbol{\mu}'$ and $\boldsymbol{\nu}'$, we obtain the canonical form of the operator Q_1'

$$Q_1' = D(a^+S_- + aS_+). \tag{39}$$

Here, we retained the notations S_- and S_+ for atomic operators in new coordinate axes. The eigenfunctions $|\Psi_{\pm n}\rangle$ and the spectrum $E_{\pm n}$, $n = 0, 1, 2\ldots$ for (39) are known [18] and have the form

$$E_{\pm n} = \pm D\sqrt{n}, \tag{40}$$

$$|\Psi_{\pm n}\rangle = (|n\rangle \cdot |-1/2\rangle \pm (|n-1\rangle \cdot |1/2\rangle))/\sqrt{2} \tag{41}$$

for the case of a single atom. Here, $|n\rangle$ and $|\pm 1/2\rangle$ are the eigenfunctions of operators a^+a and S_3, respectively. One can see from Eqs. (38) and (39) that, when the problem parameters approach to their critical values [conditions (32) are satisfied], the distance between quasi-levels tends to zero and the spectrum of Q_1 becomes continuous. In this case, the squeezing parameter ξ (37) tends to ∞, so that one of the mode quadratures becomes strongly squeezed and the dispersion of the second quadrature becomes very large. According to Eqs. (33) and (41), the eigenfunctions of the operator Q_1 (30) have the form

$$|\Psi_{\xi,\pm n}\rangle = (|\xi, n\rangle|-1/2\rangle \pm |\xi, n-1\rangle|1/2\rangle)/\sqrt{2}. \tag{42}$$

Here, we introduced the notation of squeezed Fock states

$$|\xi, n\rangle = G|n\rangle.$$

4. THE QUASI-ENERGY OPERATOR FOR A BIHARMONIC EXTERNAL FIELD

Consider as an example the case of biharmonic perturbation with two frequencies equal to $\omega_c \pm \Omega$ and

$$g(t) = F\cos(\Omega t).$$

In the case of the exact resonance with the carrier frequency $\omega_0 - \omega_c = 0$, $\omega - \omega_c = 0$, we have the required zero-order solutions (25)–(29)

$$Q_{0at} = 0, \quad u_{0at}(t) = \exp\{-i\Phi(t)S_x\},$$

$$\Phi(t) = \sigma\sin(\Omega t),$$

$$Q_{0f} = 0, \quad u_{0f} = I, \quad Q_0 = 0, \quad \sigma = 2F/\Omega.$$

We will call the parameter σ the dimensionless amplitude of a classical field. By substituting these solutions into Eqs. (14)–(16), we obtain the quasi-energy operator in the first-order approximation

$$Q_1 = \sqrt{2}\kappa(pS_x + xS_yJ_0(\sigma)). \tag{43}$$

Here, $J_n(z)$ is the Bessel function. In the above expressions, we introduced for brevity the field operators (quadratures)

$$x = \frac{i(a - a^+)}{\sqrt{2}}, \quad p = \frac{a + a^+}{\sqrt{2}}.$$

By comparing Eq. (43) with Eq. (30), we obtain the relations for parameters $\boldsymbol{\mu}$ and $\boldsymbol{\nu}$

$$\boldsymbol{\mu} = \kappa\mathbf{e}_x, \quad \boldsymbol{\nu} = \kappa\mathbf{e}_yJ_0(\sigma).$$

Because $\boldsymbol{\mu} \cdot \boldsymbol{\nu} = 0$, we have the angle $\varphi = 0$ (36), and parameters ξ and D are determined by the relations

$$\exp(2\xi) = J_0(\sigma), \quad D = \kappa\sqrt{J_0(\sigma)}. \tag{44}$$

It follows from Eqs. (38), (39), and (44) that a singularity in which the spectrum of Q_1 becomes continuous corresponds to a zero of the Bessel function:

$$\sigma = 2F/\Omega = 2.4048\ldots.$$

Analysis of the high orders of the problem shows that the operator Q can be represented in the equivalent form Q_E, which is convenient for calculating its spectrum:

$$Q = LQ_EL^+.$$

Here, the unitary operator L and the equivalent quasi-energy operator Q_E found up to the third order in κ inclusive have the form

$$Q_E = Q_1 + Q_{E3},$$

$$\begin{aligned} Q_{E3} &= \sqrt{2}\kappa\delta^2(xpxS_xF_1(\sigma) - x^3S_yF_2(\sigma)/2), \\ L &= \exp(i\sqrt{2}\delta xS_3f_1)\exp\{-i\delta^2(px + xp)S_3f_2\}, \end{aligned} \tag{45}$$

$$\delta = \kappa/\Omega.$$

The parameters f_1, f_2, $F_1(\sigma)$, and $F_2(\sigma)$ represent series in the Bessel functions of the integer index of the argument $\sigma = 2F/\Omega$. The expressions for $F_1(\sigma)$ and $F_2(\sigma)$ required for further calculations have the form

$$F_1(\sigma) = -2\sum_{k=1}^{\infty}\left(\frac{J_k(\sigma)}{k}\right)^2,$$

$$F_2(\sigma) = 2\sum_{k,k'=-\infty}^{\infty}\frac{J_{2k'+1}(\sigma)J_{2k+1}(\sigma)J_{2k+2k'+2}(\sigma)}{(2k+1)(2k'+1)} - \frac{1}{2}\sum_{\substack{k,k'=-\infty \\ k\neq 0,\, k'\neq 0 \\ k+k'\neq 0}}^{\infty}\frac{J_{2k'}(\sigma)J_{2k}(\sigma)J_{2k+2k'}(\sigma)}{2k\cdot 2k'}.$$

Here,

$$J_k(\sigma) = (-1)^kJ_{-k}(\sigma).$$

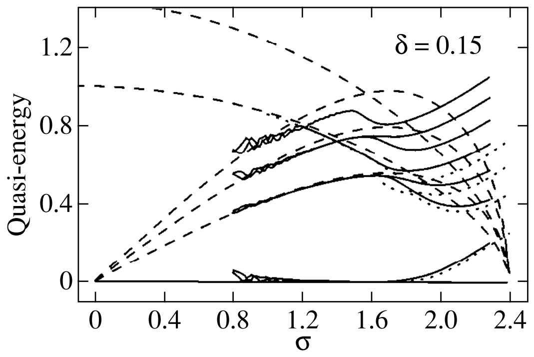

Fig. 1. Levels of the quasi-energy operator for the "open" JCM in a biharmonic field as functions of the classical-field amplitude σ. The dashed curves are levels of noninteracting "wells" (the linearization method). The solid curves are the third order of the perturbation theory. The dotted curves are calculations using the monodromy operator. $n_{\max} = 150$, $\delta = 0.15$.

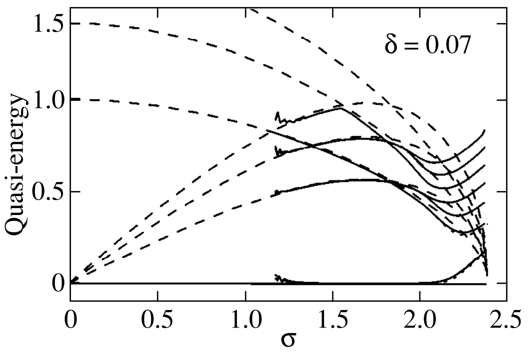

Fig. 2. The same as in Fig. 1, only for δ = 0.07.

The operator Q_{E3} is nonlinear in the "coordinate" x and, hence, determines the asymptotics of eigenfunctions of the operator Q_E for $|x| \longrightarrow \infty$. It is obvious that the asymptotics can change when the higher orders of the perturbation theory are taken into account. Below, we consider some features of the spectrum of the operator Q_E as a whole, without assuming that Q_{E3} is small compared to Q_1. Not all the results of such an approach are reliable in the quantitative respect and require verification by numerical methods.

Consider the possibility of the linearization of Q_E in the "coordinate" x. Nonlinear terms are small and can be neglected in the region of small $x \approx 0$. We will call this region a central "well." Here, $Q_E \approx Q_1$ (43). The spectral properties of this operator were studied above [see (40)–(42), (44)]. In the region of large values of $|x|$ for $0 \le \sigma \le 2.4048\ldots$, the operator Q_E can be linearized by the shift transformation

$$\exp(ix_0p)x\exp(-ix_0p) = x + x_0$$

by choosing the parameter x_0

$$|x_0| = \sqrt{2J_0(\sigma)/\delta^2F_2(\sigma)}. \quad (46)$$

The linearized operator Q_E has the form

$$\begin{aligned} Q_E^{\text{lin}} &= \sqrt{2}\kappa(pS_xJ(\sigma) - 2xS_yJ_0(\sigma)), \\ J(\sigma) &= 1 + 2F_1(\sigma)J_0(\sigma)/F_2(\sigma). \end{aligned} \quad (47)$$

The operator Q_E^{lin} determines the quasi-energy states of the atomic–field system in the regions $x \approx \pm|x_0|$, which we will call side wells:

$$E_{\pm n}^{\text{lin}} = \pm D\sqrt{n}, \quad D = \kappa\sqrt{2J_0(\sigma)J(\sigma)},$$

$$|\Psi_{\xi,\pm n}^{x_0}\rangle \quad (48)$$

$$= (|x_0, \xi, n\rangle|-1/2\rangle \pm |x_0, \xi, n-1\rangle|1/2\rangle)/\sqrt{2}.$$

Here, we introduced the notation of a shifted (coherent) squeezed Fock state of the field

$$|x_0, \xi, n\rangle = \exp(-ix_0p)G|n\rangle.$$

The squeezing parameter ξ in Eqs. (33) and (44) is defined by the relation

$$\exp(-2\xi) = J(\sigma)/2J_0(\sigma).$$

Thus, our analysis showed that there exist three regions of values of x in the third order of the perturbation theory where the quasi-energy states of the atomic–field system are described by the generalized Jaynes–Cummings Hamiltonian (30). Figures 1 and 2 show the dependences of energies of some quasi-energy levels on the amplitude σ (for δ = 0.15 and 0.07, respectively), which were obtained by three methods. The dashed, monotonically decreasing curves, which converge at the singularity $\sigma \approx 2.4048\ldots$, give the quasi-levels of the linearized quasi-energy operator in the central well of Q_1 Eqs. (40) and (44). The dashed curves issuing from the point $\sigma = 0$ and converging at the point $\sigma \approx 2.4048\ldots$ represent the doubly degenerate quasi-levels of the operator Q_E^{lin} (side wells) (48). The solid curves correspond to the energy levels of the operator Q_E (45) (the third order of the perturbation theory), which were obtained by the numerical diagonalization of its matrix in the Fock basis. The basis dimensionality was limited by the parameter $n_{\max}$ equal to 150. The dotted curves show the quasi-levels of the exact quasi-energy operator Q of the problem under study [the Hamiltonian $H(t)$ (23)], which was found numerically from the formula [15]

$$Q = \frac{i\Omega}{2\pi}\text{Ln}(U(T)).$$

Here, $U(T)$ is the evolution operator (22) during the period T. The dimensionality of the matrix Q was also limited by the parameter $n_{\max}$. As follows from Figs. 1 and 2, the calculation in the third order of the perturbation theory and the exact calculation quantitatively agree with each other. The agreement increases with decreasing parameter δ of the perturbation theory. The plots of quasi-levels obtained by the linearization method qualitatively differ from the plots obtained by more exact methods. This concerns first of all the regions of crossing of the levels of the central and side wells. Upon the refinement of the calculation, the level crossings are replaced by their anti-crossings. In addition, the double degeneracy of the side-well levels is removed upon approaching the singularity.

To elucidate the reason for the differences found, we consider the features of the field "motion" in the vicinity of the above-mentioned wells in more detail. In Fig. 3, the amplitudes of oscillations over the "coordinate" x and "momentum" p for the central well, Δx and Δp [the Hamiltonian Q_1 (43)] are compared with these quantities Δx_1 and Δp_1 [the Hamiltonian Q_E^{lin} (47)] for side wells as function of σ. Our estimate shows that the amplitudes are determined by the relations

$$\Delta x = \sqrt{1/J_0(\sigma)}, \quad \Delta p = 1/\Delta x,$$

$$\Delta x_1 = \sqrt{J(\sigma)/2J_0(\sigma)}, \quad \Delta p_1 = 1/\Delta x_1.$$

It follows from Fig. 3 that in the region $\sigma \approx 0$, the quadrature of x for oscillations in side wells is strongly squeezed. Near the point $\sigma \approx 2.4048\ldots$, the quadrature of p for oscillations in the central and side wells is strongly squeezed. In the system of units chosen, the absence of squeezing corresponds to the regions where amplitudes are close to unity. Figure 4 shows the dependence of the shift of side wells $|x_0|$ (46) on σ for several values of the interaction parameter $\delta = \kappa/\Omega$. The comparison of Figs. 3 and 4 shows that the eigenfunctions of the field mode in the x representation are strongly localized in the region of three wells at sufficiently small δ:

$$x \approx 0, \pm|x_0|.$$

The overlap of the wells appears near the value $\sigma \approx 2.4048\ldots$. The side wells are separated from the central well by a potential barrier whose penetrability is determined by the parameters σ and δ:

$$B = \exp\{-4J_0(\sigma)x_0^2/3\}. \tag{49}$$

The potential barrier penetrability increases with increasing σ for δ being fixed. The quasi-energy states localized in the central well become quasi-stationary, with the decay constant R, which can be estimated, according to [19], from the formula

$$R = \kappa\sqrt{J_0(\sigma)}B/4\pi.$$

The wells located in the vicinity of the singularity begin to interact with each other. This causes the splitting of quasi-levels.

The barrier width (over the "coordinate" x) between the central and side wells is of the order of the shift $|x_0|$ (46) and tends to infinity with decreasing σ. This circumstance substantially affects the result of numerical analysis because, due to the restriction of the dimensionality of the Fock basis ($n \le n_{\max}$), the region of variation of the "coordinate" is also restricted ($0 \le |x_0| \le x_{\max} \approx \sqrt{n_{\max}}$). For this reason, the plot of any physical quantity versus σ constructed at the fixed value of the cut-off parameter $n_{\max}$ has two regions, which are divided by the boundary value σ_0. In the region $0 \le \sigma \le \sigma_0$, the barrier width exceeds $x_{\max}$, and the influence of side wells is completely excluded. When $\sigma \ge \sigma_0$, the side wells are taken into account in the calculation, resulting in the drastic modification of the plot upon passing through σ_0. The dependence of the parameter σ_0 on δ is determined by the relation

$$\delta = \frac{J_0(\sigma_0)}{\sqrt{n_{\max}F_2(\sigma_0)}}.$$

Thus, we have $\sigma_0 \approx 0.8$ for Fig. 1 and $\sigma_0 \approx 1.2$ for Fig. 2. The above-mentioned effect is manifested in these figures as the instability of calculations upon approaching σ_0 from the left.

The presence of the boundary value σ_0 should be also taken into account in the numerical solution of the

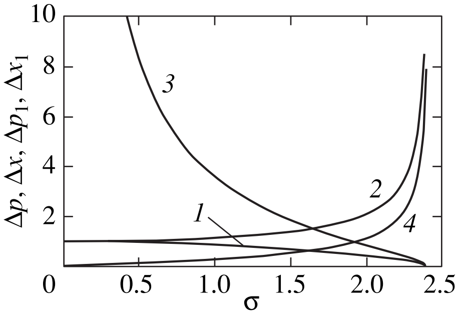

Fig. 3. Amplitudes of oscillations over the "coordinate" x and "momentum" p for noninteracting central (Δx, Δp) and side (Δx_1, Δp_1) "wells" as functions of the classical-field amplitude σ: (*1*) Δp, (*2*) Δx, (*3*) Δp_1, (*4*) Δx_1.

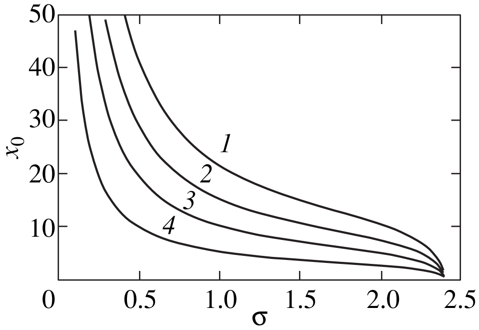

Fig. 4. Parameter x_0 of the shift of side wells from the central well as a function of the classical-field amplitude σ: δ = 0.07 (*1*), 0.1 (*2*), 0.15 (*3*), 0.3 (*4*).

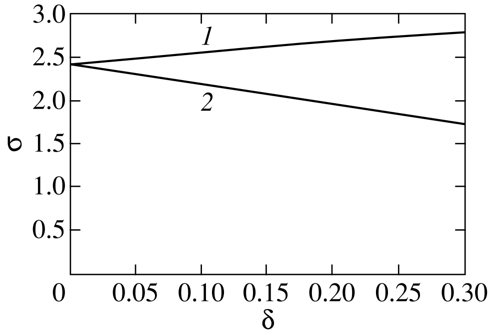

Fig. 5. Parametric resonance region in the "open" JCM in a biharmonic field on the δσ plane: (*1*) top of the region (48) and (*2*) bottom of the region (47).

problem on parametric excitation of the quantized field mode of a resonator produced by a classical field with the amplitude that smoothly increases from zero. In this case, the inaccuracy caused by the cut-off of the Fock basis can be eliminated assuming that the switching on rate on the interval $0 \le \sigma \le \sigma_0$ is sufficiently high (greater than the decay rate R), so that tunneling has no time to occur. In other words, the rate of the initial interval of the envelope of the classical-field pulse should be matched with the cut-off parameter $n_{\max}$ of the basis. The process of parametric excitation of the quantized mode of the resonator by the classical field, whose amplitude is much smaller than the critical value, is of the below-barrier transition type. Having fixed the barrier penetrability B in Eq. (49) at the 0.1 level, we obtain the estimate for the lower boundary (bottom) $\delta_b(\sigma)$ of the parametric excitation region on the δσ plane:

$$\delta_b(\sigma) = \sqrt{\frac{8J_0^2(\sigma)}{3F_2(\sigma)\mathrm{Ln}10}}. \tag{50}$$

As analysis shows, to the right of the singularity $\sigma \ge 2.4048\ldots$, the boundary curve (the top of the parametric excitation region) $\delta_t(\sigma)$ is described by the relation

$$\delta_t(\sigma) = \sqrt{\frac{4J_0^2(\sigma)}{F_1(\sigma)J_0(\sigma) - 3F_2(\sigma)/2}}. \tag{51}$$

Figure 5 shows the plot of the parametric resonance region. The singularity $\sigma = 2.4048\ldots$ corresponds to the region origin.

5. CONCLUSIONS

We have considered the problem on parametric excitation of a quantized field mode by a polychromatic classical field. Parametric processes involving the electromagnetic radiation have many practical applications and have been discussed in the literature [15, 20, 21]. According to [21, p. 303], parametric processes represent processes of energy exchange between vibrational systems due to their coupling via a nonlinear dissipative element. In the problem considered, the coupling of the fields—the classical and quantum ones—is caused by their interaction with two-level atoms placed in a resonator. The fields and atoms form a unified quantum system whose Hamiltonian depends on time. It is assumed that this Hamiltonian can be simulated by the Hamiltonian of the "open" TCM. In this paper, we have paid a special attention to the statistical properties of the quantized mode states, which are related to the parametric process under study.

We have developed the perturbation theory for constructing the quasi-energy operator Q of the problem. As a small parameter δ, we used the ratio of the constant of interaction between the mode and an atom to the modulation frequency of the amplitude of a biharmonic classical field. We derived the operator Q up to the third order in δ inclusive. We studied the spectral problem for Q analytically using linearization and numerically, by matrix diagonalization. The Q matrix was constructed in the third order and also exactly (in the truncated basis) with the help of the monodromy operator obtained by numerical methods. We studied the lower limit of the parameter δ. The opposite case of low frequencies Ω can be analyzed more easily and seems to be of little interest because the quadrature squeezing is absent in this limit. The question of the convergence of the perturbation theory series obtained by us remains open. It is not inconceivable that the quasi-energy operator under study has a continuous spectrum. In this case, the series can be treated only as asymptotic and probably diverging.

The application of the linearization method to the equivalent operator Q_E (in the "coordinate" representation) revealed the special feature of the problem, namely, the presence of the efficient potential barrier dividing the central and side wells. The term well refers to the regions of the "coordinate" change where the generalized JCM Hamiltonian Q_1 (30) can be used. The field part of the eigenfunctions of Q_1 has interesting statistical properties; namely, it represents squeezed (over one of the quadratures) field states of quantum optics. The degree of squeezing can be changed by varying the parameters of the problem: the amplitude and the modulation frequency Ω of the classical field. The presence of the potential barrier is reflected in the features of the spectrum of Q (the tunneling effect results in the interaction between the wells, the splitting of the quasi-levels, and the replacement of their crossing by anti-crossing), as well as in the dynamics of parametric excitation of the quantized field mode. The initial excitation stage is of the below-barrier transition type and therefore is improbable. As the barrier vanishes (with increasing amplitude of the classical field), a region of the parametric resonance appears on the δσ plane. The dynamics of the parametric process requires a separate study.

REFERENCES

1. P. Meystre and M. Sargent III, *Elements of Quantum Optics* (Springer-Verlag, Berlin, 1998).
2. P. Meystre, E. Geneux, A. Quattrapani, and A. Faist, Nuovo Cimento B **25**, 21 (1975).
3. B. Yurke, W. Schleich, and D. F. Walls, Phys. Rev. A **42**, 1703 (1990).
4. M. Weidinger, B. T. H. Varcoe, R. Heerlein, and H. Walther, Phys. Rev. Lett. **82**, 3795 (1999).
5. P. Filipowicz, J. Javanainen, and P. Meystre, Opt. Commun. **58**, 327 (1986).
6. C. A. Blockley, D. F. Wolls, and H. Risken, Europhys. Lett. **17**, 509 (1992).
7. Shi-Biao Zheng, Phys. Lett. A **245**, 11 (1998); Xueli Luo, Xiwen Zhu, and Ying Wu, Phys. Lett. A **237**, 354 (1998).
8. A. Sinatra, J. F. Roch, and K. Vigneron, Phys. Rev. A **57**, 2980 (1998).
9. K. Vogel, V. M. Akulin, and W. P. Schleich, Phys. Rev. Lett. **71**, 1816 (1993).
10. C. K. Law and J. H. Eberly, Phys. Rev. Lett. **76**, 1055 (1996).
11. A. S. Parkins, P. Marte, and P. Zoller, Phys. Rev. A **51**, 1578 (1995).
12. M. Z. Smirnov, Zh. Éksp. Teor. Fiz. **112**, 819 (1997) [JETP **85**, 441 (1997)]; M. Z. Smirnov, Zh. Éksp. Teor. Fiz. **114**, 474 (1998) [JETP **87**, 260 (1998)]; M. Z. Smirnov, Quantum Semiclassic. Opt. **10**, 765 (1998); M. Z. Smirnov, Phys. Rev. A **52**, 2195 (1995); M. Z. Smirnov, Kvantovaya Élektron. (Moscow) **25**, 871 (1995).
13. H. P. Yuen, Phys. Rev. A **13**, 2226 (1976).
14. Ya. B. Zel'dovich, Usp. Fiz. Nauk **110**, 139 (1973) [Sov. Phys. Usp. **16**, 427 (1973)].
15. V. A. Yakubovich and V. M. Starzhinskiĭ, *Parametric Resonance in Linear Systems* (Nauka, Moscow, 1987).
16. N. N. Bogolyubov and Yu. A. Mitropol'skiĭ, *Asymptotic Methods in the Theory of Nonlinear Oscillations* (Nauka, Moscow, 1974, 4nd ed.; Gordon and Breach, New York, 1962).
17. M. Tavis and F. W. Cummings, Phys. Rev. **170**, 379 (1968).
18. E. T. Jaynes and F. W. Cummings, Proc. IEEE **51**, 89 (1963).
19. D. I. Blokhintsev, *Principles of Quantum Mechanics* (Nauka, Moscow, 1976).
20. V. S. Butylkin, A. E. Kaplan, Yu. G. Khronopulo, and E. I. Yakubovich, *Resonant Interactions of Light with Matter* (Nauka, Moscow, 1977).
21. A. Yariv, *Quantum Electronics* (Wiley, New York, 1967; Sov. Radio, Moscow, 1973).

Translated by M. Sapozhnikov

Journal of Experimental and Theoretical Physics, Vol. 92, No. 3, 2001, pp. 390–399.
Translated from Zhurnal Éksperimental'noĭ i Teoreticheskoĭ Fiziki, Vol. 119, No. 3, 2001, pp. 452–462.
Original Russian Text Copyright © 2001 by N. Bunkin, F. Bunkin.

**ATOMS,
SPECTRA, RADIATION**

Ionic Contribution to Rayleigh Line Wing under Conditions of Light Scattering by Liquid Electrolytic Solutions

N. F. Bunkin* and F. V. Bunkin

Scientific Center of Wave Studies, Institute of General Physics, Russian Academy of Sciences, Moscow, 117942 Russia
**e-mail: nbunkin@orc.ru*

Received September 22, 2000

Abstract—A theoretical treatment is performed of the mechanism (suggested in N. F. Bunkin and A. V. Lobeev, Z. Phys. Chem. **214**, 269 (2000)) of ionic effect on the Rayleigh line wing under conditions of light scattering by liquid electrolytic solutions. The mechanism consists essentially in that the fluctuation electric field caused by Brownian motion of ions dissolved in a liquid leads, because of the Kerr polarization effect, to fluctuations of optical anisotropy of the scattering medium. The spectral characteristics of the Rayleigh line wing are obtained using the fluctuation-dissipative theorem as applied to equilibrium thermal electromagnetic field. Expressions are derived for the integral intensity and spectral width ($\Delta\nu$) of the Rayleigh line wing in terms of parameters of liquid solution such as the temperature T, the viscosity η, the concentration of dissolved ions n_i, and the coefficient of their diffusion D_i. It is demonstrated that $\Delta\nu \propto \exp(-W/2T)$, where W is the activation energy of ion mobility $b_i = D_i/T$. The possible region of validity of developed theoretical concepts as applied to the experimental data for the Rayleigh line wing in electrolytic solutions is discussed. *© 2001 MAIK "Nauka/Interperiodica".*

1. INTRODUCTION

Modern concepts of the physical nature of the Rayleigh line wing under conditions of light scattering in liquids are still far from being finalized. Although the universally accepted macroscopic model of this phenomenon, based on the results of treatment of fluctuations of optical anisotropy (fluctuations $\Delta\varepsilon_{ik}$ of the permittivity tensor) of the scattering medium [1, 2], proved to be very fruitful, it still calls for further development as regards the concretization of the physical mechanisms of such fluctuations. The difficulties encountered in the process are associated with the interpretation of the observed spectral structure of the Rayleigh line wing and, first of all, of its width $\Delta\nu$, which reaches values of the order of ~100 cm^{-1} and higher for most of the investigated liquids. With the values of $\Delta\nu$ as high as this, characteristic times $\tau \sim (\Delta\nu)^{-1} \le 10^{-13}$ s must be present in the $\Delta\varepsilon_{ik}$ fluctuation spectrum. The need for times as short as this is in conflict, first of all, with the so-called relaxation models of the phenomenon, which are based, with a number of variations, on the assumption made as early as that of Landau and Plachek [3] that the rate of fluctuations $\Delta\varepsilon_{ik}$ in a liquid is defined by the processes of rotational self-diffusion of its molecules. According to these models, only one characteristic time must be present in the $\Delta\varepsilon_{ik}$ fluctuation spectrum, namely, the time of rotational diffusion of liquid molecules, which coincides by an order of magnitude with the time of Debye relaxation $\tau_D = 4\eta\delta_l^3/T$, where η is the viscosity of the liquid, δ_l is the radius of its molecules, and T is the temperature (here and below, all quantities are given in energy units). For molecular liquids, $\tau_D \ge 10^{-11}$ s; i.e., it exceeds the time $(\Delta\nu)^{-1} \le 10^{-13}$ s by at least an order of magnitude.

At present, it is generally recognized that simple (relaxation) models are limited, which stimulated the development of other theoretical approaches to interpreting the Rayleigh line wing; many of those approaches are described in reviews [1, 4]. These new approaches, however, have likewise failed to produce an adequate explanation for the spectral structure of the Rayleigh line wing, especially in the far portion of its spectrum, i.e., at $\Delta\nu \gg 1/\tau_D$. The situation turned out to be even less predictable theoretically as papers have become available that described experiments involving observations of the Rayleigh line wing in aqueous electrolytic solutions. Gray *et al.* [5] and Lanshina *et al.* [6] have found that the characteristics of the Rayleigh line wing in such solutions depend considerably both on the concentration of dissolved electrolyte and on the type of the electrolyte. A qualitative explanation of this effect, as suggested in [5, 6], consists in that the ions dissolved in water cause a change in intermolecular interactions and, thereby, in the water structure defined by hydrogen bonds. Thus, one must bear in mind that the behavior of such variations depends on the type of ions which, according to Frank and Evans [7], may be classified as structure-forming and structure-destroying. The ions of the former type fit into the structure of water without destroying hydrogen bonds, while the ions of the latter type destroy these bonds and, thereby, distort the structure of water. This is quite a plausible assumption which, as far as we know, was not subjected to subsequent quantitative treatment; therefore, it still remains a hypothesis.

At the same time, in a recent paper [8] also dealing with the investigation of the Rayleigh line wing in aqueous solutions of some salts, another physical mechanism of the effect of dissolved ions on the spectrum of the Rayleigh line wing was suggested. This mechanism consists in that the fluctuation electric field $\mathbf{E}(t)$ caused by thermal Brownian motion of ions dissolved in a liquid leads, because of the Kerr polarization effect, to fluctuations of optical anisotropy and, as a result, to the emergence of depolarized scattering of incident light (i.e., the Rayleigh line wing). Note that the mechanism suggested in [8] applies, generally speaking, to all molecular liquids, because the latter liquids always possess ionic conduction to some or other degree. If this is not a solution of impurity electrolyte, the conduction is due to intrinsic ions which appear as a result of thermal electrolytic dissociation of molecules of the liquid proper. This dissociation is especially effective in polar liquids characterized by high values of static permittivity ε_0. The resistivity ρ of very thoroughly purified water at room temperature ($\varepsilon_0 \approx 80$) is of the order of ~10^7 Ω cm, which corresponds to the density of intrinsic ions H^+ and OH^- $n_i \approx 3 \times 10^{14}$ cm^{-3}. In pure nonpolar liquids, the density n_i is of course much lower. In solutions (for example, aqueous) of strong electrolytes, the density n_i is limited only by their saturation concentration.

Naturally, the mechanism of the effect of dissolved ions on the spectral structure of the Rayleigh line wing, treated below, cannot lay claim to universality if only for the reason that it fails to enable one to explain the dependence of the data of [5, 6] on the type of ions. Therefore, it must be regarded as one possible mechanism. It appears attractive owing to its physical clarity and to the possibility of quantitative analysis, which was first attempted in [8]. However, the quantitative estimates of the effect, which were obtained in [8], are not exhaustive: this fact caused us to resume the treatment of the problem.

This paper describes the results of detailed theoretical analysis of the mechanism suggested in [8]. The analysis is based on the general theory of equilibrium thermal electromagnetic fluctuations, which involves the use of the fluctuation-dissipative theorem; the most complete description of this theory is found in [9] (see also [10]). This approach enables one to relate the spectral intensity $F(\omega)$ of fluctuations of electric field $\mathbf{E}(t)$ in liquid with the parameters of the latter such as the resistivity ρ (or the ionic density n_i), the ionic diffusion coefficient D_i, and the temperature T. In turn, given $F(\omega)$, one can use the third-rank tensor of nonlinear polarizability of liquid χ_{ijkl} to determine the spectral intensity of fluctuations of the anisotropy tensor $\Delta\varepsilon_{ik}$ associated with the Kerr high-frequency effect. Note that the spectral characteristics of equilibrium fluctuations of the field $\mathbf{E}$, calculated using the fluctuation-dissipative theorem in terms of the linear dissipation characteristics of the medium, are completely independent of the nonlinear optical properties of the medium and, in particular, of the third-order polarizability χ. Therefore, in determining the anisotropy of liquid induced by the field $\mathbf{E}$, the field proper may be treated as external.

2. SPECTRAL INTENSITY OF FLUCTUATION OF ELECTRIC FIELD IN A LIQUID CHARACTERIZED BY IONIC CONDUCTION

As was stated above, the spectral intensity $F(\omega)$ of fluctuations of the field $\mathbf{E}(t)$ may be described using the fluctuation-dissipative theorem. Because we are interested in the contribution to the intensity $F(\omega)$ caused only by the thermal motion of ions dissolved in a liquid, the use of this theorem implies that the permittivity ε of the liquid proper is regarded as a real quantity. In further treatment of aqueous electrolytic solutions (in particular, pure water), we will represent ε in the form

$$\varepsilon = \frac{\varepsilon_0 + \varepsilon_1(\omega\tau_D)^2}{1 + (\omega\tau_D)^2}, \tag{1}$$

where $\varepsilon_0 = \varepsilon(0)$ is the static permittivity (for water, $\varepsilon_0 \approx 80$) and ε_1 is the permittivity in the IR frequency band when $(\omega\tau_D)^2 \gg \varepsilon_0/\varepsilon_1$. For water at $T = 4 \times 10^{-14}$ erg (293 K), the time $\tau_D \approx 8 \times 10^{-12}$ s. The expression for ε in the form of Eq. (1) may be used, with certain limitations, for all polar liquids. We will use the symbol ε_i to denote the contribution to the total permittivity caused by the presence of the ionic component. The dissipative properties of the ionic solution, which are responsible, according to the fluctuation-dissipative theorem, for the emergence of fluctuation field $\mathbf{E}$, are defined by the fact that the quantity ε_i is complex.

It is known [9] that the calculation of the spectral characteristics of thermal electromagnetic field inside the medium proper calls for the inclusion of spatial dispersion in this medium. In the case of the problem being treated, one must know the longitudinal component $\varepsilon_i^l(\omega, p)$ of permittivity ε_i. Because the ionic density $n_i \ll n_l$ (n_l is the density of molecules of liquid), the motion of ions under the effect of the field $\mathbf{E} \propto \exp[i(\omega t - \mathbf{p} \cdot \mathbf{r})]$ of electromagnetic wave may be described in the diffusion approximation. In so doing, $\varepsilon_i^l(\omega, p)$ is defined by formula (20.42) in monograph [9],

$$\varepsilon_i^l = \varepsilon[1 - i/(\omega\tau_0 - ip^2a^2)], \tag{2}$$

where

$$a = \sqrt{\varepsilon T/8\pi e^2 n_i}, \quad \tau_0 = a^2/D_i,$$

and D_i is the ionic diffusion coefficient (the ionic solution is assumed to be binary, symmetric, and consisting of singly charged ions of identical mobilities). The transverse component ε_i^t of permittivity in this approximation does not possess spatial dispersion and is

$$\varepsilon_i^t = \varepsilon(1 - i/\omega\tau_0).$$

The sought spectral intensity $F(\omega)$ of the field **E** is defined by the second term of formula (20.15) in [9] under conditions of $R = 0$ and substitution into this formula of expression (2) for $\varepsilon_i^l(\omega)$. Thus, integration for the region of $\omega > 0$ yields[1]

$$F(\omega) = F(0)(2^{1/3}\varepsilon_0/\varepsilon)^{3/2} \times \frac{1}{\sqrt{1 + \sqrt{1 + (\varepsilon/\varepsilon_0)^2(\omega\tau_d)^2}}} \frac{\hbar\omega/T}{e^{\hbar\omega/T} - 1}, \tag{3}$$

$$F(0) = \sqrt{\frac{2e^2 n_i T}{9\pi\varepsilon_0^3 D_i^2}}, \tag{3a}$$

$$\tau_d = \frac{\varepsilon_0 T}{8\pi e^2 n_i D_i} = \frac{a_D^2}{D_i}, \tag{3b}$$

where $a_D = \sqrt{\varepsilon_0 T/8\pi e^2 n_i}$ is the Debye length.

In the case of aqueous solutions, when ε is defined by formula (1) and the parameters $\xi \equiv \varepsilon_1/\varepsilon_0 \approx 1/40$ and $\alpha \equiv \tau_D/\tau_d \sim \mathrm{M}/10 \ll 1$ (M is the molar concentration of the solution; 1 M corresponds to the ion density $n_i = 6 \times 10^{20}\ \mathrm{cm}^{-3}$), expression (3) for the spectrum $F(\omega)$ may be represented in the form ($\omega > 0$)

$$F(\omega) = \frac{T(2\alpha)^{1/2}}{6\pi D_i \varepsilon_0 a_D}\left(\frac{1 + x^2}{1 + \xi x^2}\right)^2 \times \left[\alpha\frac{1 + x^2}{1 + \xi x^2} + x\right]^{-1/2} \frac{\beta x}{e^{\beta x} - 1}, \tag{4}$$

where $x \equiv \omega\tau_D$ and $\beta \equiv \hbar/T\tau_D$.

Until now, we talked about fluctuations of the field **E** in time only. In reality, it fluctuates in space as well. In so doing, $F(\omega)$ defines the spectral intensity of time fluctuations at a fixed point in space and, accordingly, their time correlation properties. The space–time correlation characteristics of the field $\mathbf{E}(t, \mathbf{r})$, which will be required in what follows, are given in the Appendix.

3. LIGHT SCATTERING BY FLUCTUATIONS OF OPTICAL ANISOTROPY IN LIQUID, CAUSED BY ELECTRIC FIELD OF DISSOLVED IONS

In the general case, the scattering properties of an anisotropic medium during macroscopic description are characterized by the properties of the tensor α_{ik} appearing in the constitutive equation [2]

$$D_i' = \varepsilon E_i' + \alpha_{ik} E_k^0, \tag{5}$$

where E_k^0 denotes the components of the electric field of incident wave; E_i' and D_i' are the components of the electric field and induction of scattered wave, respectively; and ε is the permittivity of the medium. The physical nature of the tensor α_{ik} may vary; its components (as well as ε), generally speaking, are characterized by frequency dispersion. Therefore, the algebraic form of notation (5) has a meaning only for monochromatic fields. In our problem, the tensor α_{ik} is defined by the Kerr high-frequency effect in the fluctuating field $\mathbf{E}(t, \mathbf{r})$, which has a continuous spectrum extending, according to Eq. (3), to frequencies $\sim T/\hbar \approx 3 \times 10^{13}\ \mathrm{s}^{-1} \sim 10^2\ \mathrm{cm}^{-1}$. Compared with the optical wave frequencies $\omega_0 \approx 3 \times 10^{15}\ \mathrm{s}^{-1}$, such fluctuations of the field **E** may be regarded as slow. Therefore, with due regard for the nonlinear electron polarizability alone and, accordingly, ignoring the dispersion of the tensor χ_{ijkl}, we will further represent the tensor α_{ik} in the algebraic form,

$$\alpha_{ik} = \alpha_{ik}(t, \mathbf{r}) = \chi_{ijkl}[E_j(t, \mathbf{r})E_l(t, \mathbf{r}) - \langle E_j E_l \rangle], \tag{6}$$

and the second, "scattering," term in Eq. (5) in the form

$$A\alpha_{ik} e_k \exp[-i(\omega_0 t - \mathbf{k} \cdot \mathbf{r})],$$

where A is the amplitude of an incident plane monochromatic wave and **e** is the unit vector defining the polarization of this wave. Because the dispersion of the tensor χ_{ijkl} is ignored, all of its components are real, and the tensor α_{ik} is also real (as regards the designations adopted for $E_k(t, \mathbf{r})$, see the Appendix). The degree of its symmetry is defined by the known symmetry of the tensor χ_{ijkl} for isotropic media (see, for example, [11]); the average values $\langle \alpha_{ik} \rangle = 0$.

We will further assume that an incident wave, which is linearly polarized along the z axis, propagates along the x axis of rectangular coordinates (x, y, z). We will be

---

[1] Formula (3) defines the spectral intensity $F(\omega)$ of a single projection E_a of the field onto the coordinate axis (average $\langle E_a \rangle = 0$). The continuation of the function $F(\omega)$ to the region of $\omega < 0$ is even, $F(-\omega) = F(\omega)$, so that

$$\langle E_a^2 \rangle = \int_{-\infty}^{\infty} F(\omega)d\omega = 2\int_0^{\infty} F(\omega)d\omega.$$

The rejection of the first term in formula (20.25) in [9] is attributed to the fact that this term defines the spectral intensity of the total thermal electromagnetic background in a liquid, which is in no way related to the presence of dissolved ions in that liquid. This term is present in the case of $n_i = 0$ as well. In addition, the zero-point vibration term $\hbar\omega/2$ is rejected in the mean oscillator energy. To ensure against misunderstanding, note that, in the notation of monograph [9], the spectral intensity $F(\omega) = \langle E_a(\mathbf{r})E_a^*(\mathbf{r})\rangle = (1/3)\langle \mathbf{E}(\mathbf{r})\mathbf{E}^*(\mathbf{r})\rangle$ (there is no summation over the indices; for more detail, see the Appendix).

interested in the wave scattered along the y axis (scattering angle of 90°); the x-component of this wave corresponds to the so-called depolarized component E'_{VH}, and the z component corresponds to the polarized component E'_{VV}. In the Fraunhofer zone, we have for these components [2]

$$E'_{VH} = E'_{VH}(t) = [C\exp(-i\omega_0 t)] \times \int \mathbf{e}_H \hat{\alpha}(t, \mathbf{r})\mathbf{e}_V e^{-i\mathbf{q}\cdot\mathbf{r}} d\mathbf{r}. \tag{7}$$

For $E'_{VV}(t)$, we have an analogous formula with $\mathbf{e}_H$ replaced by $\mathbf{e}_V$. Here,

$$C = [A\exp(ikR)]k_0^2/4\pi R,$$

$$k = k_0\sqrt{\varepsilon_1}, \quad k_0 = \omega_0/c,$$

$$\mathbf{q} = \mathbf{k}' - \mathbf{k}, \quad q = \sqrt{2}k,$$

$$\mathbf{e}_V = \{0, 0, 1\}, \quad \mathbf{e}_H = \{1, 0, 0\},$$

c is the light velocity, and R is the distance between the observation point and the scattering region ($R \gg kV^{2/3}$, V is the volume of the scattering region); integration in (7) is performed with respect to the volume V. The correlation functions of the components $E'_{VH}(t)$ and $E'_{VV}(t)$,

$$\psi^{VH}(\tau) = \frac{1}{4}[\langle E'_{VH}(t)E'^{*}_{VH}(t+\tau)\rangle - \text{c.c.}],$$

($\psi^{VV}(\tau)$ is determined analogously) in view of (7) take the form

$$\psi^{VH}(\tau) = \frac{1}{4}|C|^2 \times \left\{ \int \langle (\mathbf{e}_H\hat{\alpha}(t, \mathbf{r}')\mathbf{e}_V) \cdot (\mathbf{e}_H\hat{\alpha}(t+\tau, \mathbf{r}'')\mathbf{e}_V)\rangle \times \exp i[\omega_0\tau - \mathbf{q}\cdot(\mathbf{r}' - \mathbf{r}'')]dV'dV'' + \text{c.c.} \right\}. \tag{8}$$

According to Eqs. (6), (A.3), and (A.4), the quantity $\langle(\mathbf{e}_H\hat{\alpha}(t, \mathbf{r}')\mathbf{e}_V) \cdot (\mathbf{e}_H\hat{\alpha}(t+\tau, \mathbf{r}'')\mathbf{e}_V)\rangle$ which appears under the integration sign is real, is an even function of only τ and $\boldsymbol{\rho} = \mathbf{r}' - \mathbf{r}''$, and is given by the formula (see the Appendix)

$$\begin{aligned} &\langle (\mathbf{e}_H\hat{\alpha}(t, \mathbf{r}')\mathbf{e}_V) \cdot (\mathbf{e}_H\hat{\alpha}(t+\tau, \mathbf{r}'')\mathbf{e}_V)\rangle \\ &= \beta^{VH}_{kl\gamma\delta}K_{kl\gamma\delta}(\tau, \boldsymbol{\rho}) = \beta^{VH}_{kl\gamma\delta}K_{kl\gamma\delta}(-\tau, -\boldsymbol{\rho}), \end{aligned} \tag{8a}$$

where

$$\begin{aligned} \beta^{VH}_{kl\gamma\delta} &= (\mathbf{e}_H)_i(\mathbf{e}_H)_\alpha(\mathbf{e}_V)_j(\mathbf{e}_V)_\beta\chi_{ijkl}\chi_{\alpha\beta\gamma\delta} \\ &= \chi_{xzkl}\chi_{xz\gamma\delta}. \end{aligned} \tag{8b}$$

The substitution of Eq. (8a) into Eq. (8) and single integration yield

$$\psi^{VH}(\tau) = \frac{1}{2}|C|^2 V\cos\omega_0\tau \times \int_V \beta^{VH}_{kl\gamma\delta}K_{kl\gamma\delta}(\tau, \rho)\cos(\mathbf{q}\boldsymbol{\rho})d\rho. \tag{9}$$

For $\psi^{VV}(\tau)$, an analogous formula is derived with the tensor $\beta^{VH}_{kl\gamma\delta}$ replaced by $\beta^{VV}_{kl\gamma\delta} = \chi_{zzkl}\chi_{zz\gamma\delta}$.

The spectrum of the Rayleigh line wing is defined by the Fourier transform of the correlation functions $\psi^{VH, VV}(\tau)$. On the basis of Eqs. (9), (A.9), (A.9a), (A.9b), and (A.6), for this spectrum $G^{VH, VV}(\nu)$ ($\nu = (\omega - \omega_0)$ denotes the mismatch between the frequency ω of scattered wave and the frequency ω_0 of incident wave), we derive (the obvious condition $|\nu| \ll 2\omega_0$ is used)

$$\begin{aligned} G^{VH}(\nu) &= G^{VH}(-\nu) = \text{const}(\chi_{1212} + \chi_{1221})^2 \\ &\times \left\{ \int \cos(\mathbf{q}\cdot\boldsymbol{\rho})g_{11}(\nu, \rho)d\boldsymbol{\rho} + \int \cos(\mathbf{q}\cdot\boldsymbol{\rho})(1 - \gamma_y^2) \right. \\ &\left. \times g_{12}(\nu, \rho)d\boldsymbol{\rho} + 2\int \cos(\mathbf{q}\cdot\boldsymbol{\rho})\gamma_x^2\gamma_z^2 g_{22}(\nu, \rho)d\boldsymbol{\rho} \right\}, \end{aligned} \tag{10a}$$

$$\begin{aligned} G^{VV}(\nu) &= G^{VV}(-\nu) = \text{const}(\chi_{1111} + 2\chi_{1122}) \\ &\times \left\{ \int \cos(\mathbf{q}\cdot\boldsymbol{\rho})g_{11}(\nu, \rho)d\boldsymbol{\rho} \right. \\ &+ 4\int [\chi_{1122}^2(1 - \gamma_z^2) + \chi_{1111}^2\gamma_z^2]\cos(\mathbf{q}\cdot\boldsymbol{\rho})g_{12}(\nu, \rho)d\boldsymbol{\rho} \\ &\left. + 2\int [\chi_{1122}(1 - \gamma_z^2) + \chi_{1111}\gamma_z^2]^2\cos(\mathbf{q}\cdot\boldsymbol{\rho})g_{22}(\nu, \rho)d\boldsymbol{\rho} \right\}, \end{aligned} \tag{10b}$$

where

$$\begin{aligned} g_{11}(\nu, \rho) &= g_{11}(-\nu, \rho) = \int_{-\infty}^{\infty} L_1(\omega, \rho)L_1(\omega + \nu, \rho)d\omega, \\ g_{12}(\nu, \rho) &= g_{12}(-\nu, \rho) = \int_{-\infty}^{\infty} L_1(\omega, \rho)L_2(\omega + \nu, \rho)d\omega \\ &= \int_{-\infty}^{\infty} L_1(\omega + \nu, \rho)L_2(\omega, \rho)d\omega, \\ g_{22}(\nu, \rho) &= g_{22}(-\nu, \rho) = \int_{-\infty}^{\infty} L_2(\omega, \rho)L_2(\omega + \nu, \rho)d\omega. \end{aligned} \tag{10c}$$

In deriving these formulas, the following notation was used for components of the tensor χ_{ijkl} [11]:

$$\chi_{1111} \equiv \chi_{xxxx} = \chi_{yyyy} = \chi_{zzzz};$$

$$\chi_{1212} \equiv \chi_{xyxy} = \chi_{xzxz} = \chi_{yxyx} = \chi_{yzyz} = \chi_{zxzx} = \chi_{zyzy};$$

$$\chi_{1221} \equiv \chi_{xyyx} = \chi_{xzzx} = \chi_{yxxy} = \chi_{yzzy} = \chi_{zxxz} = \chi_{zyyz};$$

$$\chi_{1122} \equiv \chi_{xxyy} = \chi_{xxzz} = \chi_{yyxx} = \chi_{yyzz} = \chi_{zzxx} = \chi_{zzyy};$$

$$\chi_{1111} = \chi_{1122} + \chi_{1212} + \chi_{1221}.$$

The functions $L_{1,2}(\omega, \rho) = L_{1,2}(-\omega, \rho)$ are defined in the general case by formulas (A.7a) and (A.7b). For aqueous solutions, when relations (2) and (A.7c) are valid, these functions take the following form at $\omega > 0$:

$$L_1(\omega, \rho) = F(\omega)\exp[-(3/4)\kappa\rho], \tag{11a}$$

$$L_2(\omega, \rho) = -3F(\omega) \times \exp[-(3/4)\kappa\rho](1 - \exp(-\kappa\rho/4)). \tag{11b}$$

Here, $F(\omega) \equiv L_1(\omega, 0)$ is the spectral intensity of fluctuations of the field component $E_\alpha(t)$ at a fixed point in space, which is defined by formula (3c), and

$$\kappa = \frac{1}{\sqrt{2}a_D\sqrt{\alpha}}\sqrt{\alpha\frac{1 + x^2}{1 + \xi x^2} + x}, \quad x \equiv \omega\tau_D. \tag{11c}$$

If $G^{VH, VV}(\nu)$ denotes the density of the energy flux of scattered radiation (intensity) in a unit frequency range, the constant appearing in Eqs. (10a) and (10b) is equal to $I_0k_0^4V/(8\pi)^2R^2$, where $I_0 = (c\sqrt{\varepsilon_1}/8\pi|A|^2$ is the total (integral) intensity of incident light wave. The integration in Eqs. (10a) and (10b) is limited to the ranges of values of ρ, in which the functions $g_{11}(\nu, \rho)$, $g_{12}(\nu, \rho)$, and $g_{22}(\nu, \rho)$ are other than zero, i.e., in fact, to the ranges of spatial correlation of the field $\mathbf{E}(t, \mathbf{r})$. The integrals over solid angles ($d\boldsymbol{\rho} = \rho^2 d\rho d\Omega = \rho^2 d\rho\sin\theta d\theta d\varphi$), which enter Eqs. (10a) and (10b), are readily calculated and have the form

$$J_1 = \int_{4\pi}\cos(\mathbf{q}\cdot\boldsymbol{\rho})d\Omega = 4\pi\frac{\sin(q\rho)}{q\rho},$$

$$J_2 = \int_{4\pi}\gamma_y^2\cos(\mathbf{q}\cdot\boldsymbol{\rho})d\Omega = (4\pi/3)_1F_2(2;\, 5/2;\, 1;\, -(q\rho/2)^2),$$

$$J_3 = \int_{4\pi}\gamma_x^2\gamma_z^2\cos(\mathbf{q}\cdot\boldsymbol{\rho})d\Omega = (4\pi/15)_1F_2(2;\, 9/2;\, 1;\, -(q\rho/2)^2),$$

$$J_4 = \int_{4\pi}\gamma_z^2\cos(\mathbf{q}\cdot\boldsymbol{\rho})d\Omega = 4\pi\left(\frac{\sin(q\rho)}{q\rho} - \cos(q\rho)\right)1/(q\rho)^2,$$

$$J_5 = \int_{4\pi}\gamma_z^4\cos(\mathbf{q}\cdot\boldsymbol{\rho})d\Omega = 12\pi\frac{(3/(q\rho)^3 - 1)\sin(q\rho) - 3\cos(q\rho)/q\rho}{(q\rho)^3},$$

where ${}_1F_2$ is a generalized hypergeometric series. At $q\rho = 0$, the values of these integrals are as follows:

$$J_1 = 4\pi; \quad J_2 = 4\pi/3; \quad J_3 = 4\pi/15;$$

$$J_4 = 4\pi/3; \quad J_5 = 4\pi/5.$$

Therefore, formulas (10a)–(10c) and (11a)–(11c) define the spectral structure of the Rayleigh line wing for both depolarized (V, H) and polarized (V, V) components. However, it proves impossible to perform integrations indicated in these formulas; therefore, we will restrict ourselves to the calculation of only the integral intensity of scattering $I^{VH, VV}$ and the spectral width $(\Delta\nu)^{VH, VV}$ of the Rayleigh line wing. We will start with the calculation

$$I^{VH, VV} = \int_{-\infty}^{\infty}G^{VH, VV}(\nu)d\nu.$$

The substitution into this integral of the expressions for $G^{VH, VV}(\nu)$ according to formulas (10a)–(10c) gives rise to the integrals

$$\iint_{-\infty}^{\infty}L_{1,2}(\omega, \rho)L_{1,2}(\omega + \nu, \rho)d\omega\, d\rho,$$

$$\iint_{-\infty}^{\infty}L_1(\omega, \rho)L_2(\omega + \nu, \rho)d\omega\, d\nu,$$

which, in view of the fact that the functions $L_{1,2}(\omega, \rho)$ are even with respect to ω, are equal to $M_{1,2}^2(\rho)$ and $M_1(\rho)M_2(\rho)$, respectively, where

$$M_{1,2}(\rho) = 2\int_0^{\infty}L_{1,2}(\omega, \rho)d\omega, \quad M_2(0) = 0. \tag{12}$$

We substitute Eqs. (11a) and (11b) and perform integration in view of the condition $\alpha \ll 1$ to derive

$$M_1(\rho) = \frac{2\sqrt{2}T}{3\pi\varepsilon_0 a_D^3}\frac{e^{-\rho/\rho_0}}{\rho/\rho_0}, \tag{12a}$$

$$M_2(\rho) = -\frac{2\sqrt{2}T}{\pi\varepsilon_0 a_D^3}\frac{(\rho/\rho_0)e^{-\rho/\rho_0}}{6\alpha + (\rho/\rho_0)^2}, \tag{12b}$$

where $\rho_0 = (4\sqrt{2}/3)a_D$. Because $M_{1,2}^2(\rho)$ and $M_1(\rho)M_2(\rho) \propto \exp(-2\rho/\rho_0)$, the integrals $J_{1,2,3,4,5}$, which enter Eqs. (10a) and (10b), may be replaced, on the condition that $(q\rho_0/2)^2 \ll 1$, by their values at $q\rho = 0$. Assuming that this condition is valid (see below), the integrals with respect to ρ in Eqs. (10a) and (10b) reduce to the following:

$$\int_0^\infty \rho^2 M_1^2(\rho)d\rho; \quad \int_0^\infty \rho^2 M_2^2(\rho)d\rho; \quad \int_0^\infty \rho^2 M_1(\rho)M_2(\rho)d\rho. \tag{12c}$$

According to Eqs. (12a) and (12b), the respective values of these integrals are b, $9b$, and $-3b$, where

$$b = \frac{2\sqrt{2}}{3}\left(\frac{16}{9\pi}\right)^2 \frac{T^2}{a_D^3\varepsilon_0^2}. \tag{13}$$

In view of the foregoing, we derive for the intensities $I^{VH,\,VV}$, according to (10a)–(10c),

$$I^{VH} = \mathrm{const}(\chi_{1212} + \chi_{1221})^2 \times \frac{8\sqrt{2}}{15\pi}\left(\frac{16}{9}\right)^2 \frac{T}{a_D^3\varepsilon_0^2}, \tag{14a}$$

$$I^{VV} = \mathrm{const}\left(\chi_{1111}^2 + \frac{7}{2}\chi_{1122}^2 + 3\chi_{1111}\chi_{1122}\right) \times \frac{64\sqrt{2}}{15\pi}\left(\frac{16}{9}\right)^2 \frac{T}{a_D^3\varepsilon_0^2}. \tag{14b}$$

In accordance with this, the values of the scattering cross section calculated per unit volume of the scattering region (scattering coefficient), $\sigma_1^{VH,\,VV} \equiv (R^2/V)(I^{VH,\,VV}/I_0)$, are given by

$$\sigma_1^{VH} = \frac{5\sqrt{2}}{3}\left(\frac{16}{9}\right)^2 \frac{T^2}{\lambda^4\varepsilon_0^2 a_D^3}(\chi_{1212} + \chi_{1221})^2, \tag{15a}$$

$$\sigma_1^{VV} = \frac{5\sqrt{2}}{24}\left(\frac{16}{9}\right)^2 \frac{T^2}{\lambda^4\varepsilon_0^2 a_D^3} \times \left(\chi_{1111}^2 + \frac{7}{2}\chi_{1122}^2 + 3\chi_{1111}\chi_{1122}\right), \tag{15b}$$

where λ is the wavelength of incident light. (Note that, in the CGSE system of units employed by us, the quantities $\sigma_1^{VH,\,VV}$ are in cm^{-1} and the components of the tensor χ_{ijkl} are in s^2 cm/g.) According to these formulas, the degree of depolarization is

$$\Delta = \frac{I^{VH}}{I^{VV}} = \frac{1}{8}\frac{(\chi_{1212} + \chi_{1221})^2}{\chi_{1111}^2 + \frac{7}{2}\chi_{1122}^2 + 3\chi_{1111}\chi_{1122}}. \tag{15c}$$

It will be recalled that these formulas are valid subject to the condition $(q\rho_0/2)^2 \ll 1$, which, in view of the fact that $q = \sqrt{2\varepsilon_1}\,k_0$ and $\rho_0 = (4\sqrt{2}/3)a_D$, may be represented in the form

$$\lambda \ge 8\pi\varepsilon_1^{1/2}a_D = \sqrt{\frac{8\pi\varepsilon_1\varepsilon_0 T}{e^2 n_i}} \approx 10\ \mathrm{M}^{-1/2}\ \mathrm{nm} \tag{16}$$

(room temperature).

We will now turn to the calculation of the spectral half-width $(\Delta\nu)^{VH,\,VV}$ of the Rayleigh line wing, defined by the formula

$$(\Delta\nu)^{VH,\,VV} = \frac{1}{2}\sqrt{\frac{\int_{-\infty}^{\infty}\nu^2 G^{VH,\,VV}(\nu)d\nu}{\int_{-\infty}^{\infty} G^{VH,\,VV}(\nu)d\nu}}. \tag{17}$$

The substitution of expressions for $G^{VH,\,VV}(\nu)$ according to formulas (10a)–(10c) gives rise to the integrals

$$\iint_{-\infty}^{\infty} \nu^2 L_{1,2}(\omega,\rho)L_{1,2}(\omega+\nu,\rho)d\omega\,d\nu,$$

$$\iint_{-\infty}^{\infty} \nu^2 L_1(\omega,\rho)L_2(\omega+\nu,\rho)d\omega\,d\nu,$$

which, in view of the fact that the function $L_{1,2}(\omega, \rho)$ is even with respect to ω, prove to be equal to $2M_{1,2}(\rho)\bar{M}_{1,2}(\rho)$ and $[M_1(\rho)\bar{M}_2(\rho) + \bar{M}_1(\rho)M_2(\rho)]$, where $M_1(\rho)$ and $M_2(\rho)$ are defined by formulas (12), and

$$\bar{M}_{1,2}(\rho) = 2\int_0^\infty \omega^2 L_{1,2}(\omega,\rho)d\omega. \quad \bar{M}_2(0) = 0. \tag{18}$$

According to Eqs. (11a)–(11c), one can derive

$$\bar{M}_1(\rho) = \frac{16\sqrt{2}T\alpha^3}{\pi D_i\varepsilon_0 a_D\tau_D^3}\left(\frac{\rho_0}{\rho}\right)^5 e^{-\rho/\rho_0}, \tag{18a}$$

$$\bar{M}_2(\rho) = -\frac{2\sqrt{2}T\alpha^3}{\pi D_i\varepsilon_0 a_D\tau_D^3}\frac{(\rho/\rho_0)e^{-\rho/\rho_0}}{18\alpha^3 + (\rho/\rho_0)^2}. \tag{18b}$$

If the condition $(q\rho_0/2)^2 \ll 1$, i.e., condition (16), is valid, the internal integrals with respect to ρ, which enter the integral $\int_{-\infty}^{\infty}\nu^2 G^{VH,\,VV}(\nu)d\nu$ according to Eqs. (10a) and (10b), reduce to the following:

$$\int_0^\infty \rho^2 M_1\bar{M}_1 d\rho; \quad \int_0^\infty \rho^2 M_2\bar{M}_2 d\rho; \quad \int_0^\infty \rho^2\frac{M_1\bar{M}_2 + \bar{M}_1 M_2}{2}d\rho. \tag{18c}$$

One can see in Eqs. (12a), (12b), and (18a), (18b) that

$$(M_1\overline{M}_1) \propto (\rho_0/\rho)^6 e^{-2\rho/\rho_0}$$

and

$$(M_1\overline{M}_2) \propto (\rho_0/\rho)^4 e^{-2\rho/\rho_0},$$

and, therefore, the first and third of integrals in (18c) diverge at the lower limit. The formal reason for this consists in that expressions (12a), (12b) and (18a), (18b) for the functions $M_{1,2}(\rho)$ and $\overline{M}_{1,2}(\rho)$ were derived by us on the condition that the quantity ρ/ρ_0 is finite (i.e., cannot tend to zero). In calculating $I^{VH,VV}$, this limitation proved to be of no importance, because it did not result in the divergence of integrals (12c). In order to eliminate the divergence of the above-identified integrals (18c), the lower limit in them must be replaced by some finite scale $\rho_{\min} \ll \rho_0/2$. Because the divergence is caused by the fact that $\overline{M}_1 \propto (1/\rho)^5$ (see Eq. (18a)), it is natural to determine the scale $\rho_{\min}$ by equating the *a fortiori* finite quantity

$$\overline{M}_1(0) = 2\int_0^\infty \omega^2 L_1(\omega, 0)d\omega$$

$$\equiv 2\int_0^\infty \omega^2 F(\omega)d\omega = \left\langle\left(\frac{dE_\alpha}{dt}\right)^2\right\rangle$$

to the right-hand part of expression (18a), assuming that, in this part, $\rho = \rho_{\min}$. In so doing, we derive

$$\rho_{\min} = \rho_0\left[\frac{16\sqrt{2}T\alpha^3}{\pi D_i\varepsilon_0 a_D\tau_D^3\overline{M}_1(0)}\right]^{1/5}$$

and, based on Eq. (3c), we have

$$\overline{M}_1(0) = \frac{\sqrt{2\alpha}T}{3\pi D_i\varepsilon_0 a_D\tau_D^3\xi^2\beta^{3/2}}$$

and, therefore,

$$\begin{aligned}\rho_{\min} &\approx 2\rho_0(\alpha^{5/2}\beta^{3/2}\xi^2)^{1/5}\\ &\approx 4(\varepsilon_1/\varepsilon_0)^{2/5}(D_i^5\tau_r^3\tau_D^2)^{1/10}.\end{aligned} \qquad (19)$$

For aqueous solutions at room temperature,

$$\alpha \equiv \tau_D/\tau_d \equiv \tau_D D_i/a_D^2 \approx \mathrm{M}/10,$$

$$\beta \equiv \hbar/T\tau_D \approx 3\times 10^{-3},$$

$$\xi \equiv \varepsilon_1/\varepsilon_0 \approx 2.5\times 10^{-2}, \quad \tau_r \equiv \hbar/T \approx 2.5\times 10^{-14}\ \mathrm{s},$$

so that the parameter $(\alpha^{5/2}\beta^{3/2}\xi^2)^{1/5} \approx 10^{-2}\ \mathrm{M}^{1/2}$, and, therefore,

$$\rho_{\min}/(\rho_0/2) \approx 4\times 10^{-2}\ \mathrm{M}^{1/2} \ll 1.$$

One can see in Eq. (19) that, with the Stokes mechanism of ion mobility, when $b_i = D_i/T \propto 1/\eta$, the minimal scale $\rho_{\min} \propto (b_i)^{0.3}$, i.e., for the preassigned solution having the temperature T and the viscosity η, the scale $\rho_{\min}$ depends (in the manner indicated above) only on the mobility $b_i = b_i(T, \eta)$ of dissolved ions (it is assumed that the ratio $\varepsilon_1/\varepsilon_0$ is invariable).

The results of calculating integrals (18c) for the functions M_1, M_2, $\overline{M}_1$, and $\overline{M}_2$, defined by formulas (12a), (12b) and (18a), (18b), and, for the value of the scale $\rho_{\min}$ defined by formula (19), demonstrate that the main contribution to the integral $\int_{-\infty}^{\infty}\nu^2 G^{VH,VV}(\nu)d\nu$ is made by the first of the integrals (18c), i.e.,

$$\int_{\rho_{\min}}^{\infty}\rho^2 M_1\overline{M}_1 d\rho = \frac{64}{9(48)^{3/5}\pi^2}\times\frac{T^2\alpha^3\rho_0^3}{D_i\varepsilon_0^2 a_D^4\tau_D^3}\frac{1}{\alpha^{3/2}\beta^{9/10}\xi^{6/5}}.$$

In so doing, we derive for the half-width of the Rayleigh line wing, according to Eqs. (17), (10a)–(10c), (12c), and (13),

$$(\Delta\nu)^{VH} = 2\frac{(\varepsilon_0/\varepsilon_1)^{0.6}}{\tau_d^{0.25}\tau_D^{0.3}\tau_r^{0.45}}, \qquad (20a)$$

$$(\Delta\nu)^{VV} = (\Delta\nu)^{VH}\times\sqrt{\frac{\chi_{1111}^2 + 2\chi_{1122}^2}{\chi_{1111}^2 + \frac{7}{2}\chi_{1122}^2 + 3\chi_{1111}\chi_{1122}}}. \qquad (20b)$$

4. DISCUSSION OF THE RESULTS. CONCLUSION

The obtained results demonstrate that the ion contribution to the Rayleigh line wing under conditions of light scattering in electrolytic solutions, which is due to the mechanism suggested in [8], proves to be quite substantial. This is especially true of the spectral structure of the Rayleigh line wing. According to the theory described, three characteristic times define the spectral half-width of the Rayleigh line wing (of both the depolarized and polarized components), namely, $\tau_d = a_D^2/D_i$, the time of ionic diffusion through a Debye sphere; $\tau_D = 4\eta\delta_l^3/T$, the time of rotational self-diffusion of liquid molecules through a large angle (Debye relaxation time); and $\tau_r = \hbar/T$, the time of correlation of the electric field generated by the Brownian motion of ions (inverse spectral width of these fluctuations). One can see from formulas (20a) and (20b), which define the spectral half-width $\Delta\nu$ of the Rayleigh line wing, that the contribution by each one of these times to the value of $\Delta\nu$ is multiplicative, with the most significant part played by the time τ_r, and the least significant part, by the time τ_d. Note that the half-width $(\Delta\nu)^{VH}$ is independent of the components of the tensor χ_{ijkl}, while the integral intensity $I^{VH} \propto (\chi_{1212} + \chi_{1221})^2$ (see Eq. (14a)). We will give the numerical estimate of the quantity $(\Delta\nu)^{VH}$ for a typical aqueous solution of alkali salts at room temperature, assuming that $D_i = 2 \times 10^{-5}$ cm^2/s. In so doing, the time $\tau_d = (4.6 \times 10^{-11}/\mathrm{M})$ s. Formula (20a) gives $(\Delta\nu)^{VH} = 105$ M$^{1/4}$ cm^{-1}. Assuming that the diffusion coefficient for ions H^+ and OH^- in water is also equal to 2×10^{-5} cm^2/s, for purest water with pH = 7 (i.e., 10^{-7} M) we obtain $(\Delta\nu)^{VH} \approx 2$ cm^{-1}: this agrees with the result given by the simple relaxation theory with a single (rotational) relaxation time, according to which $(\Delta\nu)^{VH} = 3/\tau_D$ [1].

It is of interest to treat the temperature dependence of the spectral width $\Delta\nu$. For the quantities entering Eq. (20a), we have $\varepsilon_0 \propto 1/T$ (water), $\tau_r \propto 1/T$, and $\tau_d \propto T/n_iD_i$. Assuming further that the Stokes mechanism of ion mobility is valid, we have $D_i \propto T/\eta$; therefore, $\tau_D \propto 1/D_i$. As a result, we derive

$$\Delta\nu \propto n_i^{1/4}\exp(-W/2T),$$

where W is the activation energy for the ion mobility $b_i = D_i/T$. For weak electrolytic solutions, the density n_i, generally speaking, increases with T; therefore, the temperature-related increase in $\Delta\nu$ proves to be much faster. For the ions of K^+, Cs^+, Cl^-, and I^- in water, the energy

$$W/2 \approx 2\ \mathrm{kcal/mol} \approx 10^3\ \mathrm{K}.$$

Therefore, in heating aqueous solutions of such ions from 20 to 90°C, the width of their spectrum must increase by a factor of approximately two, i.e., for alkali salt solutions one must expect the values of

$$(\Delta\nu)^{VH} \approx 210\mathrm{M}^{1/4}\ \mathrm{cm}^{-1}.$$

According to Eqs. (14a) and (14b), the integral intensity of the Rayleigh line wing $I^{VH,\,VV} \propto T^{5/2}n_i^{3/2}$; i.e., the dependence on temperature is weaker, and that on the ion concentration is, on the contrary, stronger than for $\Delta\nu$. As follows from Eq. (15c), the degree of depolarization is independent of n_i and T and, for each liquid (solvent), is a fixed quantity (naturally, if the dependence of χ_{ijkl} on T and n_i is ignored).

The foregoing theory qualitatively explains some of the experimental data of [5, 6] and, at the same time, displays considerable contradictions to those data. For example, Gray *et al.* [5] have found a weak (nonexponential) temperature-related increase in the integral intensity of the Rayleigh line wing in aqueous solutions of KI and $MgSO_4$ salts in the concentration range of 0–3 M, which is predicted by our results. Gray *et al.* [5] have further demonstrated that, in the region of fairly high values of concentration, the integral intensity for the KI solution increases slowly (in accordance with our theory), but for $MgSO_4$ it remains almost unchanged. At the same time, for highly dilute solutions of both electrolytes, Gray *et al.* [5] observed a decrease in the intensity of the Rayleigh line wing with an increase in concentration, which may in no way be explained within our model. A similar pattern is observed in comparing our results with those of Lanshina *et al.* [6], who give the data of measurements of the half-width $(\Delta\nu)^{VH}$ in aqueous solutions of $Zn(NO_3)_2$, $Ca(NO_3)_2$, and $Mg(NO_3)_2$, as well as carbonates of alkali metals. Lanshina *et al.* [6] have found that an increase in concentration in the range of its moderate and high values (up to saturation) is accompanied by a weak increase in the values of $(\Delta\nu)^{VH}$ for electrolytes of the first group (which agrees with our results), and for electrolytes of the second group these values remain almost unchanged. However, in the range of fairly low values of concentration ($\leq 10^{-2}$ M), electrolytes of both types, on the contrary, exhibited a decrease in $(\Delta\nu)^{VH}$ as the concentration increases analogously with the behavior of integral intensity observed in [5].

The results of comparison with the experimental data lead one to conclude that the mechanism of the effect of dissolved ions on the Rayleigh line wing in water, suggested in [8], may apparently play a decisive part only in the region of fairly high values of dissolved ion concentration. Given the hypothesis about the ionic rearrangement of the structure of water, discussed in [5, 6] (see the Introduction), one can suggest that the mechanism treated by us becomes prevailing in the case of such a concentration of ions when the rearrangement of the structure of a solution is terminated as a result of its saturation. In conclusion, note that a radical experimental proof of the concepts of the importance of ions in the effect of the Rayleigh line wing, which were suggested in [8] and developed in this paper, would be given by finding the Arrhenius correlation $(\Delta\nu)^{VH} \propto \exp(-W/2T)$ in the range of high values of electrolyte concentration, as well as the independence of the degree of depolarization of scattering in the Rayleigh line wing of n_i and T.

ACKNOWLEDGMENTS

We are grateful to our colleague N.V. Suyazov for his kind assistance. This study received financial support from the Russian Foundation for Basic Research (grants nos. 99-15-96023, 00-15-96636, and 98-02-16264).

5. APPENDIX

We will give some results obtained using the correlation theory of steady-state (with respect to time), uniform, and isotropic (with respect to space) random fields that were employed in the main body of the paper. In addition, we will establish a continuity relation with the results of Levin and Rytov [9], which are also employed in the paper. Further, as in the main text of the paper, the quantity $\mathbf{E}(t, \mathbf{r})$ (which explicitly includes the time t as one of the independent variables) denotes the real value of the vector of electric field intensity. In so doing, the spectral tensor of spatial correlation of the field, defined by formula (20.24) of [9], has the form

$$\begin{aligned}&\langle E_\alpha(\mathbf{r}_1)E^*_\beta(\mathbf{r}_2)\rangle\\ &= \frac{1}{2}\pi\int_{-\infty}^{\infty}\Psi_{\alpha\beta}(\tau, \mathbf{r}_1 - \mathbf{r}_2)e^{-i\omega\tau}d\tau,\end{aligned} \qquad \text{(A.1)}$$

where

$$\begin{aligned}\Psi_{\alpha\beta}(\tau, \boldsymbol{\rho}) &= \Psi_{\alpha\beta}(-\tau, \boldsymbol{\rho})\\ &= \langle E_\alpha(t, \mathbf{r})E^*_\beta(t + \tau, \mathbf{r} + \boldsymbol{\rho})\rangle.\end{aligned}$$

The dependence of $\Psi_{\alpha\beta}$ on $|\tau|$ and $\boldsymbol{\rho}$ alone is a result of stationarity and spatial uniformity of the random field $\mathbf{E}(t, \mathbf{r})$. The tensor $\langle E_\alpha(\mathbf{r}_1)E^*_\beta(\mathbf{r})\rangle$, in turn, satisfies the equality

$$\begin{aligned}&\langle E_\alpha(\omega, \mathbf{r}_1)E^*_\beta(\omega', \mathbf{r}_2)\rangle\\ &= \langle E_\alpha(\mathbf{r}_1)E^*_\beta(\mathbf{r}_2)\rangle\delta(\omega - \omega'),\end{aligned}$$

where

$$\mathbf{E}(\omega, \mathbf{r}) = \frac{1}{2}\pi\int_{-\infty}^{\infty}\mathbf{E}(t, \mathbf{r})e^{-i\omega t}dt$$

is the random spectral amplitude density of the process $\mathbf{E}(t, \mathbf{r})$. According to the Wiener–Khintchine theorem,

$$\Psi_{\alpha\beta}(\tau, \boldsymbol{\rho}) = \int_{-\infty}^{\infty}\langle E_\alpha(\mathbf{r})E^*_\beta(\mathbf{r} + \boldsymbol{\rho})\rangle e^{i\omega\tau}d\omega. \qquad \text{(A.2)}$$

Based on the known property of Gaussian random quantities (as are the quantities entering this tensor), the tensor

$$\begin{aligned}K_{ikjl} = &\langle E_i(t, \mathbf{r})E_k(t, \mathbf{r})E_j(t + \tau, \mathbf{r} + \boldsymbol{\rho})E_l(t + \tau, \mathbf{r} + \boldsymbol{\rho})\rangle\\ &- \langle E_i(t, \mathbf{r})E_k(t, \mathbf{r})\rangle\langle E_j(t + \tau, \mathbf{r} + \boldsymbol{\rho})E_l(t + \tau, \mathbf{r} + \boldsymbol{\rho})\rangle\end{aligned}$$

is represented as

$$\begin{aligned}K_{ikjl}(\tau, \boldsymbol{\rho}) &= \Psi_{ij}(\tau, \boldsymbol{\rho})\Psi_{kl}(\tau, \boldsymbol{\rho})\\ &+ \Psi_{il}(\tau, \boldsymbol{\rho})\Psi_{kj}(\tau, \boldsymbol{\rho})\end{aligned} \qquad \text{(A.3)}$$

(if the random quantities x_1, x_2, x_3, and x_4 have a joint Gaussian probability distribution, the mean $\langle x_1x_2x_3x_4\rangle = \langle x_1x_2\rangle\langle x_3x_4\rangle + \langle x_1x_3\rangle\langle x_2x_4\rangle + \langle x_1x_4\rangle\langle x_2x_3\rangle$).

Because of both the spatial uniformity and the isotropism of the vector field $\mathbf{E}(t, \mathbf{r})$, we derive, in the general case,

$$\Psi_{\alpha\beta}(\tau, \boldsymbol{\rho}) = N_1(\tau, \rho)\delta_{\alpha\beta} + N_2(\tau, \rho)\rho_\alpha\rho_\beta/\rho^2, \qquad \text{(A.4)}$$

where $N_{1,2}(\tau, \rho)$ denotes scalar functions even with respect to τ, with $N_2(\tau, 0) \equiv 0$. The representation of the tensor

$$\begin{aligned}&\langle E_\alpha(\mathbf{r})E^*_\beta(\mathbf{r} + \boldsymbol{\rho})\rangle\\ &= L_1(\omega, \rho)\delta_{\alpha\beta} + L_2(\omega, \rho)\rho_\alpha\rho_\beta/\rho^2\end{aligned} \qquad \text{(A.5)}$$

is analogous, where $L_{1,2}(\omega, \rho)$ denotes scalar functions even with respect to ω, with $L_2(\omega, 0) \equiv 0$. According to Eqs. (A.2) and (A.4),

$$N_{1,2}(\tau, \rho) = \int_{-\infty}^{\infty}L_{1,2}(\omega, \rho)e^{i\omega\tau}d\omega. \qquad \text{(A.6)}$$

Based on formulas (20.24) and (20.25) in [9], the functions $L_{1,2}(\omega, \rho)$ may be represented as

$$\begin{aligned}L_1(\omega, \rho) &= \frac{2\theta}{\pi^2\omega}\\ &\times\int_0^\infty\mathrm{Im}\left(\frac{1}{\varepsilon_i^l}\right)\left(\frac{\sin(p\rho)}{p\rho} - \cos(p\rho)\right)\frac{p^2dp}{(p\rho)^2},\end{aligned} \qquad \text{(A.7a)}$$

$$\begin{aligned}L_2(\omega, \rho) &= \frac{2\theta}{\pi^2\omega}\int_0^\infty\mathrm{Im}\left(\frac{1}{\varepsilon_i^l}\right)\left[\frac{\sin(p\rho)}{p\rho}\right.\\ &\left.- \frac{3}{(p\rho)^2}\left(\frac{\sin(p\rho)}{p\rho} - \cos(p\rho)\right)\right]p^2dp \qquad \text{(A.7b)}\\ &= \langle\mathbf{E}(\mathbf{r})\cdot\mathbf{E}^*(\mathbf{r} + \boldsymbol{\rho})\rangle - 3L_1(\omega, \rho).\end{aligned}$$

For the medium being treated, according to Eq. (2),

$$\mathrm{Im}\left(\frac{1}{\varepsilon_i^l}\right) = \frac{1}{\varepsilon_0}\frac{\omega\tau_d}{[(\varepsilon/\varepsilon_0)\omega\tau_d]^2 + (1 + p^2a^2)^2}. \qquad \text{(A.7c)}$$

Here,

$$a^2 = \varepsilon T/8\pi e^2n_i, \quad \tau_d = \varepsilon_0T/8\pi e^2n_iD_i,$$
$$\theta = \hbar\omega/(e^{\hbar\omega} - 1).$$

It follows from (A.7a) and (A.7b) (see Footnote 1) that

$$L_1(\omega, 0) = \frac{1}{3}\langle\mathbf{E}(\mathbf{r})\cdot\mathbf{E}^*(\mathbf{r})\rangle = F(\omega), \ L_2(\omega, 0) = 0.$$

Hence, according to Eq. (A.6),

$$\begin{aligned}N_1(\tau, 0) &= \int_{-\infty}^{\infty}L_1(\omega, 0)e^{i\omega\tau}d\omega\\ &= \int_{-\infty}^{\infty}F(\omega)e^{i\omega\tau}d\omega = \psi(\tau).\end{aligned} \qquad \text{(A.8)}$$

Therefore, based on Eq. (A.4), we have

$$\Psi_{\alpha\beta}(\tau, 0) \equiv \langle E_\alpha(t, \mathbf{r})E_\beta(t + \tau, \mathbf{r})\rangle = \psi(\tau)\delta_{\alpha\beta}, \qquad \text{(A.8a)}$$

where

$$\psi(\tau) = \psi(-\tau) = \langle E_\alpha(t, \mathbf{r})E_\alpha(t+\tau, \mathbf{r})\rangle$$

is the correlation function of an individual component of the field at a fixed point in space; thus, different components are not correlated.

For the medium being treated, when $\beta^{VH}_{kl\gamma\delta} = \chi_{xzkl}\chi_{xz\gamma\delta}$ and $\beta^{VV}_{kl\gamma\delta} = \chi_{zzkl}\chi_{zz\gamma\delta}$, we have

$$\begin{gathered}\beta^{VH,\,VV}_{kl\gamma\delta}K_{kl\gamma\delta}(\tau, \boldsymbol{\rho}) = f^{VH,\,VV}_{11}N_1^2(\tau, \rho) \\ + f^{VH,\,VV}_{12}N_1(\tau, \rho)N_2(\tau, \rho) + f^{VH,\,VV}_{22}N_2^2(\tau, \rho),\end{gathered} \tag{A.9}$$

where

$$\begin{gathered}f^{VH}_{11} = (\chi_{1212} + \chi_{1221})^2, \\ f^{VH}_{12} = (\chi_{1212} + \chi_{1221})^2(1 - \gamma_y^2), \\ f^{VH}_{22} = 2(\chi_{1212} + \chi_{1221})^2\gamma_x^2\gamma_z^2,\end{gathered} \tag{A.9a}$$

$$\begin{gathered}f^{VV}_{11} = 2(\chi^2_{1111} + 2\chi^2_{1122}), \\ f^{VV}_{22} = 4[\chi^2_{1122}(1 - \gamma_z^2) + \chi^2_{1111}\gamma_z^2], \\ f^{VV}_{22} = 2[\chi_{1122}(1 - \gamma_z^2) + \chi_{1111}\gamma_z]^2.\end{gathered} \tag{A.9b}$$

Here, $\gamma_{x,\,y,\,z}$ denotes the direction cosines of the vector $\boldsymbol{\rho} = \mathbf{r}_1 - \mathbf{r}_2$. With $\rho = 0$, when $N_1(\tau, 0) = \psi(\tau)$ and $N_2(\tau, 0) \equiv 0$, formula (A.9) yields

$$\beta^{VH,\,VV}_{kl\gamma\delta}K_{kl\gamma\delta}(\tau, 0) = f^{VH,\,VV}_{11}\psi^2(\tau). \tag{A.10a}$$

With $\tau = 0$, we have, according to Eq. (A.9),

$$\begin{gathered}\beta^{VH,\,VV}_{kl\gamma\delta}K_{kl\gamma\delta}(0, \boldsymbol{\rho}) = f^{VH,\,VV}_{11}M_1^2(\rho) \\ + f^{VH,\,VV}_{12}M_1(\rho)M_2(\rho) + f^{VH,\,VV}_{22}M_2^2(\rho),\end{gathered} \tag{A.10b}$$

where (see Eq. (A.6))

$$\begin{gathered}M_{1,\,2}(\rho) = N_{1,\,2}(0, \rho) = \int\limits_{-\infty}^{\infty} L_{1,\,2}(\omega, \rho)d\omega, \\ M_2(0) = 0.\end{gathered} \tag{A.11}$$

REFERENCES

1. I. L. Fabelinskii, *Molecular Scattering of Light* (Nauka, Moscow, 1965; Plenum, New York, 1968); Usp. Fiz. Nauk **164**, 897 (1994) [Phys. Usp. **37**, 821 (1994)].
2. L. D. Landau and E. M. Lifshitz, *Course of Theoretical Physics,* Vol. 8: *Electrodynamics of Continuous Media* (Nauka, Moscow, 1982; Pergamon, New York, 1984).
3. L. Landau and G. Plachek, Phys. Z. Sowjetunion **5**, 172 (1934).
4. V. S. Vikhrenko, Usp. Fiz. Nauk **113**, 627 (1974) [Sov. Phys. Usp. **17**, 558 (1974)].
5. M. A. Gray, T. M. Loehr, and P. A. Pincus, J. Chem. Phys. **59**, 1121 (1973).
6. L. V. Lanshina, G. K. Golubovich, T. N. Kuz'mina, and M. V. Petrova, Khim. Fiz. **5**, 603 (1983).
7. H. S. Frank and M. W. Evans, J. Chem. Phys. **13**, 507 (1945).
8. N. F. Bunkin and A. V. Lobeev, Z. Phys. Chem. **214**, 269 (2000).
9. M. L. Levin and S. M. Rytov, *Theory of Equilibrium Thermal Fluctuations in Electrodynamics* (Nauka, Moscow, 1967).
10. E. M. Lifshitz and L. P. Pitaevskiĭ, *Course of Theoretical Physics,* Vol. 5: *Statistical Physics* (Nauka, Moscow, 1978; Pergamon, New York, 1980), Part 2.
11. Y. R. Shen, *The Principles of Nonlinear Optics* (Wiley, New York, 1984; Nauka, Moscow, 1989).

Translated by H. Bronstein

Journal of Experimental and Theoretical Physics, Vol. 92, No. 3, 2001, pp. 400–411.
Translated from Zhurnal Éksperimental'noĭ i Teoreticheskoĭ Fiziki, Vol. 119, No. 3, 2001, pp. 463–475.

Detachment of Electrons during the Collision of Two Negative Ions

M. I. Chibisov[a, *], **F. Brouillard**[b, **], **and M. Cherkani**[c]
[a]*Kurchatov Institute Russian Research Center, Nuclear Fusion Institute, pl. Kurchatova 1, Moscow, 123182 Russia*
[b]*Université Louvain-la-Neuve, Départment de physique, unité FYAM, B-1348 Louvain-la-Neuve, Belgium*
[c]*Université Sidi Mohamad Ben Abdollah, Faculté des Sciences Saïss, Fès, Morocco*
**e-mail: chib@qq.nfi.kiae.su*
***e-mail: brouillard@fyam.fyam.ucl.ac.be*
Received September 26, 2000

Abstract—The cross sections of the detachment of one and two electrons during the collision of two negative ions $H^- + H^-$, $H^- + Cs^-$, and $Cs^- + Cs^-$ are calculated in a wide range of collision energies: from the energy threshold to approximately 100 keV. In adiabatically slow collisions, the detachment of electrons occurs as a result of one- or two- electron Auger decays whose rates are calculated in the approximation of asymptotically large separations between ions. For high collision energies, the cross sections of the electron detachment are calculated by the method of close coupling of states. The calculated cross sections are in good agreement with the results of experimental measurements made for the $H^- + H^-$ collision. *© 2001 MAIK "Nauka/Interperiodica".*

1. INTRODUCTION

The ionization processes occurring during the collision of two negative ions are of considerable interest in connection with the problem of nuclear plasma heating by neutral atomic hydrogen beams. It is convenient to generate the beams of fast neutral atoms by accelerating and neutralizing negative ions in view of the relatively large cross section of their neutralization at targets. However, the collisions of negative ions in high-intensity beams, which occur due to the spread in their velocities, effectively suppress the intensity of such beams. The detachment of electrons during the collision between two negative ions of hydrogen atoms, $H^- + H^-$, was studied earlier both experimentally [1–3] and theoretically [4, 5].

In this paper, we analyze the following three processes of electron detachment:

$$A^- + B^- = \begin{cases} A + B^- + e, & \text{(A)} \\ A^- + B + e, & \text{(B)} \\ A + B + 2e, & \text{(AB)} \end{cases}$$

whose probabilities strongly compete with one another. For this reason, we calculate the cross sections of these processes simultaneously by solving a single wave equation. Reactions (A), (B), and (AB) will be investigated by us for the following three collisions: $H^- + H^-$, $H^- + Cs^-$, and $Cs^- + Cs^-$.

For high collision velocities, processes (A), (B), and (AB) occur as a result of direct transfer of a part of the kinetic energy of the nuclei to the electrons. In this limit, the cross sections are calculated in the dynamic approximation. For low velocities, the energy exchange between electrons and nuclei has a low probability, and another mechanism becomes effective. In view of the smallness of the binding energy of negative ions and their repulsion, several channels of autoionization decay become effective simultaneously for low velocities. When two ions approach each other, the electronic energy level rises and intersects the boundary of the continuum even for very large distances between the nuclei. As in the dynamic approximation, the Auger decays of the autoionization states formed in this process lead to considerable values of the cross sections of the above reactions.

In this paper, atomic units of measurements are used.

2. DETACHMENT OF ELECTRONS FOR HIGH COLLISION VELOCITIES. DYNAMIC DETACHMENT

All the three reactions, (A), (B), and (AB), occur predominantly at large distances R between nuclei, when the Coulomb repulsion between weakly bound electrons of the negative ions play the major role. For large R, this interaction can be expanded into a series in reciprocal powers of R:

$$\begin{gathered}\frac{1}{|\mathbf{r}_1-\mathbf{r}_2|} \approx \frac{1}{R} + \frac{z_{1a}}{R^2} + \frac{3z_{1a}^2 - r_{1a}^2}{2R^3} \\ + \frac{r_{1a}z_{1a}(5z_{1a}-3r_{1a})}{2R^4} + \ldots - \frac{z_{2b}}{R^2} + \frac{3z_{2b}^2-r_{2b}^2}{2R^3} \\ - \frac{r_{2b}z_{2b}(5z_{2b}-3r_{2b})}{2R^4} + \ldots + W(\mathbf{r}_{1a}, \mathbf{r}_{2b}) + \ldots, \\ r_{1a}, r_{2b} \ll R,\end{gathered} \tag{1}$$

where $\mathbf{r}_1$ and $\mathbf{r}_2$ are the radius vectors of electrons 1 and 2 in an arbitrary reference frame, while $\mathbf{r}_{1a}$ and $\mathbf{r}_{2b}$ are the vectors of electrons 1 and 2 relative to nuclei a and b, respectively. The correlation term $W(\mathbf{r}_{1a}, \mathbf{r}_{2b})$ is a function of the product of the coordinates of both electrons:

$$W(\mathbf{r}_{1a}, \mathbf{r}_{2b}) = \frac{\mathbf{r}_{1a}\cdot\mathbf{r}_{2b} + 3z_{1a}z_{2b}}{R^3} + \ldots, \tag{2}$$

while the remaining terms in expansion (1) depend on the coordinates of only one of the electrons, 1 or 2.

The relatively large term $1/R$ in expansion (1) affects only the energy of the system. This term does not depend on the electron coordinates and does not perturb the wave functions of weakly bound electrons. We can therefore use the unperturbed wave functions both for bound states and for the states in the continuum. The transitions between these states are determined by the terms following $1/R$ in expansion (1). In order to calculate the matrix elements for dipole transitions, we can use the following simple expressions for the wave functions of the initial bound state [6–8]:

$$\begin{gathered}\psi_0^{(-)}(r) = B(\gamma, \beta)\sqrt{\frac{\gamma}{2\pi}}\frac{e^{-\gamma r} - e^{-\beta r}}{r}, \\ B(\gamma, \beta) = \frac{\sqrt{1+\gamma/\beta}}{1-\gamma/\beta},\end{gathered} \tag{3}$$

the binding energy of a negative ion being $\varepsilon = -\gamma^2/2$, while for the P state in the continuum, we have

$$\begin{gathered}\psi_a^{\varepsilon}(\mathbf{r}) = \sqrt{\frac{2}{\pi k}}\frac{1}{r}\left[\frac{\sin(kr)}{kr} - \cos(kr)\right] \\ \times\sqrt{\frac{3}{4\pi}}\{\cos\theta;\ \sin\theta\cos\varphi;\ \sin\theta\sin\varphi\}\end{gathered} \tag{4}$$

with three components of angular functions $\cos\theta$, $\sin\theta\cos\varphi$, and $\sin\theta\sin\varphi$. The z axis of the reference frame introduced here is perpendicular to the plane of the collision. The binding energies of the ions H⁻ and Cs⁻ under investigation are given by [9]

$$\varepsilon_{\mathrm{H}^-} = -0.75421\ \mathrm{eV} \quad (\gamma_{\mathrm{H}^-} = 0.23544),$$

$$\varepsilon_{\mathrm{Cs}^-} = -0.4716\ \mathrm{eV} \quad (\gamma_{\mathrm{Cs}^-} = 0.1862).$$

In monograph [6], coefficient B was determined by joining the first term in formula (3) with the wave function of the H^- ion determined by Chandrasekhar [10] with three variable parameters; it was found that $B_{\mathrm{H}^-} = 1.183$. In our earlier publications [7, 8], we considered the wave equation satisfied by function (3). It was found by fitting the potential appearing in this equation to the static potential of a neutral hydrogen atom in the ground state that $\beta_{\mathrm{H}^-} = 2.66$ for H^-. Using formula (3) which defines coefficient B, we obtain $B_{\mathrm{H}^-} = 1.145$. The relative difference between the values of the coefficient B_{H^-} obtained in [6] and in [7, 8] amounts to only 3.3%. For Cs^-, the same approximation that was used earlier [7, 8] for H^- now yields $\beta_{\mathrm{Cs}^-} = 1.45$ (see also [11]), which gives $B_{\mathrm{Cs}^-} = 1.22$.

In view of the smallness of the binding energy for negative ions, the cross section for all the three reactions are large, and we therefore take into account only the transitions of weakly bound electrons. In this case, the wave functions of the complete set of the states of the system formed by two negative ions are given by

$$\psi_a^{(-)}(\mathbf{r}_{1a})\psi_b^{(-)}(\mathbf{r}_{2b})\exp[-i(\varepsilon_a + \varepsilon_b)t], \tag{5}$$

$$\psi_a^{\varepsilon}(\mathbf{r}_{1a})\psi_b^{(-)}(\mathbf{r}_{2b})\exp(-i\varepsilon_b t - i\varepsilon t), \tag{6}$$

$$\psi_a^{(-)}(\mathbf{r}_{1a})\psi_b^{\varepsilon}(\mathbf{r}_{2b})\exp(-i\varepsilon_a t - i\varepsilon t), \tag{7}$$

$$\psi_a^{\varepsilon}(\mathbf{r}_{1a})\psi_b^{\varepsilon'}(\mathbf{r}_{2b})\exp(-i\varepsilon t - i\varepsilon' t), \tag{8}$$

where $\psi_{a,b}^{(-)}$ are the wave functions of weakly bound electrons and $\psi_{a,b}^{\varepsilon}$ are the wave functions of neutral atoms with an electron in the continuum corresponding to energy ε. Expression (5) is the wave function of the system formed by two negative ions, i.e., the wave function of the initial state; expressions (6) and (7) describe the states in which the electron of one of the ions, A⁻ or B⁻, is detached and belongs to the continuum, while expression (8) describes the state with two detached electrons.

The complete wave function of the system is given by

$$\begin{gathered}\Psi_{\mathrm{AB}}^{(-)}(t, \mathbf{r}_{1a}, \mathbf{r}_{2b}) \\ = a_0(t)\psi_a^{(-)}(\mathbf{r}_{1a})\psi_b^{(-)}(\mathbf{r}_{2b})\exp[-i(\varepsilon_a+\varepsilon_b)t] \\ + \int a(t, \varepsilon)\psi_a^{\varepsilon}(\mathbf{r}_{1a})\psi_b^{(-)}(\mathbf{r}_{2b})\exp[-i(\varepsilon_b+\varepsilon)t]\,d\varepsilon \\ + \int b(t, \varepsilon)\psi_a^{(-)}(\mathbf{r}_{1a})\psi_b^{\varepsilon}(\mathbf{r}_{2b})\exp(-i(\varepsilon_a+\varepsilon)t)d\varepsilon \\ + \iint c(t, \varepsilon, \varepsilon')\psi_a^{\varepsilon}(\mathbf{r}_{1a})\psi_b^{\varepsilon'}(\mathbf{r}_{2b})\exp(-i\varepsilon t - i\varepsilon' t)d\varepsilon d\varepsilon',\end{gathered} \tag{9}$$

and the system of time-dependent equations for amplitudes $a_0(t)$, $a(t, \varepsilon)$, $b(t, \varepsilon)$, and $c(t, \varepsilon, \varepsilon')$ can be written in the form

$$i\frac{da_0}{dt} = \int a(t, \varepsilon)V^{\mathrm{A}}_{0,\,\varepsilon}(t)\exp[i\phi^{\mathrm{A}}_{0\varepsilon}(t)]d\varepsilon$$

$$+\int b(t, \varepsilon)V^{\mathrm{B}}_{0,\,\varepsilon}(t)\exp[i\phi^{\mathrm{B}}_{0\varepsilon}(t)]d\varepsilon$$

$$+\iint c(t, \varepsilon, \varepsilon')V^{\mathrm{AB}}_{0,\,\varepsilon,\,\varepsilon'}(t)\exp[i\phi^{\mathrm{AB}}_{\varepsilon\varepsilon'0}(t)]d\varepsilon d\varepsilon',$$

$$\dots$$

$$i\frac{da(t, \varepsilon)}{dt} = a_0(t)V^{\mathrm{A}}_{\varepsilon,\,0}(t)\exp[-i\phi^{\mathrm{A}}_{0\varepsilon}(t)], \qquad (10)$$

$$\dots$$

$$i\frac{db(t, \varepsilon)}{dt} = a_0(t)V^{\mathrm{B}}_{\varepsilon,\,0}(t)\exp[-i\phi^{\mathrm{B}}_{0\varepsilon}(t)],$$

$$\dots$$

$$i\frac{dc(t, \varepsilon, \varepsilon')}{dt} = a_0(t)V^{\mathrm{AB}}_{\varepsilon,\,\varepsilon',\,0}(t)\exp(-i\phi^{\mathrm{AB}}_{0\varepsilon\varepsilon'}(t)),$$

where

$$\begin{aligned}\phi^{\mathrm{A,\,B}}_{0\varepsilon}(t) &= -(\varepsilon - \varepsilon_{a,\,b})t,\\ \phi^{\mathrm{AB}}_{0\varepsilon\varepsilon'}(t) &= -(\varepsilon - \varepsilon_a + \varepsilon' - \varepsilon_b)t,\end{aligned} \qquad (11)$$

$a_0(t)$ is the amplitude of the initial state, $a(t, \varepsilon)$ and $b(t, \varepsilon)$ are the amplitudes of states with one electron detached from ion A^- or B^-, respectively, and $c(t, \varepsilon, \varepsilon')$ is the amplitude of the state with both electrons detached. We have neglected the transitions between states in the continuum. The system of equations (10) must be solved under the initial condition

$$a_0(t = -\infty) = 1, \quad a(-\infty) = b(-\infty) = c(-\infty) = 0.$$

Simple integration of the equations for a, b, and c,

$$a(t, \varepsilon) = -i\int\limits_{-\infty}^{t} a_0(t')V^{\mathrm{A}}_{\varepsilon 0}(t')\exp[-i\phi^{\mathrm{A}}_{0\varepsilon}(t')]dt',$$

$$b(t, \varepsilon) = -i\int\limits_{-\infty}^{t} a_0(t')V^{\mathrm{B}}_{\varepsilon 0}(t')\exp[-i\phi^{\mathrm{B}}_{0\varepsilon}(t')]dt',$$

$$c(t, \varepsilon, \varepsilon') = -i\int\limits_{-\infty}^{t} a_0(t')V^{\mathrm{AB}}_{\varepsilon\varepsilon'0}(t')\exp[-i\phi^{\mathrm{AB}}_{0\varepsilon\varepsilon'}(t')]dt',$$

and the substitution of these integrals into the first equation of system (10) leads to an integro-differential equation in one unknown function $a_0(t)$:

$$\frac{da_0}{dt} = -S_{\mathrm{A}}(t) - S_{\mathrm{B}}(t) - S_{\mathrm{AB}}(t), \qquad (12)$$

where

$$S_{\mathrm{A,\,B}}(t) = \int\limits_{-\infty}^{t} a_0(t')\exp[i\varepsilon_{a,\,b}(t - t')]K_{\mathrm{A,\,B}}(t, t')dt', \qquad (13)$$

$$S_{\mathrm{AB}}(t) = \int\limits_{-\infty}^{t} a_0(t')\exp[i(\varepsilon_a + \varepsilon_b)(t - t')]K_{\mathrm{AB}}(t, t')dt' \qquad (14)$$

and kernels $K(t, t')$ of the integro-differential equation (12) are given by

$$K_{\mathrm{A,\,B}}(t, t') \equiv \int\limits_{0}^{\infty} V^{\mathrm{A,\,B}}_{0\varepsilon}(t)V^{\mathrm{A,\,B}}_{\varepsilon 0}(t')\exp[-i\varepsilon(t - t')]d\varepsilon, \qquad (15)$$

$$\begin{aligned}K_{\mathrm{AB}}(t, t') \equiv{}& \int\limits_{0}^{\infty}\int\limits_{0}^{\infty} V^{\mathrm{AB}}_{0\varepsilon\varepsilon'}(t)V^{\mathrm{AB}}_{\varepsilon\varepsilon'0}(t')\\ &\times\exp(-i(\varepsilon + \varepsilon')(t - t'))d\varepsilon d\varepsilon'.\end{aligned} \qquad (16)$$

Equation (12) was solved numerically for each rectilinear trajectory of the classical motion of atomic nuclei. A similar integro-differential equation was used earlier [8] for evaluating the ionization cross section of the negative ion by the field of the positive ion in collision $\mathrm{H}^- + \mathrm{H}^+$.

The total probability of the detachment of an electron from ion A by the instant t of the collision is given by

$$P_{\mathrm{A}}(\rho, t) \equiv \int\limits_{0}^{\infty}|a(\varepsilon, t)|^2 d\varepsilon, \qquad (17)$$

while its derivative is

$$\frac{dP_{\mathrm{A}}(\rho, t)}{dt} = 2\mathrm{Re}\left\{\int\limits_{0}^{\infty} a(\varepsilon, t)\frac{da^*(\varepsilon, t)}{dt}d\varepsilon\right\}. \qquad (18)$$

Similar expressions can be written for P_{B} and P_{AB}. Substituting into these expressions the derivative of amplitude $da^*(\varepsilon, t)/dt$ from the system of equations (10), we obtain the total probabilities of the detachment of one and two electrons:

$$P_{\mathrm{A,\,B}}(\rho, t) = 2\mathrm{Re}\left\{\int\limits_{-\infty}^{t} a_0^*(t')S_{\mathrm{A,\,B}}(t')dt'\right\}, \qquad (19)$$

$$P_{\mathrm{AB}}(\rho, t) = 2\mathrm{Re}\left\{\int\limits_{-\infty}^{t} a_0^*(t')S_{\mathrm{AB}}(t')dt'\right\}. \qquad (20)$$

In the solution of Eq. (12), these relations make it possible to directly evaluate the total probabilities of electron detachment without additional integration over the spectra.

The matrix elements $V_{0,\,\varepsilon}$ can be calculated in the dipole approximation since the nuclear distances which make the main contribution to the detachment cross sections are very large. Using the wave functions (3) and (4), we obtain

$$|(r\cos\theta)_{0,\varepsilon}|^2 = \frac{16\gamma k^3 B^2(\gamma,\beta)}{3\pi(\gamma^2+k^2)^4} \times\left[1-\left(\frac{\gamma^2+k^2}{\beta^2+k^2}\right)^2\right]^{-2} \approx \frac{16\gamma k^3 B^2(\gamma,\beta)}{3\pi(\gamma^2+k^2)^4}. \tag{21}$$

The accuracy of the expansion carried out in (21) is determined by the small parameter $(\gamma/\beta)^2 \sim 10^{-2}$ since $k \sim \gamma$. The kernels K of Eq. (12) in this case are given by

$$K_{\mathrm{A,B}}(t,t') = \frac{4B_{a,b}^2}{3\pi|\varepsilon_{a,b}|} \times\frac{\cos[\varphi_R(t)-\varphi_R(t')]}{R^2(t)R^2(t')}F(|\varepsilon_{a,b}|(t-t')), \tag{22}$$

$$K_{\mathrm{AB}}(t,t') = \frac{16B_a^2B_b^2F(|\varepsilon_a|(t-t'))F(|\varepsilon_b|(t-t'))}{3\pi^2|\varepsilon_a\varepsilon_b|} \times\frac{3\cos^2[\varphi_R(t)-\varphi_R(t')]-1}{R^3(t)R^3(t')}, \tag{23}$$

where the spectral function

$$F(x) = \int_0^\infty \frac{y^{3/2}e^{-ixy}dy}{(1+y)^4} \tag{24}$$

is a function of only one variable, which considerably simplifies the procedure of the numerical solution of Eq. (12). This function was calculated numerically.

For large impact parameters $\rho \longrightarrow \infty$, the probabilities of the detachment of one electrons are $P_{\mathrm{A,B}} \sim \rho^{-3}$ so that $P_{\mathrm{A,B}}(\rho)\rho d\rho \sim \rho^{-2}d\rho$. The effective cross sections were determined from the numerical solution of Eq. (12) in the range of impact parameters $0 \le \rho \le \rho_{\max}$, and the contribution from large impact parameters $\rho \ge \rho_{\max}$ was calculated in the approximation of the theory of small perturbations. In the dipole approximation, the contribution from $\rho \ge \rho_{\max}$ is given by

$$\sigma_{\mathrm{A,B}}(\rho_m) = 2\pi\int_{\rho_{\max}}^\infty P_1(\rho)\rho d\rho = \frac{64B_{a,b}^2}{3v^2|\varepsilon_{a,b}|} \times\mathrm{Re}\left\{\int_0^\infty \exp[-iy\Omega(\rho_m)]F(y\Omega(\rho_m))dy\int_0^\infty f(x,y)dx\right\},$$

$$f(x,y) \equiv \frac{1+\left(x+\frac{y}{2}\right)\left(x-\frac{y}{2}\right)+q_+(x,y)q_-(x,y)}{q_+(x,y)q_-(x,y)[q_+(x,y)+q_-(x,y)]^2}, \tag{25}$$

$$q_\pm(x,y) \equiv \sqrt{1+\left(x\pm\frac{y}{2}\right)^2},$$

where v is the relative velocity of the collision.

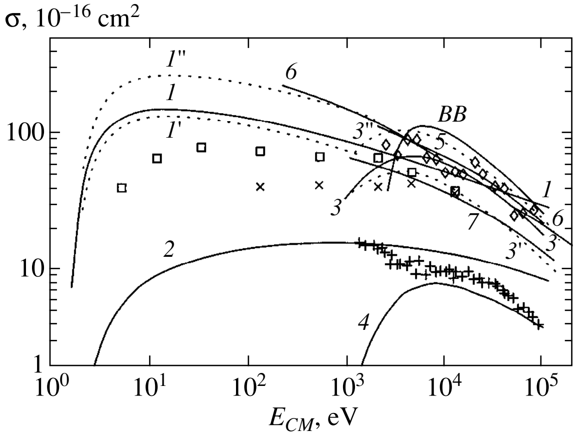

Fig. 1. Cross section of the electron detachment in the $H^- + H^-$ collision as a function of the collision energy E_{CM} in the center-of- mass system: curves *1* and *2* are obtained as a result of calculations in the approximation of the decay with one- and two-electron detachments, respectively; the dotted curves *1'* and *1"* are the cross sections of the electron "squeezing" as a result of collision with an antiproton, $H^- + \bar{p}$, calculated by us earlier [12], and the doubled antiproton cross section, respectively, □ and × are the doubled cross section of the electron detachment from H^- in a collision with an antiproton, classical approximation, the Monte Carlo method [25, 26]; curves *3* and *4* are the cross sections of one- and two electron detachments, respectively, calculated in the dynamic approximation; the dotted curves *3'* and *3"* are the cross section of the electron detachment by the impact of an antiproton, dynamic approximation, and the doubled antiproton cross section, respectively; curve *BB* is the doubled Bethe–Born cross section of the one-electron detachment [12], ◇ and + are the results of the experimental measurements of the one- and two electron detachments, respectively [1, 2, 5]; curves *5* and *6* are the theoretical estimates of the total cross section of the one-electron detachment obtained on the basis the doubled antiproton cross section [5, 24], and curve *7* is the total cross section of the one-electron detachment, calculated in the classical approximation by the Monte Carlo method [1].

The total cross sections of one- and two-electron detachment for high collision velocities, i.e.,

$$\sigma_{\mathrm{A,B,AB}} = 2\pi\int_0^\infty P_{\mathrm{A,B,AB}}(\rho)\rho d\rho,$$

were calculated using the rectilinear trajectories for the $H^- + H^-$ collision. The relative error in the calculation of the total cross section did not exceed 1%. The impact parameter $\rho_{\max}$ was chosen so that the contribution to the cross section from $\rho \ge \rho_{\max}$ was also below 1%. The total cross sections of one- and two-electron detachment are presented in Fig. 1 in comparison with the results of experimental measurements [1, 2, 5]. For a symmetric collision, the total cross section of the detachment of one electron is $\sigma_1 = \sigma_{\mathrm{A}} + \sigma_{\mathrm{B}}$ (σ_{A} is the cross section of electron detachment from the partner of collision H_A^- and σ_B is the cross section of electron detachment from H_B^-), where $\sigma_A = \sigma_B = \sigma_1/2$.

3. SMALL VELOCITIES OF COLLISION. ONE- AND TWO-ELECTRON AUGER DECAYS

For low collision velocities $v \ll 1$, the energy exchange between electrons and nuclei is hardly probable. Although the energy of heavy particles exceeds the total binding energy of weakly bound electrons, the dynamic detachment cross sections are adiabatically small. Figure 1 shows that the limiting energy for the $H^- + H^-$ collision in the center-of-mass system is equal to 2–3 keV. For low energies, however, five channels of Auger decay are open [3], and the electron detachment cross sections remain large ($\sim 10^{-14}$ cm^2) up to the threshold values of energy of the order of 1 eV, for which the cross sections decrease due to the Coulomb repulsion between negative ions.

In order to study Auger decays, we must analyze in detail the behavior of the binding energies of electrons for two negative ions approaching each other. Expansion (1) can be presented in the form

$$\begin{gathered}\frac{1}{r_{12}} = -\frac{1}{R} + \frac{1}{|\mathbf{R}-\mathbf{r}_{1a}|} + \frac{1}{|\mathbf{R}+\mathbf{r}_{2b}|} + W(\mathbf{r}_{1a}, \mathbf{r}_{2b}), \\ r_{1a}, r_{2b} \ll R,\end{gathered} \tag{26}$$

since all the power terms in the first line in expansion (1) coincide with those in the expansion of the interaction between an electron and a negative point charge, $|\mathbf{R} - \mathbf{r}_{1a}|^{-1}$. If we supplement the second line in (1) with term $1/\mathbf{R}$, the line will coincide with the expansion of interaction $|\mathbf{R} + \mathbf{r}_{2b}|^{-1}$. These coincidences follow from the Taylor expansion for the function $r_{12}^{-1}(\mathbf{r}_1, \mathbf{r}_2)$ of several variables. The power series for $W(\mathbf{r}_1, \mathbf{r}_2)$ is presented by mixed derivatives of the Taylor series.

If one of the electrons is removed to a large distance from the system, the following expansions hold:

$$\frac{1}{r_{12}} \approx \frac{1}{|\mathbf{R}-\mathbf{r}_{1a}|} - \frac{\mathbf{r}_{2b}\cdot(\mathbf{R}-\mathbf{r}_{1a})}{|\mathbf{R}-\mathbf{r}_{1a}|^3} + \dots, \quad |\mathbf{R}-\mathbf{r}_{1a}| \gg r_{2b},$$

$$\frac{1}{r_{12}} \approx \frac{1}{|\mathbf{R}+\mathbf{r}_{2b}|} - \frac{\mathbf{r}_{1a}\cdot(\mathbf{R}+\mathbf{r}_{2b})}{|\mathbf{R}+\mathbf{r}_{2b}|^3} + \dots, \quad |\mathbf{R}+\mathbf{r}_{2b}| \gg r_{1a}.$$

The presentation of the electron–electron interaction in the form of expression (26) indicates a certain analogy between the collision of two negative ions and the collision of a negative ion with a structureless negatively charges point particle (electron or antiproton), which was investigated earlier [12, 13]. In particular, a one-electron detachment in the collision between two negative ions is determined by the process of “squeezing” [12] of one electron by the field of the other electron, i.e., by the tunneling of one electron from its own ion through the potential barrier created by the other negative ion. However, in the collision of two negative ions, both electrons are subjected to squeezing, and these processes compete since after the detachment of one weakly bound electron the squeezing of the second electron becomes impossible. Such a competition does not take place, for example, in the collision of a negative ion with an antiproton.

Using expansion (26), we can write the total Hamiltonian of the system in the form

$$\hat{H} = \hat{H}_0 + W(\mathbf{r}_{1a}, \mathbf{r}_{2b}), \quad \hat{H}_0 = \hat{h}_a + \hat{h}_b, \tag{27}$$

where the one-electron Hamiltonians $\hat{h}_a$ and $\hat{h}_b$ are given by

$$\begin{gathered}\hat{h}_a = -\frac{\Delta_1}{2} + U_a(r_{1a}) + \frac{1}{|\mathbf{R}-\mathbf{r}_{1a}|} - \frac{1}{R}, \\ \hat{h}_b = -\frac{\Delta_2}{2} + U_b(r_{2b}) + \frac{1}{|\mathbf{R}+\mathbf{r}_{2b}|}\end{gathered} \tag{28}$$

and $U_{a,b}(r)$ are the energies of the interaction of weakly bound electrons a and b with their atomic residues. The wave equations for these electrons can be written in the form

$$\begin{gathered}\left(-\frac{\Delta_1}{2} + U_a(r_{1a}) + \frac{1}{|\mathbf{R}-\mathbf{r}_{1a}|} - \frac{1}{R} - E_a(R)\right) \\ \times \psi_a^{(-)}(\mathbf{r}_{1a}) = 0,\end{gathered} \tag{29}$$

$$\left(-\frac{\Delta_2}{2} + U_b(r_{2b}) + \frac{1}{|\mathbf{R}+\mathbf{r}_{2b}|} - E_b(R)\right)\psi_b^{(-)}(\mathbf{r}_{2b}) = 0 \tag{30}$$

and their energies can be presented as

$$\begin{gathered}E_a(R) \approx \varepsilon_a - \frac{\alpha_a}{2R^4} + \dots, \\ E_b(R) \approx \varepsilon_b + \frac{1}{R} - \frac{\alpha_b}{2R^4} + \dots,\end{gathered} \tag{31}$$

where $\alpha_{a,b}$ are the polarizabilities of negative ions.

The terms $-1/R$ can be attributed to either Hamiltonian $\hat{h}_a$ or Hamiltonian $\hat{h}_b$. In Eqs. (28)–(30), this term is attributed to $\hat{h}_a$. In this case, electron b possesses the excess energy $1/R$, and the change in the energy of electron a is small and can be neglected. The absolute value of $1/R$ is of the order of or greater than $|\varepsilon_{a,b}|$, and the electric field, which is of the order of $1/R^2$, is small and can be neglected. The energy $E_b(R)$ of electron b lies in the continuum for nuclear spacings $R \le R_b \equiv 1/|\varepsilon_b|$, and this electron can tunnel from ion B away from ion A. This process was investigated earlier [12] for the collision of H^- with an electron treated as a classical point particle. In contrast to the collision between a negative ion and a structureless negatively charged particle, the following two-electron process is possible for the collision of two negative ions. Electron b may transfer its excess energy $1/R$ to electron a, after which electron a will go to the continuum if $R \leq R_a \equiv 1/|\varepsilon_a|$. In these peculiar Auger processes which will be described in detail below, only one electron is detached, while the other electron remains bound to the negative ion.

If $R \leq R_{ab} \equiv |\varepsilon_a + \varepsilon_b|^{-1}$, the Auger decay with the emission of two electrons is possible from the point of view of energy. The rate of this decay is determined by the square of the matrix element of the correlation interaction W (see below).

If term $-1/R$ is added to Hamiltonian $\hat{h}_b$, we obtain an alternative representation equivalent to the previous one after the change in indices $a \longleftrightarrow b$. In order to obtain a complete description of the system, both representations should be analyzed. We will consider in detail only representation (28)–(30) since the results for the alternative representation can be written analogously.

In both representations, the total energy of the system is given by

$$E(R) = E_a(R) + E_b(R) = \varepsilon_a + \varepsilon_b + \frac{1}{R}. \tag{32}$$

The polarization terms are small and will be neglected. Melchert *et al.* [3] thoroughly investigated the change in the total energy $E(R)$ in the approximation of the δ-potential model [14] using the Coulomb Green's function [15, 16]. It was proved that the total energy obeys relation (32) after the intersection of the continuum boundary also.

The zeroth-order term $1/R$ of the electron–electron repulsion can be formally divided into two, say, equal parts, and each half can be ascribed to different electrons. In other words, instead of formulas (31), we can formally write the one-electron energies, for example, in the form

$$E_a(R) \approx \varepsilon_a + 1/2R, \quad E_b(R) \approx \varepsilon_b + 1/2R.$$

However, in this case we obtain incorrect values of the nuclear spacing for which the one-electron detachment channels are open. It follows from relations (31) and (32) that the detachment of the electron from ion a becomes possible for $R \leq |\varepsilon_a|^{-1}$, while the above formulas for $E_{a,b}(R)$ imply that this occurs at a half as large distance $R \leq |2\varepsilon_a|^{-1}$.

The rates of all the Auger decays listed above were calculated on the basis of the Fano method [17], which was also used in our earlier works [12, 18–20] (see also [21, 22]).

Distances R_a, R_b, and R_{ab} are very large since the binding energies for negative ions are very small. For example, for the $H^- + H^-$ collision, the distances are $R_a = R_b \approx 36a_0$ and $R_{ab} \approx 18a_0$. For this reason, the effective electron detachment cross sections determined by the above-mentioned Auger decays are very large ($\sim 10^{-14}$ cm^2).

3.1. "Squeezing" Process

If $R < R_b$, the energy of electron b lies in the continuum ($E_b = \varepsilon_b + 1/R > 0$), and electron b can tunnel through the potential barrier, thus going over to the continuum. The same is valid for electron a for $R < R_a$. The rate $\Gamma_{\rm sq}$ of tunneling through the barrier calculated in [12] is given by

$$\Gamma_{{\rm sq},\,(a,\,b)}(R) = \frac{B_{a,\,b}^2}{2\gamma_{a,\,b}R^2}\exp\left[-\frac{4}{\gamma_{a,\,b}}y f(y)\right],$$
$$f(y) \equiv \frac{\arcsin\sqrt{y}}{\sqrt{y(1-y)}} - 1, \quad y \equiv \frac{R}{R_{a,\,b}} \leq 1, \tag{33}$$
$$R_{a,\,b} \equiv \frac{1}{|\varepsilon_{a,\,b}|}.$$

The rate of decay $\Gamma_{{\rm sq},\,(a,\,b)}(R) \equiv 0$ for $R \geq R_{a,\,b}$ since the energy of a "tunneling" electron at such distances is negative ($E_{a,\,b}(R) < 0$) and the tunneling is ruled out. If electron a (or b) tunnels for $R \leq R_{a,\,b}$, electron b (or a) cannot tunnel to the continuum since there is no Coulomb repulsion in system $A + B^-$ (or $A^- + B$). The simultaneous tunneling of the two electrons is also impossible since, in accordance with formula (31), the energy of only one electron can acquire positive values.

Formula (33) is valid for large separations between the ions, which satisfy the condition [12]

$$\gamma R > 1. \tag{34}$$

In [3], formula (33) was derived in the δ-potential approximation using the Coulomb Green's function [15, 16] written in the semiclassical approximation.

3.2. One-Electron Auger Decay

If it is electron b that possesses the excess energy $1/R$, it can transfer it to electron a, which will go to the continuum for $R \leq R_a$. Electron b in this case remains in the bound state so that this process is a one-electron Auger decay. The rate of this decay is determined by the matrix element of the correlation interaction $W(\mathbf{r}_{1a}, \mathbf{r}_{2b})$. If we calculate this matrix element using the unperturbed wave function of electron b, this matrix element is equal to zero since the state of electron b remains unchanged. Actually, the wave functions of electron b before and after the decay are different. Before the decay, the state of electron b is perturbed by the electron–electron repulsion, and its wave function is polarized. After the decay, this electron is perturbed by the neutral atom A; the perturbation is much weaker than the Coulomb repulsion and can be neglected. The matrix element of the correlation interaction W calculated with such wave functions of electron b differs from zero. Thus, we must determine the wave function of electron b, which is polarized in the initial state due to the interaction with electron a.

The perturbed orbit $\psi_b^{(-)}(\mathbf{r}_{2b})$ is the solution of the wave equation (30). For large values of R, this equation can be written in the form

$$\left(-\frac{\Delta}{2} + U_b(r_{2b}) + \frac{r_{2b}\cos\theta}{R^2} - \varepsilon_b\right)\psi_b^{(-)}(\mathbf{r}_{2b}) = 0 \tag{35}$$

and solved by using the theory of small perturbations ($\psi_b^{(-)} = \psi_{b0}^{(-)} + \delta\psi_b^{(-)} + \ldots$):

$$\left(-\frac{\Delta}{2} + U_b(r_{2b}) - \varepsilon_b\right)\psi_{b0}^{(-)} = 0, \tag{36}$$

$$\begin{gathered}\left(-\frac{\Delta}{2} + U_b(r_{2b}) - \varepsilon_b\right)\delta\psi_b^{(-)}(\mathbf{r}_{2b}) \\ = -\frac{r_{2b}\cos\theta}{R^2}\psi_{b0}^{(-)},\end{gathered} \tag{37}$$

where the unperturbed orbit $\psi_{b0}^{(-)}$ is specified by expression (3). The exact solution of Eq. (37) with the corresponding boundary conditions is given by

$$\psi_b^{(-)} = \psi_{b0}^{(-)}(r_{2b})\left[1 - \frac{r_{2b}^2\cos\theta}{2\gamma_b R^2} + O\left(\frac{r_{2b}^3}{R^3}\right)\right]. \tag{38}$$

Substituting Eq. (38) into Eq. (37), we can verify directly that Eq. (38) is indeed the exact solution of this equation.

After the calculation of the dipole matrix elements, the two-electron matrix element of the one-electron Auger decay, i.e.,

$$\begin{gathered}W_{if} = \langle\psi_{a0}^{(-)}(\mathbf{r}_{1a})\psi_{b0}^{(-)}(\mathbf{r}_{2b})| \\ \times|W(\mathbf{r}_{1a}, \mathbf{r}_{2b})|\psi_a^{\varepsilon}(\mathbf{r}_{1a})\psi_b^{(-)}(\mathbf{r}_{2b})\rangle,\end{gathered} \tag{39}$$

has the form

$$W_{if} = \frac{1}{\gamma_a\sqrt{3\pi}}\frac{(k/\gamma_a)^{3/2}}{(1 + (k/\gamma_a)^2)^2}\frac{1}{(\gamma_a R)^5}. \tag{40}$$

Using the energy conservation law

$$\frac{k^2}{\gamma_a^2} = \frac{R_a}{R} - 1, \quad R_a \equiv \frac{1}{|\varepsilon_a|}, \tag{41}$$

we obtain the rate Γ_{1ab} of the one-electron Auger decay with the detachment of an electron from the negative ion A^- by the negative ion B^-:

$$\begin{gathered}\Gamma_{1ab}(R) = 2\pi|W_{if}|^2 = \frac{\gamma_a^8 B_a^2 B_b^4}{6\sqrt{2}}\left(\frac{\gamma_a}{\gamma_b}\right)^4\frac{(1-x)^{3/2}}{(2x)^{15/2}}, \\ x \equiv \frac{R}{R_a} < 1.\end{gathered} \tag{42}$$

Similarly, the rate $\Gamma_{1,\,ba}$ of the one-electron Auger decay with the detachment of an electron from the negative ion B^- by the negative ion A^- is given by

$$\begin{gathered}\Gamma_{1,\,ba}(R) = \frac{\gamma_b^8 B_a^4 B_b^2}{6\sqrt{2}}\left(\frac{\gamma_b}{\gamma_a}\right)^4\frac{(1-y)^{3/2}}{(2y)^{15/2}}, \\ y \equiv \frac{R}{R_b} < 1, \quad R_b \equiv \frac{1}{|\varepsilon_b|}.\end{gathered} \tag{43}$$

3.3. Two-Electron Auger Decay

The rate $\Gamma_{AB}(R)$ of the two-electron Auger decay can be calculated using the unperturbed wave functions of the initial state of the system formed by two negative ions:

$$\begin{gathered}\Gamma_{ab}(R) = 2\pi \\ \times\sum_m\left|\langle\psi_{a0}^{(-)}(\mathbf{r}_{1a})\psi_{b0}^{(-)}(\mathbf{r}_{2b})|W(\mathbf{r}_{1a}, \mathbf{r}_{2b})|\psi_a^{\varepsilon}(\mathbf{r}_{1a})\psi_b^{\varepsilon'}(\mathbf{r}_{2b})\rangle\right|^2.\end{gathered} \tag{44}$$

As a result, we obtain the partial width

$$\begin{gathered}\Gamma_{ab}(R, k_a, k_b) = \frac{2^{10}\gamma_a\gamma_b B_a^2 B_b^2}{3\pi R^6} \\ \times\frac{k_a^3 k_b^3}{(\gamma_a^2 + k_a^2)^4(\gamma_b^2 + k_b^2)^4}\end{gathered} \tag{45}$$

of the decay leading to the formation of a pair of free electrons whose momenta k_a and k_b are related through the energy conservation law:

$$k_a^2 + k_b^2 = 2\left(\frac{1}{R} - |\varepsilon_a + \varepsilon_b|\right).$$

After the integration over the electron momentum, we obtain the total rate of the two-electron Auger decay:

$$\begin{gathered}\Gamma_{ab}(R) = \frac{2^{10}\gamma_a\gamma_b B_a^2 B_b^2}{3\pi R_{ab}^2}\frac{(1-x)^4}{x^2} \\ \times\int_0^1\frac{(1-t^2)^{3/2}dt}{[1-(1-x)^2t^2]^4}, \\ R_{ab} \equiv \frac{1}{|\varepsilon_a + \varepsilon_b|}, \quad x \equiv \frac{R}{R_{ab}} < 1.\end{gathered} \tag{46}$$

The rates of all Auger decays are presented in Fig. 2 as functions of the nuclear spacing R for the $H^- + Cs^-$ collision. The squeezing rate $\Gamma_{sq}(R)$ has the maximum value in the range of distances 2 to $3 \le R \le 35$, which make the main contribution to the one-electron detachment cross section for energies of collision that are not very low. However, the squeezing rate is an exponentially decreasing function of R; at a distance $R > 25$ to 35, it becomes smaller than the rate Γ_1 of the one-electron Auger decay, which is a power function of R. As a result, for small collision energies close to the threshold value, the one-electron decay is determined by the one-electron Auger decay, i.e., by the quantity Γ_1. Such a behavior of the decay rates and the electron detachment cross sections is observed for all the three collisions under investigation: $H^- + H^-$, $H^- + Cs^-$, and $Cs^- + Cs^-$.

3.4. Probabilities and Cross Sections for a Multichannel Decay

The initial state of the system formed by two negative ions $A^- + B^-$ may decay through five different channels with the formation of three different final states: (A), (B), and (AB). The probabilities of such a decay must be calculated using the multichannel scheme. Let $P_0(\rho, t)$ be the probability of finding the system in the initial state at the instant of time t for a collision with the impact parameter ρ and $\Gamma_{\text{tot}}(R(t))$ be the total probability of the decay via all the channels; in this case,

$$P_0(\rho, t) = \exp\left[-\int_{-\infty}^{t} \Gamma_{\text{tot}}(R(t'))dt'\right], \qquad (47)$$

$$P_0(\rho) \equiv P_0(\rho, t = +\infty).$$

The probability of the decay through the ith channel is given by

$$P_i(\rho) = \int_{-\infty}^{\infty} P_0(\rho, t)\Gamma_i(R(t))dt$$
$$= \int_{-\infty}^{\infty} \Gamma_i(R(t))\exp\left[-\int_{-\infty}^{t} \Gamma_{\text{tot}}(R(t'))dt'\right]dt, \qquad (48)$$

where $\Gamma_i(R(t))$ is the rate of the decay via the ith channel and

$$\Gamma_{\text{tot}} = \sum_i \Gamma_i$$
$$= \Gamma_{\text{sq},a} + \Gamma_{\text{sq},b} + \Gamma_{1,ab} + \Gamma_{1,ba} + \Gamma_{ab}. \qquad (49)$$

The cross sections σ_A and σ_B of one-electron detachments from ions A^- and B^-, respectively,

$$\sigma_A = 2\pi\int_0^{\infty}(P_{\text{sq},a}(\rho) + P_{1,ab}(\rho))\rho d\rho,$$
$$\sigma_B = 2\pi\int_0^{\infty}(P_{\text{sq},b}(\rho) + P_{1,ba}(\rho))\rho d\rho, \qquad (50)$$

and the cross section σ_{AB} of the two-electron detachment,

$$\sigma_{AB} = 2\pi\int_0^{\infty} P_{ab}(\rho)\rho d\rho, \qquad (51)$$

were calculated using the Coulomb trajectories $R(t)$, which made it possible to correctly reproduce the behavior of the cross sections in the vicinity of energy thresholds, which is determined by the repulsion between ions A^- and B^-.

The cross sections of electron detachments in collisions $H^- + H^-$, $H^- + Cs^-$, and $Cs^- + Cs^-$ are shown in Figs. 1, 3, and 4. A comparison with the results of experimental measurements is carried out in Fig. 1 only for the $H^- + H^-$ collision since the experimental results for the collisions between other ions are not available. The total cross sections of one-electron detachments in the collisions of like ions, $H^- + H^-$ and $Cs^- + Cs^-$, presented in Figs. 1 and 4, are given by

$$\sigma_1 \equiv \sigma_A + \sigma_B = 2\pi$$
$$\times\int_0^{\infty}(P_{\text{sq},a}(\rho) + P_{\text{sq},b}(\rho) + P_{1,ab}(\rho) + P_{1,ba}(\rho))\rho d\rho, \qquad (52)$$

while the cross sections of the electron detachment from each partner in a collision are equal to half the total cross section.

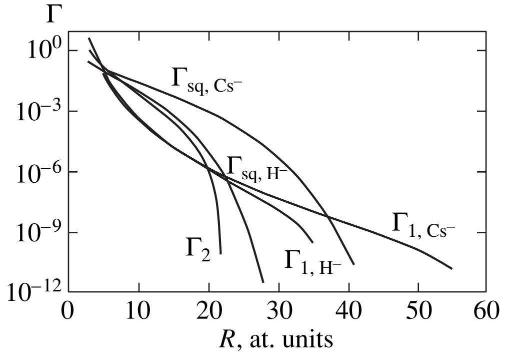

Fig. 2. Partial decay rates as functions of the nuclear spacing R for the $H^- + Cs^-$ collision: $\Gamma_{\text{sq, H}^-}$ and $\Gamma_{\text{sq, Cs}^-}$ are the rates of the electron squeezing from H^- and Cs^-, respectively, formula (33); $\Gamma_{1,\text{ H}^-}$ and $\Gamma_{1,\text{ Cs}^-}$ are the rates of the one-electron Auger decays with the electron detachment from H^- and Cs^-, respectively, formulas (42) and (43); Γ_2 is the rate of the two-electron Auger decay, formula (46).

4. RESULTS AND CONCLUSIONS

Equation (12) was solved numerically by the finite-difference method. The fifth-order recurrence relation used by us has the form

$$a_0(t_{i+1}) = a_0(t_i) + dt\left[\frac{103}{60}S(t_i) - \frac{119}{120}S(t_{i-1}) + \frac{41}{120}S(t_{i-2}) - \frac{3}{40}S(t_{i-3}) + \frac{1}{120}S(t_{i-4})\right],$$

where $S(t_i)$ is the write-hand side of Eq. (12):

$$S(t_i) \equiv S_A(t_i) + S_B(t_i) + S_{AB}(t_i).$$

These quantities were evaluated by integrating between $t = -\infty$ and t_i so that double integration was carried out for each trajectory. The stability of the computational algorithm was controlled by the equality to unity of the total probability:

$$1 = |a_0|^2 + P_A + P_B + P_{AB}.$$

The relative computational error was of the order 10^{-3}–10^{-4}.

Figure 1 shows the cross sections of one- and two-electron detachments for the $H^- + H^-$ collision in the collision energy range from the threshold values to 100 keV in comparison with the results of experimental measurements [1, 2, 5] made in the high-energy range (1–100 keV). The one-electron detachment cross section calculated by us in the dynamic approximation is on the average in good agreement with the results of experimental measurements, although a large spread of experimental points is worth noting. The calculated cross section for the two-electron detachment is 15–20% smaller than the experimental value. This discrepancy can be attributed to the contribution of reaction $H^- + H \longrightarrow H + H + e$ to the experimentally observed cross section [5], which was disregarded in our calculations. This reaction, which was theoretically investigated for the first time in [23], occurs after the one-electron detachment and leads to the detachment of two electrons. Both cross sections of the dynamic detachment calculated by us decrease exponentially for adiabatically low energies of collisions (≤2–3 keV).

Figure 2 depicts the rates of decay through all possible channels as functions of the nuclear spacing for the $H^- + Cs^-$ collision. The rates of squeezing in the range of distances $5 \le R \le (22–37)a_0$ have the highest values, the rate of squeezing of an electron from Cs^- being the largest since the binding energy for the Cs^- ion (0.4716 eV) is almost half as large as the binding of the H^- ion (0.75421 eV). The detachment of an electron from the Cs^- ion becomes possible at a distance $R \le R_{1, Cs^-} = 57.70a_0$, while the threshold distance for the H^- ion is $R \le R_{1, H^-} = 36.08a_0$. A two-electron decay is possible in such a collision at distances $R \le R_2 = 22.20a_0$, the main contribution to the two-electron decay cross section coming from distances $5 \le R \le 20a_0$. The rate of squeezing decreases exponentially upon an increase in the distance to R_{sq}, and hence the rate of the one-electron Auger decay, which decreases at a lower rate with increasing R, becomes larger than the squeezing rate at distances close to R_{sq} ($R \sim R_{sq}$).

The rates of Auger decays depicted in Fig. 2 were used by us for calculating the electron detachment cross sections for slow $H^- + H^-$ collisions. Curve *1* in Fig. 1 corresponds to the total cross section of a one-electron detachment, while curve *2* describes the cross section of a two-electron detachment. The cross section of a one-electron detachment was estimated in [5, 24] on the basis of the assumption that the total cross section of a one-electron detachment is twice as large as the cross section of the electron detachment from H^- by the impact of an antiproton, which was calculated in [25, 26], where the weakly bound electrons of both ions were treated as classical particles. Neither of these simplifying assumptions was used in our calculations and, hence, it would be interesting to compare the total cross section of the one-electron detachment obtained by us with the cross section of the electron detachment from H^- by the impact of an antiproton. Curve *1*' in Fig. 1 is the cross section of the electron detachment from H^- for small velocities of the collision with the antiproton. In this collision, the electron detachment at low collision velocities, $v < v_0$, is possible only as a result of squeezing, while at high velocities, a dynamic detachment takes place. For this reason, the cross section for small values of v was calculated by using formula (50) in which only one decay channel (squeezing of the electron from H^- by the field of the antiproton) was present, i.e., when only $\Gamma_{sq, H^-} \ne 0$, and the decay rates for all other channels were put equal to zero. Curve *1*'' in Fig.1 describes the doubled cross section *1*'. The dotted curve *3*' is also the cross section of the electron detachment from H^- by the impact of an antiproton, which was calculated by us earlier for large values of v in the dynamic approximation while solving Eq. (12), where we put $S_A \ne 0$ and $S_B = S_{AB} = 0$. The dotted curve *3*'' in Fig. 1 is the doubled cross section *3*'. These results indicate that when the collision energy $E_{CM} \le 10$ keV, the cross section of the electron detachment from H^- by the impact of an antiproton is very close to the total cross section one the one-electron detachment in the $H^- + H^-$ collision, and the doubled antiproton cross section is approximately twice as large as the latter value. The doubled antiproton cross section *3*'' in Fig. 1 approaches the cross section *3* only for high energies $E_{CM} \ge 100$ keV.

The results of the comparison can easily be interpreted. In the collision between two negative ions, the detachment of the electron from one of the ions, e.g., H_A^-, competes with the detachment of the electron from the other ion, H_B^-. The electron detachment from the H_A^- ion as a result of the Coulomb repulsion from the H_B^- ion is possible only as long as ion B is intact. If the electron of ion H_B^- has been detached, the detachment of the electron from ion H_A^- is possible only as a result of a weaker interaction with the neutral atom H_B. Consequently, the probability of the electron detachment from H_A^- should be estimated as product $P_A(1 - P_B)$, where $1 - P_B$ is the probability of ion B being undamaged. The total probability on the one-electron detachment in this case is $P_A(1 - P_B) + P_B(1 - P_A)$. For high collision energies, the main contribution to the detachment cross section comes from collisions with large impact parameters, when the detachment probabilities are low, $P_{A,B} \ll 1$. In this case, $1 - P_{A,B} \approx 1$, the total probability of the one-electron detachment is of the order of $P_A + P_B$, and the total cross section is of the order of $\sigma_A + \sigma_B$. For energies $E_{CM} \le 10$ keV, the probabilities $P_{A,B}$ of the electron detachment strongly depend on the impact parameter ρ. For large values of $\rho \gg 1$, these probabilities are close to zero, and in a small region δρ, they increase from zero to unity, remaining close to unity for smaller values of ρ. With such a behavior of the probabilities, the sum $P_A + P_B \approx 2$ in the main region of variation of ρ and, hence, the probabilities as well as cross sections cannot be summed. The detachment of an electron from ion A strongly competes with the detachment from ion B, and the total cross section of a one-electron detachment is close to the single cross section *1*' of the detachment by an antiproton rather than to the doubled cross section *1*" (see Fig. 1).

An analytic expression for the cross section of the ionization of H^- by an electron was obtained in [12] using the Bethe–Born approximation. In order to compare this formula with the results of our present calculations of the total cross section of the one-electron detachment in the $H^- + H^-$ collision, we must consider the doubled Bethe–Born cross section which, in accordance with [12], is given by

$$\sigma^{(1)}_{H^- + H^-} = 2\sigma_{e + H^-} = \frac{4\pi}{3}\frac{B^2 a_0^2}{|\varepsilon_0| v^2}\ln\frac{1.55 v^2}{\gamma B}, \qquad (53)$$
$$a_0^2 = 2.8003 \times 10^{-17}\ \text{cm}^2.$$

The cross section (53) is shown in Fig. 1 (curve *BB*). While calculating this cross section, we used the value $B = 1.145$ instead of the previous value $B = \sqrt{2.65} = 1.628$ [12]. It can be seen from the figure that even for a collision energy close to 100 keV, the Bethe–Born cross section (53) is larger than the cross section obtained by us here approximately by a factor of 1.5. In the peak region, the Bethe–Born cross section is twice as large as that calculated in the present work (curve *1*). The difference can be explained by the fact that the time-dependent problem in the Bethe–Born approximation is solved using the theory of small perturbations. In our calculations, however, we solved the time-dependent equation (12) exactly, without using any approximation. It should also be noted that formula (53) disregards the above competition between the detachments of electrons from each of the ions and holds only for very high energies of collisions, when the main contribution to the cross section comes from the region of large impact parameters, for which the detachment probability is much smaller than unity.

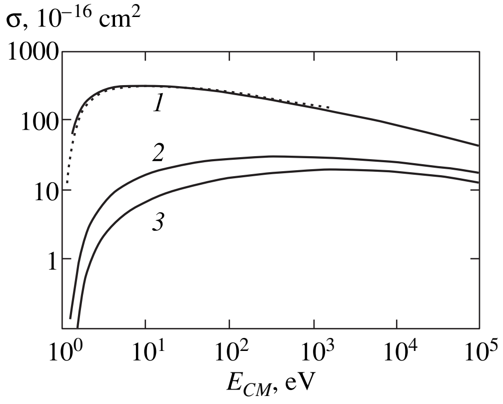

Fig. 3. Cross sections of one- and two-electron detachments calculated in the decay approximation for the $H^- + Cs^-$ collision: curves *1* and *2* are the cross sections of the electron detachment from Cs^- and H^-, respectively; the dotted curve corresponds to the cross section of the electron detachment as a result of a collision with an antiproton, $Cs^- + \bar{p} = Cs + \bar{p} + e$; curve *3* is the detachment cross sections for both weakly bound electrons, $H^- + Cs^- = H + Cs + 2e$.

For collisions of heavy particles, the Born approximation is applicable for energies differing considerably from the reaction threshold due to the presence of the logarithm in formula (53) (see Fig. 1), while for collisions with an electron, this approximation is applicable for energies whose values are closer to the threshold [12]. For collisions between two different negative ions, $A^- + B^-$, the electron detachment from one ion strongly competes with the detachment from the other ion, the ratio of the probabilities of the electron detachment from the ions depending on the ratio of their binding energies. If the binding energy for ion A^- is higher than the binding energy for ion B^-, the detachment from B^- is more probable than from A^-, the electron detachment cross section from B^- being close to the cross section of the detachment by an antiproton, while the cross section of disintegration of A^- is considerably lower than the corresponding antiproton cross section. Figure 3 presents the cross sections of the electron detachment in the $H^- + Cs^-$ collisions calculated by us. The cross

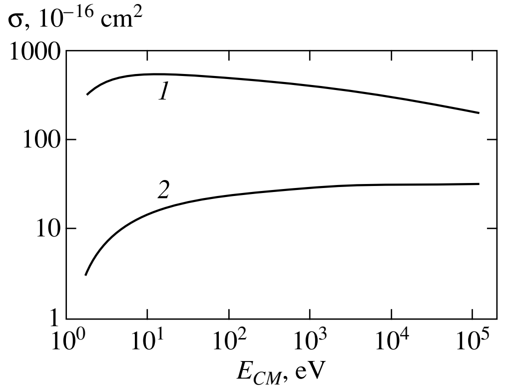

Fig. 4. Cross sections of one- and two-electron detachments calculated in the decay approximation for the $Cs_a^- + Cs_b^-$ collision: curve *1* is the total cross section of the one-electron detachment with the formation of systems $Cs_a + e + Cs_b^-$ or $Cs_a^- + Cs_b + e$; curve *2* is the cross section of the detachment of two electrons, $Cs^- + Cs^- = 2Cs + 2e$.

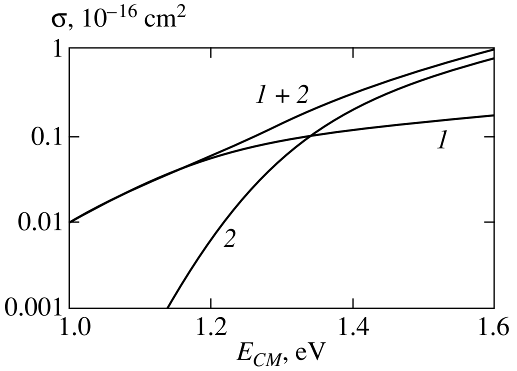

Fig. 5. Cross section of the electron detachment from H^- in collision $H^- + Cs^- = H + Cs^- + e$ in the region of threshold energies: curve *1* is the cross section of the one-electron decay of the H^- ion; curve *2* is the cross section of the electron squeezing from H^-, curve *1* + *2* is the sum of cross sections *1* and *2*.

section of the electron detachment from Cs^- (curve *1*) is very close to the cross section of the destruction of the Cs^- ion by an antiproton (dotted curve). At the same time, the cross section of the disintegration of H^- (curve *2*) is approximately half as large as the cross section of the electron detachment from one of the partners of the $H^- + H^-$ collision (see Fig. 1).

Figure 4 shows the cross sections calculated by us for the $Cs^- + Cs^-$ collision. A comparison of Figs. 1 and 4 readily shows that the ratio of the total cross sections of the one-electron detachment (curves *1* in these figures) is inversely proportional to approximately the square of the ratio of the binding energies for the negative ions. On the contrary, the cross section of the detachment of two electrons (curves *2* in Figs. 1 and 4) increases very slowly upon a decrease in the energy of the colliding ions; this is valid for slow (Auger decays) as well as rapid (dynamic detachment) collisions.

A new type of Auger decay, i.e., the one-electron Auger decay, whose rate $\Gamma_1(R)$ is approximately two orders of magnitude smaller than the rate of squeezing $\Gamma_{sq}(R)$ for nuclear spacings $R = 10–20$ (see Fig. 2), was considered in Subsection 3.2. This route of the decay is insignificant for high collision energies far from the energy threshold. However, it was mentioned above that the rate of the one-electron decay decreases upon an increase in the distance R between the ions at a much lower rate than the rate of squeezing. For collision energies close to the threshold, the colliding ions do not approach each other to a distance at which squeezing dominates because of the Coulomb repulsion, and the one-electron detachment is determined by the one-electron Auger decay. Figure 5 shows the cross section of the electron detachment from H^- in the range of threshold energies of collisions with Cs^-. The contribution to this cross section comes from the squeezing processes (curve *2*) and from the one-electron Auger decay (curve *1*). For energy $E_{CM} = 1.35$ eV, these contributions are equal (see Fig. 5). For lower energies $E_{CM} >$ 1.35 eV, the one-electron Auger decay dominates. The total cross section (curve *1* + *2*) changes its functional dependence on the collision energy in the vicinity of $E_{CM} = 1.35$ eV. This singularity in the behavior of the cross section can be investigated experimentally by the method of combined beams. It should also be noted that the dipole expansion of the electron–electron interaction used by us here is especially accurate since the negative ions do not approach each other to small distances for threshold energies, and the behavior of the cross section reproduced in Fig. 5 is also quite correct.

ACKNOWLEDGMENT

This work was supported by the Russian Foundation for Basic Research (project no. 96-15-96815) in accordance with the program supporting leading scientific schools.

REFERENCES

1. R. Schulze, F. Melchert, M. Hagman, *et al.*, J. Phys. B **24**, L7–L12 (1991).
2. M. Benner, S. Krüdener, F. Melchert, *et al.*, in *Tätigkeitsbericht – Strahlenzentrum Justus Liebig–Universität Giessen, Kernphysik* (Strahlenzentrum Justus Liebig–Universität Giessen, Giessen, 1991), p. 46.
3. F. Melchert, R. Schulze, S. Krüdener, *et al.*, J. Phys. B **28**, 3299 (1995).
4. M. I. Chibisov and Yu. N. Yavlinskiĭ, Preprint IAÉ-5738/6 (Moscow, 1994).
5. O. Busic, N. Grün, and W. Scheid, J. Phys. B **31**, 2659 (1998).

6. B. M. Smirnov, *Negative Ions* (Atomizdat, Moscow, 1978).
7. M. Chibisov, F. Brouillard, J. P. Chenu, *et al.*, J. Phys. B **30**, 991 (1997).
8. M. I. Chibisov, R. K. Janev, F. Brouillard, *et al.*, J. Phys. B **31**, 2795 (1998).
9. A. A. Radtsig and B. M. Smirnov, *Reference Data on Atoms, Molecules, and Ions* (Énergoatomizdat, Moscow, 1986; Springer-Verlag, Berlin, 1985).
10. S. Chandrasekhar, Astrophys. J. **100**, 176 (1944).
11. V. P. Zhdanov and M. I. Chibisov, Dokl. Akad. Nauk SSSR **226**, 1055 (1976) [Sov. Phys. Dokl. **21**, 94 (1976)].
12. B. M. Smirnov and M. I. Chibisov, Zh. Éksp. Teor. Fiz. **49**, 841 (1965) [Sov. Phys. JETP **22**, 585 (1966)].
13. E. A. Solov’ev, Zh. Éksp. Teor. Fiz. **72**, 2072 (1977) [Sov. Phys. JETP **45**, 1089 (1977)].
14. Yu. N. Demkov and V. N. Ostrovskii, *Zero-Range Potentials and Their Applications in Atomic Physics* (Leningr. Gos. Univ., Leningrad, 1975; Plenum, New York, 1988).
15. L. Hostler and R. H. Pratt, Phys. Rev. Lett. **10**, 469 (1963).
16. L. Hostler, J. Math. Phys. **5**, 591 (1964).
17. U. Fano, Phys. Rev. **124**, 1866 (1961).
18. B. M. Smirnov and O. B. Firsov, Pis’ma Zh. Éksp. Teor. Fiz. **2**, 478 (1965) [JETP Lett. **2**, 297 (1965)].
19. V. P. Zhdanov and M. I. Chibisov, Zh. Éksp. Teor. Fiz. **70**, 2087 (1976) [Sov. Phys. JETP **43**, 1089 (1976)].
20. V. P. Zhdanov and M. I. Chibisov, Opt. Spektrosk. **41**, 521 (1976) [Opt. Spectrosc. **41**, 307 (1976)].
21. W. H. Miller and H. Morgner, J. Chem. Phys. **67**, 4923 (1977).
22. A. Naji, K. Olamba, J. P. Chenu, *et al.*, J. Phys. B **31**, 2961 (1998).
23. B. M. Smirnov and O. B. Firsov, Zh. Éksp. Teor. Fiz. **47**, 232 (1964) [Sov. Phys. JETP **20**, 156 (1964)].
24. V. N. Ostrovskii and K. Taulbjerg, J. Phys. B **29**, 2573 (1996).
25. G. Fiorentini and R. Tripiccioni, Phys. Rev. A **27**, 737 (1983).
26. J. S. Cohen and G. Fiorentini, Phys. Rev. A **33**, 1590 (1986).

Translated by N. Wadhwa

Journal of Experimental and Theoretical Physics, Vol. 92, No. 3, 2001, pp. 412–419.
Translated from Zhurnal Éksperimental'noĭ i Teoreticheskoĭ Fiziki, Vol. 119, No. 3, 2001, pp. 476–484.
Original Russian Text Copyright © 2001 by Novikov, Senashenko.

ATOMS,
SPECTRA, RADIATION

Excitation of Autoionization Resonances in Collisions of Helium Atoms with Fast Ions

N. V. Novikov[a], * and V. S. Senashenko[b], **

[a] Nuclear Safety Institute, Russian Academy of Sciences, B. Tul'skaya ul. 52, Moscow, 113191 Russia
[b] Skobel'tsyn Research Institute of Nuclear Physics, Moscow State University,
Vorob'evy gory, Moscow, 119899 Russia
*e-mail: mit@ibrae.ac.ru
**e-mail: nrsenat@nrsenat.phys.msk.su

Received October 17, 2000

Abstract—A theoretical model of collisions between fast ions and atoms is proposed which describes the effect of projectiles on the excitation of autoionization resonances. The model takes into account the change in the binding energy of electrons in a target atom induced by the field of a projectile, the effect of the field of the atom on the kinematics of the ion scattering, as well as the effect of the intermediate $(1snl)^1L$ states on the two-electron excitation mechanism. The charge dependence of the excitation cross section of the $(2s^2)^1S$ and $(2s2p)^1P$ resonances is found to be weaker than in the first order of the perturbation theory and is in qualitative agreement with experimental data. The reasons for the emergence of such a charge dependence are analyzed. © *2001 MAIK "Nauka/Interperiodica".*

1. INTRODUCTION

The description of the scattering of structureless ions from atoms is a fundamental problem in the physics of collisions [1]. In the case of many-electron processes (whose simplest examples are the excitation and decay of autoionization resonances of the helium atom), not only the interaction between a projectile and an atom must be correctly taken into consideration, but also the electron correlations must be taken into account.

At the present time, the two-electron excitation by structureless and partially ionized ions at high and intermediate energies of collision has been experimentally investigated by many authors [2–7]. In these experiments, the profile of autoionization resonances as a function of the electron ejection angle and of the charge and velocity of the projectile was determined along with the parameters of the yield [2–4] and asymmetry [2, 4] of autoionization resonances averaged over the angles of electron ejection. It was found that upon an increase in the charge Z_p of the projectile, the yields of resonances $(2s^2)^1S$ and $(2s2p)^1P$ integrated over the ejection angles increase very slowly ($Y(Z_p) \sim Z_p^n$, $n < 2$) [2], while the averaged yield of the $(2s^2)^1S$ resonance may even decrease upon an increase in the charge of the projectile, $n < 0$ [4]. Such a weak dependence of the differential and total cross sections of the excitation of autoionization resonances on the charge of the projectile is not a specific feature of two-electron excitation. Similar dependences for total cross sections were also observed in the processes with the single ionization [8] and the one-electron excitation of an atom [9, 10] in collisions with various ions.

In order to explain the saturation of the charge dependence theoretically, it was initially assumed that in the limit as $Z_p \longrightarrow \infty$, the differential and integrated cross sections must tend to constant $d\sigma/dZ_p \longrightarrow 0$ independent of Z_p [11]. A sufficient condition for such a dependence would be the unitarity of the amplitude of the processes under investigation for $Z_p \gg 1$ [8]. Such an assumption is apparently of a purely model nature and cannot explain the physical reasons behind the observed effects. Besides, it fails to explain the decrease in the integrated yield of resonances [4] and the cross section of one-electron excitation [12] upon an increase in the charge of a projectile. The interaction of a projectile with a target atom leads to several effects determining the charge dependence of cross sections, including the modifications of the mechanism of electron excitation from the initial to the final state [13–16] due to the effect of intermediate excited states and the states corresponding to the continuous spectrum of the target, the change in the kinematics of ion scattering from the short-range potential created by a neutral target [17], and an increase in the binding energy [18] of electrons in the target atom at short nuclear distances as compared to electrons of an isolated atom. It remains unclear which of the above effects lead to the saturation of the charge dependence since most theoretical models take into account the integrated influence of these effects.

The effect of intermediate states on the mechanism of electron transitions from the initial to the final state is taken into account explicitly in perturbation theory in the interaction of a projectile with a target [13–16] or in the close coupling method with one-center wave functions [19, 20]. These approaches successfully describe the profile of autoionization resonances excited in collisions with charged particles with $Z_p = \pm 1$ [15, 16]. However, the observed charge dependence of excitation cross sections for ions with $Z_p \geq 2$ is not reproduced in these models [20, 21]. For example, the perturbation theory using a power expansion in Z_p predicts an even stronger dependence than the first Born approximation. The close coupling method also cannot reproduce the saturation of cross sections of two-electron excitation [22] as well as the parameters of the autoionization resonance yield integrated over the electron ejection angles [20].

In order to take into account all the terms of the perturbation-theory series in the expansion of the excitation amplitude, we must use the wave function that takes into account the interaction between a projectile and a target most completely. This is usually realized in theoretical models using the methods of distorted waves. For example, in the eikonal approximation [23], the wave function is constructed under the assumption that a projectile interacts independently with the nucleus of a target atom and with electrons which are stationary relative to this nucleus. In this case, the electrons of the target atom are regarded as if belonging to the continuous spectrum of the projectile, and its influence on the binding energy is disregarded. The wave function obtained in this way corresponds to partial summation of the series in perturbation theory. For fast collisions ($Z_p/V_i \ll 1$), this function is transformed into the wave function of the first Born approximation and satisfies not only the correct boundary conditions for $R \gg r$ for any nuclear charge of the target atom, bu also, in contrast to the wave function in the CDW approximation [24], to the regular normalization conditions [23].

However, a considerable disadvantage of the wave function in the eikonal approximation is that the amplitude is calculated using additional approximations since the dependence of the phase factor on the nuclear spacing $\mathbf{R}$ as well as on $\mathbf{R} - \mathbf{r}$ ($\mathbf{r}$ is the radius vector determining the position of an electron in the atom) does not permit the factorization of the six-dimensional integral over the variables of the configuration space. An amplitude with a wave function in the eikonal approximation is usually calculated with the help of two approximations: the interaction of heavy particles in the transition operator is disregarded in spite of the nonorthogonality of the wave functions used, and the following approximate relation is introduced for the phase factor:

$$\mathrm{Ln}(V_i R + \mathbf{V}_i \cdot \mathbf{R}) \longrightarrow \mathrm{Ln}(V_i|\mathbf{R} - \mathbf{r}| + \mathbf{V}_i \cdot (\mathbf{R} - \mathbf{r})).$$

These transformations are equivalent to the disregard of the interaction between heavy particles in the transition amplitude at the first stage, followed by its phenomenological inclusion in the phase factor [23]. Such an approach makes it possible to factorize the amplitude in variables $\mathbf{R} - \mathbf{r}$, $\mathbf{r}$ in analogy with the first Born approximation and to calculate it analytically. Such a transformation is obviously applicable only for $R \gg 1$ and in effect reduces the interaction of an ion with the electrons and the nucleus of an atom to the interaction of the projectile with a structureless target. This increases the discrepancy between the results of calculations based on this model and the experimental data primarily for optically forbidden transitions [25], which occur predominantly for small values of R.

The theoretical analysis of differential characteristics in the one-electron excitation of hydrogen ($1s \longrightarrow 2p$) [26] and helium ($(1s^2)^1S \longrightarrow (1snp)^1P$) atoms [19, 27] by multiply charged ions proved that the saturation of the total cross sections for optically allowed transitions is a consequence of the change in the probability distribution depending on the impact parameter ρ. As the value of Z_p increases, the position of the peak of the excitation probability function $\rho P(\rho)$ is displaced towards higher values of the impact parameter, and the height of the peak of the function $\rho P(\rho)/Z_p^2$ decreases [19, 26]. It is impossible to experimentally determine the probability distribution as a function of the impact parameter, and hence the proposed explanation of the effect of saturation in one-electron processes is purely formal. The situation for two-electron excitations is more complicated. In the case when the peak of the function $\rho P(\rho)$ is shifted towards larger values of ρ, the calculations [20] did not reveal any saturation of the integrated yield of the autoionization resonances $(2s^2)^1S$, $(2s2p)^1P$, and $(2p^2)^1D$ upon an increase in the charge of a projectile. Thus, the reasons behind the saturation of total cross sections for two-electron transitions in atoms has not been explained even qualitatively.

The present work aims at developing a theoretical model of collisions of fast ions with atoms, which would take into account the role of intermediate states in the excitation of autoionization resonances, the change in the kinematics of scattering of a projectile by the field of a target atom, and also the change in the binding energy of electrons in the field of the projectile for small nuclear spacings. The influence of these effects on the form of the charge dependence of the differential and total excitation cross sections is also analyzed.

2. THEORY

2.1. Wave Functions

Let us consider a system formed by a neutral atom containing N_e electrons and an structureless charged projectile having charge Z_p, mass M_p, and momentum $\mathbf{K}_i = M_p\mathbf{V}_i$, where $\mathbf{V}_i$ is the velocity of the particle. The position of the jth electron and the projectile relative to the target nucleus with charge Z_t will be characterized by vectors $\mathbf{r}_j$ and $\mathbf{R}$, respectively, while the set of all vectors $\mathbf{r}_j$, $j = 1, \ldots, N_e$, will be denoted by $\mathbf{r}$. The state of the target electrons in the absence of a projectile is characterized by the set of quantum numbers τ_i. We will seek the wave function of such a system in the form

$$\Psi^{+}_{\tau_i, \mathbf{K}_i}(\mathbf{r}, \mathbf{R}) = \varphi_{\tau_i}(\mathbf{r}, \mathbf{R})\xi^{+}_{\mathbf{K}_i}(\mathbf{R}), \tag{1}$$

where function $\xi^{+}_{\mathbf{K}_i}(\mathbf{R})$ describes the motion of the projectile in the effective field created by the atom in state τ_i, and function $\varphi_{\tau_i}(\mathbf{r}, \mathbf{R})$ describes the motion of the electrons in the field of two Coulomb centers. Substituting Eq. (1) into the Schrödinger equation and integrating with respect to $\mathbf{r}$ with $\varphi_{\tau_i}(\mathbf{r}, \mathbf{R})$, we obtain the following system of integro-differential equations correct to within terms of the order $O(1/M_p)$:

$$\left(-\frac{1}{2M_p}\nabla^2_{\mathbf{R}} + \frac{Z_t Z_p}{R} + U_{\tau_i}(\mathbf{R}) - \frac{K_i^2}{2M_p}\right)\xi^{+}_{\mathbf{K}_i}(\mathbf{R}) = 0, \tag{2}$$

$$\begin{gathered}(\hat{H}_A + V(\mathbf{r}, \mathbf{R}) - i\mathbf{V}_i\nabla_{\mathbf{R}}\mathrm{Ln}(\varphi_{\tau_i}(\mathbf{r}, \mathbf{R})) \\ - U_{\tau_i}(\mathbf{R}) - \varepsilon_{\tau_i}(Z_t))\varphi_{\tau_i}(\mathbf{r}, \mathbf{R}) = 0,\end{gathered} \tag{3}$$

where $U_{\tau_i}(\mathbf{R})$ is the optical potential depending on velocity, $\hat{H}_A$ and $\varepsilon_\tau(Z_t)$ are the Hamiltonian and the energy of the electrons of the isolated target, and

$$V(\mathbf{r}, \mathbf{R}) = -\sum_j \frac{Z_p}{|\mathbf{R} - \mathbf{r}_j|}$$

is the operator describing the interaction of the projectile with the electrons of the atom.

As the first approximation in the solution of the system of equations (2) and (3), we can use in $U_{\tau_i}(\mathbf{R})$ the wave function $\Phi^{Z_t}_{\tau_i}(\mathbf{r})$ for the isolated target atom instead of $\varphi_{\tau_i}(\mathbf{r}, \mathbf{R})$. In this case, disregarding the imaginary component of potential U_{τ_i}, we obtain

$$U_{\tau_i}(\mathbf{R}) \approx U'_{\tau_i}(R) = \left\langle \Phi^{Z_t}_{\tau_i}(\mathbf{r})|V(\mathbf{r}, \mathbf{R})|\Phi^{Z_t}_{\tau_i}(\mathbf{r})\right\rangle. \tag{4}$$

In this approximation the system of the integro-differential equations (2) and (3) is reduced to two independent second-order differential equations. Since

$$U'_{\tau_i}(R) \longrightarrow -\frac{Z_p N_e}{R} \quad \text{for} \quad R \longrightarrow \infty,$$

the potential of the interaction between the projectile with the neutral ($Z_t = N_e$) target appearing in Eq. (2) has a short range and the solution of Eq. (2) for $M_p \gg 1$ can be found in the eikonal approximation.

Let us first consider the solution of Eq. (3) for the ground state of the helium atom with $\tau_i = (1s^2)^1S$. Taking into account the normalization conditions, we will seek the solution of Eq. (3) in the form of an expansion in the electron wave functions for an isolated helium-like atom:

$$\begin{gathered}\varphi_{\tau_i}(\mathbf{r}, \mathbf{R}) = \left(\Phi^{Z_i(R)}_{\tau_i}(\mathbf{r}) + i\sum_{n, L} C_{n, L}(\rho, t)\right. \\ \left.\times \sum_M \sqrt{\frac{4\pi}{2L+1}} Y^{*}_{L, M}(\hat{R})\Phi^{Z_i(R)}_{nLM}(\mathbf{r})\right)\left(1 + \sum_{n, L} C^2_{n, L}(\rho, t)\right)^{-1/2},\end{gathered} \tag{5}$$

where $\Phi^{Z}_{\tau_i}(\mathbf{r})$ and $\Phi^{Z}_{nLM}(\mathbf{r})$ are the wave functions of the ground state and the excited $(1snL)^1L$ states of the isolated helium-like ion with the nuclear charge Z, M is the component of the total orbital angular momentum L, $Y_{L, M}(\hat{R})$ is a spherical function, $\boldsymbol{\rho}$ is the impact parameter, and t is time. The expansion coefficients $C_{n, L}(\rho, t)$ and the effective charge $Z_i(R)$ are unknown real-valued functions. It should be noted that the wave function (5) cannot be characterized by a definite parity since the electrons move in the field of two Coulomb centers, which is not centrosymmeric.

We will assume that the effective charge $Z_i(R)$ is a slowly varying function. This leads to the following equations in $Z_i(R)$ and $C_{n, L}(\rho, t)$:

$$\begin{gathered}\left\langle \Phi^{Z_i(R)}_{\tau_i}(\mathbf{r})|\hat{H}_A + V(\mathbf{r}, \mathbf{R})|\Phi^{Z_i(R)}_{\tau_i}(\mathbf{r})\right\rangle \\ = \varepsilon_{\tau_i}(Z_t) + U'_{\tau_i}(R),\end{gathered} \tag{6}$$

$$\frac{\partial C_{n, L}(\rho, t)}{\partial t} = V^{Z_{\tau_i}(R)}_{n, L}(R)\left(1 + \sum_{n, L} C^2_{n, L}(\rho, t)\right) \tag{7}$$

with the boundary conditions

$$\begin{gathered}Z_i(R) \longrightarrow Z_t \quad \text{for} \quad R \longrightarrow \infty, \\ C_{n, L}(\rho, t) \longrightarrow 0 \quad \text{for} \quad t \longrightarrow -\infty,\end{gathered} \tag{8}$$

where $V^{Z_i(R)}_{n, L}(R)$ are the reduced matrix elements. The choice of the wave function in form (5) makes it possible to single out explicitly the dependence of the wave function on $\mathbf{r}$ and to determine numerically the effective charge $Z_i(R)$ of the centrosymmetric field for fixed values of R and Z_p from the condition of the minimum of functional (6). The increase in the effective charge for small R in Eq. (5) takes into account the fact that with decreasing R, the electrons of the atom fall in a deeper potential well, and functional (6) in the limit $R \longrightarrow 0$ tends to the energy in an isolated ion with charge $Z = Z_t + Z_p$. Consequently, the effective charge can be approximated, to a high degree of accuracy, by the function

$$Z_i(R) = Z_t + Z_p \exp(-Z_t R).$$

Functional (6) corresponds to the sum of the binding energy of the electrons in the target atom and the energy of the interaction of the atom with the projectile. In order to separate these quantities, we assume that the binding energy of the electrons for a fixed value of R coincides with the binding energy in an isolated helium-like ion with a nuclear charge equal to the effective charge $Z_i(R)$, and the difference between functional (6) and the binding energy determined in this way corresponds to the energy of interaction between the atom and the projectile. In this case, the dependence of the binding energy of the electrons in the target atom on the nuclear distance R and on the charge Z_p of the projectile is determined by the behavior of the effective charge as a function of R and Z_p: $\varepsilon_{\tau_i}(Z_i(R))$. It should be noted that the variational method used for determining the effective charge in one-electron functions as a function of the nuclear spacing was also used in [28]. After determining the effective charge $Z_i(R)$, we can calculate the matrix elements $V_{n,L}^{Z_i(R)}$ appearing in Eq. (7). Since $|C_{n,L}(\rho, t)| < 1$, we can disregard the quadratic terms in Eq. (7), which gives

$$C_{n,L}(\rho, t) = -\int_{-\infty}^{t} dt' V_{n,L}^{Z_i(R(t'))}\left(\sqrt{\rho^2 + V_i^2 t'^2}\right). \tag{9}$$

The same method can be used for determining the wave functions for the excited states τ_f of the target atom. However, since we must take into account the conditions of orthogonality to all wave functions corresponding to the states with a lower energy, the wave functions for the highly excited and autoionization states obtained in this way turn out to be quite cumbersome since

$$\left\langle \Phi_{\tau_i}^{Z_i}(\mathbf{r}) | \Phi_{\tau_f}^{Z_f}(\mathrm{r}) \right\rangle \neq 0 \quad \text{for} \quad Z_i \neq Z_f.$$

It is more convenient to use the approximation describing all the states of the target atom in a unified effective centrosymmetric field. In this case, the effective charge $Z_f(R)$ in the excited states τ_f, as well as in the states of the continuous spectrum, coincides with the effective charge in the ground state:

$$Z_f(R) = Z_i(R) = Z(R). \tag{10}$$

With this approximation, which provides a unique description for the evolution of all atomic states, the conditions of orthogonality of the initial and final states are satisfied automatically due to the properties of the wave functions of isolated helium-like ions defined for the same nuclear charge. As the nuclear spacing R decreases, the depth of the potential well in which the electrons in any state τ of the target atom are located increases, and the larger the charge of the projectile, the deeper the well. This leads to an increase in the excitation energy,

$$\Delta\varepsilon_{if}(Z(R)) = \varepsilon_{\tau_f}(Z(R)) - \varepsilon_{\tau_i}(Z(R)), \tag{11}$$

for small values of R, which considerably affects the dynamics of the processes occurring in the region of strong interaction.

2.2. Excitation of the Target Atom in Collisions with Multiply Charged Ions

Let us first consider the process of excitation $\tau_i \longrightarrow \tau_f$ for a fixed scattering angle, i.e., for

$$\mathbf{Q} = \mathbf{q}_\perp(R) + \mathbf{q}_\parallel(R) = \text{const},$$

where $\mathbf{Q} = \mathbf{K}_f - \mathbf{K}_i$ is the momentum transferred to the target atom, $\mathbf{K}_f$ is the momentum of the scattered ion, and $\mathbf{q}_\parallel(R)$ and $\mathbf{q}_\perp(R)$ are its components along the direction of the incident beam and the direction perpendicular to the incident beam of projectiles,

$$q_\parallel(R) = \Delta\varepsilon_{if}(Z(R))/V_i.$$

For

$$Q \le \Delta\varepsilon_{if}(Z(R))/V_i,$$

a transition of the target atom to state τ_f is forbidden. In the case of scattering of projectiles through small angles, when

$$\Delta\varepsilon_{if}(Z_t) \le QV_i \le \Delta\varepsilon_{if}(Z_t + Z_p), \tag{12}$$

there exists a region of atomic spacings $R < R_{\min}(Q)$ in which the energy QV_i transferred to the atom is insufficient for its transition to the final state τ_f. In other words, because of an increase in the binding energy of electrons for small nuclear spacings, a projectile must fly to a large distance $R \ge R_{\min}(Q)$ for the process of the electron transition $\tau_i \longrightarrow \tau_f$ in the target to become possible from the point of view of energy. For large values of the transferred momenta $QV_i \ge \Delta\varepsilon_{if}(Z_t + Z_p)$, the transition of the target atom to the excited state τ_f is possible for any R.

The amplitude of the excitation from the initial state τ_i to the final state τ_f can be written in the form

$$\begin{aligned} T_{if}(\mathbf{Q}) &= \int d\mathbf{R} \sqrt{\frac{4\pi}{2L_f + 1}} Y^*_{L_f M_f}(\hat{R}) V_{if}(\rho, t) \\ &\times \exp(i\mathbf{Q}\cdot\mathbf{R} + i\alpha^+_{\tau_i}(\rho, t) - i\alpha^-_{\tau_f}(\rho, t)), \end{aligned} \tag{13}$$

$$V_{if}(\rho, t) = \Bigg(V_{L_f}^{Z(R)}(\tau_i \longrightarrow \tau_f, R) + i\sum_{n,L} C_{n,L}(\rho, t)$$

$$\left.\times \sum_{l} \langle L0l0|L_f0\rangle V_l^{Z(R)}(nL \longrightarrow \tau_f, R)\right) \qquad (14)$$

$$\times\left(1 + \sum_{n,L} C^2_{n,L}(\rho, t)\right)^{-1/2},$$

where $\langle L0l0|L_f0\rangle$ is the Clebsch–Gordan coefficient, $V_{L_f}^{Z(R)}(\tau_i \longrightarrow \tau_f, R)$ and $V_L^{Z(R)}(nL \longrightarrow \tau_f, R)$ are the reduced matrix elements describing the transitions from the ground state and from the $(1snL)^1L$ state to the autoionization state τ_f, and $\alpha^-_{\tau_f}(\rho, t)$ and $\alpha^+_{\tau_i}(\rho, t)$ are the eikonal phases. Thus, the two-electron excitation amplitude (13) and (14) can be presented in the form of a sum in which the first term in Eq. (14) corresponds to the excitation mechanism such that only one electron of the atom interacts with the projectile, while the other electron is excited due to electron correlations. The remaining terms in Eq. (14) correspond to the mechanism of excitation of the autoionization state via the intermediate $(1snL)^1L$ energy levels, in which both electrons of the atoms interact with the projectile. In this case, the amplitudes corresponding to these two mechanisms of excitation do not interfere with each other in the differential cross section. As in perturbation theory, the amplitude of the excitation via intermediate energy levels has a stronger charge dependence since $C_{n,L}(\rho, t) \sim Z_p$ (9). However, in contrast to the amplitude in the second order of the perturbation theory, amplitude (13) and (14) contains the normalization factor

$$\left(1 + \sum_{n,L} C^2_{n,L}(\rho, t)\right)^{-1/2},$$

which is a function of Z_p and can noticeably change the charge dependence of the cross section. Integration in Eq. (13) is carried out over the entire region in which $QV_i \geq \Delta\varepsilon_{if}(Z(R))$. Thus, the inclusion of the effect of the projectile on the binding energy of the electrons in the target atom not only modifies the transition operator in Eq. (13), but also leads to the exclusion of a part of the configuration space $R < R_{\min}(Q)$ from the amplitude.

3. RESULTS OF CALCULATIONS

We calculated the differential and total excitation cross sections for the autoionization resonances $(2s^2)^1S$, $(2s2p)^1P$, and $(2p^2)^1D$ of helium, which are excited by structureless ions with energies of 0.5 and 1.5 MeV/amu. The effect of the degenerate continuous spectrum on the autoionization states is disregarded. The integration with respect to ρ and t in Eq. (13) in the region $R \leq R_{\max}$, where $R_{\max} = 20$, was carried out numerically, and the contribution of the region $|V_it| > R_{\max}$, $\rho \leq R_{\max}$ was estimated using asymptotic methods. The wave functions of isolated helium-like ions with a continuous dependence of all parameters on the nuclear charge were obtained by using the variational method [29, 30]. In the sum over intermediate states in Eq. (14), only states $(1snL)^1L$, where $n = 2, 3$, were taken into consideration.

The excitation amplitude (13) and (14) was calculated in the following approximations:

(1) the first Born approximation ($C_{n,L}(\rho, t) = 0$, $\alpha^+_{\tau_i}(\rho, t) = 0$, $\alpha^-_{\tau_f}(\rho, t) = 0$, and $Z(R) = Z_t$);

(2) only the transitions through intermediate levels were taken into account ($C_{n,L}(\rho, t) \neq 0$, $\alpha^+_{\tau_i}(\rho, t) = 0$, $\alpha^-_{\tau_f}(\rho, t) = 0$, and $Z(R) = Z_t$);

(3) the transitions through intermediate levels and the change in the kinematics of the projectiles were taken into consideration ($C_{n,L}(\rho, t) \neq 0$, $\alpha^+_{\tau_i}(\rho, t) \neq 0$, $\alpha^-_{\tau_f}(\rho, t) \neq 0$, and $Z(R) = Z_t$);

(4) complete analysis was carried out taking into account the effect of the projectile on the binding energy of the electrons in the target ($C_{n,L}(\rho, t) \neq 0$, $\alpha^+_{\tau_i}(\rho, t) \neq 0$, $\alpha^-_{\tau_f}(\rho, t) \neq 0$, $Z(R) \geq Z_t$).

The table contains the results of the calculations of the parameter determining the charge dependence

$$n(Z_p) = \mathrm{Ln}\left(\frac{\sigma_{if}(Z_p)}{\sigma_{if}(Z_p = 1)}\right)/\mathrm{Ln}(Z_p)$$

of the excitation cross sections for the autoionization resonances formed as a result of collisions with structureless ions with energy 0.5 MeV/amu, which are compared with the parameter describing the charge dependence of the experimental yield of resonance from [2] integrated over the ejection angles. It should be noted that $n(Z_p) = 2$ in the first order of perturbation theory. The inclusion of the transitions through intermediate energy levels (second version of the calculations) leads to an increase in $n(Z_p)$ for all resonances ($2 \leq n(Z_p) \leq 4$), the value of $n(Z_p)$ increasing with Z_p. The largest increase is observed for the parameter $n(Z_p)$ for the $(2p^2)^1D$ resonance since the transitions

$$(1s^2)^1S \longrightarrow (1snL)^1L \longrightarrow (2p^2)^1D$$

through intermediate levels make the main contribution to the excitation cross section of this resonance for the collision energy in question. Our results also indicate the weak effect of the intermediate states in the excitation of the $(2s2p)^1P$ resonance in the given energy range. The inclusion of the interaction between the atom and the projectile on the kinematics (third version of the calculations) leads to a noticeable decrease in parameter $n(Z_p)$. The charge dependence of the excitation cross section for resonances $(2s^2)^1S$ and $(2s2p)^1P$ is found to be weaker than in the first order of perturbation theory ($n(Z_p) < 2$), which is in qualitative agreement with the experimental data. The influence of two factors producing opposite effects on the charge dependence of the excitation cross section qualitatively explains the difference in the dependences $n(Z_p)$ for the $(2s^2)^1S$ and $(2s2p)^1P$ resonances. The transitions through intermediate levels accompanied by an increase in Z_p produce a strong effect on the excitation cross section for the $(2s^2)^1S$ resonance, and the parameter $n(Z_p)$ for this resonance increases with Z_p. On the contrary, the parameter of charge dependence for the $(2s2p)^1P$ resonance decreases upon an increase in Z_p like in the experiment [2]. In the case of the $(2p^2)^1D$ resonance, parameter $n(Z_p)$ changes insignificantly when the change in the kinematics of the scattered ion is taken into account and, hence, the charge dependence of the excitation cross section for this resonance is determined predominantly by two-step transitions. The inclusion of the effect of the projectile on the binding energy of the electrons in the atom in the most complete version of the calculations leads to a decrease in the excitation cross section. However, this decrease for the $(2s2p)^1P$ and $(2p^2)^1D$ resonances actually does not change the charge dependence parameter for these resonances. Potential (14) for resonances $(2s2p)^1P$ and $(2p^2)^1D$ decreases rapidly upon a decrease in R,

$$V_{if}(\rho, t) \sim R^{L_f+1} \quad \text{for} \quad R \longrightarrow 0,$$

and slowly for large R,

$$V_{if}(\rho, t) \sim R^{-(L_f+1)} \quad \text{for} \quad R \longrightarrow \infty.$$

As a result, refining the value of amplitude (13) in the range of small R for moderate value of Z_p weakly affects the charge dependence of the excitation cross section. On the other hand, the charge dependence of the excitation cross section for the $(2s^2)^1S$ resonance taking into account the effect of the projectile on the binding energy of the electrons in the atom is modified significantly. The excitation of this resonance takes place only for small values of R since potential $V_{if}(\rho, t)$ has a short range ($V_{if}(\rho, t) \longrightarrow 0$ for $R \longrightarrow \infty$ and $V_{if}(\rho, t) \longrightarrow \text{const}$ for $R \longrightarrow 0$).

The differential cross section of the excitation of the $(2s^2)^1S$ resonance for small scattering angles of structureless triply charged ions with an energy of 0.5 MeV/amu is presented in Fig. 1. The inclusion of the transitions through intermediate energy levels increases the differential excitation cross section for small scattering angles as compared to the cross section in the first order of perturbation theory. A change in the kinematics of the projectiles strongly diminishes the differential cross section in the range of small scattering angles. The short-range potential with a Coulomb kernel in Eq. (2) leads to a rapid change in scattering phases in Eq. (13) for small ρ and, hence, to a quasiperiodic variation of the differential cross section. The larger Z_p, the stronger the Coulomb repulsion of the projectile by the nucleus of the target atom for small R, the higher the rate of variation of scattering phases for small ρ, and the weaker the charge dependence of the differential cross section. In other words, the Coulomb repulsion of the projectile by the nucleus of the target atom lowers the probability of finding the projectile in the region of small nuclear spacings; however, it is this region that makes the main contribution to the excitation amplitude for the $(2s^2)^1S$ resonance. The inclusion of the effect of the projectile on the binding energy of the electrons in the target atom modifies the excitation amplitude for small values of R also. However, in contrast to the change in the kinematics of the scattered ion, this effect is manifested most clearly for small scattering angles, for which the energy transferred to the target atom may turn out to be insufficient for a transition of the atom to an excited state for small R. As a result, a peak which was not observed in the previous versions of the calculation is formed in the differential cross section for the $(2s^2)^1S$ as well as $(2s2p)^1P$ and $(2p^2)^1D$ resonances for small scattering angles. Thus, the presence of a peak in the differential cross section

Parameter characterizing the charge dependence of the excitation cross section for the autoionization resonances formed as a result of collision with 0.5-MeV/amu ions

Z_p	$(2s2s)^1S$	$(2s2p)^1P$	$(2p2p)^1D$
Experimental data [2]			
2	1.6	2.1	3.4
3	1.3	1.7	2.9
Our calculations (version 2)			
2	2.1	2.3	3.6
3	2.2	2.4	3.7
5	2.3	2.5	3.7
Our calculations (version 3)			
2	1.5	2.0	3.7
3	1.6	2.0	3.7
5	1.8	1.8	3.6
Our calculations (version 4)			
2	1.3	2.0	3.8
3	1.6	1.9	3.8
5	1.9	1.7	3.6

Note: The results obtained in different versions of calculation are denoted by 2 when only intermediate levels are taken into account, by 3 when the transitions between intermediate levels and the change in the kinematics of the projectile are included, and by 4 when the transitions through intermediate levels, the change in the kinematics of the projectile, and its effect on the binding energy of the target electrons are taken into consideration.

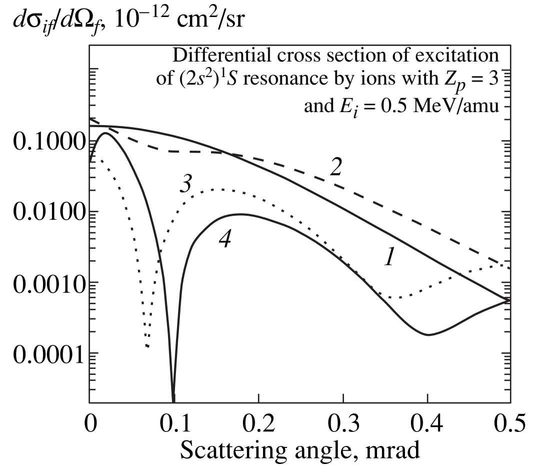

Fig. 1. Differential cross section of excitation of the $(2s^2)^1S$ resonance for small angles of scattering by ions with $Z_p = 3$ and with an energy of 0.5 MeV/amu. The results are obtained using various versions of calculation: (*1*) first Born approximation, (*2*) taking into account only the transitions through intermediate levels; (*3*) taking into account the transitions through intermediate levels and the change in the kinematics of the projectile, and (*4*) taking into account the transitions through intermediate levels, the change in the kinematics of the projectile, and its effect on the binding energy of the target electrons.

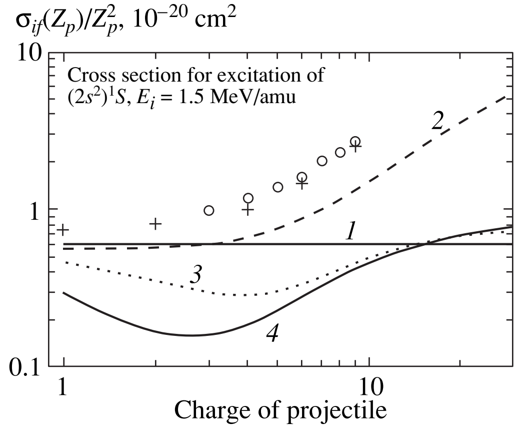

Fig. 2. Cross section of excitation of the $(2s^2)^1S$ resonance by ions with energy 1.5 MeV/amu. The results of calculations obtained by other authors are marked with crosses [22] and circles [31]. The remaining notation is the same as in Fig. 1.

of excitation for small scattering angles is associated with the effect of the projectile on the binding energy of electrons in the target atom.

Figure 2 shows the results of calculation for the cross section of excitation of the $(2s^2)^1S$ resonance by structureless ions with energy 1.5 MeV/amu. The cross section calculated taking into account only the transitions through intermediate states reproduces qualitatively and quantitatively the results of the calculations using the method of close coupling between channels [22] as well as the calculations based on the perturbation theory [31] disregarding the effect of the degenerate continuous spectrum. Refining the kinematics of the projectiles leads to a value of the excitation cross section smaller than in the first order of the perturbation theory, and the increase in the cross section for small values of Z_p is slower than in proportion to Z_p^2; i.e., $\sigma_{if}(Z_p)/Z_p^2$ decreases with increasing Z_p. However, as the value of Z_p increases further, function $\sigma_{if}(Z_p)/Z_p^2$ starts increasing due to a stronger charge dependence of the amplitude of excitation through intermediate states. It should be noted that experimental data for this collision energy are available only for a very narrow region of ejection angles [5], and the procedure of deriving the resonance yield integrated over ejection angles [5] from these data appears to us as not quite correct.

4. CONCLUSIONS

In the present paper, we propose a theoretical model of two-electron excitation, which has made it possible for the first time to take into account explicitly the effect of the Coulomb field of a projectile on the binding energy of the electrons in a target atom along with the transitions through intermediate states and the change in the kinematics of the projectile. The cross section of the excitation of autoionization resonances, which is calculated taking into account only the transitions through intermediate states, increases with the charge of the projectile at a rate higher than in the first order of perturbation theory. However, the inclusion of the change in the kinematics of the projectile and its effect on the binding energy of the electrons in the target atom reduces the excitation cross section and suppresses the charge dependence. The charge dependence of the excitation cross section for resonances $(2s^2)^1S$ and $(2s2p)^1P$ becomes weaker as compared to the first order of perturbation theory, which is in qualitative agreement with the experimental data. The modification of the kinematics of the projectile by the short-range potential of the interaction with the atom and a rapid change in the scattering phases may lead to oscillations in the differential excitation cross section in a wide range of scattering angles. On the other hand, the effect of the field of the projectile on the binding energy of the electrons in the target atom leads to a decrease in the differential cross section for small scattering angles since, in the case of small transferred momenta, there exists a region of nuclear spacings in which electron transitions to an excited state are forbidden by the energy conservation law.

ACKNOWLEDGMENT

This research was supported by the program “Universities of Russia. Fundamental Research” (grant no. 98-1-5247).

REFERENCES

1. L. P. Presnyakov, V. P. Shevel’ko, and R. K. Yaneev, *Elementary Processes Involving Multiply Charged Ions* (Énergoizdat, Moscow, 1986).
2. P. W. Arcuni and D. Shneider, Phys. Rev. A **36**, 3059 (1987).
3. J. O. P. Pedersen and P. Hvelplund, Phys. Rev. Lett. **62**, 2373 (1989).
4. N. Stolterfoht, Nucl. Instrum. Methods Phys. Res. B **53**, 477 (1991).
5. J. P. Giese, M. Schulz, J. H. Swenson, *et al.*, Phys. Rev. A **42**, 1231 (1990).
6. A. Bordenave-Montesquieu, A. Gleizes, *et al.*, J. Phys. B **25**, L367 (1992).
7. A. Bordenave-Montesquieu, P. Moretto-Capelle, A. Gleizes, *et al.*, J. Phys. B **28**, 653 (1995).
8. J. H. McGuire, A. Muller, B. Schuch, *et al.*, Phys. Rev. A **35**, 2479 (1987).
9. D. Defleffsen, M. Anton, A. Werner, and K. H. Schartner, J. Phys. B **27**, 4195 (1994).
10. K. Reymann, K. H. Schartner, B. Sommer, *et al.*, Phys. Rev. A **38**, 2290 (1988).
11. B. Brendle, R. Gayet, J. P. Rozet, and K. Wohrer, Phys. Rev. Lett. **54**, 2007 (1985).
12. R. K. Janev, Phys. Rev. A **53**, 219 (1996).
13. J. H. McGuire and J. C. Stratton, Phys. Rev. A **46**, 5514 (1992).
14. A. L. Godunov, N. V. Novikov, and V. S. Senashenko, J. Phys. B **24**, L173 (1991).
15. A. L. Godunov, J. H. McGuire, and V. A. Schipakov, J. Phys. B **30**, 3227 (1997).
16. N. V. Novikov and V. S. Senashenko, Zh. Éksp. Teor. Fiz. **109**, 1551 (1996) [JETP **82**, 833 (1996)].
17. Sh. D. Kunikeev, Zh. Éksp. Teor. Fiz. **109**, 44 (1996) [JETP **82**, 22 (1996)].
18. N. Stolterfoht, D. Brandt, and M. Prost, Phys. Rev. Lett. **43**, 1654 (1979).
19. F. Martin and A. Salin, J. Phys. B **28**, 671 (1995).
20. F. Martin and A. Salin, J. Phys. B **28**, 2159 (1995).
21. A. L. Godunov and V. A. Schipakov, Nucl. Instrum. Methods Phys. Res. B **98**, 354 (1995).
22. W. Fritsch and C. D. Lin, Phys. Rev. A **41**, 4776 (1990).
23. C. O. Reinhold and J. E. Miraglia, J. Phys. B **20**, 1069 (1987).
24. D. S. F. Crothers, J. Phys. B **15**, 2061 (1982).
25. A. Bugacov, J. M. Maidagan, R. D. Rivarola, and R. Shingal, Phys. Rev. A **47**, 1052 (1993).
26. V. D. Rodriguez and A. Salin, J. Phys. B **25**, L467 (1992).
27. V. D. Rodriguez, C. A. Ramirez, R. D. Rivarola, and J. E. Miraglia, Phys. Rev. A **55**, 4201 (1997).
28. É. S. Parilis, L. M. Kishinevskiĭ, V. I. Matveev, and B. G. Karkov, *Auger Processes in Atomic Collisions* (Fan, Tashkent, 1989).
29. N. V. Novikov and V. S. Senashenko, Opt. Spektrosk. **86**, 371 (1999) [Opt. Spectrosc. **86**, 320 (1999)].
30. N. V. Novikov and V. S. Senashenko, Vestn. Mosk. Univ., Ser. 3: Fiz., Astron., No. 6, 37 (2000).
31. V. A. Sidorovich, Nucl. Instrum. Methods Phys. Res. B **154**, 131 (1999).

Translated by N. Wadhwa

Journal of Experimental and Theoretical Physics, Vol. 92, No. 3, 2001, pp. 420–440.
Translated from Zhurnal Éksperimental'noĭ i Teoreticheskoĭ Fiziki, Vol. 119, No. 3, 2001, pp. 485–508.
Original Russian Text Copyright © 2001 by Shevkunov.

PLASMA,
GASES

Scattering of Centimeter Radiowaves in a Gas Ionized by Radioactive Radiation: Cluster Plasma Formation

S. V. Shevkunov
St. Petersburg State Technical University, ul. Politekhnicheskaya 29, St. Petersburg, 195251 Russia
e-mail: root@shevk.hop.stu.neva.ru

Received June 23, 2000

Abstract—A theoretical explanation is proposed for an anomalously high reflectivity of air masses exposed to radioactive radiation relative to electromagnetic waves from the rf range. The mechanism of formation of the reflected signal is connected with a change in the electric parameters of the ionized gas. The concentration of free charges under the typical conditions of radioactive contamination is ten orders of magnitude lower than that required for the formation of an experimentally detectable reflected signal. The discrepancy between the values of reflectivity observed under the real conditions of radar probing and predicted theoretically on the basis of the elementary theory of a weakly ionized gas amounts to 20 orders of magnitude. It is shown that the inclusion of the variation of the mass and the critical capture radius of ions due to their hydration changes the difference between the theoretical predictions and the experimental observations insignificantly. The discrepancy becomes smaller (but only by 1.5 orders of magnitude) when the scattering of radiowaves from turbulent vortices is taken into account. The mechanism of the formation of the high reflectivity is associated with slowing down the recombination and with the accumulation of a profuse population of unrecombined ionic pairs stabilized in the clusters of water molecules. The steady-state concentration of such electrically neutral clusters is several orders of magnitude higher than the concentration of free hydrated ions. A variation of the intensity of ionizing radiation is accompanied by proportional variations of both components. The recombination barrier is formed as a result of drawing dipole molecules into the gap between ions at the final stage of motion of counterions towards one another before their recombination. The accumulation of ionic pairs ensures the multiple enhancement of the sensitivity of the electric properties of cold plasma to the effect of ionizing radiation. A quantitative kinetic theory of the effect is constructed. The numerical calculations of the parameters of the prerecombination states of ions against the background of the molecular component are made using computer simulation at the microscopic level. The steady-state recombination rate is an exponential function of the prerecombination barrier height and decreases rapidly even upon an insignificant change in the number of molecules involved in an ion recombination act. The obtained theoretical conclusions are confirmed by the independent results of observations of the strong absorption band in the atmosphere in the middle part of the IR spectrum, which is attributed to the anomalously high concentration of electrically neutral water clusters. *© 2001 MAIK "Nauka/Interperiodica".*

1. RESULTS OF RADAR PROBING

The first observations of the reflected radar signal from a radioactive burst in the atmosphere were made in 1986 by the group headed by V. B. Bogdanov [1] in the region of the Chernobyl nuclear power plant. Subsequently, the presence of the reflected signal was confirmed by several independent groups of scientists [1–3]. The experiments were made using various types of industrial radars in the centimeter and decimeter ranges at the South-Ukrainian, Zaporozh'e, St. Petersburg, Balaklava, Udomlya, and other nuclear power plants as well as on the research reactors at Gatchina and other towns. Burst flames were observed at distances ranging from 11 to 65 km. The limiting range in one of the experiments amounted to 500 km [2], and the limiting sensitivity to radioactive impurity bursts attained several curies per day. The total number of independent observations reaches several hundreds.

The reflection of a radio signal takes place at the boundaries of macroscopic fluctuations of electric parameters such as permittivity ε and conductivity σ. The variations of ε and σ are associated with the ionization of the gas in a radioactive cloud. According to the results of preliminary calculations, the values of the equilibrium concentration of free charges calculated using the classical theory of ionization of gases are 9 to 10 orders of magnitude lower than those corresponding to the experimentally observed intensity of the reflected signal. The measured signal intensity was used in [1] to estimate value of the effective reflecting surface of a radioactive cloud. The calculations were made according to the formula [4]

$$S_{\mathrm{eff}} = (4\pi)^3 \frac{R_0^4 N k_{\mathrm{B}} T m_{\mathrm{noise}} \Delta f}{\bar{p}(\tau_r/\tau_p) G_{\mathrm{dir}}^2 \lambda^2}, \tag{1}$$

where R_0 is the distance to the object, λ is the radiation wavelength, Δf is the transmission band, N is the noise factor, k_B is Boltzmann's constant, m_{noise} is the signal-to-noise power ratio, $\bar{p}$ is the average power of the transmitter, and τ_r and τ_p are the radar pulse repetition and duration time, respectively. The antenna power gain G_{dir} is equal to $4\pi s_a/\lambda^2$, where $s_a = \zeta\pi\alpha_1\alpha_2$ is the effective area of the antenna, ζ is the antenna efficiency, $\alpha_n = 0.61\lambda/\Delta\varphi_n$, $\Delta\varphi_1$ and $\Delta\varphi_2$ are the azimuthal and angular sizes of the antenna. The numerical estimate obtained using formula (1) for the typical experimental conditions [1] ($\lambda = 6$ cm, $\bar{p} = 300$ W, $\tau_r = 2.5$ μs, $\tau_p = 1.7$ μs, $R_0 = 42$ km, $m_{\text{noise}} = 2.5 \times 10^3$, $N = 12$, $\Delta f = 2$ MHz, $\zeta = 0.4$, $\Delta\varphi_1 = 2.3°$, and $\Delta\varphi_2 = 0.5°$) is $S_{\text{eff}} = 5.1$ m^2, which agrees with the result of blank experiments. The estimate given by formula (1) varies from 0.1 m^2 (the level corresponding to the limiting sensitivity of the method) to 100 m^2 depending on the experimental conditions. The obtained value of S_{eff} makes it possible to estimate the required degree of ionization ρ_i in a radioactive cloud. In the model of a random charge distribution in a cylindrical gas column of length L and radius r_0 [5], the following expression is derived:

$$S_{\text{eff}} \approx 0.6\pi r_0^2 \frac{L^{1/3}}{\lambda^{1/3}} (\Delta\varepsilon)^2. \tag{2}$$

The mean square of permittivity fluctuations is given by

$$(\Delta\varepsilon)^2 = \left(\frac{q_i^2 \rho_i \lambda^2}{\pi c^2 m_i}\right)^2, \tag{3}$$

where q_i, ρ_i, and m_i are the charge, concentration, and mass of free charge carriers and c is the velocity of light. Substituting $m_i \approx 10^{-23}$ g for ions into formula (3) and $L = 3$ km and $r_0 = 0.1$ km into formula (2), for $S_{\text{eff}} = (1\text{–}100)$ m^2, we obtain $\rho_i = (4 \times 10^{12}\text{–}4 \times 10^{13})$ cm^{-3}. A similar estimate for the electron concentration gives $\rho_e = (4 \times 10^8\text{–}4 \times 10^9)$ cm^{-3}. Both estimates are much higher than the values predicted by the standard theory of ionization–recombination equilibrium in gases. In [2], such calculations were made under the assumption that free charge carriers in the atmosphere are mainly ions O_2^+, N_2^+, and O_2^-. Free electrons are absent since they are trapped by oxygen molecules in the case of their relatively high concentration ($\rho_{O_2} = 0.54 \times 10^{19}$ cm^{-3}) and form negative ions. The system of equations describing the time evolution of the concentrations of positive (ρ_+) and negative (ρ_-) ions as well as electrons (ρ_e) has the form

$$\begin{aligned} \frac{d\rho_e}{dt} &= WY - k_{oe}\rho_e - k_{ie}\rho_+\rho_e, \\ \frac{d\rho_+}{dt} &= WY - k_{ii}\rho_+\rho_- - k_{ie}\rho_e\rho_+, \\ \frac{d\rho_-}{dt} &= k_{oe}\rho_{O_2}\rho_e - k_{ii}\rho_+\rho_-, \\ \rho_+ &= \rho_- + \rho_e, \end{aligned} \tag{4}$$

where $k_{oe} = 8.8 \times 10^{-11}$ cm^3/s is the electron trapping coefficient, $k_{ie} = 7 \times 10^{-7}$ cm^3/s and $k_{ii} = 1.4 \times 10^{-6}$ cm^3/s are the ion–electron and ion–ion recombination coefficients, $W = 2.08 \times 10^9$ R^{-1} cm^{-3} is the radiation yield of electron–ion pairs, and Y is the dose rate. The steady-state solution of Eqs. (4) for $Y = 1$ R/h gives the following concentrations: $\rho_+ \approx \rho_- = 6.5 \times 10^5$ cm^{-3} and $\rho_e = 3.5 \times 10^{-3}$ cm^{-3}. The electron component is virtually absent, while the ionic concentration is 7–8 orders of magnitude lower than the value obtained in the experiments on the measurement of the intensity of the reflected radar signal.

Didenko *et al.* [3] estimated S_{eff} on the basis of the rated degree of ionization in accordance with formula (2) using the expression for fluctuations in which the corrections for collisions of ions with gas molecules and the frequency-dependent phase shifts between the field of the wave and the displacement of charges in the plasma associated with these collisions are taken into account [5]:

$$\Delta\varepsilon = \sum_i \frac{\omega_{ik}^2}{\omega^2 + \nu_{ik}^2} + i\sum_i \frac{\omega_{ik}^2 \nu_{ik}}{\omega(\omega^2 + \nu_{ik}^2)}. \tag{5}$$

Here, summation is carried out over all species of ions, the second sum being the imaginary component of the complex quantity $\Delta\varepsilon$; ω_{ik} is the plasma frequency of ions and ν_{ik} is the frequency of collisions of ions with neutral particles. The ionic concentrations required for calculating the plasma frequencies ω_{ik} are estimated on the basis of the elementary theory of the ionization–recombination equilibrium for a gas ionization rate of 10^5–10^6 cm^{-3} s^{-1}, which corresponds to a specific activity of impurities of the order of $(3\text{–}30) \times 10^{-6}$ Cu cm^{-3} typical of highly radioactive wastes. Under these conditions, the expected equilibrium concentration of ions is of the order of 10^6 cm^{-3}, while the electron concentration is seven orders of magnitude lower. Substituting the values of ω_{ik} calculated for this concentration into formula (5) and then Eq. (5) into formula (2) for $\lambda = 10$ cm, we obtain a negligibly low estimate for the radioactive cloud reflectivity: $S_{\text{eff}} \approx 2 \times 10^{-16}$ m^2. This value is 16 orders of magnitude smaller than that obtained from the measurements of the reflected signal intensity. The actual discrepancy is still larger since the theoretical estimates were obtained for ionic concentrations corresponding to the limiting contamination by radioactive wastes, while the reflected radio signal is detected in experiments when the burst intensity exceeds the background level just by a factor of several units. The calculations based on the refined formula (5) instead of Eq. (3) do not significantly change the general pattern of mismatching between the measured intensities of the reflected signal and the rated degree of ionization in a radioactive burst.

Thus, the application of the standard theory of ionization in plasma to the problem of reflection of a radio signal from a radioactive cloud leads to a discrepancy between the theoretical and measured values of the reflected signal intensity of more than 16 orders of magnitude. According to these estimates, the reflected signal could not be detected even by using the most powerful and sensitive radar systems. The results of experiments renounce this conclusion. Obviously, Eqs. (4) do not take into account all circumstances affecting the electric parameters of cold plasmas.

2. SCATTERING OF AN ELECTROMAGNETIC WAVE IN A TURBULENT PLASMA FLOW

We consider a plane sinusoidal electromagnetic wave with the cyclic frequency $\omega = 2\pi\nu$ and the wave number k_0, which is incident along the normal to the plane boundary at which the electric parameters suffer discontinuity:

$$E(t, x) = E_0 \exp(i\omega t - k_0 x). \tag{6}$$

The reflected electromagnetic wave has the complex-valued amplitude E_1:

$$E'(t, x) = E_1 \exp(i\omega t + k_0 x). \tag{7}$$

The "joining" of the solutions of Maxwell's equations on both sides of the reflection plane leads to the well-known [6] amplitude–phase relation

$$\frac{E_1}{E_0} = \frac{\tilde{n} - \tilde{n}_0}{\tilde{n} + \tilde{n}_0} = \frac{n - n_0 - i\kappa(n - n_0)}{n + n_0 - i\kappa(n + n_0)}, \tag{8}$$

where $\tilde{n} = n(1 - i\kappa)$ and $\tilde{n}_0 = n_0(1 - i\kappa_0)$ are complex refractive indices on the sides of the reflection boundary. The reflection coefficient is given by

$$R_e = \frac{E_1}{E_0}\left(\frac{E_1}{E_0}\right)^* = \frac{(n - n_0)^2 + (\kappa n - \kappa_0 n_0)^2}{(n + n_0)^2 + (\kappa n + \kappa_0 n_0)^2}. \tag{9}$$

Substituting Eq. (6) into Maxwell's equations for a conducting medium,

$$\begin{gathered} \operatorname{curl}\mathbf{H} = \frac{4\pi}{c}\mathbf{j} + \frac{1}{c}\frac{\partial \mathbf{D}}{\partial t}, \\ \mathbf{j} = \sigma\mathbf{E}, \quad \mathbf{D} = \boldsymbol{\varepsilon}\mathbf{E}, \end{gathered} \tag{10}$$

where σ is the conductivity and $\mathbf{j}$ is the current density, leads to the complex permittivity

$$\tilde{\varepsilon} = \varepsilon - \frac{4\pi\sigma}{\omega} i,$$

$$\varepsilon - \frac{2\sigma}{\nu} i = n^2(1 - i\kappa)^2.$$

The last relation can be written separately for the real and imaginary components in the form

$$\begin{gathered} n = \sqrt{0.5(\varepsilon + \sqrt{\varepsilon^2 + 4\sigma^2\nu^{-2}})}, \\ n\kappa = \frac{\sigma\nu^{-1}}{\sqrt{0.5(\varepsilon + \sqrt{\varepsilon^2 + 4\sigma^2\nu^{-2}})}}. \end{gathered} \tag{11}$$

Expanding expressions (11) into a two-dimensional Taylor series and retaining the principal powers of the small parameters $\varepsilon - \varepsilon_0$, $\sigma_0\nu^{-1}$, $\sigma\nu^{-1}$, and $(\sigma^2 - \sigma_0^2)\nu^{-2}$, we obtain the following expressions for the optical density jump in the leading order in $(\varepsilon - 1) \ll 1$ and $(\varepsilon_0 - 1) \ll 1$:

$$\begin{gathered} n - n_0 = \frac{1}{2}(\varepsilon - \varepsilon_0) + \ldots, \\ \kappa n - \kappa_0 n_0 = (\sigma - \sigma_0)\nu^{-1} + \ldots. \end{gathered} \tag{12}$$

Substituting these expressions into relation (9) and retaining the main powers of the small parameters, we arrive at the following expression:

$$R_e = \frac{1}{16}(\varepsilon - \varepsilon_0)^2 + \frac{1}{4}(\sigma - \sigma_0)^2\nu^{-2} + \ldots. \tag{13}$$

It can be seen that the role of conductivity in the formation of the reflectivity at high frequencies ν decreases.

The vortices formed as a result of the turbulent mixing of a radioactive burst with uncharged masses of air induce additional spatial fluctuations of ρ_i, ε, and σ from which the electromagnetic waves emitted by the radar will be scattered. The strongest scattering effect should be expected from vortices with a size of the order of the radiation wavelength λ since the scattering of waves from vortices with a size smaller than λ decreases strongly. The criterion of the turbulent flow is the Reynolds number $\mathrm{Re} = \rho_g V l/\mu_g$, where ρ_g is the gas density, μ_g is the gas viscosity, V is the jet velocity, and l are the characteristic linear dimensions of the region. Substituting the numerical values for air under standard conditions ($\rho_g = 1.29$ kg m^{-3}, $\mu_g = 17.2 \times 10^{-6}$ N s m^{-2}), the characteristic velocity $V \approx 1$ m s^{-1} of convective displacements in the atmosphere, and the spatial scale of the order of the wavelength, $l \approx \lambda \approx 0.1$ m, we obtain $\mathrm{Re} = 7.5 \times 10^3 \gg 1$, which corresponds to the boundary of the transition from a laminar to a turbulent flow. In the first approximation, the effective scattering surface is comparable with the total surface of the vortices. If volume V contains approximately V/λ^3 vortices with a size comparable with the radar wavelength, their total surface is of the order of V/λ. The effective reflection surface of a radioactive cloud (whose geometrical surface is of the order of $V^{2/3}$) increases due to scattering from turbulent vortices by a factor of $k_{\text{turb}} = V^{1/3}/\lambda$. Typically, for $V = 10^9$ m^3 and $\lambda = 6$ cm, we have the "gain factor" $k_{\text{turb}} = 1.7 \times 10^4$:

$$S_{\text{eff}} \approx k_{\text{turb}} R_e V^{2/3}. \tag{14}$$

Let us set a limit on the sensitivity of a radar with a moderate resolving power, which is capable of detecting a radio signal reflected from a metallic surface of area $S_{\text{eff}} = 0.1$ m^2 at a distance of 30 km. The substitution of this value into relation (14) leads to $R_e = 6 \times 10^{-12}$. Using this result in (13), we find that the permittivity jump must be $\varepsilon - \varepsilon_0 > 10^{-5}$. The same effect will be observed at frequency $\nu = 10^{10}$ s^{-1} due to the conductivity jump $\sigma - \sigma_0 > 5 \times 10^4$ s^{-1}.

The general theory of transport [7, 8] implies that the static conductivity jump is connected with a jump in the concentration of singly charged ions through the relation

$$\begin{aligned} \sigma - \sigma_0 &= (\rho - \rho_0)e^2[l_i^+(m_i^+ + \gamma^+ m_{\mathrm{H_2O}})^{-1} \\ &\times v_+^{-1}\sqrt{1 + (m_i^+ + \gamma^+ m_{\mathrm{H_2O}})/\tilde{m}} + l_i^-(m_i^- + \gamma^- m_{\mathrm{H_2O}})^{-1} \\ &\times v_-^{-1}\sqrt{1 + (m_i^- + \gamma^- m_{\mathrm{H_2O}})/\tilde{m}}], \end{aligned} \tag{15}$$

where γ^+ and γ^- are the equilibrium mean numbers of water molecules trapped in the electric field of ions (the degree of hydration), $\tilde{m}$ is the effective average mass of air molecules, and the terms containing $\tilde{m}$ take into account the effect of the difference in the masses of ions and molecules on the ionic mobility. Substituting the expressions for the thermal velocities of hydrated ions

$$v_+ = \sqrt{\frac{9\pi k_{\mathrm{B}} T}{8(m_i^+ + \gamma^+ m_{\mathrm{H_2O}})}},$$

$$v_- = \sqrt{\frac{9\pi k_{\mathrm{B}} T}{8(m_i^- + \gamma^- m_{\mathrm{H_2O}})}}$$

at temperature $T = 300$ K as well as the numerical values of the mass of the $\mathrm{H^+}$ and $\mathrm{OH^-}$ ions and assuming that the mean free paths for ions in the first approximation are $l_i^+ = l_i^- = 4 \times 10^{-6}$ cm, we obtain the lower estimate for the concentration of free ions in the case when the reflection coefficient is formed due to the conductivity jump:

$$\begin{aligned} \rho - \rho_0 > 2.68 \times 10^{10}&\left[\frac{\sqrt{1 + (1 + 18\gamma^+)/29}}{\sqrt{1 + 18\gamma^+}}\right. \\ &\left.+ \frac{\sqrt{1 + (17 + 18\gamma^-)/29}}{\sqrt{17 + 18\gamma^-}}\right]^{-1} [\mathrm{cm}^{-3}]. \end{aligned} \tag{16}$$

It can be seen from this expression that hydration does not affect the order of magnitude of $\rho - \rho_0$. For typical values of $\gamma^+ = \gamma^- = 10$, we obtain

$$\rho - \rho_0 > 6.72 \times 10^{10} \ \mathrm{cm}^{-3}. \tag{17}$$

The change in the permittivity of air due to the binding of water molecules at ions is connected with the jump of the ionic concentration through the following relation:

$$\begin{aligned} \varepsilon - \varepsilon_0 &= (\rho - \rho_0) \\ &\times [\chi_{\mathrm{cl}}^+ + \chi_{\mathrm{cl}}^- - (\gamma^+ + \gamma^-) p_{\mathrm{H_2O}}^2/3k_{\mathrm{B}}T]. \end{aligned} \tag{18}$$

For $\varepsilon - \varepsilon_0 > 10^{-5}$, this leads to the following lower estimate for the equilibrium concentration of hydrated ions in the case when the reflection coefficient for a radiowave is formed due to the permittivity jump:

$$\begin{aligned} &\rho - \rho_0 > 10^{-5} \\ &\times \left|\chi_{\mathrm{cl}}^+ + \chi_{\mathrm{cl}}^- - (\gamma^+ + \gamma^-) p_{\mathrm{H_2O}}^2/3k_{\mathrm{B}}T\right|^{-1} [\mathrm{cm}^{-3}], \end{aligned} \tag{19}$$

where χ_{cl}^+ and χ_{cl}^- are the equilibrium polarizabilities of hydrated ionic shells associated with the rotation of intrinsic dipole moments of water molecules and $p_{\mathrm{H_2O}}^2/3k_{\mathrm{B}}T$ is the polarizability associated with the rotation of free molecules in the gas phase, $p_{\mathrm{H_2O}} = 1.83 \times 10^{-18}$ CGS units being the intrinsic dipole moment of a water molecule.

We calculated the quantities χ_{cl} and $\gamma^{+(-)}$ using computer simulation on the molecular level. For obtaining numerical estimates, it suffices for us to use the obtained orders of magnitudes of the quantities $\gamma^+ = \gamma^- = 10$ and $\chi_{\mathrm{cl}} \sim 10^{-22}$ cm^3, whose substitution into (19) gives $\rho - \rho_0 > 2.9 \times 10^{16}$ cm^{-3}. While writing expression (19), we disregarded the effect of amplification due to scattering from thermal fluctuations. The inclusion of this effect may subdue the constraint imposed on the concentration, but not more than by one or two orders of magnitude:

$$\rho - \rho_0 > (10^{14}\text{–}10^{15}) \ \mathrm{cm}^{-3}, \tag{20}$$

which is 9 to 10 orders of magnitude higher than the value obtained from equations (4) of the ionization–recombination kinetics. The concentration (20) of hydrated ions is only 1.5 orders of magnitude lower than the theoretical limit set by a finite concentration of water in the atmosphere. At temperature $T = 300$ K and a relative humidity of 80%, the vapor pressure $p_s \approx 2.4 \times 10^{-2}$ bar, while the volume concentration of water molecules amounts to $p_s/k_BT = 5.8 \times 10^{17}$ cm^{-3}. For the degree of hydration $\gamma \approx 10$, this concentration is sufficient for the formation of 2.9×10^{16} cm^{-3} pairs of ions. In other words, for the concentration of ionic pairs defined by condition (20), 3% of moisture is bound at the ions. Thus, the model of a turbulent plasma fails to explain the experimentally observed reflectivity by the permittivity jump.

Let us now consider the mechanism associated with conductivity. Substituting the values of γ^+ and $\gamma^- = 10$ into Eq. (15) and taking into account the criterion $\sigma - \sigma_0 > 5 \times 10^4$ s^{-1}, we obtain

$$\rho > 1.4 \times 10^{10} \text{ cm}^{-3}. \tag{21}$$

A comparison of this relation with the estimate following from Eqs. (4) shows that the concentration of free charge carriers required for obtaining a reflected signal is at least 4–5 orders of magnitude higher than that ensured by the mechanism laid in Eqs. (4). In actual practice, the discrepancy is still larger since the estimates were made with a considerable margin. Consequently, the increase in the reflection coefficient by a factor of $k_{\text{turb}} = 1.7 \times 10^4$ due to scattering from turbulent vortices does not remove the discrepancies between the results of experimental observations and the theoretical estimates, but makes them less profound.

3. EFFECT OF HYDRATION ON THE CRITICAL RADIUS OF ION TRAPPING IN A COLD PLASMA

Hydration of ions is absent in hot plasmas, but must be taken into account in ionized gases. Water molecules possess relatively large intrinsic dipole moments $\mu_{H_2O} = 1.85 \times 10^{-8}$ CGS units [9] and are the first to be pulled into the field of ions. The energy of binding between a water molecule and an ion is of the order of 1 eV (approximately $39k_BT$). Ions are coated with a layer of water molecules, and their effective mass and collision cross sections change as a result. In fact, we are dealing with a cluster plasma.

If we disregard the electronic component, the time evolution of the volume concentration of free ions in a gas can be described by the dynamic equation

$$\frac{d\rho}{dt} = -k_{ii}\rho^2 + I, \tag{22}$$

where ρ is the number of ions of the same polarity per unit volume; I is the number of pairs generated per unit time per unit volume under the action of ionizing radiation; $k_{ii}\rho^2$ is the number of recombination acts per unit time per unit volume; $k_{ii} = \pi d^2(v_+^2 + v_-^2)^{1/2}$, πd^2 being the effective collision cross section; and $v_{+(-)} = (8k_BT/\pi M_{+(-)})^{1/2}$, the average velocity of an ion of mass $M_{+(-)}$ at temperature T. The solution of Eq. (22) with the initial condition $\rho(0) = 0$ has the form

$$\rho(t) = \frac{\sqrt{I/k_{ii}}[1 - \exp(-2\sqrt{k_{ii}I}t)]}{1 + \exp(-2\sqrt{k_{ii}I}t)} \tag{23}$$

with the characteristic relaxation time $\tau = (2\sqrt{k_{ii}I})^{-1}$ and the asymptotic form

$$\rho(t) \approx \rho_\infty[1 - 2\exp(-t/\tau)] \tag{24}$$

for large values of $t \gg \tau$, where $\rho_\infty = \sqrt{I/k_{ii}}$ is the steady-state concentration of ions, and

$$\tau = \frac{1}{2\rho_\infty k_{ii}}. \tag{25}$$

It can be seen from relation (25) that the macroscopically long relaxation times detected in experiments can be ensured either by the small value of coefficient k_{ii}, or in a system with a low degree of ionization ρ_∞.

The integrals of motion make a transition from the electrostatic energy of ions to the kinetic energy almost impossible without the participation of a third particle. The recombination occurs via one of the following channels:

$$\begin{gathered} A^+ + B^- + M^0 \longrightarrow AB + M^0, \\ A^+ + B^- \longrightarrow AB + h\nu, \\ A^+ + B^- \longrightarrow A^* + B^*. \end{gathered} \tag{26}$$

The second and third channels presenting the radiation-induced recombination and mutual neutralization with charge reversal dominate under a gas pressure below 10^{-3} bar [8, 10]. The recombination involving a third particle prevails under atmospheric pressure.

While estimating the effective reaction cross section, we must take into account the long-range Coulomb interaction between ions. In a system of singly charged ions, we can single out at least two characteristic distances for the interactions between ions, i.e., the Debye radius $r_D = (k_BT/4\pi\rho e^2)^{1/2}$, where e is the elementary charge [11], and the Bjerrum radius $r_B = 2e^2/3k_BT$. Debye screening is of the collective origin and is observed when the number of ions in the Debye sphere is much greater than unity, $(4/3)\pi r_D^3\rho \gg 1$, or, after the substitution of temperature $T = 300$ K, for $\rho \ll 5 \times 10^{13}$ cm^{-3}. For such concentrations of ions, we obtain $r_D \gg 1.7 \times 10^{-5}$ cm for the Debye radius, while the Bjerrum radius at the same temperature amounts to $r_B = 3.7 \times 10^{-6}$ cm. At distance $r < r_B$, the necessary condition for the linearization of the Poisson–Boltzmann equation forming the basis of the Debye–Hückel theory [11] is violated, and the collective screening degenerates into the screening by a counterion. The statistical analysis of the system of charged particle by the computer experiment methods [12–24] revealed that the collective nature of screening changes upon an increase in density, when the Bjerrum radius becomes comparable with the Debye radius: contact pairs of ions start to form, and the radius of correlations between the ions continues to decrease monotonically, attaining its minimum value at a point where the formation of ionic triplets begins. At the point corresponding to the minimum of the ionic correlation radius, the monotonic behavior of the correlation functions changes to the oscillating behavior, and the correlation radius starts increasing with the density of the system up to the condensation into the ionic liquid. Thus, the region of high ionic concentrations $\rho > 5 \times 10^{13}$ cm^{-3} cannot be attained in actual practice in ionized air if only due to the fact that the intense formation of contact pairs of ions, which is inevitable at such concentrations, would indicate a sharp increase in the recombination rate k_{ii}, which obstructs the increase in the ionic concentration. This limitation on the concentration of ions is in serious contradiction to the requirements on the ionic concentration (20).

For $r > r_B$, the total energy of two counterions is negative on the average and corresponds to the bound state, while the probability of counterion trapping is close to unity. Consequently, under atmospheric conditions, when $r_D > r_B$, the effective scattering radius d can be estimated by the Bjerrum radius r_B. Under standard conditions, the Bjerrum sphere contains 5.2×10^3 electrically neutron air molecules with the mean free path $l_{mol} = (\sqrt{2}\, d^2_{mol} p/k_B T)^{-1} \approx 10^{-5}$ cm. The mean free path l_i of an ion in the gas depends on the degree of its hydration γ since the latter increases the integrated cross section of collisions of a hydrated ion with molecules. For $\gamma = 10$, $l_i = (0.3–0.5)l_{mol} = (3–5) \times 10^{-6}$ cm, i.e., it amounts to a value of the order of the Bjerrum radius. Molecules carry away the excess of the kinetic energy of ions liberated due to the work done by the Coulomb attractive force, thus ensuring their convergence to a distance of the order of a molecular radius. Since the linear size of the Bjerrum sphere is comparable with the mean free path, this convergence is preceded by several cycles of finite motion of two interacting counterions, which are accompanied by collisions with molecules. The electrically neutral component plays the role of a viscous medium ensuring the collision with the counterion captured in the electric field even if the impact parameter is larger than the diameter of the ion.

There exist three classical theories of the ion–ion recombination involving a third particle: Langevin's theory [25] valid for high pressures (considerably exceeding 10 bar), which describes the motion of ions as a drift in a continuous viscous medium, Thomson's theory [26, 27], applicable for low pressures (below 10 bar), and the more universal Natanson's theory [28]. In Thomson's theory, the critical radius of counterion capture is equal to the Bjerrum radius ($r_c = r_B$). The averaging over various direction of entrance into the capturing sphere of radius r_c leads to the integrated probability of collision with a third particle [26]:

$$W = 1 - \frac{l_i}{2r_c}\left[1 - \exp\left(-\frac{2r_c}{l_i}\right)\right]. \qquad (27)$$

It is assumed that one collision is sufficient for getting rid of the excess kinetic energy e^2/r_c relative to the average thermal energy $3k_B T/2$. In Natanson's theory, a correction to r_c is introduced to take into account the fact that the kinetic energy of the relative motion decreases after the collision with the third particle only by $e^2/4r_c$. Accordingly, another condition for r_c can be derived:

$$\frac{3}{2}k_B T + \frac{3e^2}{8r_c} = \frac{e^2}{r_c},$$

whence

$$r_c = \frac{5e^2}{12k_B T} = 2.3 \times 10^{-6} \text{ cm}.$$

For the atmosphere, another correction must be introduced to take into account a considerable difference between the mass of an air molecule $\tilde{m} = 29m_p$, where m_p is the proton mass, and the mass of a hydrated ion, $M_\alpha = m_\alpha + \gamma^\alpha m_{H_2O}$, with the degree of hydration γ^α, where $\alpha = +, -$. For $M_\alpha \gg \tilde{m}$, the average amount of energy transferred from ions to a molecule during the act of collision is

$$\frac{e^2}{4r_c}\tilde{m}\left(\frac{1}{M_+} + \frac{1}{M_-}\right).$$

This corresponds to the critical capture radius for hydrated ions:

$$r_c = \frac{2e^2}{3k_B T}\left[1 - \frac{3}{8}\tilde{m}\left(\frac{1}{M_+} + \frac{1}{M_-}\right)\right] \approx 3.3 \times 10^{-6} \text{ cm}, \qquad (28)$$

where the numerical value is given for the H^+ and OH^- ions with $\gamma^+ = \gamma^- = 10$. It can be seen from relation (28) that the inclusion of hydration increases the critical capture radius for ions by a factor of 1.4.

Substituting Eq. (27) for positive and negative ions with $l_i^+ = l_i^- = 4 \times 10^{-6}$ cm and (28) into the formula for the recombination coefficient, we obtain

$$\begin{aligned} k_{ii} &= \pi r_c^2 \sqrt{v_+^2 + v_-^2}(W^+ + W^-) \\ &= 4.6 \times 10^{-7} \text{ cm}^3 \text{ s}^{-1}. \end{aligned} \qquad (29)$$

The inclusion of hydration increases the value of r_c^2 by a factor of 2.3, simultaneously reducing the velocity

$$\sqrt{v_+^2 + v_-^2} = \sqrt{\frac{8k_BT}{\pi M_r}} = 2.62 \times 10^4 \text{ cm s}^{-1}$$

(M_r is the reduced mass) to one third of its initial value, while the probability $W^+ + W^-$ increases by a factor of 1.8 and the recombination coefficient, by a factor of 1.4. The inclusion of hydration of ions does not reduce the recombination coefficient and cannot explain the anomalously intense accumulation of ions in the atmosphere.

4. FORMATION OF CLUSTER PLASMA

The presence of ion-hydrate clusters in the atmosphere is confirmed by studies using the methods of mass spectrometry [29–33]. The thermodynamic stability of clusters is determined by the dependence of the work of their formation $A(N) = G^{\text{cl}}(N) - \mu N$ from a vapor with the chemical potential μ on the cluster size N. The equilibrium size corresponds to the extremum of the work of formation $\partial G^{\text{cl}}(N)/\partial N = \mu$, while the sign of the second derivative of the free energy $G^{\text{cl}}(N)$determines the stability of an equilibrium cluster. As a rule, the clusters of electrically neutral particles are unstable.

The atmosphere contains various types of ions. The most numerous populations are formed by the H^+, N_4^+, OH^-, O^{2-}, and CO_4^- ions. Our goal is to determine a typical pattern of cluster formation on ions. For this reason, computer simulation has been carried out only for two types of ions, H^+ and OH^-. A free proton H^+ formed as a result of the dissociation of a water molecule is rapidly captured by another water molecule, forming a hydronium ion H_3O^+. The energy of addition of the first water molecule to a proton is anomalously high and amounts to 7.18 eV $\approx 280k_BT$. The energies of the addition of next molecules are much lower: 1.6, 0.97, 0.74, 0.67, 0.57, and 0.51 eV. In these calculations, we disregard the dissociation of this particle, which has a low probability. The H_3O^+ ion is regarded as rigid since the intraionic vibrational degrees of freedom are “frozen” in view of the smallness of the thermal energy k_BT as compared to the vibrational quantum. The Hamiltonian of the system is written in the form of a combination of multicenter potentials. The numerical values of the potential parameters are set so that they reproduce the experimentally measured free energy and entropy of clusters [34, 35]. The potential is described in detail in [36–44]. The interaction includes the Coulomb, exchange, and dispersion interactions, as well as the energy of the polarization of molecules in the field of ions, the energy of covalent bonds, and the contributions associated with the transport of the excess charge from an ion to molecules. The interaction is of an unpaired type. Strong many-particle interactions at the contact distances to the ion are explicitly taken into account. In the present work, we refine the numerical values of parameters as compared to those contained in [36–44] on the basis of more exact experimental data [34, 35] taken instead of the results presented in [45, 46]. The Hamiltonian of the system is supplemented with the interaction of the dipoles induced on the molecules with one another and with the molecular electrostatic field. The following numerical values of parameters have been established for the H_3O^+ ion (in the notation adopted in [36–44]): the polarizability $\alpha_w = 1.44$ Å^3 of a water molecule, the ionic charge $Q^+ = 4.80298 \times 10^{-10}$ CGS units being screened, the Lennard–Jones potential parameters $\varepsilon_0^+ = 0.515 \times 10^{-13}$ erg and $\sigma^+ = 2.959$ Å, the amplitude and the limiting radii of the isotropic component of covalent interactions $U_0^+ = 0.17025 \times 10^{-11}$ erg, $R_L^+ = 4.410$ Å, and $R_U^+ = 5.372$ Å, the amplitude, the preexponential parameter, and the parameter characterizing the many-particle nature of unpaired interactions $a_0^+ = 0.9285 \times 10^{-12}$ erg, $b_0^+ = 25.2$ Å, and $n^+ = 1.323$, the radii of unpaired interactions $\tilde{R}_L^+ = 4.425$ Å and $\tilde{R}_U^+ = 5.458$ Å, the parameter $\kappa^+ = 0.195$ characterizing the intensity of excess charge transport, and the correction $\chi^+ = 0.92$ to the non-pointlike nature of the induced dipoles. Four point charges simulating the anisotropic component of the ionic field and of covalent bonds are arranges at the following points in the local system of coordinates:

$$x_1 = 0, \quad y_1 = 1.0171 \text{ Å}, \quad z_1 = 0.2961 \text{ Å},$$

$$q_1 = 2.129 \times 10^{-10} \text{ CGS units},$$

$$x_2 = -0.8809 \text{ Å}, \quad y_2 = -0.5086 \text{ Å}, \quad z_2 = 0.2961 \text{ Å},$$

$$q_2 = 2.129 \times 10^{-10} \text{ CGS units},$$

$$x_3 = 0.8809 \text{ Å}, \quad y_3 = -0.5086 \text{ Å}, \quad z_3 = 0.2961 \text{ Å},$$

$$q_3 = 2.129 \times 10^{-10} \text{ CGS units},$$

$$x_4 = 0, \quad y_4 = 0, \quad z_4 = 0.128 \text{ Å},$$

$$q_4 = -6.387 \times 10^{-10} \text{ CGS units}.$$

The corresponding parameters for the OH^- ion have the following values:

$$Q^- = -2.30298 \times 10^{-10} \text{ CGS units}, \quad \varepsilon_0^- = 0.155 \times 10^{-13} \text{ erg},$$

$$\sigma^- = 3.2835 \text{ Å}, \quad U_0^- = 0.924 \times 10^{-12} \text{ erg},$$

$$R_L^- = 4.760 \text{ Å}, \quad R_U^- = 5.275 \text{ Å},$$

$$a_0^- = 0.306 \times 10^{-12} \text{ erg},$$

$$b_0^- = 28.8\ \text{Å}, \quad n^- = 0.55, \quad \tilde{R}_L^- = 4.770\ \text{Å},$$

$$\tilde{R}_U^- = 5.067\ \text{Å}, \quad \kappa^- = 0.$$

Two point charges simulating the anisotropic component of the field created by the OH^- ion are located at the following points and have the following values:

$$x_1 = 0, \quad y_1 = 0, \quad z_1 = 0.78\ \text{Å},$$

$$q_1 = 1.758 \times 10^{-10}\ \text{CGS units},$$

$$x_2 = 0, \quad y_2 = 0, \quad z_2 = 0, \quad q_2 = -4.258 \times 10^{-10}\ \text{CGS units}.$$

The Monte Carlo method was used to calculate the Gibbs free energy of clusters (Tables 1 and 2). The calculations were made on a bicanonical statistical ensemble [47–52]. The free energy of the addition reaction is calculated through the ratio of the probabilities of two classes of microscopic states with the numbers of molecules n and $n-1$:

$$\begin{aligned}&\frac{w(n)}{w(n-1)}\\ &= \exp\left(-\frac{G^{\text{cl}}(n, p, T) - G^{\text{cl}}(n-1, p, T) - \mu(p, T)}{k_B T}\right).\end{aligned} \tag{30}$$

The numerical calculation of $G^{\text{cl}}(k, p, T)$ is reduced to the summation of differences $\Delta G^{\text{cl}}(n, p, T) = G^{\text{cl}}(n, p, T) - G^{\text{cl}}(n-1, p, T)$ for $n = 1, 2, 3, \ldots, N$. In fact, we calculate the configuration components

$$\begin{aligned}\Delta G^{\text{cl, conf}}(n, p, T) &= \Delta G^{\text{cl}}(n, p, T)\\ &\quad - [-k_B T \ln(Z_{\text{tr}}^{\text{kin}} Z_{\text{rot}}^{\text{kin}} v_{\text{ref}})]\end{aligned} \tag{31}$$

and

$$\begin{aligned}\mu^{\text{conf}}(p, T) &= \mu(p, T) - [-k_B T \ln(Z_{\text{tr}}^{\text{kin}} Z_{\text{rot}}^{\text{kin}} v_{\text{ref}})]\\ &= k_B T \ln\left(\frac{\sigma}{8\pi^2} \frac{p}{k_B T} v_{\text{ref}}\right),\end{aligned} \tag{32}$$

where

$$Z_{\text{tr}}^{\text{kin}} = \left(\frac{h}{\sqrt{2\pi m k_B T}}\right)^{-3} = \frac{1}{\Lambda^3}$$

is the result of integration over the momenta of the translational motion in the statistical sum;

$$Z_{\text{rot}}^{\text{kin}} = \frac{(2k_B T)^{3/2}(I_1 I_2 I_3)^{1/2}\pi^{3/2}}{h^3}$$

is the result of integration over the rotational momenta of molecules; Λ is the thermal de Broglie wavelength; σ is the parameter characterizing the rotational symmetry of molecules ($\sigma = 2$ for water); and v_{ref} is an arbitrary fixed volume. The substitution of expressions (31) and (32) into Eq. (30) leads to the following relations:

$$\frac{w(n)}{w(n-1)} = \exp\left(-\frac{\Delta G^{\text{cl, conf}}(n, p, T) - \mu^{\text{conf}}(p, T)}{k_B T}\right) \tag{33}$$

and

$$\begin{aligned}&\Delta G^{\text{cl, conf}}(n, p, T)\\ &= -k_B T \ln\left(\frac{w(n)}{w(n-1)}\right) + \mu^{\text{conf}}(p, T).\end{aligned} \tag{34}$$

The chemical potential $\mu^{\text{conf}}(p, T)$ of vapor is an input parameter, while the ratio $w(n)/w(n-1)$ is calculated by directly counting the numbers of n- and $(n-1)$-states in a Markov random process of roaming over microscopic states. The fluctuational computation errors of a bounded sampling strongly depend on the value of $\mu^{\text{conf}}(p, T)$. The optimal value corresponding to the $w(n) = w(n-1)$ mode is unknown beforehand and is determined at the initial stage of computations by using a special iterative procedure.

The transitions between microscopic states with the numbers of particles $n-1$ and n occur with the probabilities p_{ij} ensuring the limiting distribution over microscopic states ρ_i:

$$\begin{aligned}\frac{p_{i,j}}{p_{j,i}} &= \frac{\rho_j}{\rho_i}\\ &= \frac{\dfrac{1}{n!}(Z_{\text{tr}}^{\text{kin}})^n (Z_{\text{rot}}^{\text{kin}})^n \exp\left(\dfrac{n\mu(p, T) - U_n}{k_B T}\right) d\Omega dV}{\dfrac{1}{(n-1)!}(Z_{\text{tr}}^{\text{kin}})^{n-1} (Z_{\text{rot}}^{\text{kin}})^{n-1} \exp\left(\dfrac{(n-1)\mu(p, T) - U_{n-1}}{k_B T}\right)}\\ &= \frac{1}{n}\exp\left(\frac{\mu^{\text{conf}}(p, T) - (U_n - U_{n-1})}{k_B T}\right)\frac{1}{v_{\text{ref}}} d\Omega dV \qquad (35)\\ &= \frac{d\Omega}{8\pi^2/\sigma} \frac{dV}{V} \frac{V}{n} \frac{1}{v_{\text{ref}}} \exp\left(\frac{\mu^c(p, T) - (U_n - U_{n-1})}{k_B T}\right)\\ &= \frac{d\Omega}{8\pi^2/\sigma} \frac{dV}{V} \frac{pV}{n k_B T} \exp\left(-\frac{U_n - U_{n-1}}{k_B T}\right),\end{aligned}$$

where $d\Omega$ and dV are the elementary volumes in the space of the orientations and the coordinates of the molecular centers of mass, and $\mu^c \equiv \mu^{\text{conf}} - k_B T \ln(\sigma/8\pi^2)$. The probabilities $d\Omega/(8\pi^2/\sigma)$ and dV/V are realized when a molecule is cast out at a randomly chosen point of the system. The remaining factors in (35) are played in the standard manner using the program of random numbers [53]. In addition to the steps of casting in and omitting, the steps of translation and rotation of molecules were made in accordance with the standard Metropolis procedure for a canonical statistical ensemble [54, 55]. The maximum length of a step in the translation of the molecular center of mass

Table 1. Experimental values of $\Delta H^{\rm exp}$ and $\Delta G^{\rm exp}$ [34] and the values of $\Delta H^{\rm theor}$ and $\Delta G^{\rm theor}$ for the enthalpy H and the Gibbs free energy G of the reaction of addition of a water molecule to a cluster based on the hydronium ion H_3O^+ at $T = 300$ K calculated by the Monte Carlo method for the standard conditions of vapor at $p = 1$ atm. All values are in kcal/mole

n	$-\Delta H^{\rm exp}$	$-\Delta H^{\rm theor}$	$-\Delta G^{\rm exp}$	$-\Delta G^{\rm theor}$
1	31.6	31.6	24.3	24.3
2	19.5	19.5	13.0	13.0
3	17.9	17.8	9.5	9.5
4	12.7	13.4	5.6	5.7
5	11.6	11.1	4.1	4.2
6	10.7	10.7	3.0	3.5

Table 2. The same as in Table 1 for the oxonium ion OH^- with the experimental values from [35] at $T = 297$ K

n	$-\Delta H^{\rm exp}$	$-\Delta H^{\rm theor}$	$-\Delta G^{\rm exp}$	$-\Delta G^{\rm theor}$
1	24.0	24.00	17.8	17.80
2	17.9	17.90	11.6	11.69
3	15.1	15.11	7.7	6.50
4	14.2	14.29	5.4	5.40
5	14.1	13.80	4.2	4.31

was 0.3 Å, while the maximum rotation step was 20°. The frequency of acquiring new configurations upon translations and rotations of molecules varied from 30 to 50%, while the corresponding value for casting in and omitting of molecules varied approximately by 0.5%. An attempt of a translation with a rotation was accompanied by five attempts of casting in or omitting a molecule. The system was placed in a spherical cavity of radius 10 Å, and an ion was fixed at the center. The length of the Markov process used for calculating canonical averages amounted to 5×10^8 steps, which is one to two orders of magnitude larger than the adopted standards and ensures a high reliability of calculated averages. The calculation of a point for a cluster formed by 10 molecules on a 600-MHz PENTIUM-III computer takes approximately 10 hours. Table 1 contains the numerical results obtained for the H_3O^+ ion. The dependences for the OH^- ion are similar.

The work of formation of clusters as a function of size (Fig. 1) has a clearly manifested minimum indicating the stability of clusters formed at ions. The depth of the minimum is estimated at $U_{\rm min} = 1$ eV $\approx 39k_BT$. The probability of cluster disintegration is negligibly low as compared to the probability of cluster formation. Almost all ions in the cold plasma are hydrated. The position of the minimum corresponds to a stable size of the cluster and is displaced upon an increase in the vapor pressure to larger sizes. However, the degree of hydration even in a conventionally "dry" atmosphere with a relative humidity of 10% (which corresponds to vapor pressure $p \approx 300$ Pa at $T = 300$ K [56]) amounts to $\gamma = N \approx 10$. As the moisture content decreases to one third of the initial value, the equilibrium size of the cluster decreases, remaining larger than $\gamma = 8$. Clusters with a size $\gamma > 20$ are formed only in the vicinity of the point of equilibrium between vapor and liquid. For $\gamma = 10$, the difference between the free and internal energies of the cluster is of the order of $\Delta = 3$ eV $\approx 116k_BT$ (Fig. 2). This means that the substitution of the internal energy for the free energy is ruled out even in estimates since it would lower the probability of cluster formation approximately by a factor of $\exp(-\Delta) \approx 10^{-50}$. For $\gamma = 12$, the entropy per molecule attains its maximum value, indicating qualitative rearrangements in the cluster. For $\gamma > 12$, the coupling of water molecules changes from the confinement due to the direct interaction with the ion to the collective interactions between the molecules. Under the conditions corresponding to lower layers of the atmosphere, the hydrate shell is formed by a single layer located at a distance of 2.6 Å from the ion. The growth of the second hydrate layer at a distance of 5.1 Å and a transition to the confinement of the molecules due to collective interactions start only when the pressure approaches saturation (Fig. 3). The mass of the ion increases as a result of hydration by an order of magnitude, and the effective radius is doubled. The degree of hydration weakly depends on the moisture content in the atmosphere and is close to $\gamma = 10$ under typical conditions. The cluster remains in a metastable state for a threefold–fivefold supersaturation. When supersaturation is approximately tenfold, the cluster loses its stability and experiences an avalanche-type growth (Fig. 4).

5. MECHANISM OF RECOMBINATION RETARDATION IN A CLUSTER PLASMA

The calculations made in the previous sections prove that the concentration of free charges formed as a result of the air mass ionization is insufficient for the formation of the experimentally observed reflectivity. The reason behind the high reflectivity is obviously associated not with free charges as such, but with side effects accompanying their formation. According to estimates, a cold plasma must contain, apart from clusters, a large population of electrically neutral complexes stabilized by ions.

In the absence of ions, water clusters are thermally unstable. The intrusion of an ion stabilizes a cluster [36–42], but the latter loses its electroneutrality. On the other hand, the results of previous investigations show [13–24, 57] that the intense pairing of charges accompanied by the formation of water clusters at two counterions should be expected in the density and temperature ranges under investigation. In view of their electrical neutrality, water clusters cannot be detected in electrometric experiments. The presence of this component in the atmosphere is confirmed by the anoma-

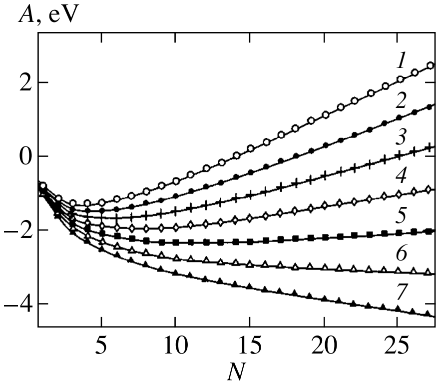

Fig. 1. The work of formation of the hydrate shell of a H_3O^+ ion from vapor at temperature $T = 300$ K under various pressures: 10 Pa (*1*), 50 Pa (*2*), 250 Pa (*3*), 1.25 kPa (*4*), 6.25 kPa (*5*), 31.25 kPa (*6*), and 156.25 kPa (*7*).

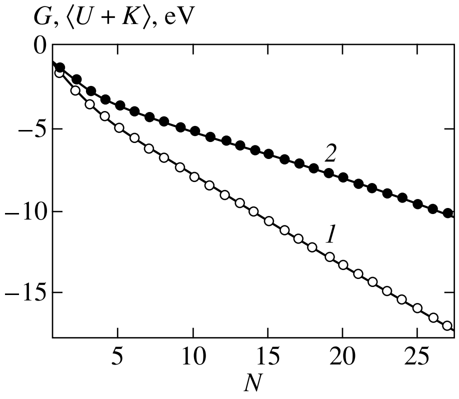

Fig. 2. Gibbs free energy (*1*) and internal energy (*2*) of the hydrate shell of an H_3O^+ ion at temperature $T = 300$ K.

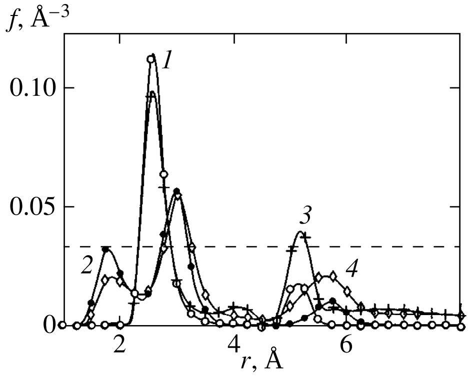

Fig. 3. Binary atom–atom correlations in the hydrate shell of an H_3O^+ ion in water vapor at $T = 300$ K: correlations between the ion and the oxygen atom in a water molecule (*1, 3*), between the ion and the hydrogen atom in a water molecule (*2, 4*); $p = 2.75$ kPa (close to the saturation pressure) (*1, 2*) and $p = 10.0$ kPa (supersaturated vapor) (*3, 4*). The functions are normalized to the number of molecules in the system. The dashed line corresponds to the gross density of water under standard conditions.

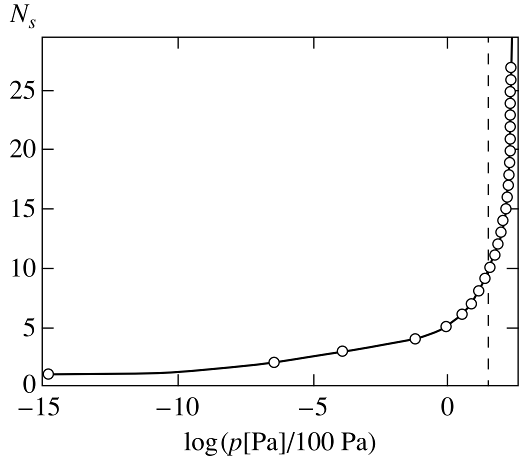

Fig. 4. Equilibrium number of particles in the hydrate shell of an H_3O^+ ion as a function of vapor pressure. The dashed curve corresponds to the saturation vapor pressure above the plane boundary at $T = 300$ K [56].

lously strong absorption of electromagnetic radiation at the middle of the infrared range [29, 58, 59]. The absorption wavelength corresponds to the characteristic frequency of vibrations in hydrogen bonds and indicates the presence of high concentrations of water clusters in the atmosphere. Indirect estimates based on spectroscopic measurements indicate [29, 30, 33] that under standard conditions, a free charge in the atmosphere corresponds to at least 10^6–10^7 electrically neutral water clusters. After the formation of a cluster, its future depends on the type of ions contained in it. The ions of solvable salts and acids remain in a cluster, ensuring its stability. Their coagulation leads to the formation of coarse drops of strong electrolytes. Unstable ions formed as a result of ionization recombine in a water cluster with a certain characteristic recombination time τ_{rec}. In a thermodynamically equilibrium state that sets in when there are no source of ionization, all unstable ions recombine, and the clusters formed on their basis are destroyed. Under natural conditions, free charges are permanently supplied due to ionization. In the case of the steady-state production and recombination of charges, the finiteness of the lifetime τ_{rec} of electrically neutral clusters is responsible for their invariable presence in a cold plasma. The steady-state concentration of clusters is equal to the radio τ_{rec}/τ_{cr} of the characteristic time of the recombination of ions in a cluster to the characteristic time of production of a cluster per unit volume, $\tau_{cr} = I^{-1}$ s cm^3. A long lifetime τ_{rec} ensures a high concentration of electrically neutral clusters under steady-state conditions even in the case of their absolute instability under equilibrium conditions. An increase in τ_{rec} indicates the retardation of recombination and their relative instability.

In a cold rarefied plasma, the energy of interaction between ions and molecules is comparable with the energy of interaction between ions and exceeds the thermal energy $k_B T$. As cluster ions approach one another, a region of a strong electric field formed in the gap between the ions pulls in water molecules. The energy of interaction of a water molecule with the electric field in the gap between two monovalent counterions separated by 4.1 nm amounts to $-k_B T$, and the probability of finding a molecule in this region is thrice as high as outside the gap. This is equivalent to a local elevation of the pressure of vapor, which provokes its condensation. The collective interactions between molecules render the process an avalanche-type, but its evolution is limited in space to the region of ionic gap.

Each ion carries a thermally stable hydrate shell formed by $\langle N_+\rangle$ and $\langle N_-\rangle$ molecules. In view of a nonlinear dependence of the statistical weights of microscopic states on their energy, the total number $\langle N\rangle$ of the molecules bound in the field of two counterions increases as the ions approach one another and the total (negative) energy $\langle U\rangle$ of interaction ion the cluster decreases. The potential of the average force for two counterions is given by

$$\Phi(R) = -k_B T \ln(\rho_{+-}(R)/\rho) = \langle U\rangle - \langle U_+\rangle - \langle U_-\rangle,$$

where $\rho_{+-}(R)$ is the equilibrium density of counterions at a distance R from the ions, $\langle U_+\rangle$ and $\langle U_-\rangle$ are the equilibrium potential energies of hydrate shells of the ions separated by an infinitely long distance, and $\rho \equiv \rho_+ = \rho_-$. The potential $\Phi(R)$ includes the direct interaction between the ions and the indirect interaction through water molecules. The two types of interaction display different dependences on the distance R between the ions. The relative motion of the centers of mass of the ions is determined by the potential $\Phi(R)$ of the average force, which is the result of averaging of energy over the positions of molecules and orientations of two interacting counterions for a fixed distance R between them. At distances much smaller than the average separation between cluster ions, the contribution of the interaction with a third ion to $\Phi(R)$ is insignificant.

Such a pattern corresponds to a hypothetic equilibrium state of a cold plasma in the absence of ionic recombination and the sources of ionizing radiation. Under natural conditions, the number of ions and clusters in the plasma is a result of the dynamic equilibrium between opposite processes of ionization and recombination. For times longer than the relaxation time, the steady-state regime corresponding to equal numbers of generated and recombining charges sets in. The calculation of the concentration of electrically neutral clusters on recombining ionic pairs is a typical kinetic problem, but its considerable part can be solved by the methods of equilibrium statistics. In a weakly ionized gas with a charge density of 10^3–10^5 cm^{-3}, the time τ_{int} of relaxation of the internal degrees of freedom for cluster is much shorter than the mean free time τ_{life} of cluster ions before their collision and recombination. Under these conditions, a cluster ions should be regarded as an internally equilibrium system. The characteristic time of interaction of cluster ions with vapor is determined by the frequency of collisions of the cluster with water molecules. The volume density of vapor under typical conditions is approximately 12 to 13 orders of magnitude higher than the density of charges, but it is 5 to 6 orders of magnitude lower than the density of molecules in a cluster. For this reason, the time τ_{vap} of stabilization of a local equilibrium between a cluster and vapor occupies an intermediate position in the time hierarchy: $\tau_{int} \ll \tau_{vap} \ll \tau_{life}$. For a large distance between ions, the conditions of the interaction between a cluster and vapor remain unchanged during almost the entire time interval τ_{life} of diffusion counterflow. During this time, the thermal and material equilibrium of the cluster and vapor sets in, and its hydrate shell is formed. The conditions of interaction of charged clusters with vapor change radically only at the final stage of this motion for an ionic spacing of the order of 3 nm. The process of convergence of hydrated ions is accompanied by the intense pulling of vapor molecules into the ionic gap. The time of motion of ions in this final region is comparable with the characteristic time of exchange of molecules between the cluster and vapor. The average distance between vapor molecules is approximately equal to 15 nm, but water molecules are approximately an order of magnitude lighter than clusters. Their thermal velocity is approximately thrice as high as that of clusters, while the cross section of their collisions with gas molecules equal to a quarter of the value corresponding to clusters. For this reason, the mobility of water molecules is an order of magnitude higher. It can be expected that in the final stage of motion before recombination, a partial equilibrium sets in between clusters and vapor: only those molecules which are separated from colliding clusters by a distance not exceeding a certain radius r_{rel} of relaxation are pulled into the ionic gap. The remaining molecules moving in the gas cannot reach the ionic gap during the collision time. The value of r_{rel} depends of the time of the head-on motion of clusters at the final stage before their collision, when polar water molecules are intensely pulled into the ionic gap. The number of vapor molecules getting into the sphere of radius r_{rel} is given by

$$N_{rel} = \frac{4}{3}\pi r_{rel}^3 \rho_w, \tag{36}$$

where ρ_w is the vapor density. The quantity N_{rel} is smaller than the number of vapor molecules which would have been pulled into the ionic gap under the equilibrium conditions. Consequently, the relative motion of two recombining counterions under steady-state conditions corresponds not to the equilibrium function $\Phi(R)$, but to its analogue $\Phi(R, r_{\mathrm{rel}})$. During the time of formation of the dense phase in the ionic gap, a local equilibrium has time to set in only in the sphere of radius r_{rel} surrounding the recombining ions, and the number of molecules pulled into the ionic gap does not exceed N_{rel}. The characteristic relaxation time within a cluster is much shorter than the time of interaction of the cluster with vapor. For this reason, the cluster formed from vapor remains a locally equilibrium system against the background of a relatively slow variation of the number of molecules, and the motion of ions is controlled by the average force potential $\Phi(R, r_{\mathrm{rel}})$ formally in the same way as in the thermodynamic equilibrium. The limiting case of an infinitely slow counter motion of ions corresponds to the condition of a transition from a local to the global equilibrium: $\Phi(R, \infty) \equiv \Phi(R)$.

The calculation of r_{rel} is a complex kinetic problem even when the computer simulation technique is used. Difficulties are encountered in the calculation due to a considerable difference in the time scales of the diffusion motion of water molecules in a gas and the relaxation movements in a nucleus of the dense phase. An estimate of r_{rel} can be obtained from the following considerations. During the counter motion of ions from R_3, at which the dense phase starts being formed in the ionic gap, to the retarding barrier R_m, vapor molecules during their relaxation motion towards an ionic pair are displaced only through a distance not exceeding

$$\begin{aligned} r_{\mathrm{rel}} &\approx \frac{\alpha_{\mathrm{H_2O}}}{\alpha_+ + \alpha_-}(R_3 - R_m) \\ &\approx \frac{\sqrt{M_i^+}\sqrt{M_i^-}}{(\sqrt{M_i^+} + \sqrt{M_i^-})\sqrt{m_{\mathrm{H_2O}}}}\frac{d_i^2}{d_{\mathrm{H_2O}}^2}(R_3 - R_m), \end{aligned} \tag{37}$$

where $\alpha_{\mathrm{H_2O}}$, α_+, and α_- are the mobilities of vapor molecules and hydrated ions in the gas, $d_{\mathrm{H_2O}}$ and d_i are their effective radii of collision with gas molecules, and $M_i^{+(-)} = m_i^{+(-)} + \gamma^{+(-)} m_{\mathrm{H_2O}}$ is the mass of a hydrated ion. Putting $R_3 = 3$ nm, $R_m = 0.80$ nm (see below), and $d_i/d_{\mathrm{H_2O}} \approx 2$, we obtain $r_{\mathrm{rel}} \approx 14$ nm. The substitution of this value into (37) and then into Eq. (36) gives $N_{\mathrm{rel}} \approx 6$. This is approximately one-fourth of the number of water molecules which would be pulled into the ionic gap in thermodynamic equilibrium.

The values of $\Phi(R)$ and $\Phi(R, r_{\mathrm{rel}})$ were calculated for $r_{\mathrm{rel}} = 14$ nm and $T = 300$ K numerically using the Monte Carlo method on a large canonical statistical ensemble. For this purpose, the centers of mass of two ions (H_3O^+ and OH^-) were fixed in a spherical cavity at a distance R. The ions were allowed to rotate freely. The interaction of water molecules was described by the five-center ST2 Raman–Stillinger potential [36–44] supplemented with the interaction of the dipoles induced in the ionic field. Use was made of the potential of interaction of ions with water molecules (the reconstruction of this potential from the experimental data on the free energy of cluster formation was described in the previous section). The direct interaction between the ions includes the Coulomb interaction between the charges, between a charge and a dipole, between the dipoles, and the energy of the polarization-induced interaction between a charge and the induced dipole. The dipole interaction and the induced interactions between ions at distance $R > 1$ nm are relatively weak, and the variations in the values of the parameters of these interactions virtually do not affect the formation of the barrier $\Phi(R, r_{\mathrm{rel}})$. The induced interaction $(-\alpha/2)(e/R^2)^2$ between ions separated by a distance $R > 1$ nm is weaker than the interaction of an ion with a water molecule pulled into the ionic gap by a factor of 50 and amounts to less than $0.05k_{\mathrm{B}}T$; for this reason, it can be disregarded altogether. We take it into account only from the considerations of the formal completeness of the pattern, ascribing to the ions the polarization coefficients α the same as for an isoelectronic water molecule, $\alpha_w = 1.44 \times 10^{-24}$ cm^3 [9].The ion–dipole interaction $-ep/R^2$ is approximately an order of magnitude stronger than the induced interaction, but it is an order of magnitude weaker than the average interaction of an ion with a water molecule pulled into the ionic gap and is of minor importance against the background of molecular component fluctuations. The dipole moment of an ion depends on the point relative to which it is calculated. The indeterminacy in the dipole moment of an ion is equivalent to a certain indeterminacy in the position of the point relative to which its rotation in the field of the other ion is described. It can easily be seen that the indeterminacy in the value of the dipole moment of an ion of 1 D is equivalent to the indeterminacy in the position of a singly charged ion amounting approximately to 0.02 nm, which is an order of magnitude smaller than the error in the value of ionic spacing admissible in our computations, and it suffices for us to take into account only the order of magnitude of the ion-dipole interaction. Therefore, in our numerical calculations, we ascribe to ions the same dipole moment as that of a water molecule, $p_w = 1.85 \times 10^{-18}$ CGS units [9]. The main mechanism responsible for the formation of a potential well and a barrier at such distances lies in the interaction between ions and their hydrate shells against the background of the Coulomb interaction of ions. For this reason, we pay the greatest attention here to a detailed description of the interaction between ions and water molecules. The exchange and dispersive interactions between ions is described by the Lennard–Jones potential with the same numerical values as in the ST2 model for water molecules. Their contribution at such distances is negligibly small and is taken into account only from the considerations of the formal completeness of the pattern. The number of water molecules was not fixed, but fluctuated in accordance with the distribution function of a large canonical ensemble

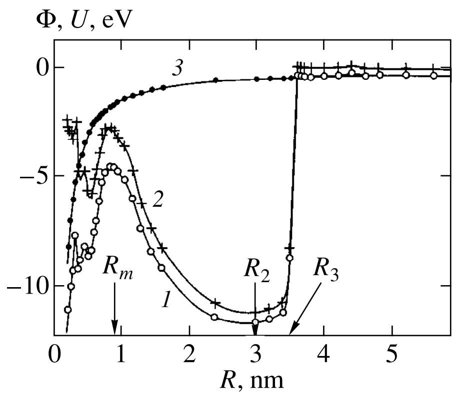

Fig. 5. Mean force potential $\Phi(R, \infty)$ of the interacting H_3O^+ and OH^- ions in water vapor under pressure p = 2 kPa at temperature T = 300 K (*1*), the equilibrium mean energy of interaction between water molecules and the ions (*2*), and the equilibrium mean energy of direct interaction between the ions (*3*).

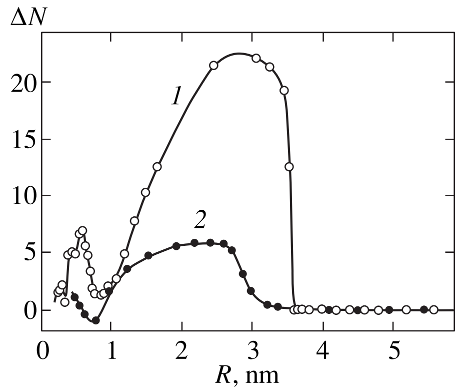

Fig. 6. The number $\Delta N = \langle N\rangle - \langle N_+\rangle - \langle N_-\rangle$ of vapor molecules pulled into the ionic gap as a function of the distance between the H_3O^+ and OH^- ions at T = 300 K and p = 2 kPa: $r_{\rm rel} = \infty$ (*1*) and 14 nm (*2*).

[51–53]. The chemical potential of vapor, which is an initial parameter in the computations, corresponded to a vapor pressure of 2 kPa, which is observed for an air humidity of 65%. Configuration averaging was used to determine the equilibrium energy $\langle U\rangle$ of the system, the direct interaction $\langle U_{+-}\rangle$ between ions, and the average number $\langle N\rangle$ of molecules for various ionic spacings R. The length of the Markov process used for calculating each point was 5×10^8 steps. The values of $\langle U_+\rangle$, $\langle U_-\rangle$, $\langle N_+\rangle$, and $\langle N_-\rangle$ were calculated separately for each ion. In these computations, the system contained only one ion. The average force potential $\Phi(R, r_{\rm rel})$ was obtained as the difference $\langle U\rangle - \langle U_+\rangle - \langle U_-\rangle$ and was subjected to the condition $\Phi(\infty, r_{\rm rel}) \longrightarrow 0$. The value of $\Phi(R, r_{\rm rel})$ was calculated using a modified large canonical ensemble in which the transitions to microscopic states with a number of particles greater than $\langle N_+\rangle + \langle N_-\rangle + N_{\rm rel}$ are forbidden. In the calculation of $\Phi(R)$, the constraint imposed on the number of particles pulled into the ionic gap was removed, which corresponds to $N_{\rm rel} = \infty$.

As the ions approach one another to a distance $R = R_3$, the average force potential $\Phi(R)$ decreases abruptly due to the pulling of additional water molecules into the ionic gap (Figs. 5 and 6). The sharp decrease in the potential, which resembles a phase transition, is associated with collective phenomena in the molecular ensemble. The stability of the molecular component in the ionic gap is partially ensured by molecular interactions. As the separation between ions decreases further, the volume of the ionic gap decreases, and a fraction of molecules is expelled from it. As a result of the decrease in the number of interacting molecules, potential $\Phi(R)$ decreases in magnitude down to contact ionic spacings, at which it starts increasing due to the direct interaction between the ions. The $\Phi(R)$ curve acquires two deep minima at R_1 = 0.3 nm and R_2 = 3 nm, separated by a peak at the point R_m = 0.89 nm (see Fig. 5). The peak height is approximately equal to $278k_BT$. This means that the density of the probability of finding two counterions separated by distance R_m in a thermodynamically equilibrium state is lower than the corresponding value for distance R_2 by a factor of $\exp(278) \approx 10^{121}$. At the same time, the density of the probability of finding the ions at distance R_2 is approximately $\exp(452) \approx 10^{197}$ times higher than at any other distance $R > R_3$, at which the pulling of molecules into the ionic gap ceases. Thus, in the resultant interaction between the ions separated by distance R_2, a minimum is formed on the $\Phi(R)$ curve due to the pulling of water molecules into the field of the ionic gap, while the $\rho_{+-}(R)$ dependence acquires an intense peak corresponding to a locally stable state of the ionic pair. The thermal stabilization of the ionic pair is achieved due to the molecular component in the ionic gap. The total number of molecules participating in the stabilization is approximately equal to 40, from which approximately 25 molecules are additionally pulled into the ionic gap.

In the steady state, the orders of magnitude of the quantities change, but the typical prevailing of ionic pairs with a spacing close to R_2 persists. As a result of a decrease in the number of water molecules pulled into the ionic gap, the depth of the minimum at distance R_2 decreases to one-fourth the initial value, and the minimum itself is displaced towards shorter distances (Fig. 7). Since the barrier height is measured from the bottom of this minimum, the barrier becomes lower, but slightly wider. The position of the barrier changes insignificantly. Since the probability of the barrier surmounting depends exponentially on its height and linearly on its width (see below), the resultant effect of nonequilibrium conditions for the accumulation of water molecules in the ionic gap lies in an increase in the recombination probability. The same figure shows the $\Phi(R, r_{\rm rel})$ curve calculated by the Monte Carlo method for the hypothetical conditions $r_{\rm rel}$ = 0 corresponding to the prohibition of pulling water molecules into the ionic gap. The recombination minimum and barrier on this curve are absent altogether. It can be seen that at distances $R < R_m$, the curves are close and their behavior is determined mainly by the direct interactions between the ions. Against the background of this interaction, only relatively small energy oscillations associated with a nonmonotonic variation of the number of molecules in hydrate shells are observed. The separations ranging from 0.8 to 0.9 nm are unfavorable and the cluster size at such distances attains its minimum value, amounting approximately to five molecules. On the contrary, the separation $R = 0.6$ nm at which the size of the ionic gap coincides with the size of a molecule is most favorable for hydration (see Fig. 6).

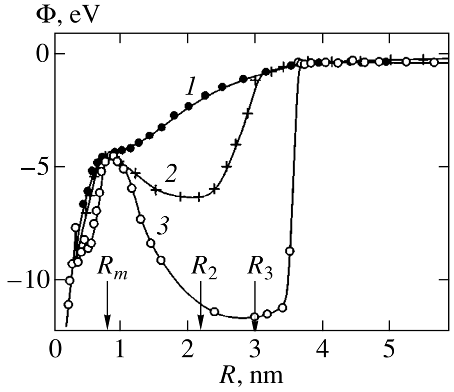

Fig. 7. Mean force potential $\Phi(R, r_{\rm rel})$ of the interaction between the H_3O^+ and OH^- ions in water vapor at $T = 300$ K and $p = 2$ kPa: $r_{\rm rel} = 0$ (*1*), 14 nm (*2*), and $r_{\rm rel} = \infty$ (*3*). The values of R_m, R_2, and R_3 indicated in the figure correspond to $r_{\rm rel} = 14$ nm.

The finite value of $r_{\rm rel}$ in $\Phi(R, r_{\rm rel})$ indicates the inclusion of the nonequilibrium conditions of cluster formation at ionic pairs, but does not take into account the nonequilibrium conditions of generation and recombination of the ions themselves. Let us consider an ensemble of pairs of recombining counterions. The recombination of two ions is preceded by their counter diffusion involving the overcoming of the potential barrier $\Phi(R, r_{\rm rel})$. The presence of the barrier hinders the convergence of the ions and decelerates their recombination. The rate of recombination in an ensemble of particles is determined by the total steady-state counterflow of ions having opposite signs:

$$\begin{aligned}\mathbf{J}^s(R) &= \mathbf{J}^s_+(R) + \mathbf{J}^s_-(R) = -\kappa_+\nabla\rho^s_{+-}(R) \\ &- \alpha_+\rho^s_{+-}(R)\nabla\Phi(R, r_{\rm rel}) - \kappa_-\nabla\rho^s_{-+}(R) \\ - \alpha_-\rho^s_{-+}(R)\nabla\Phi(R, r_{\rm rel}) &= -(\kappa_+ + \kappa_-)\nabla\rho^s_{+-}(R) \\ &- (\alpha_+ + \alpha_-)\rho^s_{+-}(R)\nabla\Phi(R, r_{\rm rel}),\end{aligned} \tag{38}$$

where κ_+ and κ_- are the diffusion coefficients for the positive and negative ions, $\alpha_+ = \kappa_+/k_BT$ and $\alpha_- = \kappa_-/k_BT$ are their mobilities, and $\rho^s_{+-}(R)$ is the spatial correlation function for the counterions in the steady-state recombination mode, normalized by the condition $\rho^s_{+-}(\infty) = \rho_-$, ρ_- being the gross density of negative ions. The last equality in Eq. (38) is valid for an electrically neutral plasma with $\rho_+ = \rho_- = \rho$ since $\rho^s_{+-}(R) = \rho^s_{-+}(R)$ in this case. The average force potential $\Phi(R) = \Phi(R, r_{\rm rel})$ for two counterions corresponds to the hypothetic equilibrium conditions between paired and unpaired ions as if the irreversible recombination of ions did not occur even at contact distances, but the ions formed instead a contact ionic pair, and the reverse process of pair dissociation were possible in principle. In this case, the number of molecules pulled into the ionic gap is subjected to the formal constraint of the finiteness of the value of $r_{\rm rel}$. The substitution of the equilibrium binary correlation function for the counterions,

$$\rho_{+-}(R, r_{\rm rel}) = \rho_-\exp[-\Phi(R, r_{\rm rel})/k_BT],$$

for $\rho^s_{+-}(R)$ into Eq. (38) would lead to the equilibrium result $\mathbf{J}^s = 0$. Recombination is a nonequilibrium process, and a steady-state mode is possible only in the presence of a permanent source of ions pumping new charges instead of recombining ones. We assume that the distance between an ion and the potential barrier $\Phi(R, r_{\rm rel})$ is much smaller than the average separation between ions. In this case, we can conjecture that a new ion is generated at an infinitely large distance from the ion which it approaches and recombines with. Each act of recombination is preceded by overcoming the potential barrier. Since the averaging over the rotational degrees of freedom of ions has already been carried out in $\Phi(R, r_{\rm rel})$, the problem is spherically symmetric. The projection of Eq. (38) on vector $\mathbf{R}$ connecting two counterions in the reference frame of one of these ions has the form

$$\begin{aligned}J^s(R) &= -\kappa(R)\left(\frac{\partial\rho^s_{+-}(R)}{\partial R} + \frac{1}{k_BT}\frac{\partial\Phi(R, r_{\rm rel})}{\partial R}\rho^s_{+-}(R)\right) \\ &= -\kappa(R)\left(\frac{\partial\rho^s_{+-}(R)}{\partial R} - \frac{\rho^s_{+-}(R)}{\rho_{+-}(R, r_{\rm rel})}\frac{\partial\rho_{+-}(R, r_{\rm rel})}{\partial R}\right) \\ &= -\kappa(R)\rho_{+-}(R, r_{\rm rel})\left(\frac{\partial[\rho^s_{+-}(R)/\rho_{+-}(R, r_{\rm rel})]}{\partial R}\right),\end{aligned} \tag{39}$$

where the counter-diffusion coefficient $\kappa(R) \equiv \kappa_+ + \kappa_-$ is a function of the separation between the ions since the gas density in the ionic gap changes with the distance R, and the ionic diffusion mode varies accordingly. The counterflow of ions corresponds to the negative sign in Eq. (39). Since we are dealing with a steady-state flow of ions into the sphere of radius R, it is equal to the number of recombination acts per unit time at the ion located at the center of the sphere. Consequently, the number of pairs recombining per unit volume per unit time is given by

$$I = 4\pi R^2 |J^s(R)| \rho = 4\pi\rho\kappa(R) R^2 \rho_{+-}(R, r_{\mathrm{rel}}) \times \left(\frac{\partial[\rho^s_{+-}(R)/\rho_{+-}(R, r_{\mathrm{rel}})]}{\partial R} \right) \equiv k_{ii}\rho^2, \tag{40}$$

where k_{ii} is the recombination coefficient. Since the recombination rate I is independent of R, Eq. (40) can be written in the following form convenient for integration:

$$\frac{I}{4\pi\rho} \frac{1}{\kappa(R) R^2 \rho_{+-}(R, r_{\mathrm{rel}})} = \frac{\partial[\rho^s_{+-}(R)/\rho_{+-}(R, r_{\mathrm{rel}})]}{\partial R}. \tag{41}$$

The integration of Eq. (41) between the ionic spacing R_r at which recombination takes place and infinity with the boundary conditions

$$\frac{\rho^s_{+-}(R_r)}{\rho_{+-}(R_r, r_{\mathrm{rel}})} = 0, \quad \frac{\rho^s_{+-}(\infty)}{\rho_{+-}(\infty, r_{\mathrm{rel}})} = 1$$

leads to the following expression for the recombination rate at an ion:

$$I = 4\pi\rho \left[\int_{R_r}^{\infty} \frac{dR}{\kappa(R) R^2 \rho_{+-}(R, r_{\mathrm{rel}})} \right]^{-1}. \tag{42}$$

We divide the integration interval in (42) into two intervals: from the distance R_r at which the recombination takes place and the distance R_2 at which ions are accumulated, and from R_2 to infinity. The results of computer simulation show that in the first interval of interionic distances, the system is essentially a cluster formed by water molecules and two counterions immersed in them. The cluster density has the same order of magnitude as the density of water under the standard conditions. The mechanism of diffusion in this case differs qualitatively from the diffusion mechanism in the second interval of interionic distances, $R > R_2$, in which the cluster disintegrates and two independent cluster ions are formed. In the former case, the distances between the molecules in the cluster are comparable with the molecular size, and the diffusion mode is close to diffusion in liquids. In the latter case, the diffusion of hydrated ions takes place in the gas with a mean free path of the order of $l_i = (3–5) \times 10^{-6}$ cm according to the estimates presented in Section 3; i.e., it is two orders of magnitude larger than the molecular size. Since the formation of a cluster as a result of convergence of ions is abrupt in nature, it is sufficient for obtaining the order-of-magnitude estimates to assume that the density of the medium in the region of ionic diffusion changes abruptly from the typically liquid mode in the first interval of ionic spacings to the typically gas mode in the second interval. At the same time, the diffusion coefficient $\kappa(R)$ also changes jumpwise from the value κ_{cl} typical of diffusion in a liquid to the value κ_g typical of diffusion in a gas. Accordingly, the expression for the recombination rate assumes the form

$$I = 4\pi\rho \left[\frac{1}{\kappa_{cl}} \int_{R_r}^{R_2} \frac{dR}{R^2 \rho_{+-}(R, r_{\mathrm{rel}})} + \frac{1}{\kappa_g} \int_{R_2}^{\infty} \frac{dR}{R^2 \rho_{+-}(R, r_{\mathrm{rel}})} \right]^{-1}. \tag{43}$$

In view of the exponential dependence of $\rho_{+-}(R, r_{\mathrm{rel}})$ on $\Phi(R, r_{\mathrm{rel}})$, the main contribution to the integrals in (43) comes from the region of maximum values of $\Phi(R, r_{\mathrm{rel}})$. For the first integral, this is the neighborhood of the minimum of the function $R^2\rho_{+-}(R, r_{\mathrm{rel}})$ at point $\tilde{R}_m$. For the second integral, this is the region $R > R_3$, where the value of $\rho_{+-}(R, r_{\mathrm{rel}})$ decreases, approaching asymptotically the gross density ρ of ions. Taking into account this circumstance, we write expression (43) substituting ρ for $\rho_{+-}(R, r_{\mathrm{rel}})$ in the second integral and changing the lower integration limit to R_3. This gives the following expression for the recombination coefficient:

$$k_{ii} = \frac{I}{\rho^2} = 4\pi \times \left[\frac{1}{\kappa_{\mathrm{cl}}} \int_{R_r}^{R_2} \frac{\tilde{R}_m^{-2} dR}{\exp\{-[\Phi(R, r_{\mathrm{rel}}) - 2k_{\mathrm{B}}T \ln(R/\tilde{R}_m)]/k_{\mathrm{B}}T\}} + \frac{1}{\kappa_g} \int_{R_3}^{\infty} \frac{dR}{R^2} \right]^{-1}. \tag{44}$$

In view of the strong exponential dependence of the integrand in the first integral of (44), the main contribution to the integral comes from the neighborhood of the maximum of the function $\tilde{\Phi}(R, r_{\mathrm{rel}}) \equiv \Phi(R, r_{\mathrm{rel}}) - 2k_{\mathrm{B}}T\ln(R/\tilde{R}_m)$ at point $R = \tilde{R}_m$. Expanding $\tilde{\Phi}(R, r_{\mathrm{rel}})$ into a Taylor series in the vicinity of $\tilde{R}_m$, retaining the first two leading terms, and integrating (44), we obtain

$$k_{ii} = \left\{ \frac{1}{\kappa_{\mathrm{cl}}} \left[-8\pi \left(\frac{\Phi''(\tilde{R}_m, r_{\mathrm{rel}})}{k_{\mathrm{B}}T} + \frac{2}{\tilde{R}_m^2} \right) \right]^{-1/2} \times \frac{1}{\tilde{R}_m^2} \exp\left(\frac{\Phi(\tilde{R}_m, r_{\mathrm{rel}})}{k_{\mathrm{B}}T} \right) + \frac{1}{4\pi\kappa_g R_3} \right\}^{-1}, \tag{45}$$

where $\Phi''(R, r_{\mathrm{rel}}) \equiv \partial^2\Phi(R, r_{\mathrm{rel}})/\partial R^2$. The expression in the braces in (45) is the sum of two terms. The first term is the contribution to k_{ii} associated with the diffusion flow of ions in the interval from R_r to R_2, and the second term, the same in the interval from R_2 to ∞. The substitution of numerical values into (45) shows that the leading role is played by the second term $(4\pi\kappa_g R_3)^{-1}$ whose value is of the order of 10^9 cm s^{-3}. The first term is small due to the exponential factor $\exp[\Phi(\tilde{R}_m)/k_{\rm B}T] \approx \exp(-174) \approx 10^{-75}$. This small factor is not compensated by the relation between other factors appearing in the first and second terms, the ratio $k_g/k_{\rm cl} < 10^3$–10^4 being the next in the hierarchy of values. Consequently, expression (45) can be replaced, with an excessive degree of accuracy, by

$$k_{ii} = 4\pi\kappa_g R_3. \qquad (46)$$

The physical meaning of this result is obvious. The main obstacle for the probability flux of diffusing ions is the interval from infinity to R_3. The relatively low resistance to the probability flux of diffusing ion in a short interval from R_3 to R_r is due to low values of the average force potential (see Fig. 7) and, hence, exponentially high values of ionic concentration at such distances. However, the potential barrier existing within this interval at the point $\tilde{R}_m \approx R_m$ decelerates the counter diffusion of ions and leads to the accumulation of ionic pairs in front of the barrier in the interval $R_m < R < R_3$. Under natural conditions, the continuous recombination of ionic pairs and the "pumping" of new charges from the sources of ionizing radiation take place. The steady-state distribution $\rho^s_{+-}(R)$ is the result of the dynamic equilibrium between these opposite processes. The number of ionic pairs formed as a result of deceleration and recombination in front of the barrier can be expressed in terms of function $\rho^s_{+-}(R)$ which differs significantly from the equilibrium distribution $\rho_{+-}(R, r_{\rm rel})$ in the interval $R_m < R < R_2$ in view of a considerable difference in the probabilities of traversing the intervals $[\infty \longrightarrow R_2]$ (formation of an ionic pair) and $[R_2 \longrightarrow R_r]$ (its recombination) by ions. The first process occurs at a much lower rate than the second, and the predominant "pumping" of ionic pairs from the region $[R_m, R_3]$ in front of the barrier would occur until their number would drop to the value compensating for the difference between the probabilities of single acts of formation and recombination. Consequently, it should be expected that the following relation between the equilibrium and steady-state correlation functions is observed in the region in front of the barrier:

$$\rho_{+-}(R_2, r_{\rm rel}) \gg \rho^s_{+-}(R_2) \gg \rho. \qquad (47)$$

In order to verify the validity of these inequalities, we derive an expression for the recombination coefficient k_{ii} in terms of $\rho^s_{+-}(R_2)$. For this purpose, we return to the differential equation (41) and integrate it from R_r to R_2. This gives

$$I = 4\pi\rho\kappa_{\rm cl}\frac{\rho^s_{+-}(R_2)}{\rho_{+-}(R_2, r_{\rm rel})}\left[\int\limits_{R_r}^{R_2}\frac{dR}{R^2\rho_{+-}(R, r_{\rm rel})}\right]^{-1}, \qquad (48)$$

instead of (42) and

$$k_{ii} = \frac{\rho^s_{+-}(R_2)}{\rho_{+-}(R_2, r_{\rm rel})}$$
$$\times\left\{\frac{1}{\kappa_{\rm cl}}\left[-8\pi\left(\frac{1}{k_{\rm B}T}\Phi''(\tilde{R}_m, r_{\rm rel}) + \frac{2}{\tilde{R}_m^2}\right)\right]^{-1/2} \qquad (49)$$
$$\times\frac{1}{\tilde{R}_m^2}\exp\left[\frac{\Phi(\tilde{R}_m, r_{\rm rel})}{k_{\rm B}T}\right]\right\}^{-1}$$

instead of (45). Equating the right-hand sides of Eqs. (46) and (49), solving the equation for $\rho^s_{+-}(R_2)$, and using the expression for $\rho_{+-}(R, r_{\rm rel})$ in terms of $\Phi(R, r_{\rm rel})$, we obtain

$$\rho^s_{+-}(R_2) = 4\pi\rho\frac{\kappa_g}{\kappa_{\rm cl}}\frac{R_3}{\tilde{R}_m}$$
$$\times\left[-8\pi\left(\tilde{R}_m^2\frac{\Phi''(\tilde{R}_m, r_{\rm rel})}{k_{\rm B}T} + 2\right)\right]^{-1/2}\exp\left[\frac{\Delta\Phi(r_{\rm rel})}{k_{\rm B}T}\right], \qquad (50)$$

where $\Delta\Phi(r_{\rm rel}) = \Phi(\tilde{R}_m, r_{\rm rel}) - \Phi(R_2, r_{\rm rel})$ is the recombination barrier height. It can be seen from Eq. (50) that the number of ionic pairs is an exponential function of the barrier height $\Delta\Phi(r_{\rm rel})$ and depends almost linearly on the barrier width. With decreasing temperature, the number of ionic pairs increases almost exponentially. The steady-state volume density of ionic pairs can be obtained by integrating from the recombination distance to the distance of disintegration of an ionic pair:

$$\rho^s_2 = \rho\int\limits_{R_r}^{R_3} 4\pi R^2\rho^s_{+-}(R)dR. \qquad (51)$$

The integral in (51) weakly depends on the limits of integration since in view of exponentially strong variations of $\rho^s_{+-}(R)$ with the distance, the main contribution to the integral comes from a narrow neighborhood of the peak of function $\rho^s_{+-}(R)R^2$ at point $\tilde{R}_2 \approx R_2$. It follows from Eq. (50) that in the vicinity of point R_2, the profile of function $\rho^s_{+-}(R)$, as well as the profile of $\rho_{+-}(R, r_{\rm rel})$, is determined by the exponential dependence $\rho^s_{+-}(R) \propto \exp[-\Phi(R, r_{\rm rel})/k_{\rm B}T]$. Expanding the exponent in the integrand in (51) into a Taylor series in the vicinity of point $\tilde{R}_2$, retaining the first two leading terms, and integrating between infinite limits taking into account the exponentially rapid decrease of the integrand, we obtain

$$\begin{aligned} \rho_2^s &= 4\pi\tilde{R}_2^2\rho\rho_{+-}^s(\tilde{R}_2) \\ &\times \int_{-\infty}^{\infty} \exp\left[-\frac{1}{2}\left(\frac{\Phi''(\tilde{R}_2, r_{\text{rel}})}{k_\text{B}T} + \frac{2}{\tilde{R}_2^2}\right)(R-\tilde{R}_2)^2\right]dR \\ &= 8\pi^2\frac{\kappa_g}{\kappa_{\text{cl}}}\frac{R_3}{\tilde{R}_m}\tilde{R}_2^3\left(-\tilde{R}_m^2\frac{\Phi''(\tilde{R}_m, r_{\text{rel}})}{k_\text{B}T} - 2\right)^{-1/2} \\ &\times \left(\tilde{R}_2^2\frac{\Phi''(\tilde{R}_2, r_{\text{rel}})}{k_\text{B}T} + 2\right)^{-1/2}\exp\left(\frac{\Delta\Phi(r_{\text{rel}})}{k_\text{B}T}\right)\rho^2. \end{aligned} \tag{52}$$

The height, width, and position of the barrier as well as the position and the width of the minimum of potential $\Phi(R, r_{\text{rel}})$ required for the calculations based on formula (52) were computed using the Monte Carlo method. In the typical case of $r_{\text{rel}} = 14$ nm, the following results were obtained:

$$\Delta\Phi(r_{\text{rel}}) = 1.60 \text{ eV}, \quad \tilde{R}_m = 0.80 \text{ nm},$$

$$\Phi''(\tilde{R}_m) = -45 \text{ eV nm}^{-2}, \quad \tilde{R}_2 = 2.2 \text{ nm},$$

$$\Phi''(\tilde{R}_2) = 8.3 \text{ eV nm}^{-2}, \quad R_3 = 3.0 \text{ nm}$$

(see Fig. 7). In the limiting case when $r_{\text{rel}} = \infty$, the values of the same parameters are as follows:

$$\Delta\Phi(r_{\text{rel}}) = 7.18 \text{ eV}, \quad \tilde{R}_m = 0.89 \text{ nm},$$

$$\Phi''(\tilde{R}_m) = -61 \text{ eV nm}^{-2}, \quad \tilde{R}_2 = 3.0 \text{ nm},$$

$$\Phi''(\tilde{R}_2) = 2.8 \text{ eV nm}^{-2}, \quad R_3 = 3.5 \text{ nm}$$

(see Fig. 5). The diffusion coefficient for a positive ion in the gas is $\kappa_+^g = \langle v_+^{\text{rel}}\rangle l_i/3$, where

$$\langle v_+^{\text{rel}}\rangle = \left(\frac{8k_\text{B}T}{\pi M}\right)^{1/2}$$

is the average relative velocity of collision of a cluster with gas molecules and

$$M = \frac{(m_i^+ + \gamma^+ m_{\text{H}_2\text{O}})m_g}{m_i^+ + \gamma^+ m_{\text{H}_2\text{O}} + m_g}$$

is the reduced mass, m_g being the mass of a gas molecule. The substitution of the numerical values of $l_i = 4 \times 10^{-6}$ cm and $m_g = 0.49 \times 10^{-22}$ g for air leads to the estimate $\kappa_+^g = 0.032$ cm^2 s^{-1} for a hydrated H$^+$ ion. The diffusion flow of hydrated ions in the gas is mainly controlled by collisions of gas molecules with the hydrate shells of ions and is independent of the details of interaction at the contact with an ion. Since the sizes of the hydrate shells of the H$^+$ and OH$^-$ ions are close, their mean free paths and diffusion coefficients also differ insignificantly. Assuming that the diffusion coefficients of the hydrated H$^+$ and OH$^-$ ions in the gas are approximately identical, we obtain for the counter diffusion coefficient the estimate $\kappa_g = \kappa_+^g + \kappa_-^g \approx 0.06$ cm^2 s^{-1}, which is in satisfactory agreement with the diffusion coefficient of the H$_3$O$^+$ ion measured under the same conditions in gaseous nitrogen, which is equal to 0.071 cm^2 s^{-1} [56]. The calculation of the diffusion coefficient κ_{cl} for a cluster is a laborious computational problem. For calculations based on formula (52), it is sufficient to estimate the order of magnitude. Since the density of molecules in a cluster is close to the density of water under the standard conditions, we can naturally expect that the value of κ_{cl} is close to the corresponding diffusion coefficient for water, whose value can be reconstructed from the experimental values of the ionic conductivity $\sigma_+^{\text{liq}} = 350$ A (g-equiv.)/(cm^4 V) and $\sigma_-^{\text{liq}} = 189$ A (g-equiv.)/(cm^4 V) [56]:

$$\kappa_+^{\text{liq}} = \frac{k_\text{B}T\sigma_+}{\rho e^2} = 0.94 \times 10^{-4} \text{ cm}^2 \text{ s}^{-1},$$

$$\kappa_-^{\text{liq}} = 0.51 \times 10^{-4} \text{ cm}^2 \text{ s}^{-1}.$$

The counter diffusion coefficient is given by

$$\kappa_{\text{cl}} \approx \kappa_{\text{liq}} = \kappa_+^{\text{liq}} + \kappa_-^{\text{liq}} = 1.45 \times 10^{-4} \text{ cm}^2 \text{ s}^{-1}.$$

Substituting into (52) these numerical values and the characteristics of the potential barrier $\Phi(R, r_{\text{rel}})$ calculated by the Monte Carlo method for $r_{\text{rel}} = 14$ nm as well as the experimentally measured free carrier concentration $\rho = 10^3$ cm^{-3} typical of the background radiation level at temperature $T = 300$ K, we obtain $\rho_2^s = 7.6 \times 10^{14}$ cm^{-3}. The predicted steady-state concentration of clusters is in fact higher:

$$\rho_2^s + \rho_3^s + \rho_4^s + \ldots > 7.6 \times 10^{14} \text{ cm}^{-3}, \tag{53}$$

since while calculating the right-hand side of this relation, we assumed that the value $r_{\text{rel}} = 14$ nm is preserved for all recombining pairs irrespective of the type of the relative motion of ions. In actual practice, this value is correct only for pairs overcoming the prerecombination barrier during one cycle of the finite counterflow. The remaining (unrecombined) ionic pairs continue accumulating water molecules in their ionic gaps, which leads to an increase in the barrier height, a decrease in the recombination probability, and the stabilization of a cluster. Against the background of such a retardation, slower recombination channels are activated. The most probable channel is the recombination in ionic chains. Detailed studies of strongly nonideal ionic systems by the computer simulation methods revealed [14–24] that ionic pairs form ionic clusters with a chain structure (+ – + – + – + –) in a rarefied system at temperatures satisfying the condition $0.02u_0 < k_BT < 0.1u_0$, where u_0 is the energy of interaction of counterions at the contact distance. The coiling of chains into compact clusters is disadvantageous from the entropy point of view in the range of densities and temperatures under investigation. The reason behind this effect is studied in detail in [21, 60, 61]. The chains correspond to a higher entropy S, and the free energy $G = U - TS + pV$ of the chains at temperatures exceeding a certain threshold value T turns out to be lower than for compact structures. The energy U of a system of charged particles decreases due to screening upon the coiling of the chains to a smaller extent than in systems of electrically neutral particles and cannot compensate the loss in the entropy. The system considered by us here is not identical to ions in a vacuum, but the presence of electric charges of the opposite polarity will inevitably lead to the competition between compact and chain-type clusters in this case also. The effective diameter of an ion increases due to hydration approximately to $r_0 = 1–2$ nm (see Fig. 5). If we disregard the effects associated with the expulsion of molecules from ionic gaps, the electrostatic energy of interaction between the ions of such a size at the contact distance would be $u_0 \approx (1–2) \times 10^{-12}$ erg, or $k_BT = (0.02–0.04)u_0$, which falls into the temperature interval of the stability of ionic chains. The stability condition for the chains in the gross charge density [21, 60, 61] $\rho < (10^{-4}–10^{-3})r_0^{-3} = (10^{17}–10^{18})$ cm^{-3} is satisfied with a considerable margin. The presence of the dipole component in the system in the form of water molecules must catastrophically increase the probability of chain formation and to extend the chain stability interval since the molecules are mainly pulled into the gap between ions of opposite signs. Against such a background, the interactions between like ions whose fraction in a compact cluster is larger appear as especially disadvantageous. The coiling would lead to the expulsion of a part of molecules from the cluster, which is also disadvantageous from the energy point of view.

An ionic chain is formed as a result of a complex many-particle collision whose probability is lower that for a collision of two ions, and this process is kinetically slower. However, recombination within a chain cluster is more probable and occurs at a higher rate than in a cluster formed on an ionic pair. In a chain-like cluster, there exists a trajectory of the counter motion of ions, which is not accompanied by the expulsion of dipole molecules from the cluster and, hence, does not involve the surmounting of a potential barrier. When two counterions move towards each other along the chain, the molecules expelled from the ionic gap may go over to the neighboring ionic gaps in the chain so that the total number of molecules in the cluster changes insignificantly. The larger the cluster size, the greater the number of such collective relaxation modes bypassing the potential barrier of recombination in it. In the limiting case of a macroscopic liquid phase, the effect of pulling in and expulsion of molecules from the interionic gap to the gaseous phase disappears altogether with the recombination barrier. We can expect that ionic pairs that escaped recombination in the first cycle of finite motion will recombine in large clusters, and the recombination rate will be controlled by the rate of cluster formation. The presence of such clusters in the case of anomalously high concentrations is confirmed by the results of measurements of IR absorption spectrum in the atmosphere [29, 58, 59]. The measurements of electric parameters in water vapor prove that the accumulation of clusters is an extremely slow process, while the relaxation time is of the order of tens of minutes and hours [29–33]. These experimental results can easily be interpreted by estimating the lifetime $\tau_{rec} = \rho_n^s/I$ of clusters in a cold plasma. Substituting estimate (53) for ρ_n^s and using the value of $I = 10^5$ cm^{-3} s^{-1}, we obtain $\tau_{rec} \approx 10^{10}$ s. This result is obviously exaggerated since it takes into account only one mechanism of cluster destruction through the recombination of ions. However, the order of magnitude of this quantity shows that the stability of clusters to recombination is extremely high even on macroscopic time scales.

Estimate (53) is one or two orders of magnitude higher than the minimal concentration of clusters sufficient for detecting a radioactive cloud according to calculations (1)–(3) made on the basis of the threshold sensitivity of standard radars. Estimate (53) also satisfies the requirement (20) for the threshold concentration obtained on the basis of the theoretical analysis of the scattering of radiowaves from permittivity fluctuations in a clustered plasma. At the same tame, the value given by (53) is nine orders of magnitude higher than the ionic concentration following from the solution of the ionization–recombination kinetics equation (4) disregarding the dipole component. This resolves the contradiction between the low concentration following from Eqs. (4) and the requirements to the threshold values given by (1)–(3) and (20). The nine-orders-of-magnitude difference was due to the disregard of the recombination retardation associated with the dipole component in the plasma.

In actual practice, the intensity of the reflected signal is higher than that obtained from formulas (12), (13), and (18) after the substitution of the cluster concentration (53), and the conclusion following from estimate (53) and concerning the possibility of radar probing of radioactive bursts to the atmosphere has a "margin" of at least several orders of magnitude. This is due to unique electrical properties of ionic pairs formed in the atmosphere, which magnify the polarizability of the medium by several orders of magnitude and change its permittivity. The discussion of these effects is beyond the scope of this article.

6. CONCLUSION

The presence of dipole particles radically affects the equilibrium and kinetic parameters of a cold plasma. The role of such particles in the ionized atmosphere is played by water molecules. Dipole particles are pulled into the electric field of ions and coat them as a stable envelope. As a result of hydration, the effective mass of the ions increases by an order of magnitude, and the critical radius of capture increases by a factor of 1.5. The interaction between the ions and the dipole component qualitatively changes the nature of correlations between the ions. The pulling of dipole particles into the field of an ionic gap leads to the formation of a deep minimum in the effective ionic interaction potential at a separation of 2–4 nm between the ions and of a high-intensity recombination barrier at a distance of the order of 1 nm. The barrier significantly increases the lifetime of ionic pairs in the prerecombination state. However, in thermodynamic equilibrium in the absence of ionizing radiation, the charges remaining after switching off the external sources of radiation ultimately recombine, and the plasma as such ceases to exist. The existence of a cold plasma requires a permanent supply of new ions. Under natural conditions, the role of such a source of ions is played by radioactive radiation. The presence of the barrier strongly suppresses the recombination and leads to the accumulation of a considerable population of ionic pairs with an ionic gap of 2–4 nm filled with water molecules under the steady-state condition of the cold plasma. The ionic pairs in the prerecombination state are not absolutely stable, but the lifetime of such formations, which is extremely long on the molecular scale, leads to their accumulation in amounts exceeding the number of free charges in the plasma by 8–9 orders of magnitude. Under steady-state conditions, the volume concentration of ionic pairs is proportional to the power of ionizing radiation and repeats its variation in time, although with a delay determined by the relaxation time.

The formation of a large population of electrically neutral water clusters at ionic pairs make the interaction of electromagnetic waves with the natural atmosphere extremely sensitive to the presence of ionization sources. Although the concentration of free charges formed as a result of radioactive irradiation of a moderate intensity is insufficient for the formation of the experimentally observed reflectivity of a radioactive cloud relative to centimeter radiowaves, the role of free charges is played by clusters formed at ionic pairs. The prerecombination barrier decelerates the recombination and ensures the mechanism of enhancement of the effect of ionizing radiation on the electrical properties of the medium through the accumulation of ionic pairs. The effect of enhancement is proportional to the number of the accumulated ionic pairs, which in turn depends exponentially of the recombination barrier height. If the counter motion of ions prior to their recombination were slow enough so that the equilibrium density of water molecules could follow the increasing electric field, the number of molecules drawn into the ionic gap under the natural atmospheric conditions would be of the order of 25, which would lead to the formation of an extremely deep minimum (of approximately $280k_BT$) and an intense barrier (of approximately $450k_BT$) in the ionic interaction at distances smaller than the recombination radius. According to the results of calculations, all the ions under the steady-state conditions would be coupled into ionic pairs. The number of such pairs would be independent of the power of the ionization source and would be limited only by the moisture content in the atmosphere. Vapor would be completely bound in clusters on ionic pairs. This is not observed in actual practice since the density of water molecules in the ionic gap is much lower than a local equilibrium value, and just a few molecules can get into the ionic gap at the final stage of the counter motion of the ions. Thus, in contrast to the equilibrium conditions, the height of the prerecombination barrier under the steady-state conditions is a result of a compromise between the dynamics of the counterflow of hydrated ions and the mobility of vapor molecules. A higher mobility would correspond to a higher barrier and a more intense accumulation of ionic pairs.

The formation of clusters on ionic pairs noticeably changes the dielectric properties of the air mass since the rotational mobility of a molecule bound to a cluster and its contribution to the polarizability of the medium change radically. The giant (on the molecular scale) value of the dipole moment of a bound ionic pair, which is 2 or 3 orders of magnitude higher than the dipole moment of a water molecule, ensures the elevated polarizability of the ionized gas. In view of the quadratic dependence of rotational polarizability on the dipole moment of particles [51], the formation of an ionic pair makes the same contribution to the polarizability of the gas as the addition of 10^4–10^6 free water molecules to it.

A detailed analysis of the permittivity and the reflectivity associated with the formation of ionic pairs is beyond the scope of this paper. However, even the obtained order-of-magnitude estimates (up to 9 orders of magnitude in the concentration of ionic pairs and 4–6 orders in their polarizability) undoubtedly prove that it is just ionic pairs formed as a “side product” of ionization that ensure more than 8 to 10 orders of magnitude in the relative change in the permittivity of the natural atmosphere, which were missing in theoretical calculations, and eliminate the discrepancy between the results of theoretical calculations and experimental observations on the scattering of radiowaves from radioactive bursts in the atmosphere.

Finally, it should be observed that the problem investigated here has basically common roots with a number of other important phenomena in the atmosphere, including the well-known problem of an anomalously high absorbability of higher atmospheric layers in the middle part of the IR spectrum. The most reasonable explanation of this phenomenon is associated with the formation of a large population of electrically neutral water clusters stabilized by ionic pairs [29–31, 58, 59]. Another example is the problem of a globular discharge. Although a number of daring and sometimes exotic hypotheses have been put forth [62–64], Stakhanov's model [65, 66] appears the most plausible in view of its quantitative consistency. According to this model, the energy of a globular discharge is accumulated in ionic pairs stabilized by water molecules. The unique condition for the formation of a globular discharge is apparently an intense cold ionization. The temperature of the plasma must be low for the formation of molecular clusters on ions. The cold nonequilibrium glow of a plasma globe is formed as a result of relatively rare acts of recombination, which is hampered by the hydrate shells of ions. The heating of the globe by internal electric currents as a result of the mechanical contact with the conducting surface leads to the destruction of hydrate shells, the intensification of recombination, and the avalanche-type liberation of thermal energy. The evolution of instability terminates by the burst of the globular lightning and is accompanied by rapid heating to a temperature of thousands of degrees. In our opinion, the formation of the reflectivity of the ionized atmosphere and the globular electric discharge are based on the same phenomenon and differ in the scale of the spatial concentration of energy. In both cases, we are dealing with a cold plasma, but the high concentration of unrecombined ionic pairs in the case of globular lightning leads to the energy instability which evolves into a burst, while in a weakly ionized atmosphere, the process evolves to a steady-state mode. The mechanisms of retardation of recombination also differ in their spatial scales. According to the hypothesis developed on the basis of Stakhanov's model [67], the stabilization of ions in a globular lightning occurs at distances of the order of the thickness of the first hydrate shell of an ion (0.3–0.5 nm), while in the steady-state process initiated by a radioactive radiation, the leading role is played by another thermodynamic barrier located at a distance of the order of 1 nm. The origin of this barrier is qualitatively different and is associated with the rapid expulsion of molecules from the ionic gap. In Stakhanov's model, the retardation of recombination is mainly determined by the probability of electron tunneling through a monomolecular hydrate layer, while in our model of the cold plasma with a low charge concentration, the recombination rate is determined by the deceleration of the counter diffusion flows of ions in the region in front of the barrier at atomic spacings larger by a factor of 7–8 than in the former case.

REFERENCES

1. K. A. Boyarchuk, E. N. Kononov, and G. A. Lyakhov, Pis'ma Zh. Tekh. Fiz. **19** (6), 67 (1993) [Tech. Phys. Lett. **19**, 184 (1993)].
2. A. P. Elokhin and E. N. Kononov, At. Énerg. **80**, 129 (1996).
3. A. N. Didenko, Yu. P. Usov, Yu. G. Yushkov, *et al.*, At. Énerg. **80**, 47 (1996).
4. *Contemporary Radiolocation*, Ed. by Yu. B. Kozyrev (Sov. Radio, Moscow, 1969).
5. S. M. Rytov, Yu. A. Kravtsov, and V. I. Tatarskiĭ, in *Introduction to Statistical Radio Physics* (Nauka, Moscow, 1978), Part 2.
6. N. I. Kaliteevskiĭ, *Wave Optics* (Nauka, Moscow, 1971).
7. L. B. Loeb, in *Kinetic Theory of Gases* (McGraw-Hill, New York, 1961), p. 547.
8. E. W. McDaniel, *Collision Phenomena in Ionized Gases* (Wiley, New York, 1964).
9. A. A. Radtsig and B. M. Smirnov, *Reference Data on Atoms, Molecules, and Ions* (Atomizdat, Moscow, 1980; Springer-Verlag, Berlin, 1985).
10. S. Ya. Pshezhetskiĭ, *Mechanism of Radiation-Chemical Reactions* (Khimiya, Moscow, 1968).
11. P. Debye and E. Hückel, Z. Phys. **24**, 185 (1923).
12. B. V. Zelener, G. É. Norman, and V. S. Filinov, Teplofiz. Vys. Temp. **11**, 922 (1973).
13. V. P. Chasovskikh, P. N. Vorontsov-Vel'yaminov, and A. M. El'yashevich, Dokl. Akad. Nauk Tadzh. SSR **16**, 23 (1973).
14. V. P. Chasovskikh and P. N. Vorontsov-Vel'yaminov, Teplofiz. Vys. Temp. **14**, 379 (1976).
15. P. N. Vorontsov-Vel'yaminov and V. P. Chasovskikh, Vestn. Leningr. Univ., No. 10, 30 (1975).
16. P. N. Vorontsov-Vel'yaminov and V. K. Shiff, Teplofiz. Vys. Temp. **15**, 1137 (1977).
17. P. N. Vorontsov-Vel'yaminov and V. P. Chasovskikh, Teplofiz. Vys. Temp. **13**, 1153 (1975).
18. P. N. Vorontsov-Vel'yaminov and V. K. Shiff, Available from VINITI No. 2086-79 (1979).
19. V. K. Shiff, Teplofiz. Vys. Temp. **26**, 1072 (1988).
20. P. N. Vorontsov-Vel'yaminov and S. V. Shevkunov, Fiz. Plazmy **4**, 1354 (1978) [Sov. J. Plasma Phys. **4**, 756 (1978)].
21. S. V. Shevkunov and P. N. Vorontsov-Vel'yaminov, Teplofiz. Vys. Temp. **20**, 1025 (1982).
22. S. V. Shevkunov and P. N. Vorontsov-Vel'yaminov, Teplofiz. Vys. Temp. **21**, 625 (1983).
23. S. V. Shevkunov, P. N. Vorontsov-Vel'yaminov, and N. B. Gromova, Teplofiz. Vys. Temp. **24**, 998 (1986).
24. A. A. Martsinovski, S. V. Shevkunov, and P. N. Vorontsov-Velyaminov, Mol. Simul. **6**, 143 (1991).
25. P. Langevin, Ann. Chim. Phys. **28**, 289 (1903); **28**, 433 (1903).
26. J. J. Thomson, Philos. Mag. **47**, 337 (1924).
27. J. Sayers, Proc. R. Soc. London, Ser. A **169**, 83 (1938).
28. G. L. Natanson, Zh. Tekh. Fiz. **29**, 1373 (1959) [Sov. Phys. Tech. Phys. **4**, 1263 (1960)].
29. H. R. Carlon, J. Appl. Phys. **52**, 3111 (1981).
30. H. R. Carlon, Appl. Opt. **20**, 1316 (1981).
31. H. R. Carlon, J. Chem. Phys. **76**, 5523 (1982).
32. H. R. Carlon, J. Chem. Phys. **78**, 1622 (1983).
33. H. R. Carlon, J. Appl. Phys. **52**, 2638 (1981).

34. Y. K. Lau, S. Ikuta, and P. Kebarle, J. Am. Chem. Soc. **104**, 1462 (1982).
35. J. D. Payzant, R. Yamdagni, and P. Kebarle, Can. J. Chem. **49**, 3308 (1971).
36. S. V. Shevkunov, Dokl. Akad. Nauk **356**, 652 (1997).
37. S. V. Shevkunov, Kolloidn. Zh. **60**, 111 (1998).
38. S. V. Shevkunov, Dokl. Akad. Nauk **363**, 215 (1998).
39. S. V. Shevkunov, Élektrokhimiya **34**, 860 (1998).
40. S. V. Shevkunov, Élektrokhimiya **34**, 869 (1998).
41. S. V. Shevkunov, Kolloidn. Zh. **61**, 275 (1999).
42. S. V. Shevkunov, Khim. Vys. Énerg. **33**, 325 (1999).
43. S. V. Shevkunov and A. Vegiri, J. Chem. Phys. **111**, 9303 (1999).
44. S. V. Shevkunov and A. Vegiri, Mol. Phys. **98**, 149 (2000).
45. P. Kebarle, S. K. Searles, A. Zolla, *et al.*, J. Am. Chem. Soc. **89**, 6393 (1967).
46. M. Arshadi and P. Kebarle, J. Phys. Chem. **74**, 1483 (1970).
47. S. V. Shevkunov, A. A. Martsinovskiĭ, and P. N. Vorontsov-Vel'yaminov, in *Physics of Clusters*, Ed. by A. A. Vostrikov and A. A. Rebrov (Inst. Teplofiz. Akad. Nauk SSSR, Novosibirsk, 1987), p. 98.
48. S. V. Shevkunov, A. A. Martsinovskiĭ, and P. N. Vorontsov-Vel'yaminov, Teplofiz. Vys. Temp. **26**, 246 (1988).
49. S. V. Shevkunov, A. A. Martsinovskiĭ, and P. N. Vorontsov-Vel'yaminov, in *Current Problems of Statistical Physics*, Ed. by I. R. Yukhnovskiĭ *et al.* (Naukova Dumka, Kiev, 1989), Vol. 1, p. 385.
50. S. V. Shevkunov, A. A. Martsinovski, and P. N. Vorontsov-Velyaminov, Mol. Simul. **5**, 119 (1990).
51. T. L. Hill, *Statistical Mechanics. Principles and Selected Applications* (McGraw-Hill, New York, 1956).
52. C. Kittel, *Thermal Physics* (Wiley, New York, 1973; Nauka, Moscow, 1977).
53. V. M. Zamalin, G. É. Norman, and V. S. Filinov, *Monte Carlo Method in Statistical Thermodynamics* (Nauka, Moscow, 1977).
54. N. Metropolis, A. W. Rosenbluth, M. N. Rosenbluth, and H. A. Teller, J. Chem. Phys. **21**, 1087 (1953).
55. M. N. Rosenbluth and A. W. Rosenbluth, J. Chem. Phys. **22**, 881 (1954).
56. *Physical Quantities. Handbook*, Ed. by I. S. Grigor'ev and E. Z. Meĭlikhov (Énergoizdat, Moscow, 1991).
57. Y. Guissani and B. Guillot, J. Chem. Phys. **101**, 490 (1994).
58. H. R. Carlon, Appl. Opt. **19**, 2210 (1980).
59. H. R. Carlon, Appl. Opt. **17**, 3192 (1978).
60. S. V. Shevkunov and P. N. Vorontsov-Vel'yaminov, Khim. Fiz., No. 1, 83 (1983).
61. S. V. Shevkunov and P. N. Vorontsov-Vel'yaminov, Teplofiz. Vys. Temp. **21**, 625 (1983).
62. O. A. Sinkevich, Teplofiz. Vys. Temp. **35**, 651 (1997); **35**, 968 (1997).
63. V. N. Kunin, V. S. Pleshivtsev, and L. V. Furov, Teplofiz. Vys. Temp. **35**, 866 (1997).
64. B. M. Smirnov, *Problem of Globular Lightning* (Nauka, Moscow, 1988).
65. I. P. Stakhanov, Zh. Tekh. Fiz. **46**, 82 (1976) [Sov. Phys. Tech. Phys. **21**, 44 (1976)].
66. I. P. Stakhanov, *On the Physical Origin of Globular Lightning* (Énergoatomizdat, Moscow, 1985).
67. A. N. Gudzenko, V. I. Derzhiev, and S. I. Yakovlenko, Tr. Fiz. Inst. Akad. Nauk SSSR **120**, 50 (1980).

Translated by N. Wadhwa

Journal of Experimental and Theoretical Physics, Vol. 92, No. 3, 2001, pp. 441–453.
Translated from Zhurnal Éksperimental'noĭ i Teoreticheskoĭ Fiziki, Vol. 119, No. 3, 2001, pp. 509–523.
Original Russian Text Copyright © 2001 by Novikov, Vorob'ev, D'yachkov, Nikiforov.

PLASMA, GASES

Effect of a Magnetic Field on the Radiation Emitted by a Nonequilibrium Hydrogen and Deuterium Plasma

V. G. Novikov[a], V. S. Vorob'ev[b], L. G. D'yachkov[b]*, and A. F. Nikiforov[a]

[a]*Keldysh Institute of Applied Mathematics, Russian Academy of Sciences, Miusskaya pl. 4, Moscow, 125047 Russia*
[b]*Institute of High Temperatures Scientific Association (IVTAN), Russian Academy of Sciences,*
Izhorskaya ul. 13/19, Moscow, 127412 Russia
**e-mail: dyachk@mail.ru*

Received July 5, 2000

Abstract—Radiative transfer in a nonequilibrium plasma in an external electric field is considered. The system of kinetic equations determining the populations of atomic levels is written taking into account the combination of collision and radiative processes and is solved together with the kinetic equation for photon of various frequencies, which are emitted and absorbed in the radiative transitions from the states of the continuous and discrete spectra. The shape of spectral lines is determined from the solution of the quantum-mechanical problem on the emission of an atom in the electric field of the plasma and an external magnetic field, taking the Doppler effect into consideration. The developed approach is used in the model calculation of radiative transfer under the conditions corresponding to the edge plasma in a tokamak, which is simulated by a homogeneous plane layer of a deuterium plasma. It is shown that the joint action of the external magnetic field and the electric plasma fields considerably affects the spectral and integrated characteristics of the radiation. *© 2001 MAIK “Nauka/Interperiodica”.*

1. INTRODUCTION

In order to analyze the radiation emitted by a nonequilibrium plasma, one must determine the concentrations of all emitting components and solve the radiative transfer equation for photons in the entire spectral range. In the presence of reabsorption of the radiation, the populations are nonlinear functions of radiation parameters. For this reason, the system of kinetic balance equations determining the level populations must be solved together with the radiative transfer equation. In the presence of externally applied and intrinsic plasma fields, the problem is complicated since the effect of these fields on the emission and absorption coefficients for photons of various frequencies must be taken into consideration. The practical need in formulating such problem emerges, for example, in an analysis of radiative transfer in the low-temperature edge plasma of a tokamak. For instance, in the deuterium plasma in the edge region of the Alcator C-Mod tokamak [1, 2] at temperature $T_e \sim 1$ eV, for the electron number density $n_e \approx 3 \times 10^{15}$ cm^{-3}, and the atomic density $n_a \approx 10^{13}$–10^{16} cm^{-3} in a magnetic field $B \approx 6$–8 T, the emission in spectral lines plays a decisive role in the energy transfer process. As a result of intense recombination and the emergence of radiation with a partial reabsorption of the lines from the Lyman series, the plasma becomes nonequilibrium. Transport processes are very sensitive to the shape of the lines, which is strongly affected by the magnetic field of the tokamak and the electric fields produced by the plasma ions and electrons. Under such conditions, the Zeeman, Stark, and Doppler effects for the lower lines in the Lyman and Balmer series are approximately of the same order of magnitude and must therefore be taken into account simultaneously.

This work is devoted to the analysis of radiation parameters of such plasmas. For this purpose, the equations of radiation–collision kinetics for excited states are solved together with the radiative transfer equation. The populations are determined from the direct numerical solution of these equations as well as using the modified diffusion approximation [3]. The calculation of the spectral line profile is a separate problem. To this end, we obtained the solution of the quantum-mechanical problem on the shape of the spectral lines emitted by an atom in the electric microscopic field of the plasma and in an external magnetic field in the presence of the Doppler effect. The electric microfield created by the plasma ions is taken into account in the quasi-static approximation. Together with the magnetic field, this field removes degeneracy and leads to the splitting of spectral lines into components. For a fixed ionic microfield, the broadening of the components is due to the interaction with plasma electrons and the Doppler effect. The resultant profiles of the lines determined in this way are averaged over the magnitude and direction of the ionic microfield and are used in the equations of kinetics and radiative transfer. We consider the simplest geometry of the emitting volume, i.e., a homogeneous plane plasma layer. In view of the presence of the magnetic field, the problem is not one-dimensional, which

1063-7761/01/9203-0441$21.00 © 2001 MAIK “Nauka/Interperiodica”

complicates computations significantly. The inclusion of the magnetic field may change the radiation energy transferred in spectral lines and may considerably modify the intensity and shape of the lines emitted from the bulk of the plasma.

2. POPULATION OF LEVELS

The populations of the excited states $n_k = n_k(\mathbf{r}, t)$ can be determined proceeding from the equations of energy level kinetics:

$$\frac{dn_k}{dt} = \sum_{q = c, r}\sum_{k' \neq k}(W^{(q)}_{k'k}n_{k'} - W^{(q)}_{kk'}n_k). \tag{1}$$

Here, k determines the electron state corresponding to the discrete level $k = 1, 2, \ldots, k_m$ or to the continuous spectrum $k = e$. We assume that the population of levels with $k > k_m$ are in equilibrium with the continuous spectrum, and these level can be effectively taken into account by ascribing them to the continuous spectrum e. Symbol q denotes the collision-induced ($q = c$) processes of excitation, ionization, quenching, three-particle recombination as well as radiative ($q = r$) processes such as transitions in the discrete spectrum, photorecombination, and photoionization. The probabilities $W^{(q)}_{nm}$ of the $n \longrightarrow m$ transitions in a q process were calculated using the formulas from [4].

According to estimates, the formation and destruction of negative and molecular ions at temperatures $T \sim 1$ eV are not essential for calculating the populations of excited states and the radiative transfer. For this reason, we considered plasmas consisting of atoms, electrons, and singly charged positive ions.

In the quasi-stationary approximation, putting $dn_k/dt = 0$, we obtain a system of algebraic equations in the collision–radiation approximation, which was solved in a given radiation field. Besides, to reduce the computation time, we used the modified diffusion approximation (MDA) in which analytic formulas were derived for calculating the populations [3]. This approximation is constructed on the analogy between the motion of an electron in the discrete space of atomic energy levels and the random roaming of a Brownian particle; this leads to the discrete version of the Fokker–Planck equation. Its solution directly specifies the values of populations taking into account radiative and collision processes (see [3, p. 133]).

In this paper, atomic units are used.

3. RADIATIVE TRANSFER

If we disregard scattering processes, the spectral intensity of radiation at frequency ω with polarization ρ in a certain direction defined by the unit vector $\mathbf{\Omega}$ ($\mathbf{\Omega} = \mathbf{k}/|\mathbf{k}|$, where $\mathbf{k}$ is the wave vector of the electromagnetic radiation) satisfies the transfer equation

$$\frac{dI_{\omega\rho}}{ds} + \kappa_{\omega\rho}I_{\omega\rho} = j_{\omega\rho}, \tag{2}$$

where s is the coordinate along the beam in the preset direction, $j_{\omega\rho}$ is the bulk emissive power, and $\kappa_{\omega\rho}$ is the absorption coefficient taking into account the induced emission. The solution of Eq. (2) has the form

$$I_{\omega\rho}(s) = \int_{-\infty}^{s} j_{\omega\rho}(s')\exp\left(-\int_{s'}^{s}\kappa_{\omega\rho}(s'')ds''\right)ds'. \tag{3}$$

For the isolated spectral line corresponding to transition $n \longrightarrow m$, in the approximation of the total redistribution over frequency and polarization, we have

$$j^{nm}_{\omega\rho}(\mathbf{r}, \mathbf{\Omega}) = \frac{\omega}{4\pi}A_{nm}n_n(\mathbf{r})\frac{1}{2}\Phi^{nm}_{\omega\rho}(\mathbf{r}, \mathbf{\Omega}), \tag{4}$$

where A_{nm} is the Einstein coefficient for the spontaneous emission of a photon, and $\Phi^{nm}_{\omega\rho}(\mathbf{r}, \mathbf{\Omega})$ is the line profile for such an emission in direction $\mathbf{\Omega}$, normalized to unity. In the presence of a magnetic field $\mathbf{B}$, the emissive power and the absorption coefficient depend on the magnitude of the magnetic field as well as its direction. If there exists a preferred direction, the anisotropy in the properties of the plasma may become significant and, hence, the electromagnetic radiation in the general case is determined by the four Stokes parameters. In an optically inactive medium, under the condition of complete mixing of polarizations, it is sufficient to write the transfer equations for each polarization separately. The necessary condition for complete mixing in frequency and polarization is that the frequency of collisions between an atom and electrons is much higher than the frequency of radiative transitions.

In the case of a plane plasma layer ($0 \le z \le L$) in a uniform magnetic field directed at angle β to the z axis (which is normal to the layer), the intensity of radiation (3) emitted from the layer in direction $\mathbf{\Omega}(\vartheta, \varphi)$ (ϑ is the angle between the direction $\mathbf{\Omega}$ of the beam and the z axis and φ is the angle between the projections of $\mathbf{\Omega}$ and $\mathbf{B}$ on the plane perpendicular to the z axis) can be written in the form

$$\begin{aligned} I_\omega(\vartheta, \varphi) &= \sum_\rho I_{\omega\rho}(z, \vartheta, \varphi)\big|_{z = L} \\ &= \frac{1}{\cos\vartheta}\sum_\rho\int_0^L j_{\omega\rho}(z, \chi)\exp\left(-\frac{1}{\cos\vartheta}\int_z^L\kappa_{\omega\rho}(z', \chi)dz'\right)dz, \end{aligned} \tag{5}$$

where χ is the angle between $\mathbf{\Omega}$ and $\mathbf{B}$:

$$\cos\chi = \cos\beta\cos\vartheta + \sin\beta\sin\vartheta\cos\varphi. \tag{6}$$

In the problem of plasma radiation energy losses, it is important to calculate the emissive power carried through a unit area element on the surface of the layer. For the spectral line corresponding to the $n \longrightarrow m$ transition, the radiation yield in the half-space corresponding to the positive direction of the z axis is defined as

$$J_{nm} = \int d\omega \int_0^{\pi/2} \sin\vartheta d\vartheta \int_0^{2\pi} d\varphi \sum_\rho I_{\omega\rho}(\vartheta, \varphi)\cos\vartheta$$

$$= \frac{\omega_{nm}}{4\pi} A_{nm} \int_0^L dz n_n(z) \int d\omega \int_0^{\pi/2} \sin\vartheta d\vartheta \qquad (7)$$

$$\times \int_0^{2\pi} d\varphi \frac{1}{2} \sum_\rho \Phi^{nm}_{\omega\rho}(z, \chi) \exp\left(-\int_z^L \frac{\kappa_{\omega\rho}(z', \chi) dz'}{\cos\vartheta}\right),$$

where we have taken into account the fact that the line width is much smaller than the radiation frequency ω_{nm}.

In Eqs. (1) of the energy-level kinetics, the emission and absorption processes in the spectral line $n \longrightarrow m$ appear in the form of the combination

$$W^{(r)}_{nm}(\mathbf{r}) n_n(\mathbf{r}) - W^{(r)}_{mn}(\mathbf{r}) n_m(\mathbf{r}) = A_{nm} n_n(\mathbf{r})$$

$$+ \frac{1}{c} \int d\omega \int d\Omega \sum_\rho [B_{nm} n_n(\mathbf{r}) \tilde{\Phi}^{nm}_{\omega\rho}(\mathbf{r}, \mathbf{\Omega}) \qquad (8)$$

$$- B_{mn} n_m(\mathbf{r}) \Phi^{mn}_{\omega\rho}(\mathbf{r}, \mathbf{\Omega})] I^{nm}_{\omega\rho}(\mathbf{r}, \mathbf{\Omega}).$$

Here, c is the velocity of light, B_{mn} and B_{nm} are the Einstein coefficients for absorption and induced emission, $\Phi^{mn}_{\omega\rho}(\mathbf{r}, \mathbf{\Omega})$ and $\tilde{\Phi}^{nm}_{\omega\rho}(\mathbf{r}, \mathbf{\Omega})$ are the spectral line profiles for the emission in direction $\mathbf{\Omega}$ corresponding to these processes, and $d\Omega$ is the solid angle element for the direction of emission ($d\Omega = \sin\vartheta d\vartheta d\varphi$). Quantity (8) defines the number of photons corresponding to transition $n \longrightarrow m$, which emerge from the unit volume of the plasma surrounding point $\mathbf{r}$ per unit time. It is convenient to introduce the so-called effective probability of radiation,

$$A^*_{nm}(\mathbf{r}) = A_{nm}$$

$$- \frac{1}{n_n(\mathbf{r})} \int \frac{d\omega}{\hbar\omega} \int d\Omega \sum_\rho \kappa_{\omega\rho}(\mathbf{r}, \mathbf{\Omega}) I^{nm}_{\omega\rho}(\mathbf{r}, \mathbf{\Omega}), \qquad (9)$$

where $\kappa_{\omega\rho}(\mathbf{r}, \mathbf{\Omega})$ is the absorption coefficient corresponding to the given isolated line,

$$\kappa_{\omega\rho}(\mathbf{r}, \mathbf{\Omega}) = -\frac{\omega}{c}$$

$$\times [B_{nm} n_n(\mathbf{r}) \tilde{\Phi}^{nm}_{\omega\rho}(\mathbf{r}, \mathbf{\Omega}) - B_{mn} n_m(\mathbf{r}) \Phi^{mn}_{\omega\rho}(\mathbf{r}, \mathbf{\Omega})].$$

Relations (8) and (9) are of a general nature and are valid for an arbitrary geometry of the emitting system. Using relation (9), we obtain instead of (8) the following expression for the radial component of the equations of the energy-level kinetics:

$$W^{(r)}_{nm}(\mathbf{r}) n_n(\mathbf{r}) - W^{(r)}_{mn}(\mathbf{r}) n_m(\mathbf{r}) = A^*_{nm} n_n(\mathbf{r}). \qquad (10)$$

Substituting the solution of the transfer equation in form (3) and the emissive power (4) into Eq. (9), we obtain

$$A^*_{nm}(\mathbf{r}) = A_{nm}\left[1 - \frac{1}{n_n(\mathbf{r})} \int n_n(\mathbf{r}') \mathcal{K}(\mathbf{r}, \mathbf{r}') d\mathbf{r}'\right], \qquad (11)$$

where the integral is taken over the entire plasma volume, and

$$\mathcal{K}(\mathbf{r}, \mathbf{r}') = \frac{1}{4\pi|\mathbf{r} - \mathbf{r}'|^2} \frac{1}{2} \sum_\rho \int \kappa_{\omega\rho}(\mathbf{r}, \mathbf{\Omega}) \Phi^{nm}_{\omega\rho}(\mathbf{r}', \mathbf{\Omega})$$

$$\times \exp\left(-\int_0^{|\mathbf{r} - \mathbf{r}'|} \kappa_{\omega\rho}(\mathbf{r}'', \mathbf{\Omega}) dq\right) d\omega.$$

Here, point $\mathbf{r}''$ runs along the straight line from point $\mathbf{r}$ to point $\mathbf{r}'$, so that

$$\mathbf{\Omega} = \frac{\mathbf{r} - \mathbf{r}'}{|\mathbf{r} - \mathbf{r}'|}, \quad q = |\mathbf{r}' - \mathbf{r}''|.$$

Following Biberman [5], we assume that $n_n(\mathbf{r})$ is a slowly varying function of $\mathbf{r}$ (at least in the major part of the integration domain). In this case, $n_n(\mathbf{r}')$ in Eq. (11) can be taken out of the integral. According to calculations, such a representation holds well for the model problem with a plasma layer of thickness L since the value of $n_n(\mathbf{r})$ varies only slightly except in narrow surface regions ($z \approx 0$, $z \approx L$) of thickness $\Delta z \ll L$ making a small contribution to the integral (see Section 5).

As a result, we obtain the following expression for the effective emission probability A^*_{nm} in the problem with a plane layer under consideration:

$$A^*_{nm}(z) = A_{nm}[\Theta_{nm}(z, 0) + \Theta_{nm}(z, L)], \qquad (12)$$

$$\Theta_{nm}(z_1, z_2) = \frac{1}{2} - \frac{\delta}{4\pi} \int d\omega \int_{z_1}^{z_2} dz \int_{(\pi/2)(1-\delta)}^{\pi/2} \tan\vartheta d\vartheta \qquad (13)$$

$$\times \int_0^{2\pi} d\varphi \frac{1}{2} \sum_\rho \kappa_{\omega\rho}(z_1, \chi) \Phi^{nm}_{\omega\rho}(z, \chi) \exp\left(-\int_{z_1}^{z} \frac{\kappa_{\omega\rho}(z', \chi) dz'}{\cos\vartheta}\right),$$

where $\delta = 1$ for $z_2 > z_1$ and $\delta = -1$ for $z_1 > z_2$.

In zero magnetic field, we have

$$\Theta_{nm}(z_1, z_2) = \frac{1}{2} - \frac{1}{2} \int d\omega \kappa_\omega(z_1)$$

$$\times \int_{z_<}^{z_>} \Phi^{nm}_\omega(z) E_1\left(\left|\int_{z_1}^{z} \kappa_\omega(z') dz'\right|\right) dz, \qquad (14)$$

where $z_<$ and $z_>$ are respectively the smallest and largest values of z_1 and z_2, and $E_1(y)$ is the integral exponential function:

$$E_1(y) = \int_1^\infty \frac{e^{-yt}}{t}dt.$$

4. SPECTRAL LINE PROFILE IN A MAGNETIC FIELD

The problem on a hydrogen atom in cross electric and magnetic fields was considered by many authors both analytically, using perturbation theory [6–9], and by solving equations numerically in the case of ultrastrong magnetic fields [10, 11]. A much more complicated problem of spectral line broadening in the case when an emitting atom is under the action of an external magnetic field and the fluctuating electric microscopic field of a plasma was studied in detail in [12–14] using the quasi-static approximation for ions. The first two Lyman lines and a Balmer line were calculated. Mathys [14] took into account the Doppler broadening. The effect of ionic dynamics was studied by Günter and Könies in their recent work [15].

An externally applied magnetic field and the electric field produced by ions and electrons of a plasma strongly affect the shape of spectral lines. As a rule, the ions can be considered in the quasi-static approximation, while the electrons should be analyzed in the impact approximation [16]. In crossed electric and magnetic fields, the degeneracy is removed, and the spectral lines corresponding to transitions between the levels with the principal quantum numbers $\bar{n}$ and n split into individual components. The structure of such a splitting is more complex than in the presence of one of the field. The shift of each component and its intensity are determined by the magnetic field induction **B**, the strength of the quasi-static ionic microfield **E**, and the angle between vectors **E** and **B**. Besides, the intensity of a component (but not its shift) depends on the direction **Ω** of radiation, to be more precise, on the angles between **Ω** and vectors **E** and **B**. The profile of each component is determined by the Doppler effect and by the interaction between an atom and free electrons. The resultant profile of the line corresponding to the $\bar{n} \longrightarrow n$ transition can be calculated by averaging over the magnitude and direction of the quasi-static ionic microfield:

$$\Phi_{\omega\rho}^{\bar{n}n}(\mathbf{r}, \mathbf{\Omega}) = \frac{1}{4\pi}\int P(E) \times \sum_{\bar{\nu}\nu} R_{\bar{\nu}\nu\rho}(\mathbf{E})\phi_{\bar{\nu}\nu\rho}(\omega, \mathbf{E})d\mathbf{E}. \tag{15}$$

Here, $P(E)$ is the probability distribution function for the electric ionic (quasi-static) microfield, which is assumed to be isotropic, $R_{\bar{\nu}\nu\rho}(\mathbf{E})$ and $\phi_{\bar{\nu}\nu\rho}(\omega, \mathbf{E})$ are the relative intensity and the profile of an individual component $\bar{\nu} \longrightarrow \nu$ into which transition $\bar{n} \longrightarrow n$ splits in the given magnetic (**B**) and electric (**E**) fields (here and below in this section, the dependence on the magnetic field and on **r** is not manifested explicitly). By $\bar{\nu}$ and ν we denote the sets of quantum numbers determining the initial and final states for each component (see below).

In contrast to [12–14], where the energy matrix could be diagonalized numerically in the basis of the angular momentum eigenstates, we develop here an approach using the analytical results obtained in [6] for energy level splitting. This allows us to present analytically the dipole matrix elements between the basis wave functions.

The profile of each component is determined by the Doppler effect and by the interaction of the atoms with free electrons. These mechanisms are treated as statistically independent, and the resultant contour $\phi_{\bar{\nu}\nu\rho}(\omega, \mathbf{E})$ can be calculated as a convolution of the corresponding profiles:

$$\phi_{\bar{\nu}\nu\rho}(\omega, \mathbf{E}) = \frac{1}{\sqrt{\pi}D_{\bar{\nu}\nu}} \times \int \psi_{\bar{\nu}\nu\rho}(\omega - \omega_{\bar{\nu}\nu} - s, \mathbf{E})\exp[-(s/D_{\bar{\nu}\nu})^2]ds, \tag{16}$$

where $\omega_{\bar{\nu}\nu}$ is the position of the center of the component corresponding to $\bar{\nu} \longrightarrow \nu$,

$$D_{\bar{\nu}\nu} = (\omega_{\bar{\nu}\nu}/c)(2T_a/M)^{1/2}$$

is the Doppler broadening parameter, T_a is the temperature of atoms, and M is the atomic mass. For the electronic profile $\psi_{\bar{\nu}\nu\rho}(\omega, \mathbf{E})$, we use the approximation proposed by Seaton [17] for calculating the broadening of Stark components by electrons. In the given case, the line splitting is associated with a combination of the Stark and Zeeman effects, which renders specific features to the line profiles and requires a certain modification of the theory [17]. This problem is considered in the Appendix.

The relative intensities of the components corresponding to the $\bar{\nu} \longrightarrow \nu$ transition in the dipole approximation are defined as

$$R_{\bar{\nu}\nu\rho} = \frac{|\mathbf{e}_\rho\langle\nu|\mathbf{r}|\bar{\nu}\rangle|^2}{\sum_{\bar{\nu}\nu}|\mathbf{e}_\rho\langle\nu|\mathbf{r}|\bar{\nu}\rangle|^2} = \frac{2\omega_{\bar{n}n}}{n^2 f_{n\bar{n}}}|\mathbf{e}_\rho\langle\nu|\mathbf{r}|\bar{\nu}\rangle|^2, \tag{17}$$

where $\mathbf{e}_\rho$ is the unit vector of photon polarization and $f_{n\bar{n}}$ is the total oscillator force for the $n \longrightarrow \bar{n}$ transition.

We assume that the lines are isolated. In this case, the characteristic line width is smaller than the separation between the lines, which imposes the following limitations on the magnetic field and the plasma density for a given line:

$$B < c/\bar{n}^4, \quad n_e < 0.05/\bar{n}^{15/2}. \tag{18}$$

It should be noted that the approximation of the rectilinear classical trajectories of perturbing electrons, which is conventional in the theory of atomic spectral line broadening, does not lead to any additional constraint on the magnitude of the magnetic field. Indeed, this condition requires that the Larmor frequency be smaller than the plasma frequency, or $B < \sqrt{8\pi c^2 n_e}$. It can easily be verified, however, that the latter inequality always holds when inequalities (18) are satisfied. We can neglect the spin–orbit interaction since the fine structure splitting at temperatures $T \sim 1$ eV, which are typical of divertor plasmas, is smaller than the Doppler width of the levels.

It was proved by Epstein in the framework of the old Born theory (see [18, 19]) that the combined effect of the magnetic and electric fields on the orbit of an electron in a state with the principal quantum number n and the orbital quantum number l in the first approximation in the field can be described as a uniform and independent precession of vectors

$$\frac{3}{2}n\mathbf{L} \mp \mathbf{r}_a$$

($\mathbf{L}$ is the angular momentum and $\mathbf{r}_a$ is the radius vector of the electron, averaged over its orbital motion) with the angular velocities

$$\boldsymbol{\omega}_{1,2} = \frac{1}{2c}\mathbf{B} \mp \frac{3}{2}n\mathbf{E}, \tag{19}$$

respectively.

In the same approximation, the corrections to the electron energies have been obtained [18]. The quantum-mechanical analysis in the first order of perturbation theory leads to the same result [6]. Hamiltonian $\mathcal{H}$ can be written as the sum

$$\mathcal{H} = \mathcal{H}_0 + \mathcal{H}_1$$

of the unperturbed Hamiltonian

$$\mathcal{H}_0 = -\Delta/2 - r^{-1}$$

and the perturbation

$$\mathcal{H}_1 = (2c)^{-1}\mathbf{B}\cdot\mathbf{L} + \mathbf{E}\cdot\mathbf{r},$$

which can be presented in the subspace of states with a preset value of n in the form

$$\mathcal{H}_1 = \frac{1}{2c}\mathbf{B}\cdot\mathbf{L} - \frac{3}{2}n\mathbf{E}\cdot\mathbf{A} = \omega_1\cdot\mathbf{I}_1 + \omega_2\cdot\mathbf{I}_2,$$

where

$$\mathbf{I}_{1,2} = \frac{1}{2}(\mathbf{L} \pm \mathbf{A})$$

and $\mathbf{A}$ is the Runge–Lenz vector satisfying in this subspace the relation [6]

$$\mathbf{A} = -2\mathbf{r}/3n.$$

Operators $\mathbf{I}_{1,2}$ commute with $\mathcal{H}_0$ and satisfy the conventional commutation relations for the angular momentum operator. It follows hence that

$$I_1^2 = I_2^2 = j(j+1),$$

where j is determined by the number of possible states, i.e., $2(2j+1)^2 = 2n^2$, and hence $j = (n-1)/2$, and the components $\mathbf{I_1}$ along the ω_1 axis and $\mathbf{I_2}$ along the ω_2 axis (we will denote them by n' and n'', respectively) may assume $2j + 1$ integer or half-integer values $-j, -j+1, \ldots, j-1, j$.

In the first order of perturbation theory, we can write

$$\varepsilon_{nn'n''m_s} = -\frac{1}{2n^2} + \omega_1 n' + \omega_2 n'' + \frac{1}{c}Bm_s, \tag{20}$$

where $m_s = \pm 1/2$ is the spin projection on the axis directed along the magnetic field.

The corresponding wave function $\psi_{nn'n''}$ can be written as a linear combination of wave functions in the parabolic coordinates with the z axis directed along the electric field $\mathbf{E}$:

$$\psi_{nn'n''} = \sum_{i_1=-j}^{j}\sum_{i_2=-j}^{j} d^j_{n'i_1}(\alpha_1)d^j_{n''i_2}(\alpha_2)\psi_{ni_1i_2}, \tag{21}$$

where $d^j_{kk'}(\alpha) = D^j_{kk'}(0, \alpha, 0)$ is the Wigner function [20] corresponding to the rotation about the z axis through angle α and $\psi_{ni_1i_2} \equiv \psi_{n_1n_2m}$ are the wave function in the parabolic coordinates. In the present case, it is convenient to characterize these functions by quantum numbers i_1 and i_2, which are the components of operators $\mathbf{I}_1$ and $\mathbf{I}_2$ along the z axis and are connected with the conventional parabolic quantum numbers n_1, n_2 and the magnetic quantum number m ($n_1 + n_2 + |m| + 1 = n$) through the following relations:

$$i_1 + i_2 = m, \quad i_1 - i_2 = n_2 - n_1.$$

Angles α_1 and α_2 are formed by vector $\mathbf{E}$ with vectors $\boldsymbol{\omega}_1$ and $\boldsymbol{\omega}_2$, respectively, i.e.,

$$\cos\alpha_{1,2} = \frac{(1/2c)B\cos\vartheta' \mp (3/2)nE}{\omega_{1,2}},$$

where ϑ' is the angle between $\mathbf{E}$ and $\mathbf{B}$.

The shift of component $\bar{\nu} \longrightarrow \nu$ (ν denotes the set of quantum numbers $nn'n''$) relative to the center of the line can be obtained from Eq. (20) if we disregard the spin-orbit interaction:

$$\omega_{\bar{\nu}\nu} - \omega_{\bar{n}n} = \bar{\omega}_1\bar{n}' + \bar{\omega}_2\bar{n}'' - \omega_1 n' - \omega_2 n''.$$

The dipole matrix elements appearing in (17) with the wave functions (21) can be presented in the form of linear combinations of the matrix elements calculated in parabolic coordinates. Let $e_{\rho x}$, $e_{\rho y}$, and $e_{\rho z}$ be the Cartesian coordinates of the unit polarization vector $\mathbf{e}_\rho$ in a coordinate system with the z axis directed along $\mathbf{E}$ and the x axis lying in the plane of vectors $\mathbf{E}$ and $\mathbf{B}$. In this case, we have

$$\mathbf{e}_\rho\langle\nu|\mathbf{r}|\bar{\nu}\rangle = \sum_{a = x, y, z} e_{\rho a}\langle\nu|a|\bar{\nu}\rangle,$$

$$\langle\nu|a|\bar{\nu}\rangle \equiv \langle nn'n''|a|\bar{n}\bar{n}'\bar{n}''\rangle$$

$$= \sum_{i_1 = -j}^{j}\sum_{i_2 = -j}^{j}\sum_{\bar{i}_1 = -\bar{j}}^{\bar{j}}\sum_{\bar{i}_2 = -\bar{j}}^{\bar{j}} d^j_{n'i_1}(\alpha_1)d^j_{n''i_2}(\alpha_2)d^{\bar{j}}_{\bar{n}'\bar{i}_1}(\bar{\alpha}_1) \quad (22)$$

$$\times d^{\bar{j}}_{\bar{n}''\bar{i}_2}(\alpha_2)\langle n_1n_2m|a|\bar{n}_1\bar{n}_2\bar{m}\rangle,$$

where the matrix elements $\langle n_1n_2m|a|\bar{n}_1\bar{n}_2\bar{m}\rangle$ in the parabolic coordinates are calculated by the Gordon formulas [21].

We direct one of the polarization vectors, $\mathbf{e}_1$, along the normal to the plane of vectors $\mathbf{\Omega}$ and $\mathbf{B}$ and choose the other vector $\mathbf{e}_2$ so that it lies in this plane and is perpendicular to Ω. It is convenient to carry out the averaging in Eq. (15) over the directions of $\mathbf{E}$ in a reference frame associated with the magnetic field. Let φ' be the angle between the projections of vectors $\mathbf{\Omega}$ and $\mathbf{E}$ on a plane perpendicular to vector $\mathbf{B}$. In this case, we can write

$$e_{1x} = \cos\vartheta'\sin\varphi', \quad e_{1y} = \cos\varphi', \quad e_{1z} = \sin\vartheta'\sin\varphi',$$

$$e_{2x} = -\cos\chi\cos\vartheta'\cos\varphi' - \sin\chi\sin\vartheta',$$

$$e_{2y} = \cos\chi\sin\varphi',$$

$$e_{2z} = -\cos\chi\sin\vartheta'\cos\varphi' + \sin\chi\cos\vartheta',$$

where angle χ is defined by Eq. (6).

The Wigner function $d^j_{kk'}(\alpha)$ in formulas (21) and (22) can be expressed in terms of the Jacobi polynomials [20]:

$$d^j_{kk'}(\alpha) = \xi_{kk'}\left[\frac{s!(s+\mu+\nu)!}{(s+\mu)!(s+\nu)!}\right]^{1/2}$$

$$\times\left(\sin\frac{\alpha}{2}\right)^{\mu}\left(\cos\frac{\alpha}{2}\right)^{\nu}P_s^{(\mu,\nu)}(\cos\alpha),$$

where

$$\mu = |k-k'|, \quad \nu = |k+k'|, \quad s = j - \frac{1}{2}(\mu+\nu),$$

$$\xi_{kk'} = \begin{cases} 1 \text{ for } k' \ge k, \\ (-1)^{k'-k} \text{ for } k' < k. \end{cases}$$

The Jacobi polynomials $P_s^{(\mu,\nu)}$ can be conveniently evaluated using the recurrence relations [22].

For calculating the broadening by electrons, we will use an approximation in which the profiles of individual components are independent of angle φ' (see the Appendix). In this case, the integration with respect to φ' in Eq. (15) is carried out analytically, which gives

$$\Phi^{\bar{n}n}_{\omega\rho} = \frac{1}{2}\int_0^\infty dEP(E)\sum_{\nu\bar{\nu}}\int_0^\pi d\vartheta'\sin\vartheta'\phi_{\bar{\nu}\nu\rho}(\omega,\vartheta')\langle R_{\bar{\nu}\nu\rho}\rangle, \quad (23)$$

$$\langle R_{\bar{\nu}\nu\rho}\rangle = \frac{1}{2\pi}\int_0^{2\pi} R_{\bar{\nu}\nu\rho}d\varphi'. \quad (24)$$

For $\rho = 1$, we have

$$\langle R_{\bar{\nu}\nu1}\rangle = \frac{\omega_{\bar{n}n}}{n^2 f_{n\bar{n}}}[(x^{\bar{\nu}}_\nu\cos\vartheta' + z^{\bar{\nu}}_\nu\sin\vartheta')^2 + (y^{\bar{\nu}}_\nu)^2],$$

while for $\rho = 2$, the following expression holds:

$$\langle R_{\bar{\nu}\nu2}\rangle = \frac{\omega_{\bar{n}n}}{n^2 f_{n\bar{n}}}\{2\sin^2\chi(x^{\bar{\nu}}_\nu\sin\vartheta' - z^{\bar{\nu}}_\nu\cos\vartheta')^2$$

$$+ \cos^2\chi[(x^{\bar{\nu}}_\nu\cos\vartheta' + z^{\bar{\nu}}_\nu\sin\vartheta')^2 + (y^{\bar{\nu}}_\nu)^2]\},$$

where the matrix elements $a^{\bar{\nu}}_\nu \equiv \langle\nu|a|\bar{\nu}\rangle$ ($a = x, y, z$) are defined by expression (22).

5. RESULTS OF CALCULATIONS

We studied a plane layer of a homogeneous deuterium plasma at temperature $T_e = 1$ eV, with the electron number density $n_e = 3 \times 10^{15}$ cm^{-3} and atomic densities $n_a = 10^{13}$–10^{16} cm^{-3}, which simulates a plasma with a varying optical density. Although the total number density of atoms was assumed to be fixed for definiteness, the populations of individual levels depend, among other things, on the optical density of the layer and is a function of coordinate z (the z axis is perpendicular to the plane of the layer). In order to determine the extent to which the magnetic field affects the radiative transfer, we made calculations for zero magnetic field ($B = 0$) as well as with a magnetic field $B = 8$ T directed at various angles to the plane of the layer. In the conditions under investigation, the Zeeman, Stark, and Doppler effects for the lower lines in the Lyman and Balmer series are of the same order of magnitude, which means that these effects must be taken into account simultaneously.

The relevant quantities are given in the table. The electronic width is estimated by using the approximate formula [23, 24], the Stark shift is included as the second term on the right-hand side in formula (19) for the upper energy level in the transition in the normal (Holzmark) field of ions, and the shift in the magnetic field is taken into account as the first term in the same formula.

In our calculations, we assumed that the profiles of the spectral line corresponding to spontaneous emission, absorption, and induced emission are the same, which corresponds to the approximation of the complete redistribution of photons over frequency [25]. In the static approximation for ions, the participation of collisions with the ions in this redistribution is neglected. However, in the conditions of our problem, almost complete redistribution is attained due to impact collisions with electrons and the Doppler effect. The frequency of the collisions with electrons is much higher than the spontaneous emission probability, and the overlapping of the Zeeman–Stark components ensures the frequency redistribution within the entire line profile (see the table).

It should be noted that the application of the quasi-static approximation for ions in the central region of spectral lines is incorrect. In zero magnetic field, the width of this region for the *Ly*-α line is of the order of the width of the line itself. Consequently, the accuracy in the calculation of the *Ly*-α profile is lower than for other lines. However, in the presence of a magnetic field, the linewidth increases significantly, and the relative role of the ionic dynamics decreases. For this reason, “switching on” the magnetic field slightly improves the accuracy of calculation of line profiles, and the inclusion of the ionic dynamics becomes relatively less important [15]. A similar conclusion about a lower line shape sensitivity to the broadening mechanisms in the presence of a magnetic field was drawn long ago by Mathys [14].

Parameters of line broadening (in electronvolts) for various mechanisms responsible for broadening in deuterium plasma for $T_e = 1$ eV, $n_e = 3 \times 10^{15}$ cm^{-3}, $n_a = 3 \times 10^{15}$ cm^{-3}, and $B = 8$ T

Line	Electronic width	Doppler parameter	Stark shift	Shift in magnetic field
Ly-α	4.1×10^{-5}	3.3×10^{-4}	1.2×10^{-4}	4.6×10^{-4}
Ly-β	1.7×10^{-4}	3.7×10^{-4}	1.9×10^{-4}	4.6×10^{-4}
Ly-γ	4.7×10^{-4}	4.2×10^{-4}	2.5×10^{-4}	4.6×10^{-4}
D-α	1.7×10^{-4}	6.2×10^{-5}	1.9×10^{-4}	4.6×10^{-4}

The population distribution over the plasma layer was calculated by the method of iterations. First, the populations were assumed to have equilibrium values $n_n = n_n^{(0)}$ and a modified diffusion approximation was used. At the last stage (third or fourth iteration), the system of equations (1) was solved. To describe the spectrum, 3100 groups had to be chosen on a special nonequilibrium mesh in ω (100–200 points for each of the principal lines of deuterium). The calculations were made using a multiprocessor computer. Parallelizing was carried out by splitting the problem over the spectrum paying attention to the uniform loading of the processors.

The distribution of deuterium atoms over the energy levels in a plasma layer of thickness 1 cm is shown in Fig. 1. The role of the radiation yield in the lines

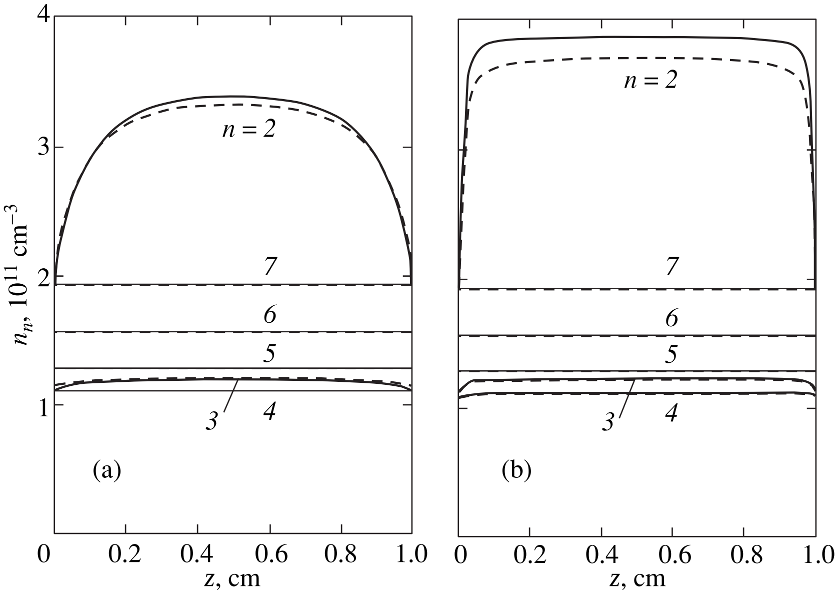

Fig. 1. Populations of excited levels of deuterium in a plasma layer of thickness 1 cm for $T_e = 1$ eV, $n_e = 3 \times 10^{15}$ cm^{-3}, (a) $n_a = 3 \times 10^{14}$ cm^{-3} and (b) 3×10^{15} cm^{-3} as a function of coordinate z perpendicular to the plasma layer.

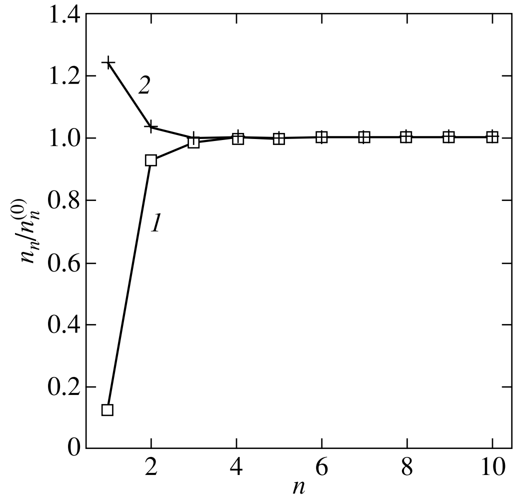

Fig. 2. Population of deuterium levels at the center of the layer normalized to their equilibrium values for $T_e = 1$ eV, $n_e = 3 \times 10^{15}$ cm^{-3}, $n_a = 3 \times 10^{14}$ (*1*) and 3×10^{15} cm^{-3} (*2*).

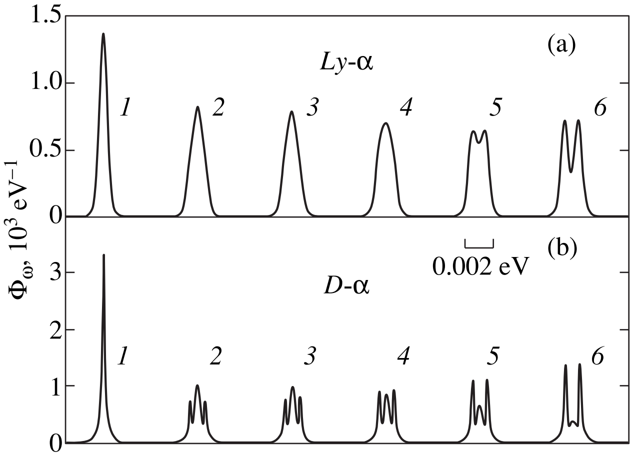

Fig. 3. Profiles of the *Ly*-α and *D*-α spectral lines of deuterium (in the absence of reabsorption) for $T_e = 1$ eV, $n_e = 3 \times 10^{15}$ cm^{-3}, $B = 0$ (*1*) and 8 T (*2*–*6*) for various directions of the magnetic field relative to the direction of observation: $\cos\chi = 0$ (*2*), 1/4 (*3*), 1/2 (*4*), 3/4 (*5*), and 1 (*6*).

belonging to the Lyman series increases strongly as we approach the edge of the layer; for this reason, the population of the first excited energy level ($n = 2$) at the layer edge decreases abruptly. The width Δz of the region where this decrease takes place corresponds to the optical width $\kappa_\omega \Delta z \sim 1$. For other energy levels, this effect is less pronounced, and their populations rapidly approach equilibrium values (according to Saha) with increasing n (Fig. 2). In this case, the magnetic field virtually does not affect their values. “Switching on” the field $B = 8$ T leads to a change in the population by less than 0.3%, and the dependence on the direction of the field is even weaker. The populations of all energy levels turn out to be weakly dependent on coordinate z except for the level with $n = 2$ for which the population in the surface regions decreases considerably (see Fig. 1).

Specifying the atomic concentration n_a below or above the equilibrium value (which amounts to $n_a^{(0)} = 2.4 \times 10^{15}$ cm^{-3} for $n_e = 3 \times 10^{15}$ cm^{-3} and $T_e = 1$ eV), we simulate the recombination or ionization mode, respectively, in the nonequilibrium plasma. This leads to an underpopulation ($n_n/n_n^{(0)} < 1$) or overpopulation ($n_n/n_n^{(0)} > 1$) of lower atomic levels, while upper levels are always in equilibrium with free electrons. In fact, a considerable departure from equilibrium population under our conditions is observed only for the ground level $n = 1$ (see Fig. 2). Figure 1 also shows the results of calculations in a modified diffusion approximation, which ensures virtually the same accuracy as in the numerical solution, but the computation time becomes much shorter, which is important for the numerical realization of complex computational algorithms in the calculation of radiative transfer in a nonequilibrium plasma in the 2D or 3D geometries.

The effect of the magnetic field on the profiles of the first lines in the Lyman (*Ly*-α) and Balmer (*D*-α) spectral series of deuterium is illustrated in Fig. 3. Each profile is the result of averaging of profiles (23) for polarizations $\rho = 1, 2$ and is normalized by the condition

$$\int \Phi_\omega^{\bar{n}n} d\omega = 1.$$

For the resultant profile, the direction of the magnetic field is as important as its strength. The line profile changes significantly depending on the angle χ between the direction of the magnetic field and the direction of radiation (direction of observation). The results of calculation are in agreement with the data obtained in [12–14].

The combined effect of radiation reabsorption and of magnetic fields of various orientations is illustrated in Figs. 4–6, which show the variation of the profiles of the spectral lines emitted by a plasma layer in a direction normal to the layer depending on the layer thicknesses. The results of calculation by formula (5) are given for two values of atomic number density $n_a = 3 \times 10^{14}$ cm^{-3} (Figs. 4a, 5a, and 6a) and 3×10^{15} cm^{-3} (Figs. 4b, 5b, and 6b). Each figure shows the profiles of three Lyman and one Balmer line (*Ly*-α, *Ly*-β, *Ly*-γ, and *D*-α from left to right) whose centers are separated by 0.005 eV for five values of the layer thickness. All the lines are given on the same intensity scale and on the energy scale relative to the center of the lines.

It can be seen from the figures that the *Ly*-α line is trapped in a layer of thickness $L = 0.1$ cm for $n_a = 3 \times 10^{15}$ cm^{-3} and in a layer of thickness $L = 0.6$ cm for $n_a = 3 \times 10^{14}$ cm^{-3}. As the layer thickness increases further, the line intensity changes insignificantly. The *Ly*-β line is trapped for $L \approx 2$ cm if $n_a = 3 \times 10^{14}$ cm^{-3}; if the atomic density is an order of magnitude higher, it occurs for the layer thickness which is an order of magnitude smaller. Indeed, the populations of the absorbing energy level $n = 1$ in the Lyman series differ in these two cases almost by an order of magnitude (see Fig. 2). The features of self-absorption for *Ly*-γ appear only for $n_a = 3 \times 10^{15}$ cm^{-3}, while for $n_a = 3 \times 10^{14}$ cm^{-3}, the line intensity increases in proportion to the layer thickness, which is typical of optically transparent plasmas. For the *D*-α line, the plasma layer is optically transparent, the line intensity remaining virtually unchanged upon an order-of-magnitude change in the value of n_a since in these two cases, the population of the upper ($n = 3$) and the lower ($n = 2$) energy level are close (see Figs. 1 and 2).

The dip at the center of a line typical of self-absorption appears only on the *Ly*-α contour since the population of the energy level $n = 2$ emitting this line decreases noticeably at the layer surface (see Fig. 1). This can be seen in Fig. 4 (**B** = 0) and Fig. 5 (**B** is perpendicular to the direction of observation), where the *Ly*-α line is not split by the magnetic field. In the case when the magnetic field is parallel to the direction of observation, the *Ly*-α line is split by the magnetic field, and the self-absorption effects emerge on each of the two peaks (Fig. 6; cf. Fig. 3). The central part of the *Ly*-β and *Ly*-γ lines remains flat after their reabsorption since the populations of the levels emitting these lines remain virtually unchanged in the surface regions.

The magnetic field affects the line width and the structure of the profile, the magnetic field direction playing a significant role in the latter case. However, the integrated characteristic, i.e., the radiation yield from the layer surface, is virtually independent of the field direction since a change in the direction does not lead to a noticeable redistribution of intensity between the center of the line and its wings (see Fig. 3). The radiation yield was calculated by formula (7) taking into account the dependence of the population of levels on the radiation field in accordance with the system of kinetic equations (1) and relations (10), (12)–(14).

Figure 7 shows the radiation yield from one of the two surfaces of a plane plasma layer as a function of its thickness for two values of atomic number density in zero magnetic field as well as in the field $B = 8$ T directed perpendicularly ($\beta = 0$) to the plasma layer and parallel to it ($\beta = \pi/2$). In the last two cases, the curves almost merge into one. The magnetic field leads to an increase in the radiation yield for partially locked spectral lines due to an increase in their width. The plasma layer is optically transparent for the *D*-α line and, hence, the magnetic field does not affect its yield. The yield of the trapped *Ly*-α line for $n_a = 3 \times 10^{15}$ cm^{-3} and $L > 1$ cm is also affected by the magnetic field insignificantly. The relative role of the magnetic field in the line broadening decreases as we go over to higher terms in a spectral series. The presence of the field $B = 8$ T virtually does not affect the radiation yield even for *Ly*-γ

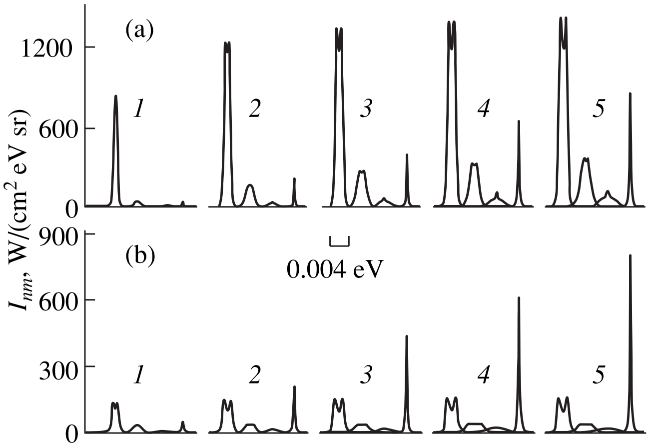

Fig. 4. Profiles of the *Ly*-α, *Ly*-β, *Ly*-γ, and *D*-α spectral lines emitted by a plane layer of deuterium plasma in zero magnetic field in a direction normal to the layer for T_e = 1 eV, $n_e = 3 \times 10^{15}$ cm^{-3}, (a) $n_a = 3 \times 10^{14}$ cm^{-3} or (b) 3×10^{15} cm^{-3}; the plasma layer thickness is 0.1 (*1*), 0.6 (*2*), 1.1 (*3*), 1.6 (*4*), and 2.1 cm (*5*). For each value of the layer thickness, the centers of the lines are separated from one another by 0.005 eV.

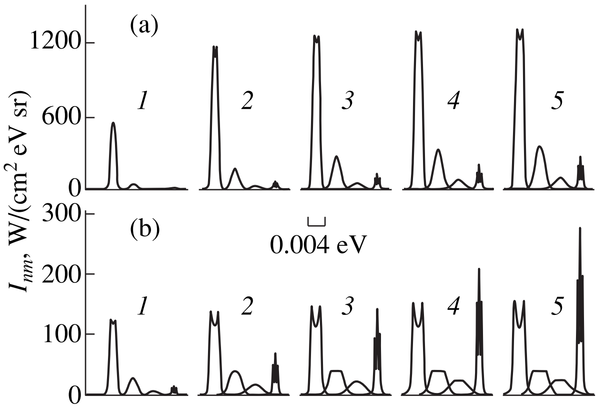

Fig. 5. The same as in Fig. 4 but in a magnetic field $B = 8$ T perpendicular to the direction of observation.

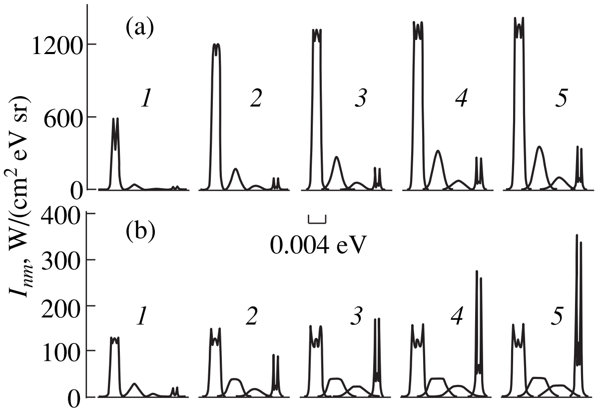

Fig. 6. The same as in Fig. 4 but in a magnetic field $B = 8$ T parallel to the direction of observation.

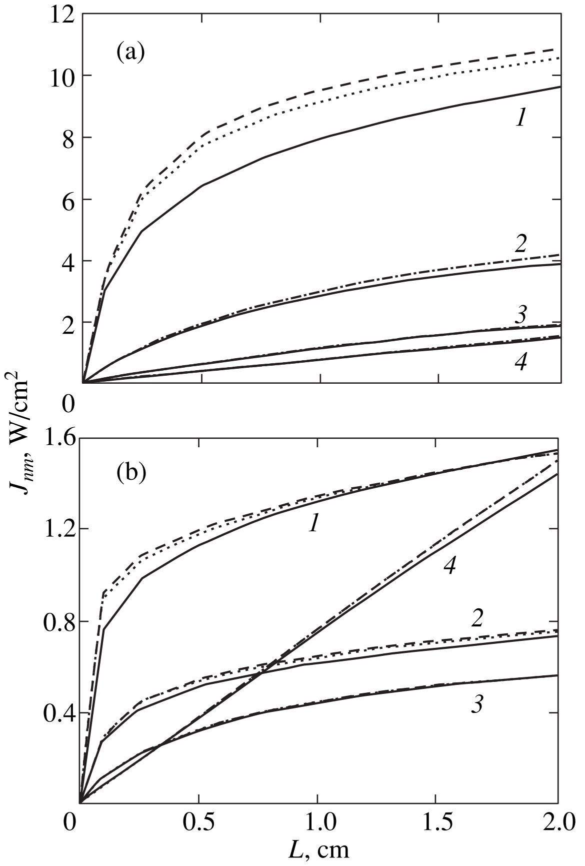

Fig. 7 Radiation yield for spectral lines *Ly*-α (*1*), *Ly*-β (*2*), *Ly*-γ (*3*), and *D*-α (*4*) as a function of the plasma layer thickness for $T_e = 1$ eV, $n_e = 3 \times 10^{15}$ cm^{-3}, (a) $n_a = 3 \times 10^{14}$ cm^{-3} and (b) 3×10^{15} cm^{-3}; solid curves correspond to $B = 0$, dotted curves to $B = 8$ T, $\beta = 0$, and dashed curves to $B = 8$ T, $\beta = \pi/2$.

for both values of n_a considered above, although the effect of reabsorption in these two cases is different.

6. CONCLUSION

The shape of the spectral lines of deuterium and the radiation yield from a plane layer of a deuterium plasma of various thicknesses are calculated for $T = 1$ eV, $n_e \approx n_a \approx 10^{15}$ cm^{-3}, and $B = 8$ T.

It is shown that the magnitude as well as the direction of the magnetic field considerably affect the shape of spectral lines. The contour of a spectral line may acquire a complex structure. For example, when the direction of observation is parallel to the magnetic field, a dip appears at the center of the *Ly*-α line. As the principal quantum numbers of the lower and upper states of the transition increase, the contour structure becomes more complicated. It should be noted that in order to single out the effect of the magnetic field and to simplify our computations to the maximum possible extent, we disregarded the dynamics of ions. Obviously, its inclusion must lead to a partial smoothing of the obtained structures.

The spectral line profile may be considerably deformed as a result of reabsorption. This effect is obviously manifested most clearly for the first lines in the Lyman series and depends on the optical thickness of the plasma layer. Operating together with the magnetic field, it may either additionally complicate or simplify the observed contour of the spectral line. This is primarily determined by the form of the spatial dependence of the population of the upper and lower levels of the transition in the vicinity of the surface of the emitting layer.

The radiation yield from the plasma layer for a given line integrated over the spectrum depends on the magnitude of the magnetic field, but is virtually independent of its direction since the magnetic field direction affects the structure of the spectral line profile, but not the line width. This allows us to use in the radiation–collision kinetics the radiation parameters averaged over the directions and simplifies the inclusion of the magnetic field effect on the energy balance in the edge region of a tokamak. The factors leading to spectral line broadening, in particular, strong magnetic fields, considerably affect the radiation yield for partially reabsorbed lines. In the limiting cases of small or large optical width, the radiation yield is virtually independent of the line width and shape.

ACKNOWLEDGMENTS

The authors are grateful to A.V. Nedospasov, who directed their attention to this problem, the late L.M. Biberman, who took part in discussing the formulation of the problem, and also to A.Yu. Pigarov for numerous fruitful discussions.

This work was supported by the Russian Foundation for Basic Research (project nos. 99-02-17640, 99-01-00121, and 00-15-96529). The calculations were made at the Interdepartmental Computer Complex, Russian Academy of Sciences.

APPENDIX

Broadening by Electrons

A simple model for calculating the electron broadening of hydrogen lines was proposed by Seaton [17]. It is based on the Bethe–Born approximation for the binary interaction of an emitting atom with a perturbing electron, the truncation in the orbital angular momentum, and the analytic approximation of the line profile taking into account its normalization to unity. This approximation ensures the correct frequency dependence both in the profile core, where it corresponds to the impact approximation, and at the wings in the region of transition from the impact to the static approximation. The static electron wing for the plasma parameters under investigation falls to the frequency range in which the approximation of isolated lines is violated and was not considered by us here. The profile associated with electron broadening can be approximated by the expression

$$\psi_\xi(u) = \frac{\gamma_\xi(u)/2\pi}{u^2 + g_\xi^2(u)/4}, \tag{A.1}$$

where ξ denotes the component $\bar{\nu} \longrightarrow \nu$ ($\bar{n}\bar{n}'\bar{n}'' \longrightarrow nn'n''$) of line $\bar{n} \longrightarrow n$ and $u = \omega - \omega_{\bar{\nu}\nu}$ is the distance from the center of the given component.

Profile (A.1) is symmetric; consequently, we will henceforth assume that $u > 0$. Functions $\gamma_\xi(u)$ and $g_\xi(u)$ satisfy the following formulas derived by Seaton [17] for a hydrogen plasma in zero magnetic field:

$$\gamma_\xi(u) = \sqrt{\frac{2\pi}{T}} n_e F_\xi w(u), \tag{A.2}$$

$$g_\xi(u) = \sqrt{\frac{2\pi}{T}} n_e F_\xi u \int_u^\infty \frac{w(u')}{u'^2} du'. \tag{A.3}$$

Here, function $w(u)$ depends only on the principal quantum numbers of the transition and is the same for all components. On the contrary, factor F_ξ is determined by all quantum numbers of the initial and final states and does not depend on u. In the presence of a magnetic field, function $w(u)$ remains the same as in [17] and factor F_ξ must change. For $w(u)$, we have

$$w(u) = \begin{cases} w_0, & u < u_1 \\ w_\infty(u), & u > u_1, \end{cases}$$

where u_1 is determined from the equation

$$w_\infty(u_1) = w_0.$$

In the case of a neutral hydrogen (or deuterium) atom, we have

$$w_0 = \frac{1}{2}\left[\ln\left(\frac{2Tr_D^2}{3\bar{n}^2(\bar{n}^2-1)}\right) - \gamma_0 - E_1\left(\frac{24\bar{n}^2(\bar{n}^2-1)}{(5\bar{n}^2+1)^2 T}\right)\right],$$

$$w_\infty = \ln\left(1 + \frac{C + Du/T}{1 + Qu/T}\frac{T}{u}\right),$$

where r_D is the Debye radius and $\gamma_0 = 0.5772$ is the Euler constant. The parameters C, D, and Q depend on $\bar{n}$ and are given in [17]. The integral with respect to u' in (A.3) can be evaluated in elementary functions.

The diagonal matrix $\boldsymbol{\gamma}$ approximates the electron–electron interaction matrix $\boldsymbol{\Gamma}$ and is defined so that [17] its elements are proportional to the diagonal elements of the interaction matrix, and the matrix product $\mathbf{D}^+\boldsymbol{\Gamma}\mathbf{D}$ does not change as a result of approximation, i.e.,

$$\gamma_\xi = b\Gamma_{\xi\xi}, \quad \mathbf{D}^+\boldsymbol{\gamma}\mathbf{D} = \mathbf{D}^+\boldsymbol{\Gamma}\mathbf{D}.$$

Here, $\mathbf{D}$ is the column matrix consisting of the transition probability amplitudes D_ξ whose squares of the moduli are equal to the relative intensities of components (17). For this reason, factor F_ξ is the product of the proportionality factor b and the diagonal element $G_{\xi\xi}$ of matrix $\mathbf{G}$ ($F_\xi = bG_{\xi\xi}$), which is connected with $\boldsymbol{\Gamma}$ in the same way as F_ξ is connected with γ_ξ through relation (A.2):

$$\boldsymbol{\Gamma} = \sqrt{2\pi/T} n_e \mathbf{G} w(u).$$

Coefficient b is defined as

$$b = \frac{\sum_{\xi\xi'} D_\xi^* G_{\xi\xi'} D_{\xi'}}{\sum_\xi |D_\xi|^2 G_{\xi\xi}}. \tag{A.4}$$

The explicit form of $\mathbf{G}$ is defined in [17] in the representation of states $|nlm\rangle$ (the corresponding matrix will be denoted by $\mathbf{G}^{(L)}$) and the transition to the representation of the parabolic states $|n_1n_2m\rangle$ is indicated. In the case of crossed electric and magnetic fields, we must go over to the basis of states (21). In the *nlm* representation, the matrix element $G_{s,t}^{(L)}$ (s, t are transitions between the $\bar{n}\bar{l}\bar{m}$ and *nlm* states) has the form

$$G_{s,t}^{(L)} = C(\bar{l}_s, 1, l_s; \bar{m}_s, m_s - \bar{m}_s, m_s)$$
$$\times C(\bar{l}_t, 1, l_t; \bar{m}_t, m_t - \bar{m}_t, m_t) G^{(L)}(l_s, \bar{l}_s; l_t, \bar{l}_t)$$
$$\times [(2l_s + 1)(2l_t + 1)]^{-1/2},$$

where $C(j_1, j_2, j; m_1, m_2, m)$ are the Clebsch–Gordan coefficients and $G^L(l_s, \bar{l}_s; l_t, \bar{l}_t)$ is the reduced matrix element which may differ from zero only if

$$\bar{l}_s - l_s = \pm 1, \quad \bar{l}_t - l_t = \pm 1,$$
$$l_t - l_s = 0, \pm 1, \quad \bar{l}_t - \bar{l}_s = 0, \pm 1.$$

For $l_s = l_t = l$ (in this case, $\bar{l}_s = \bar{l}_t = \bar{l}$ also), we have

$$G^{(L)}(l, \bar{l}, l, \bar{l})$$
$$= 6[n^2(n^2 - l^2 - l - 1) + \bar{n}^2(\bar{n}^2 - \bar{l}^2 - \bar{l} - 1)],$$

while for $l_s \neq l_t$, we have

$$G^{(L)}(l_s, \bar{l}_s; l_t, \bar{l}_t)$$
$$= -12\begin{Bmatrix} 1 & l_s & \bar{l}_s \\ 1 & \bar{l}_t & l_t \end{Bmatrix} d(n, l_s, l_t) d(\bar{n}, \bar{l}_s, \bar{l}_t),$$

where

$$d(n, l, l') = (l - l')[nl_>(n^2 - l_>^2)]^{1/2}$$

and $l_>$ is the larger of numbers l and l'.

A transition to representation (21) is carried out with the help of the transformation matrix **Y**, which is constructed from the coefficients of the expansion of states $|nn'n''\rangle$ in states $|nlm\rangle$:

$$\mathbf{G} = \mathbf{Y}\mathbf{G}^{(L)}\mathbf{Y}^{+},$$

$$Y(\xi, s) = \langle nlm|nn'n''\rangle\langle\bar{n}\bar{l}\bar{m}|\bar{n}\bar{n}'\bar{n}''\rangle.$$

The expansion of the $nn'n''$ states in the states in parabolic coordinates is determined by formula (21), while the expansion of the latter in the nlm states is carried out with the help of the Clebsch–Gordan coefficients [26, 27, 19]:

$$\langle nlm|nn'n''\rangle = \sum_{i_1=-j}^{j}(-1)^{n_2}d^{j}_{n'i_1}(\alpha_1)$$
$$\times d^{j}_{n''i_2}(\alpha_2)C(j, j, l; i_1, i_2, m),$$

where $i_2 = m - i_1$, $n_2 = j + i_1 - (m + |m|)/2$.

The numerator in formula (A.4) can be calculated in any representation, but the easiest way is to make calculation in the nlm representation. The denominator is calculated in the $nn'n''$ representation. In this case, the relative intensities of the components $|D_\xi|^2 = R_{\bar{\nu}\nu\rho}$ and, hence, profiles (A.1) are complex functions of angles ϑ' and φ' over which the integration in Eq. (15) is carried out. In order to simplify calculations, we use the following approximation. Instead of $|D_\xi|^2$, we substitute into Eq. (A.4) relation (24), i.e., the result of averaging of this quantity over φ', and also carry out the averaging over polarizations in the numerator and denominator of Eq. (A.4) separately. This gives

$$b = 4\sum_{l_s\bar{l}_s l_t\bar{l}_t}(l_s - \bar{l}_s)(l_t - \bar{l}_t)(l_{s>}l_{t>})^{1/2}$$
$$\times R^{\bar{n}\bar{l}_s}_{nl_s}R^{\bar{n}\bar{l}_t}_{nl_t}G^{(L)}(l_s, \bar{l}_s; l_t, \bar{l}_t)$$
$$\times\left\{3\sum_{\xi}G_{\xi\xi}\{2\sin^2\chi(x^{\bar{\nu}}_{\nu}\sin\vartheta' - z^{\bar{\nu}}_{\nu}\cos\vartheta')^2\right. \tag{A.5}$$
$$\left.+ (1 + \cos^2\chi)[(x^{\bar{\nu}}_{\nu}\cos\vartheta' + z^{\bar{\nu}}_{\nu}\sin\vartheta')^2 + (y^{\bar{\nu}}_{\nu})^2]\}\right\}^{-1},$$

where $l_{s>}$ is the larger of the values of l_s and $\bar{l}_s$, $l_{t>}$ is the larger of the values of l_t and $\bar{l}_t$, and $R^{\bar{n}\bar{l}}_{nl}$ is the radial matrix element calculated by using Gordon's formula [21, 28]. In order to justify this approximation, we note, first, that the broadening of individual components is determined by three factors: the Doppler effect and the interaction with ions and electrons, while the application of approximation (A.5) roughens the effect of only one (the latter) of these factors. Second, factor b appears in the approximation of the interaction matrix which is computed using a number of approximations; consequently, it is meaningless to require a high accuracy of its calculation. Finally, the dependence of the final result on b will be masked to a considerable extent as a result of averaging over the magnitude and direction of the quasi-static microfield in Eq. (15). For this reason, approximation (A.5) is justified, which was confirmed by approximate calculations. The application of this approximation makes the profile of component (16) independent of angle φ' and simplifies the integration in Eq. (15).

REFERENCES

1. B. L. Welch, H. R. Griem, J. Terry, *et al.*, Phys. Plasmas **2**, 4246 (1995).
2. A. Yu. Pigarov, J. L. Terry, and B. Lipschultz, Plasma Phys. Controlled Fusion **40**, 2055 (1998).
3. L. M. Biberman, V. S. Vorob'ev, and I. T. Yakubov, *Kinetics of Nonequilibrium Low-Temperature Plasmas* (Nauka, Moscow, 1982; Consultants Bureau, New York, 1987).
4. L. C. Johnson, Astrophys. J. **174**, 227 (1972).
5. L. M. Biberman, Dokl. Akad. Nauk SSSR **59**, 659 (1948).
6. Yu. N. Demkov, B. S. Monozon, and V. N. Ostrovskiĭ, Zh. Éksp. Teor. Fiz. **57**, 1431 (1969) [Sov. Phys. JETP **30**, 775 (1970)].
7. E. A. Solov'ev, Zh. Éksp. Teor. Fiz. **85**, 109 (1983) [Sov. Phys. JETP **58**, 63 (1983)].
8. A. V. Turbiner, Zh. Éksp. Teor. Fiz. **84**, 1329 (1983) [Sov. Phys. JETP **57**, 770 (1983)].
9. P. A. Braun and E. A. Solov'ev, Zh. Éksp. Teor. Fiz. **86**, 68 (1984) [Sov. Phys. JETP **59**, 38 (1984)].
10. V. S. Melezhik, Phys. Rev. A **48**, 4528 (1993).
11. P. Fassinder and W. Schweizer, Phys. Rev. A **53**, 2135 (1996).
12. Nguyen-Hoe, H.-W. Drawin, and L. Herman, J. Quant. Spectrosc. Radiat. Transf. **7**, 429 (1967).
13. G. Mathys, Astron. Astrophys. **125**, 13 (1983).
14. G. Mathys, Astron. Astrophys. **139**, 196 (1984).
15. S. Günter and A. Könies, J. Quant. Spectrosc. Radiat. Transf. **62**, 425 (1999).
16. H. R. Griem, *Spectral Line Broadening by Plasmas* (Academic, New York, 1974; Mir, Moscow, 1978).
17. M. J. Seaton, J. Phys. B **23**, 3255 (1990).
18. M. Born, in *The Mechanics of the Atom* (G. Bell and Sons, London, 1927; ONTI, Kharkov, 1934), p. 235.
19. L. A. Bureeva and V. S. Lisitsa, in *Perturbed Atom* (IzdAT, Moscow, 1997), p. 221.
20. D. A. Varshalovich, A. N. Moskalev, and V. K. Khersonskiĭ, *Quantum Theory of Angular Momentum* (Nauka, Leningrad, 1975, p. 64; World Scientific, Singapore, 1988).

21. H. A. Bethe and E. E. Salpeter, *Quantum Mechanics of One- and Two-Electron Atoms* (Academic Press, New York, 1957; Fizmatgiz, Moscow, 1960, pp. 412, 432).
22. A. F. Nikiforov and V. B. Uvarov, *Special Functions of Mathematical Physics* (Nauka, Moscow, 1984, p. 38; Birkhauser, Basel, 1987).
23. L. A. Vainshtein, I. I. Sobelman, and E. A. Yukov, *Excitation of Atoms and Broadening of Spectral Lines* (Nauka, Moscow, 1979, p. 298; Springer-Verlag, Berlin, 1981).
24. V. S. Lisitsa, Usp. Fiz. Nauk **122**, 449 (1977) [Sov. Phys. Usp. **20**, 603 (1977)].
25. V. A. Abramov, V. I. Kogan, and V. S. Lisitsa, in *Reviews of Plasma Physics*, Ed. by M. A. Leontovich and B. B. Kadomtsev (Énergoatomizdat, Moscow, 1982, Vol. 12, p. 114; Consultants Bureau, New York, 1987).
26. J. W. B. Hughes, Proc. Phys. Soc. London **91**, 810 (1967).
27. L. D. Landau and E. M. Lifshitz, *Course of Theoretical Physics*, Vol. 3: *Quantum Mechanics: Non-Relativistic Theory* (Nauka, Moscow, 1974; Pergamon, New York, 1977).
28. V. B. Berestetskiĭ, E. M. Lifshitz, and L. P. Pitaevskiĭ, *Quantum Electrodynamics* (Nauka, Moscow, 1980, p. 222; Pergamon, Oxford, 1982).

Translated by N. Wadhwa

Journal of Experimental and Theoretical Physics, Vol. 92, No. 3, 2001, pp. 454–461.
Translated from Zhurnal Éksperimental’noĭ i Teoreticheskoĭ Fiziki, Vol. 119, No. 3, 2001, pp. 524–532.
Original Russian Text Copyright © 2001 by Samaryan, Chernyshev, Petrov, Nefedov, Fortov.

An Analysis of Acoustic Oscillations in Dust Plasma Structures

A. A. Samaryan, A. V. Chernyshev, O. F. Petrov*, A. P. Nefedov, and V. E. Fortov
Institute for High Energy Densities, Russian Academy of Sciences, Moscow 127412 Russia
**e-mail: ipdustpl@redline.ru*

Received November 9, 2000

Abstract—Low-frequency oscillations in the density of dust particles, which are spontaneously excited in the standing plasma column of a dc glow discharge in neon, were experimentally studied. The longitudinal waves were monitored by a special visualization technique, and the dust sound oscillation characteristics were determined and analyzed using specially developed algorithm and data processing software. It was established that the longitudinal waves propagate from anode to cathode, the frequency and wavevector of the dust sound oscillations being dependent on the discharge current, gas pressure, particle density in the dust cloud, and spatial coordinates. Two-dimensional (2D) fields of the main wave characteristics were studied using an original algorithm. The possible mechanisms of excitation of the dust sound oscillations is discussed. The experimental spatial distributions of the wave parameters are compared to the patterns obtained within the framework of various theoretical models. *© 2001 MAIK “Nauka/Interperiodica”.*

1. INTRODUCTION

In the absence of an applied magnetic field, a plasma may exhibit three oscillation branches, representing transverse (electromagnetic) and longitudinal (Langmuir and ion sound) modes. The presence of macroscopic particles changes the charge distribution in the plasma and introduces new time and space scales into the system. This results in modification of the longitudinal plasma oscillation modes, the appearance of new modes, and a change in the dispersion relationships. A new branch of the low-frequency oscillations appears, representing the dust sound [1, 2], and the system is characterized by the dust plasma frequency in addition to the electron and ion plasma frequencies characterizing the dust-free system. The physical nature of the dust sound is analogous to that of the ion sound, the dust particles (instead of ions) representing the inertial component of the system. Depending on the interparticle interaction parameter Γ, the low-frequency oscillations in the dust plasma can be divided into two types: dust acoustic waves (DAW) and dust lattice waves (DLW). The DAW modes are excited in a plasma featuring weak electrostatic interactions between particles, while DLW modes (i.e., waves in the plasma crystal lattice) appear when the dust particles oscillate in strongly correlated structures with large values of the coupling parameter Γ.

At present, there are many theoretical papers devoted to thorough analysis of the waves of both types in dust plasmas with various sets of parameters [3–18]. The DLW modes excited under RF discharge conditions were specially studied in [19–21]. Zuzic *et al.* [19] analyzed induced oscillations in a plasma crystal and their influence upon phase transitions in the system. Pieper and Goree [20] also studied the induced dust sound oscillations in a plasma crystal and used an experimental dispersion relationship to determine the particle charge.

The dust sound waves in a *Q*-plasma were experimentally observed for the first time in 1995 [22]. The particle density waves in a dc gas discharge were reported in [23]. Experimental investigations of the acoustic (DAW) modes reported in [22–26] were restricted to determining averaged parameters of the dust plasma oscillations. The lack of systematic data on the wave parameters as functions of the plasma characteristics hindered a correct comparison of the available theoretical models with experiment.

The purpose of this work was to develop methods for visualization of the dust sound waves in a gas plasma and to use these methods in the experimental study of acoustic oscillations in the dust plasma column of a dc glow discharge.

2. EXPERIMENTAL

The experiments were carried out with a dc glow discharge in neon at pressures in the range from 0.1 to 2 Torr. The concentration of dust particles in the system was 10^2–10^4 cm^{-3}, the density of electrons and ions in the plasma was 10^7–10^8 cm^{-3}, the electron temperature was 2–8 eV, and the temperature of ions and atoms was 300–400 K. The experimental setup was similar to that used in our previous investigations of the dust plasma column formed under dc glow discharge conditions [27]. A schematic diagram of this system is depicted in Fig. 1. The discharge tube had an internal diameter of 55 mm and a length of 800 mm; the distance between electrodes (arranged in side fingers) was 600 mm. The plasma parameters were determined using a single cylindrical probe.

Iron particles with a diameter of 6 μm were introduced into a stratified region of the positive gas-discharge plasma column. The micron particles were initially charged into a cylindrical container mounted in the top part of the discharge tube (Fig. 1). The container bottom was made of a 40-μm mesh metal grid. The suspended dust particles were illuminated with a ribbon-shaped beam of an argon laser. The probing beam could be moved in both vertical and radial directions. The light scattered from the microscopic dust particles was detected with the aid of a CCD video camera at an angle of 90° and recorded on a video tape recorder. The parameters of acoustic oscillations were determined using a specially developed algorithm. Correctness of this determination was checked with the aid of an additional photomultiplier detector (FEU-106) linked to an S9-8 oscillograph. The oscillograms were analyzed by conventional methods to determine the oscillation frequency.

3. RESULTS AND DISCUSSION

Our experiments showed that low-frequency longitudinal waves of the dust particle density appear in the system and can be clearly observed for certain plasma parameters. The waves propagate in the discharge tube downward from anode to cathode. The character of this wave motion significantly depends on the discharge current, gas pressure, and particle density in the dust cloud. As the discharge current and particle density increase, the wave amplitude grows and the wave process can observed by naked eye. The waves of large amplitude are also observed at low gas pressures. An analysis of the experimental data showed that waves spread over the entire dust volume, rather than restrict to the bottom part of the tube as was indicated in [23, 26]. The wave amplitude is coordinate-dependent: greater waves were observed in the dust plasma region close to a head of the column. The size of this region varies from 0.1Z to 0.8Z (Z is the vertical size of the dust plasma column), depending on the discharge parameters and particle density.

Figure 2 shows typical video images of the dust plasma column observed in the course of the particle density wave propagation. An analysis of the sequence of such images allows the wavelength, frequency, and phase velocity of the density wave to be determined. We have used the following algorithm for determining the density wave parameters. The initial image was considered as an array of pixels representing the scattered laser radiation intensity distribution $I_s(i, j)$, where i and j are the pixel indexes. Since the scattering objects in our case are the dust particles, the scattered light intensity is proportional to the particle density $I_s = \gamma n_p$. For determining the particle density wave amplitude, it is necessary to find the coefficient γ. The other quantities (wavelength λ, frequency ω, and phase velocity V) can be determined from analysis of the relative I_s values. For this purpose, the time sequence of 2D arrays $I_s(i, j)$ is represented by a 3D array $f(x, y, t)$, where $x = \alpha i$ and $y = \beta j$ are the spatial coordinates and t is the time. The discreteness of data in the $f(x, y, t)$ array with respect to the spatial coordinates is determined by the values

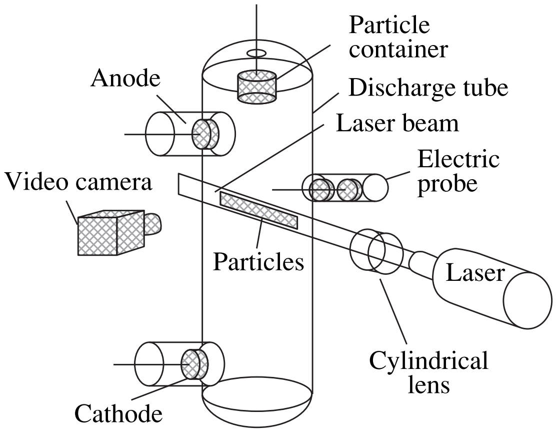

Fig. 1. A schematic diagram of the experimental setup.

$$\Delta^{\min} x = P_x M_x, \quad \Delta^{\min} y = P_y M_y, \qquad (1)$$

where P_x, P_y are the pixel dimensions and M_x, M_y are the magnification coefficients of the detecting system along the x and y axis, respectively. The discreteness $t - \Delta^{\min} t$ with respect to the time is determined by a minimum time interval t_r between two sequential images (in our experiment, t_r = 20 ms). The values of $\Delta^{\min} y$, x (depending on the registration system characteristics) in our experiments were varied from 10 to 30 μm.

For determining the particular λ, ω, and V values, we used the $f(x, y, t)$ arrays at each point with the coordinates (x, y) to construct the following functions:

$$\varphi_\omega^{x,y}(\Delta t) = \sum_t f(x, y, t) f(x, y, t + \Delta t), \qquad (2a)$$

$$\varphi_\lambda^{x,y}(\Delta y) = \sum_t f(x, y, t) f(x, y + \Delta y, t), \qquad (2b)$$

$$\varphi_V^{x,y}(\Delta y) = \sum_t f(x, y, t) f(x, y, t + t_r). \qquad (2c)$$

The analysis of variation of the $\varphi_\omega(\Delta t)$, $\varphi_\lambda(\Delta y)$, and $\varphi_V(\Delta y)$ values allowed the corresponding parameters of the wave process to be determined. For example, the circular frequency ω is obtained by plotting $\varphi_\omega(\Delta t)$, determining the period of this periodic function τ, and using the formula $\omega = 2\pi/\tau$.

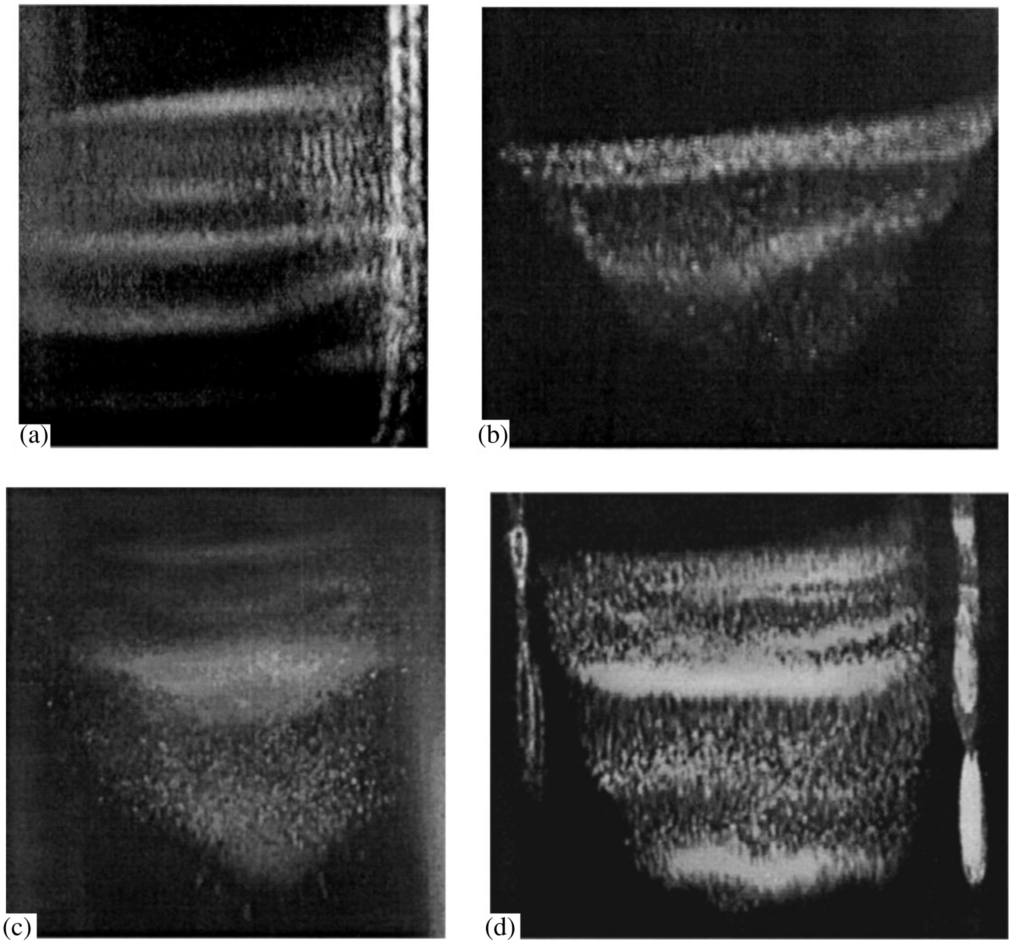

Fig. 2. Typical video images of the acoustic waves observed in a dust plasma column in a dc glow discharge under various conditions: (a) $P = 1.2$ Torr, $I = 2$ mA; (b) $P = 1$ Torr, $I = 0.8$ mA; (c) $P = 0.8$ Torr, $I = 0.3$ mA. (d) $P = 0.3$ Torr, $I = 0.4$ mA.

Using the above algorithm, we can determine the local parameters of the density waves studied and construct the corresponding 2D fields of phase velocity, frequency, and wavelength. The local character of the algorithm used for determining the wave parameters is very important for the study of acoustic oscillations in the dust plasma structures formed in a dc glow discharge, where the oscillations spread in a strongly inhomogeneous medium and the wave parameters are different at various points of the plasma column.

Figure 3 shows the maps of the 2D fields of main parameters determined for the acoustic oscillations observed in a cloud of iron particles with a radius of $r_p = 3$ μm. As is seen, the fields are inhomogeneous: all the parameters exhibit spatial variations. The most pronounced variation of the dust density wave parameters are observed along the vertical coordinate y. For a more thorough investigation of the general pattern, we have analyzed the wave behavior in the central region of the dust plasma in more detail. Figure 4 shows the variation of the frequency, phase velocity, and wavelength in the wave propagating in the dust plasma column at various parameters of the gas discharge. In order to check the correctness of determining the parameters of oscillations, we have compared the frequency values obtained using the algorithm based on Eqs. (1) and (2) to the values determined by a standard method employing a photodetector and digital oscillograph. The results obtained by the two methods showed good coincidence; a difference (<5%) can be explained by different dimensions of the plasma region probed.

The results of our experiments showed that the frequency and wavevector of the dust plasma oscillations not only vary in space, but depend on the discharge current, gas pressure, and particle density in the dust cloud. Figure 5 shows a region in the $k\omega$ phase plane representing the domain of existence of acoustic oscillations in the dust plasma formed in a dc glow discharge.

The acoustic oscillations in the dust plasma structures observed in our experiments are of interest both from the fundamental standpoint, as a physical phenomenon, and from the standpoint of applications, as a method of dust plasma diagnostics. In particular, using

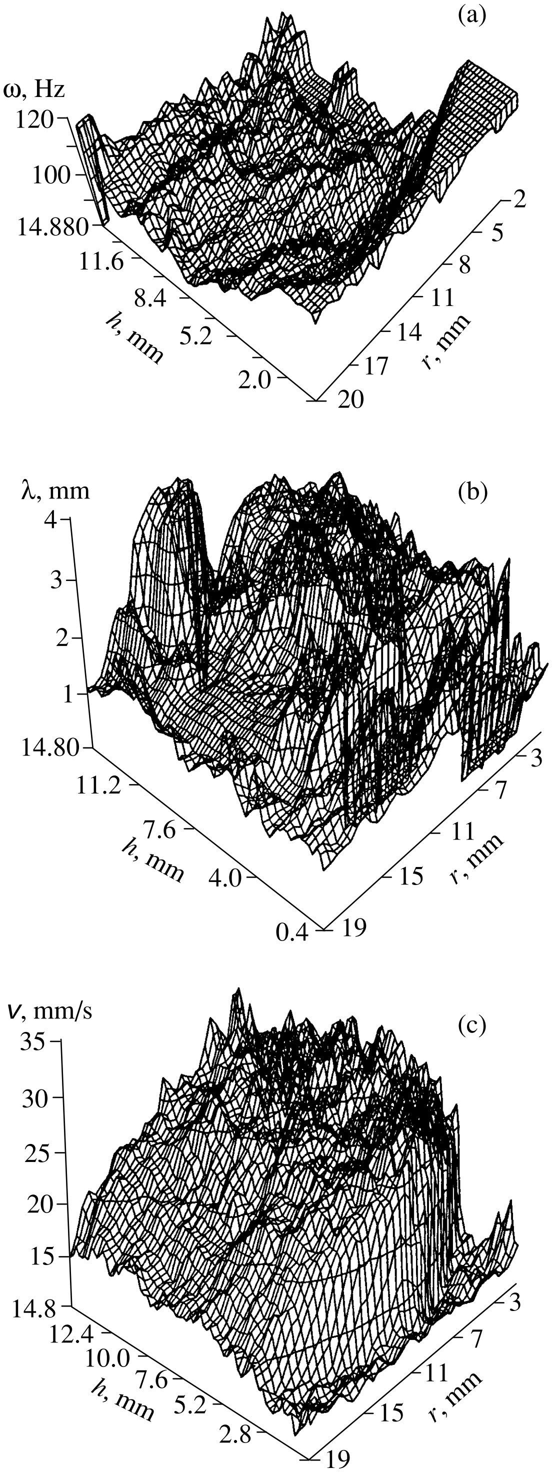

Fig. 3. 2D fields of (a) frequency ω, (b) wavelength λ, and (c) phase velocity v for the acoustic waves in dust plasma structures (P = 0.23 Torr; I = 0.28 mA).

the existing models of wave processes in a dust plasma and the experimentally measured values of parameters of the acoustic waves, we may evaluate the charge of dust particles.

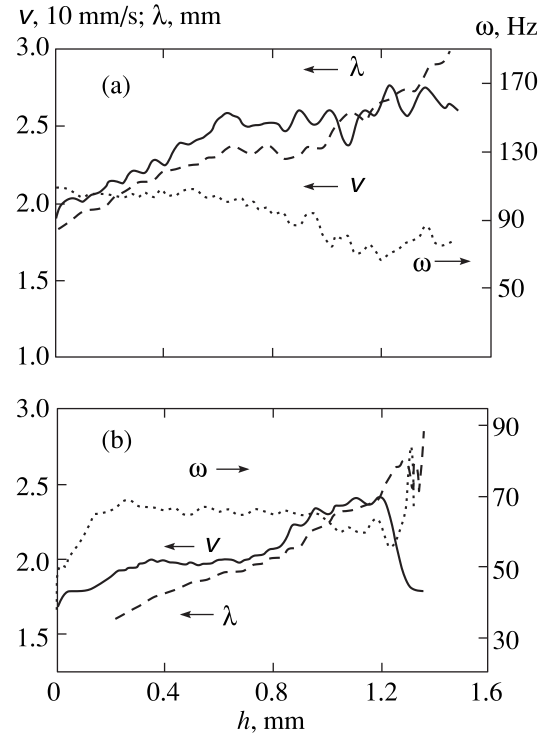

Fig. 4. Vertical profiles of the wavelength λ, frequency ω, phase velocity v of dust plasma oscillations under various discharge conditions: (a) P = 1.2 Torr, I = 2 mA; (b) P = 0.3 Torr, I = 0.4 mA.

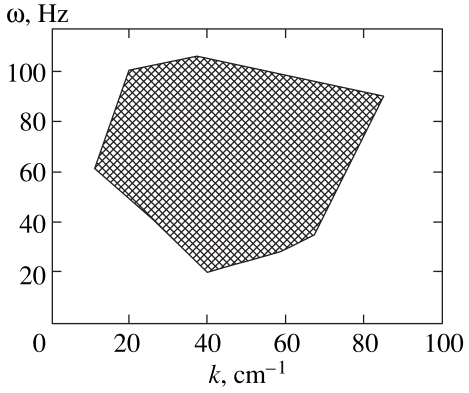

Fig. 5. The domain of existence of self-excited low-frequency dust density oscillations in a dc glow discharge for the discharge current varied from 0.2 to 0.4 mA and the gas pressure, from 0.2 to 4 Torr.

The law of dispersion for the acoustic (DAW) modes in a two-stream approximation is given by the formula [1]

$$\omega^2 = \omega_d^2 \frac{k^2\lambda_d^2}{1 + k^2\lambda_d^2}, \tag{3}$$

where $\omega_d = \sqrt{4\pi n_d Z_d^2 e^2/M}$ is the dust sound frequency and λ_d is the Debye screening radius.

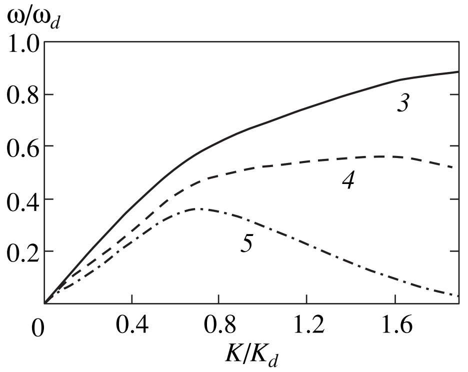

Fig. 6. Model dispersion relationships determined by Eqs. (3)–(5) (number of equation indicated at the curve; $K_d = 2\pi/\lambda$).

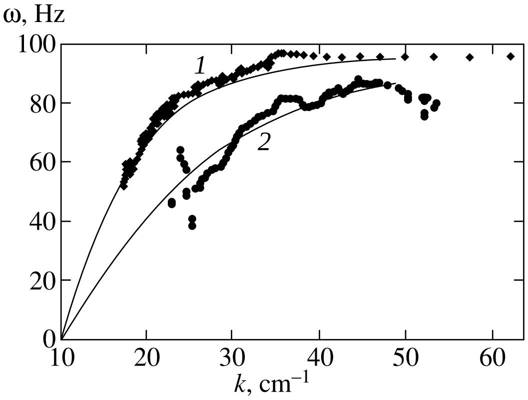

Fig. 7. Dispersion relationships for the dust sound waves in a dc discharge under various conditions: (*1*) $P = 1.2$ Torr, $I = 2$ mA, $Z = 10^4$ e; $n_i = 10^7\ \mathrm{cm}^{-3}$; (*2*) $P = 0.3$ Torr, $I = 0.4$ mA, $Z = 10^4$ e; $n_i = 4 \times 10^7\ \mathrm{cm}^{-3}$. Black circles represent experimental points; solid curves show the approximations calculated using Eq. (3).

With the interparticle interactions taken into account, the dispersion relationship acquires the following form [18]:

$$\omega^2 = \omega_d^2 \frac{k^2\lambda_d^2}{1 + k^2\lambda_d^2} \frac{16}{16 + k^2\lambda_d^2}. \qquad (4)$$

The values of charge on dust particles calculated by Eqs. (7) and (8)

P, Torr	I, mA	Z_d, e
1.2	2	2.2×10^4
1.2	1.4	4.3×10^4
1.2	0.8	1.6×10^4
0.8	0.4	2.8×10^4
0.3	0.6	3.3×10^4
0.3	0.4	5.6×10^4

For the dispersion of the dust plasma lattice (DLW) waves, the model of crystal modes yields [8]

$$\omega \approx 2\tilde{\omega}_{pd}\sqrt{1 + K + K^2/2}\exp(-K/2)\sin(k\Delta/2), \qquad (5)$$

where $K = \Delta/\lambda_d$,

$$\tilde{\omega}_{pd}^2 = \frac{2Z_d^2e^2}{m_d\Delta^3},$$

and Δ is the interparticle distance.

Some other dispersion relationships for DAW and DLW modes were reported in [4, 7, 8, 16–18]. However, these expressions are not quite convenient for analyzing our experimental data. For this reason, we will restrict the consecration to the three cases given above. The dispersion curves described by formulas (3)–(5) are depicted in Fig. 6. Figure 7 presents the experimental plots of ω versus k and shows the approximation of these data by curves constructed using formula (3). The best fit observed for this approximation indicates that the corresponding model quite adequately describes the law of dispersion for the longitudinal waves propagating in the system studied. Once the dispersion law is established, we may use the approximated curves to evaluate the charge on dust particles and the ion concentration. The particle charge estimated using the data depicted in Fig. 8 was 10^4, and the ion concentration was $n_i \sim 10^7\ \mathrm{cm}^{-3}$.

A simpler algorithm for evaluation of dust the particle charge can be used in the case when $\lambda \gg \lambda_D$. Indeed, the condition $k\lambda_D \ll 1$ allows the dispersion relationship for the dust sound to be written as

$$\omega = V_d k, \qquad (6)$$

where V_d is the dust sound velocity. In our case, $\lambda_D \sim 200\ \mu\mathrm{m}$ and the condition $k\lambda_D \ll 1$ is valid for the waves with $\lambda > 2$ mm. The dust sound velocity is determined by the formula

$$V_d = \omega_d\lambda_d = \frac{Z_d}{n_i^{1/2}}\sqrt{\frac{n_dT_i}{m}}. \qquad (7)$$

When the wavelength is comparable to the interparticle spacing (or $k \longrightarrow \pi/\langle r\rangle$), the phase velocity of the wave tends to zero and the frequency–to a certain fixed value called the dust plasma frequency ω_d. This value is given by the formula

$$\omega_d = \sqrt{\frac{4\pi n_d Z_d^2 e^2}{m}}. \qquad (8)$$

Thus, the particle charge is readily estimated from the wave phase velocity and the ion density by formula (7) (for $\lambda \gg \lambda_D$) or from the limiting dust plasma frequency and the dust particle size and density by formula (8). The particle charge values *Zpe* calculated using formulas (7) and (8) for various discharge parameters are summarized in the table.

Using Eq. (6), we may also determine variation of the dust particle charge $Z_d(y)$ depending on the vertical coordinate in the dust plasma column. Variation of the phase velocity in the vertical direction is determined experimentally (see Fig. 3). Using a single probe available in the setup, we may also determine the ion concentration. Since the measurements were performed at a single point (at the upper boundary of the dust plasma column), the $Z_d(y)$ function was approximated using the known variation of the relative value $n_i(y)$ taken from [28] (Fig. 8).

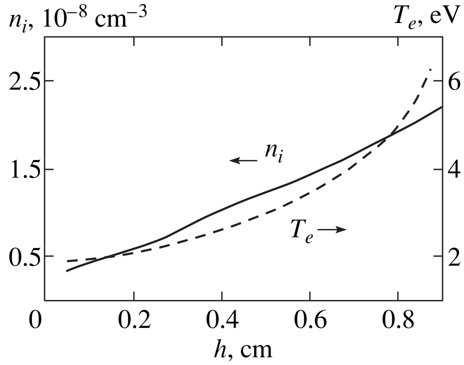

Fig. 8. Vertical profiles of the ion density n and the electron temperature T_e. Coordinate h measured from the upper boundary of the dust plasma structure.

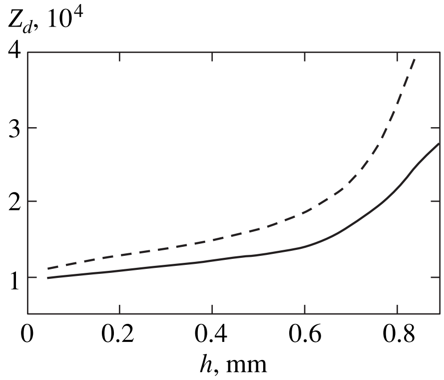

Fig. 9. Variation of the charge Z_d on dust particles along the vertical axis: dashed curve shows the profile calculated by Eq. (6) using our data on the wave velocity and the $n_i(h)$ curve depicted in Fig. 8; solid profile was calculated within the framework of the OML model [29] for $T_i = 0.03$ eV and the $T_e(h)$ curve from Fig. 8.

The $Z_d(y)$ values determined by this method are presented in Fig. 9 (dashed curve). As seen, the charge exhibits a considerable (more than twofold) variation along the height of the dust plasma column. In order to analyze these results, we calculated the charge on dust particles within the framework of the orbital motion (OML) model [29] using the following parameters: $T_i = 0.03$ eV; $T_e(y)$ as in Fig. 8 [28]; $n_i(y) = n_e(y)$. The results of these calculations are presented in Fig. 9 (solid curve). As seen in Fig. 9, the values of the particle charge determined by two methods almost coincide, but the curve based on our experimental data markedly deviates from the calculated curve at the distant end of the plasma column (the coordinate was measured from the top of the dust plasma column), that is, in the region of high field strength. This deviation can be explained by uncontrolled polydispersity of the iron dust particles. Particles with greater mass will tend to the region of greater field strength (i.e., to the bottom of the plasma column). This factor may account for the particle charge variation along the vertical axis, since the charge of a particle is directly proportional to its size. The same reason may explain a difference between the data obtained in this experiment and the results of numerical modeling [30] of a gas-discharge dust plasma with close parameters, where it was established that a change in the particle charge along the vertical axis does not exceed 20%. Our analysis indicates that this estimate is valid only for the dust plasma in the upper part of the column.

We have experimentally observed spontaneous excitation of the low-frequency oscillations in the dust particle density, which indicates that there are mechanisms of instability development in the oscillation process studied. Various possible models of the instability development in a dust plasma were proposed in the literature. These models were used to analyze the influence of fluctuations in the charge of dust particles [3, 4, 17, 18, 26], the role of nonlinearity [7–9] and nonideality of the dust plasma [10–12], and the effects of ionization and ion entrainment [13, 15, 16] on the dust sound wave propagation. The mechanisms of wave instability caused by the electron and ion drift relative to the charged dust particles were analyzed in [5, 6, 23, 26].

Fortov *et al.* [26] most exhaustively described and analyzed various mechanisms for the excitation of oscillations in the positive plasma column of a dc glow discharge. According to this analysis, the mechanism of instability is related to the nature of forces holding particles within the positive discharge region and to the particle charge variations during the plasma density wave propagation. However, despite the large number of proposed models, the question as to whether a common driving force and mechanism are responsible for the excitation of density oscillations in a dust plasma observed in the laboratory experiments is still open. This situation is explained by the fact that no experimental evidence is available for any of the proposed models. The comparison of experiment and theory in [23–26] was performed on a qualitative level and did not provide sufficient grounds for unambiguously selecting one or another mechanism on the instability development in the system studied.

We have attempted to compare the experimental profile of the wavevector variation in height of the dust plasma column to the analogous distributions obtained within the framework of various theoretical models. Figure 10 shows plots of the wavevector versus height

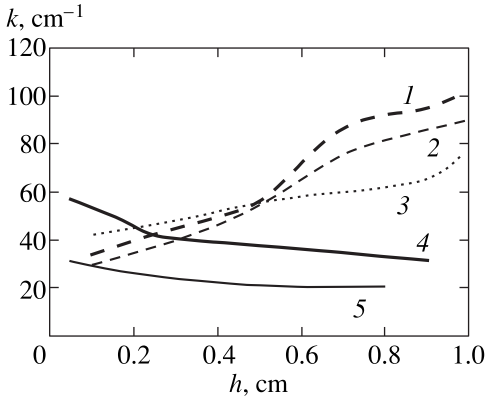

Fig. 10. Plots of the wavevector k versus height h calculated within the framework of various models: (*1*) model [5]; (*2*) model [16]; (*3*) model [26]; (*4*, *5*) experimental data for iron dust particles measured in a discharge tube operated at $P = 0.8$ Torr and $I = 0.5$ (*4*) and 0.22 mA (*5*).

calculated using the models described in [5, 16, 26] (dashed curves) and the profiles experimentally measured under various discharge conditions. As seen from this comparison, the theoretical curves differ rather significantly from the experimental profiles. A possible explanation is offered by the fact that models based on the analysis of linear dispersion relationships for the low-frequency oscillations cannot adequately describe wave processes in the dust plasma systems. Indeed, the dust plasma column belongs to the class of nonlinear thermodynamically nonequilibrium open dissipative systems [31, 32]. For a correct analysis of this system, we should employ an adequate physical model. The most interesting case is offered by a model of the autooscillating system with the parameters independent of the initial conditions and determined completely by properties of the medium [33].

The appearance of stable oscillatory motions of macroparticles in a dust plasma is possible only provided that there are potential sources capable of compensating for the energy dissipation. There must be a dynamic equilibrium between the amounts of supplied and dissipated energy. Under equilibrium conditions, the dissipative effects would level off any inhomogeneity, thus leading to the thermodynamic equilibrium. In a nonlinear open system, the dissipation plays a quite different role. Acting jointly with some other processes, the energy dissipation may lead both to the appearance of stable stationary structures and complicated oscillatory regimes [32, 34].

In the case of a laboratory gas-discharge plasma, it is obvious that stationary autooscillations in the dust plasma column must be maintained at the expense of the energy taken from the power source in the discharge circuit. A possible mechanism capable of converting the potential energy of the external electric field into the energy of moving dust particles is related to the presence of spatial gradients of the system parameters such as temperature, ionization, and charge. In particular, a possible mechanism considered in [35] is based on the presence of space charge gradient in a dust cloud formed in a trap under the action of electric field and the Earth gravity field.

4. CONCLUSION

Thus, we have experimentally studied the low-frequency oscillations in the density of dust particles, which are spontaneously excited in the stationary plasma column of a dc glow discharge in neon. The longitudinal dust sound wave parameters were determined using a special visualization technique. The dust sound oscillation characteristics were determined and analyzed using specially developed algorithm and data processing software. Based on these data, two-dimensional fields of the main wave characteristics were constructed.

Using the values of the phase velocity of the wave studied, the charge on the dust particles was evaluated and the profile of its spatial variation in the dust plasma column was determined. Under the experimental conditions studied, the charges on particles occurring in various regions of the dust cloud may differ by a factor of more than two, and the particles carrying a greater charge are found in the bottom part of the plasma column.

The experimental spatial distributions of the wave parameters were compared to the distributions obtained within the framework of various theoretical models. The results of this comparison showed that the principal mechanisms of the oscillation excitation cannot be based on linear analytical models. It is necessary to perform numerical modeling of the wave process taking into account the nonlinear dissipative character of the system studied.

ACKNOWLEDGMENTS

The authors are grateful to O.S. Vaulina for fruitful discussions and valuable remarks. The work was partly supported by the Russian Foundation for Basic Research, project nos. 00-02-32281, 00-02-17520, and 98-02-16828.

REFERENCES

1. N. Rao, P. K. Shukla, and M. Y. Yu, Planet. Space Sci. **38**, 543 (1990).
2. V. N. Tsytovich, Usp. Fiz. Nauk **167**, 57 (1997) [Phys. Usp. **40**, 53 (1997)].
3. R. Varma, P. K. Shukla, and V. Krishan, Phys. Rev. E **47**, 3612 (1993).
4. V. Jana, A. Sen, and P. K. Kaw, Phys. Rev. E **48**, 3930 (1993).
5. M. Rosenberg, Planet. Space Sci. **41**, 229 (1993).
6. M. Rosenberg, J. Vac. Sci. Technol. A **14**, 631 (1996).
7. N. Rao, J. Plasma Phys. **59**, 561 (1998).
8. Y. Ma and J. Liu, Phys. Plasmas **4**, 253 (1997).

9. D. Winske and M. Rosenberg, IEEE Trans. Plasma Sci. **26**, 92 (1998).
10. M. Rosenberg and G. Kalman, Phys. Rev. E **56**, 7166 (1997).
11. M. Murillo, Phys. Plasmas **5**, 3116 (1998).
12. D. Winske, M. S. Murillo, and M. Rosenberg, Phys. Rev. E **59**, 2263 (1999).
13. P. Shukla and G. Morfill, Phys. Lett. A **216**, 153 (1996).
14. F. Melandso, Phys. Plasmas **3**, 3890 (1996).
15. N. D’Angelo, Phys. Plasmas **5**, 3155 (1998).
16. A. Ivlev, D. Samsonov, J. Goree, *et al.*, Phys. Plasmas **6**, 741 (1999).
17. A. Ivlev, G. Morfill, and J. R. Jokipii, Phys. Rev. Lett. **83**, 971 (1999).
18. K. N. Ostrikov, S. V. Vladimirov, M. Y. Yu, and G. E. Morfill, Phys. Plasmas **7**, 461 (2000).
19. M. Zuzic, H. Tomas, and G. Morfill, J. Vac. Sci. Technol. A **14**, 496 (1996).
20. J. Pieper and J. Goree, Phys. Rev. Lett. **77**, 3137 (1996).
21. A. Homann, A. Melzer, R. Madani, and A. Piel, Phys. Lett. A **242**, 173 (1998).
22. A. Barkan, N. D’Angelo, and R. L. Merlino, Phys. Plasmas **2**, 3563 (1995).
23. V. I. Molotkov, A. P. Nefedov, V. M. Torchinskiĭ, *et al.*, Zh. Éksp. Teor. Fiz. **116**, 902 (1999) [JETP **89**, 477 (1999)].
24. R. L. Merlino, A. Barkan, C. Thompson, and N. D’Angelo, Phys. Plasmas **5**, 1607 (1998).
25. H. R. Prabhakara and V. L. Tana, Phys. Plasmas **3**, 3176 (1996).
26. V. E. Fortov, A. G. Khrapak, S. A. Khrapak, *et al.*, Phys. Plasmas **7**, 1374 (2000).
27. A. M. Lipaev, V. I. Molotkov, A. P. Nefedov, *et al.*, Zh. Éksp. Teor. Fiz. **112**, 2030 (1997) [JETP **85**, 1110 (1997)].
28. Yu. B. Golubovskiĭ, S. U. Nisimov, and I. E. Suleimenov, Zh. Tekh. Fiz. **64** (10), 54 (1994) [Tech. Phys. **39**, 1005 (1994)]; Yu. B. Golubovskiĭ and S. U. Nisimov, Zh. Tekh. Fiz. **65** (1), 46 (1995) [Tech. Phys. **40**, 24 (1995)].
29. J. E. Allen, Phys. Scr. **45**, 497 (1992).
30. O. M. Belotserkovskiĭ, I. E. Zakharov, A. P. Nefedov, *et al.*, Zh. Éksp. Teor. Fiz. **115**, 819 (1999) [JETP **88**, 449 (1999)].
31. V. Tsytovich, S. Benkada, and S. Vladimirov, Plasma Phys. Controlled Fusion **34**, 123 (1999).
32. G. Nicolis and I. Prigogine, *Self-Organization in Non-Equilibrium Systems* (Wiley, New York, 1977; Mir, Moscow, 1979).
33. R. K. Dodd, J. C. Eilbeck, J. Gibbon, and H. C. Morris, *Solitons and Nonlinear Wave Equations* (Academic Press, New York, 1982; Mir, Moscow, 1988).
34. T. Akhromeeva, S. Kurdyumov, and G. Malinetskiĭ, in *Computers and Nonlinear Phenomena* (Nauka, Moscow, 1988), p. 44.
35. O. S. Vaulina, A. P. Nefedov, O. F. Petrov, and V. E. Fortov, Zh. Éksp. Teor. Fiz. **118**, 1325 (2000) [JETP **91**, 1147 (2000)].

Translated by P. Pozdeev

Journal of Experimental and Theoretical Physics, Vol. 92, No. 3, 2001, pp. 462–473.
Translated from Zhurnal Éksperimental'noĭ i Teoreticheskoĭ Fiziki, Vol. 119, No. 3, 2001, pp. 533–545.
Original Russian Text Copyright © 2001 by Loshkareva, Sukhorukov, Gan'shina, Mostovshchikova, Kumaritova, Moskvin, Panov, Gorbenko, Kaul'.

SOLIDS
Structure

The Isotope Effect and Phase Separation in $(La_{0.5}Pr_{0.5})_{0.7}Ca_{0.3}MnO_3$ Films: Optical Data

N. N. Loshkareva[a], Yu. P. Sukhorukov[a], E. A. Gan'shina[b], *, E. V. Mostovshchikova[a], R. Yu. Kumaritova[b], A. S. Moskvin[c], Yu. D. Panov[c], O. Yu. Gorbenko[b], and A. R. Kaul'[b]
[a]*Institute of Metal Physics, Ural Division, Russian Academy of Sciences, Yekaterinburg, 620219 Russia*
[b]*Moscow State University, Moscow, 119899 Russia*
[c]*Ural State University, Yekaterinburg, 620083 Russia*
**e-mail: eagan@magn.phys.msu.su*

Received September 15, 2000

Abstract—A new approach to the study of phase separation in lanthanum manganites is proposed based on the combined investigation of their optical and magnetooptical characteristics providing information about the conducting and ferromagnetic regions, respectively. Effects of the ^{18}O isotope substitution for ^{16}O in the epitaxial films of $(La_{0.5}Pr_{0.5})_{0.7}Ca_{0.3}MnO_3$ (grown on $SrTiO_3$ or $LaAlO_3$ substrates) upon the IR absorption spectra and the equatorial Kerr effect measured in the 1.5–3.8 eV range were studied. A giant drop in the temperature of maximum resistance of the film grown on $SrTiO_3$ and disappearance of the metal-insulator transition in the film on $LaAlO_3$, observed upon the isotope exchange, are accompanied by a decrease in the contribution of free charge carriers to the absorption spectra, by the appearance of bands due to localized states, and by a decrease in magnitude of the equatorial Kerr effects. Measurements of the Kerr effect and the temperature variation of the optical transmission show evidence of the presence of ferromagnetic metal regions in the ^{18}O-isotope-substituted $(La_{0.5}Pr_{0.5})_{0.7}Ca_{0.3}MnO_3/LaAlO_3$ film at low temperatures, with a general semiconductor character of the resistivity behavior in the entire temperature range studied. Changes observed in the absorption spectra are explained based on a model of the pseudo-Jahn–Teller polar centers and phase separation. The optical and magnetooptical data show evidence of a percolation nature of the giant isotope effect in manganites. *© 2001 MAIK "Nauka/Interperiodica".*

1. INTRODUCTION

Manganites with a perovskite structure are extensively studied in the context of a problem of the giant magnetoresistance (GMR) phenomenon. The unusual properties of manganites are related to the interaction of charge, spin, orbital, and local structural (Jahn–Teller) degrees of freedom with a strong charge inhomogeneity, static and dynamic phase separations, and percolation effects [1–3].

One of the brightest phenomena in GMR manganites is the giant isotope shift. A decrease in the Curie temperature T_C upon substituting the ^{18}O oxygen isotope for ^{16}O in $La_{0.8}Ca_{0.2}MnO_3$ reaches 21 K [4]. The same substitution in a $(La_{1-y}Pr_y)_{0.7}Ca_{0.3}MnO_3$ system composition with $y = 0.75$ results in the transition from ferromagnetic metal to antiferromagnetic insulator state [5]. The main reasons for such a strong variation of the material properties upon the isotope exchange are associated with a change in the electron–phonon interaction [4, 5] and with the phenomena arising near the percolation threshold [2, 3]. A strong isotope effect is observed near a ferromagnetic–antiferromagnetic phase boundary of manganite compositions possessing the narrowest electron e_g band, where the charge carrier localization processes become substantial. This group of materials includes $La_{0.8}Ca_{0.2}MnO_3$ [4], $(La_{1-y}Pr_y)_{0.7}Ca_{0.3}MnO_3$ with $y = 0.75$ and 0.5 [5, 6], and $(La_{0.5}Nd_{0.5})_{2/3}Ca_{1/3}MnO_3$ [7].

Systems featuring a strong isotope effect also exhibit phase separation, significant hysteresis effect during the heating–cooling cycles, and relaxation processes with large characteristic times. These essentially inhomogeneous systems should be studied by local methods capable of providing information on the separate components of the system. Below we propose a new quasilocal approach to the study of inhomogeneous systems based on the combined measurement of their optical (absorption spectra) and magnetooptical (the equatorial Kerr effect) properties. The main idea of applying the optical methods to the study of phase separation and percolation phenomena is naturally related to a difference in the optical response of various phases. In the absence of percolation, the metal inclusions in a dielectric matrix cannot be detected by dc conductivity measurements but are well manifested in the IR absorption spectra.

In application to the GMR manganites, a quasilocal character of the optical methods is related to the fact that the optical absorption in a spectral range corresponding to the light interaction with the charge carriers provides information about the conducting (i.e., light-absorbing) regions in the insulator (transparent) matrix, thus revealing the charged phase separation [8]. At the same time, the Kerr effect taking place in the ferromagnetic crystal regions allows us to make a judgment on the magnetic phase separation [9]. In addition, the optical absorption spectra of manganites also clearly reveal the delocalized and localized states [10], which allows us to follow the process of charge carrier localization during the isotope exchange.

The purpose of this work was to use the new approach in studying the nature of the giant isotope effect observed upon substituting the ^{18}O isotope for ^{16}O in the epitaxial films of $(La_{0.5}Pr_{0.5})_{0.7}Ca_{0.3}MnO_3$ manganite. The results obtained by the optical methods are compared to the data obtained by the resistivity measurements.

2. SAMPLE PREPARATION AND EXPERIMENTAL METHODS

The films of $(La_{0.5}Pr_{0.5})_{0.7}Ca_{0.3}MnO_3$ manganite composition with a thickness of 60 nm were obtained by a chemical vapor deposition (CVD) method on single crystal $LaAlO_3$ (LAO) and $SrTiO_3$ (STO) perovskite substrates [11, 12]. The results of X-ray diffraction, Raman spectroscopy, and high-resolution transmission electron microscopy investigation confirmed the epitaxial character and the structural and chemical homogeneity of the sample films.

The crystal lattice parameters of the films on LAO substrates are

$$\frac{a}{2} = \frac{b}{2} = 0.3846 + 0.0003\ \text{nm},$$

$$\frac{c}{2} = 0.3872 + 0.0002\ \text{nm},$$

and on the STO substrates,

$$\frac{a}{2} = \frac{b}{2} = 0.3879 + 0.0003\ \text{nm},$$

$$\frac{c}{2} = 0.3823 + 0.0002\ \text{nm}$$

(the c-axis corresponds to the normal to the film surface); tetragonal distortions for films on the LAO and STO substrates were 0.7 and –1.5%, respectively.

The neutron diffraction measurements on ceramic samples of the same bulk composition [13] showed that this compound is a collinear ferromagnet at temperatures below $T_C = 175$ K. The charge ordering temperature is $T_0 = 200$ K. Because of the epitaxial stresses, the properties of manganite films usually differ from those of the bulk ceramic samples of the same nominal composition [11].

The process of isotope exchange, leading to the substitution of ^{18}O for ^{16}O in the samples, was performed at the Kurchatov Institute as described in [5]. The exchange process resulted in that about 85% of ^{16}O oxygen ions were replaced by ^{18}O ions.

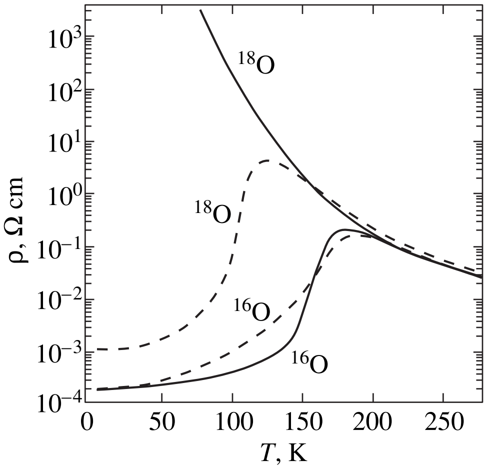

Fig. 1. The temperature dependence of resistivity for the $(La_{0.5}Pr_{0.5})_{0.7}Ca_{0.3}MnO_3$ films annealed in ^{16}O and ^{18}O. Dashed and solid curves refer to the films grown on $SrTiO_3$ (STO) and $LaAlO_3$ (LAO) substrates [14].

The IR absorption spectra of the manganite films were measured using an automated IKS-21 spectrometer in the 0.09–0.9 eV spectral range and using an MDR-4 monochromator in the 1.0–3.6 eV range. The temperature-induced variations in the spectra were studied in the 80–293 K range by heating samples preliminarily cooled in the presence or in the absence of external magnetic field. A magnetic field with a strength of 0.8 T was directed along the normal to the sample surface.

The equatorial Kerr effect was measured in a spectral range of 1.5–3.8 eV for the sample temperature varied from 20 to 300 K (cooling–heating cycles) and the magnetic field (0.1 T) normal to the film surface.

3. EXPERIMENTAL RESULTS

As is seen from Fig. 1 (reproduced from [14]), the resistivity ρ of the $(La_{0.5}Pr_{0.5})_{0.7}Ca_{0.3}MnO_3$ manganite films with ^{16}O isotope on both substrates (denoted below as ^{16}O/LAO and ^{16}O/STO) exhibits a maximum at a temperature of 189 K, below which the samples exhibit a dielectric–metal transition. The isotope exchange does not lead to any increase in the room-temperature resistivity. However, the resistance of an ^{18}O/LAO film at low temperatures is considerably greater as compared to that of the ^{16}O/LAO film, the difference reaching more that six orders of magnitude at 80 K. For the films on STO substrates, the difference is about 1.5 orders of magnitude. The position of maximum resistivity shifts by approximately 60 K upon the isotope exchange in films on the STO substrates, while the ^{18}O/LAO films exhibit no such maximum at all in a temperature range down to 4.2 K.

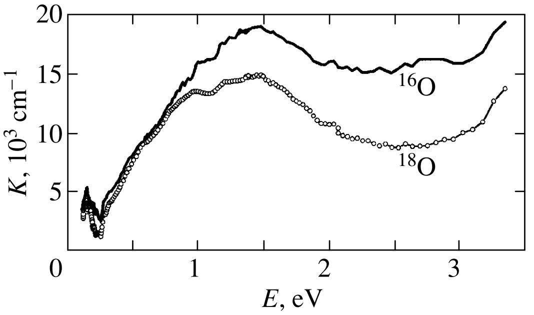

Fig. 2. Room-temperature optical absorption spectra of the $(La_{0.5}Pr_{0.5})_{0.7}Ca_{0.3}MnO_3$ films with ^{16}O and ^{18}O isotopes on STO substrates.

According to [15], the resistivity measurements in the cooling–heating cycle mode with a magnetic field applied in the plane of the film reveal a hysteresis with a loop width reaching 60 K at a field strength of 1 T.

Figure 2 presents the IR absorption spectra of the films with ^{16}O and ^{18}O on STO. As seen, the room-temperature spectra are much alike, showing a broad band with a maximum at 1.5 eV, a small peak at 0.14 eV, and a growth of the absorption above 2.5 eV. However, the spectra of the ^{16}O/STO and ^{18}O/STO samples measured at 80 K exhibit a considerable difference (Fig. 3). The film with ^{16}O (Fig. 3a) is characterized by an increase in the absorption intensity with decreasing energy, which is characteristic of the interaction of light with free charge carriers. In contrast, the free carrier contribution to the absorption at 0.2 eV in the film with ^{18}O is small. For the ^{16}O/STO film, the low-energy wing of the absorption band at 1.5 eV exhibits no features (except a weak shoulder at 1.2 eV) at all temperatures. The spectrum of ^{18}O/STO in the same region (Fig. 3b), and especially that of the samples cooled in the magnetic field (Fig. 4a), shows evidence of a complicated structure of the 1.5 eV absorption band edge, suggesting the presence of localized states in both paramagnetic and ferromagnetic regions. The room-temperature spectra of samples on STO show weakly pronounced absorption bands at 0.95 and 1.2 eV; on cooling in the absence of the magnetic field, these features transform into shoulders and shift toward higher energies. The spectra of the films cooled from room temperature to liquid nitrogen temperature in a field of 0.8 T (Fig. 4) show (in a 80–150 K interval) a pronounced absorption band at 0.80–0.95 eV and a less intense band at 0.40–0.50 eV.

Similar variations of the optical absorption spectra are observed for the manganite films with ^{16}O and ^{18}O on LAO substrates. The difference is that the absorption

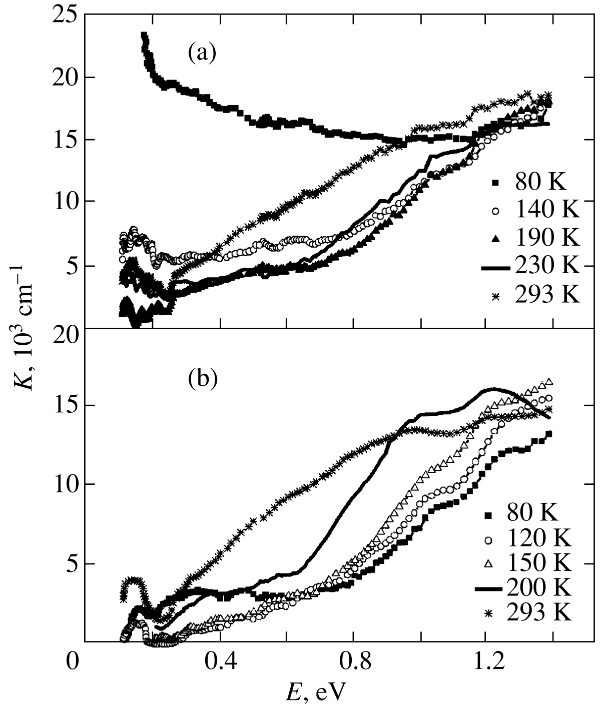

Fig. 3. Optical absorption spectra of the $(La_{0.5}Pr_{0.5})_{0.7}Ca_{0.3}MnO_3$ films with (a) ^{16}O and (b) ^{18}O isotopes on STO substrates. The samples were cooled to various temperatures in the absence of external magnetic field.

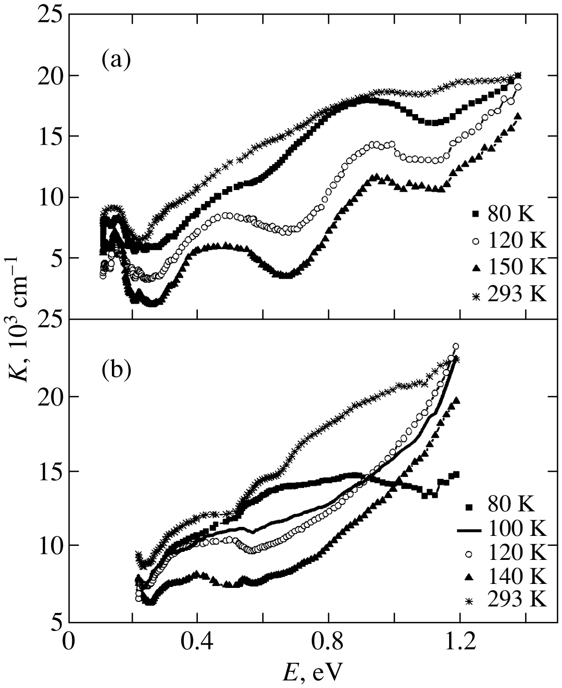

Fig. 4. Optical absorption spectra of the $(La_{0.5}Pr_{0.5})_{0.7}Ca_{0.3}MnO_3$ films with ^{18}O isotope on (a) STO and (b) LAO substrates. The samples were cooled to various temperatures in the presence of external magnetic field with a strength of 0.8 T. For clarity, the curves are shifted along the ordinate axis.

band at 0.9 eV for ^{18}O/LAO is clearly observed only at 80 K (Fig. 4b) and the energy positions of the absorption bands are generally somewhat lower as compared to those of the manganite films on STO substrates. Figure 5 shows the temperature variation of the optical transmission for the manganite films with ^{16}O and ^{18}O on LAO substrates. As seen, the curves for the ^{16}O/LAO films heated upon cooling with and without magnetic field differ rather insignificantly (Fig. 5a). As for the ^{18}O/LAO film (Fig. 5b), a monotonic variation observed for the sample cooled without magnetic field (curve *1*) changes to a curve with maximum at about 120 K for the sample cooled in the field (curve *2*). The repeated experiment on the latter sample (cooled in the field) with a magnetic field of 0.8 T applied during the optical transmission measurements showed a shift in the transmission maximum to $T \approx 135$ K (Fig. 5b, curve *3*).

The value of magnetotransmittance (the ratio of the sample transmittances with and without applied field) was determined during heating of the samples preliminarily cooled in a magnetic field; the field was switched on and off at each point. The magnetotransmittance ratio of the ^{16}O/LAO film is about 6% for a magnetic field strength of 0.8 T (Fig. 6). The magnetotransmittance of the ^{18}O/LAO film measured under the same conditions is markedly lower. It should be noted that repeated transmission (absorption) measurements reproduced only the general behavior of the spectral and temperature dependences, while the absolute transmittance values exhibited a systematic variation. The most significant variation of the results of repeated measurements, which was especially pronounced for large time intervals between the measurements, were observed for the manganite films with ^{18}O isotope.

The spectra of the equatorial Kerr effect (EKE) of the manganite films with ^{16}O on both STO and LAO substrates measured at low temperatures ($T < 80$ K) are virtually identical (Fig. 7) and coincide with the spectra reported for both ceramic and film samples of $(La, Pr)_{0.7}Ca_{0.3}MnO_3$ [9, 16]. The isotope exchange leads to a decrease in the EKE intensity, which is most pronounced for ^{18}O/LAO. The ^{18}O/STO film sample exhibits a considerable change in the EKE spectrum as compared to that of the ^{16}O/STO film: the main extremum shifts toward lower energies and an additional peak appears at 3.25 eV. Analogous changes were reported for the EKE in $(La_{1-x}Pr_x)_{0.7}Ca_{0.3}MnO_3$ samples with $x = 0.75$ measured in the course of cooling [9].

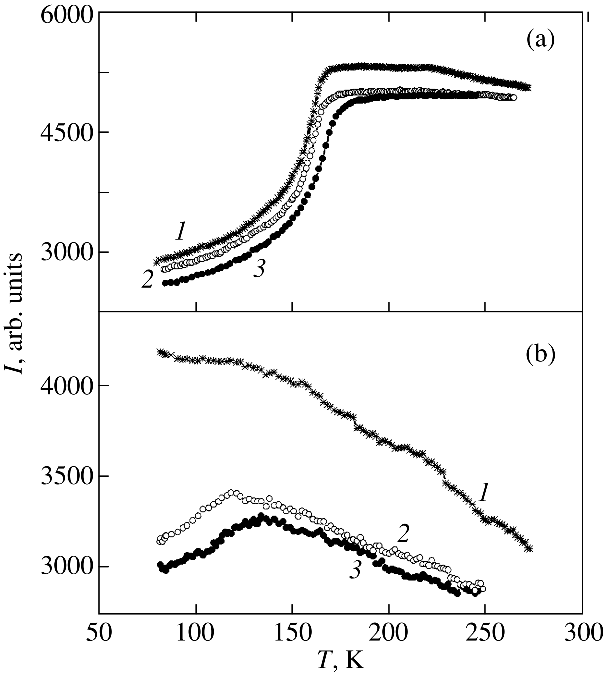

Fig. 5. Temperature variation of the optical transmittance at 0.4 eV for the $(La_{0.5}Pr_{0.5})_{0.7}Ca_{0.3}MnO_3$ films with (a) ^{16}O and (b) ^{18}O isotopes on LAO substrates: (*1*) cooled without field; (*2*) cooled in the field; (*3*) cooled and measured in a magnetic field with a strength of 0.8 T.

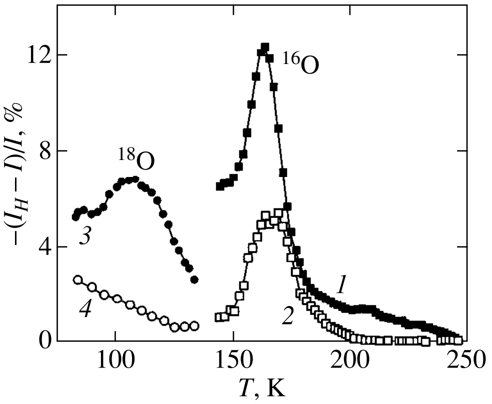

Fig. 6. The plots of magnetotransmittance at 0.4 eV versus temperature for the $(La_{0.5}Pr_{0.5})_{0.7}Ca_{0.3}MnO_3$ films with ^{16}O and ^{18}O isotopes on LAO substrates measured (*1, 3*) in a constant magnetic field with a strength of 0.8 T and (*2, 4*) using the same field switched on and off at each point.

The temperature variation of the EKE magnitude measured at $E = 2.9$ eV differs considerably in the samples of all the four types studied (Fig. 8). A common feature of these temperature dependences is a considerable hysteresis revealed by measurements in the heating–cooling cycles. The temperature below which the EKE is manifested (that is, a ferromagnetic order appears) is close to the temperature of maximum resistance observed for all films during heating in the field. The EKE magnitudes for the manganite films with ^{16}O on both substrates are approximately equal. The ^{18}O isotope substitution for ^{16}O leads to a decrease in the EKE magnitude in the saturated state. A minimum EKE value was observed for the ^{18}O/LAO sample.

A comparison of the temperature variation of the EKE and transmission values at 0.14 eV (and at 0.4 eV)

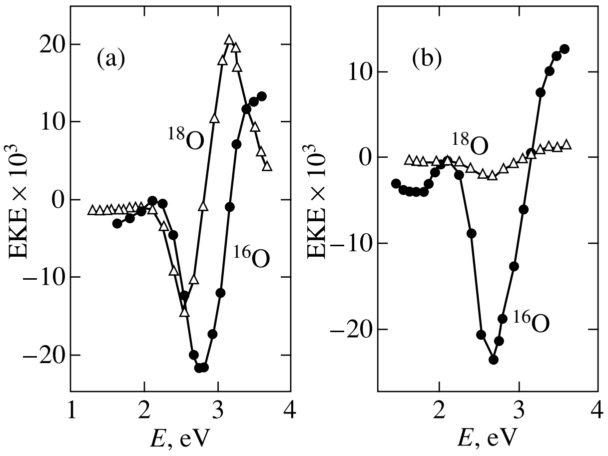

Fig. 7. The spectra of equatorial Kerr effect (EKE) for the $(La_{0.5}Pr_{0.5})_{0.7}Ca_{0.3}MnO_3$ films with ^{16}O and ^{18}O isotopes on (a) STO and (b) LAO substrates.

for the samples cooled in a magnetic field shows close values of the temperature at which the EKE appears and the transmittance exhibits a maximum for the films of all types. It should be noted that the EKE measurements for the ^{16}O/STO sample at 150–200 K gave a value of the opposite sign as compared to that observed in the low-temperature region. The EKE measurements on the substrate side did not show the change in sign. This observation is a direct evidence of the surface magnetism manifestations in the films studied.

4. DISCUSSION OF RESULTS

4.1. The Electron Structure of Doped Manganites

The traditional approach to describing the electron structure of manganites is based on the assumption of applicability of the standard energy band models with an allowance for a strong electron–vibrational interaction. The “low-energy physics” of doped manganites (on a scale below 4 eV) is determined by the e_g states of Mn ions coupled by a strong Hund’s exchange to the localized t_{2g} states of Mn, as well as by the Jahn–Teller interaction with the lattice. Thus, the model of double exchange with a strong Jahn–Teller interaction assumes a pronounced Mne_g band character of the injected holes in systems of the $La_{1-x}Sr_xMnO_3$ type.

However, the experimental data are not as unambiguous in determining the character of injected holes in these manganite systems. In particular, the study of electron energy losses near the O1*s*–O2*p* transition in $La_{1-x}Sr_xMnO_3$ led Ju *et al.* [17] to a rather unexpected conclusion about an O2*p* character of holes generated in this system in a broad range of doping ($0 \le x \le 0.7$). The same character of holes was indicated by the results of investigating the exchange splitting of the Mn3*s* level in the X-ray photoelectron spectra (which

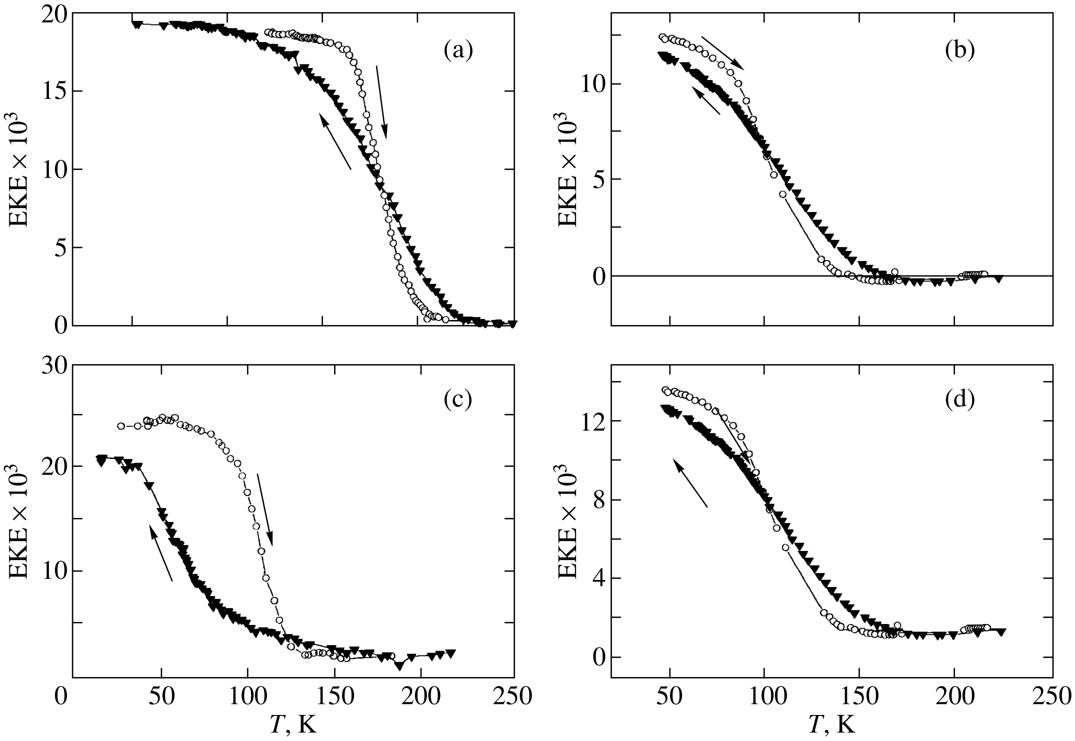

Fig. 8. Temperature dependence of the EKE magnitude for the $(La_{0.5}Pr_{0.5})_{0.7}Ca_{0.3}MnO_3$ films with (a, b) ^{16}O and (c, d) ^{18}O isotopes on (a, c) STO and (b, d) LAO substrates measured in the cooling–heating cycles (arrows indicate the direction of temperature variation).

are highly sensitive to the valence state of manganese) [18]. It was demonstrated [18] that the exchange splitting of the Mn3*s* level in systems of the $La_{1-y}MnO_3$ and $La_{1-x}Sr_xMnO_3$ remains virtually unchanged when the formal valence of Mn in this composition changes from 3.0 to 3.3. The same study presented convincing evidence for the appearance of Mn^{2+} ions in oxygen-depleted compositions of the $LaMnO_{3-\delta}$ type. For a low doping level ($x < 0.3$), the Mn K_β X-ray photoelectron spectra of the $La_{1-x}Ca_xMnO_3$ [19] even showed a "monovalent" Mn^{3+} state, with the O2*p* character of holes being most probable. For a high doping level ($x > 0.3$) the X-ray photoelectron spectra were indicative of a mixed valence state Mn^{3+}–Mn^{4+} with a component ratio corresponding to the *x* value (which implies predominantly Mn3*d* character of the injected holes).

The experimentally observed redistribution of the spectral density from high-energy charge-transfer band (O2*p*–Mn3*d*) to the region of lower energies upon the hole injection agrees with the notion that this must lead to the appearance of a considerable concentration of O2*p* holes.

A potentially more complicated character of the charge transfer process in doped manganites is indicated by the results of a high-temperature investigation of $LaMnO_3$ [20]. These data show evidence of the instability of manganites with respect to a disproportionation reaction, which can be schematically represented as a process

$$2MnO_6^{9-} \longrightarrow MnO_6^{8-} + MnO_6^{10-}$$

leading to the formation of hole and electron centers with the structure admitting a mixed valence of manganese ions (of the Mn^{3+}–Mn^{4+} type for the hole centers).

On the whole, the character of charge fluctuations in GMR manganites is still one of the central points of discussion from both theoretical and experimental standpoint. The state with $x = 0.3$ for the $(La, Pr)_{0.7}Ca_{0.3}MnO_3$ composition studied most probably corresponds to a mixed Mn3*d*–O2*p* character of the charge fluctuations.

4.2. Electron Inhomogeneity, Phase Separation, and Percolation Phenomena in Manganites

There is increasing evidence that doped manganites, as well as many other strongly correlated oxides such as cuprates, nickelates, and vanadites, are capable of occurring in a complicated inhomogeneous state exhibiting a metal–dielectric dualism.

Generally speaking, such systems can be characterized by a certain self-consistent distribution of various charge, spin, orbital, and structural fluctuations with the corresponding lifetimes and correlation lengths. The possibility of using the approximation of an effective homogeneous medium for describing the properties of systems with strongly developed static and dynamic fluctuations is disputable.

The heterovalent doping of manganites leads to the appearance of strong local inhomogeneities in the potential distribution. The corresponding potential wells may serve both as the centers of charge (hole or electron) localization and as the centers of nucleation for the phase providing the most effective screening of the charge inhomogeneity. These charge inhomogeneity centers may possess a complex structure featuring charge, spin, orbital, and structural fluctuations, each type with a character of its own. As the concentration of dopant ions (Ca^{2+}, Sr^{2+}, …) and, hence, of the charge inhomogeneity centers increases, these centers may exhibit a superposition leading to an increase in the correlation length of various charge, spin, and orbital fluctuations and, eventually, to the corresponding long-range ordering.

In the simplest case, when the charge inhomogeneity centers can be considered as microscopic domains of a new (ferromagnetic metal) phase, the process can be described within the framework of a model of percolation phase transition. According to this model, the conductivity (as well as some other values) in the vicinity of the percolation threshold is described by a power function of certain "geometric order parameter" $p - p_c$ [21]. In the simplest variant, this parameter can be represented by deviation of the bulk fraction *p* of the metal phase from a critical value p_c corresponding to the percolation limit, for example,

$$\sigma \propto (p - p_c)^t, \tag{1}$$

where *t* is the critical exponent [21]. In turn, the geometric order parameter near the percolation threshold can be related to the concentration of the charge inhomogeneity centers:

$$p - p_c \propto (x - x_c)^a,$$

where x_c is the critical concentration, which yields

$$\sigma \propto |x - x_c|^{at}.$$

By the same token, the critical temperature T_{MI} corresponding to the percolation breakage and the metal–dielectric transition at $p \geq p_c$ can be expressed as

$$T_{MI} \approx T_{MI}^0 (p - p_c)^\gamma, \tag{2}$$

where γ is the critical exponent and T_{MI}^0 is a certain characteristic temperature determined by their microscopic transport parameters.

Urushibara *et al.* [22] showed that the concentration dependence of the low-temperature conductivity of $La_{1-x}Sr_xMnO_3$ in the region of $x < 0.3$ can be presented as

$$\sigma(x) \propto (x - x_c)^{at}$$

with a critical concentration of $x_c = 0.174$ and the exponent $at = 0.5$, which also well falls within the framework of the percolation model.

A principal difference of this variant of the percolation model for GMR manganites is the (ferro)magnetic character of the metal regions, which leads to certain anomalies in the magnetic behavior. The first of these effects is a sharp increase in the relative volume of ferromagnetic metal regions at temperatures below the critical value T_C^0 corresponding to the “local” ferromagnetic ordering. The temperature dependence of magnetization and the magnetization curve reflect the superposition of two effects: the “internal” effect of spin ordering in the metal regions and the “external” effect of increasing volume of the magnetically ordered phase with a characteristic effective “Curie temperature” $T_C < T_C^0$. In the simplest model, T_C can be represented by the temperature of maximum of the average “thermal expansion” coefficient $\alpha(T) = \partial p/\partial T$ of the magnetically ordered metal phase. It is this external effect that can lead to the metal–dielectric percolation transition at $T_{MI} < T_C^0$. In the general case, the temperatures T_{MI} and T_C may differ.

The metal–dielectric percolation transition with a critical fraction $p = p_c$ of the metal phase volume in GMR manganites can be shifted toward either smaller or greater concentration x of divalent elements, for example, by selecting a dopant with appropriate ion radius to provide for a necessary relative decrease in the energy of metal or dielectric phase. In particular, these conditions are satisfied for $La_{5/8-y}Pr_yCa_{3/8}MnO_3$ with $y = 3/8$ [23] and for the composition studied in this work. All features in the thermal, electron, and magnetotransport properties of $La_{5/8-y}Pr_yCa_{3/8}MnO_3$ are related to the dominating contribution of the percolation conductivity through ferromagnetic metal regions coexisting with charge-ordered insulating regions. Note that the percolation transition is accompanied by strong fluctuations of the geometric order parameter and by the anomalous relaxation phenomena, hysteresis, and memory effects.

The results of measurements of the 1/*f* noise in poly- and single-crystalline samples of $(La, Pr)_{5/8}Ca_{3/8}MnO_3$ with low values of the effective temperature T_C of magnetic ordering [24] are indicative of a percolation mechanism of the transition from an inhomogeneous charge-ordered state to the ferromagnetic metal state. It is necessary to note several features characteristic of the first-order phase transitions, including a large temperature hysteresis of the resistivity and magnetization. In contrast to the behavior typical of the phase transitions in homogeneous systems, the magnetization of crystals under consideration varies smoothly in the vicinity of T_C and remains a linear function of $T_C–T$ even in a weak magnetic field.

The results of analysis of the scaling behavior of the 1/*f* noise and resistance agree with predictions of the percolation model concerning the pattern of phase separation, with the formation of conducting phase regions chaotically distributed in the insulating matrix. It is interesting to note that Podzorov *et al.* [24] even revealed a difference in the critical behavior of poly- and single-crystalline samples. Although the values of resistivities in the two cases are close, the temperature variation of ρ near T_C in single crystals exhibits reproducible jumps by more than one order of magnitude. For explaining this phenomenon, it was suggested [24] that the jumps of resistance are related to a large size of conducting regions in single crystals, which exceeds that in polycrystalline samples and cannot be considered small as compared to the characteristic system size (which is a necessary assumption in percolation models).

4.3. Percolation and the Giant Isotope Effect in Doped Manganites

The isotope exchange in a homogeneous system must not lead to any substantial changes in the optical properties beyond the phonon spectrum. Indeed, neither the energy spectrum of the optically active centers, nor the oscillator strengths for the optical transitions are significantly modified by the exchange. The main effect of the isotope substitution is related to the lattice oscillations and, hence, pronounced manifestations can be expected only in systems featuring strong electron–phonon interactions or the Jahn–Teller systems. The ^{16}O–^{18}O isotope exchange, owing to a relatively large mass increment (12.5%), produces a considerable stabilization of the (pseudo)-Jahn–Teller centers (Jahn–Teller polarons) on the one hand, and leads to a significant vibronic reduction of various electron matrix elements (e.g., the electron or hole transfer integrals) on the other hand.

All the above manifestations of the isotope exchange can be related to a vibronic mechanism of the isotope effect. In a homogeneous regular lattice, this mechanism leads to an increase in the effective mass of the Jahn–Teller polarons and favors their localization accompanied, in particular, by a small modification of the polaron IR absorption spectrum. In contrast, the ^{16}O–^{18}O isotope exchange in inhomogeneous systems with phase separation will lead to an additional increase in the relative volume of a dielectric phase of the localized Jahn–Teller polarons. This will be accompanied by anomalous phenomena near the percolation threshold. It is this “percolation” mechanism that may account for the anomalous response to the isotope exchange in the systems with phase separation [2, 3].

Using Eq. (1), we may establish a relationship between the constant α (characterizing the isotope effect with respect to the critical temperature T_{MI} of the metal–insulator transition) and the parameter p in the vicinity of the percolation threshold ($x \geq x_c$):

$$\begin{aligned}\alpha_0 &= \left(-\frac{\partial \ln T_{MI}}{\partial \ln M_0}\right) \approx \left(-\frac{\partial \ln T_{MI}^0}{\partial \ln M_0}\right)\\ &+ \gamma \frac{p_c}{p - p_c}\left(-\frac{\partial \ln p}{\partial \ln M_0}\right) = \alpha_{vibr} + \alpha_{perc}.\end{aligned} \tag{3}$$

In other words, the isotope effect includes two additive contributions–vibronic (α_{vibr}) and percolation (α_{perc}). The former term is of a purely microscopic electron nature and describes the influence of the isotope exchange on the microscopic parameters of electron transport. The latter term reflects the phase separation and describes the isotope-exchange-induced variation in the relative phase volume.

An important consequence of relationship (3) is the appearance of a power divergence

$$\alpha_{perc} \propto |x - x_c|^{-a}$$

in the isotope effect constant α near the critical point corresponding to the percolation threshold. This fact of proximity to the percolation threshold may explain the anomalously large α values observed in the $La_{1-x}Ca_xMnO_3$ system for $x_c \approx 0.18$ [4]. In this system, the character of the temperature dependence of magnetization in a weak external field and the concentration dependence of the constant reflecting the isotope effect with respect to the effective Curie temperature (determined as the temperature at which the magnetization reaches half of the maximum value) agrees with predictions of the percolation model for both $x > x_c$ and $x < x_c$.

It should be noted that the constant $\alpha_p = -\partial \ln p / \partial \ln M_0$ of the isotope effect with respect to the relative phase volume can be considered as an effective "isotope pliability" of a system with phase separation. This quantity characterizes the influence of the isotope exchange on the relative phase volume and on the effectiveness of the percolation isotope effect. Note that large values of this constant far from the percolation threshold may be accompanied by a relatively small contribution to the isotope effect for T_C.

4.4. Optical Properties of Manganites

Manganites with giant magnetoresistance, in contrast to many other typical systems based on 3*d* elements, exhibit anomalously strong fluctuations of the charge state and the crystal field in both Mn3*d* and O2*p* sublattices and may occur in a multiphase state with coexistence of metal and dielectric regions. This behavior markedly complicates interpretation of the optical properties of GMR manganites. The model of phase separation implies the existence of an optically inhomogeneous medium, many properties of which are analogous to those of the well-known and extensively studied dielectric systems such as glasses with metal inclusions [25–27]. For example, this refers to manifestations of the (quasi)-Drude with an integral weight proportional to the relative volume *p* of the metal regions. In addition to this (quasi)-Drude contribution of charge carriers, the optical spectra of manganites also reveal sufficiently narrow resonance transitions related to the hole and electron centers. Measurements of the optical properties of manganites are an important tool in studying their electron structure and multiphase composition.

The photoconductivity spectrum of undoped $LaMnO_3$ manganite exhibits a low-energy band in the region of 2.4 eV and a high-energy band at 5.2 eV [28], which are naturally assigned to the *d–d* type transition ^5E_g–$^5T_{2g}$ in Mn^{3+} ions and the lowest allowed charge-transfer transition O2*p*–Mn3*d* in the octahedral complexes $(MnO_6)^{9-}$, respectively [29]. The introduction of Ca^{2+} and Sr^{2+} ions (hole doping) leads to a significant modification of the optical properties in a broad spectral range. The low-energy band at 2.4 eV sharply drops in intensity, while the high-energy band gradually shifts toward lower energies. As a result, the spectral weight is generally transferred toward the IR range, with a pronounced maximum appearing at 1.5 eV [28, 30]. The nature of this peak was actively discussed. According to Takenaka *et al.* [28], this peak is related to the charge-transfer transition O2*p*–Mn3*d*, while most of the other researchers attribute this peak to various one-center or two-center *d–d* transitions. For example, Jung *et al.* [31] believe that this absorption is most probably due to indirect transitions between occupied ($e_{g\uparrow}^{(1)}$) and empty ($e_{g\uparrow}^{(2)}$) states (the $e_g^{(1)}$ and $e_g^{(2)}$ states belong to the e_g band of Mn^{3+} ions, which splits as a result of the Jahn–Teller interaction).

The *d–d* electric-dipole transitions become possible due to hybridization of the e_g states of Mn and the 2*p* states of oxygen. The observed band shift and the increase in the IR absorption coefficient in the region of ferromagnetic ordering are due to the appearance of a contribution from carriers in the conduction band and to the spectral weight redistribution from high- to low-energy region [32]. In our opinion, the *d–d* transition may also include the ^5E_g–$^5T_{2g}$ transition in Mn^{3+} ions because the crystal field for these ions in doped manganites is screened by the hole density partly delocalized on the surrounding oxygen ions. Indeed, a partial screening of the negative charge of the oxygen ions will lead to a decrease in the parameter of crystal-field splitting which, in turn, may result in decreasing energy of the ^5E_g–$^5T_{2g}$ transition from 2.4 eV in pure manganite to 1.5 eV in substituted compositions.

The main body of the optical data for manganites was obtained by measuring and processing the reflectance spectra, which cannot provide for the detection (and the more so, the detailed investigation) of many important features manifested by relatively weak (but highly informative) *d–d* transitions and forbidden charge-transfer transitions. In particular, this is valid for the transitions in Mn^{4+} ions and octahedral complexes $(MnO_6)^{8-}$ appearing in systems of the $La_{1-x}Sr_xMnO_3$ type as a result of the hole doping. Balykina *et al.* [33] studied the magnetooptical activity of these transitions in $A_2Mn_2O_7$ pyrochlores with the octahedral complexes $(MnO_6)^{8-}$ in the 1.5–4.5 eV range by measuring the Kerr effect. These measurements revealed the bands at 2.6 and 3.1 eV assigned to the *d–d* type transitions

$^4A_{2g}$–$^4T_{2g}$ and $^4A_{2g}$–$^4T_{1g}$ in Mn^{4+} ions and octahedral complexes $(MnO_6)^{8-}$, respectively. The band at 3.8 eV and a very intense band with a maximum at $E \geq 4.3$ eV can be attributed to the forbidden and allowed charge-transfer transitions, respectively, This assignment generally agrees with the data reported in [34] for a series of systems containing Mn^{4+}.

One of the first measurements of the Faraday effect in manganites was reported by Lawler *et al.* [35] for $La_{1-x}Ca_xMnO_3$ in the 1.5–3.0 eV range. These measurements showed evidence of a large Faraday rotation with maxima in the regions of the ^5E_g–$^5T_{2g}$ transition in Mn^{3+} (1.5 eV) and the charge-transfer transition (3.1 eV). Yamaguchi *et al.* [36] studied the magnetooptical Kerr effect in the $La_{1-x}Sr_xMnO_3$ system in the 0.9–5.3 eV range. The obtained spectral dependences of the polar Kerr effect (more precisely, the nondiagonal components of the dielectric permittivity tensor calculated from these data) were processed within the framework of the simplest two-oscillator model. This model satisfactorily described the low-frequency band with a maximum at 1.2 eV, but a discrepancy between the behavior observed in the 2–5 eV interval and the contribution of one model oscillator with an energy of 3.1 eV exceeded the experimental error. The magnetooptical activity in the latter interval was explained by a contribution from charge-transfer transitions O2*p*–Mn3*d*. Gan'shina *et al.* [9, 16] measured the equatorial Kerr effect in the $(La_{1-x}Pr_x)_{0.7}(CaSr)_{0.3}MnO_3$ system [9, 16] and established that the magnetooptical activity in this case must be assigned to transitions in the octahedral complexes of Mn^{3+} and Mn^{4+}.

On the whole, we may expect that the doped manganites must exhibit a considerable optical activity in the region of 2–3 eV, which is related to the Mn^{3+} and Mn^{4+} ions responsible for the unique properties of these oxide systems.

Let us consider the general features of the optical and magnetooptical spectra of the epitaxial manganite films studied in our experiments. The absorption spectra presented in Figs. 3 and 4 show evidence of a complicated character of the absorption band at 1.5 eV. The low-energy edge of this band clearly reveals a contribution due to the localized states. The appearance of bands due to localized states, called the middle infrared (MIR) bands, is a general feature in the optical absorption of many transition metal oxides representing strongly correlated systems. The two bands mentioned above (0.14 and 0.45 eV) were also observed in our investigations of the optical absorption of $La_{0.9}MnO_3$ and $(La_{0.9}Sr_{0.1})_{0.9}MnO_3$ single crystals [10, 37]. The photoconductivity band at 0.4 eV reported for singe-crystalline $La_{0.9}Sr_{0.1}MnO_3$ [30] and polycrystalline $La_{7/8}Sr_{1/8}MnO_3$ [31] was attributed to the polaron effects. The phonon absorption in manganites with a perovskite structure takes place in the region of energies below 0.09 eV. The appearance of bands due to localized states at a high carrier concentration created by doping cannot be explained within the framework of a one-electron band model. The existence of these bands together with the Drude or quasi-Drude contribution is important evidence for the electron inhomogeneity and phase separation in the system.

The nature of bands related to the localized states and many other features in the properties of transition metal oxides are successfully explained based on a cluster model [2] assuming the existence of the pseudo-Jahn–Teller electron and hole clusters characterized by the two-electron (boson, bipolaron) nature of the carriers. Transitions in the main clusters [MnO_6^{9-}] form the fundamental absorption band (above 3 eV), while the low-energy transitions in the electron and hole clusters account for the MIR bands. The origin of the MIR bands is related to a strong correlation effect produced by an additional hole (or electron) appearing in the main cluster. This correlation leads to a pseudo-degeneracy in the energy of states with the hole (electron) localized in the Mn3*d* and O2*p* states and, hence, to a valence resonance (of the Mn^{3+}-Mn^{4+} type in the hole cluster) and a decrease in the energy of a charge-transfer transition. The MIR bands are essentially related to the charge-transfer transitions Mn3*d*–O2*p* inside the electron and hole clusters.

In the above model [2], the electron and hole clusters MnO_6 form the centers of charge inhomogeneity. These centers may possess a complicated structure and contain various numbers of clusters. The energy states of the polar clusters (and of the charge inhomogeneity centers) are determined by the charge, sin, and orbital degrees of freedom. therefore, the charge inhomogeneity centers are essentially the large Jahn–Teller magnetic polarons. The formation of these centers is favored by the local potential inhomogeneity caused by a nonisovalent substitution or by the vacancy formation. The appearance of the charge inhomogeneity centers may account for the metal phase nucleation in manganites with a perovskite structure and, hence, for the static ad/r dynamic phase separation in the systems [2].

The experimental results presented in this paper can also be explained within the framework of the model proposed in [2]. Indeed, the band at 0.14 eV observed in $La_{0.9}MnO_3$ and $(La_{0.9}Sr_{0.1})_{0.9}MnO_3$ single crystals was previously assigned to transitions in the hole closer MnO_6^{8-}, while the band at 0.4 eV was attributed to transitions in the corresponding electron cluster [10]. According to an alternative interpretation, the band at 0.4 eV is explained by the delocalization of polar clusters [2], that is, by a fast two-electron exchange between coupled electron and hole clusters. This exchange may give rise to a common band centered at the energy

$$\Delta_M = c_e\Delta_e + c_h\Delta_h,$$

where $c_{e,h}$ are the concentrations of electrons and holes, respectively, and $\Delta_{e,h}$ are the corresponding MIR peak energies. Assuming that transitions in the electron cluster account for the band at 0.95 eV (i.e., $\Delta_h = 0.14$ eV and $\Delta_e = 0.95$ eV), we obtain $\Delta_M \approx (\Delta_h + \Delta_e)/2 \approx 0.5$ eV. This delocalization is accompanied by an increase in the conductivity and leads to the formation of a Drude-like metal contribution. This very situation is observed below the metal–dielectric transition (accompanied by an additional absorption at 0.2 eV). The intensity of absorption in the region of the "hole" peak at 0.14 eV also increases below the metal–dielectric transition, which can be explained both by an increase in the Drude-like contribution and by a change in the overall peak intensity.

As is seen from Fig. 5, the intensity of absorption bands at 0.14 and 0.4 eV is strongly affected by the magnetic order, which allows us to assign the bands of localized states to the magnetic polarons. In the general case, the intensity of polaron absorption bands reflects the conductivity in the polaron system. This temperature dependence of the absorption bands at 0.14 and 0.4 eV (Fig. 5 shows data only for the band at 0.4 eV), as well as a similar variation observed for $La_{0.9}MnO_3$ and $(La_{0.9}Sr_{0.1})_{0.9}MnO_3$ single crystals [2, 10] that indicates that these bands belong to the same object—the charge inhomogeneity center containing electron and hole clusters. It should be noted that we failed to reveal the trends in the temperature variation of the intensity of absorption at 0.9 eV because this band exhibited a temperature-dependent shift (see Figs. 3 and 4) because of the superposition of other absorption bands.

A comparison of the EKE spectra of the ^{18}O/LAO and ^{18}O/STO samples (Fig. 7) to the absorption spectra of the same films (Figs. 3 and 4) shows that the appearance of an intense band at 0.9 eV in the absorption spectrum coincides with the shift of the EKE spectrum toward lower energies. Apparently these effects are interrelated. Assuming that the band at 0.9 eV is due to the low-energy transitions in the electron clusters, the growth in intensity of this band observed for the ^{18}O/STO sample implies an increase in the number of these electron clusters. A change in the ratio of hole end electron clusters in the charge inhomogeneity centers (in the ferromagnetic regions) can modify the energies of transitions in the Mn^{3+} and Mn^{4+} clusters. This can result from a change in the crystal field screening by carriers and must apparently affect the EKE spectrum. In the spectrum of the ^{18}O/LAO sample, the band at 0.9 eV is less pronounced; accordingly, no shift is observed in the EKE spectrum (Fig. 7). The drop in the EKE intensity upon the isotope exchange in these samples is related to a decrease in the volume fraction of ferromagnetic regions at the expense of growing charge-ordered antiferromagnetic regions. A difference in the degree of the EKE intensity drop for the films on STO and LAO substrates is probably related to differences in the character of the process of charge carrier localization in these samples. These distinctions are caused by the different character of stresses developed in the films grown on different substrates.

Previously [8, 10], we demonstrated that a decrease in the intensity of optical absorption in the region of energies corresponding to the light interaction with the charge carriers observed on cooling the samples below the Curie temperature ("metal" contribution), together with retained "semiconductor" character of the temperature variation of then dc resistivity $\rho(T)$, is evidence of the phase separation in the system, representing metal "droplets" distributed in an insulating matrix. A comparison of the optical and magnetooptical data to the results of resistivity measurements indicates that the phase separation phenomenon is most pronounced in the ^{18}O/LAO samples. Indeed, a decrease in the absorption intensity of this film (cooled in a magnetic field) at temperatures below 120 K (Fig. 5) demonstrates the presence of a "metal" contribution related to the metal–dielectric transition. Simultaneously, this film exhibits a growth in the EKE intensity below 125 K (Fig. 8). Thus, both the absorption and Kerr effect measurements are indicative of the presence of ferromagnetic conducting regions in the ^{18}O/LAO film. However, the resistivity of this film in a zero magnetic field keeps monotonically increasing below 125 K (Fig. 1). These facts show that the optical methods are more sensitive than the electrical measurements with respect to the presence of a small fraction of ferromagnetic metal droplets in the insulating matrix.

From the standpoint of the optical properties, the ^{18}O isotope substitution for ^{16}O in manganites leads to a decrease in the contribution related to the free carriers and to an increase in intensity of bands related to the localized states, which is indicative of a considerable localization of the charge carriers. This localization apparently has a percolation character [2, 3]. A system occurring near the percolation threshold is extremely sensitive with respect to various external factors (light, electric field, pressure, etc.). In our case, the external action consists in substituting the ^{18}O oxygen isotope for ^{16}O. As a result of this isotope exchange, the fraction of ferromagnetic metal droplets decreases and the proportion of antiferromagnetic charge-ordered regions increases. Assuming that the charge carriers take the form of polarons, an increase in their localization caused by the growth of the oxygen ion mass can be explained by the polaron band narrowing [3].

Application of a magnetic field during cooling of the film is an additional external factor that strongly affects the character of the inhomogeneous multiphase state of the composition studied. This factor leads, in particular, to an increase in the relative volume and size of the ferromagnetic metal regions which, in turn, results in the growth in intensity of the MIR absorption bands accompanied by suppression of the inhomogeneous broadening effects characteristic of the small metal droplets. The curves of the EKE magnitude versus temperature measured in the heating mode for the samples preliminarily cooled in the magnetic field exhibit a sharper decay in the vicinity of T_C.

During the magnetotransmittance measurements, when the field is switched at every point (Fig. 6), the system of charge carriers cannot relax during the time of measurement. For this reason, the measured magnetotransmittance values is considerably (at least, by half) smaller that those calculated using the data of Fig. 5 (measured with a constant magnetic field applied during the sample heating from 80 K to room temperature). The existence of long-term relaxation and irreversible phenomena is an important feature typical of inhomogeneous systems.

A considerable difference in the results of isotope exchange in the manganite films on LAO and STO substrates is related to a difference in the character of stresses developed in the films grown on different substrates–expanding on STO and contracting on LAO. This difference is related to the fact that the substrate lattice parameter a in the lateral direction is greater (for LAO) and smaller (STO) as compared to that of the film material [14, 38]. This circumstance also accounts for the different character of the magnetic anisotropy of the manganite films on STO and LAO substrates, which is manifested by a change in the EKE sign in the temperature interval 145 K < T < 205 K observed for the ^{16}O/STO film.

5. CONCLUSION

The effects of temperature, external magnetic field, isotope exchange, and illumination on the doped manganites lead to a strong modification of their optical absorption spectrum in a broad spectral range (up to 5 eV). Taking into account the very small energy scale of these perturbations (especially of the external magnetic field and isotope exchange), the observed anomalous changes can be related to the percolation phenomena.

The results of the optical and magnetooptical measurements for the epitaxial $(La_{0.5}Pr_{0.5})_{0.7}Ca_{0.3}MnO_3$ films with a partial ^{18}O isotope substitution for ^{16}O show evidence in favor of the model of phase separation and confirm the percolation character of changes cased by the isotope exchange. The observed spectral features can be interpreted within the framework of the model of the pseudo-Jahn–Teller electron and hole cluster formation.

ACKNOWLEDGMENTS

The authors are grateful to N.A. Babushkina for preparing the isotope substituted samples. The work was supported by the Russian Foundation for Basic Research (project no. 99-02-16595) and the INTAS Foundation (project nos. 97-30252 and 97-11954).

REFERENCES

1. É. L. Nagaev, Usp. Fiz. Nauk **166**, 833 (1996) [Phys. Usp. **39**, 781 (1996)].
2. A. S. Moskvin, Physica B (Amsterdam) **252**, 186 (1998).
3. D. Khomskii, Physica B (Amsterdam) **280**, 325 (2000).
4. G. Zhao, K. Conder, H. Keller, and K. A. Müller, Nature **381**, 676 (1996); Phys. Rev. B **60**, 11 914 (1999).
5. N. A. Babushkina, L. M. Belova, O. Yu. Gorbenko, *et al.*, Nature **391**, 159 (1998).
6. N. A. Babushkina, L. M. Belova, A. N. Taldenkov, *et al.*, J. Phys.: Condens. Matter **11**, 5865 (1999).
7. G. Zhao, H. Keller, J. Hofer, *et al.*, Solid State Commun. **104**, 57 (1997); M. R. Ibarra, G. Zhao, J. M. de Teresa, *et al.*, Phys. Rev. B **57**, 7446 (1998).
8. N. N. Loshkareva, Yu. P. Sukhorukov, S. V. Naumov, *et al.*, Pis'ma Zh. Éksp. Teor. Fiz. **68**, 89 (1998) [JETP Lett. **68**, 97 (1998)].
9. E. A. Gan'shina, O. Yu. Gorbenko, A. R. Kaul, *et al.*, J. Phys.: Condens. Matter **12**, 2857 (2000).
10. N. N. Loshkareva, Yu. P. Sukhorukov, É. A. Neĭfel'd, *et al.*, Zh. Éksp. Teor. Fiz. **117**, 440 (2000) [JETP **90**, 389 (2000)].
11. O. Yu. Gorbenko, A. R. Kaul, A. A. Bosak, *et al.*, in *High-Temperature Superconductors and Novel Inorganic Materials*, Ed. by G. van Tendeloo, E. V. Antipov, and S. N. Putilin (Kluwer, Dordrecht, 1999), p. 233.
12. B. Guettler, L. Skuja, O. Yu. Gorbenko, *et al.*, Mater. Res. Soc. Symp. Proc. **517**, 111 (1998).
13. A. M. Balagurov, V. Yu. Pomyakushin, V. L. Aksenov, *et al.*, Pis'ma Zh. Éksp. Teor. Fiz. **67**, 672 (1998) [JETP Lett. **67**, 705 (1998)].
14. O. Yu. Gorbenko, A. R. Kaul, N. A. Babushkina, *et al.*, Aust. J. Phys. **52**, 269 (1999).
15. N. A. Babushkina, L. M. Belova, D. I. Khomskii, *et al.*, Phys. Rev. B **59**, 6994 (1999).
16. E. A. Gan'shina, O. Yu. Gorbenko, N. A. Babushkina, *et al.*, in *Non-Linear Electromagnetic Systems* (IOS Press, Amsterdam, 1998), p. 325.
17. H. L. Ju, H.-C. Sohn, and Kannan M. Krishnan, Phys. Rev. Lett. **79**, 3230 (1997).
18. V. R. Galakhov, M. Demeter, S. Bartkowski, *et al.*, submitted to Phys. Rev. Lett.
19. T. A. Tyson, Q. Qian, C.-C. Kao, *et al.*, Phys. Rev. B **60**, 4665 (1999).
20. J.-S. Zhou and J. B. Goodenough, Phys. Rev. B **60**, R15002 (1999).
21. D. Staufer and A. Aharoni, *Introduction to Percolation Theory* (Taylor and Francis, London, 1992).
22. A. Urushibara, Y. Moritomo, T. Arima, *et al.*, Phys. Rev. B **51**, 14 103 (1995).
23. K. H. Kim, M. Uehara, C. Hess, *et al.*, Phys. Rev. Lett. **84**, 2961 (2000).
24. V. Podzorov, M. Uehara, M. E. Gershenson, *et al.*, Phys. Rev. B **61**, R3784 (2000).
25. J. A. A. Perenboom, P. Wyder, and F. Meyer, Phys. Rep. **78**, 173 (1981).
26. Ping Sheng, Phys. Rev. Lett. **45**, 60 (1980).
27. N. Del Fatti, F. Vallee, C. Flytzanis, *et al.*, Chem. Phys. **251**, 215 (2000).

28. K. Takenaka, K. Iida, Y. Sawaki, *et al.*, J. Phys. Soc. Jpn. **68**, 1828 (1999).
29. J. M. D. Coey, M. Viket, and S. von Molnar, Adv. Phys. **48**, 167 (1999).
30. Y. Okimoto, T. Katsufuji, T. Ishikawa, *et al.*, Phys. Rev. B **55**, 4206 (1997).
31. J. H. Jung, K. H. Kim, H. J. Lee, *et al.*, Phys. Rev. B **59**, 3793 (1999).
32. N. N. Loshkareva, Yu. P. Sukhorukov, V. E. Arkhipov, *et al.*, Fiz. Tverd. Tela (St. Petersburg) **41**, 475 (1999) [Phys. Solid State **41**, 426 (1999)].
33. E. A. Balykina, E. A. Ganshina, G. S. Krinchik, *et al.*, J. Magn. Magn. Mater. **117**, 259 (1992).
34. A. G. Paulusz and H. I. Burrus, Chem. Phys. Lett. **17**, 527 (1972).
35. J. F. Lawler, J. G. Lunney, and J. M. D. Coey, Appl. Phys. Lett. **65**, 3017 (1994).
36. S. Yamaguchi, Y. Okimoto, K. Ishibashi, and Y. Tokura, Phys. Rev. B **58**, 6862 (1998).
37. N. N. Loshkareva, Yu. P. Sukhorukov, B. A. Gizhevskii, *et al.*, Phys. Status Solidi A **164**, 863 (1997).
38. O. Yu. Gorbenko, M. A. Novojilov, I. E. Graboy, *et al.*, in *Book of Abstracts of E-MRS Spring Meeting, Strasbourg, 2000*, p. P-22.

Translated by P. Pozdeev

Journal of Experimental and Theoretical Physics, Vol. 92, No. 3, 2001, pp. 474–479.
Translated from Zhurnal Éksperimental'noĭ i Teoreticheskoĭ Fiziki, Vol. 119, No. 3, 2001, pp. 546–552.
Original Russian Text Copyright © 2001 by Barabanenkov, V. Ivanov, S. Ivanov, Taranov, Khazanov.

SOLIDS
Structure

Investigation of Nanoceramics Based on Aluminum and Zirconium Oxides Using the Heat Pulse Method

Yu. N. Barabanenkov[a], **V. V. Ivanov**[b, *], **S. N. Ivanov**[a], **A. V. Taranov**[a], **and E. N. Khazanov**[a]
[a]*Institute of Radio Engineering and Electronics, Russian Academy of Sciences, Moscow, 103907 Russia*
[b]*Institute of Electrophysics, Ural Division, Russian Academy of Sciences, Yekaterinburg, 620219 Russia*
**e-mail: ivanov@mail.cplire.ru*

Received September 20, 2000

Abstract—The processes of phonon transport in ceramics and composites based on aluminum and zirconium oxides are studied experimentally in the region of helium temperatures. It is demonstrated that, for the ceramic grain size R within two orders of magnitude and more (up to nanosizes), the phonon diffusion coefficient $D_{\text{eff}} \propto R$ and exhibits a decreasing temperature dependence. In aluminum-based nanoceramics with $R < 200$ nm, the phonon diffusion coefficient decreases abruptly by two orders of magnitude, and its temperature dependence becomes increasing. A model of temperature dependence of the diffusion coefficient is suggested. *© 2001 MAIK "Nauka/Interperiodica".*

1. INTRODUCTION

Interest in nanocrystal materials is associated with expectations of high mechanical and other functional characteristics of such materials, as well as of new properties resulting from the dimensional effect of the crystals or grains that form those materials and structural changes of the boundaries between them [1, 2].

One of the methods of preparing dense nanostructure ceramics, for example, ZrO_2 and Al_2O_3, and composites on their basis, involves making the process of compaction more important compared with the process of subsequent sintering. Such a method was provided by pulsed compaction using shock waves up to 22 GPa [3] and soft pressure waves generated by the magnetic pulse method [4]. The stage of sintering, i.e., the final operation in the preparation of nanoceramics, differs from the conventional modes of preparing ceramics by lower ($(0.5–0.6)T_{ml}$) temperatures of treatment and shorter (by two–three orders of magnitude) exposure times. This stage defines both the grain size and the structure of interfaces between the grains [4].

A number of methods exist for the investigating the structure of nanoceramics. They include, first of all, X-ray techniques whereby one can use the broadening of X-ray diffraction peaks compared with the lines of standards such as coarse-grained ceramics to estimate the average grain size. An analysis of the type of boundaries between grains proves to be a more complicated problem to be solved by high resolution microscopy. Nevertheless, numerous questions as to the type of boundaries, the pore structure, and the pore and grain dispersion remain open.

This paper deals with the investigation of nanoceramics and composites on the basis of α-Al_2O_3 and ZrO_2 using the heat pulse method. The use of weakly nonequilibrium phonons with a temperature of 2 to 4 K and, accordingly, with the wave vector for the main group of phonons $q_s \approx 2.7kT/\hbar v_s \approx (1.0–2.0) \times 10^6$ cm^{-1} or $\lambda_s \approx 30–60$ nm makes it possible to "sense" the size of nanocrystallites. The transmission of a phonon or acoustic wave from grain to grain via a boundary layer of thickness l_{gb}, whose properties differ from those of the grains, is defined within the laws of acoustic matching [5] by the quantity $ql_{gb} \le \pi$, which enables one, with the acoustic wavelengths employed, to identify the thickness, density, and other quantitative parameters of this boundary layer.

2. EXPERIMENTAL PROCEDURE

We investigated samples of high-density α-Al_2O_3 and ZrO_2 ceramics and composites on their basis, which were prepared from nanopowders of oxides produced by electric explosion of metallic aluminum and zirconium in an oxygen-containing atmosphere. The average size of powder particles of a close-to-spherical shape did not exceed 30 nm. The powder was pressed by the magnetic pulse technique in a hard mold with the maximum pressure pulse of 1.2 GPa for a period of 200–300 μs. The compaction was performed in vacuum ($p \approx 1$ Pa) at room temperature with preliminary degassing of the powder. Compacts in the form of disks with the diameter of 3.0 cm and thickness of up to 0.35 cm had a relative density of 0.7–0.8.

The compacts were sintered in the air in a laboratory resistance furnace at temperatures $T_{\text{bur}} \approx 1400$°C. The exposure time at the synthesis temperature ranged from zero to 60 min; it was this time that defined the obtained values of the grain size R (crystallites) and the quality of the boundaries between them. In preparing Al_2O_3–ZrO_2

composites, the sintering temperature of 1410°C was selected for the composition of $0.4Al_2O_3$–$0.6ZrO_2$ (A40–Z60) and 1450°C for the composition of $0.85Al_2O_3$–$0.15ZrO_2$ (A85–Z15). In both cases, the exposure time amounted to 15 min; as a result, approximately similar (~70 nm) grain sizes of the ZrO_2 phase could be obtained. As to the grain sizes of the α-Al_2O_3 phase, they were different for different compositions, namely, approximately 120 nm for the first composition and approximately 180 nm for the second composition in which the α-Al_2O_3 phase predominates. Also investigated were ceramics prepared by the conventional technology and produced commercially (sapphirite, polycor). The characteristics of the investigated samples are given in the table.

The microstructure of the surface (spallation) of ceramic samples was investigated using a JSM-840 scanning electron microscope manufactured by Jeol.

The kinetics of phonons at helium temperatures were investigated by the “heat pulse” method. A film of gold, which was heated by a short (($\approx 10^{-7}$ s) pulse of current and served as an injector of nonequilibrium phonons, was deposited on one side of a plate of material being investigated. A bolometer of Sn in the form of a meander with an area of 0.3×0.25 mm^2 was applied onto the other side of the plate. The displacement of the working point of the bolometer under the effect of magnetic field ($\approx 160 \times 10^2$ A/m) enabled one to obtain the dependence of scattering of nonequilibrium phonons on the temperature in the sample being investigated in the range from 1.7 to 3.8 K. The power dissipated in the heater was selected to be sufficiently low so that the injected phonons could be assigned the thermostat (bath) temperature with the frequency distribution close to Planckian.

3. RESULTS AND DISCUSSION

Examples of microphotographs of the spallation surface of ceramic samples, obtained by scanning microscopy, are given in Fig. 1 for α-Al_2O_3 samples. One can see that, both for commercially produced ceramic (Fig. 1a) and for nanoceramic prepared by magnetic pulse compaction with subsequent sintering (Fig. 1b), the grains of ceramic are close-packed crystallites (or single crystals), which leads one to assume their high structural perfection. At the same time, the employed procedure leaves open the question of the type of boundaries between grains of ceramic.

Before turning to the analysis of the main experimental results, we will briefly dwell on the theoretical prerequisites of applying the heat pulse method to ceramic materials, as described in [6]. In the model of [6], it is assumed that the free path of phonons considerably exceeds the grain size, $l_{tr} \gg R$, as follows obviously from the perfect structure of the grain (Fig. 1) and low temperature of the experiment. In this situation, the scattering of nonequilibrium phonons reflects only the structure and properties of boundaries between grains. According to [6], the expression for the arrival time of the maximum of the signal $t_{\max}$ of a pulse of nonequilibrium phonon radiation under conditions of diffuse propagation of phonons in a ceramic sample of thickness $L \gg R$ has a conventional form of

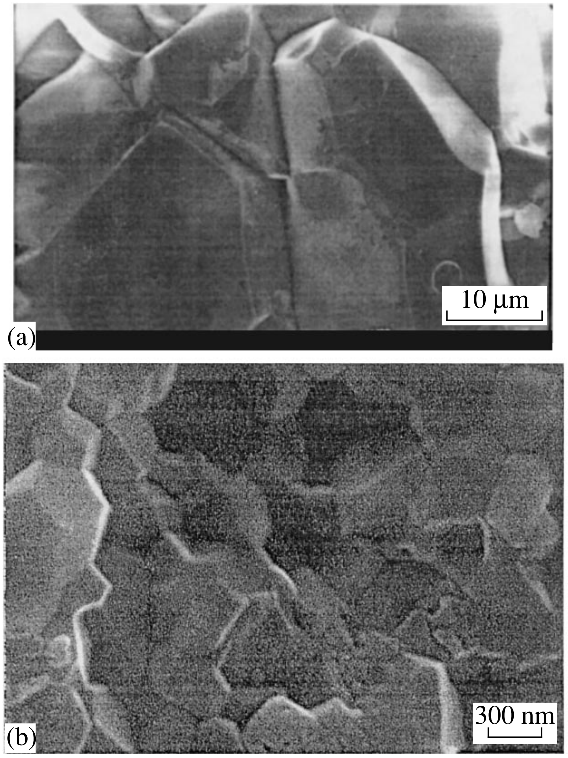

Fig. 1. The microstructure of the spallation surface of ceramic samples: (a) VK-100 (polycor); (b) nanoceramic, sample no. (N1862).

$$t_{\max} \approx L^2/D_{\text{eff}}$$

and

$$D_{\text{eff}} = v_s R f_\omega \Sigma / S. \quad (1)$$

Here, v_s is the velocity of sound in a grain of ceramic, S is the area of the grain surface, Σ is the total area of contact sites per single grain, and f_ω is the probability of transmission of a phonon of frequency ω through a contact site. The expression Σ/S reflects the possibility of open and closed porosity on the grain boundaries in ceramic samples. In what follows, we will demonstrate that, for dense ceramics with open porosity (of approximately 1–2%) investigated in our experiments, $\Sigma/S \approx 1$; the average velocity of sound in the ceramics and composites being investigated within the experimental errors and estimates may be assumed to be the same and equal to $v_s \approx 7 \times 10^5$ cm/s.

The behavior of the effective diffusion coefficient D_{eff} as a function of temperature, ceramic grain size, Parameters of samples of Al_2O_3 and ZrO_2 ceramics and composites on their basis investigated by us

No. of sample	Powder	*T* of sintering, °C	Density, g/cm^3	Grain size *d*, nm	Exposure time, min	Phase composition
1604	AT-1s2	1410	3.74	200–300	0	
1862	AM1-1	1410	3.80	~300	2	
1868	AM1-1	1310	3.62	~100	3	
1863	AM1-1-s5	1410	3.87	~1000	60	
1872	AM1-1-s5	1410	3.86	~500	20	
1623.7	AM1-1-s5	1230	3.25	94		α-Al_2O_3–96%, spinel–4%
1623.3	AM1-1-s5	1310	3.60	164		α-Al_2O_3–96%, spinel–4%
1466	AM1-1-s2	1370	3.724	~100		α-Al_2O_3–96%, spinel–4%
88	ZrO_2	1050	5.28	45		Monoclinic
196	ZrO_2	1100	5.52	~70		Monoclinic
2071	A40-Z60	1410	5.01	120/70*	15	
2036	A85-Z15	1450	4.07	180/70*	15	
VK100-1 (Polycor)			3.96	20000		99% α-Al_2O_3
VK98-1 (Sapphirite)			3.88	7000		98% α-Al_2O_3
VK-94-1 (22KhS)			3.65	12000		98.4% α-Al_2O_3

* The numerator gives the size of Al_2O_3 crystallites, and the denominator, that of ZrO_2.

and the properties and area of the intergrain boundaries fully describes the properties of ceramic material.

Examples of curves of heat pulse propagation for a number of temperatures in an α-Al_2O_3 sample with an average grain size $R \geq 0.2$ μm are given in Fig. 2; shown in the inset are analogous curves for a sample with $R \leq 0.2$ μm. In both cases, the curves of the signal on the bolometer have a bell shape with a well-defined maximum, that is characteristic of diffuse propagation of injected phonons. The condition $t_{max} \propto L^2$ is valid for all investigated samples, which points to the diffuse behavior of the motion of nonequilibrium phonons. Note that, for α-Al_2O_3 ceramics with $R \geq 0.2$ μm and for all ZrO_2 samples, as well as for composites, the time of the maximum of the bolometer signal t_{max} increases with the temperature of injected phonons ($\partial t_{max}/\partial T > 0$); for α-$Al_2O_3$ nanoceramics with $R \leq 0.1$ μm, the time t_{max} increases by two orders of magnitude, and its temperature dependence becomes decreasing ($\partial t_{max}/\partial T < 0$).

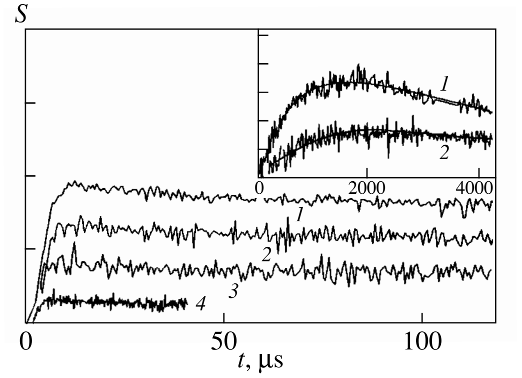

Fig. 2. The amplitude of the signal of nonequilibrium phonon radiation as a function of time in samples of α-Al_2O_3 nanoceramics: sample no. 1862, $R = 300$ nm, $L = 3.75 \times 10^{-2}$ cm, $T = 3.83$ (*1*), 3.43 (*2*), 3.03 (*3*), and 2.62 K (*4*). The inset corresponds to sample no. 1868, $R \approx 100$ nm, $L = 1.7 \times 10^{-2}$ cm, $T = 3.85$ (*1*) and 3.46 K (*2*).

For investigated samples (see table), the curve of $D_{eff} \approx L^2/t_{max}$ dependence on the ceramic grain size was constructed at the fixed temperature $T = 3.8$ K (Fig. 3). For ceramics with $\partial t_{max}/\partial T > 0$ in the range of values of R within two orders of magnitude, it turns out that $D_{eff} \propto R$ (curve *1*); it was for the first time that such correlations were obtained. A deviation from the linear dependence (decrease in the values of D_{eff}) occurs at $R \leq 100$ nm for ZrO_2 ceramics and ZrO_2–Al_2O_3 composites. A deviation from the linear dependence $D_{eff} \propto R$ may be due either to the variation of the properties of intercrystallite boundaries, i.e., of the quantity f_ω, or to the manifestation of the effects of diffraction (interference) of the phonon flux because of the comparability of the wavelengths of phonons used in the experiment with the grain size of ceramic crystallites. This interpretation of the behavior of the $D_{eff} \propto \varphi(R)$ for the grain size $R \leq 40$ nm appears possible, in particular, because of dispersion in the sizes of nanocrystallites of ceramic material. The results obtained by a number of authors for α-Al_2O_3 ceramics [7, 8] "fit" the linear portion of curve *1* well (Fig. 3). This points to the validity of formula (1) for describing the diffusion of phonons in ceramics, and the quantity $f_\omega \Sigma/S$ defined by the properties of boundaries between crystallites turns out to be within the experimental error, which is the same for the samples being investigated (irrespective of the time of exposure and the temperature during sintering, which define the size of grain in ceramics) and for high-quality commercially produced ceramics. A quantitative comparison of the experimental data with Eq. (1) leads one to argue that the boundary between grains is fairly perfect and well formed, and one can assume that $\Sigma/S \approx 1$ and $f_\omega \approx 0.8$–0.9.

As was already mentioned above, the situation changes radically for α-Al_2O_3 nanoceramics with $R < 0.2$ μm, which have a decreasing temperature dependence of t_{max}; the value of D_{eff} at $T = 3.8$ K decreases by two orders of magnitude. Therefore, a change of mechanism of phonon scattering on the boundaries between grains occurs as a result of variation of the structure of those boundaries. One can assume that, because of the singularities of the process (rapid sintering at a lower temperature, see table), the boundaries in these samples are not fully formed and have a low-density interlayer between them, this leading to effective reflection of phonons from the boundary. We will perform numerical estimation; namely, for a value of $D_{eff} \approx 10^{-1}$ cm²/s and grain size $R \approx 10^{-5}$ cm (see Fig. 3), we have $l_{eff} \approx D_{eff}/v_s \approx 1.5 \times 10^{-7}$ cm $\ll R$ for the effective free path; i.e., a phonon “dangles” in crystallite for quite some time and is reflected from the boundaries before moving over to the adjacent crystallite ($f_\omega \Sigma/S \approx 10^{-2}$). Note further that, for these samples, $qR \gg 1$, and this rules out any significant manifestation of diffraction effects. Feofilov *et al.* [9] arrived at the same conclusion studying α-Al_2O_3 ceramic with a grain size of approximately 10^{-5} cm by the optical methods. They believe that the dynamics of phonons with the energy of 29 cm^{-1} differ sharply from those for α-Al_2O_3 with a grain size of the order of $\sim 10^{-3}$ cm. The variation of the phonon dynamics is associated with the variation of the conditions of phonon transmission between the crystallite boundaries rather than with the decrease in the crystallite size. In some of our previous experiments, $\partial t_{max}/\partial T < 0$ was observed for a number of single-phase ceramics with a large grain size (5.0 to 10 μm), namely, α-Al_2O_3 [6], and SiC and AlN [10]. The diffusion coefficients for these samples at $T = 3.8$ K are also given in Fig. 3. They are matched with the data for nanocrystals given by curve *2*, which also obeys the $D_{eff} \propto R$ correlation. For a large class of ceramics with $\partial t_{max}/\partial T < 0$, there is much in common in the structure of boundaries between grains, this defining the weak transparency ($f_\omega \Sigma/S \approx 10^{-2}$) of these boundaries for phonons.

We will treat the possible resonance mechanism [11] explaining the origin of the experimentally revealed increasing and decreasing forms of the temperature dependence for the arrival time t_{max} of the maximum for the signal of a pulse of nonequilibrium phonon radiation, as illustrated by the example of the structure shown in Fig. 4, which is a simplified model of a phonon (high-frequency acoustic wave) propagating from grain *3* to grain *1* via the boundary layer *2*. The materials of the structure of Fig. 4 are assumed to be isotropic and homogeneous with preassigned values of density ρ_i and group velocity of sound v_i (i = 1, 2, 3), with the grains *1* and *3* assumed to be semibounded plane layers of thickness l_{gb}. We follow the method of acoustic matching of media [12] to estimate the probability f_ω of phonon transmission from grain *3* to grain *1* via the boundary layer *2* as the ratio of the power of radiation transmitted to grain *1* to the power of radiation incident on the boundary layer, with due regard for all angles of incidence θ_3 and transmission θ_1 (Fig. 4). This determination gives

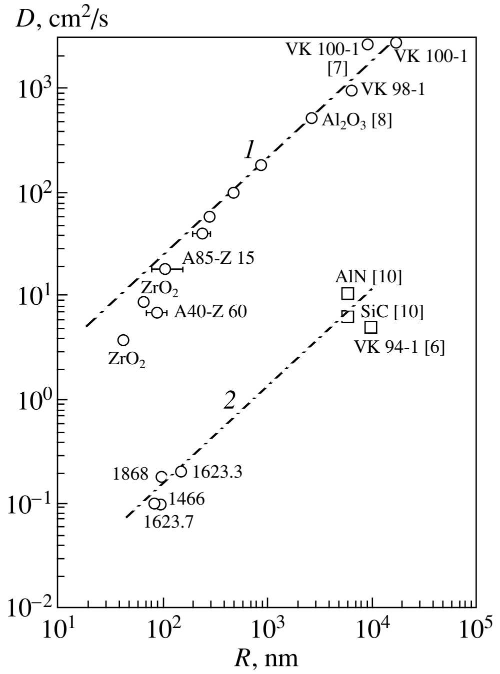

Fig. 3. The effective diffusion coefficient of phonons as a function of the average grain size of ceramic sample, $T = 3.8$ K. Curve *1* indicates the increasing temperature dependence of t_{max}, and curve *2* indicates the decreasing temperature dependence of t_{max}. References for ceramic samples investigated in other studies or by other authors are given in square brackets.

$$f_\omega = \frac{\int_0^{\pi/2} \alpha(\theta_3)\cos\theta_3 \sin\theta_3 d\theta_3}{\int_0^{\pi/2} \cos\theta_3 \sin\theta_3 d\theta_3}. \tag{2}$$

Here, the coefficient $\alpha(\theta_3)$ is written as

$$\alpha(\theta_3) = (Z_3/Z_1)|W|^2, \tag{3}$$

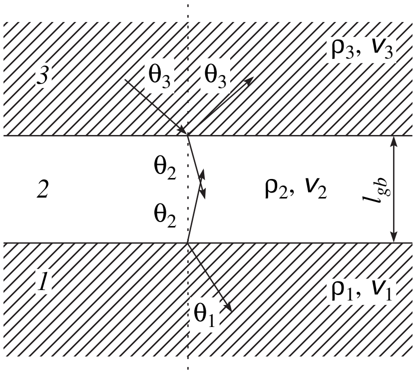

Fig. 4. The acoustic model of phonon transmission from grain to grain via plane boundary layer.

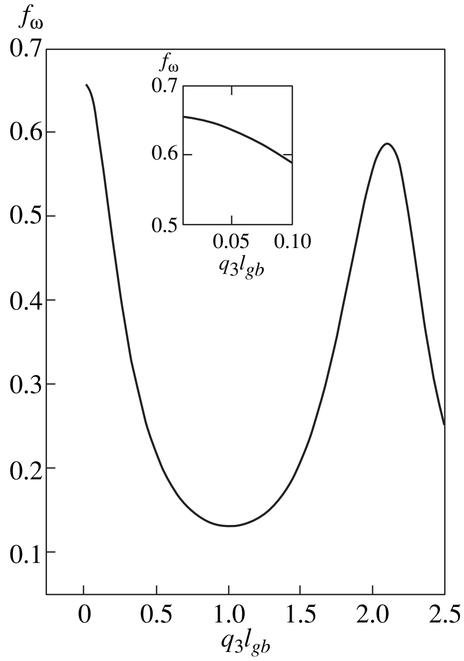

Fig. 5. Predicted curves of probability f_ω of the transmission of a phonon of frequency ω from grain *3* to grain *1* via boundary layer *2* of thickness l_{gb} as a function of the layer thickness q_3l_{gb}, where $q_3 = \omega/v_3$. The other parameters: $v_1/v_2 = 1.83$, $v_2/v_3 = 0.6$, $\rho_2v_2/\rho_1v_1 = 0.32$, $\rho_3v_3/\rho_2v_2 = 3.5$. Given in the inset is the value of f_ω for small values of q_3l_{gb}.

where $Z_i = \rho_iv_i/\cos\theta_i$ is the acoustic impedance of the medium, $i = 1, 2, 3$, and W is the coefficient of transparency of the boundary layer with respect to the wave amplitude [5], that is equal to

$$W = \frac{4Z_1Z_2}{(Z_1+Z_2)(Z_2+Z_3)} \times \frac{1}{\exp(-i\gamma_2l_{gb}) + V_{12}V_{23}\exp(i\gamma_2l_{gb})} \tag{4}$$

with the quantities V_{12} and V_{23} having the meaning of the coefficients of wave reflection at the boundaries of the medium 2, 1 and 3, 2, i.e.,

$$V_{12} = \frac{Z_1 - Z_2}{Z_1 + Z_2}, \quad V_{23} = \frac{Z_2 + Z_3}{Z_2 + Z_3}. \tag{5}$$

and with the wave number $\gamma_2 = q_2\cos\theta_2$ of wave propagation inside the boundary layer in the direction transverse to its boundaries, $q_2 = \omega/v_2$.

We used Eqs. (3)–(5) and preassigned the parameters of the structure shown in Fig. 4 to perform numerical integration (2) and obtain the dependence of the coefficient of transmission of phonon flux through the boundary between grains on the acoustic thickness of the boundary ql_{gb}. The calculation results are given in Fig. 5. For a thin (perfect) boundary between grains, $ql_{gb} \ll 1$ and $f_\omega \approx 0.7$ (see the inset in Fig. 5), the value of f_ω decreases as the frequency (or the phonon temperature) increases, and, therefore, the value of $t_{\max}$ increases. The absolute value of f_ω for this case agrees with our estimates based on the experimental curve *1* in Fig. 3 for $\Sigma/S \approx 1$.

In the case of a fairly thick boundary layer, $ql_{gb} \geq 1$, for the preassigned parameters of the layer $\rho_2/\rho_{1,3} \approx 0.6$ and $v_2/v_{1,3} \approx 0.6$, the transparency of the boundary to the phonon flux decreases, $f \approx 0.1$, and may exhibit an increasing temperature dependence, and, consequently, $t_{\max}$ will decrease as the temperature increases. The estimates based on the condition $ql_{gb} \approx 1$ give $l_{gb} \geq 5$ nm for the thickness of the intergrain layer, which appears to be a reasonable value.

The results given in Fig. 3 (curve *2*), i.e., for samples with a decreasing temperature dependence of $t_{\max}$, were used to estimate the value of $f_\omega\Sigma/S \approx 10^{-2}$.

For the model shown in Fig. 4 and for the boundary layer thickness $l_{gb} \geq 5$ nm, we have $f_\omega \approx 0.1$, and, consequently, $\Sigma/S \approx 10^{-1}$, i.e., the porosity or closed porosity in the region of the boundary between grains in such ceramics is high, and the contact between grains in the region of this layer is poor.

In conclusion, note that the method of propagation of nonequilibrium phonons in ceramic samples, employed by us, makes it possible to suggest a model of the boundary between grains in Al_2O_3 and ZrO_2 ceramics and in composites on their basis in the case of change of process conditions of preparation with a view to reducing the grain size (for example, in Al_2O_3 ceramic) to the nanolevel. Of course, the suggested model is not final, and its development calls for further studies.

ACKNOWLEDGMENTS

We are grateful to researchers from the Institute of Electrophysics of the Ural Division of the Russian Academy of Sciences Yu.A. Kotov for placing nanopowders at our disposal, and S.N. Paronin and V.R. Khrustov for assistance in synthesizing nanoceramics.

This study received financial support from the Russian Foundation for Basic Research (project 00-02-17426) and from the International Scientific-and-Technical Center (program no. 1030).

REFERENCES

1. R. W. Siegel, Nanostruct. Mater. **4**, 121 (1994).
2. A. I. Gusev, Usp. Fiz. Nauk **168**, 55 (1998) [Phys. Usp. **41**, 49 (1998)].
3. B. G. Adamenko, P. O. Pashkov, and L. N. Tambovtsev, Poroshk. Metall. **190**, 93 (1978).
4. V. V. Ivanov and V. R. Khrustov, Neorg. Mater. **34**, 495 (1998).
5. L. M. Brekhovskikh and O. A. Godin, *Acoustics in Continuous Media* (Nauka, Moscow, 1989).
6. S. N. Ivanov, A. G. Kozorezov, A. V. Taranov, and E. N. Khazanov, Zh. Éksp. Teor. Fiz. **102**, 600 (1992) [Sov. Phys. JETP **75**, 319 (1992)].
7. A. A. Kaplyanskiĭ, M. B. Mel’nikov, and S. P. Feofilov, Fiz. Tverd. Tela (St. Petersburg) **38**, 1434 (1996) [Phys. Solid State **38**, 792 (1996)].
8. J. E. Graebner and B. Golding, Phys. Rev. B **34**, 5788 (1986).
9. S. P. Feofilov, A. A. Kaplyanskii, A. B. Kulinkin, and R. I. Zakharchenya, Physica B (Amsterdam) **263–264**, 695 (1999).
10. S. N. Ivanov, E. N. Khazanov, W. Lojhowski, and L. M. Zhukova, Physica B (Amsterdam) **263–264**, 698 (1999).
11. M. P. Albada, B. A. Tiggelen, Ad Lagendijk, and A. Tip, Phys. Rev. Lett. **66**, 3132 (1991).
12. W. A. Little, Can. J. Phys. **37**, 334 (1959).

Translated by H. Bronstein

Journal of Experimental and Theoretical Physics, Vol. 92, No. 3, 2001, pp. 480–492.
Translated from Zhurnal Éksperimental'noĭ i Teoreticheskoĭ Fiziki, Vol. 119, No. 3, 2001, pp. 553–566.
Original Russian Text Copyright © 2001 by Kuchinskiĭ, Sadovskiĭ.

SOLIDS
Electronic Properties

Superconductivity in the Pseudogap State Induced by Short-Order Fluctuations

É. Z. Kuchinskiĭ* and M. V. Sadovskiĭ**
Institute of Electrophysics, Ural Division, Russian Academy of Sciences,
ul. Komsomol'skaya 34, Yekaterinburg, 620016 Russia
**e-mail: kuchinsk@iep.uran.ru*
***e-mail: sadovski@iep.uran.ru*

Received September 5, 2000

Abstract—Peculiarities of the superconducting state (s and d pairing) are considered in a simple model of the pseudogap state caused by short-range fluctuations (e.g., of the antiferromagnetic type), which is based on the model of a Fermi surface with "hot" regions. A system of Gor'kov recurrence equations is constructed taking into account all diagrams in perturbation theory in the electron interaction with short-range fluctuations. The superconducting transition temperature is determined, and the temperature variation of the energy gap depending on the pseudogap width and the correlation length of short-range fluctuations is analyzed. In a similar approximation, a microscopic derivation of the Ginzburg–Landau expansion is carried out, and the behavior of the main physical parameters of the superconductor near the transition temperature is studied depending on the pseudogap width as well as the correlation length of the fluctuations. The obtained results are in qualitative agreement with a number of experiments with underdoped HTSC cuprates. *© 2001 MAIK "Nauka/Interperiodica".*

1. INTRODUCTION

The pseudogap state observed in a wide region on the phase diagram for HTSC cuprates leads to numerous anomalies in their properties in the normal as well as superconducting states [1]. These anomalies can be explained using two basic theoretical scenarios. The first is based on the model of the formation of Cooper pairs even above the superconducting transition temperature [2–4], followed by the stabilization of their phase coherence at $T < T_c$. The second assumes that the origin of the pseudogap state is associated with fluctuations of the antiferromagnetic (AFM) short-range order existing in the region of underdoped compositions on the phase diagram [5–7]. A number of recent experimental results convincingly demonstrate the validity of the second scenario [8, 9].

Most of theoretical publications are devoted to an analysis of the models of the pseudogap state in the normal phase at $T > T_c$. We proposed [10, 11] a very simple exactly solvable model of the pseudogap, which is based on the concept of "hot" (planar) regions existing on the Fermi surface. In the framework of this model, the Ginzburg–Landau expansion was constructed for various types of Cooper pairing [10] and the peculiarities of the superconducting state in the range of $T < T_c$ [11], caused by short-range fluctuations of the AFM type, were analyzed. We used an extremely simplified model of Gaussian short-range fluctuations with an infinitely large correlation length, which allowed us to obtain the exact solution for the pseudogap state. In real systems, the correlation length of AFM fluctuations is finite and comparatively small [6]. The present work is mainly devoted to the generalization of the main results obtained by us earlier [10, 11] to the case of finite correlation lengths of the short-range AFM fluctuations and to the analysis of the main parameters of the superconducting state as functions of this correlation length and the effective width of the pseudogap.

2. MODEL OF THE PSEUDOGAP STATE

The simplified model of the pseudogap state [10, 11] under investigation is based on the pattern of well-developed fluctuations of the antiferromagnetic short-range order and is close to the model of "hot points" on the Fermi surface [6]. We assume that the Fermi surface of a 2D electronic system has the form depicted in Fig. 1. Such a Fermi surface was observed in a number of ARPES experiments on HTSC cuprates [12, 13]. It should be noted that the assumption concerning the existence of plane regions is not of fundamental importance for our model. However, it considerably simplified the calculations which could also be in principle made in a more realistic model of hot points. Such a model of the Fermi surface was applied long ago to HTSC cuprates by many authors [14–16] who thoroughly analyzed, among other things, the microscopic criteria for the existence of the antiferromagnetic and superconducting phases. We will be using a purely phenomenological model presuming the existence in a system of static Gaussian fluctuations of a short-range order with a correlation function (structural factor) of the form [5]

$$S(\mathbf{q}) = \frac{1}{\pi^2}\frac{\xi^{-1}}{(q_x - Q_x)^2 + \xi^{-2}}\frac{\xi^{-1}}{(q_y - Q_y)^2 + \xi^{-2}}, \qquad (1)$$

where ξ is the correlation length of the fluctuations, and the scattering vector is taken in the form $Q_x = \pm 2k_F$, $Q_y = 0$, or $Q_y = \pm 2k_F$, $Q_x = 0$, which envisages the presence of incommensurate fluctuations. The factorized form of correlator (1) introduced in [5] considerably simplifies the calculations and is virtually identical quantitatively to the conventional isotropic Lorentzian in the range $|\mathbf{q} - \mathbf{Q}| < \xi^{-1}$, which is the most important for our analysis [7].

The least physically justified assumption concerns the static form of fluctuations and can be used only at high temperatures [6, 7]. At low temperatures, including those corresponding to the superconducting phase, the spin dynamics may naturally turn out to be quite significant. This also applies to the microscopic theory of Cooper pairing in the model of a "nearly antiferromagnetic" Fermi liquid [17, 18]. However, we assume that the static approximation used here is sufficient for an analysis of the qualitative effect of pseudogap formation on the superconductivity, which will be described by using a purely phenomenological approach of the BCS theory.

We present the effective interaction of electrons with AFM fluctuations in the form

$$V_{\text{eff}} = (2\pi)^2 W^2 S(\mathbf{q}), \qquad (2)$$

where parameter W determines the energy scale (width) of the pseudogap. We assume that only the electrons belonging to planar (hot) regions on the Fermi surface interact with fluctuations, so that the value of W effectively differs from zero only for these electrons [10, 11]. We completely disregard the spin structure of the interaction, which could be easily taken into account [6], but this would make our calculations more cumbersome. In this sense, our analysis can be applied literally to a description of the interaction between short-range fluctuations and charge density waves rather than spin density waves. We also assume that this simplifying assumption is insignificant for an analysis of the qualitative effects of the pseudogap state on superconductivity that we are interested in.

The factorized form of correlator (1), and hence of the effective interaction (2), makes the scattering from fluctuations one-dimensional. In the limit of an infinitely large correlation length ($\xi \longrightarrow \infty$), the model of scattering from such fluctuations has an exact solution [10, 11, 19]. For a finite ξ, we can construct an "almost exact" solution [7] generalizing the one-dimensional approach proposed in [20]. In this case, the sum of the entire diagrammatic series for the one-particle Green's function for electrons from the planar regions on the Fermi surface (where the nesting condition $\xi_{\mathbf{p} \pm \mathbf{Q}} = -\xi_{\mathbf{p}}$ for the electron spectrum is satisfied) can be (approximately) determined.

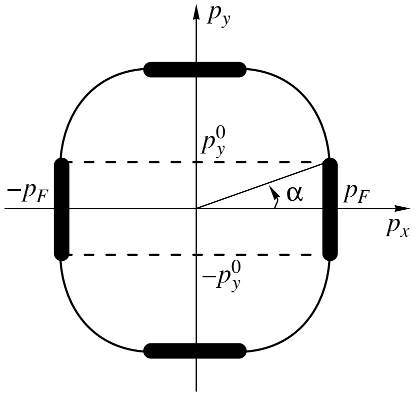

Fig. 1. Fermi surface of a two-dimensional system. Hot regions are shown by bold lines of thickness $\sim\xi^{-1}$.

For the contribution of an arbitrary diagram, we can write the following ansatz for the N-order eigenenergy component in the interaction (2) [7, 20]:

$$\begin{gathered} \Sigma^{(N)}(\varepsilon_n, \mathbf{p}) = W^{2N}\prod_{j=1}^{2N-1} G_{0k_j}(\varepsilon, \mathbf{p}), \\ G_{0k_j}(\varepsilon_n, \mathbf{p}) = \frac{1}{i\varepsilon_n - (-1)^j \xi_{\mathbf{p}} + ik_j\kappa}, \end{gathered} \qquad (3)$$

where $\kappa = v_F\xi^{-1}$ (v_F is the Fermi velocity), k_j is the number of interaction curves embracing the jth electron line in the diagram (starting from the origin), and $\varepsilon_n = 2\pi T(n + 1/2)$ (we assume for definiteness that $\varepsilon_n > 0$). Thus, the contribution of any diagram is actually determined only by the set of integers k_j. Any diagram with the intersection of the lines of interaction is identical to a certain diagram of the same order without intersection of interaction lines, and the contribution of all diagrams with intersections can be taken into account through the combinatorial factors $v(k_j)$ ascribed to interaction lines on diagrams without intersections [20, 7, 6]. In the model of incommensurate fluctuations under investigation, we have

$$v(k) = \begin{cases} \dfrac{k+1}{2} & \text{for odd} \quad k, \\ \dfrac{k}{2} & \text{for even} \quad k. \end{cases} \qquad (4)$$

As a result, we arrive at the following recurrence procedure (presentation in the form of a chain fraction) for

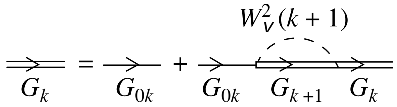

Fig. 2. Diagrammatic representation of the recurrence relation for a one-particle Green's function.

the one-particle Green's function $G(\varepsilon_n, \mathbf{p})$ for electrons from hot regions [20, 7, 6]:

$$G_k(\varepsilon_n, \mathbf{p}) = \frac{1}{i\varepsilon_n - (-1)^k\xi_{\mathbf{p}} + ik\kappa - W^2 v(k+1)G_{k+1}(\varepsilon_n\mathbf{p})}, \quad (5)$$
$$G(\varepsilon_n, \mathbf{p}) \equiv G_0(\varepsilon_n, \mathbf{p}).$$

The diagrammatic representation of this procedure is illustrated in Fig. 2.

Ansatz (3) for the contribution of an arbitrary N-order diagram is usually not exact [7, 21]. However, in the 2D case, we can indicate the topologies of the Fermi surface for which representation (3) is exact [7]. In the remaining cases, it can be proved [7] that this representation exaggerates (in a certain sense) the role of the finiteness of the correlation length ξ in the given order of perturbation theory. In the 1D case, when this problem is especially vital [7, 21], it turns out that the calculations of the density of states on the basis of approximation (3) for incommensurate fluctuations give a nearly perfect quantitative coincidence [22] with the results of the exact numerical simulation of this problem, which was carried out in [23, 24].[1] In the limit $\xi \longrightarrow \infty$, ansatz (3) can be reduced to the exact solution [19], while in the limit $\xi \longrightarrow 0$, it leads to a physically correct limit of free electrons for a fixed value of W.

Outside hot regions, electrons do not interact with fluctuations altogether in our model, and the Green's function remains free:

$$G(\varepsilon_n\mathbf{p}) = G_{00}(\varepsilon_n\mathbf{p}) = \frac{1}{i\varepsilon_n - \xi_{\mathbf{p}}}. \quad (6)$$

The model considered above leads to a non-Fermi-liquid (two-hump) behavior of the spectral density in hot regions on the Fermi surface and to a blurred pseudogap in the density of states (cf. similar results in the model of hot points [6, 7]). In cold regions of the Fermi surface, we observe the conventional Fermi-liquid behavior (free electrons).

3. GOR'KOV EQUATIONS FOR A SUPERCONDUCTOR WITH A PSEUDOGAP

In our previous publications [10, 11], we analyzed the peculiarities of the superconducting state in the exactly solvable model of the pseudogap state induced by short-range AFM fluctuations with an infinitely large correlation length ($\xi \longrightarrow \infty$). Among other things, it was proved [11] that AFM fluctuations may lead to strong fluctuations of the semiconducting order parameter (energy gap Δ), which violate the standard assumption concerning the self-averaging of the gap [25–27]. This assumption makes it possible to average (over the configurations of the random field of static short-range fluctuations) the order parameter Δ and various combinations of the electron Green's functions appearing in the basic equations of the theory. The conventional arguments in favor of such an independent averaging are usually formulated as follows [25, 27]. The value of Δ varies over characteristic scales of length of the order of the coherence length $\xi_0 \sim v_F/\Delta_0$ in the BCS theory, while Green's functions vary rapidly over much smaller scales of the order of atomic spacings. Naturally, the latter assumption becomes incorrect when a new characteristic length $\xi \longrightarrow \infty$ appears for the electronic subsystem. At the same time, if the antiferromagnetic correlation length $\xi \ll \xi_0$ (i.e., if AFM correlations correlate over distances smaller than the characteristic size of Cooper pairs), the assumption concerning the self-averaging of Δ must be preserved, being violated only in the region where $\xi > \xi_0$. For this reason, the subsequent analysis will be carried out assuming self-averaging of the energy gap of a superconductor over AFM fluctuations. This allows us to use the standard approach of the theory of disordered superconductors (mean-field approximation in the language of [11]). In this case, the interesting question concerning superconductivity in the absence of self-averaging of the order parameter is not considered. It should be noted that for real HTSC cuprates, we apparently always have $\xi \sim \xi_0$, so that these materials fall in the most complicated range of parameters of the theory.

Following [10, 11], we assume that the superconducting pairing is governed by the attraction potential of the following simplest form:

$$V(\mathbf{p}, \mathbf{p}') = V(\phi, \phi') = -Ve(\phi)e(\phi'), \quad (7)$$

where ϕ is the polar angle determining the direction of the electron momentum $\mathbf{p}$ in a plane, and for $e(\phi)$ we assume the following simplest model dependence:

$$e(\phi) = \begin{cases} 1 \quad (s\text{-pairing}), \\ \sqrt{2}\cos(2\phi) \quad (d\text{-pairing}). \end{cases} \quad (8)$$

As usual, the constant of attraction V is assumed to be other than zero in a certain layer of width $2\omega_c$ in the vicinity of the Fermi level (ω_c is the characteristic fre-

---

[1] In the case of a one-dimensional problem with commensurate fluctuations, ansatz (3) fails to describe only a weak Dyson singularity in the density of states near the center of the pseudogap [23, 24], also providing a quantitatively good approximation to the exact results beyond the pseudogap. Note that in the 2D case, the Dyson singularity in the density of states is just absent in all probability.

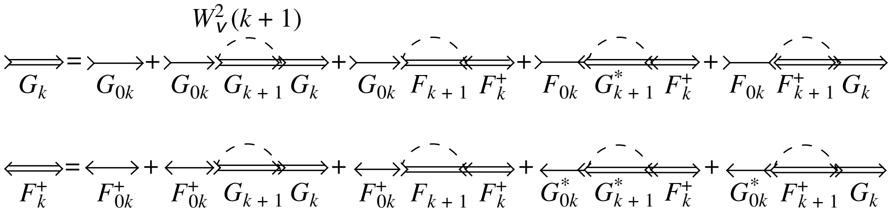

Fig. 3. Diagrammatic representation of the recurrence relation for Gor'kov's equations.

quency of quanta ensuring the attraction of electrons). In this case, the superconducting gap has the form

$$\Delta(\mathbf{p}) \equiv \Delta(\phi) = \Delta e(\phi). \tag{9}$$

In order to simplify the notation, we will henceforth assume that the gap Δ just stands for $\Delta(\phi)$ and will write explicitly the angular dependence only when required.

The perturbation theory in the interaction with AFM fluctuations (1) for the superconducting state must be constructed on "free" normal and anomalous Green's functions for the superconductor:

$$\begin{aligned} G_{00}(\varepsilon_n, \mathbf{p}) &= -\frac{i\varepsilon_n + \xi_{\mathbf{p}}}{\varepsilon_n^2 + \xi_{\mathbf{p}}^2 + |\Delta|^2}, \\ F_{00}^+(\varepsilon_n, \mathbf{p}) &= \frac{\Delta^*}{\varepsilon_n^2 + \xi_{\mathbf{p}}^2 + |\Delta|^2}. \end{aligned} \tag{10}$$

In the adopted model with planar regions on the Fermi surface, the electron spectrum in the regions orthogonal to the p_x axis has the form $\xi_{\mathbf{p}} = v_F(|p_x| - p_F)$ since the electron velocity $\mathbf{v}$ is perpendicular of the p_y axis (a symmetric situation is also observed in the regions orthogonal to p_y). Consequently, in the case of s-pairing, when the value of Δ is independent of the direction of the momentum, the problem becomes completely one-dimensional in the model with an interaction of form (1) and (2). In the case of d-pairing, the situation is more complicated since the value of $\Delta(\phi)$ depends on p_y even in the planar regions orthogonal to p_x (and, symmetrically, on the regions orthogonal to p_y). For this reason, it is convenient to analyze d-pairing by using instead of Eq. (1) the correlator of fluctuations in the form

$$\begin{aligned} S(\mathbf{q}) = \frac{1}{\pi}\Bigg\{ & \frac{\xi^{-1}}{(q_x \mp 2p_F)^2 + \xi^{-2}}\delta(q_y) \\ & + \frac{\xi^{-1}}{(q_y \mp 2p_F)^2 + \xi^{-2}}\delta(q_x)\Bigg\}. \end{aligned} \tag{11}$$

In this case, the interaction does not affect p_y and p_x in the planar regions orthogonal, respectively, to p_x and p_y, and the problem becomes completely one-dimensional again.

We can now formulate an analogue of approximation (3) for the superconducting state also. The details of the substantiation of the relations presented below are given in Appendix A. The contribution of an arbitrary N-order diagram in interaction (2) to the total normal or anomalous Green's function has the form of a product of $N + 1$ "free" normal G_{0k_j} and anomalous ($F^+_{0k_j}$) Green's functions with frequencies and gaps renormalized in a certain way (see below). Here k_j is the number of the interaction curves embracing the given jth electron line (starting from the origin of the diagram). As in the normal phase, the contribution of any diagram is determined by the set of integers k_j, and each diagram with the intersection of interaction curves is equivalent to a certain diagram of the same order without intersection of these curves. Consequently, we can again consider only diagrams without intersections of interaction curves, taking into account the contribution of the remaining diagrams through the same combinatorial factors $v(k)$ ascribed to the interaction curves as in the normal phase. As a result, we obtain a diagrammatic analogue of the Gor'kov equations [28] presented in Fig. 3. Accordingly, we have two coupled recurrence equations for the normal and anomalous Green's functions:

$$\begin{aligned} G_k &= G_{0k} + G_{0k}\tilde{G}G_k - G_{0k}\tilde{F}F_k^+ \\ &\quad - F_{0k}\tilde{G}^*F_k^+ - F_{0k}\tilde{F}^+G_k, \\ F_k^+ &= F_{0k}^+ + F_{0k}^+\tilde{G}G_k + -F_{0k}^+\tilde{F}F_k^+ \\ &\quad + G_{0k}^*\tilde{G}^*F_k^+ + G_{0k}^*\tilde{F}^+G_k, \end{aligned} \tag{12}$$

where

$$\tilde{G} = W^2 v(k+1)G_{k+1}, \quad \tilde{F}^+ = W^2 v(k+1)F_{k+1}^+, \tag{13}$$

$$\begin{aligned} G_{0k}(\varepsilon_n, \mathbf{p}) &= -\frac{i\varepsilon_n + (-1)^k\xi_{\mathbf{p}}}{\tilde{\varepsilon}_n^2 + \xi_{\mathbf{p}}^2 + |\tilde{\Delta}|^2}, \\ F_{0k}^+(\varepsilon_n, \mathbf{p}) &= \frac{\tilde{\Delta}^*}{\tilde{\varepsilon}_n^2 + \xi_{\mathbf{p}}^2 + |\tilde{\Delta}|^2}. \end{aligned} \tag{14}$$

and the renormalized frequency $\tilde{\varepsilon}$ and gap $\tilde{\Delta}$

$$\tilde{\varepsilon}_n = \eta_k\varepsilon_n, \quad \tilde{\Delta} = \eta_k\Delta, \quad \eta_k = 1 + \frac{k\kappa}{\sqrt{\varepsilon_n^2 + |\Delta|^2}} \tag{15}$$

have been introduced in analogy with the case of superconductors with impurities [28].

Equations (12)–(15) can easily be used to derive a system of recurrence relations directly for the real and imaginary components of the normal Green's function and for the anomalous Green's function:

$$\mathrm{Im}G_k = \frac{\tilde{\varepsilon} - \mathrm{Im}\tilde{G}}{(\tilde{\varepsilon} - \mathrm{Im}\tilde{G})^2 + ((-1)^k\xi_{\mathbf{p}} + \mathrm{Re}\tilde{G})^2 + |\tilde{\Delta} + \tilde{F}|^2},$$

$$\mathrm{Re}G_k = \frac{(-1)^k\xi_{\mathbf{p}} + \mathrm{Re}\tilde{G}}{(\tilde{\varepsilon} - \mathrm{Im}\tilde{G})^2 + ((-1)^k\xi_{\mathbf{p}} + \mathrm{Re}\tilde{G})^2 + |\tilde{\Delta} + \tilde{F}|^2}, \tag{16}$$

$$F_k^+ = \frac{\tilde{\Delta}^* + \tilde{F}^+}{(\tilde{\varepsilon} - \mathrm{Im}\tilde{G})^2 + ((-1)^k\xi_{\mathbf{p}} + \mathrm{Re}\tilde{G})^2 + |\tilde{\Delta} + \tilde{F}|^2}.$$

Let us introduce the following notation:

$$\mathrm{Im}G_k = -\varepsilon_n J_k, \quad \mathrm{Re}G_k = -(-1)^k\xi_{\mathbf{p}}R_k, \quad F_k^+ = \Delta^* f_k. \tag{17}$$

It turns out that the recurrence relations for J_k and f_k are completely identical in this case so that $J_k = f_k$. Finally, we arrive at the following system of recurrence relations for J_k and R_k:

$$\begin{aligned} J_k &= [\eta_k + W^2 v(k+1)J_{k+1}] \\ &\times [(\varepsilon_n^2 + \Delta^2)^{1/2}(\eta_k + W^2 v(k+1)J_{k+1})^2 \\ &+ \xi_{\mathbf{p}}^2(1 + W^2 v(k+1)R_{k+1})^2]^{-1}, \\ R_k &= [1 + W^2 v(k+1)R_{k+1}] \\ &\times [(\varepsilon_n^2 + \Delta^2)^{1/2}(\eta_k + W^2 v(k+1)J_{k+1})^2 \\ &+ \xi_{\mathbf{p}}^2(1 + W^2 v(k+1)R_{k+1})^2]^{-1}. \end{aligned} \tag{18}$$

The normal and anomalous Green's functions for the superconductor we are interested in can be defined in terms of R_0 and J_0,

$$\mathrm{Im}G = -\varepsilon_n J_0, \quad \mathrm{Re}G = -\xi_{\mathbf{p}}R_0, \quad F^+ = \Delta^* J_0, \tag{19}$$

and have the form of a totally summed series in the perturbation theory in the interaction of an electron with short-range antiferromagnetic fluctuations in the semiconductor.

4. SUPERCONDUCTING TRANSITION TEMPERATURE AND THE TEMPERATURE DEPENDENCE OF THE GAP

The energy gap in a superconductor is defined by the equation

$$\Delta(\mathbf{p}) = -T\sum_{\mathbf{p}'}\sum_{\varepsilon_n} V_{sc}(\mathbf{p}, \mathbf{p}')F(\varepsilon_n, \mathbf{p}'). \tag{20}$$

The anomalous Green's function on planar regions of the Fermi surface can be determined from Eqs. (19) by using the recurrence procedure (18). In our model, the scattering from AFM fluctuations on the remaining (cold) part of the Fermi surface is absent, and the anomalous Green's function has the same form as in Eqs. (10). As a result, Eq. (20) for *s*-pairing taking into account dependence (8) assumes the form

$$1 = \lambda\left\{\tilde{\alpha}T\sum_{\varepsilon_n}\int_{-\omega_c}^{\omega_c} d\xi J_0(\varepsilon_n\xi) + (1 - \tilde{\alpha})\int_0^{\omega_c} d\xi \frac{\tanh\frac{\sqrt{\xi^2 + \Delta^2}}{2T}}{\sqrt{\xi^2 + \Delta^2}}\right\}, \tag{21}$$

where $\lambda = VN_0(0)$ is the dimensionless constant of the pairing interaction ($N_0(0)$ is the density of states for free electrons at the Fermi level) and $\tilde{\alpha} = 4\alpha/\pi$, where α is the angular dimension of a planar region on the Fermi surface (see Fig. 1). In our further numerical calculations, we will assume (quite arbitrarily) that $\tilde{\alpha} = 2/3$, i.e., $\alpha = \pi/6$, which is close, for example, to the results obtained in [12].

In the case of *d*-pairing, we must take into account the angular dependence of gap (9), and Eq. (20) assumes the form

$$1 = \lambda\frac{4}{\pi}\left\{T\int_0^{\alpha} d\phi e^2(\phi)\sum_{\varepsilon_n}\int_{-\omega_c}^{\omega_c} d\xi J_0(\varepsilon_n\xi) + \int_{\alpha}^{\pi/4} d\phi e^2(\phi)\int_0^{\omega_c} d\xi \frac{\tanh\frac{\sqrt{\xi^2 + \Delta^2 e^2(\phi)}}{2T}}{\sqrt{\xi^2 + \Delta^2 e^2(\phi)}}\right\}. \tag{22}$$

Figure 4 shows the temperature dependences of the gap width calculated from Eq. (21) in the case of *s*-pairing for various values of correlation length (parameter $\kappa = v_F\xi^{-1}$) of the fluctuations. In the case of *d*-pairing, the corresponding qualitative dependences are quite similar.

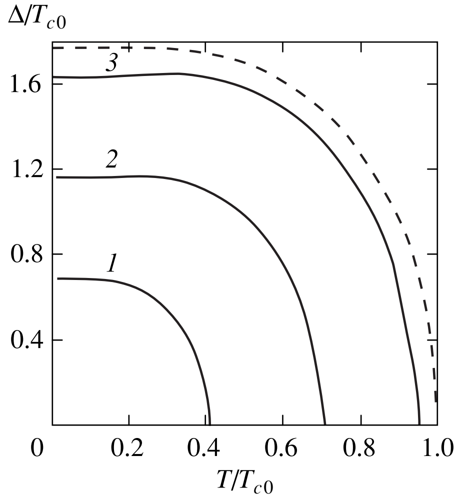

Fig. 4. Temperature dependence of the superconducting gap width in the case of *s*-pairing for various values of correlation length (parameter $\kappa = v_F\xi^{-1}$) for AFM fluctuations, calculated for $\lambda = 0.4$, $\omega_c/W = 3$, $\kappa/W = 0$ (*1*), 1.0 (*2*), and 10.0 (*3*). The dashed curve describes $\Delta(T)$ in the absence of a pseudogap.

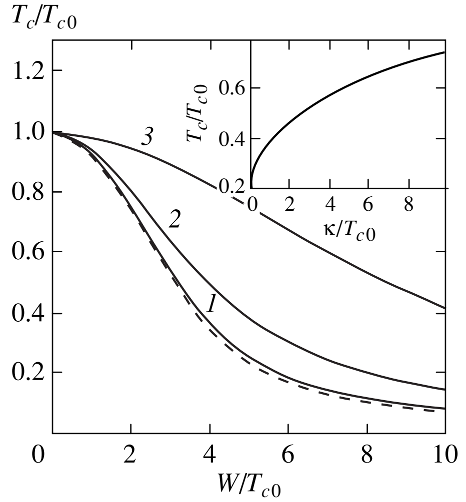

Fig. 5. Dependence of the superconducting transition temperature on the pseudogap width W and the correlation length (parameter $\kappa = v_F\xi^{-1}$) for AFM fluctuations: κ/W = 0.1 (*1*), 1.0 (*2*), and 10.0 (*3*). The dashed curve corresponds to $\kappa = 0$ [10]. The inset shows the dependence of T_c on κ for $W/T_{c0} = 5$.

The equation for the superconducting transition temperature T_c follows directly from Eqs. (21) and (22) for $\Delta \longrightarrow 0$. In this case, $J_0(\Delta \longrightarrow 0)$ is independent of ϕ and is the same for *s*- and *d*-pairing. Accordingly, the equation for T_c has the form

$$1 = \lambda\left\{\alpha_{\rm eff}T_c\sum_{\varepsilon_n}\int\limits_{-\omega_c}^{\omega_c}d\xi J_0(\varepsilon_n\xi;\Delta\longrightarrow 0) + (1-\alpha_{\rm eff})\int\limits_0^{\omega_c}d\xi\frac{\tanh\xi/(2T_c)}{\xi}\right\}, \qquad (23)$$

where the "effective" fraction of planar regions on the Fermi surface is defined as

$$\alpha_{\rm eff} = \begin{cases}\tilde{\alpha} & (s\text{-pairing}),\\ \tilde{\alpha} + \dfrac{1}{\pi}\sin(\pi\tilde{\alpha}) & (d\text{-pairing}).\end{cases} \qquad (24)$$

The theoretical dependence of T_c on the pseudogap width W and correlation length (parameter $\kappa = v_F\xi^{-1}$) are shown in Fig. 5 (T_{c0} is the superconducting transition temperature in the absence of a pseudogap).

The general qualitative conclusion is the same as in [10, 11]: the pseudogap suppresses superconductivity due to a partial "dielectrization" of the electron spectrum in hot regions on the Fermi surface. The suppression effect is the strongest for $\kappa = 0$ (infinitely large correlation length of AFM fluctuations) [10, 11] and decreases with the correlation length, which is quite in accordance with the experimental phase diagram of HTSC systems.

It should be emphasized once again that all the results described above are valid under the assumption of the self-averaging of the superconducting order parameter (gap) in AFM fluctuations (mean-field approximation [11]), which holds for not very large values of the correlation length $\xi < \xi_0$, where ξ_0 is the coherence length for the superconductor (the size of Cooper pairs at $T = 0$). For $\xi \gg \xi_0$, considerable non-self-averaging effects appear, which are manifested in the emergence of characteristic "tails" on the temperature dependence of the averaged gap in the temperature range $T_c < T < T_{c0}$ [11].

5. COOPER INSTABILITY. RECURRENCE PROCEDURE FOR THE VERTEX PART

It is well known that the superconducting transition temperature can also be determined in a different way, namely, from the equation for the Cooper instability of the normal phase:

$$1 - V\chi(0, 0) = 0, \qquad (25)$$

where the generalized Cooper susceptibility is described by the graph in Fig. 6. In this case, we are dealing with the problem of calculation of the "triangular" vertex component taking into account the interaction with AFM fluctuations. For the one-dimensional analogue of our problem (and for real frequencies, $T = 0$), the corresponding recurrence procedure was formulated in [29]. For the 2D model considered by us

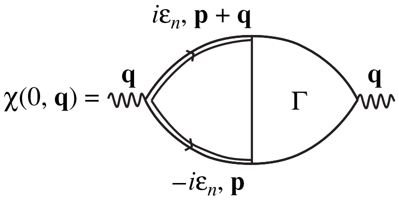

Fig. 6. Diagram for the generalized Cooper susceptibility.

here, this procedure was used for calculating the optical conductivity [30]. The procedure can easily be generalized to the case of Matsubara frequencies. Henceforth, we will assume for definiteness that $\varepsilon_n > 0$. This gives

$$\Gamma_{k-1}(\varepsilon_n, -\varepsilon_n, \mathbf{q}) = 1 + W^2 v(k) G_k \bar{G}_k$$
$$\times \left\{1 + \frac{2ik\kappa}{2i\varepsilon_n - (-1)^k v_F q - W^2 v(k+1)(G_{k+1} - \bar{G}_{k+1})}\right\}$$
$$\times \Gamma_k(\varepsilon_n, -\varepsilon_n, \mathbf{q}), \qquad (26)$$
$$\Gamma(\varepsilon_n, -\varepsilon_n, \mathbf{q}) \equiv \Gamma_0(\varepsilon_n, -\varepsilon_n, \mathbf{q}),$$

where $G_k = G_k(\varepsilon_n, \mathbf{p}+\mathbf{q})$ and $\bar{G}_k = G_k(-\varepsilon_n, \mathbf{p})$ are calculated in accordance with relations (5).

In order to find T_c, we consider the vortex where $\mathbf{q} = 0$. In this case, $\bar{G}_k = G_k^*$, and the vertices Γ_k become real-valued, which considerably simplifies procedure (26). Using a notation similar to (17), we obtain from relations (5) and (26)

$$\Gamma_{k-1} = 1 + W^2 v(k) \frac{J_k}{1 + W^2 v(k+1) J_{k+1}} \Gamma_k, \qquad (27)$$

while for R_k and J_k we have recurrence relations coinciding with Eqs. (18) for $\Delta = 0$.

The following exact relation (which will be proved below) of the type of the Word identity holds:

$$G(\varepsilon_n, \mathbf{p}) G(-\varepsilon_n, \mathbf{p}) \Gamma(\varepsilon_n, -\varepsilon_n, 0)$$
$$= (\xi_{\mathbf{p}}^2 R_0^2(\varepsilon_n, \xi_{\mathbf{p}}) + \varepsilon_n^2 J_0(\varepsilon_n, \xi_{\mathbf{p}})) \qquad (28)$$
$$\times \Gamma_0(\varepsilon_n, -\varepsilon_n, 0) \equiv J_0(\varepsilon_n, \xi_{\mathbf{p}}) = -\frac{1}{\varepsilon_n}(\varepsilon_n, \mathbf{p}).$$

A numerical analysis completely confirms the validity of this relation, demonstrating complete matching between the recurrence procedures for the one-particle Green's function and for the vertex component.[2] Since $J_0(\Delta \longrightarrow 0)$ coincides with J_0 in the normal phase, relation (28) just leads to the coincidence of the equation for T_c obtained from the Cooper instability condition (25),

$$1 = \lambda \left\{ \alpha_{\text{eff}} T_c \sum_{\varepsilon_n} \int_{-\omega_c}^{\omega_c} d\xi (\xi_{\mathbf{p}}^2 R_0^2(\varepsilon_n, \xi_{\mathbf{p}}) + \varepsilon_n^2 J_0(\varepsilon_n, \xi_{\mathbf{p}})) \right. \qquad (29)$$
$$\left. \times \Gamma_0(\varepsilon_n, -\varepsilon_n, 0) + (1 - \alpha_{\text{eff}}) \int_0^{\omega_c} d\xi \frac{\tanh(\xi/2T_c)}{\xi} \right\}$$

and Eq. (23) obtained as a result of the linearization of the equation for the gap in spite of the apparently different recurrence procedures used for their derivation and taking into account AFM fluctuations.

6. THE GINZBURG–LANDAU EXPANSION

The Ginzburg–Landau expansion in the exactly solvable model of a pseudogap with an infinitely large correlation length of AFM fluctuations was constructed in [10]. Here, we will generalize these results to the case of finite correlation lengths.

We write the Ginzburg–Landau expansion for the difference in the free energy densities of the superconducting and normal states in the standard form

$$F_s - F_n = A|\Delta_{\mathbf{q}}|^2 + q^2 C |\Delta_{\mathbf{q}}|^2 + \frac{B}{2}|\Delta_{\mathbf{q}}|^4, \qquad (30)$$

where $\Delta_{\mathbf{q}}$ is the amplitude of the Fourier component of the order parameter:

$$\Delta(\phi, \mathbf{q}) = \Delta_q e(\phi). \qquad (31)$$

Expansion (30) is determined by the graphs of the loop-type expansion for the free energy in the field of order parameter fluctuations with a small wave vector $\mathbf{q}$ [10].

We present the Ginzburg–Landau coefficients in the form

$$A = A_0 K_A, \quad C = C_0 K_C, \quad B = B_0 K_B, \qquad (32)$$

where A_0, C_0, and B_0 denote the standard expressions for these coefficients in the case of an isotropic s-pairing:

$$A_0 = N_0(0)\frac{T - T_c}{T_c}, \quad C_0 = N_0(0)\frac{7\zeta(3)}{32\pi^2}\frac{v_F^2}{T_c^2}, \qquad (33)$$
$$B_0 = N_0(0)\frac{7\zeta(3)}{8\pi^2 T_c^2}.$$

In this case, all the peculiarities of the model under investigation, which are associated with the emergence of a pseudogap, are contained in the dimensionless coefficients K_A, K_C, and K_B. In the absence of a pseudogap, all these coefficients are equal to unity ($K_B = 3/2$ only in the case of d-pairing). For this reason, we will normalize coefficient K_B for d-pairing to this value, presenting the numerical results for $\tilde{K}_B = (2/3)K_B$.

---

[2] Note that an analytic proof of this relation through a direct comparison of the recurrence procedures themselves for the Green's function and the vertex component is not at all obvious.

Let us consider the generalized Cooper susceptibility (Fig. 6)

$$\chi(\mathbf{q}, 0; T) = -T\sum_{\varepsilon_n}\sum_{\mathbf{p}} G(\varepsilon_n, \mathbf{p}+\mathbf{q}) \times G(-\varepsilon_n, \mathbf{p})e^2(\phi)\Gamma(\varepsilon_n, -\varepsilon_n, \mathbf{q}). \tag{34}$$

Using relations (28), we can easily write coefficients K_A and K_C in the form

$$K_A = \frac{\chi(\mathbf{q}, 0; T) - \chi(0, 0; T_c)}{A_0} = \alpha_{\text{eff}}\frac{T_c}{T - T_c} \times\left\{T\sum_{\varepsilon_n = \pi T(2n+1)}\int_{-\omega_c}^{\omega_c} d\xi J_0(\varepsilon_n, \xi) - T_c\sum_{\varepsilon = \pi T_c(2n+1)}\int_{-\omega_c}^{\omega_c} d\xi J_0(\varepsilon_n, \xi)\right\} + 1 - \alpha_{\text{eff}}, \tag{35}$$

$$K_C = \lim_{q\to 0}\frac{\chi(\mathbf{q}, 0; T) - \chi(0, 0; T_c)}{q^2 C_0} = \frac{32\pi^2 T_c^3}{7\zeta(3)v_F q^2} = \alpha_{\text{eff}}\left\{\sum_{\varepsilon_n = \pi T(2n+1)}\int_{-\omega_c}^{\omega_c} d\xi J_0(\varepsilon_n, \xi) - \sum_{\varepsilon = \pi T_c(2n+1)}\int_{-\omega_c} d\xi G\left(\varepsilon_n, \xi + \frac{1}{2}v_F q\right) \times\Gamma(\varepsilon_n, -\varepsilon_n, q)G\left(-\varepsilon_n, \xi - \frac{1}{2}v_F q\right)\right\} + 1 - \alpha_{\text{eff}}. \tag{36}$$

The situation with coefficient B in the general case is much more complicated. Considerable simplifications can be made by confining the analysis to the case of $q = 0$ in the order $|\Delta_q|^4$, as is usually done in actual practice. Then coefficient B can be determined directly from the anomalous Green's function F for which we already have the recurrence procedure (18) and (19). Indeed, let us consider the diagrammatic series for the anomalous Green's function presented in Fig. 7a. It can easily be seen that

$$\lim_{\Delta\to 0}\frac{F(\varepsilon_n, \mathbf{p})}{\Delta} = G(\varepsilon_n, \mathbf{p})G(-\varepsilon_n, \mathbf{p}) + \dots = G(\varepsilon_n, \mathbf{p})G(-\varepsilon_n, \mathbf{p})\Gamma(\varepsilon_n, -\varepsilon_n, 0), \tag{37}$$

which, by the way, immediately proves relation (28) taking into account Eqs. (19). Consequently, for the

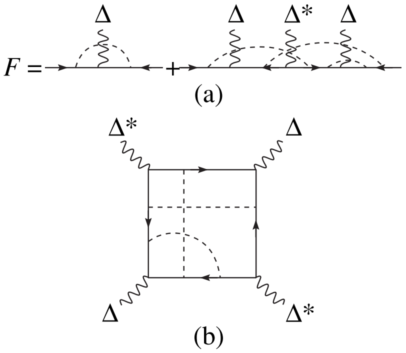

Fig. 7. (a) Diagrammatic series for the anomalous Green's function; dashed curves correspond to AFM fluctuations; (b) diagram defining coefficient K_B.

bipartite loop $\chi(0, 0)$, we have

$$\chi(0, 0) = T\sum_{\mathbf{p}}\sum_{\varepsilon_n}\lim_{\Delta\to 0}\frac{F(\varepsilon_n, \mathbf{p})}{\Delta} = T\sum_{\mathbf{p}}\sum_{\varepsilon_n} J_0(\Delta = 0). \tag{38}$$

For the "four-tail" diagram in Fig. 7b defining coefficient B, we similarly obtain

$$-T\sum_{\mathbf{p}}\sum_{\varepsilon_n}\lim_{\Delta\to 0}\frac{F(\varepsilon_n, \mathbf{p})/\Delta - \lim\limits_{\Delta\to 0} F(\varepsilon_n\mathbf{p})/\Delta}{|\Delta|^2} = -T\sum_{\mathbf{p}}\sum_{\varepsilon_n}\lim_{\Delta\to 0}\frac{J_0(\Delta) - J_0(\Delta = 0)}{|\Delta|^2}, \tag{39}$$

where $J_0(\Delta)$ is determined through the recurrence procedure (18). As a result, for the dimensionless coefficient K_B, we have

$$K_B = \alpha_B\frac{8\pi^2 T_c^3}{7\zeta(3)} \times\sum_{-\omega_c}^{\omega_c} d\xi\lim_{\Delta\to 0}\frac{J_0(\Delta = 0) - J_0(\Delta)}{|\Delta|^2} + 1 - \alpha_B, \tag{40}$$

where

$$\alpha_B = \begin{cases}\tilde{\alpha} \quad (s\text{-pairing}),\\ \tilde{\alpha} + \dfrac{4}{3\pi}\sin\pi\tilde{\alpha} + \dfrac{1}{6\pi}\sin 2\pi\tilde{\alpha} \quad (d\text{-pairing}).\end{cases} \tag{41}$$

The obtained relations allow us to carry out direct numerical calculations of the coefficients K_A, K_C, and K_B. Figure 8 shows, by way of an example, the calculated dependence of K_C on the pseudogap width W and on the correlation length of AFM fluctuations (parameter $\kappa = v_F\xi^{-1}$). The corresponding dependences for K_A and K_B are qualitatively similar. In particular, for $\kappa = 0$, we just have $K_B = K_C$ [10].

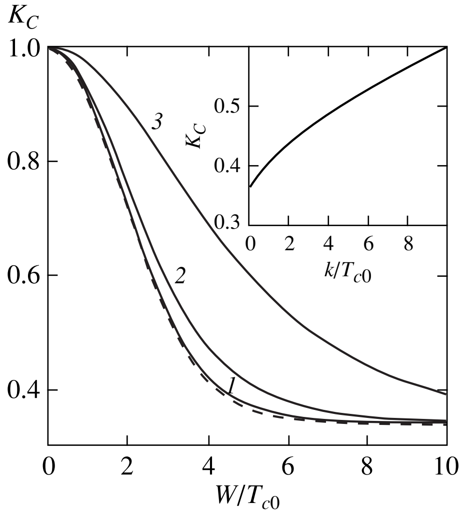

Fig. 8. Dependence of coefficient K_C on the pseudogap width W and the correlation length (parameter $\kappa = v_F\xi^{-1}$) for AFM fluctuations: $\kappa/W = 0.1$ (*1*), 1.0 (*2*), and 10.0 (*3*). The dashed curve corresponds to $\kappa = 0$ [10]. The inset shows the dependence of K_C on κ for $W/T_{c0} = 5$.

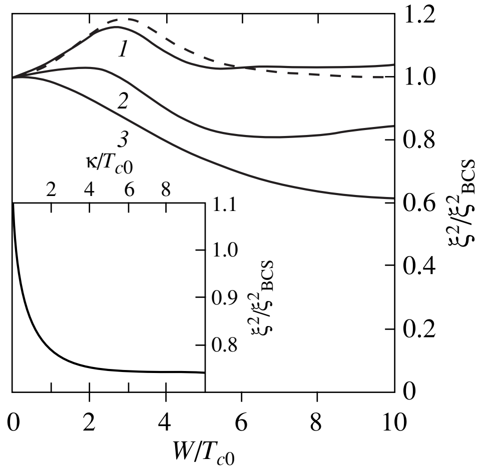

Fig. 9. Dependence of the coherence length on the pseudogap width W and the correlation length (parameter $\kappa = v_F\xi^{-1}$) for AFM fluctuations: $\kappa/W = 0.1$ (*1*), 1.0 (*2*), and 10.0 (*3*). The dashed curve corresponds to $\kappa = 0$ [10]. The inset shows the dependence of the coherence length on κ for $W/T_{c0} = 5$.

7. PHYSICAL PARAMETERS OF SUPERCONDUCTORS WITH A PSEUDOGAP

The Ginzburg–Landau equations define two characteristic lengths for superconductors: the coherence length and the magnetic field penetration depth.

The coherence length $\xi(T)$ at a given temperature determines the characteristic scale of inhomogeneities in the order parameter Δ:

$$\xi^2(T) = -C/A. \tag{42}$$

In the absence of a pseudogap, we have

$$\xi^2_{\rm BCS}(T) = -C_0/A_0, \tag{43}$$

$$\xi_{\rm BCS}(T) \approx 0.74\xi_0/\sqrt{1-T/T_c}, \tag{44}$$

where $\xi_0 = 0.18v_F/T_c$. In the model under investigation, we can write

$$\xi^2(T)/\xi^2_{\rm BCS}(T) = K_C/K_A. \tag{45}$$

The corresponding dependences of $\xi^2(T)/\xi^2_{\rm BCS}(T)$ on the pseudogap width W and on the correlation length of fluctuations (parameter κ) in the case of d-pairing are presented in Fig. 9. Note that the coherence length varies insignificantly.

For the magnetic field penetration depth in a superconductor without a pseudogap, we have

$$\lambda_{\rm BCS}(T) = \frac{1}{\sqrt{2}}\frac{\lambda_0}{\sqrt{1-T/T_c}}, \tag{46}$$

where $\lambda_0^2 = mc^2/4\pi ne^2$ defines the penetration depth at $T = 0$. In the general case, we have

$$\lambda^2(T) = -\frac{c^2}{32\pi e^2}\frac{B}{AC}. \tag{47}$$

Then, in the model under investigation, we can write

$$\frac{\lambda(T)}{\lambda_{\rm BCS}(T)} = \left(\frac{K_B}{K_A K_C}\right)^{1/2}. \tag{48}$$

The dependences of these quantity in the case of d-pairing are presented graphically in Fig. 10.

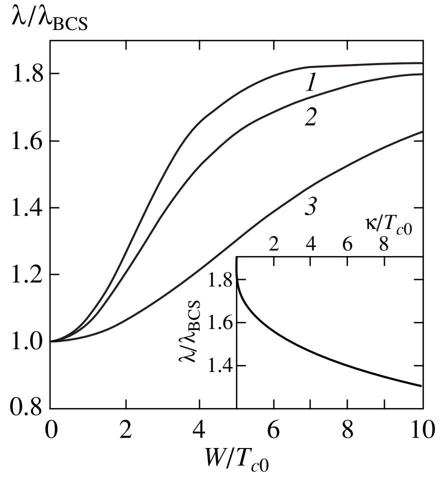

Fig. 10. Dependence of the penetration depth on the pseudogap width W and the correlation length (parameter $\kappa = v_F\xi^{-1}$) for AFM fluctuations: $\kappa/W = 0.1$ (*1*), 1.0 (*2*), and 10.0 (*3*). The inset shows the dependence of the penetration depth on κ for $W/T_{c0} = 5$.

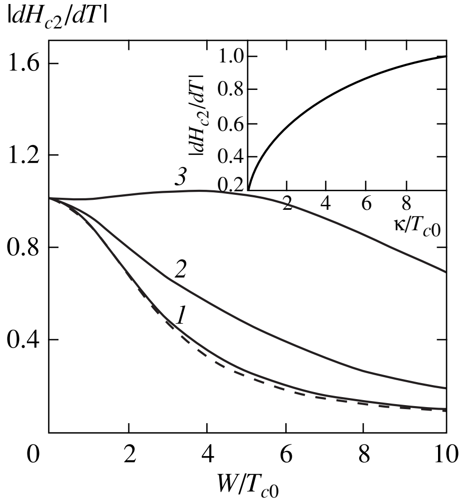

Fig. 11. Dependence of the slope of the upper critical field on the pseudogap width and on the correlation length (parameter $\kappa = v_F\xi^{-1}$) for AFM fluctuations: $\kappa/W = 0.1$ (*1*), 1.0 (*2*), and 10.0 (*3*). The dashed curve corresponds to $\kappa = 0$ [10]. The inset shows the dependence of the slope of H_{c2} on κ for $W/T_{c0} = 5$.

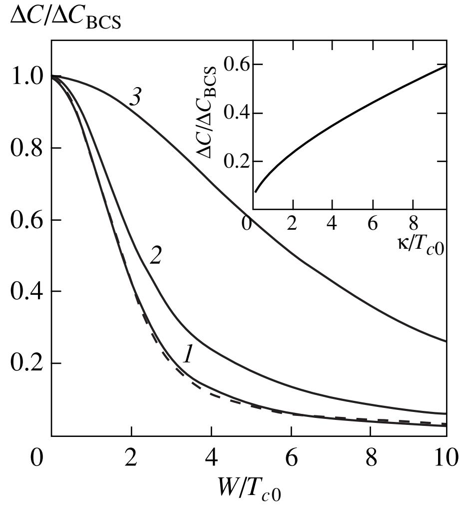

Fig. 12. Dependence of the heat capacity on the pseudogap width and jump on the correlation length (parameter $\kappa = v_F\xi^{-1}$) for AFM fluctuations: $\kappa/W = 0.1$ (*1*), 1.0 (*2*), and 10.0 (*3*). The dashed curve corresponds to $\kappa = 0$ [10]. The inset shows the dependence of the heat capacity jump on κ for $W/T_{c0} = 5$.

In the vicinity of T_c, the upper critical field H_{c2} can be expressed in terms of the Landau–Ginzburg coefficients:

$$H_{c2} = \frac{\phi_0}{2\pi\xi^2(T)} = -\frac{\phi_0}{2\pi}\frac{A}{C}, \tag{49}$$

where $\phi_0 = c\pi/e$ is the magnetic flux quantum. In this case, the slope of the curve describing the upper critical field in the vicinity of T_c is given by

$$\left|\frac{dH_{c2}}{dT}\right|_{T_c} = \frac{24\pi\phi_0}{7\zeta(3)v_F^2}T_c\frac{K_A}{K_C}. \tag{50}$$

Figure 11 shows graphically the derivative $|dH_{c2}/dT|_{T_c}$ normalized to the derivative at temperature T_{c0} as a function of the effective width W of the pseudogap and the correlation parameter κ in the case of *d*-pairing. It can be seen that for large correlation lengths, the derivative of the field decreases rapidly with increasing pseudogap width. However, for small correlation lengths, this parameter can slightly increase for small values of the pseudogap width. For a fixed pseudogap width, the function dH_{c2}/dT increases noticeably for a decreasing correlation length of fluctuations.

Finally, let us consider the heat capacity jump at the transition point:

$$\frac{C_s - C_n}{\Omega} = \frac{T_c}{B}\left(\frac{A}{T - T_c}\right)^2, \tag{51}$$

where C_s and C_n are the heat capacities of the superconducting and normal states and Ω is the sample volume. At temperature T_{c0} (in the absence of a pseudogap, $W = 0$), we have

$$\left(\frac{C_s - C_n}{\Omega}\right)_{T_{c0}} = N(0)\frac{8\pi^2 T_{c0}}{7\zeta(3)}. \tag{52}$$

The relative jump in the heat capacity in the model under investigation can be written as

$$\frac{(C_s - C_n)_{T_c}}{(C_s - C_n)_{T_{c0}}} = \frac{T_c}{T_{c0}}\frac{K_A^2}{K_B}. \tag{53}$$

The corresponding dependences on the effective pseudogap width W and the correlation length parameter κ in the case of *d*-pairing are presented in Fig. 12. It can be seen that the heat capacity jump decreases rapidly with increasing pseudogap width and, on the contrary, increases upon a decrease in the correlation length of AFM fluctuations.

For superconductors with *s*-pairing, the dependences of the physical quantities considered above are basically quite similar. The only difference is a larger scale of W for which the corresponding changes take place. This corresponds to a higher stability of isotropic superconductors to a partial dielectrization of the electron spectrum due to the formation of a pseudogap in hot regions on the Fermi surface [10, 11].

From the physical parameters of a superconductor, detailed experimental data have been obtained for heat capacity jump [8]. In complete qualitative agreement with our conclusions, the heat capacity jump for the Bi-2212 system decreases rapidly upon a transition to the range of underdoped compositions for which the pseudogap width increases. According to the results obtained by Tallon and Loram [8], the pseudogap width (parameter $2W$ in our case) varies from a value of the order of 700 K for the hole concentration $p = 0.05$ to a value of the order of $T_c \sim 100$ K in the vicinity of the optimal concentration $p = 0.16$, vanishing for $p = 0.19$. In this case, a clearly manifested correlation between the decrease in the heat capacity jump and the increase in the effective pseudogap width is observed. Unfortunately, we are not aware of detailed results on the concentration dependence of correlation length of fluctuations and, accordingly, of the corresponding dependences of physical parameters of a superconductor. Qualitatively, the correlation length increases as we go over to the range of underdoped compositions, so that the effect of a decrease in the heat capacity jump is quite justified from this point of view.

8. CONCLUSION

In this work, we continue our study of the peculiarities of the superconducting state on the basis of a rather rough model of the pseudogap state of a two-dimensional electronic system [10, 11], which nevertheless is in qualitative agreement with a number of observed singularities in the electronic structure of underdoped HTSC cuprates. In our earlier publications [10, 11], we considered a nonrealistic limit of an infinitely large correlation length of fluctuations with the short-range antiferromagnetic order, which, however, allowed us to find the exact analytic solution of the problem. Here, we have carried out a generalization to the realistic case of finite correlation lengths, which takes into account all the diagrams of perturbation theory in the interaction of electrons with short-range fluctuations in the same way as in [10, 11]. The analysis was carried out using the standard (mean-field in terms of [11]) approach based on the assumption of the self-averaging of the superconducting order parameter in the fluctuations of the random field induced by AFM fluctuations. It was proved in [11] that this assumption is not substantiated in the limit $\xi \longrightarrow \infty$. At the same time, it is undoubtedly valid for $\xi \ll \xi_0$ (where ξ_0 is the coherence length of the superconductor at $T = 0$, i.e., the size of Cooper pairs). Thus, it remains for us to solve the extremely complicated problem of taking into account the non-self-averaging effects for $\xi > \xi_0$. It was mentioned above that in real HTSC systems, ξ is in all probability of the order of ξ_0 so that non-self-averaging effects for the superconducting gap of the type of those considered in [11] can be quite significant. These effects are manifested of the form of “tails” on the temperature dependence of the averaged gap at $T > T_c$ (the pattern of superconducting “drops” [11]).

Another significant simplification in our model is the assumption concerning the static (Gaussian) type of short-range fluctuations. This assumption is justified only in the limit of high temperatures $T \gg \omega_{sf}$ (where ω_{sf} is the characteristic frequency of spin fluctuations) [6, 7]. For this reason, its application to the superconducting phase for $T < T_c$ is quite dubious. We believe, however, that the simplified analysis carried out above can be used for describing the most significant effects of variation of the electron spectrum (formation of a pseudogap in hot regions on the Fermi surface) on the superconductivity in such a system. If we took into account the dynamics of spin fluctuations, we would inevitably leave the limits of the simple phenomenology of the BCS model and would have to analyze in detail the microscopic aspects of the pairing interaction. Such a program can hardly be realized at present. Moreover, the problem of inclusion of all orders of perturbation theory in AFM fluctuations appears as completely futile on account of the dynamics of the spin subsystem.

ACKNOWLEDGMENTS

This research was partly supported by the Russian Foundation for Basic Research (project no. 99-02-16285) and CRDF (grant no. REC-005) as well as by the State program “Statistical Physics” (project no. 108-11(00-P)) and the State program on HTSC (project no. 96-051).

APPENDIX

Coordinate Representation: Normal and Anomalous Green’s Functions

Let us consider some technical aspects of the derivation of the recurrence relation for Gor’kov’s equations (12)–(15). We will confine our analysis to two regions on the Fermi surface, which are orthogonal to the p_x axis and coupled though the scattering vector $\mathbf{Q} = (\pm 2p_F, 0)$. In this case, the problem becomes purely one-dimensional since the velocity component $v_y = 0$ and the electron spectrum in the linearized form $\xi_{p_x \mp p_F} = \pm v_F p_x$ is completely independent of the y-component of the momentum. For the sake of brevity, we will henceforth assume that $v_F = 1$.

It is convenient to carry out the calculations in the coordinate representation [21], analyzing the motion of an electron in the field of Gaussian AFM fluctuations $W(x) \neq W^*(x)$ (incommensurate case) with the correlator

$$\langle W^*(x)W(x')\rangle = W^2 e^{-\kappa|x - x'|}. \tag{A.1}$$

In this case, the propagators corresponding to the normal and anomalous Green’s functions (10) of the superconductor assume the form

$$G_{00}(x) = \int_{-\infty}^{\infty} \frac{dp_x}{2\pi} e^{ip_x x} G_{00}(p_x)$$

$$= -\frac{i}{2}\left(\frac{\varepsilon_n}{\sqrt{\varepsilon_n^2+|\Delta|^2}} + \sigma_3 \operatorname{sgn} x\right)\exp(-\sqrt{\varepsilon_n^2+|\Delta|^2}x), \tag{A.2}$$

$$F_{00}(x) = \int_{-\infty}^{\infty}\frac{dp_x}{2\pi}e^{ip_x x}F^+_{00}(p_z)$$

$$= \frac{\Delta^*}{\sqrt{\varepsilon_n^2+|\Delta|^2}}\exp(-\sqrt{\varepsilon_n^2+|\Delta|^2}x),$$

where $\sigma_3 = 1$ for particles moving to the right and $\sigma_3 = -1$ for particles moving to the left. Scattering at fluctuations transforms "right" particles to "left" ones, and vice versa. It can be seen from expressions (A.2) that a particle traversing a distance of length l gives the factor $\exp(-\sqrt{\varepsilon_n^2+|\Delta|^2}l)$.

For calculating specific diagrams, is it convenient [21] to go over from the integration with respect to coordinates x_k of interaction vertices to the integration over paths l_k traversed by a particle between individual scattering acts by fixing the total displacement $x - x'$. The interaction curve connecting vertices m and n on the electron line in this case corresponds to the factor

$$W^2|\Delta|^2\exp(-\kappa|x_m - x_n|)$$
$$= W^2|\Delta|^2\exp\left(-\kappa\left|\sum_{k=m}^{n-1}(-1)^k l_k\right|\right). \tag{A.3}$$

The integration over all values of l_k is carried out from 0 to ∞.

Thus, considering the finiteness of the correlation length of fluctuations leads to the emergence of a certain "damping" of the corresponding transition amplitude in each diagram with increasing distance traversed by an electron. It is very difficult to take into account this effect exactly. In [7], however, we used the obvious inequality

$$\exp\left(-\kappa\left|\sum_{k=m}^{n-1}(-1)^k l_k\right|\right) > \exp\left(-\kappa\sum_{k=m}^{n-1} l_k\right) \tag{A.4}$$

and replaced the exponential in (A.3) by the exponential from the right-hand side of (A.4). This is equivalent to the replacement of the correlator (A.1) of random fields by an analogous expression in which the distance $|x - x'|$ in the exponent is replaced by the total distance traversed by a particle between the scattering acts at points x and x'. Therefore, in accordance with Eq. (A.4), we slightly overestimate the role of the damping factor κ in each diagram of the series in perturbation theory. As a result of such a substitution, the diagrams of all orders can be calculated easily and reproduce exactly ansatz (3) for the normal phase [21]. It was mentioned above that the results obtained in this way, for example, for the density of states are in good agreement with the results of exact numerical simulation of the problem under investigation [23, 24]. This is an additional argument in favor of the approximation used, extending the qualitative estimates obtained in [7].

We will use the same approximation for analyzing the diagrams in perturbation theory in the superconducting phase, which are constructed on propagators (A.2). In this case, the role of interaction with fluctuations is reduced only to the addition of the factor $e^{-\kappa l_k}$ to each normal or anomalous Green's function (A.2), which is embraced by the given interaction curve or, which is the same, to the addition of κ to $\sqrt{\varepsilon_n + |\Delta|^2}$ in the exponent of each such Green's function. Returning to the momentum representation, we can easily verify that the contribution of any higher-order diagram is determined by the product of the corresponding number of normal and anomalous Green's functions of the form

$$G_{0k}(p) = -\frac{i\varepsilon_n\frac{\varepsilon_k}{\sqrt{\varepsilon_n + |\Delta|^2}} + (-1)^k\xi_p}{\varepsilon_k^2 + \xi_p^2},$$
$$F^+_{0k}(p) = \frac{\Delta^*\frac{\varepsilon_k}{\sqrt{\varepsilon_n + |\Delta|^2}}}{\varepsilon_k^2 + \xi_p^2}, \tag{A.5}$$

where $\varepsilon_k = \sqrt{\varepsilon_n + |\Delta|^2} + k\kappa$, k being the number of interaction curves embracing a given Green's function. The factor $(-1)^k$ appears due to the fact that the scattering transforms "right" particles into "left" ones, and vice versa. Introducing the renormalized frequency and gap width in accordance with relations (15), we see that relations (A.5) can be reduced to the standard form (14), which completes the justification of the recurrence procedure (12) and (15).

REFERENCES

1. T. Timusk and B. Statt, Rep. Prog. Phys. **62**, 61 (1999).
2. V. B. Geshkenbein, L. B. Ioffe, and A. I. Larkin, Phys. Rev. B **55**, 3173 (1997).
3. V. Emery, S. A. Kivelson, and O. Zachar, Phys. Rev. B **56**, 6120 (1997).
4. V. P. Gusynin, V. M. Loktev, and S. G. Sharapov, Zh. Éksp. Teor. Fiz. **115**, 1243 (1999) [JETP **88**, 685 (1999)].
5. A. P. Kampf and J. R. Schrieffer, Phys. Rev. B **41**, 6399 (1990); **42**, 7967 (1990).
6. J. Schmalian, D. Pines, and B. Stojkovic, Phys. Rev. Lett. **80**, 3839 (1998); Phys. Rev. B **60**, 667 (1999).
7. É. Z. Kuchinskiĭ and M. V. Sadovskiĭ, Zh. Éksp. Teor. Fiz. **115**, 1765 (1999) [JETP **88**, 968 (1999)]; cond-mat/9808321 (1998).

8. J. L. Tallon and J. W. Loram, cond-mat/0005063 (2000); Physica C (Amsterdam) (2000) (in press).
9. V. M. Krasnov, A. Yurgens, D. Winkler, *et al.*, Phys. Rev. Lett. **84**, 5860 (2000); cond-mat/0006479 (2000).
10. A. I. Posazhennikova and M. V. Sadovskiĭ, Zh. Éksp. Teor. Fiz. **115**, 632 (1999) [JETP **88**, 347 (1999)]; cond-mat/9806199 (1998).
11. É. Z. Kuchinskiĭ and M. V. Sadovskiĭ, Zh. Éksp. Teor. Fiz. **117**, 613 (2000) [JETP **90**, 535 (2000)]; cond-mat/9910261 (1999).
12. R. Gatt, S. Christensen, B. Frazer, *et al.*, cond-mat/9906070 (1999).
13. D. L. Feng, W. J. Zheng, K. M. Shen, *et al.*, cond-mat/9908056 (1999).
14. A. Virosztek and J. Ruvalds, Phys. Rev. B **42**, 4064 (1990).
15. J. Ruvalds, C. T. Rieck, S. Tewari, *et al.*, Phys. Rev. B **51**, 3797 (1995).
16. A. T. Zheleznyak, V. M. Yakovenko, and I. E. Dzyaloshinskii, Phys. Rev. B **55**, 3200 (1997).
17. P. Monthoux, A. V. Balatsky, and D. Pines, Phys. Rev. B **46**, 14 803 (1992).
18. P. Monthoux and D. Pines, Phys. Rev. B **47**, 6069 (1993); **49**, 4261 (1994).
19. M. V. Sadovskiĭ, Zh. Éksp. Teor. Fiz. **66**, 1720 (1974) [Sov. Phys. JETP **39**, 845 (1974)]; Fiz. Tverd. Tela (Leningrad) **16**, 2504 (1974) [Sov. Phys. Solid State **16**, 1632 (1974)].
20. M. V. Sadovskiĭ, Zh. Éksp. Teor. Fiz. **77**, 2070 (1979) [Sov. Phys. JETP **50**, 989 (1979)].
21. O. Tchernyshyov, Phys. Rev. B **59**, 1358 (1999).
22. M. V. Sadovskiĭ, cond-mat/9912318 (1999); Physica C (Amsterdam) (2000) (in press).
23. L. Bartosch and P. Kopietz, Phys. Rev. B **60**, 15 488 (1999).
24. A. Millis and H. Monien, Phys. Rev. B **61**, 12 496 (2000).
25. L. P. Gor'kov, Zh. Éksp. Teor. Fiz. **37**, 1407 (1959) [Sov. Phys. JETP **10**, 998 (1960)].
26. P. G. de Gennes, *Superconductivity of Metals and Alloys* (Benjamin, New York, 1966; Mir, Moscow, 1968).
27. M. V. Sadovskiĭ, *Superconductivity and Localization* (World Scientific, Singapore, 2000); Phys. Rep. **282**, 225 (1997); Sverkhprovodimost': Fiz., Khim., Tekh. **8**, 337 (1995).
28. A. A. Abrikosov, L. P. Gor'kov, and I. E. Dzyaloshinskiĭ, *Methods of Quantum Field Theory in Statistical Physics* (Fizmatgiz, Moscow, 1963; Prentice-Hall, Englewood Cliffs, 1963).
29. M. V. Sadovskiĭ and A. A. Timofeev, Sverkhprovodimost': Fiz., Khim., Tekh. **4**, 11 (1991); J. Mosc. Phys. Soc. **1**, 391 (1991).
30. M. V. Sadovskiĭ, Pis'ma Zh. Éksp. Teor. Fiz. **69**, 447 (1999) [JETP Lett. **69**, 483 (1999)]; cond-mat/9902192 (1999).

Translated by N. Wadhwa

Journal of Experimental and Theoretical Physics, Vol. 92, No. 3, 2001, pp. 493–499.
Translated from Zhurnal Éksperimental'noĭ i Teoreticheskoĭ Fiziki, Vol. 119, No. 3, 2001, pp. 567–573.
Original Russian Text Copyright © 2001 by Sinyavskiĭ, Grebenshchikova.

SOLIDS
Electronic Properties

The Theory of the Cyclotron Resonance Line Half-Width in Limited-Size Systems

É. P. Sinyavskiĭ* and E. I. Grebenshchikova
Institute of Applied Physics, Academy of Sciences of Moldova, Chisinau, 277028 Moldova
**e-mail: exciton@cc.acad.md*

Received April 24, 2000

Abstract—Many-phonon optical transitions between Landau levels and size quantization levels in a longitudinal magnetic field are investigated in solitary quantum wells. The developed theory makes it possible to describe the intensity of the cyclotron resonance line as well as the temperature and field dependences of its half-width. The theoretical results are compared with experimental data. It is shown that when the interaction between electrons and optical phonons is taken into account, phonon satellites may appear as a result of an electron transition between the size quantization levels and magnetic levels. *© 2001 MAIK “Nauka/Interperiodica”.*

1. INTRODUCTION

If the direction of a magnetic field is normal to the surface of a quantum well, the electron energy is fully quantized. For a rectangular quantum well of width *a* with infinitely high walls, the energy of an electron with the effective mass *m* is defined as

$$E_{nN} = \hbar\omega_c\left(N + \frac{1}{2}\right) + \varepsilon_0 n^2.$$

Here, ω_c is the cyclotron frequency and $\varepsilon_0 = \hbar^2\pi^2/2ma^2$ is the spatial quantization step.

The experiments on light absorption determined by an electron transition between Landau levels were made in superlattices [1], heterostructures [2–6], metal–insulator–semiconductor systems [7], and in quantum wells [8, 9]. The experimental results show that with increasing magnetic field strength, the absorption peak is displaced to the short-wave region, and the cyclotron resonance line half-width Δ varies over a wide range $\Delta = 0.1$–2 meV depending on the quasi-two-dimensional system under investigation. The half-width of the optical absorption line associated with an electron transition between discrete states is of fundamental importance. This is due to the fact that the inelastic scattering of charge carriers from vibrations, which reflects the nonstationary nature of electronic states, determines the value $\Delta < 10^{-3}$ meV, which is much smaller than the experimental results. In the theoretical analysis of the shape of the cyclotron resonance line [10–12], it is assumed that it is described by a Lorentzian curve. The half-width of the cyclotron resonance line may be determined by nonuniform broadening (in the case of superlattices), while for a degenerate electron gas, it is determined by the Coulomb interaction between electrons [8], long-range impurity potentials [13], the interaction with soft magnetoplasmon modes [8], center-of-mass fluctuations (phonons and impurities are regarded as fluctuations of forces) [14, 15], and the interaction of electrons with surface phonons [16]. The half-width of the cyclotron resonance line in rectangular quantum wells [17, 18], heterostructures [5], and structures of the metal–insulator–semiconductor type [7, 14] noticeably depends on temperature. The value of Δ increases upon heating, the increase being nonlinear for $T > 1$ K. The latter circumstance clearly indicates that phonons play a significant role in the formation of the frequency dependence of the cyclotron resonance line.

We investigate here the many-phonon absorption of an electromagnetic wave, which is determined by an electron transition between Landau levels (cyclotron resonance) as well as between size quantization levels (size resonance). The inclusion of many vibrational quanta in an optical transition makes it possible to explain the half-width of the cyclotron resonance line as well as its temperature and field dependences. The mechanism proposed by us is apparently the only possible mechanism which provides a description of the shape of the cyclotron resonance line in solitary quantum wells.

2. FORMULATION OF THE PROBLEM. GENERAL RELATIONS

In accordance with the Kubo formula [19], the absorption coefficient for light of frequency Ω is defined through the correlation function of dipole moment operators:

$$K(\Omega) = \frac{4\pi\Omega}{Vn_0\hbar c}\sum_{\alpha,\alpha',\beta,\beta'} d_{\alpha\alpha'}d_{\beta\beta'} \times \int_{-\infty}^{\infty} dt e^{i\Omega t}\langle a_\alpha^+(t)a_{\alpha'}(t)a_\beta^+a_{\beta'}\rangle. \tag{1}$$

Here, $d_{\alpha\alpha'}$ is the matrix element of the dipole moment on the electron wave functions $|\alpha\rangle$ in a limited-size system in the presence of a magnetic field directed along the spatial quantization axis z, $\alpha = (N, n, K_x)$ is the set of quantum numbers describing the state of a charged particle, K_x is the wave vector of the electron along the x axis, $\overset{+}{a}_\alpha$ (a_α) are the creation (annihilation) operators for a charge carrier in state α, V is the volume of the quantum system under investigation, n_0 is the refractive index in the quantum well, and c is the velocity of light in a vacuum:

$$\overset{+}{a}_\alpha(t) = e^{itH/\hbar}\overset{+}{a}_\alpha e^{-itH/\hbar}, \tag{2}$$

$$H = H_0 + V, \tag{3}$$

$$H_0 = \sum_\alpha E_\alpha \overset{+}{a}_\alpha a_\alpha + \sum_{\mathbf{q}} \hbar\omega_{\mathbf{q}} \overset{+}{b}_{\mathbf{q}} b_{\mathbf{q}}, \tag{4}$$

$$V = \sum_{\mathbf{q},\,\alpha,\,\beta} C_{\mathbf{q}} V_{\alpha\beta}(b_{\mathbf{q}} + \overset{+}{b}_{-\mathbf{q}})\overset{+}{a}_\alpha a_\beta, \tag{5}$$

where H_0 is the Hamiltonian for free electrons and phonons, $\overset{+}{b}_{\mathbf{q}}$ $(b_{\mathbf{q}})$ are the creation (annihilation) operators for phonons with energy $\hbar\omega_{\mathbf{q}}$ and the wave vector $\mathbf{q}$, $C_{\mathbf{q}}$ is the coefficient function of the electron–phonon interaction, and

$$V_{\alpha\beta} = \left\langle \alpha \middle| e^{i\mathbf{qr}} \middle| \beta \right\rangle. \tag{6}$$

The angle brackets in relation (1) describe statistical averaging with Hamiltonian (3). While writing Eq. (1), we consider that the electron spin does not change as a result of the optical transition (the summation over the spin states gives factor 2).

In accordance with Eq. (2), the operator $\overset{+}{a}_\alpha(t)$ satisfies the equation of motion:

$$\begin{aligned}\dot{\overset{+}{a}}_\alpha(t) = \frac{i}{\hbar}\Big\{ & E_\alpha \overset{+}{a}_\alpha(t) \\ & + \sum_{\mathbf{q},\,\beta} C_{\mathbf{q}} \overset{+}{a}_\beta(t)\, V_{\beta\alpha}(b_{\mathbf{q}}e^{-i\omega_{\mathbf{q}}t} + \overset{+}{b}_{-\mathbf{q}}e^{i\omega_{\mathbf{q}}t})\Big\}.\end{aligned} \tag{7}$$

While writing Eq. (7), we assume that electrons do not modify the phonon spectrum of the system, i.e.,

$$b_{\mathbf{q}}(t) \approx e^{-i\omega_{\mathbf{q}}t} b_{\mathbf{q}}, \quad \overset{+}{b}_{\mathbf{q}}(t) \approx e^{i\omega_{\mathbf{q}}t}\overset{+}{b}_{\mathbf{q}}.$$

The last approximation is justified for a nondegenerate electron gas since the corrections introduced into $\omega_{\mathbf{q}}$ are proportional to the charge carrier concentration.

It follows from Eq. (7) that the equation of motion for the operator

$$\overset{+}{\xi}_\alpha(t) = \overset{+}{a}_\alpha(t)\exp\left\{-\frac{itE_\alpha}{\hbar}\right\} \tag{8}$$

is defined by the relation

$$\begin{aligned}\dot{\overset{+}{\xi}}_\alpha(t) = {} & \frac{i}{\hbar}\sum_{\mathbf{q},\,\beta} C_{\mathbf{q}} \overset{+}{\xi}_\beta(t) V_{\beta\alpha} \\ & \times \exp\left\{-\frac{it}{\hbar}(E_\alpha - E_\beta)\right\}(b_{\mathbf{q}}e^{-i\omega_{\mathbf{q}}t} + \overset{+}{b}_{-\mathbf{q}}e^{i\omega_{\mathbf{q}}t}),\end{aligned} \tag{9}$$

where $\beta = (n', N', K'_x)$.

Subsequent calculations will be carried out in the approximation diagonal in the quantum numbers ($N = N'$, $n = n'$). Putting $N = N'$, $n = n'$ in Eq. (9), we arrive at the following approximate equation for operators $\overset{+}{\xi}_\alpha(t)$:

$$\dot{\overset{+}{\xi}}_{\nu,\,K_x}(t) = \frac{i}{\hbar}\sum_{K'_x} \overset{+}{\xi}_{\nu,\,K'_x}(t)\langle K'_x|V_\nu(t)|K_x\rangle, \tag{10}$$

where $|K_x\rangle$ are the wave function for a free electron:

$$V_\nu(t) = \sum_{\mathbf{q}} C_{\mathbf{q}} V_\nu(q) e^{iA}(b_{\mathbf{q}}e^{-i\omega_{\mathbf{q}}t} + \overset{+}{b}_{-\mathbf{q}}e^{i\omega_{\mathbf{q}}t}). \tag{11}$$

For a rectangular quantum well with infinitely high walls, we have

$$\begin{aligned}V_\nu(\mathbf{q}) = {} & \frac{4i\pi^2 n^2}{(q_z a)^2 - (2\pi n)^2}\,\frac{\exp\{iq_z a\} - 1}{q_z a} \\ & \times \exp\left\{-\frac{R^2(q_x^2 + q_y^2)}{4}\right\} L_N\left(\frac{R^2(q_x^2 + q_y^2)}{2}\right),\end{aligned} \tag{12}$$

$$A = iq_x x + iq_y\frac{R^2 P_x}{\hbar}, \quad P_x = -i\hbar\frac{\partial}{\partial x}, \quad R^2 = \frac{\hbar}{m\omega_c},$$

where $L_N(z)$ are the Laguerre polynomials.

The solution of Eq. (10) taking into account the initial conditions $\overset{+}{\xi}_{\nu K_x}(0) = \overset{+}{\xi}_{\nu K_x} = \overset{+}{a}_{\nu K_x}$ has the form

$$\overset{+}{\xi}_{\nu K_x}(t) = \sum_{K'_x} \overset{+}{\xi}_{\nu K'_x}\left\langle K'_x \middle| \overset{+}{U}_\nu(t) \middle| K_x \right\rangle. \tag{13}$$

Here, the following notation has been introduced:

$$U_\nu^+(t) = \exp\left\{\frac{it}{\hbar}(H_f + V_\nu)\right\}\exp\left\{\left(-\frac{it}{\hbar}\right)H_f\right\},$$

$$H_f = \sum_{\mathbf{q}} \hbar\omega_q b_{\mathbf{q}}^+ b_{\mathbf{q}}, \tag{14}$$

$$V_\nu = \sum_{\mathbf{q}} C_q V_\nu(\mathbf{q})(b_{\mathbf{q}} + b_{-\mathbf{q}}^+)\exp\{iA\}.$$

Consequently, in accordance with Eq. (8), we have

$$a_{\nu K_x}^+(t) = \sum_{K'_x} a_{\nu K'_x}^+ \exp\left\{\frac{itE_\nu}{\hbar}\right\}\left\langle K'_x\middle|U_\nu^+(t)\middle|K_x\right\rangle. \tag{15}$$

The validity of solution (13) can easily be verified by substituting it into Eq. (10) and taking into account the equation of motion for the evolution operators

$$\dot{U}_\nu^+(t) = \frac{1}{\hbar}U_\nu^+(t)V_\nu(t)$$

as well as the condition of the completeness of the wave functions for a free electron along the x axis:

$$\sum_{K''_x} |K''_x\rangle\langle K''_x| = I,$$

where I is the unit operator.

The operator $a_\alpha(t)$ can be calculated in a similar way.

Substituting the values of $a_\alpha^+(t)$ and $a_\alpha(t)$ into relation (1), we obtain the following expression for the optical absorption coefficient:

$$\begin{aligned} K(\Omega) = \frac{4\pi\Omega}{Vn_0c\hbar} & \sum_{\nu, \nu_1, K_x, K'_x} f_{\nu K'_x} d_{\nu K_x, \nu_1 K_x} d_{\nu_1 K'_x, \nu K'_x} \\ & \times \int_{-\infty}^{\infty} dt \exp\left\{\frac{it}{\hbar}(E_\nu - E_{\nu_1} + \hbar\Omega)\right\} \\ & \times \left\{\langle K'_x|U_\nu^+(t)|K_x\rangle\langle K_x|U_{\nu_1}|K'_x\rangle\right\}_0, \end{aligned} \tag{16}$$

where

$$f_\alpha = \langle a_\alpha^+ a_\alpha\rangle = 2\pi R^2 aDn_e \sinh(\beta\hbar\omega_c/2)$$
$$\times \exp\{-\beta\hbar\omega_c/2\}\exp\{-\beta(N\hbar\omega_c + \varepsilon_0 n^2)\},$$

$$D^{-1} = \sum_{n=1} \exp\{-\beta\varepsilon_0 n^2\}, \quad \beta = \frac{1}{k_0 T},$$

$$U_{\nu_1}(t) = \exp\left\{\frac{it}{\hbar}H_f\right\}\exp\left\{-\frac{it}{\hbar}(H_f + V_{\nu_1})\right\},$$

f_α is the equilibrium distribution function for electrons in the nondegenerate limited-size system under investigation, and n_e is the electron concentration.

While writing expression (16), we disregarded the polaron effects; consequently, $\{\ldots\}_0$ denotes the averaging over the system of the free phonon field. The averaging over the system of noninteracting electrons was carried out in the lowest approximation in electron concentration:

$$\left\langle a_{\alpha_1}^+ a_{\alpha_2} a_{\alpha_3}^+ a_{\alpha_4}\right\rangle_0 \approx \left\langle a_{\alpha_1}^+ a_{\alpha_4}\right\rangle_0 \delta_{\alpha_1\alpha_4}\delta_{\alpha_2\alpha_3}.$$

If the linearly polarized electromagnetic wave being absorbed is incident along the normal to the surface of a limited-size system, we have

$$\begin{aligned} d_{\alpha\alpha_1} &= \frac{eR}{\sqrt{2}}\delta_{n, n_1}\delta_{K_x, K'_x} \\ &\times \{\sqrt{N}\delta_{N, N_1+1} + \sqrt{N+1}\delta_{N, N_1-1}\}. \end{aligned} \tag{17}$$

In accordance with this relation, direct optical transitions are possible in this case only between nearest Landau levels without a change in the quantum numbers n of size quantization.

We will henceforth consider the case when all electrons are in the lowest state ($N = 0$, $n = 1$); i.e.,

$$\hbar\omega_c > k_0 T, \quad 3\varepsilon_0 > k_0 T, \quad f_{\nu K_x} = f_{01K_x} = \pi n_e a R^2.$$

The substitution of relation (17) into (16) leads to the following form of the optical absorption coefficient:

$$\begin{aligned} K_\perp(\Omega) &= \frac{2\pi^2\Omega e^2 R^4 n_e a}{Vn_0c\hbar} \\ &\times \int_{-\infty}^{\infty} dt \exp\{-it(\omega_c - \Omega)\} \sum_{K_x} \{\langle K_x|U_{01}^+ U_{11}|K_x\rangle\}_0. \end{aligned} \tag{18}$$

If an electromagnetic wave propagates along the surface of a quantum well and the polarization vector is parallel to the space quantization axis, the matrix element of the dipole moment is defined by the relation

$$\begin{aligned} d_{\alpha\alpha_1} &= \frac{ea}{\pi^2}\delta_{N, N_1} \\ &\times \left\{\frac{\cos\pi(n + n_1) - 1}{(n + n_1)^2} - \frac{\cos\pi(n - n_1) - 1}{(n - n_1)^2}\right\}\delta_{K_x, K_{x_1}}. \end{aligned} \tag{19}$$

Consequently, direct optical transitions are possible in the case in question between the space quantization levels ($n \neq n_1$) without a change in the number of the Landau level ($N = N_1$).

Let us analyze the absorption of light determined by a transition from the lowest state ($N = 0$, $n = 1$) to the next size-quantized state ($N_1 = 0$, $n_1 = 2$). The substitution of relation (19) into (16) leads to the following expression for the optical absorption coefficient:

$$K_{\parallel}(\Omega) = \frac{4\pi^2\Omega e^2 R^2 n_e a}{V n_0 c\hbar}\left(\frac{16a}{9\pi^2}\right)^2 \times \int_{-\infty}^{\infty} dt \exp\left\{-\frac{it}{\hbar}(3\varepsilon_0 - \hbar\Omega)\right\}\sum_{K_x}\{\langle K_x|U_{01}^{\dagger}U_{02}|K_x\rangle\}_0. \tag{20}$$

The averaging over the system of free phonons in expressions (18) and (20) can be carried out exactly using the methods of the theory of many-phonon transitions [20] or the algebra of Bose operators [21]. This gives

$$\{U_{\nu}^{\dagger}(t)U_{\nu_1}(t)\}_0 = \exp\{-g_{\nu\nu_1}(t)\}, \tag{21}$$

$$\begin{aligned} g_{\nu\nu_1}(t) &= \frac{it}{\hbar}\sum_{\mathbf{q}}\frac{|C_{\mathbf{q}}|^2}{\hbar\omega_{\mathbf{q}}}[|V_{\nu}(\mathbf{q})|^2 - |V_{\nu_1}(\mathbf{q})|^2] \\ &+ \sum_{\mathbf{q}}\frac{2N_{\mathbf{q}}+1}{(\hbar\omega_{\mathbf{q}})^2}|C_{\mathbf{q}}|^2|V_{\nu}(\mathbf{q}) - V_{\nu_1}(\mathbf{q})|^2(1-\cos\omega_{\mathbf{q}}t) \\ &- i\sum_{\mathbf{q}}\frac{|C_{\mathbf{q}}|^2}{(\hbar\omega_{\mathbf{q}})^2}[|V_{\nu}(\mathbf{q})|^2 - |V_{\nu_1}(\mathbf{q})|^2]\sin\omega_{\mathbf{q}}t. \end{aligned} \tag{22}$$

Taking relation (21) into consideration, we can write, in accordance with (18), the optical absorption coefficient associated with a transition from the lower Landau level in the form

$$K_{\perp}(\Omega) = \frac{\pi\Omega e^2 R^2 n_e}{n_0 c\hbar} \times \int_{-\infty}^{\infty} dt \exp\{-it(\omega_c - \Omega)\}\exp\{-g_{01,\,11}(t)\}. \tag{23}$$

Similarly, we can write the expression for the absorption coefficient of light whose polarization vector is directed along the space quantization axis:

$$K_{\parallel}(\Omega) = \frac{2\pi\Omega e^2 n_e}{n_0 c\hbar}\left(\frac{16a}{9\pi^2}\right)^2 \times \int_{-\infty}^{\infty} dt \exp\left\{-\frac{it}{\hbar}(3\varepsilon_0 - \hbar\Omega)\right\}\exp\{-g_{01,\,02}(t)\}. \tag{24}$$

3. DISCUSSION OF RESULTS AND COMPARISON WITH EXPERIMENT

Relations (23) and (24) describe the frequency dependence of the optical absorption coefficient, associated with the transition of an electron between Landau levels and size-quantized states and taking into account many phonons involved in the process.

Let us consider a quantum system in which electrons interact most actively with long-wave acoustic phonons. If electrons are described in the quasiclassical approximation, the function $g_{\nu\nu_1}(t)$ in (22) can be expanded into a series in t up to terms with t^2 inclusively. (The main criteria of such an approximation can be found in [22].) This gives

$$g_{\nu\nu_1}(t) \approx B_{\nu\nu_1}t^2, \qquad B_{\nu\nu_1} = \frac{1}{2}\sum_{\mathbf{q}}\frac{1+2N_{\mathbf{q}}}{\hbar^2}|C_{\mathbf{q}}|^2|V_{\nu}(\mathbf{q}) - V_{\nu_1}(\mathbf{q})|^2. \tag{25}$$

Consequently, in accordance with Eq. (23), the optical absorption coefficient associated with an electron transition from the lowest Landau level [ν(0, 1)] to the nearest Landau level [ν(1, 1)] assumes the form

$$K_{\perp}(\Omega) = \frac{\pi\Omega e^2 R^2 n_e}{n_0 c\hbar}\sqrt{\frac{\pi}{B}}\exp\left\{-\frac{(\hbar\Omega - \hbar\omega_c)^2}{4\hbar^2 B}\right\}, \qquad B = \sum_{\mathbf{q}}\frac{1+2N_{\mathbf{q}}}{2\hbar^2}|C_{\mathbf{q}}|^2|V_{01}(\mathbf{q}) - V_{11}(\mathbf{q})|^2. \tag{26}$$

In the case of high temperatures at which $N_{\mathbf{q}} \approx k_0T/\hbar\omega_{\mathbf{q}} > 1$, we obtain

$$B = \frac{3k_0TE_1^2}{4\hbar^2\rho v^2\pi aR^2}, \tag{27}$$

where ρ is the density of the quantum well, E_1 is the deformation potential constant for electrons, and v is the velocity of sound in the limited-size system.

It follows directly from Eqs. (26) that the frequency dependence of the absorption coefficient for an electromagnetic wave is described by a Gaussian curve with the half-width

$$\Delta = 4\sqrt{B\hbar^2\ln 2} \approx 2\sqrt{\frac{3k_0TE_1^2m\omega_c}{\pi\hbar a\rho v^2}\ln 2}. \tag{28}$$

For typical quantum wells with $\rho = 5.4$ g/cm^3, $v = 3 \times 10^3$ m/s, and $m = 0.06m_0$, for $B = 8$ T, $T = 50$ K, $a = 50$ Å, and $E_1 = 10$ eV, we have $\Delta = 3$ meV, which is in the range of experimental data [1, 4]. In accordance with (28), the half-width of the cyclotron absorption line increases with T ($\Delta \propto \sqrt{T}$). Such an obviously nonlinear temperature dependence of Δ (at $T > 10$ K) was observed in experiments [5–7, 16, 17]. The half-width of the cyclotron resonance line increases with the magnetic field strength ($\Delta \approx \sqrt{B}$). Hopkins *et al.* [5] experimentally observed an increase in Δ in the range of strong magnetic fields (the value of B was varied from 6 to 14 T).

In accordance with Eq. (24), the optical absorption coefficient for an electromagnetic wave whose polarization vector is directed along the space quantization axis is defined by the relation

$$K_{\parallel}(\Omega) = \frac{2\pi\Omega e^2 n_e}{n_0 c\hbar}\left(\frac{16a}{9\pi^2}\right)^2\sqrt{\frac{\pi}{B_1}} \times \exp\left\{-\frac{(\hbar\Omega - 3\varepsilon_0)^2}{4\hbar^2 B_1}\right\}. \tag{29}$$

For an electron transition between two nearest size-quantized states, we have

$$B_1 = \sum_{\mathbf{q}}\frac{1+2N_{\mathbf{q}}}{2\hbar^2}|C_{\mathbf{q}}|^2|V_{01}(\mathbf{q}) - V_{02}(\mathbf{q})|^2 \approx \frac{1}{3}B. \tag{30}$$

Consequently, the frequency dependence of the optical absorption coefficient is described by a Gaussian curve whose half-width is smaller than in the case of the cyclotron resonance by a factor of $1/\sqrt{3}$.

If a circularly polarized electromagnetic wave propagates along the surface of a quantum well, the optical absorption coefficient is defined by the sum of Eqs. (26) and (29):

$$\begin{aligned} K(\Omega) &= K_{\perp}(\Omega) + K_{\parallel}(\Omega) \\ &= \frac{\pi\Omega e^2 R^2 n_e}{n_0 c\hbar}\sqrt{\frac{\pi}{B}}\left\{\exp\left(-\frac{[\hbar\Omega - \hbar\omega_c]^2}{4\hbar^2 B}\right) + 0.55\frac{\hbar\omega_c}{\varepsilon_0}\exp\left(-\frac{[\hbar\Omega - 3\varepsilon_0]^2}{4\hbar^2 B_1}\right)\right\}. \end{aligned} \tag{31}$$

Consequently, for $\hbar\omega_c < 3\varepsilon_0$, the frequency dependence $K(\Omega)$ is described by two Gaussians. The first peak with half-width $\Delta = 4\sqrt{B\hbar^2\ln 2}$ and a maximum at $\hbar\Omega = \hbar\omega_c$ is associated with the cyclotron absorption of light, while the second peak with half-width $\Delta_1 = \Delta/\sqrt{3}$ and a maximum at $\hbar\Omega = 3\varepsilon_0$ is determined by an electron transition from the lowest state to the next size-quantized state. It should be noted that the maximum of the second absorption peak differs in absolute value from the cyclotron resonance peak by the quantity $\delta = 0.55(\hbar\omega_c/\varepsilon_0)$. Similar results are obtained when a linearly polarized electromagnetic wave being absorbed is incident at an angle to the surface of a limited-size system. It is in this case that the influence of size-quantized states on the cyclotron resonance was observed in heterostructures [23].

For narrow rectangular quantum wells of space quantization, $\varepsilon_0 = (5 \times 10^2/a_0^2)$ eV (a_0 is the quantum well width); for $a_0 = 100$ Å, $3\varepsilon_0 = 0.15$ eV, which exceeds the energy $\hbar\omega_0$ of the limiting optical phonon. Consequently, on account many optical phonons, the absorption of light is possible between spatially quantized states.

If we consider the interaction between an electron and optical phonons, the quantity $g_{\nu\nu_1}$ in Eq. (22) can be presented in the form

$$g_{\nu\nu_1} = it\omega_0 B_0 + A - Z\cos(\omega_0 t - \varphi). \tag{32}$$

Here, the following notation has been introduced:

$$B_0 = \sum_{\mathbf{q}}\frac{|C_{\mathbf{q}}|^2}{(\hbar\omega_0)^2}[|V_\nu(\mathbf{q})|^2 - |V_{\nu_1}(\mathbf{q})|^2],$$

$$A = (1+2N_0)\sum_{\mathbf{q}}\frac{|C_{\mathbf{q}}|^2}{(\hbar\omega_0)^2}|V_\nu(\mathbf{q}) - V_{\nu_1}(\mathbf{q})|,$$

$$Z^2 = A^2 - B_0^2, \quad \tan\varphi = i\frac{B_0}{A},$$

where N_0 is the distribution function for equilibrium phonons with energy $\hbar\omega_0$.

If we use the equality [24]

$$\exp\{Z\cos(\omega_0 t - \varphi)\} = \sum_n I_n(Z)\exp\{in(\omega_0 t - \varphi)\}$$

($I_n(Z)$ is a modified Bessel's function), the optical absorption coefficient determined by an electron transition from the lowest state ($N = 0$, $n = 1$) to the next size-quantized state ($N = 0$, $n = 2$) assumes the form

$$K_{\parallel}(\Omega) = \frac{4\pi^2\Omega e^2 n_e}{n_0 c}\left(\frac{16a}{9\pi^2}\right)^2\exp\{-A\} \times \sum_n I_n(Z)\left[\frac{A+B_0}{A-B_0}\right]^{n/2}\delta(3\varepsilon_0 - \hbar\Omega - n\hbar\omega_0 - B_0\hbar\omega_0). \tag{33}$$

The term with $n = 0$ describes a phonon-free electron transition. If $Z > 1$, the processes of light absorption accompanied by the emission ($n > 0$) or absorption ($n < 0$) of phonons occur actively. Consequently, along with the phonon-free absorption of light at frequency $\hbar\Omega = 3\varepsilon_0 - B_0\hbar\omega_0$, vibrational satellites separated by $\hbar\omega_0$ appear. If we take into account the interaction between an electron and acoustic vibrations, the shape of the phonon-free absorption line as well as of phonon satellites is described by a Gaussian curve with half-width $\Delta/\sqrt{3}$. The constants B and A are calculated directly. This gives

$$Z = Z_0 D(N, \tilde{\xi}), \quad Z_0 = \frac{e^2 c_0}{4\hbar\omega_0 a}, \tag{34}$$

$c_0 = 1/\varepsilon_\infty - 1/\tilde{\varepsilon}_0$, where $\tilde{\varepsilon}_0$ and ε_∞ are the static and high-frequency dielectric constants, respectively.

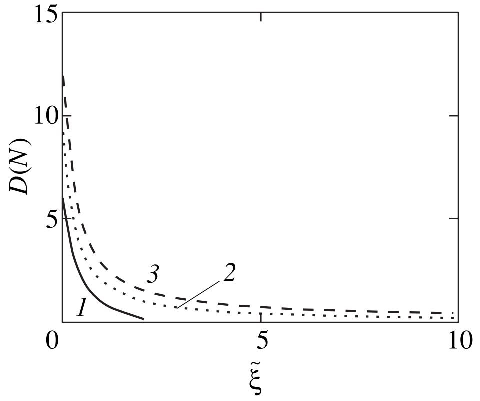

Fig. 1. Dependence of $D(N)$ on $\tilde{\xi}$. Curves *1*, *2*, and *3* were obtained for $N_0 = 0.5$, 1, and 1.5, respectively.

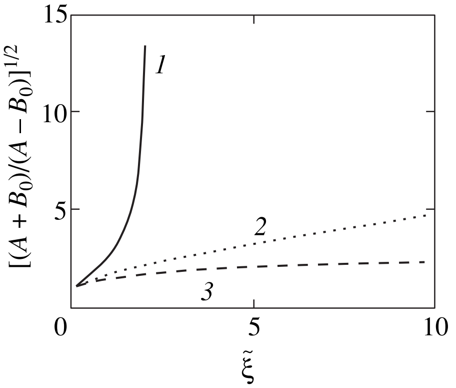

Fig. 2. Dependence of $[(A + B_0)/(A - B_0)]^{1/2}$ on $\tilde{\xi}$. Curves *1*, *2*, and *3* were obtained for $N_0 = 0.5$, 1, and 1.5, respectively.

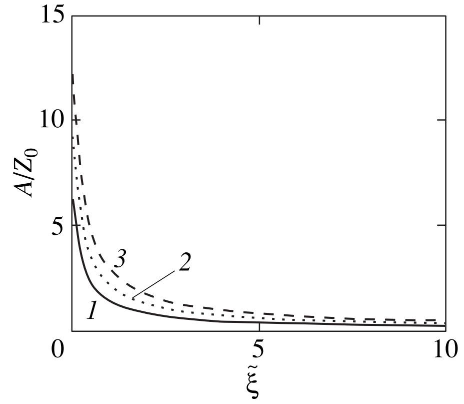

Fig. 3. Dependence of A/Z_0 on $\tilde{\xi}$. Curves *1*, *2*, and *3* were obtained for $N_0 = 0.5$, 1, and 1.5, respectively.

Figure 1 shows the dependence of $D(N, \tilde{\xi})$ on $\tilde{\xi} = \pi^{-2}(\varepsilon_0/\hbar\omega_c)$ for various values of N_0. Curves *1*, *2*, and *3* are obtained for $N_0 = 0.5$, 1, and 1,5, respectively. Figures 2 and 3 depict, respectively, the dependences of $[(A + B_0)/(A - B_0)]^{1/2}$ and A/Z_0 on $\tilde{\xi}$ for various values of N_0.

For quantum wells with $a = 50$ Å in GaAs/Al$_x$Ga$_{1-x}$As ($c_0 = 1.4 \times 10^{-2}$, $\hbar\omega_0 = 0.03$ eV), $Z_0 \approx 0.03$; for InP/In$_x$Ga$_{1-x}$As ($c_0 = 1.73 \times 10^{-2}$, $\hbar\omega_0 = 0.03$ eV), we have $Z_0 \approx 0.04$, while for GaN/AlGaN ($c_0 = 9 \times 10^{-2}$, $\hbar\omega_0 = 0.05$ eV), the value of $Z_0 \approx 0.13$. In accordance with Eqs. (34), for $\xi = 1$ ($N = 1.5$), for example, for quantum wells in GaN/AlGaN, we have $Z \approx 0.39$, while for GaAs/Al$_x$Ga$_{1-x}$As, the value of $Z \approx 0.09$. Consequently, limited-size systems with a strong polar bond must display vibrational satellites appearing upon the absorption of an electromagnetic wave whose polarization vector is directed along the spatial quantization axis.

In an analysis of optical many-phonon transitions, the diagonal approximation in the quantum numbers N and n was used (see Eq. (10)). This approximation has made it possible to carry out the exact averaging over the vibrational subsystem. The contribution of nondiagonal elements to the optical spectra can be estimated as follows. It can easily be verified that the solution of Eq. (9) can be written in the form

$$\xi_\alpha^+(t) = \sum_\beta \xi_\beta^+(0)\langle\beta|\exp\left\{\frac{it}{\hbar}(H_0 + V)\right\}\exp\left\{\frac{-it}{\hbar}H_0\right\}|\alpha\rangle.$$

Here,

$$V = \sum_{\mathbf{q}} C_{\mathbf{q}}(b_{\mathbf{q}} + b_{-\mathbf{q}}^+)\exp\{i\mathbf{qr}\}.$$

Consequently, in accordance with Eq. (8), we can easily determine $a_\alpha^+(t)$. The operator $a_{\alpha'}(t)$ can be calculated similarly. If we substitute $a_\alpha^+(t)$ and $a_{\alpha'}(t)$ into the sought relation (1) for the optical absorption coefficient, the averaging over the phonon subsystem can be carried out approximately by using the cumulative expansion [25] and confining the analysis to the second cumulant. According to the results of our earlier investigations [26], in the theory of magnetooptical phenomena, this approximation corresponds (in the language of the Konstantinov–Perel diagrammatic technique) to the summation of graphs which do not intersect phonon lines [27] and to the ordinary breaking of a chain for the Green's function [28]. According to the results of calculations, the contribution of terms with $N \neq N'$ and $n \neq n'$ to the parameter $B_{\nu\nu_1}$ (25), which determines the halfwidth of the absorption line, and to Z (34), which describes the intensity of vibrational satellites, amounts to less than 10% for $\tilde{\xi} > 1$.

Consequently, the diagonal approximation is quite reasonable for an analysis of many-phonon processes in the optical spectra for limited-size systems.

REFERENCES

1. T. Diffield, R. Bhat, M. Koza, *et al.*, Solid State Commun. **65**, 1483 (1988).
2. W. Seidenbusch, Phys. Rev. B **36**, 1877 (1987).
3. K. Ensslin, D. Heitmann, H. Sigg, *et al.*, Phys. Rev. B **36**, 8177 (1987).
4. M. J. Chou, D. C. Tsui, and G. Weimann, Phys. Rev. B **37**, 848 (1988).
5. M. A. Hopkins, R. J. Nicholas, D. J. Bernes, *et al.*, Phys. Rev. B **39**, 13 302 (1989).
6. L. K. Orlov, J. Leotin, F. Yang, and N. L. Orlova, Fiz. Tverd. Tela (St. Petersburg) **39**, 2096 (1997) [Phys. Solid State **39**, 1875 (1997)].
7. R. J. Wagner, T. A. Kennedy, B. D. McCombe, *et al.*, Phys. Rev. B **22**, 945 (1980).
8. Z. Schlesinger, S. J. Allen, and J. C. M. Hwang, Phys. Rev. B **30**, 435 (1984).
9. M. O. Manasreh, D. W. Fischer, K. R. Evans, *et al.*, Phys. Rev. B **43**, 9772 (1991).
10. Xiaoguang Wu and F. M. Peeters, Phys. Rev. B **41**, 3109 (1990).
11. Mahendra Prasad and Mahiradhwaj Singh, Phys. Rev. B **29**, 4803 (1984).
12. M. P. Chaubey and C. M. van Vliet, Phys. Rev. B **34**, 3932 (1986).
13. W. Cai and C. S. Ting, Phys. Rev. B **33**, 3967 (1986).
14. G. Y. Hu and R. F. O'Connel, Phys. Rev. B **40**, 11 701 (1989).
15. G. Y. Hu and R. F. O'Connel, Phys. Rev. B **37**, 10 391 (1988).
16. M. A. Brummel, R. J. Nicholas, and M. A. Hopkins, Phys. Rev. Lett. **58**, 77 (1987).
17. B. Tanatar and M. Singh, Phys. Rev. B **43**, 6612 (1991).
18. Z. Schlesinger, W. I. Wang, and A. M. MacDonald, Phys. Rev. Lett. **58**, 73 (1987).
19. R. Kubo, J. Phys. Soc. Jpn. **12**, 570 (1957).
20. Yu. E. Perlin, Usp. Fiz. Nauk **80**, 553 (1963) [Sov. Phys. Usp. **6**, 542 (1964)].
21. W. H. Louisell, *Radiation and Noise in Quantum Electronics* (McGraw-Hill, New York, 1964; Nauka, Moscow, 1972).
22. Yu. E. Perlin and B. S. Tsukerblat, *The Effects of Electron-Vibrational Interaction in Optical Spectra of Impurity Ions* (Shtiintsa, Kishinev, 1974).
23. S. I. Gubarev, A. A. Dremin, K. von Klitzing, *et al.*, Pis'ma Zh. Éksp. Teor. Fiz. **54**, 361 (1991) [JETP Lett. **54**, 355 (1991)].
24. I. S. Gradshteyn and I. M. Ryzhik, *Table of Integrals, Series, and Products* (Nauka, Moscow, 1971; Academic, New York, 1980).
25. R. Kubo, J. Phys. Soc. Jpn. **17**, 1100 (1962).
26. É. P. Sinyavskiĭ, *Kinetic Effects in Electron-Phonon Systems in Laser Radiation Field* (Shtiintsa, Kishinev, 1976).
27. L. I. Korovin and E. V. Kharitonov, Fiz. Tverd. Tela (Leningrad) **7**, 2162 (1965) [Sov. Phys. Solid State **7**, 1740 (1965)].
28. G. Giobanu and L. Banyani, Phys. Status Solidi **3**, 2299 (1963).

Translated by N. Wadhwa

Journal of Experimental and Theoretical Physics, Vol. 92, No. 3, 2001, pp. 500–513.
Translated from Zhurnal Éksperimental'noĭ i Teoreticheskoĭ Fiziki, Vol. 119, No. 3, 2001, pp. 574–589.
Original Russian Text Copyright © 2001 by Yakimov, Dvurechenskiĭ, Stepina, Nikiforov, Nenashev.

SOLIDS
Electronic Properties

Contribution of the Electron–Electron Interaction to the Optical Properties of Dense Arrays of Ge/Si Quantum Dots

A. I. Yakimov[a], * A. V. Dvurechenskiĭ[a], N. P. Stepina[a], A. I. Nikiforov[a], and A. V. Nenashev[b]
[a]*Institute of Semiconductor Physics, Siberian Division, Russian Academy of Sciences, Novosibirsk, 630090 Russia*
[b]*Novosibirsk State University, Novosibirsk, 630090 Russia*
**e-mail: yakimov@isp.nsc.ru*

Received June 14, 2000

Abstract—We present the results of an investigation of the light absorption due to interband and interlevel transitions and the photoconductivity in dense arrays of Ge quantum dots (QDs) in Si formed using the effect of self-organization during molecular-beam heteroepitaxy. It was found that the formation of charged exciton complexes composed of two holes and one electron, as well as of the be-exciton complexes in QDs of type II, leads to an increase in the energy of indirect (in real space) exciton transition, which is explained by the spatial separation of electron and hole. Self-consistent calculations of the wavefunctions for electrons and holes in exciton and in the exciton complexes showed that an electron in a single exciton is localized in the region of maximum stress for Si in the vicinity of the Ge pyramid apex, while a hole is localized near the pyramid base. In a be-exciton complex, electrons exhibit repulsion leading to their spatial separation. As a result, the second electron is bound at the boundary between Si and a continuous Ge layer in which the pyramid bases reside. The experimental data show that an increase in the charge carrier concentration in the ground state of QDs leads to a shortwave shift of the interband resonance and to the narrowing and shape change of the light absorption band, which is explained by depolarization of the external electromagnetic wave due to interaction with the collective charge density oscillations in the lateral direction of the array of Ge nanoclusters. It is established that the hole injection into an excited state of QDs leads to a longwave shift of the photoconductivity peak as a result of decay of the collective excitations and suppression of the depolarization effect. *© 2001 MAIK “Nauka/Interperiodica”.*

1. INTRODUCTION

Quantum dots (QDs) represent a limiting case of the systems with reduced dimensionality (quantum-confined systems), since the motion of charge carriers in these structures is spatially restricted in three dimensions. From the standpoint of device operation, the size of these nanostructures must be on the order of a few nanometers so as to avoid thermal blurring of the discrete energy spectrum at room temperature. Moreover, in order to provide for a high modal gain in lasers, a high quantum efficiency in photodetectors, a significant shift of the threshold voltage in single-electron transistor memory elements, and fast data transfer in quantum networks, it is necessary to create dense QD arrays with a layer density of QDs exceeding $\geq 10^{11}$ cm^{-2}.

The requirement of nanoscale dimensions and large density of QDs considerably restrict the possibility of using traditional methods of heterostructure fabrication based on the lithographic process and require the development of new approaches. In the search for new technologies, very good prospects are offered by the idea of using changes in the surface morphology involved in the growth of mismatched heteroepitaxial systems for the formation of arrays of atomic nanoclusters on the passage from 2D to 3D growth by the Stranski–Krastanow mechanism. We have implemented this idea for the first time in 1992 in the Ge/Si system [1]. The investigation of this system showed evidence of the presence of single-electron effects in nanostructures of the new type. Subsequently, this principle of obtaining the QD arrays was referred to as “self-organization” because it was necessary to explain the formation of an array of nanoclusters with sufficiently homogeneous size distribution [2, 3].

A special interest of researchers in the Ge nanoclusters in Si is related to the following circumstances. First, a decrease in the temperature of heteroepitaxy and increase in the deposition rate allowed the size of Ge nanoclusters to be reduced to ~10 nm. These dimensions ensured the manifestation of the quantum-confinement and single-electron effects up to room temperature and provided for the QD layer density as high as 3×10^{11} cm^{-2} [3, 4]. In addition, methods developed for the formation of Ge nanoclusters proved to be compatible with the world-spread silicon technology used for the fabrication of discrete devices and integrated circuits.

The strained layers of Ge/Si(001) belong to the heterostructures of type II. The characteristic features of systems of this type are determined by a special mutual arrangement of the energy band edges of the component semiconductors at the heterojunction. The conduc-

1063-7761/01/9203-0500$21.00 © 2001 MAIK “Nauka/Interperiodica”

tion band of one material (Si) in this region is close to the valence band of another component (Ge), which results in the spatial separation of charge carriers. In the system under consideration, the holes are localized within the Ge quantum dots, while electrons in Ge encounter a potential barrier. However, a positive charge created by holes and an inhomogeneous deformation of the structure as a result of the lattice mismatch between Ge and Si may result in the appearance of a potential well for nonequilibrium electrons in the conduction band of silicon near the Ge/Si heterojunction (Fig. 1). Thus, a distinctive feature of the QDs of type II is the possibility of formation of an indirect (in real space) exciton, whereby a hole is localized within the Ge island and an electron moves in the self-consistent potential of Si in the vicinity of the hole. At present, the properties of indirect excitons in QDs are studied rather insufficiently, although these systems are of considerable interest from the standpoint of both basic research and the technology of devices which cannot be implemented using the heterostructures of type I [5]. In particular, no data are available concerning the spectrum and structure of multiparticle exciton complexes formed in the QDs described above.

The urgent importance of investigations into the optical properties of QDs is explained by the pronounced practical orientation of this research toward the creation of photodetectors and light-emitting devices, which offer a number of advantages in comparison with 2D systems. Important features of QDs are as follows: (i) the possibility of controlling the spectral band (i.e., the color) of photoemission and photoresponse by populating discrete states with a necessary transition energy; (ii) reduced threshold current density and high temperature stability of diode lasers [2]; (iii) the lateral quantum confinement removes prohibition of the optical transitions with polarization in the photodetector plane, which provides for the possibility of photon absorption at normal incidence without using additional gratings and reflectors; and (iv) large expected lifetimes of photoexcited carriers, which are due to the so-called “phonon bottleneck effect” [6]. The last property is related to the fact that the scattering on *LO*-phonons is suppressed when a distance between discrete levels differs significantly from the phonon energy.

Until recently, optical measurements were performed for the most part in low-density systems of QDs, where the interaction effects can be ignored [7–9]. Basically, the optical measurements in dense QD arrays must reveal some new phenomena related to a large-scale Coulomb interaction. In a high-density system of atomic islands, where the distance between islands is comparable with their dimensions ($L \sim 10$ nm), the interaction between charge carriers localized in the neighboring QDs becomes a significant factor determining, in particular, the dark conductivity along the Ge layers containing QDs [10]. The characteristic magnitude of this interaction, $U \approx e^2/4\pi\epsilon\epsilon_0 L \approx 10$ meV (where ϵ_0 is the permittivity of vacuum and ϵ is the relative permittivity of the medium), is comparable with room-temperature kT and is no longer negligibly small in comparison to the characteristic energy separation of levels (70–80 meV) in the quantum-confined system [3, 11].

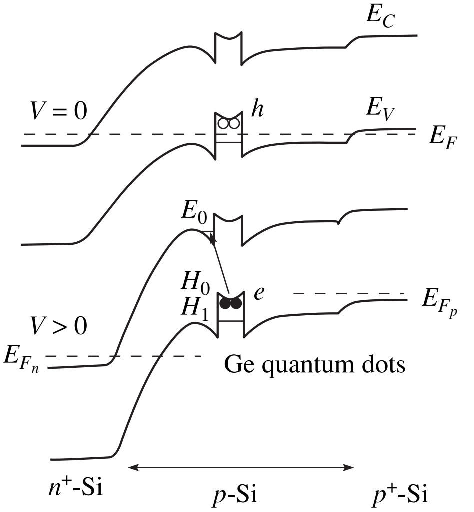

Fig. 1. Schematic diagrams of the energy band structure of a p^+–p–n^+-Si diode with Ge quantum dots under conditions of zero and reverse bias. The arrow indicates the optical transition accompanied by the formation of an implicit exciton in the ground state.

The purpose of this work was to study the process of light absorption and photoconductivity in the region of photon energies corresponding to interband and interlevel transitions in Ge/Si heterostructures with QDs. The measurements were performed in the geometry of normal incidence of the excitation light wave (propagating perpendicularly to the sample surface). The paper is arranged as follows. Section 2 presents the results of investigation of the light absorption by excitons in QDs (at a wavelength of $\simeq 1.6$ μm). Based on these experimental data, it is concluded that the formation of charged exciton complexes (each comprising two holes and one electron), as well as of the two-exciton complexes in the QDs of type II leads to an increase in the energy of exciton transition, which is explained by the spatial separation of the electron and hole in these QDs. Section 3 is devoted to the light absorption and photoconductivity in the region of photon energies corresponding to the transitions between ground and excited states of holes in Ge quantum dots (photon wavelength, $\simeq 15$–18 μm). We observed a shortwave shift of the interband resonance and the narrowing and shape change of the absorption band accompanying an increase in the concentration of carriers in the ground state of QDs. This is explained by depolarization of the external electromagnetic wave due to interaction with the collective charge density oscillations in the lateral direction. It is shown that the hole lifetime in the excited state is comparable to the values typical of two-dimensional quantum

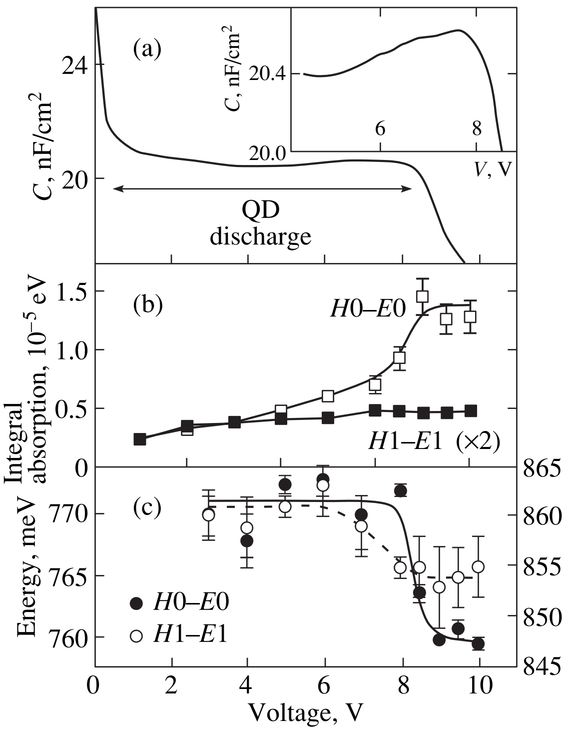

Fig. 2. The plots of (a) room-temperature capacitance of a p^+–p–n^+-Si diode with Ge quantum dots measured at 100 kHz, (b) integral IR absorption measured in the region of *H*0–*E*0 and *H*1–*E*1 exciton transitions, and (c) energy of the exciton transitions *H*0–*E*0 (left ordinate scale) and *H*1–*E*1 (right ordinate scale) versus reverse bias voltage amplitude (modulating the QD occupancy by holes).

wells, which casts some doubt concerning validity of the phonon bottleneck effect.

2. EXCITONS AND EXCITON COMPLEXES IN QUANTUM DOTS OF TYPE II

2.1. The Method of Electron Occupancy Modulation

Effects of the charged state of QDs on the interband optical transitions were studied by the method of electron occupancy modulation. Previously, this technique was successfully employed for the investigation of luminescence [12] and reflectance [13] in the arrays of QDs based on InAs/GaAs and $In_xGa_{1-x}As$/GaAs systems. According to this approach, a layer of Ge atomic islands is introduced into the base region of an n^+–p–p^+-Si diode. In this structure, the hole level occupancy in the QDs is controlled by a bias voltage applied to the diode (Fig. 1). Once a level in the valence band of Ge is filled with holes, the transition to the conduction band from this level is blocked; should the bias voltage be such that the QD is neutral (i.e., contains no holes), an electron in the valence band may absorb a photon to form an indirect exciton. By applying a time-modulated bias voltage (leading to the time-modulated QD occupancy by the holes) and measuring the IR photon transmission through the QD structure at the modulation frequency, we can obtain the spectrum of absorption due to the quantum dots. The measurements at various modulated bias amplitudes allow us to study the effect of the charge on islands (QDs) on the corresponding transition energies. An advantage of this method is that the lock-in detection suppresses the nonmodulated system response (related to the absorption in substrate, atmosphere, etc.).

The samples were grown by molecular beam epitaxy (MBE) on (001)-oriented Si substrates with a resistivity of 4.5 Ω cm. The layers of Si preceding and following the Ge layer were grown at 800 and 500°C, respectively. The growth rates were controlled on a level of 0.3 nm/s for Si and 0.03 nm/s for Ge. The layer of Ge islands with a rated thickness corresponding to 10 atomic monolayers (1 monolayer = 1.4 Å) was formed at 300°C in the middle of a 1-μm-thick *p*-Si layer (boron-doped to 5×10^{16} cm^{-3}). The bottom (buried) contact was provided by depositing a 50-nm-thick p^+-Si layer (boron-doped to 2×10^{18} cm^{-3}). The heterostructure growth was completed by forming an n^+–p junction, which was provided by a a 50-nm-thick n^+-Si layer (Sb-doped to 1×10^{19} cm^{-3}). Previously, we studied Ge quantum dots in these structures by the methods of scanning tunneling microscopy and high-resolution transmission electron microscopy. It was established that Ge islands have the shape of pyramids with a 15 × 15 nm base and a 1.5 nm height [14]. The QD size scatter was characterized by a standard deviation not exceeding 20%.

The IR absorption measurements were performed at room temperature in the normal incidence geometry. The radiation transmitted through a sample was monitored by a germanium photodetector. The occupancy of QDs by holes was modulated by applying rectangular reverse bias pulses at a frequency of 700 Hz. In order to determine the necessary pulse amplitude and establish a relationship of this value to the charged state of QDs, we have measured the capacitance-voltage (*C*–*V*) characteristic of the heterostructure at a frequency of 100 kHz. The results of these measurements are presented in Fig. 2a. At a zero bias, the QDs are filled by holes and possess a positive charge. The space charge region occurs in *p*-Si above the Ge layer. As the bias amplitude increases to $V \approx 0.5$ V, the boundary of the space charge region reaches the QD array and the holes begin to leave the energy levels of islands. Here, the capacitance *C* of the structure is virtually independent of the voltage *V* and is entirely determined by the depth of QDs. We can estimate this depth using the approximate relationship $x \approx \epsilon\epsilon_0/C$. For $C \approx 20$ nF/cm^2, this yields $x = 0.5$ μm in agreement with the value stipulated by the growth procedure. At a bias voltage exceeding 8.5 V, the holes completely leave the QDs (making the ground state empty). The QDs become electrically neutral and the structure capacitance begins to decrease again because the space charge region penetrates into silicon. Note a weakly pronounced maximum in the *C–V* curve at $V = 6–8$ V (see the inset in Fig. 2a), which a characteristic feature of the δ-shaped spectrum of the density of states in islands [15]. Based on these data, subsequent measurements of the differential absorption of QDs were performed using the QD level occupancy modulated by the reverse bias voltage varying from zero to $V = 2–10$ V.

2.2. The Interband Optical Absorption

Figure 3 shows the differential absorption spectra measured for various values of the bias modulation amplitude. In the region of energies from 650 to 850 meV (below the fundamental absorption edge of Si equal to ~1.12 eV), we observe an absorption band with a width of ~70 meV. Previously [14], we observed a similar maximum (at 730–750 meV) in the spectra of photocurrent measured in a silicon *p–i–n* diode with Ge quantum dots. Note that the same energy region (~800 meV) contains a peak (with close width) of the photoluminescence due to the exciton transition in Ge/Si(001) quantum dots [16–19]. An analysis of the shape of the absorption maximum showed that a good approximation is provided by a superposition of two Gaussian components (Fig. 4).

We assign the absorption peaked at 760–770 meV to the electron excitation from the valence band of Ge quantum dots to the conduction band of Si, which leads to the formation of the ground state of an indirect exciton (with a hole in the ground state *H*0 of QD and an electron localized in the ground state *E*0 of Si near the heterojunction). The absorption band of lower intensity at 850–860 meV is attributed to the excited state of exciton (with both hole and electron in the excited states *H*1 and *E*1, respectively). A large width of the bands is related to fluctuations of the Ge island dimensions.

Photons with higher energies excite the transitions to localized states of the conduction band, which increases the probability of absorption. Certain features on this background are probably related to participation of the higher excited states of excitons.

The assignment of the *H*0–*E*0 absorption band to the interband transitions in QDs is confirmed by analysis of the integral absorption intensity *I* as a function of the bias voltage modulation amplitude (Fig. 2b). The area under the peak was determined by approximating the absorption band shape with a Gaussian curve. For the exciton transition,

$$I = he^2 nf/2m_0\epsilon_0 c(1+\sqrt{\epsilon}), \qquad (1)$$

where *f* is the oscillator strength, *n* is the concentration of carriers involved in the absorption, m_0 is the free electron mass, and *c* is the speed of light. Since $I \propto n$, the plot of $I(V)$ directly reflects a change in the degree of QD occupancy by holes caused by variation of the reverse bias applied to the diode. In the region of $V > 8.5$ V, the integral intensity ($I \approx 1.4 \times 10^{-5}$ eV) is independent of the bias voltage because all QDs are neutral (this situation is most favorable for the interband transitions). On decreasing the modulation amplitude, the integral absorption decreases as well because holes begin to occupy the ground state of QDs and suppress the interband transitions. This scenario completely agrees with the *C–V* characteristic of the heterostructure presented in Fig. 2a.

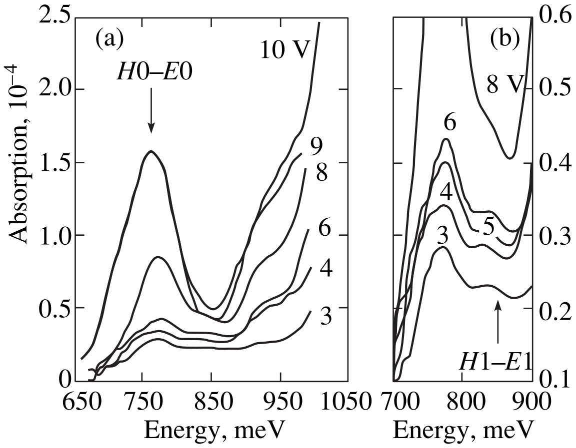

Fig. 3. Optical absorption spectra of a $p^+–p–n^+$-Si diode structure with Ge quantum dots measured at various values of the reverse bias voltage (indicated in volts by figures at the curves): (a) *H*0–*E*0 transitions; (b) *H*1–*E*1 transitions.

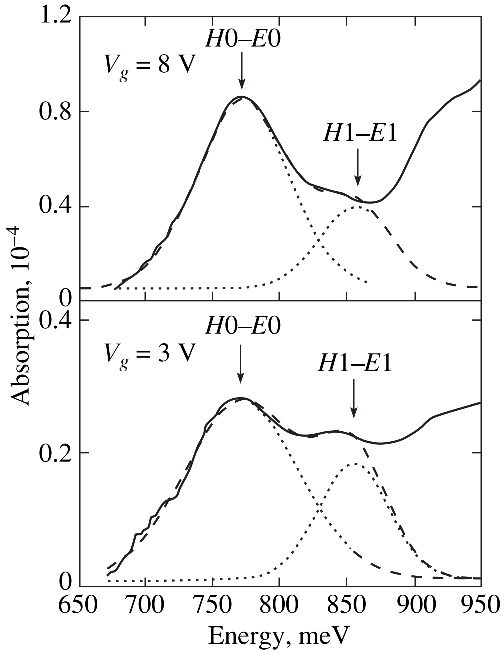

Fig. 4. Low-energy region of the absorption spectra corresponding to exciton transitions measured at two values of the reverse bias (gate) voltage (3 and 8 V). Solid curves represent the experimental spectrum, dashed curves show the results of decomposition into two Gaussian components.

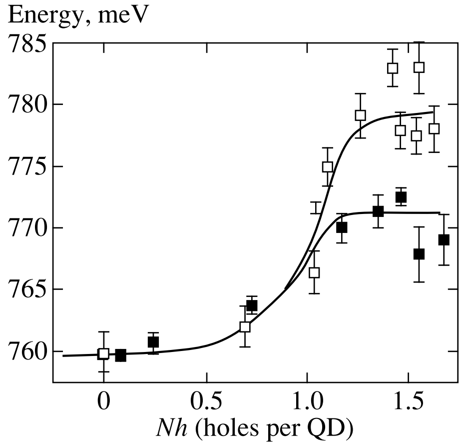

Fig. 5. Plots of the exciton transition energy versus average number of holes (occupancy) in the ground state of QDs. Black squares refer to a situation where the holes injected into QDs under the action of applied bias (no illumination) form complexes of the exciton–hole type. Open squares correspond to the case of optical injection of electrons and holes into QDs at a fixed reverse bias of $V = 9$ V, which results in the formation of two-exciton complexes.

It should be noted that the area of the band corresponding to the excited state of excitons becomes almost constant when the bias voltage varies from 4 to 10 V, which is explained by the fact that, in this interval, the energy level corresponding to the excited state of the islands contains no holes.

The experimental values of the integral absorption measured for $V > 8.5$ V can be used for determining the oscillator strength f characterizing the exciton transition. Since the maximum number of holes present in the ground state of QDs is two, n is equal to the double density of QD (6×10^{11} cm^{-2}). Taking $I \approx 1.4 \times 10^{-5}$ eV, we obtain $f = 0.5$. This value is about 1/20 of the oscillator strength for direct excitons in the InAs/GaAs system ($f = 10.9$ [21]), which is a consequence of the spatial separation of electron and hole in the QD with indirect exciton. In addition, the absolute value of the absorption intensity ($\alpha = 1.6 \times 10^{-4}$ at $V = 10$ V) can be used to estimate the equivalent cross section of interband absorption in Ge quantum dots, which yields 2.5×10^{-16} cm^2.

2.3. The Exciton–Hole Interaction

When the bias voltage decreases to 8.5 V and below (Fig. 2c) and the holes are injected into Ge islands, the energy of the exciton absorption peak exhibits an 11 meV shift toward shorter wavelengths. This result is opposite to that observed previously for the direct (in real space) excitons in InAs/GaAs quantum dot arrays [12, 21], where the exciton transition energy decreased upon the formation of charged complexes. We estimated the average hole occupancy N_h for the ground state of QDs at various bias voltages using the oscillator strength evaluated above and the experimental values of integral absorption. The N_h values were calculated taking into account that the hole injection into an island decreases by one the number of possible interband transitions (the total number of transitions related to the ground state at each QD is two). A plot of the exciton transition energy versus N_h is presented in Fig. 5 (black symbols). Here, an important point is that the energy sharply increases when one hole is injected into the ground state of QDs and then only slightly varies with further increase in the hole concentration.

It must be noted that QDs occur in the region of sufficiently strong electric field. Under the conditions studied, the field strength may reach up to 10^4 V/cm and lead to a shift of the quantum confinement levels according to the quantum Stark effect [22]. However, we can present at least three arguments against using the Stark effect in explaining the observed shift. First, the Stark shift would monotonically increase with the electric field strength, whereas we observe a steplike change in the transition energy precisely at the bias voltage producing a change in the charged state of QDs. Second, the magnitude of the Stark effect should be obviously very small because the island size in the vertical direction (QD height) is only 1.5 nm. Indeed, Miesner *et al.* [23] observed a Stark shift of about 60 meV for the levels of Ge/Si structures with 7.5-nm-high quantum dots for a field strength on the order of 10^4 V/cm. Since the shift magnitude is proportional to L^4, where L is the quantum well size [24], the resonance shift in our structures must be as small as 0.1 meV. Third, the electric field shifts the hole energy level in Ge/Si heterostructures with QDs toward delocalized states in the valence bands [23]. This implies an increase in the interband transition energy–in contrast to our experimental data. Thus the shift in the exciton energy observed in our experiments cannot be interpreted within the framework of the quantum Stark effect.

Let us consider in more detail the interactions between all particles in the system during the exciton absorption. Upon the exciton excitation, a singly-charged QD features the formation of an exciton–hole complex with an electron bound near two holes in the ground sage. One of these holes is injected due to the bias application and the other hole is generated when an electron passes from the valence band of Ge to the conduction band of Si. There are two additional contributions to the energy of charged exciton. The first is the energy of repulsion between injected and photoexcited holes (E_{hh}). The second is the energy of attraction between the injected hole and the photoexcited electron (E_{eh}). The resulting additional energy for the charged exciton is determined as the difference $\Delta E_{ex-h} = E_{hh} - E_{eh}$. Since two holes in the ground sate exhibit an antiparallel spin orientation, the contribution due to exchange interaction is absent [25]. In the case of direct excitons, the electron–hole interaction dominates and the absorption band of charged exciton exhibits a "red" (longwave) shift [21]. The spatial separation of carriers in the QDs of type II allows us to expect that the energy E_{eh} is smaller than E_{hh} and the exciton absorption band would shift toward shorter wavelengths upon the charged complex formation.

Taking into account experimental values of the exciton shift $\Delta E_{ex-h} = 11$ meV and $E_{hh} = 36$ meV [26], we may estimate the electron–hole interaction energy in QDs as $E_{eh} = 25$ meV. This value agrees with the results of self-consistent-field (SCF) calculations of the exciton binding energy in the structures studied (see Section 2.5 below). Note that this value is almost ten times greater as compared to the free exciton energy in bulk Ge and is approximately two times the exciton binding energy in bulk Si. This result, theoretically predicted for the quantum dots of type II by Rorison [27], is related to two factors. First, the spatial localization of at least one particle (in our case, a hole) leads to correlated motion of the second particle (electron). Second, the final height of the potential barrier in a real system (energy band breaks) leads to the penetration of particles into the barrier regions, which results in a considerable overlap of their wavefunctions.

It should be also noted that a shift in the absorption maximum corresponding to the excited exciton state is much less pronounced when a hole appears in the ground state of QDs (Fig. 2). This is related to an obvious fact that, because of a smaller overlap of the wavefunctions, the energy of interaction between a hole in the excited state and a hole in the ground states is lower than the energy of interaction between two holes in the ground state.

2.4. The Exciton–Exciton Interaction in Quantum Dots

Additional evidence for assigning the absorption maximum in the region of 760 meV to an exciton transition in the QD was obtained in experiments with the optical pumping of diode structures with the light of a halogen lamp. Figure 6 shows the absorption spectra measured at a fixed bias modulation amplitude ($V = 9$ V) and various pumping intensities. Under the conditions of additional interband optical excitation, the levels of holes in QDs and those of electrons in Si near the heterojunction are occupied by nonequilibrium charge carriers. At a sufficiently high illumination intensity, the ground state levels are completely filled and the *H*0–*E*0 exciton transition under the action of probing IR radiation becomes impossible (blocked). Indeed, the data presented in Fig. 6 show evidence that the absorption intensity drops with increasing intensity of the pumping radiation.

Figure 5 (open symbols) shows a plot of the exciton transition energy versus the average number of holes (per QD) generated by the interband optical pumping. As seen, the optical carrier generation leads to a more pronounced shift of the absorption maximum (in the same direction) as compared to the bias-induced hole production. A difference between the experiments with electric and optical pumping consists in that the probing (IR) photon absorption in the latter case takes place in a QD with exciton excited by the additional illumination. Thus, the experiment with illumination corresponds to the case of two excitons in the same QD, one of which is excited by the optical pumping and the other is generated by the probing radiation. In comparison with the isolated exciton, the interaction between two excitons increases the energy by $\Delta E_{ex-ex} = E_{hh} + E_{ee} - 2E_{eh}$, where E_{ee} is the energy of interaction between two electrons bound at a QD by the Hartree potential of two holes. Similarly to the above case, the spatial separation of the exciton components results in that $E_{hh} > E_{eh}$, $E_{hh} > E_{eh}$, and $\Delta E_{ex-ex} > 0$. This means that two excitons formed in the same QD of a heterostructures of type II exhibit repulsion and a be-exciton molecule is not formed.

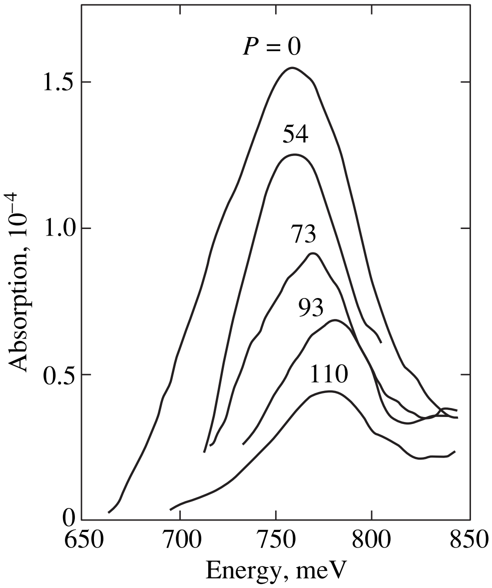

Fig. 6. The exciton optical absorption band measured at various intensities of additional optical pumping *P* (indicated in mW/cm^2 by figures at the curves).

2.5. Self-consistent Calculation of the Energy Structure of Indirect Excitons

The wavefunctions and energy spectra of electrons and holes in indirect excitons for a Ge pyramid with a 15×15 nm base and 1.5 nm height were determined by numerical modeling. The pyramid occurs in a continuous 5-monolayer (7-Å-thick) layer of Ge surrounded by Si. The substrate and pyramid orientations corresponded to the experimental situation (see Section 2.1). The *z*-axis direction is parallel to the principal symmetry axis of the pyramid; the *x*- and *y*-axes are lying in the pyramid base (continuous Ge layer). In the first stage, we calculated the distribution of elastic stresses in this model structure. The calculation was performed

Energy parameters of exciton and exciton complexes

Source of data	E_l, meV	E_{eh}, meV	ΔE_{ex-h}, meV	E_{ex-ex}, meV
Experiment	–	25	$+(11 \pm 3)$	$+(19 \pm 5)$
Calculation	38	31	+9.7	+10.2

Note: sign (+) indicates a shortwave shift.

within the framework of the valence force field (VFF) model with a Keating potential [28], based on the elastic force potential considered as a function of interatomic distances and angles. An advantage of this model as compared to the continuum theory is the possibility of determining real atomic positions. The results of the model calculations showed that a most stressed region in the vicinity of the pyramid is that outside the apex, while the apex region inside the pyramid is characterized by most relaxed elastic stresses. Taking into account the obtained 3D distribution of elastic deformations inside and outside the pyramidal QD and the known deformation potentials of Si and Ge [29], we calculated the valence and conduction band breaks at the Ge/Si heterojunction. In particular, it was established that the lowest minima in the stressed structure are represented by two Δ-valleys oriented in the [001] and $[00\bar{1}]$ directions.

In the second stage of modeling, we solved a set of two 3D Schrödinger equations for electron and hole in the effective mass approximation. The electron and hole were considered as moving in a self-consistent field created by the band breaks and the second particle. The system Hamiltonian was written in the following form:

$$\hat{H} = \hat{H}_e + \hat{H}_h + \hat{H}_{eh}, \tag{2}$$

where the terms $\hat{H}_e$ and $\hat{H}_h$ include operators of the kinetic and potential energy of noninteracting electron and hole, respectively, and $\hat{H}_{eh}$ describes the electron–hole interaction. For modeling the exciton–hole or exciton–exciton complexes, the set of equations was supplemented with one or two self-consistent equations for the hole or the hole and electron, respectively. The interaction between particles was described by a Coulomb potential:

$$U_{ij}(\mathbf{r}_i, \mathbf{r}_j) = e^2/4\pi\epsilon\epsilon_0|\mathbf{r}_i - \mathbf{r}_j|.$$

The exciton wavefunction was written in the Hartree form as

$$\psi_{ex}(\mathbf{r}_h, \mathbf{r}_e) = \psi_h(\mathbf{r}_h)\psi_e(\mathbf{r}_e),$$

where $\psi_h(\mathbf{r}_h)$ and $\psi_e(\mathbf{r}_e)$ are the wavefunctions of hole and electron, respectively. A solution to the Schrödinger equation was obtained on a network with a step equal to half of a lattice constant (0.27 nm) containing 80 × 80 × 50 nodes with a Dirichlet boundary conditions. The calculation was performed for the following energy band parameters. The conduction band break between the corresponding Δ-minima of unstressed Ge and Si was taken equal to 340 meV; the analogous valence band break was taken equal to 610 meV. The effective masses of carriers were $m_z = 0.92m_0$ and $m_{xy} = 0.19m_0$ in the conduction band and $m_z = 0.2m_0$ and $m_{xy} = 0.39m_0$ in the valence band.

The experimental and calculated values of the electron localization energy on the exciton formation E_l, the exciton binding energy E_{eh}, and the exciton transition energy shifts for the exciton–hole (ΔE_{ex-h}) and exciton–exciton (ΔE_{ex-ex}) complexes in comparison with the energy of a single exciton in QD are summarized in the table. As seen, the theoretical and experimental data are in satisfactory agreement in all respects. The modeling gives a somewhat smaller exciton transition energy shift ΔE_{ex-ex} as compared to the experimental value. This difference can be explained by the neglect of a contribution due to the interaction of electrons localized in the neighboring QDs. The calculations show that $E_l = 38$ meV, the main fraction of this value being due to the electron–hole interaction $\left\langle \psi_{ex} \middle| \hat{H}_{eh} \middle| \psi_{ex} \right\rangle =$ 31 meV and the remainder $\left\langle \psi_{ex} \middle| \hat{H}_e \middle| \psi_{ex} \right\rangle = 7$ meV, due to a potential well formed at the Ge/Si interface as a result of the inhomogeneous strain distribution.

Figure 7a presents the calculated profile (in the direction of the *z*-axis passing through the pyramid apex) of a potential binding electron and hole in an exciton. Figure 7b shows the absolute values of the electron and hole wavefunctions in the cross section of a quantum dot. As is seen, an electron in the ground state is localized in the vicinity of the pyramid apex in silicon (the region of maximum compression in the vertical direction and maximum extension in the lateral direction), while a hole in the ground state is localized at the pyramid base. The wavefunction of the ground state of the hole is characterized by a 15% overlap with that of the ground electron state. If a direct exciton in the InAs/GaAs heterosystem with an 80% overlap [30] has an oscillator strength of $f = 10.9$ [21], the indirect exciton with a 15% overlap in our system can be expected to have $f \approx 0.4$, which is close to the experimental value ($f = 0.5$). This result suggests that a relatively high oscillator strength observed for indirect excitons in QDs of the Ge/Si heterostructure studied is related to the penetration of electrons and holes into the barrier regions.

The structure of a complex composed of two excitons bound at a common quantum dot is illustrated in Fig. 8. It was found that, upon the excitation of two excitons, the Coulomb repulsion of electrons leads to their separation in space; as a result, the second electron is localized in Si at the rear side of QDs, that is, at the boundary between Si and the continuous Ge layer.

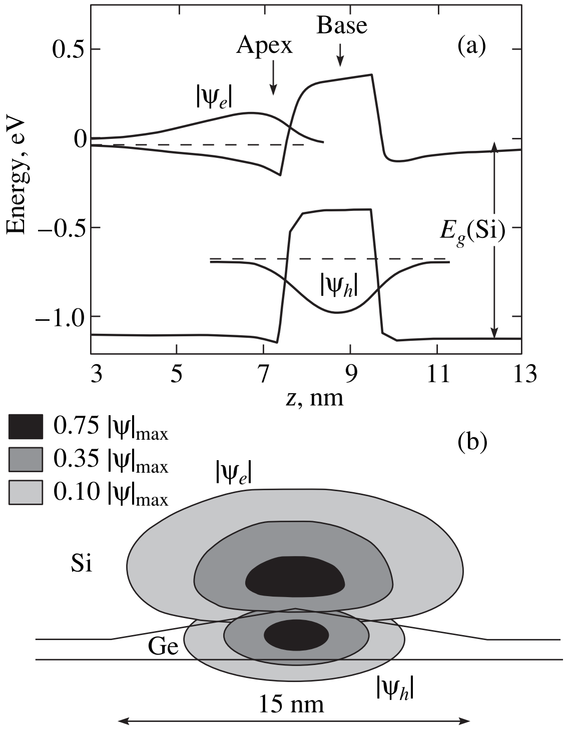

Fig. 7. (a) The calculated profile (in the direction of the z-axis passing through the Ge pyramid apex) of a potential binding electron and hole in an indirect exciton. (b) A 2D map of the absolute values of the electron $|\psi_e|$ and hole $|\psi_h|$ wavefunctions in the cross section of a quantum dot. The boundaries of differently shadowed regions correspond to the wavefunction amplitude decreasing to 75, 35, and 10% of the maximum level.

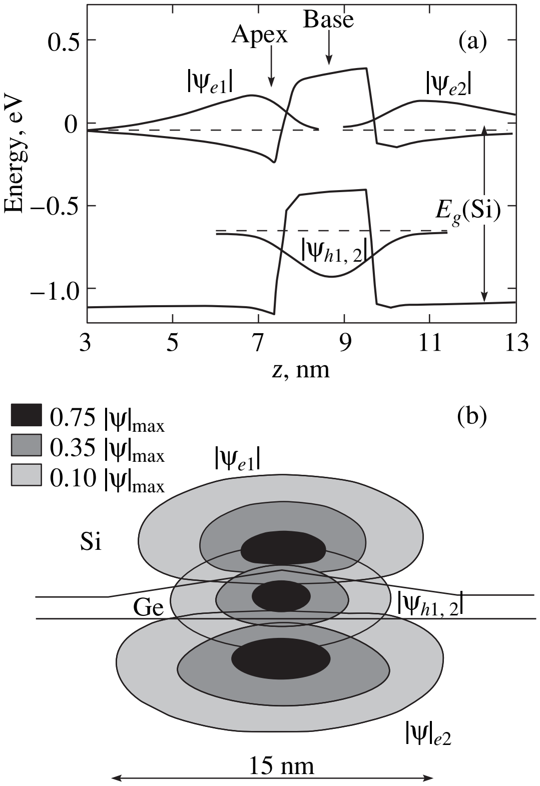

Fig. 8. (a) The calculated potential profile and (b) a 2D map of the absolute values of the electron $|\psi_e|$ and hole $|\psi_h|$ wavefunctions in the cross section of complex of two excitons bound at a common quantum dot. The boundaries of differently shadowed regions correspond to the wavefunction amplitude decreasing to 75, 35, and 10% of the maximum level.

3. INTERLEVEL OPTICAL TRANSITIONS IN MULTILAYER STRUCTURES WITH QUANTUM DOTS

3.1. Collective Phenomena in 2D Systems

The motion of electrons in 2D systems is confined in the transverse direction (i.e., along the z-axis). The IR radiation polarized in this direction can be absorbed by a 2D electron gas, which leads to the excitation of transitions between subbands in the quantum valley. As is known, the energy of the inter-subband absorption may significantly differ from the distance between single-particle quantum-confinement levels, provided that the carrier concentration in the subband is sufficiently high (10^{11}–10^{12} cm^{-2}) [31]. The difference is explained by the appearance of collective electron of spin density oscillations under the action of the incident electromagnetic wave, which results in a shift of the corresponding resonance. One of such collective effects is the resonance screening of an external electric field by self-sustained electron density oscillations related to a long-range dynamic electron–electron interaction (depolarization effect). In experiment, the depolarization effect is manifested by a shift of the intersubband resonance toward shorter wavelengths with increasing carrier concentration in the first subband. In systems with a nonparabolic binding potential, this effect is additionally manifested by narrowing of the resonance line and by a change in the line shape [32].

Investigation of the arrays of quantum dots, in which the charge carriers are additionally confined in the lateral direction, posed a question as to whether there exist collective excitations polarized in the plane of the QD structure. Recently, Metzner and Döhler [33] pointed out that a dynamic multiparticle Coulomb interaction must be also operative between electrons oscillating in the lateral direction. However, Sauvage *et al.* [8], employing the light polarized in the plane of InAs/GaAs layers containing QDs, observed the interlevel transitions in this structure but did not reveal any depolarization shift. The reason is very simple: the layer density of QDs (4×10^{10} cm^{-2}) was insufficient for providing a manifestation of the electron–electron interaction and for binding the optical excitations in a collective mode. In this context, it was especially important to study the Ge/Si structures with a QD density in the array reaching 3×10^{11} cm^{-2}.

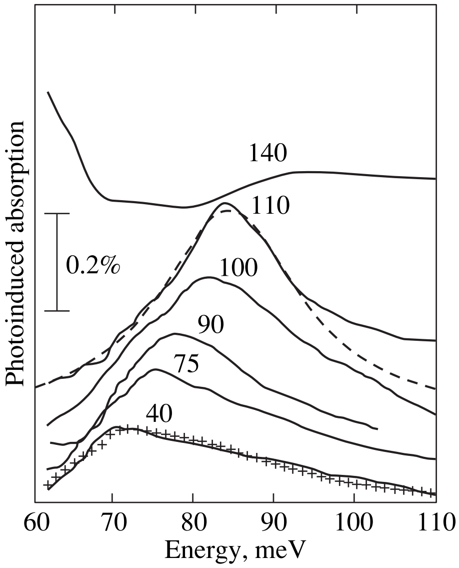

Fig. 9. The photoinduced IR absorption spectra of interlevel transitions in Ge/Si quantum dots measured at various optical pumping power density (indicated in mW/cm^2 by figures at the curves). For clarity, the curves are shifted upward with a step of 5×10^{-4}. An increase in the optical pumping power density corresponds to the growing hole concentration in the ground state of Ge nanocrystal ensemble. Crosses show the result of modeling of the absorption band for $P = 40$ mW/cm^2 using Eqs. (3) and (4) with the asymmetry parameter $\gamma = 1.25$. Dashed curve presents the approximation of the absorption band for $P = 110$ mW/cm^2 by the Lorentz function according to Eq. (5) describing the collective mode excitation.

3.2. The Method of Photoinduced Absorption

The sample structures were grown on *n*-Si(001) substrates with a resistivity of 5 Ω cm under the conditions analogous to those described in Section 2.1. A difference was in the number of Ge island layers, which was equal to ten. The QD layers were separated by 30-nm-thick Si spacers. The concentration of phosphorus (dopant) in the epitaxial Si layers was about 2.5×10^{16} cm^{-3}.

Since the doping level was relatively low, the islands contain virtually no free carriers (holes) and exhibit no interband transitions. Occupation of the ground state levels with holes can be provided by two methods. First, by means of the field effect, whereby a gate is formed in the sample structure and the corresponding potential is applied. Second, by means of an additional interband optical excitation ensuring a large concentration of nonequilibrium charge carriers. A disadvantage of the first method is the presence of a strong electric field and, hence, of the unavoidable (more or less pronounced) stark effect. On the other hand, electrons excited by the optical pumping may affect the energy spectrum of holes in QDs. However, the results of numerical calculations of the exciton structure (see Section 2.5) showed that a change in the hole energy induced by the electron field does not exceed 0.1 meV. For this reason, we injected holes into QDs by means of a high-power optical pumping with modulated radiation of a halogen lamp (Fig. 9). After passage through an interference filter, the pumping radiation exhibited a maximum intensity at a wavelength of 0.67 μm (photon energy $h\nu = 1.85$ eV). The integral pumping power density was measured using a Si photodiode and could be varied from 40 to 140 mW/cm^2. The samples were probed by IR radiation from a Globar source. The probing beam transmitted through a sample was detected with a lock-in bolometer circuit tuned to the pumping modulation frequency (1.7 Hz). Similarly to the experiments described above, the IR absorption measurements were performed in the normal incidence geometry. The photoinduced absorption spectra were normalized to the reference bolometer signal intensity measured without additional illumination of the sample.

It was very important to know the concentration of holes optically injected into quantum dots. There are two channels for the photoproduction of holes during interband optical excitation. The first is the hole generation immediately in Ge. In a linear regime, the 2D density of holes in a Ge layer with QDs can be estimated as $n = G\tau_{Ge}$, where $G = \alpha P/h\nu$ is the carrier generation rate, α is the absorption probability, and τ_{Ge} is the time of interband recombination in Ge. For $\alpha \approx 2 \times 10^{-4}$ (see Section 2.2), $P \approx 100$ mW/cm^2, $h\nu = 1.85$ eV, and $\tau_{Ge} \approx 10$ μs [34, 35], we obtain $n \approx 5 \times 10^8$ cm^{-2}. This value is three orders of magnitude lower than the QD density (3×10^{11} cm^{-2}). Therefore, the optical generation of holes immediately in Ge cannot significantly affect the QD occupancy.

We must take into account that nonequilibrium carriers are generated not only in Ge, but in the surrounding Si as well (the penetration depth of photons with a wavelength of 0.67 μm in Si is ≈2 μm). Under the experimental conditions employed, the characteristic lengths of the system studied—the hole diffusion length L_D (typically, 100–1000 μm [36]) and the light attenuation depth d_a—obey the relationship $L_D \gg d_a$. For this reason, a considerable part of the photogenerated charge carriers is carried away by diffusion from the absorption region in silicon to be effectively trapped on the bound states of germanium QDs. In this situation, the concentration of holes optically injected into QDs is given by a simple relationship $n = P\tau_{Si}/h\nu$, where τ_{Si} is the lifetime of nonequilibrium holes in silicon. By measuring the kinetics of the intensity of light absorption by free carriers in analogous Si layers containing no QDs, we established that the latter quantity is $\tau_{Si} = 15$ μs (in agreement with the published data [37]). Since $\tau_{Si} \approx \tau_{Ge}$, the recombination of electrons and holes trapped on the QDs does not lead to a change in the concentration of holes in these islands. For $P = 100$ mW/cm^2, $h\nu = 1.85$ eV, and $\tau_{Si} = 15$ μs, we obtain $n = 5.1 \times 10^{12}$ cm^{-2}. Taking into account that the structure under consideration comprises 10 germanium layers with QDs and the QD density in each layer is 3×10^{11} cm^{-2}, we conclude that the optical pumping with a power density of

100 mW/cm^2 provides for an almost complete occupation of the ground state in QDs (two holes per island).

3.3. The Effect of Lateral Depolarization in Quantum Dot Arrays

Figure 9 shows the photoinduced absorption spectra measured at room temperature for various intensities of the optical injection. The absorption peak observed in the 70–90 meV energy interval (15–18 μm) corresponds to the hole transition from ground to excited state in QDs. Approximately the same energy separation (~75 meV) of the first two levels in germanium QDs was previously observed in experiments on the resonant tunneling in structures with a single layer of Ge islands [3]. The fact that the photon absorption is observed in the normal light incidence geometry is evidence of the lateral polarization of the hole states in QDs. The spectrum measured with a maximum optical injection intensity (140 mW/cm^2) exhibits a background absorption increasing with the wavelength, which is probably explained by the absorption related to free carriers in Si not trapped by QDs. The integral absorption intensity (area under curve) for $P < 140$ mW/cm^2 is proportional to the pumping power density (Fig. 10a). This fact indicates that recombination of the nonequilibrium carriers occurs in a linear regime and implies that the concentration of holes injected into QDs is a linear function of the optical pumping power density. At $P \approx 140$ mW/cm^2, the ground state is completely filled and the absorption intensity ceases to grow.

For a small concentration of holes in the islands, the absorption band has a clearly pronounced asymmetric shape: the absorption intensity drops sharply at lower energies and exhibits an extended "tail" on the side of higher energies relative to the peak. The asymmetric shape can be described within the framework of the following simple model. In the absence of collective effects, the interlevel resonance exhibits inhomogeneous broadening caused by fluctuations of the island size within the array. Let us make an obvious assumption that the distribution of islands with respect to size L is described by the Gaussian function (which is valid with high precision in all the known experimental situations),

$$D(L) = \frac{1}{\sqrt{2\pi}\sigma}\exp\left[-\frac{(L-L_0)^2}{2\sigma^2}\right], \qquad (3)$$

where L_0 is the average island size. The distribution of distances $D(E)$ between energy levels in QDs is connected to the island size distribution by the relationship $D(E) \propto D(L)(dE/dL)^{-1}$. In the case when the quantum confinement energy decreases with increasing QD size by the power law $1/L^\gamma$, we obtain

$$D(E) \propto D(L)/E^{(1+\gamma)/\gamma}. \qquad (4)$$

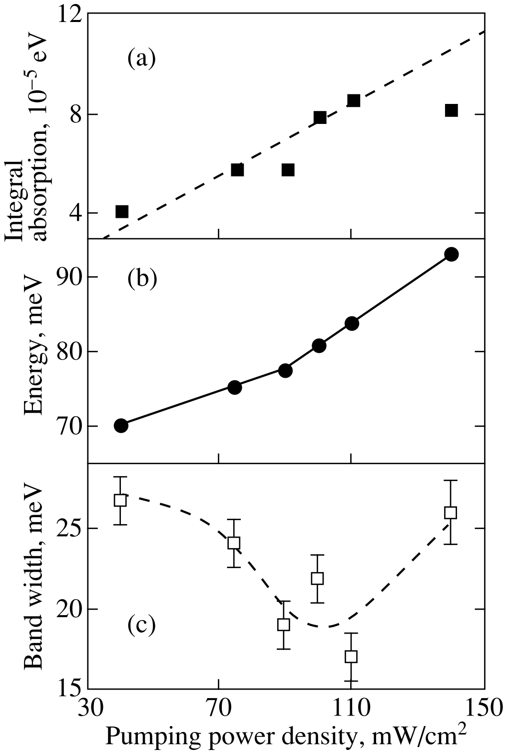

Fig. 10. The plots of (a) integral IR absorption intensity, (b) interlevel resonance energy, and (c) full resonance width at half maximum versus optical pumping power density.

With neglect of the energy dependence of the oscillator strength, the distribution (4) must describe the shape of the absorption band. The result of approximating the band measured at $P = 40$ mW/cm^2 by the curve corresponding to Eq. (4) is depicted by crosses in Fig. 9. The fitting parameters were the position of the band maximum and the asymmetry parameter γ. As seen, the resonance shape is adequately reproduced for $\gamma = 1.25$. This result indicates that the distance between energy levels varies with a QD size slower than $1/L^2$. Previously, this fact was repeatedly pointed out in calculations of the electron spectrum for nanoclusters of pyramidal and lenticular shapes [38–40].

As the hole concentration in the ground state of QDs increases, the absorption band shifts toward greater energy, decreases in width, and becomes more symmetrical (Fig. 10). For $P > 110$ mW/cm^2, the band width increases again because the interaction between QDs is screened by the free charge carriers. This behavior is indicative of the presence of collective electron density excitations polarized in the lateral direction. It must be noted that, in the case of electron QDs with a parabolic potential shape, the positions of interlevel absorption peaks depend neither on the number of electrons in the quantum well nor on the Coulomb interaction between these electrons (generalized Kohn theorem [41]). This is explained by the possibility of separating the motion of the center of mass and the relative motion of electrons. However, the Kohn theorem may fail to be valid in systems with a nonparabolic potential and in the QDs with holes [42]. In this case, an increase in the number of carriers on a given level is accompanied by the growth in their energy because of the electrostatic Coulomb interaction. Thus, if the observed band shift were related to the hole interaction, the energy of the transition from ground to excited state would decrease by E_{hh} upon occupation of the ground state. However, this contradicts our experimental results and we conclude that the observed shortwave shift cannot be related to the electrostatic charging of QDs with holes.

In the regime of collective electron modes, the individuality of QDs in the array is lost as a result of multiparticle effects. In this case, the width of the interlevel resonance must be determined only by the carrier lifetime in the excited sate, rather than by the island size fluctuations. The energy dependence of the absorption probability is described by the Lorentz function

$$\alpha = \frac{fNne^2\hbar}{2m_0\Gamma n_r c\epsilon_0}\frac{1}{1+[(E+E_0)/\Gamma]^2}, \qquad (5)$$

were $N = 10$ is the number of quantum dot layers, Γ is the rate of the excited carrier relaxation to the ground state (determined by the scattering mechanism), and n_r is the index of refraction. By approximating the experimental absorption band measured at $P = 110$ mW/cm^2 with a curve according to Eq. (5) (dashed curve in Fig. 9), we determined the full resonance width at half-maximum $2\Gamma = 17$ meV and the oscillator strength $f = 0.95$. The width $2\Gamma = 17$ meV corresponds to the hole lifetime in the excited state $\tau_{ex} = \hbar/\Gamma = 0.8 \times 10^{-13}$ s, which is also a typical value for 2D systems [43]. The presence of effective relaxation is evidence that the phonon bottleneck effect does not play any significant role for the interlevel transitions in QDs. Previously, an analogous conclusion was derived from the analysis of exciton transitions in InAs/GaAs quantum dots [2]. In our case, this behavior can be explained by the proximity of the interlevel resonance energy (~80 meV) to a double value of the *LO*-phonon energy in Ge (≈40 meV), which must simulate the two-phonon scattering processes.

As noted above, the optical transitions are often characterized by the equivalent absorption cross section in addition to the oscillator strength and lifetime. Taking into account the absorption band amplitude (4×10^{-3} for the system with 10 QD layers) and the carrier concentration in each QD layer (5×10^{11} cm^{-2}, see Section 3.2), we estimate the absorption cross section at 8×10^{-16} cm^2. Note that a significantly smaller value (1.6×10^{-16} cm^2) was obtained previously for the interlevel hole transitions in InAs/GaAs quantum dots [8].

The experimental value of the oscillator strength $f = 0.95$ corresponds to a dipole length of $\langle x\rangle = \sqrt{\hbar^2 f/2m_0(E_1 - E_0)} = 0.7$ nm in the sample plane for $E_1 - E_0 \approx 70$ meV. We performed a theoretical analysis of the polarization selection rules for the main interlevel transition in a tight binding approximation using $sp^3d^5s^*$ atomic orbitals. In calculating the optical transitions, we also took into account the spatial distribution of elastic deformations in the structure studied [28]. It was found that the hole transition from ground to excited state has a nonzero matrix element only in the lateral direction and is characterized by an oscillator strength of $f = 0.7$ and a dipole length of $\langle x\rangle \approx 0.9$ nm, in agreement with experimental data.

3.4. Photoconductivity in the Region of Interlevel Transitions

The photoconductivity was studied in a multilayer sample structure with eight QD layers grown on a highly doped p^+-Si substrate, which also served as the bottom electric contact. The top contact was obtained by depositing a 50-nm-thick layer of p^+-Si doped with boron to $\approx 10^{19}$ cm^{-3}. The thickness of Si regions separating the Ge layers was 110 nm. Within a 10-nm distance from each Ge layer, Si was δ-doped with boron at a layer concentration of 6×10^{11} cm^{-2}, which ensured nearly complete filling of the island ground state with holes. The photoconductivity measurements were performed in the vertical geometry. The temperature dependence of the dark conductivity within the ohmic region of the current–voltage curve in these structures follows the activation law with an activation energy close to the depth of the ground energy level of holes (~400 meV). When the applied voltage increased above 0.1 V, the current exhibited a quadratic dependence on the voltage explained by the hole injection into the first excited state. In this regime, the conductivity activation energy decreased to ~300 meV, which is actually close to the ionization energy of the excited state in charged Ge quantum dots [44].

Figure 11 shows the spectra of photoresponse measured at various applied voltages. The curves exhibit two photoconductivity peaks: the low-energy peak corresponds to the hole transitions from the ground to the first excited state, and the high-energy peak apparently reflects the transitions to a third excited level of QDs. The energy positions of the peaks agree with the distances from the first to second and from the first to third levels determined previously for Ge quantum dots by the method of resonance tunneling spectroscopy [3]. The appearance of photoconductivity in the vertical geometry of the experiment is determined by two processes. The first is the photoexcitation of holes from the ground to excited state. The second is the thermal ionization of the excited level, which transfers the hole to the band of delocalized states and allows it to contribute to the photocurrent.

Figure 12 shows the behavior of the photoconductivity amplitude as a function of the applied voltage. In the region of voltages above 0.4 V, the signal intensity begins to decrease because holes are accumulated in the

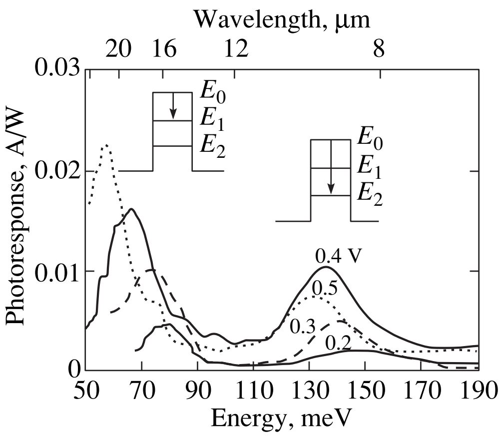

Fig. 11. The photoconductivity spectra measured in the vertical geometry at various applied voltages (indicated in volts by figures at the curves). The ground state of QDs is filled with holes as a result of δ-doping. At an applied voltage above 0.1 V, holes are injected into the excited state. Insets in the top part show the optical transitions of holes in the valence band corresponding to the observed photocurrent peaks.

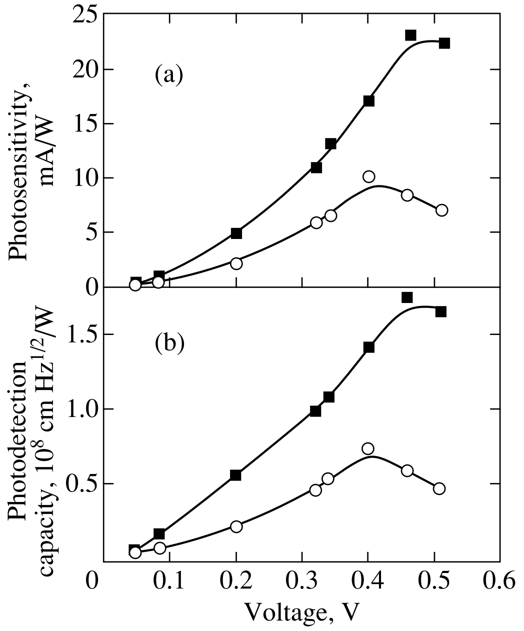

Fig. 12. The plots of (a) photoconductivity amplitude (photosensitivity) and (b) photodetection capacity versus applied voltage. Black and open squares correspond to low- and high-energy photoconductivity peaks, respectively (see Fig. 11).

excited states and the optical transitions are blocked. Combining these data with the results of noise current measurements, we evaluated the maximum detection capacity of the structure studied as a photodetector: 1.7×10^8 (cm $Hz^{1/2}$)/W at a wavelength of 20 μm and 0.7×10^8 (cm $Hz^{1/2}$)/W at a wavelength of 10 μm (at room temperature and a quantum efficiency of 0.1%). Note that, even without optimization of the structure parameters, these values exceed the analogous characteristics presently achieved using InAs/GaAs heterostructures with quantum dots [45].

From the standpoint of fundamental knowledge, an important result consists in the shift of the photoconductivity peaks toward higher energies observed with increasing applied voltage (independently of the voltage polarity). The “red” shift of the intersubband resonance position previously observed for the carrier injection into excited subbands in 2D systems [46] was related to the suppression of the depolarization effect [47]. We believe that a similar phenomenon must take place in the QD arrays as well. At low applied voltages (in the absence of injection), the depolarization effect shifts the interlevel resonance toward greater energies relative to the quantum-confinement energy. According to the Pauli principle, occupation of the excited state decreases the probability of interlevel transitions and leads to the decay of the collective excitation. As a result, the resonance must return to the initial position (unperturbed by the collective interaction). Analogous behavior must be observed in the photoinduced absorption spectra at large optical pumping intensities (Section 3.3). However, a strong background absorption by free carriers hinders the manifestation of this phenomenon.

4. CONCLUSIONS

The results of this investigation of the optical properties of Ge/Si heterostructures with quantum dots allowed us to draw the following conclusions:

1. We have studied the properties of indirect (in real space) excitons bound at the Ge quantum dots. It was shown that the binding energy of these excitons exceeds that of the free excitons both in Si and Ge, which is related to the spatial confinement of the hole motion in Ge nanocrystals and the underbarrier penetration of electron to the region of hole localization. The exciton absorption energy shifts toward shorter wavelengths upon the formation of exciton–hole and exciton–exciton complexes in charged quantum dots. This effect is explained by the spatial separation of exciton components. For this reason, the Coulomb interaction between two holes in a quantum dot, as well as that between two electrons localized in Si near this quantum dot, dominates over the electron–hole interaction.

Our theoretical analysis, conducted within the framework of the SCF approximation with allowance for the inhomogeneous distribution of elastic deformation in the structure, showed the following. In a quantum dot with single exciton, the electron is localized in Si in the vicinity of the Ge pyramid apex (the region of maximum stresses in Si), while the hole is localized at the pyramid base. In a complex of two excitons, the repulsion of electrons leads to their spatial separation and the second electron is localized in Si under the Ge pyramid base.

2. We have studied the IR absorption and photoconductivity for the vertical geometry of light incidence in the region of photon energies from 60 to 100 meV. The IR and photoconductivity spectra exhibit maxima corresponding to the hole transitions between the first two quantum confinement levels in Ge nanocrystals. It was found that an asymmetric shape of the absorption band observed for low occupancies of the ground state of Ge quantum dots corresponds to a Gaussian distribution of the nanocrystal dimensions with a 20% dispersion.

The absorption band exhibited a shift toward shortwave region, a decrease in width, and a change in shape (from asymmetric to symmetric) with increasing concentration of holes in the ground sate of quantum dots. These observations are explained based on the concept of self-sustained collective oscillations of the hole density in the lateral direction. The collective oscillations are due to a long-range dynamic electron–electron interaction (lateral depolarization effect).

It is established that the hole injection into an excited state leads to a longwave shift of the photoconductivity peak, which is caused by decay of the collective excitation and by suppression of the lateral depolarization effect.

ACKNOWLEDGMENTS

This study was supported by the Russian Foundation for Basic Research (project no. 99-02-17019), by the Interinstitution Scientific Program “Russian Universities: Basic Research” (project no. 015.01.01.34), by the Federal Program “Surface Atomic Structures” (project no. 1.14.99), and by a joint RFBR–SFNS Program (project no. 99-02-39051 GFEN).

REFERENCES

1. A. I. Yakimov, V. A. Markov, A. V. Dvurechenskii, and O. P. Pchelyakov, Philos. Mag. **65**, 701 (1992).
2. N. N. Ledentsov, V. M. Ustinov, V. A. Shchukin, *et al.*, Fiz. Tekh. Poluprovodn. (St. Petersburg) **32**, 385 (1998) [Semiconductors **32**, 343 (1998)].
3. A. V. Dvurechenskiĭ and A. I. Yakimov, Izv. Vyssh. Ucheb. Zaved., Mater. Élektron. Tekh. **4**, 4 (1999).
4. A. I. Yakimov, V. A. Markov, A. V. Dvurechenskii, and O. P. Pchelyakov, J. Phys.: Condens. Matter **6**, 2573 (1994).
5. Zh. I. Alferov, Fiz. Tekh. Poluprovodn. (St. Petersburg) **32**, 3 (1998) [Semiconductors **32**, 1 (1998)].
6. U. Bockelman and G. Bastard, Phys. Rev. B **42**, 8947 (1990).
7. H. Drexler, D. Leonard, W. Hansen, *et al.*, Phys. Rev. Lett. **73**, 2252 (1994).
8. S. Sauvage, P. Boucaud, J.-M. Gérard, and V. Thierry-Mieg, Phys. Rev. B **58**, 10562 (1998).
9. A. Weber, O. Gauthier-Lafaye, F. H. Julien, *et al.*, Appl. Phys. Lett. **74**, 413 (1999).
10. A. I. Yakimov, A. V. Dvurechenskii, V. V. Kirienko, *et al.*, Phys. Rev. B **61**, 10 868 (2000).
11. A. I. Yakimov, C. J. Adkins, R. Boucher, *et al.*, Phys. Rev. B **59**, 12598 (1999).
12. K. H. Schmidt, G. Medeiros-Ribeiro, and P. M. Petroff, Phys. Rev. B **58**, 3597 (1998).
13. T. M. Hsu, W.-H. Chang, K. F. Tsai, *et al.*, Phys. Rev. B **60**, R2189 (1999).
14. A. I. Yakimov, A. V. Dvurechenskiĭ, Yu. Yu. Proskuryakov, *et al.*, Appl. Phys. Lett. **75**, 1413 (1999).
15. A. J. Chiquito, Yu. A. Pusep, S. Mergulhão, *et al.*, Phys. Rev. B **61**, 5499 (2000).
16. H. Sunamura, N. Usami, Y. Shiraki, and S. Fukatsu, Appl. Phys. Lett. **66**, 3024 (1995).
17. E. Palange, G. Capellini, L. Di Gaspare, and F. Evangelisti, Appl. Phys. Lett. **68**, 2982 (1996).
18. Feng Liu and M. G. Lagally, Surf. Sci. **386**, 169 (1997).
19. P. A. M. Rodrigues, F. Cerdeira, and J. C. Bean, Appl. Phys. Lett. **75**, 145 (1999).
20. V. Ya. Aleshkin and N. A. Bekin, J. Phys.: Condens. Matter **9**, 4841 (1997).
21. R. J. Warburton, C. S. Dürr, K. Karrai, *et al.*, Phys. Rev. Lett. **79**, 5282 (1997).
22. A. Harwit and J. S. Harris, Appl. Phys. Lett. **50**, 685 (1987).
23. C. Miesner, O. Röthig, K. Brunner, and G. Abstreiter, Physica E (Amsterdam) **7**, 146 (2000).
24. G. Bastard, E. E. Mendez, L. L. Chang, and L. Esaki, Phys. Rev. B **28**, 3241 (1983).
25. A. Wojs and P. Hawrulak, Phys. Rev. B **55**, 13066 (1997).
26. A. I. Yakimov, A. V. Dvurechenskiĭ, A. I. Nikiforov, and O. P. Pchelyakov, Pis’ma Zh. Éksp. Teor. Fiz. **68**, 125 (1998) [JETP Lett. **68**, 135 (1998)].
27. J. M. Rorison, Phys. Rev. B **48**, 4643 (1993).
28. A. V. Nenashev and A. V. Dvurechenskiĭ, Zh. Éksp. Teor. Fiz. **118**, 570 (2000) [JETP **91**, 497 (2000)].
29. C. G. van de Walle, Phys. Rev. B **39**, 1871 (1989).
30. M. Grundmann, O. Stier, and D. Bimberg, Phys. Rev. B **52**, 11969 (1995).
31. T. Ando, A. B. Fowler, and F. Stern, Rev. Mod. Phys. **54**, 437 (1982).
32. M. Załużny, Phys. Rev. B **49**, 2923 (1994).
33. C. Metzner and G. H. Döhler, Phys. Rev. B **60**, 11005 (1999).
34. S. Fukatsu, H. Sunamura, Y. Shiraki, and S. Komiyama, Appl. Phys. Lett. **71**, 258 (1997).
35. A. O. Shegaĭ, K. S. Zhuravlev, V. A. Markov, *et al.*, Fiz. Tekh. Poluprovodn. (St. Petersburg) **34**, 1363 (2000) [Semiconductors **34**, 1311 (2000)].

36. J. A. del Alamo, in *Properties of Silicon*, Ed. by T. H. Ning (INSPEC, The Institute of Electrical Engineers, London, 1988), p. 164.
37. L. Passari and E. Susi, J. Appl. Phys. **54**, 3935 (1983).
38. J. Kim, Lin-Wang Wang, and A. Zunger, Phys. Rev. B **57**, R9408 (1998).
39. J. Kim, Lin-Wang Wang, and A. Zunger, Phys. Rev. B **59**, 5678 (1999).
40. T. Brunhes, P. Boucaud, S. Sauvage, *et al.*, Phys. Rev. B **61**, 5562 (2000).
41. L. Jacak, P. Hawrylak, and A. Wójs, in *Quantum Dots* (Springer-Verlag, Berlin, 1998), p. 196.
42. T. Darhofer, U. Rössler, and D. A. Broido, Phys. Rev. B **52**, R14376 (1995).
43. B. F. Levine, J. Appl. Phys. **74**, R1 (1993).
44. A. I. Yakimov, A. V. Dvurechenskiĭ, A. I. Nikiforov, and O. P. Pchelyakov, Phys. Low-Dimens. Struct. **3/4**, 99 (1999).
45. T. Cho, J.-W. Kim, J.-E. Oh, and S. Hong, Tech. Dig. Int. Electron Devices Meet. **1**, 441 (1998).
46. K. Craig, B. Galdrikian, J. N. Heyman, *et al.*, Phys. Rev. Lett. **76**, 2382 (1996).
47. M. Załużny, Phys. Rev. B **47**, 3995 (1993).

Translated by P. Pozdeev

Journal of Experimental and Theoretical Physics, Vol. 92, No. 3, 2001, pp. 514–518.
Translated from Zhurnal Éksperimental'noĭ i Teoreticheskoĭ Fiziki, Vol. 119, No. 3, 2001, pp. 590–594.
Original Russian Text Copyright © 2001 by Arkhincheev, Garmaev.

SOLIDS
Electronic Properties

Duality Relations in the Nonlinear Percolation Problem: Theory and Numerical Simulation

V. E. Arkhincheev* and B. A. Garmaev

Buryat Science Center, Siberian Division, Russian Academy of Sciences, Ulan-Ude, 670047 Buryat Republic, Russia
**e-mail: varkhin@bsc.buryatia.ru*

Received September 26, 2000

Abstract—The problem of a nonlinear current flow in a heterophase medium formed by a random mixture of linear and nonlinear phases is investigated. The duality relation is derived for the critical indices describing the effective response of a heterogeneous system. The critical index is calculated at the percolation threshold (for equal concentrations of the phases). The nonlinear percolation problem is simulated numerically for degrees $k = 3$, 5, and 7 of the nonlinear phase. The existence of a duality relation for critical indices is established in a range of phase concentrations. *© 2001 MAIK “Nauka/Interperiodica”.*

1. INTRODUCTION

The problem of determining the effective conductivity of macroscopically heterogeneous two-phase media in the linear ohmic approximation was studied most thoroughly in the 2D case. It was proved that for equal concentrations of the phases, the effective conductivity of randomly heterogeneous two-phase media is equal to the geometrical mean of the conductivities of the phases:

$$\sigma_e = \sqrt{\sigma_1\sigma_2} \tag{1}$$

and for arbitrary concentrations of the phases, the following duality relation holds:

$$\sigma_e(\varepsilon)\sigma_e(-\varepsilon) = \sigma_1\sigma_2. \tag{2}$$

These results were obtained in [1, 2] and, according to Dykhne [2], are consequences of the symmetry of the 2D equations for direct current relative to the linear transformations of rotation.

However, in the critical region, in the vicinity of the metal–insulator transitions, nonlinear effects become significant in view of anomalously strong fluctuations of fields and currents. The necessity of including nonlinear effects in the critical region was demonstrated in [3–5], where an anomalous behavior of critical fields (currents) as a function of the closeness to the percolation threshold was observed. Besides, additional information concerning the microscopic structure of heterogeneous media can be obtained from higher-order correlators of fields (currents) [6].

In the weak-nonlinearity approximation, the problem is reduced to the inclusion of the cubic term in the expansion of the current in the field:

$$\mathbf{j} = \sigma_e\mathbf{e} + \chi e^2\mathbf{e}. \tag{3}$$

Nonlinear effects become significant when both terms become of the same order of magnitude [7–9]. The effective nonlinearity coefficient χ is determined from the expression for energy dissipation and is defined as

$$\chi_e = \frac{\langle\chi e^4\rangle}{E^4} = \frac{\chi_1\langle e^4\rangle_1 + \chi_2\langle e^4\rangle_2}{2E^4}. \tag{4}$$

This expressions also implies that the reason behind the increase in the effective nonlinearity of the structure are singularities in the field correlators $\langle e^4\rangle_1$ and $\langle e^4\rangle_2$. An anomalous increase in the nonlinear conductivity indicates that the system goes over to the nonlinear percolation mode. This is observed for the critical fields

$$E_c = \sqrt{\sigma_e/\chi_e} \tag{5}$$

and the critical currents

$$\mathbf{J}_c = \sigma_e\mathbf{E}_c. \tag{6}$$

A considerable number of publications is devoted to an analysis of the properties of the nonlinearity coefficient in the critical region as well as outside it [10, 11].

We will analyze here the nonlinear percolation problem in the following formulation. Suppose that we have a random mixture of two phases: a linear ohmic phase with $j_1 = \sigma_1 e$ and a nonlinear cubic phase $j_2 = \chi_2 e^3$. We are interested in the effective response of such a system at the percolation threshold,

$$J \propto E^{\nu}, \tag{7}$$

and in the value of the index ν describing the nonlinear response of the system.

In order to solve this problem, we generalize the linear transformations of rotation to the nonlinear case and use these generalized transformations to determine the nonlinear response. This will lead us to the duality relations for the critical indices ν_+ and ν_- of the nonlinear percolation problem, which describe the response of the system above and below he percolation threshold:

$$\nu_+\nu_- = k. \qquad (8)$$

Here, $k = 3, 5, 7, \ldots$ is the degree of system nonlinearity. In the second part of this paper, we present the results of the numerical simulation of nonlinear percolation for various values of conductivities of the phases and in a wide range of concentrations. The numerical simulation is used to establish the existence of a duality relation for the critical indices (8) of the nonlinear percolation problem in randomly heterogeneous media.

2. ROTATION TRANSFORMATIONS AND A GENERALIZATION TO THE NONLINEAR CASE

We will briefly recall the main lines of reasoning used for solving the problem of the effective characteristics of a randomly heterogeneous medium. In the 2D case, the equations for direct current and Ohm's law (linear relation between the current and the field),

$$\operatorname{div}\mathbf{j} = 0, \quad \operatorname{curl}\mathbf{e} = 0, \quad \mathbf{j} = \sigma\mathbf{e}, \qquad (9)$$

are invariant to the linear transformations of rotation:

$$\mathbf{j} = b[\mathbf{n}\times\mathbf{e}'], \quad \mathbf{e} = d[\mathbf{n}\times\hat{\mathbf{e}}']. \qquad (10)$$

Here, $\mathbf{n}$ is the unit normal to the plane, $\mathbf{j}'$ and $\mathbf{e}'$ are the electric current and the field in the new primed system, and $\mathbf{b}$ and $\mathbf{d}$ are constant coefficients. In the primed system, Ohm's law also holds:

$$\mathbf{j}' = \sigma'\mathbf{e}, \qquad (11)$$

where $\sigma' = b/d\sigma$ is the conductivity of the transformed medium. For an appropriate choice of the coefficients, i.e., for

$$b = \frac{1}{d} = \sqrt{\sigma_1\sigma_2}, \qquad (12)$$

we obtain a system differing from the initial system in the transmutation of phases:

$$\sigma' = \frac{\sigma_1\sigma_2}{\sigma}. \qquad (13)$$

Such a system is referred to as dual relative to the initial one. Repeating the same arguments for averaged quantities, we obtain a similar relation for the effective parameters of the two-phase medium also:

$$\sigma'_e(\varepsilon)\sigma_e(\varepsilon) = \sigma_1\sigma_2. \qquad (14)$$

Since the initial and primed systems differ only in the phase transmutation, we have

$$\sigma'_e(\varepsilon) = \sigma_e(-\varepsilon). \qquad (15)$$

Consequently, the effective conductivity of a two-dimensional randomly heterogeneous two-phase system satisfies the duality relation (2). This means that the effective conductivity at the percolation threshold ($\varepsilon = 0$) is given by

$$\sigma_e(0) = \sqrt{\sigma_1\sigma_2}. \qquad (16)$$

This duality relation turns out to be helpful for deriving approximate expressions for the effective conductivity also. For example, the expressions for the effective conductivity of two-phase media with a low concentration of inclusions can easily be derived from this relation. It also allows us to find the conductivity of the system in the entire range of concentrations if we know the concentration dependence of σ_e above or below the percolation threshold. Besides, the duality relation also makes it possible to establish the general form of effective conductivity (structural dependence):

$$\sigma_e(\varepsilon) = \chi(\varepsilon) + \sqrt{\chi(\varepsilon)^2 + \sigma_1\sigma_2}. \qquad (17)$$

Here, $2\chi(\varepsilon) = \sigma_e(\varepsilon) - \sigma_e(-\varepsilon)$ is the odd component of the effective conductivity as a function of variable ε. It is described by the functional equation

$$\chi\left(\varepsilon, \frac{1}{h}\right) = h\chi(\varepsilon, h), \qquad (18)$$

where $h = \sigma_2/\sigma_1$ is the ratio of the conductivities of the phases.

Note that formula (16) is valid both for randomly heterogeneous media with an isotropic structure, and for two-periodic media [12, 13]. Recently, this formula has been derived anew in a different way for the media with a staggered structure [14].

We will now generalize the rotation transformations to the nonlinear case. For the sake of definiteness, we first consider a cubic nonlinearity. We will seek the generalized nonlinear transformations in the form

$$\mathbf{j} = b[\mathbf{n}\times\mathbf{e}']e'^2, \quad \mathbf{e} = d[\mathbf{n}\times\mathbf{j}']. \qquad (19)$$

It can easily be verified that these transformations convert the linear phase with conductivity σ into a nonlinear phase: $j' = \chi' e'^3$. Here, the coefficient χ' is given by

$$\chi'_1 = \frac{b}{d\sigma_1}. \qquad (20)$$

Let us now prove that the same transformations convert the nonlinear phase into the linear one. The conductivity of the transformed linear phase in this case is

$$\sigma'_2 = \frac{b^{1/3}}{d\chi_2^{1/3}}. \qquad (21)$$

Consequently, the proposed generalized nonlinear transformations make it possible to establish the one-to-one correspondence (isomorphism) between nonlinear and linear phases. By averaging transformations (19) over a random distribution of the phases, we obtain the following relations for the averaged characteristics of the initial and the primed system:

$$J = \langle j \rangle = AE'^3, \quad E = \langle e \rangle = BJ', \tag{22}$$

where A and B are constant coefficients. Further, we assume that the average currents in the initial and the transformed system are nonlinear functions of the field:

$$J \propto E^{\nu_+}, \quad J' \propto E'^{\nu_-}. \tag{23}$$

Formulas (22) and (23) readily lead to the following relation between the critical indices describing the system response above and below the percolation threshold:

$$\nu_+\nu_- = 3. \tag{24}$$

The relation has a simple meaning. Away from the percolation threshold, when the current can flow only through the linear phase, the effective response is linear (index $\nu_+ = 1$). In this case, the effective response of the dual primed system (differing from the initial system in the phase transmutation) away from the percolation threshold, which is accompanied by the formation of an infinite cluster from the nonlinear phase, will be nonlinear. The nonlinearity index is equal to the index of the nonlinear phase: $\nu_- = 3$.

At the percolation threshold (for equal concentrations of the phases), when both phases must take part in the conduction of current, and in the case of the macroscopic equivalence of the initial and primed systems, relation (24) leads to the exact expression for the nonlinearity index at the percolation threshold. It has a root dependence on the initial nonlinearity:

$$\nu_0 = \sqrt{3}. \tag{25}$$

The condition of the macroscopic equivalence of the initial and primed systems is important for deriving result (25) and will be considered here in greater detail. In accordance with relations (19), the primed system in the general case is microscopically nonequivalent to the initial system since the local field is not of the potential type:

$$\operatorname{div}\mathbf{j} = b\mathbf{n}[\mathbf{e}'^2\operatorname{curl}\mathbf{e}' - \mathbf{e}' \cdot \nabla(\mathbf{e}'^2)] = 0. \tag{26}$$

Thus, in order to obtain the transformed local electric field of the potential type, we must impose an additional constraint of axial symmetry on randomly heterogeneous media. In this case, local two-dimensional fields are directed along the radius, and the condition that the fields are of the potential type is naturally satisfied. (By way of an example, we can consider a cylindrical capacitor filled with a random mixture of linear and nonlinear phases and study the effective response of such a system.)

In the general case of a power nonlinearity, we must use the generalized transformations:

$$\mathbf{j} = [\mathbf{n} \times \mathbf{e}'^k], \quad \mathbf{e} = [\mathbf{n} \times \mathbf{j}']. \tag{27}$$

Repeating the above arguments, we derive relation (8) for the critical indices of type (24) for an arbitrary power nonlinearity:

$$\nu_+\nu_- = k. \tag{28}$$

At the percolation threshold and for the macroscopic equivalence of the initial and primed systems, the nonlinear response index for the general case of a power nonlinearity is given by

$$\nu_0 = \sqrt{k}. \tag{29}$$

It should be noted that, strictly speaking, the obtained relations (24) and (28) are valid only for a limited class of systems with axial symmetry. We will now verify the applicability of the obtained duality relation in the absence of such limitations using numerical simulation, thus extending the region of applicability of the obtained results.

3. NUMERICAL SIMULATION

Let us briefly describe the algorithm of simulation. As the initial model, we considered a square network of conducting links. The values of the conductivities of the links were chosen at random: a link has conductivity σ_1 with probability p and conductivity σ_2 with probability $1 - p$. (In the limit $\sigma_2 \longrightarrow 0$, this problem is transformed into the familiar problem of links in the percolation theory [15, 16].) Then we calculated the values of currents I and potentials U in such a medium. The distributions of currents and potentials in a conducting medium are described by Kirchhoff's laws:

$$\sum_i J_i = 0, \quad \sum_i J_i R_i + \sum U_i = 0. \tag{30}$$

Using the simulation program, we studied the flow of current along the diagonal (from the upper left to the lower right corner). The current was specified at the initial point and then was divided into parts depending on the relation between the conductivities of the phases. The value of the current arriving at the next node was divided accordingly, and so on. The operation was repeated until the paths with a higher conductivity started to converge to the opposite node (sink) and, accordingly, the currents started to add up. The distribution of potentials at the nodes of the network can be determined from the Kirchhoff's second law taking into account the magnitude of the current and the conductivity of the links; in other words, the potential drop across each link was taken into consideration.

The effective conductivity is determined as the proportionality factor between the average current and the average field:

$$\sigma_e = \langle J \rangle / \langle E \rangle.$$

The correctness of the program operation was verified by calculating the effective conductivity of a two-phase medium at the percolation threshold. The results of

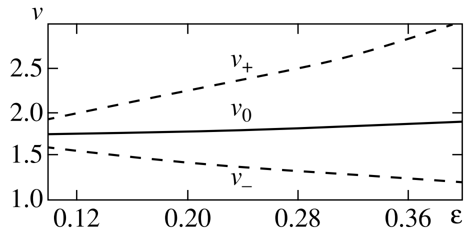

Fig. 1. Dependence of critical indices on the concentration of the phase with a cubic nonlinearity ($k = 3$).

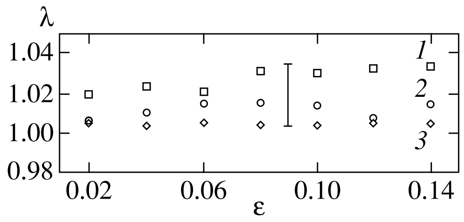

Fig. 2. Values of the parameter $\lambda = \nu_+\nu_-/\nu_0^2$ near the percolation threshold for various degrees of nonlinearity k: 3 (*1*), 5 (*2*), and 7 (*3*).

simulation coincide with the exact solution of the problem to a high degree of accuracy.

In the case of a nonlinear percolation in our formulation of the problem, one phase is a linear ohmic phase, while the other phase is nonlinear: $j = \chi e^k$, $k = 3$, 5, 7, 9. As described above, first a random medium consisting of a mixture of the linear and nonlinear phases was generated, then the current in the system was calculated and the potential drop was determined using the linear or nonlinear expression depending on the properties of the conducting phases. Further, the averaging over a large number of configurations (of the order of 1000) was carried out to find the effective parameters of the system. The results of simulation are presented graphically. Figure 1 shows the values of critical indices above and below the percolation threshold as well as their products (the value at the percolation threshold) for a cubic nonlinearity (similar results can also be obtained for other degrees of nonlinearity). Figure 2 presents the values of the product of the critical indices for various degrees of nonlinearity and near the percolation threshold. It can be seen that the results of the numerical simulation are in good agreement with the predictions of the above theory based on nonlinear transformations of rotation.

4. CONCLUSION

Let us discuss our results. A generalization of linear transformations to the case of nonlinear media has been carried out. The generalized nonlinear transformations are used to establish the one-to-one correspondence (isomorphism) between linear ohmic and nonlinear phases. The relation for the critical indices describing the effective response of the system under investigation above and below the percolation threshold (relation (28)) is derived for a random mixture of linear and nonlinear phases (with an arbitrary power-type nonlinearity). In the linear approximation, the problem of current flow through the system is reduced to determining the effective conductivity of a heterogeneous medium. Accordingly, the relation (28) between the indices is transformed into the duality relation for the effective conductivity of randomly heterogeneous media. At the percolation threshold, as well as in the case when the initial and primed systems are macroscopically equivalent, this relation in the linear approximation leads to the exact expression for the effective conductivity at the percolation threshold (root dependence on the conductivities of the phases). In our case, we obtain the exact expression for the critical nonlinearity index at the percolation threshold. It is also a root function of the initial nonlinearity (formula (29)).

Moreover, it can be verified that although the local field in the primed system subjected to transformations (19) is not of the potential type, the averaged electric field is of the potential nature. For this purpose, we average Eq. (26) over space. The second term in the sum vanishes after the averaging over space as the projection of a two-dimensional vector lying in the plane on the direction of the electric field. Consequently, the averaged electric field is of the potential type. Thus, the initial and primed systems are macroscopically equivalent at the percolation threshold and, hence, the effective response of the system to the external electric field can be found and the degree of nonlinearity at the percolation threshold can be determined.

ACKNOWLEDGMENTS

This work was financed by the Russian Foundation for Basic Research (project no. 99-02-17355).

One of the authors (V. E. A.) is grateful to É.G. Batyev, É.M. Baskin, A.O. Govorov, S.K. Savvinykh, A.V. Chaplik, and M.V. Éntin for fruitful discussions and also to Yu.N. Ovchinnikov for providing the reprints of publications.

REFERENCES

1. J. B. Keller, J. Math. Phys. **5**, 548 (1964).
2. A. M. Dykhne, Zh. Éksp. Teor. Fiz. **59**, 110 (1970) [Sov. Phys. JETP **32**, 63 (1971)]; Zh. Éksp. Teor. Fiz **59**, 641 (1970) [Sov. Phys. JETP **32**, 348 (1971)].
3. D. Stroud and P. M. Hui, Phys. Rev. B **37**, 8719 (1989).
4. D. J. Bergman, Phys. Rev. B **39**, 4598 (1988).
5. A. M. Dykhne, V. V. Zosimov, and S. A. Rybak, Dokl. Akad. Nauk **345**, 467 (1995) [Phys. Dokl. **40**, 613 (1995)].
6. A. A. Snarskiĭ, Pis'ma Zh. Tekh. Fiz. **21** (1), 3 (1995) [Tech. Phys. Lett. **21**, 1 (1995)].

7. Y. Gefen, W. H. Shin, R. B. Laibowitz, and J. M. Viggano, Phys. Rev. Lett. **57**, 3097 (1986).
8. R. K. Chakrabarty, K. Bardan, and A. Basu, Phys. Rev. B **44**, 6773 (1991).
9. M. A. Dubson, Y. C. Hui, M. B. Weisman, and J. C. Garland, Phys. Rev. B **39**, 6807 (1989).
10. A. M. Satanin, V. V. Skuzovatkin, and S. V. Khor’kov, Pis’ma Zh. Éksp. Teor. Fiz. **65**, 521 (1997) [JETP Lett. **65**, 544 (1997)].
11. A. M. Satanin, A. A. Snarskiĭ, K. V. Slipchenko, and I. V. Bezsudnov, Zh. Tekh. Fiz. **68** (5), 132 (1998) [Tech. Phys. **43**, 602 (1998)].
12. Yu. P. Emets, *Electrical Properties of Composites with Regular Structure* (Naukova Dumka, Kiev, 1986).
13. Yu. P. Emets, Zh. Éksp. Teor. Fiz. **96**, 701 (1989) [Sov. Phys. JETP **69**, 397 (1989)].
14. Yu. N. Ovchinnikov and A. M. Dyugaev, Zh. Éksp. Teor. Fiz. **117**, 162 (2000) [JETP **90**, 144 (2000)].
15. B. I. Shklovskii and A. L. Efros, Phys. Status Solidi B **76**, 475 (1976).
16. D. Stauffer, Phys. Rep. **54**, 1 (1979).

Translated by N. Wadhwa

Journal of Experimental and Theoretical Physics, Vol. 92, No. 3, 2001, pp. 519–528.
From Zhurnal Éksperimental'noĭ i Teoreticheskoĭ Fiziki, Vol. 119, No. 3, 2001, pp. 595–605.
Original English Text Copyright © 2001 by Larkin, Ovchinnikov.

SOLIDS
Electronic Properties

Nonlinear Fluctuation Phenomena in the Transport Properties of Superconductors¶

A. I. Larkin[a, b] and Yu. N. Ovchinnikov[a, *]
[a]*Landau Institute for Theoretical Physics, Russian Academy of Sciences, Moscow, 117940 Russia*
[b]*Theoretical Physics Institute, University of Minnesota, 116 Church Street SE, Minneapolis, Minnesota USA*
**e-mail: ovchin@labs.polycnrs-gre.fr*

Received September 28, 2000

Abstract—There exists a wide temperature region (Gi$T < T - T_c < T\sqrt{\text{Gi}}$) where the influence of fluctuations on the thermodynamic properties of superconductors can be taken into account in the linear (Gaussian) approximation, while their influence on the kinetic properties is strongly nonlinear. The Maki–Thompson contribution to the conductivity saturates in this region. However, the Aslamazov–Larkin contribution becomes even more singular. This enhancement is related to the fact that nonlinear effects increase the lifetime of fluctuating pairs. The pair breaking and energy relaxation processes can decrease the nonlinear effects. *© 2001 MAIK "Nauka/Interperiodica".*

1. INTRODUCTION

The electron scattering from usual impurities leads to a temperature-independent residual resistance of normal metal [1]. The conductivity of bulk samples and films can be measured with a very high accuracy. This allows one to study different mechanisms leading to temperature-dependent conductivity at low temperatures. One of these mechanisms is related to thermal fluctuations above the superconducting transition temperature T_c [2–5]. There are two kinds of fluctuation corrections leading to temperature-dependent conductivity above T_c. The first one is known as the Maki–Thompson (MT) contribution and the second is the conductivity of fluctuating pairs (the Aslamazov–Larkin (AL) contribution). These corrections depend differently on the spin flip scattering time τ_s. The characteristic temperature range for the contributions of both types is determined by the Ginzburg parameter Gi, which depends on dimensionality; for films, Gi = $\tau_0 = 1/32\nu Dd = e^2/16\hbar\sigma_\square$, where $\nu = mp^2/2\pi^2$ is the electron density of states per spin, $D = v_F l_{\text{tr}}/3$ is the diffusion coefficient, d is the film thickness, l_{tr} is the electron mean free path, p is the Fermi momentum, and $\sigma_\square$ is the conductance of a square film. It has been found in [6] that nonlinear fluctuation phenomena lead to a new temperature scale $T_c\sqrt{\text{Gi}}$ (see also [7–10]). In this paper, we obtain expressions for the conductivity in the temperature region Gi $< \tau < \sqrt{\text{Gi}}$, where the Gaussian approximation works well and the nonlinear fluctuation effects are important.

In [6], an attempt to find the fluctuating correction to the conductivity was made. The main point was that long-wave fluctuations with $Dk^2 < T\tau$ are essential. These fluctuations can be considered as a Bose condensate. The dynamics of superconductors must be considered in the background of these fluctuations. They lead to a pseudogap in the excitation spectrum. In this paper, we show that shortwave fluctuations with $Dk^2 \gg T\tau$ can be important. It was found in [11] that short-wave fluctuations of the order parameter Δ affect the electron Green's functions as paramagnetic impurities with the depairing factor $\Gamma = \tau_s^{-1} = \langle|\Delta|^2\rangle/\varepsilon$. Essential values of the energy ε are of the order $\varepsilon \sim \Delta \sim T\sqrt{\text{Gi}}$, and therefore, Γ is of the order $T\sqrt{\text{Gi}}$. This large value of the depairing factor leads to saturation of the MT contribution to conductivity in the temperature region $\tau < \sqrt{\text{Gi}}$.

A more complicated situation occurs for the AL contribution. This contribution is proportional to the density of pairs and their lifetime. For sufficiently large values of τ, the time-dependent Ginzburg–Landau (TDGL) equation can be used to obtain this lifetime. It is proportional to $\hbar/(T - T_c)$, and hence, the AL contribution is proportional to τ^{-1}. If the concentration of paramagnetic impurities is large or if the energy relaxation time is short, the TDGL equation can be used for all temperatures T. In this case, the AL contribution is valid in the temperature range $\tau >$ Gi. In the opposite limiting case, the nonlinear fluctuation effects destroy the applicability of the TDGL equation and increase the lifetime of fluctuating pairs. As a result, the AL contribution to the conductivity becomes more singular in the temperature region $\sqrt{\text{Gi}} > \tau >$ Gi.

¶This article was submitted by the authors in English.

1063-7761/01/9203-0519$21.00 © 2001 MAIK "Nauka/Interperiodica"

2. QUALITATIVE PICTURE

In the temperature region $1 \gg \tau \gg \mathrm{Gi}$, thermodynamic fluctuations of the order parameter Δ can be considered as Gaussian. The corresponding correlator is given by

$$\langle \Delta_k^* \Delta_k \rangle = \frac{T}{\nu d} \frac{1}{\tau + \pi D k^2/8T} = \frac{256}{\pi} \frac{\mathrm{Gi} T^2}{k^2 + 8T\tau/\pi D}. \quad (1)$$

To calculate thermodynamic quantities in the temperature region $\tau > \mathrm{Gi}$, it is sufficient to know only this correlator. However, a more complicated problem must be solved in order to calculate kinetic coefficients. One must find how the Gaussian fluctuations change the one-particle excitation spectrum. The long-wavelength fluctuations with $k^2 < k_{\mathrm{min}}^2 = 8T\tau/\pi D$ can be considered as a local condensate. They lead to the formation of a pseudogap in the one-particle spectrum of excitations. It follows from Eq. (1) that the pseudogap is equal to

$$\Delta_{PG} = \frac{8}{\pi} \sqrt{\mathrm{Gi}} T. \quad (2)$$

At some distance from the transition (for $\tau > \sqrt{\mathrm{Gi}}$), only excitations with the energy $\omega > \Delta_{PG}$ are significant. The pseudogap does not play any role in these excitations. It is therefore sufficient to consider fluctuations in the linear approximation (see [3–5]). It is important, however, that the excitations with the energy $\omega < \Delta_{PG}$ become essential in the temperature region $\tau < \sqrt{\mathrm{Gi}}$. In [6], the fluctuation correction to the conductivity was considered with the pseudogap taken into account in the same way as the gap below the transition temperature. This approximation gives a correct estimate for the width of the temperature region where the nonlinear effects are important.

However, the model with a constant Δ considered in [6] cannot reproduce the correct temperature dependence of the conductivity in the temperature region $\tau < \sqrt{\mathrm{Gi}}$.

To describe the nonlinear effects, we consider fluctuations of Δ in the statical approximation. This is eligible, because the fluctuation lifetime $(T\tau)^{-1}$ is large compared to the inverse pseudogap. However, the spatial dispersion of the pseudogap changes the physical picture significantly. To take the spatial variations into account, we must calculate the conductivity as a function of the order parameter $\Delta(\mathbf{r})$, which is an arbitrary function of $\mathbf{r}$, and average the result over the Gaussian fluctuations with correlator (1). We accomplish this program up to a numerical coefficient in the limiting case where the energy relaxation rate is large ($\tau_\varepsilon \ll (T\tau)^{-1}$). In other cases, we obtain a functional form of the temperature dependence of the conductivity with undetermined coefficients.

To consider the spatial dependence of the order parameter, we use the results obtained in [11], where the spatial variations of Δ were shown to act on one-particle excitations in the same way as the magnetic impurities. In this case, the total pair breaking rate Γ can be written as a sum of the pair breaking rate due to the magnetic impurities and the fluctuation term. Thus, the self-consistent equation for Γ becomes

$$\Gamma = \int \frac{d^2 k}{(2\pi)^2} \frac{\langle \Delta_k^* \Delta_k \rangle}{\omega + Dk^2/2 + \Gamma} + \frac{1}{\tau_s}. \quad (3)$$

It is important to mention that Eq. (3) is exact if either $\omega \gg \Gamma$ or τ_s is very small such that the first term in Eq. (3) is a small correction to the second one. In the other cases, the self-consistent equation (3) can be considered as an approximation and gives the result valid by the order of magnitude only.

In the region where $\omega < \Gamma$ and $\Gamma \gg T\tau$, we obtain from Eqs. (1) and (3) that

$$\Gamma = \frac{8T}{\pi} \left(\mathrm{Gi} \ln \frac{\Gamma}{T\tau} \right)^{1/2}, \quad (4)$$

which coincides with the value obtained in [7, 12] up to the logarithmic term. In what follows, we repeat the derivation in [11] and show that the pseudogap does not change result (4) qualitatively.

We note that the pair breaking rate Γ is of the order of the pseudogap Δ_{PG}. Thus, a wide maximum of the density of states appears at $\omega \sim \Delta_{PG}$.

As known from [5], the MT correction to the conductivity saturates for $T\tau < \Gamma$ and takes the form

$$\frac{\delta\sigma^{MT}}{\sigma_0} = \frac{8T\mathrm{Gi}}{\pi\Gamma} \ln \frac{\pi\Gamma}{4T\tau}. \quad (5)$$

As can be seen from Eqs. (4) and (5), this saturation occurs for $\tau < \sqrt{\mathrm{Gi}}$. Similar results have been obtained in [7, 8, 10]. However, numerical coefficients are different.

We note that the numerical coefficient in Eq. (5) depends on how the summation of higher-order diagrams is made. However, its exact value is not very important because in the region $T\tau < \Gamma$, the MT contribution is less singular than the AL contribution and can be neglected. The AL contribution does not saturate as T tends to T_{c} but becomes more and more singular.

To estimate the AL contribution due to the appearance of fluctuating Cooper pairs, we use the simple Drude formula

$$\delta\sigma^{\mathrm{AL}} = \frac{ne^2}{m} \tau_{\mathrm{fl}}, \quad (6)$$

where n, m, and τ_{fl} are the concentration, the mass, and the lifetime of the fluctuating Cooper pairs. The ratio

n/m can be estimated from Eq. (1), while the lifetime follows from the TDGL equations,

$$\left(a\frac{\partial}{\partial t} + Dk^2 + \frac{8}{\pi}T\tau\right)\Delta_k(t) = \zeta(t), \tag{7}$$

where ζ is the Langevin noise. In the two-dimensional case, we have

$$\frac{n}{m} \approx \frac{T}{2\pi d\hbar^2}$$

and

$$\tau_{\mathrm{fl}} = \frac{\pi\hbar}{8(T - T_c)a}.$$

At a sufficient distance from the transition ($T\tau > \Delta_{PG}$) or for a very large energy relaxation rate, we can set $a = 1$, because the quasiparticles are at the thermal equilibrium. Thus, we have

$$\frac{\delta\sigma_{\mathrm{AL}}}{\sigma} = \frac{\mathrm{Gi}}{\tau}. \tag{8}$$

In the presence of the pseudogap, there is no equilibrium and the coefficient a becomes greater than one. We recall that below the transition temperature the coefficient a in the TDGL equations for $|\Delta|$ similarly changes (see, e.g., [13–17]). The growth of a and, consequently, the growth of the fluctuation lifetime occur because the quasiparticles require more time to attain the thermal equilibrium (let τ_e denote the corresponding time). A rough estimate gives $a \sim \Delta_{PG}\tau_e$. For a weak energy relaxation, τ_e must be determined from the diffusion equation with the pseudogap taken into account (see [18–20]). We note that in this complicated case, the coefficient a becomes a nonlocal operator. Rough estimates give the thermal equilibrium transition time $\tau_e \sim (Dk^2_{\min})^{-1} \sim (T\tau)^{-1}$. Taking Eq. (2) into account, we obtain

$$\delta\sigma/\sigma_0 = \mathrm{Gi}^{3/2}/\tau^2. \tag{9}$$

We see that paraconductivity can exceed the normal conductivity σ_0 in the region $\mathrm{Gi}^{3/4} > \tau > \mathrm{Gi}$. We emphasize that corrections to all the thermodynamic coefficients are small in this region and are adequately described by the linear theory.

We now discuss the role of the energy relaxation processes characterized by the quasiparticle lifetime τ_ε. In the two-dimensional case, the nonelastic electron–electron scattering in dirty metals leads to the electron–electron collision time:

$$\tau_\varepsilon^{-1} \sim Tdlp^2 \sim \mathrm{Gi}T.$$

Such a large collision time does not change nonlinear effects. However, the nonelastic electron scattering from phonons and other possible collective excitations can decrease τ_ε significantly. These processes, together with additional pair breaking processes (due to magnetic impurities or a magnetic field), decrease the nonlinear effects. The energy relaxation reduces the thermal equilibrium transition time τ_e. If these processes are very strong (for example, if the temperature is relatively large), the transport equation for the distribution function becomes local, and in the limit $T\tau \sim Dk^2 \ll \tau_\varepsilon^{-1}$, we can write $\tau_e = \tau_\varepsilon$. Thus, in the temperature region under consideration, we have

$$\frac{\delta\sigma}{\sigma_0} = \frac{\mathrm{Gi}^{3/2}T\tau_\varepsilon}{\tau}. \tag{10}$$

The elastic scattering from magnetic impurities and the magnetic field also tend to diminish the nonlinear fluctuation effects in conductivity, but in a different way. These scattering processes (as well as scattering from the static fluctuations of the order parameter) do not affect the quasiparticle motion nor, hence, τ_ε. However, if the pair breaking rate is sufficiently large ($\Gamma > \Delta_{PG}$), these processes lead to the reduced pseudogap $\Delta_{PG} \sim \langle|\Delta|^2\rangle/\Gamma$ (we recall that $\Delta_{PG} \sim \sqrt{\langle|\Delta|^2\rangle} \sim T\mathrm{Gi}^{1/2}$ without pair breaking). Thus, the fluctuation correction can be written as

$$\delta\sigma/\sigma_0 = \mathrm{Gi}^2T/\tau^2\Gamma. \tag{11}$$

In the presence of both a strong pair breaking and a large energy relaxation, exact expressions for the coefficient a in the TDGL equation, which is local in this case, and for paraconductivity can be derived with a logarithmic accuracy. The main contribution to a then comes from the fluctuations with $T\tau < Dk^2 < \tau_\varepsilon^{-1}$. The first inequality allows us to consider only the leading terms in the expansion of a with respect to Δ, and the second one implies a local approximation in the transport equation. The result is

$$a = \frac{\tau_\varepsilon\langle\Delta^2\rangle}{2\Gamma}, \tag{12}$$

$$\frac{\delta\sigma}{\sigma_0} = \frac{32\mathrm{Gi}^2T^2\tau_\varepsilon}{\pi^2\Gamma\tau}\ln\frac{\pi}{8T\tau_\varepsilon\tau}. \tag{13}$$

We note that Eqs. (9)–(13) are valid only if the parameters Γ and τ_ε are such that the contribution to the conductivity $\delta\sigma$ is larger than the usual Aslamazov–Larkin contribution in Eq. (8). If $\Gamma > T$ and $T\tau_\varepsilon < \sqrt{\mathrm{Gi}}$ or if $T^2\tau_\varepsilon/\Gamma < \mathrm{Gi}$, the nonlinear effects are negligible and the usual result (8) is valid for all $\tau > \mathrm{Gi}$. We note that the MT contribution saturates at the temperatures such that $T\tau \sim \max[\Gamma, 1/\tau_\varepsilon, T\sqrt{\mathrm{Gi}}]$.

3. DEPAIRING FACTOR INDUCED BY FLUCTUATIONS

A nonzero fluctuating order parameter Δ and the Gor'kov–Green function β [6] exist above the transition temperature. In the temperature region $\tau > \mathrm{Gi}$, the main contribution to the order parameter Δ arises from zero "frequency." The momentum space can be separated into two parts: $\pi Dk^2/8T < \tau$ and $\pi Dk^2/8T > \tau$. The fluctuations with $\pi Dk^2/8T > \tau$ can be considered as "fast" variables created in the background of slow fluctuations with $\pi Dk^2/8T < \tau$. The "fast" fluctuations induce the intrinsic depairing factor Γ even if the external depairing factor related to paramagnetic impurities is missing ($\tau_s \longrightarrow \infty$). A similar phenomenon was studied in [11]. Using the method developed in that paper, we obtain expressions for the statical Green's functions α and β and the depairing factor Γ. We start from the Usadel equation for Green's functions α and β in the dirty limit (see [6, 21]),

$$\Delta\alpha - \omega\beta + \frac{D}{2}(\alpha\nabla^2\beta - \beta\nabla^2\alpha) = \alpha\beta\Gamma. \tag{14}$$

Following [11], we present Green's functions α and β in the field of "fast" fluctuations of the order parameter $\Delta(k)$ as

$$\alpha = \langle\alpha\rangle + \alpha_1, \quad \beta = \langle\beta\rangle + \beta_1. \tag{15}$$

The deviations of Green's functions from their mean values can be found using the perturbation theory [11]:

$$\alpha_1(k) = -\frac{\Delta(k)\langle\alpha\rangle\langle\beta\rangle}{\omega\langle\alpha\rangle + \langle\Delta\rangle\langle\beta\rangle + Dk^2/2}. \tag{16}$$

The "mean" Green's functions $\langle\alpha\rangle$ and $\langle\beta\rangle$ are solutions of the system of equations

$$\langle\alpha\rangle^2 + \langle\beta\rangle^2 = 1, \quad \langle\alpha\rangle\langle\Delta\rangle - \omega\langle\beta\rangle = \langle\alpha\rangle\langle\beta\rangle\Gamma. \tag{17}$$

The value of the parameter Γ is determined by Eq. (16) and is equal to

$$\Gamma = \int\frac{d^2k}{(2\pi)^2}\frac{\langle\Delta_k^*\Delta_k\rangle}{\langle\alpha\rangle\omega + \langle\Delta\rangle\langle\beta\rangle + Dk^2/2}, \tag{18}$$

where $\langle\Delta\rangle = \langle|\Delta|^2\rangle^{1/2}$. The quantity $\langle\Delta\rangle$ in Eqs. (16) and (17) must be understood as the integral over k of expression (18) over the range $\pi Dk^2/8T \le \tau$; it then becomes

$$\langle\Delta\rangle = \left[\frac{T}{\nu d}\int\frac{d^2k}{(2\pi)^2}\frac{1}{\tau + \pi Dk^2/8T}\right]^{1/2} \approx T\left[\frac{64\mathrm{Gi}}{\pi^2}\right]^{1/2}. \tag{19}$$

From Eqs. (1) and (18), we obtain

$$\Gamma = \frac{16T\mathrm{Gi}}{\pi\tau}\frac{1}{(\pi/4T\tau)(\omega\langle\alpha\rangle + \langle\Delta\rangle\langle\beta\rangle) - 1} \times \ln\left(\frac{\pi(\omega\langle\alpha\rangle + \langle\Delta\rangle\langle\beta\rangle)}{4T\tau}\right). \tag{20}$$

As can be seen from Eq. (20), $\Gamma(\omega)$ is a function of the energy ω. In the range $\tau \le \sqrt{\mathrm{Gi}}$, essential values of ω are of the order Γ. Thus, Γ itself is of the order $\langle\Delta\rangle$ (see (19)). This order of Γ is related to fluctuations of the order parameter modulus. This value is much larger than the one due to the phase fluctuations of the order parameter (see [6]).

4. EQUATIONS FOR THE TIME-DEPENDENT ORDER PARAMETER

The static Ginzburg–Landau equations are valid the in the wide temperature region

$$\mathrm{Gi} \ll |1 - T/T_c| \ll 1. \tag{21}$$

The TDGL equations are valid if the energy relaxation time τ_ε or the pair breaking time $\tau_s = \Gamma^{-1}$ is sufficiently short [13–16]. For large τ_ε, the dynamics of normal excitations becomes essential. As a result, the dynamical term in the equation for the order parameter becomes more complicated. We now derive the corresponding equation.

The order parameters $\Delta_{1,2}(t)$ can be written as

$$\Delta_{1,2}(t) = \frac{\pi\lambda_{\mathrm{eff}}}{2}F^K_{1,2}(t, t) \tag{22}$$

with Green's function $\hat{G}$ presented in the form [18]

$$\hat{G} = \begin{pmatrix} G^R & G^K \\ 0 & G^A \end{pmatrix}, \tag{23}$$

where $G^{R,A,K}$ are the retarded, advanced, and Keldysh Green's functions. Each of these is a Gor'kov–Nambu matrix

$$G^{R,A,K} = \begin{pmatrix} g_1 & F_1 \\ -F_2 & g_2 \end{pmatrix}^{R,A,K}, \qquad \tilde{\Delta} = \begin{pmatrix} 0 & \Delta_1 \\ -\Delta_2 & 0 \end{pmatrix}, \tag{24}$$

where $\Delta_2(\omega) = \Delta_1^*(-\omega)$.

In the dirty limit, we have the system of equations for $G^{R,A}$ (see [19])

$$-D\partial_\mp\left(g^{R,A}\partial_\mp F^{R,A}_{1,2} - F^{R,A}_{1,2}\frac{\partial g^{R,A}}{\partial r}\right) + 2i\Delta_{1,2}g^{R,A} - 2i\varepsilon F^{R,A}_{1,2} + \frac{2}{\tau_s}g^{R,A}F^{R,A}_{1,2} = -I^{\mathrm{Ph}(R,A)}_{1,2}, \tag{25}$$

where $I_{1,2}^{\mathrm{Ph}(R,A)}$ is the electron–phonon collision integral; in the vicinity of the transition temperature T_c for small energy values $|\varepsilon| \ll T$, this quantity is equal to

$$I_{1,2}^{\mathrm{Ph}(R,A)} = \pm\frac{1}{\tau_\varepsilon}F_{1,2}^{R,A}. \tag{26}$$

The Keldysh–Green function G^K can be written as [20]

$$G = \int dt_1 (G^R \hat{f} - \hat{f} G^A), \tag{27}$$

where the distribution function $\hat{f}$ is given by [20]

$$\hat{f} = f + \tau_z f_1. \tag{28}$$

Equations for the distribution functions $f_{1,2}$ have been derived in [20] and have the form

$$-D\frac{\partial}{\partial r}\left\{\frac{\partial f}{\partial r}(1 - G^R G^A)\right\} - D\frac{\partial}{\partial r}(f_1 j_\varepsilon) + 2\frac{\partial f}{\partial t}\mathrm{Sp}\alpha$$

$$+\frac{\partial f}{\partial \varepsilon}\left\{eD\frac{\partial A}{\partial t}j_\varepsilon - 2\mathrm{Sp}\frac{\partial \hat{\Delta}}{\partial t}\delta\right\} + 4I_1^{\mathrm{Ph}}(f) = 0,$$

$$-D\frac{\partial}{\partial r}\mathrm{Sp}\left\{\frac{\partial f_1}{\partial r}(1 - \tau_z G^R \tau_z G^A)\right\} - D\frac{\partial f}{\partial r}j_\varepsilon \tag{29}$$

$$+2\frac{\partial}{\partial t}(f_1 \mathrm{Sp}\alpha) - 4if_1\mathrm{Sp}(\gamma\hat{\Delta})$$

$$+2\frac{\partial f}{\partial \varepsilon}\mathrm{Sp}\left\{e\frac{\partial \varphi}{\partial t}\alpha - \frac{\partial \hat{\Delta}}{\partial t}\tau_z\gamma + \frac{i}{2}\frac{\partial^2 \hat{\Delta}}{\partial t^2}\frac{\partial \delta}{\partial \varepsilon}\right\} + 4I_2^{\mathrm{Ph}}(f_1) = 0,$$

where

$$j_\varepsilon = \mathrm{Sp}\tau_z(G^R \partial G^R - G^A \partial G^A),$$

$$\partial = \frac{\partial}{\partial r} - ieA\tau_z, \tag{30}$$

$$2\alpha = G^R\tau_z - \tau_z G^A, \quad 2\delta = G^R - G^A, \quad 2\gamma = G^R + G^A.$$

In the important limiting case where $\varepsilon \sim \Gamma \gg \Delta$, Eqs. (25) and (29) can be simplified and we obtain

$$F_1^{R,A} = -i\left(\Gamma \mp i\varepsilon - \frac{D}{2}\frac{\partial^2}{\partial r^2}\right)^{-1}\Delta,$$

$$F_2^{R,A} = -i\left(\Gamma \mp i\varepsilon - \frac{D}{2}\frac{\partial^2}{\partial r^2}\right)^{-1}\Delta^*, \tag{31}$$

$$-D\frac{\partial^2 f}{\partial r^2} - \frac{D}{4}\frac{\partial}{\partial r}(j_\varepsilon f_1) + \frac{\partial f}{\partial t}$$

$$+\frac{1}{4}\frac{\partial f}{\partial \varepsilon}\left\{\frac{\partial \Delta_1}{\partial t}(F_2^R - F_2^A) + \frac{\partial \Delta_2}{\partial t}(F_1^R - F_1^A)\right\} + I_1^{\mathrm{Ph}}(f) = 0,$$

$$-D\frac{\partial^2 f_1}{\partial r^2} - \frac{D}{4}j_\varepsilon\frac{\partial f_1}{\partial r} + \frac{\partial f_1}{\partial t}$$

$$+\frac{i}{2}f_1(\Delta(F_2^R + F_2^A) + \Delta^*(F_1^R + F_1^A)) + \frac{\partial f}{\partial \varepsilon}\left\{e\frac{\partial \varphi}{\partial t}\right.$$

$$\left.+\frac{1}{4}\left(-\frac{\partial \Delta_1}{\partial t}(F_2^R + F_2^A) + \frac{\partial \Delta_2}{\partial t}(F_1^R + F_1^A)\right)\right\} + I_2^{\mathrm{Ph}}(f_1) = 0,$$

where

$$j_\varepsilon = -F_1^R\frac{\partial F_2^R}{\partial r} + F_2^R\frac{\partial F_1^R}{\partial r} + F_1^A\frac{\partial F_2^A}{\partial r} - F_2^A\frac{\partial F_1^A}{\partial r}. \tag{32}$$

The general expression for the collision integrals $I_{1,2}^{\mathrm{Ph}}$ is given in [20, 22]. For small energy values $|\varepsilon| \ll T$, these integrals can be taken in the simple form:

$$I_1^{\mathrm{Ph}}(f) = \frac{1}{\tau_\varepsilon}\left(-\tanh\left(\frac{\varepsilon}{2T}\right) + f\right),$$

$$I_2^{\mathrm{Ph}}(f_1) = \frac{1}{\tau_\varepsilon}f_1, \tag{33}$$

$$\tau_\varepsilon^{-1} = 7\zeta(3)\pi\nu g^2 T^3/2(sp)^2,$$

where s is the velocity of sound in the metal and g is the electron-phonon coupling constant.

In the limiting case of strong energy relaxation with $\tau_\varepsilon\Delta \ll 1$, the distribution function $\hat{f}$ can be taken as the equilibrium one,

$$f = \tanh(\varepsilon/2T), \quad f_1 = 0. \tag{34}$$

In this case, Eqs. (22), (31), and (34) allow one to obtain the time-dependent Ginzburg–Landau equation in the standard form:

$$\left(1 - T/T_c - \frac{7\zeta(3)}{8\pi^2 T^2}|\Delta|^2\right)\Delta + \frac{\pi D}{8T}\partial_-^2\Delta$$

$$-\frac{\pi}{8T}\left(\frac{\partial}{\partial t} + 2ie\varphi\right)\Delta = 0. \tag{35}$$

If the condition $\tau_\varepsilon\Delta \ll 1$ is not satisfied, the deviation of the distribution function $\hat{f}$ from its equilibrium value can change the last term in Eq. (35).

In the range $\Gamma \gg \Delta$, the crossing term in Eq. (31) has a smallness of $(\Delta/\Gamma)^2$. In the leading approximation, system (31) is therefore diagonal.

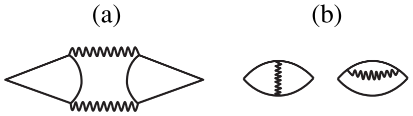

Fig. 1. The Aslamov–Larkin contribution to the conductivity (a); the Maki–Thompson contributions to the conductivity (b).

With the aid of Eqs. (27), (28), and (31), we can rewrite Eq. (22) as

$$\left[\tau + \frac{\pi}{8T}\left(-i\omega_1 - D\frac{\partial^2}{\partial r^2}\right)\right]\Delta_1 - \frac{\pi}{2}\int_{-\infty}^{\infty}\frac{d\varepsilon}{2\pi}[\delta f(F_1^R - F_1^A) - f_1(F_1^R + F_1^A)] = 0,$$
$$\left[\tau + \frac{\pi}{8T}\left(-i\omega_1 - D\frac{\partial^2}{\partial r^2}\right)\right]\Delta_2 - \frac{\pi}{2}\int_{-\infty}^{\infty}\frac{d\varepsilon}{2\pi}[\delta f(F_2^R - F_2^A) - f_1(F_2^R + F_2^A)] = 0, \tag{36}$$

where we set

$$f = \tanh(\varepsilon/2T) + \delta f. \tag{37}$$

In (36), the contributions of the second terms are of the order $(\Delta/\Gamma)^2$. This result is due to the cancellation of the terms coming from δf and f_1, but in the next orders of the perturbation theory, the quantity f_1 becomes small and the main contribution arises from the distribution function δf beyond perturbation theory.

5. THE CONDUCTIVITY OF FLUCTUATING PAIRS (THE ASLAMAZOV–LARKIN CONTRIBUTION)

The conductivity of fluctuating pairs is given by the diagrams in Fig. 1a. In what follows, we assume that the order parameters $\Delta_{1,2}$ can be written as the sums of two terms. One of them is related to the statical thermodynamic fluctuations Δ and Δ^*. In the range $\tau > \mathrm{Gi}$, these fluctuations are Gaussian with the correlator given by Eq. (1). The wavy line in Fig. 1a gives the dynamical fluctuations $\tilde{\Delta}_{1,2}$ of the order parameter. The correlators of these fluctuations $\hat{K}_{ij}$ must be found in the background of thermodynamic fluctuations,

$$\hat{K}_{ij}(\omega_1) = \nu\langle\Delta_i^*\Delta_j\rangle_{\omega_1}. \tag{38}$$

The contribution to the conductivity can be expressed through the correlators $\hat{K}$ in the same way as for weak fluctuations [3].

First, we must find the conductivity as a function of the Matzubara frequency ω_0 and then perform the analytical continuation in ω_0. The correction to the current was found in [6] with the aid of the equations for the Green's function in the dirty limit in high-frequency fields,

$$j_{\omega_0}^{\alpha} = \frac{1}{2d}\int d^2r_1 T \times \sum_{\omega_1}\mathrm{Sp}\hat{L}_r^{\alpha}\hat{K}(\omega_1 + \omega_0, r, r_1)\hat{L}_{r_1}^{\beta}\hat{K}(\omega_1, r_1, r)A_{\omega_0}^{\beta}, \tag{39}$$

where A_{ω_0} is the vector potential of the external field and the matrix $\hat{L}$ is given by

$$\hat{L}_{12}^{\alpha} = L_{21}^{\alpha} = 0, \quad \hat{L}_{11}^{\alpha}(r) = -\frac{\pi e D}{2T}\frac{\partial}{\partial r^{\alpha}}, \qquad \hat{L}_{22}^{\alpha} = -\hat{L}_{11}^{\alpha}. \tag{40}$$

After the analytical continuation with respect to ω_0 in Eq. (39), we obtain

$$j_{\omega}^{\alpha} = -\frac{1}{2d}\int d^2r_1\frac{iT}{2\pi}\int_{-i\infty}^{i\infty}d\omega_1\left[\frac{1}{\omega_1 - i\omega - \delta} - \frac{1}{\omega_1 + \delta}\right] \times \mathrm{Sp}(\hat{L}_r^{\alpha}\hat{K}(\omega_1 - i\omega + \delta, r, r_1)\hat{L}_{r_1}^{\beta}\hat{K}(\omega_1 - \delta, r_1, r))A_{\omega}^{\beta}. \tag{41}$$

It was found in [6] that the fluctuations are weak in the range $\tau > \mathrm{Gi}^{1/2}$. In this region, we have

$$K_{11}(\omega_1 + \delta) = K_{22}(\omega_1 + \delta) = \frac{1}{\tau + (\pi/8T)(\omega_1 + Dk^2)}. \tag{42}$$

From Eqs. (40)–(42), we obtain the well-known result for the paraconductivity [3],

$$\sigma^{(a)}/\sigma_0 = \mathrm{Gi}/\tau. \tag{43}$$

To obtain the conductivity in the temperature region $\tau < \mathrm{Gi}^{1/2}$, we must find the correlation functions $\hat{K}$ in the field of thermodynamic fluctuations Δ. We must then average the expression for conductivity over Δ. The correlation functions $\hat{K}$ can be found from Eq. (36),

---

$$\hat{K}^{-1} = \begin{pmatrix} \tau + \frac{\pi}{8T}\left(\omega_1 - D\frac{\partial^2}{\partial r^2}\right) - C_{11} & -C_{12} \\ -C_{21} & \tau + \frac{\pi}{8T}\left(\omega_1 - D\frac{\partial^2}{\partial r^2}\right) - C_{22} \end{pmatrix}, \tag{44}$$

where the operators C_{ij} are given by

$$\begin{aligned} C_{11} &= \frac{\pi}{2}\int_{-\infty}^{\infty}\frac{d\varepsilon}{2\pi}[(F_1^R - F_1^A)\delta f^{(1)} - f_1^{(1)}(F_1^R + F_1^A)], \\ C_{12} &= \frac{\pi}{2}\int_{-\infty}^{\infty}\frac{d\varepsilon}{2\pi}[(F_1^R - F_1^A)\delta f^{(2)} - f_1^{(2)}(F_1^R + F_1^A)], \\ C_{21} &= \frac{\pi}{2}\int_{-\infty}^{\infty}\frac{d\varepsilon}{2\pi}[(F_2^R - F_2^A)\delta f^{(1)} + (F_2^R + F_2^A)\delta f_1^{(1)}], \\ C_{22} &= \frac{\pi}{2}\int_{-\infty}^{\infty}\frac{d\varepsilon}{2\pi}[(F_2^R - F_2^A)\delta f^{(2)} + (F_2^R + F_2^A)\delta f_1^{(2)}]. \end{aligned} \tag{45}$$

In Eqs. (45), the operators $\delta f^{(1,\,2)}$ and $f_1^{(1,\,2)}$ are such that

$$\begin{aligned} \delta f &= \delta f^{(1)}\tilde{\Delta}_1 + \delta f^{(2)}\tilde{\Delta}_2, \\ f_1 &= f_1^{(1)}\tilde{\Delta}_1 + f_1^{(2)}\tilde{\Delta}_2, \end{aligned} \tag{46}$$

with δf and f_1 being the respective solutions of system (31) in the field of $\tilde{\Delta}_1$ and $\tilde{\Delta}_2$. System (31) cannot be solved analytically for an arbitrary function $\Delta(r)$. Nevertheless, in the range $\tau < \mathrm{Gi}^{1/2}$, the expression for the correlation functions $\hat{K}$ can be found with the logarithmic accuracy if the value of the external depairing factor Γ is larger than Δ. In this case, simple expressions for the Green's functions $F_{1,\,2}^{R,\,A}$ can be used,

$$F_1^{R,\,A} = \frac{-i\Delta}{\Gamma \mp i\varepsilon}, \quad F_2^{R,\,A} = \frac{-i\Delta^*}{\Gamma \mp i\varepsilon}. \tag{47}$$

If $Dk^2 \gg |\Delta|^2/\Gamma$, the contribution of $\delta f^{(1,\,2)}$ is cancelled out in the expressions for C_{11} and C_{22}. We note that $Dk^2 \ll |\Delta|^2/\Gamma$ implies $f_1^{(1,\,2)} \ll \delta f^{(1,\,2)}$. Thus, this region gives the dominant contribution to C_{ij}. Equations (44) and (45) can then be reduced to

$$\begin{aligned} &\left[\tau + \frac{\pi}{8T}\left(\omega_1 - D\frac{\partial^2}{\partial r^2}\right)\right]K_{11} \\ &+ \frac{\pi\omega_1\Delta}{16T\Gamma}\left(\omega_1 + \tau_\varepsilon^{-1} - D\frac{\partial^2}{\partial r^2}\right)^{-1}(\Delta^* K_{11}) \\ &+ \frac{\pi\omega_1\Delta}{16T\Gamma}\left(\omega_1 + \tau_\varepsilon^{-1} - D\frac{\partial^2}{\partial r^2}\right)^{-1}(\Delta K_{21}) = \delta(r - r_1), \\ &\left[\tau + \frac{\pi}{8T}\left(\omega_1 - D\frac{\partial^2}{\partial r^2}\right)\right]K_{12} \end{aligned}$$

$$\begin{aligned} &+ \frac{\pi\omega_1\Delta}{16T\Gamma}\left(\omega_1 + \tau_\varepsilon^{-1} - D\frac{\partial^2}{\partial r^2}\right)^{-1}(\Delta^* K_{12}) \\ &+ \frac{\pi\omega_1\Delta}{16T\Gamma}\left(\omega_1 + \tau_\varepsilon^{-1} - D\frac{\partial^2}{\partial r^2}\right)^{-1}(\Delta K_{22}) = 0, \\ &\left[\tau + \frac{\pi}{8T}\left(\omega_1 - D\frac{\partial^2}{\partial r^2}\right)\right]K_{21} \\ &+ \frac{\pi\omega_1\Delta^*}{16T\Gamma}\left(\omega_1 + \tau_\varepsilon^{-1} - D\frac{\partial^2}{\partial r^2}\right)^{-1}(\Delta K_{21}) \\ &+ \frac{\pi\omega_1\Delta^*}{16T\Gamma}\left(\omega_1 + \tau_\varepsilon^{-1} - D\frac{\partial^2}{\partial r^2}\right)^{-1}(\Delta^* K_{11}) = 0, \\ &\left[\tau + \frac{\pi}{8T}\left(\omega_1 - D\frac{\partial^2}{\partial r^2}\right)\right]K_{22} \\ &+ \frac{\pi\omega_1\Delta^*}{16T\Gamma}\left(\omega_1 + \tau_\varepsilon^{-1} - D\frac{\partial^2}{\partial r^2}\right)^{-1}(\Delta K_{22}) \\ &+ \frac{\pi\omega_1\Delta^*}{16T\Gamma}\left(\omega_1 + \tau_\varepsilon^{-1} - D\frac{\partial^2}{\partial r^2}\right)^{-1}(\Delta^* K_{12}) = \delta(r - r_1). \end{aligned} \tag{48}$$

This system can be solved with the logarithmic accuracy for strong energy relaxation $\tau_\varepsilon^{-1} > T\tau$. In this region, it follows from Eq. (1) that

$$\begin{aligned} &\left\langle \Delta^*\left(\omega_1 + \tau_\varepsilon^{-1} - D\frac{\partial^2}{\partial r^2}\right)^{-1}\Delta\right\rangle \\ &= \frac{64\mathrm{Gi}}{\pi^2}T^2\tau_\varepsilon\ln\left(\frac{\pi}{8T\tau\tau_\varepsilon}\right). \end{aligned} \tag{49}$$

Equations (1), (48), and (49) now imply the relations for the correlators $\hat{K}$,

$$\begin{aligned} &\left\{\tau + \frac{\pi D}{8T}K^2 + \frac{4\mathrm{Gi}T\tau_\varepsilon\omega_1}{\pi\Gamma}\ln\left(\frac{\pi}{8T\tau\tau_\varepsilon}\right)\right. \\ &\left. - \frac{2}{\tau}\left(\frac{4\mathrm{Gi}T\tau_\varepsilon\omega_1}{\pi\Gamma}\right)^2 I\right\}K_{11} = 1, \quad K_{22} = K_{11}, \end{aligned} \tag{50}$$

where

$$\begin{aligned} I &= \int_0^\infty \frac{dxdy}{(x+1)(y+1)\sqrt{(x-y)^2 + 2(x+y)a + a^2}}, \\ a &= 1 + \frac{4\omega_1 T\tau_\varepsilon\mathrm{Gi}}{\pi\Gamma\tau}\ln\left(\frac{\pi}{8T\tau\tau_\varepsilon}\right). \end{aligned} \tag{51}$$

The nondiagonal elements in $\hat{K}$ give a logarithmically small contribution to the conductivity. As a result, we obtain

$$\frac{\sigma^a}{\sigma_0} = \frac{32\mathrm{Gi}^2 T^2\tau_\varepsilon}{\pi^2\Gamma\tau}\ln\left(\frac{\pi}{8T\tau\tau_\varepsilon}\right). \tag{52}$$

The situation becomes more complicated if the energy relaxation time τ_ε is large. From (48), we then obtain the equation for the correlator K_{11}

$$\begin{gathered}\left[\tau + \frac{\pi}{8T}\left(\omega_1 - D\frac{\partial^2}{\partial r^2}\right)\right]K_{11} \\ + \frac{\pi\omega_1\Delta}{16T\Gamma}\left(\omega_1 + \tau_\varepsilon^{-1} - D\frac{\partial^2}{\partial r^2}\right)^{-1}(\Delta^* K_{11}) - \left(\frac{\pi\omega_1}{16T\Gamma}\right)^2 \\ \times\Delta\left(\omega_1 + \tau_\varepsilon^{-1} - D\frac{\partial^2}{\partial r^2}\right)^{-1}\Delta\left[\tau + \frac{\pi}{8T}\left(\omega_1 - D\frac{\partial^2}{\partial r^2}\right)\right. \\ \left. + \frac{\pi\omega_1}{16T\Gamma}\Delta^*\left(\omega_1 + \tau_\varepsilon^{-1} - D\frac{\partial^2}{\partial r^2}\right)^{-1}\Delta\right]^{-1} \\ \times\Delta^*\left(\omega_1 + \tau_\varepsilon^{-1} - D\frac{\partial^2}{\partial r^2}\right)^{-1}(\Delta^* K_{11}) = \delta(r - r_1).\end{gathered} \tag{53}$$

We next find the mean value

$$\begin{gathered}\left\langle\Delta^*\left(\omega_1 - D\frac{\partial^2}{\partial r^2}\right)^{-1}(\Delta\exp(ikr))\right\rangle \\ = \frac{64T^2\mathrm{Gi}}{\pi^2}\frac{1}{Dk^2 + 8T\tau/\pi}\ln\left(\frac{\pi(Dk^2 + 8T\tau/\pi)^2}{8T\tau\omega_1}\right).\end{gathered} \tag{54}$$

This implies that the coefficient at ω_1 in the equation for K_{11} is logarithmically large. Contrary to the previous case ($\tau_\varepsilon^{-1} \gg T\tau$), the last term in the right-hand side of Eq. (53) is essential; together with off-diagonal elements in $\hat{K}$, it leads to the cancellation of large terms in the conductivity. To verify this, we must find the mean value of the product of four Δ in the last term in Eq. (53). We have

$$\begin{gathered}I_1 = \left(\frac{\pi}{16T\Gamma}\right)^2\left\langle\Delta\left(\omega_1 - D\frac{\partial^2}{\partial r^2}\right)^{-1}\Delta\left[\tau + \frac{\pi}{8T}\left(\omega_1 - D\frac{\partial^2}{\partial r^2}\right)\right.\right. \\ \left. + \frac{\pi\omega_1}{16T\Gamma}\Delta^*\left(\omega_1 - D\frac{\partial^2}{\partial r^2}\right)^{-1}\Delta\right]^{-1} \\ \left.\times\Delta^*\left(\omega_1 - D\frac{\partial^2}{\partial r^2}\right)^{-1}\Delta^*\exp(ikr)\right\rangle = \exp(ikr) \\ \times\left(\frac{\pi}{16T\Gamma\nu d}\right)^2\int\frac{d^2k_1}{(2\pi)^2}\int\frac{d^2k_2}{(2\pi)^2} \\ \times\left[\left(\tau + \frac{\pi D}{8T}k_1^2\right)\left(\tau + \frac{\pi D}{8T}k_2^2\right)\right]^{-1}\left[(\omega_1 + D(k - k_2)^2)\right. \\ \left.\times(\omega_1 + D(k - k_1)^2)\left(\tau + \frac{\pi}{8T}Dk_3^2 + \omega_1\alpha_{k_3}\right)\right]^{-1},\end{gathered} \tag{55}$$

where

$$\begin{gathered}k_3 = k - k_1 - k_2, \\ \alpha_k = \frac{4T\mathrm{Gi}}{\pi\Gamma}\frac{1}{Dk^2 + 8T\tau/\pi}\ln\left(\frac{\pi(Dk^2 + 8T\tau/\pi)^2}{8T\tau\omega_1}\right).\end{gathered} \tag{56}$$

The $\ln^2$ term can be easily separated in expression (55). As a result, we obtain

$$I_1 = \frac{1}{\tau + (\pi D/8T)k^2 + \omega_1\alpha_k}\left\{\alpha_k^2 - \frac{4\pi\alpha_k\mathrm{Gi}}{\Gamma}\int\frac{d^2k_1}{(2\pi)^2}\frac{(\pi D/8T)(k_1^2 - k^2) + \omega_1(\alpha_{k_1} - \alpha_k)}{(\tau + (\pi D/8T)k_1^2)(k_1 - k)^2(\tau + (\pi D/8T)(k_1 - k)^2 + \omega_1\alpha_{k_1 - k})}\right\}. \tag{57}$$

In Eq. (55), we omitted the “diagonal” term with the denominator of the type $[\omega_1 + D(k + k_1)^2]^2$. This term leads to a small correction to the coefficient at ω_1 in (53).

With the same accuracy, we now present the expression for the nondiagonal elements K_{12} and K_{21} as

$$\begin{gathered}K_{21} = -\frac{\pi\omega_1}{16T\Gamma}\int\frac{d^2k_1 d^2k_2}{(2\pi)^4}\frac{\Delta_{k_1}^*\Delta_{k_2}^* K_{11}(k)}{(\omega_1 + D(k - k_1)^2)[\tau + (\pi D/8T)(k - k_1 - k_2)^2 + \omega_1\alpha_{k - k_1 - k_2}]}, \\ K_{12} = -\frac{\pi\omega_1}{16T\Gamma}\int\frac{d^2k_3 d^2k_4}{(2\pi)^4}\frac{\Delta_{k_3}\Delta_{k_4} K_{22}(k)}{(\omega_1 + D(k + k_3)^2)[\tau + (\pi D/8T)(k + k_3 + k_4)^2 + \omega_1\alpha_{k + k_3 + k_4}]}.\end{gathered} \tag{58}$$

Using Eqs. (57) and (58), we obtain the correction to the conductivity as

$$\frac{\sigma^a}{\sigma_0} \approx \frac{4T\mathrm{Gi}^2}{\pi\Gamma\tau^2}. \qquad (59)$$

This expression is valid up to a numerical factor of the order unity.

If the external depairing factor Γ is zero (a superconductor without paramagnetic impurities), the quantity Γ in Eqs. (51) and (59) must be replaced by its intrinsic value

$$\Gamma \approx T\mathrm{Gi}^{1/2} \qquad (60)$$

(see Eq. (18)). In the temperature region $\mathrm{Gi} < \tau < \mathrm{Gi}^{1/2}$, we then obtain

$$\sigma^a/\sigma_0 \approx 4\mathrm{Gi}^{3/2}/\pi\tau^2. \qquad (61)$$

Equation (61) implies that the AL contribution to the conductivity is strongly enhanced in the temperature region $\mathrm{Gi} < \tau < \mathrm{Gi}^{1/2}$.

6. THE MAKI–THOMPSON CONTRIBUTION TO CONDUCTIVITY IN THE NONLINEAR FLUCTUATION REGION

The general expression for the MT contribution to the conductivity (σ^b) was given in [6]. Equation (28) in [6] can be considered as the interpolation of the MT contribution that is valid in the entire temperature region $\tau > \mathrm{Gi}$. The depairing factor Γ in Eq. (28) in [6] must be changed to a sum of two terms: the external depairing factor τ_s^{-1} related to the spin flip scattering on magnetic impurities and the intrinsic depairing factor given by Eq. (20). As a result, we obtain

$$\begin{aligned}\frac{\sigma^b}{\sigma_0} &= \frac{\pi}{8d\nu}\int\frac{d^2k}{(2\pi)^2}\frac{1}{\Gamma + Dk^2/2}\frac{1}{\tau + (\pi D/8T)k^2} \\ &= \frac{2\mathrm{Gi}}{\tau}\frac{1}{\pi\Gamma/4T\tau - 1}\ln\left(\frac{\pi\Gamma}{4T\tau}\right).\end{aligned} \qquad (62)$$

In the range $\mathrm{Gi} < \tau < \mathrm{Gi}^{1/2}$, the MT contribution reaches its saturation value and effectively becomes temperature independent,

$$\frac{\sigma^b}{\sigma_0} = \mathrm{Gi}^{1/2}\ln\left(\frac{\mathrm{Gi}^{1/2}}{\tau}\right). \qquad (63)$$

The correction remains small in the entire region $\mathrm{Gi} < \tau < \mathrm{Gi}^{1/2}$, where nonlinear effects are important.

We note that real superconductors are always inhomogeneous. The finite value of the transition width leads to the appearance of an effective depairing factor [11]. The value of this depairing factor can be sufficiently large in the units of $T\mathrm{Gi}$. In this case, the MT contribution to the conductivity is small compared to the AL contribution in the entire temperature region.

7. CONCLUSIONS

We have seen that nonlinear fluctuation effects are much stronger in kinetics phenomena than in thermodynamics. If the external depairing factor is absent, the nonlinear effects lead to a saturation of the MT contribution to the conductivity in the temperature region $\tau \le \mathrm{Gi}^{1/2}$. In this temperature region, the AL contribution becomes even stronger and grows as $\sigma^a/\sigma_0 \approx \mathrm{Gi}^{3/2}/\tau^2$. In a superconductor with a sufficiently large external depairing factor $\Gamma = \tau_s^{-1} > T\mathrm{Gi}^{1/2}$ or a short energy relaxation time $\tau_\varepsilon^{-1} > T\mathrm{Gi}^{1/2}$, the MT contribution saturates in the temperature region $T\tau \le \Gamma$ or $T\tau \le \tau_\varepsilon^{-1}$. It is not very sensitive to nonlinear effects. Magnetic impurities and the energy relaxation act on the AL contribution in different ways. Energy relaxation leads to the appearance of a collision integral in the kinetic equation for the distribution functions of normal excitations. This collision integral diminishes the nonequilibrium contributions to the distribution functions. Magnetic impurities and the magnetic field act only on the superconductivity and do not lead to the relaxation of the distribution functions. However, the TDGL equation essentially depends on the electron distribution function. If $\tau_\varepsilon^{-1} > T\mathrm{Gi}^{1/2}$, the nonlinear fluctuation effects are not essential and the AL contribution remains the same, $\sigma^a/\sigma_0 \approx \mathrm{Gi}/\tau$, in the entire temperature region $\tau > \mathrm{Gi}$. If the inequality $\tau_\varepsilon^{-1} < T\mathrm{Gi}^{1/2}$ is satisfied, the law $\sigma^a/\sigma_0 \approx \mathrm{Gi}^{3/2}/\tau^2$ applies in the temperature region $T\tau > \tau_\varepsilon^{-1}$. In the region $(T\tau_\varepsilon)^{-1} > \tau > \mathrm{Gi}$, the correction to the conductivity is given by $\sigma^a/\sigma_0 \sim \mathrm{Gi}^{3/2}T\tau_\varepsilon/\tau$ (see Eq. (52)). Magnetic impurities (or a current) suppress nonlinear fluctuation effects in σ^a, but the effect is not as strong as for the energy relaxation. In the range $T\mathrm{Gi}/\Gamma > \tau > \mathrm{Gi}$, the correction to the conductivity σ^a is given by Eq. (59), $\sigma^a/\sigma_0 \sim T\mathrm{Gi}^2/(\Gamma\tau^2)$. In the temperature region $\tau > T\mathrm{Gi}/\Gamma$, the correction σ^a is given by Eq. (43) in the linear approximation.

It is essential that the conductivity of fluctuating pairs can be larger than the conductivity of normal electrons in the temperature region where the correction to the thermodynamic quantities is still small (see Eq. (61)).

ACKNOWLEDGMENTS

A.I. Larkin thanks M.Yu. Reizer and V.M. Galitski for discussions. The work of A.L. was supported by NSF grant DMR-9812340. The research of Yu. O. made possible in part by Award No. RP1-2251 of the U.S. Civilian Research & Development Foundation for the Independent States of the Former Soviet Union (CRDF). Research of Yu. O. is also supported by the Russian Foundation for Basic Research.

REFERENCES

1. A. A. Abrikosov, L. P. Gor’kov, and I. E. Dzyaloshinskiĭ, *Methods of Quantum Field Theory in Statistical Physics* (Fizmatgiz, Moscow, 1962; Prentice-Hall, Englewood Cliffs, 1963).
2. R. E. Glover, Phys. Lett. A **25**, 542 (1967).
3. L. G. Aslamazov and A. I. Larkin, Fiz. Tverd. Tela (Leningrad) **10**, 1106 (1968) [Sov. Phys. Solid State **10**, 875 (1968)]; Phys. Lett. A **26**, 238 (1968).
4. K. Maki, Prog. Theor. Phys. **39**, 897 (1968).
5. R. S. Thompson, Phys. Rev. B **1**, 327 (1970).
6. A. I. Larkin and Yu. N. Ovchinnikov, J. Low Temp. Phys. **10**, 407 (1973).
7. B. R. Patton, Phys. Rev. Lett. **27**, 1273 (1971).
8. J. Keller and V. Korenman, Phys. Rev. B **5**, 4367 (1972).
9. A. A. Varlamov and V. V. Dorin, Zh. Éksp. Teor. Fiz. **84**, 1868 (1983) [Sov. Phys. JETP **57**, 1089 (1983)].
10. M. Reiser, Phys. Rev. B **45**, 12 949 (1992).
11. A. I. Larkin and Yu. N. Ovchinnikov, Zh. Éksp. Teor. Fiz. **61**, 2147 (1971) [Sov. Phys. JETP **34**, 1144 (1972)].
12. W. Breing, M. C. Chang, E. Abrahams, and P. Wölfle, Phys. Rev. B **31**, 7001 (1985).
13. E. Abrachams and T. Zsuneto, Phys. Rev. **152**, 416 (1966).
14. A. Schmid, Phys. Condens. Mater. **5**, 302 (1966).
15. L. P. Gor’kov and G. M. Eliashberg, Zh. Éksp. Teor. Fiz. **54**, 612 (1968) [Sov. Phys. JETP **27**, 328 (1968)].
16. A. Schmid and G. Schön, J. Low Temp. Phys. **20**, 207 (1975).
17. G. Schön and V. Ambegaokar, Phys. Rev. B **19**, 3515 (1979).
18. A. I. Larkin and Yu. N. Ovchinnikov, Zh. Éksp. Teor. Fiz. **68**, 1916 (1975) [Sov. Phys. JETP **41**, 960 (1975)].
19. A. I. Larkin and Yu. N. Ovchinnikov, in *Nonequilibrium Superconductivity,* Ed. by D. N. Langenberg and A. I. Larkin (Elsevier, Amsterdam, 1986).
20. A. I. Larkin and Yu. N. Ovchinnikov, Zh. Éksp. Teor. Fiz. **73**, 299 (1977) [Sov. Phys. JETP **46**, 155 (1977)].
21. K. S. Usadel, Phys. Rev. Lett. **25**, 507 (1970).
22. Yu. N. Ovchinnikov, J. Low Temp. Phys. **31**, 785 (1978).

Journal of Experimental and Theoretical Physics, Vol. 92, No. 3, 2001, pp. 529–534.
Translated from Zhurnal Éksperimental'noĭ i Teoreticheskoĭ Fiziki, Vol. 119, No. 3, 2001, pp. 606–612.
Original Russian Text Copyright © 2001 by Slyunyaev.

MISCELLANEOUS

Dynamics of Localized Waves with Large Amplitude in a Weakly Dispersive Medium with a Quadratic and Positive Cubic Nonlinearity

A. V. Slyunyaev
Institute of Applied Physics, Russian Academy of Sciences, ul. Ul'yanova 46, Nizhni Novgorod, 603600 Russia
**e-mail: avs@appl.sci-nnov.ru*

Received March 22, 2000

Abstract—The dynamics of localized waves is analyzed in the framework of a model described by the Korteweg–de Vries (KdV) equation with account made for the cubic positive nonlinearity (the Gardner equation). In particular, the interaction process of two solitons is considered, and the dynamics of a “breathing” wave packet (a breather) is discussed. It is shown that solitons of the same polarity interact as in the case of the Korteweg–de Vries equation or modified Korteweg–de Vries equation, whereas the interaction of solitons of different polarity is qualitatively different from the classical case. An example of “unpredictable” behavior of the breather of the Gardner equation is discussed. *© 2001 MAIK “Nauka/Interperiodica”.*

1. INTRODUCTION

The Korteweg–de Vries (KdV) equation provides a basis for the description of wave processes in dispersive media. It includes a nonlinear (quadratic) and a dispersive term, which appear in the first order approximation in perturbation theory with respect to two small parameters, the amplitude and the wave number. The KdV equation, which provides a model for describing surface and internal waves in oceans and the Rossby waves, can be also used to describe various wave processes in the atmosphere, plasma, astrophysics, and transmission lines (see, e.g., [1–3]). In a number of physical applications, the nonlinearity of the lowest order is cubic. In this case, the problem is reduced to the modified Korteweg–de Vries equation. For example, it describes acoustic waves in plasma, the propagation of an elastic quasi-plane wave in a lattice, and internal ocean waves under certain stratification [4–6]. If the solution of the modified KdV equation on a pedestal is considered (which tends to a constant at infinity), which often corresponds to an external confining force or flow, then this problem is described by an evolutionary equation with two nonlinear terms, which is a generalization of the KdV equation and is called the Gardner equation. It is written as

$$\frac{\partial u}{\partial t} + (c + \alpha u + \alpha_1 u^2)\frac{\partial u}{\partial x} + \beta\frac{\partial^3 u}{\partial x^3} = 0. \qquad (1)$$

Two nonlinear terms in Eq. (1) correspond to the case of large amplitude waves. The coefficients in Eq. (1) can take various values depending on a concrete application. In physical problems, the KdV equation must be replaced by the Gardner equation (1) in the case when the coefficient of the quadratic nonlinearity is very small. In physical problems, the nonlinear coefficients in Eq. (1) can vary within a wide range and can change their sign (for example, in [7], an analysis of the nonlinear coefficients for model cases of the stratification of internal ocean waves is given), which results in nontrivial effects in the wave transformation [8–10]. All three models mentioned can be integrated by the inverse scattering transform [11–14] and have an infinite set of time-independent integrals and elastically interacting soliton solutions.

It is also known that in the case of a positive cubic nonlinearity, the modified KdV and Gardner equations have breather solutions corresponding to “breathing” wave packets [3, 15, 16]. Breathers, along with solitons, determine the asymptotics of the wave field. The KdV and modified KdV equations have long become classical, and the dynamics of their solitons is well understood (see, e.g., [1–3, 15]).

Notwithstanding the increased interest in nonlinear evolutionary equations with higher order nonlinear and dispersive terms (see, e.g., [17–19]), the completely integrable Gardner equation has not been studied from the viewpoint of soliton interaction. In the papers [20, 21], the interaction of solitons was analyzed for the case of a negative cubic nonlinearity ($\alpha_1 < 0$), and the special role played by the limit (“broad”) soliton in the evolution of the wave field was demonstrated. The phenomenon of peculiar interaction with a “broad” soliton has been recently validated in the framework of the fully nonlinear model of the two-layer water [22]. In this case, the second soliton changes its polarity and propagates on the back of the “broad” soliton. The wave dynamics of the Gardner equation (1) with a positive nonlinearity ($\alpha_1 > 0$) is qualitatively different from

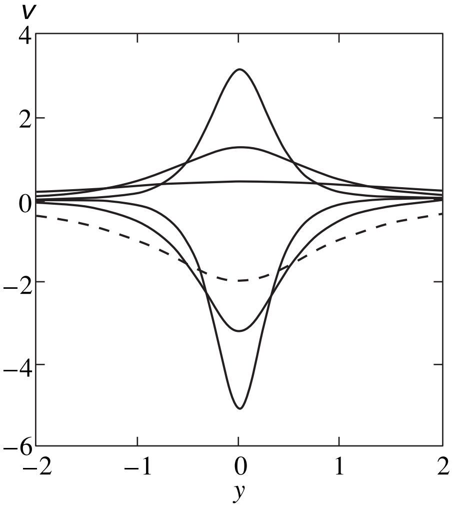

Fig. 1. Solitons of the Gardner equation with a positive cubic nonlinearity. The dashed curve represents the "algebraic" soliton.

that of the former case. The present paper gives an analysis of the soliton interaction for this equation.

2. SOLITON SOLUTIONS TO THE GARDNER EQUATION

For simplicity, we use dimensionless variables; then, Eq. (1) for the function $v(y, \tau)$ is written in the form

$$\frac{\partial v}{\partial \tau} + 6v(1+v)\frac{\partial v}{\partial y} + \frac{\partial^3 v}{\partial y^3} = 0. \tag{2}$$

It is well known that Eq. (2) has soliton solutions

$$v_{\text{sol}}(y,\tau) = \frac{\Gamma_1^2}{1 + s_1\sqrt{1+\Gamma_1^2}\cosh Z_1}, \tag{3}$$
$$Z_1 = \Gamma_1(y - V_1\tau - y_1), \quad V_1 = \Gamma_1^2, \quad s_1 = \pm 1.$$

The parameter Γ_1 determines the size of the soliton, and the sign $s_1 = \pm 1$ determines its polarity.

The shape of positive solitons is the same as that of the solitons of the KdV equation in the limit $\Gamma \longrightarrow 0$ (small amplitudes), and they tend to the solitons of the modified KdV equation as Γ (the amplitude) increases (Fig. 1). The amplitude of negative solitons cannot be less than the critical one, which is

$$v_{\text{cr}} = -2. \tag{4}$$

A soliton with such an amplitude (for it, $\Gamma_1 = 0$ and $s_1 = -1$) is called algebraic, since its value at infinity decreases as a power function rather than as an exponential one (the dashed curve in Fig. 1):

$$v_{\text{alg}}(y,\tau) = \lim_{\Gamma_1 \to 0} v_{\text{sol}}(y,\tau) = -\frac{2}{1+y^2}. \tag{5}$$

This soliton does not move and is unstable [16]. In the limit $\Gamma_1 \longrightarrow \infty$, the shape of negative solitons tends to that of the solitons of the modified KdV equation.

It must be noted that Γ has a clear physical meaning: its square equals the propagation speed of the solitary wave V. For the KdV and modified KdV equations, the greater soliton propagates faster; however, for the Gardner equation with a positive cubic nonlinearity, this is true only for solitons of the same polarity.

Since the Gardner equation is integrable, it possesses an infinite number of time-independent integrals. The simplest of them are the mass and energy integrals:

$$M = \int_{-\infty}^{\infty} v(y,\tau)dy, \quad E = \int_{-\infty}^{\infty} v^2(y,\tau)dy. \tag{6}$$

They are often used for qualitative reasoning and to control the accuracy of numerical experiments. For solitons (3), these integrals have the form

$$\begin{aligned} M_{\text{sol}}^{+} &= 2\arctan\Gamma_1, \\ M_{\text{sol}}^{-} &= M_{\text{sol}}^{+} - 2\pi, \\ E_{\text{sol}}^{\pm} &= 2\Gamma_{\text{sol}} - M_{\text{sol}}^{\pm}, \end{aligned} \tag{7}$$

where the signs "+" and "–" correspond to the polarity of the soliton.

The simplest multisoliton solution (the two-soliton one) can be obtained by the inverse scattering transform, by the Hirota method, and by the Darboux transformation (these methods were adapted for the Gardner equation with a negative cubic nonlinearity in [14, 23] and [21], respectively). In the most compact form, the two-soliton solution to Eq. (2) is written as

$$v_{2\text{sol}}(y,\tau) = \frac{i}{2}(\Gamma_2^2 - \Gamma_1^2)\left(\frac{1}{\Gamma_2\coth Z_{2+} - \Gamma_1\tanh Z_{1+}} - \frac{1}{\Gamma_2\coth Z_{2-} - \Gamma_1\tanh Z_{1-}}\right),$$

$$Z_{j\pm} = \frac{\Gamma_j}{2}(y - V_j\tau \pm \delta_j - y_j), \tag{8}$$

$$\tanh(\Gamma_j\delta_j) = -i\Gamma_j,$$

$$V_j = \Gamma_j^2, \quad j = 1, 2, \quad \Gamma_2 > \Gamma_1 > 0.$$

The expression for $v_{2\text{sol}}(y, \tau)$ was obtained by the Darboux transformation (see [21]) for Eq. (2); it describes the real solution, although it is complex in its form.

When written in the real form, it is much more complicated:

$$v_{2\mathrm{sol}}(y, \tau) = (\Gamma_2^2 - \Gamma_1^2)(\Gamma_2^2 d_{1+} - \Gamma_1^2 d_{2-})$$

$$\times [\Gamma_2^2 d_{1+} d_{2+} + \Gamma_1^2 d_{1-} d_{2-}$$

$$+ 2\Gamma_1\Gamma_2(\Gamma_1\Gamma_2 - D_1 D_2 \sinh Z_1 \sinh Z_2)]^{-1},$$

$$d_{j+} = 1 + D_j \cosh Z_j, \quad d_{j-} = 1 - D_j \cosh Z_j, \qquad (9)$$

$$D_j = s_j\sqrt{1 + \Gamma_j^2},$$

$$Z_j = \Gamma_j(y - V_j\tau - y_j), \quad V_j = \Gamma_j^2,$$

$$s_j = \pm 1, \quad j = 1, 2, \quad \Gamma_2 > \Gamma_1 > 0.$$

The subscript j indexes the solitons, and the sign $s_j = \pm 1$ in the expression for D_j determines the polarity of the corresponding soliton.

3. INTERACTION OF SOLITONS

Formulas (8) and (9) describe the interaction of two solitons of any polarity. In the framework of Eq. (2), two solitons with an equal speed cannot exist as stationary: they would interact. As was already mentioned, the amplitude of every type of solitons (the positive and the negative ones) monotonically depends on the speed; however, the negative of two solitons of different polarity propagating with the same speed is greater in amplitude (in the absolute value). Hence, the positive of two solitons of different polarity and the same amplitude is faster.

The interaction of solitons of the same polarity is qualitatively similar to that of the KdV solitons or of the modified KdV solitons of the same polarity: if their amplitudes are significantly different, then one soliton overtakes the other, and a single-hump symmetric profile appears; otherwise, an exchange of energy takes place, but no single hump appears.

It is convenient to introduce a parameter equal to the ratio of the amplitudes, $r = A_1/A_2$, where the soliton with the subscript 2 is the faster one and $\Gamma_2 > \Gamma_1$ (for solitons of the same polarity, $A_2 > A_1$ and, therefore, $0 < r < 1$). Then, the boundary value of this parameter, which separates two possible interaction scenarios, can be found from the two-soliton solution (9). It depends on the amplitude of the interacting solitons; the plot is shown in Fig. 2. The curve $A_2 = -2/r$, which limits the domain of feasible values of the parameters in Fig. 2, appears due to the existence of the minimal negative soliton, the algebraic one. For demonstrative purposes, Fig. 2 is not to scale. In reality, the range of values of r is very small for various amplitudes A_2: for positive solitons, it is $0.33 < r < 0.38$, and for negative ones, $0.38 < r < 0.40$. In the limit, this parameter tends to the values corresponding to the KdV equation (small amplitudes) and to the modified KdV equation (infinitely large amplitudes). For this reason, the inclusion of two nonlinear terms in the equation is of no qualitative importance for describing the interaction of solitons of the same polarity.

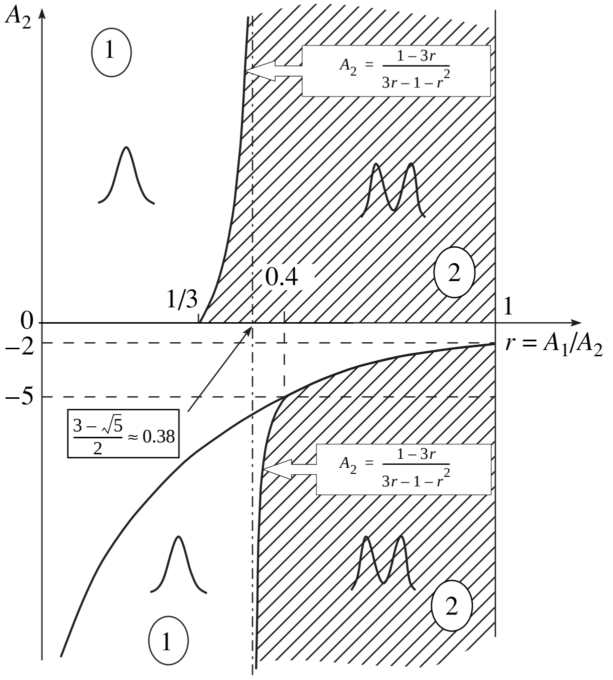

Fig. 2. The domains of parameters of the Gardner equation solitons interacting with overtaking (domain 1) or energy exchange (domain 2).

While interacting, the solitons of the Gardner equation of different polarity pass through one another, forming a single-hump symmetric shape at time $\tau = 0$. This situation is similar to that for the modified KdV equation. For interacting solitons of the Gardner equation, the relation

$$v_2(y = 0, \tau = 0) = A_2 - A_1 \qquad (10)$$

holds. For solitons of different polarity, this means that the height of the central point is equal to the difference of the amplitudes of the solitons at the moment when the symmetric wave profile is formed. Thus, the interaction of solitons of different polarity increases the amplitude of the wave. The polarity of the combined wave is determined by the faster soliton, which is different from the similar problem for the modified KdV equation, in which the greater soliton is faster. Neglecting the quadratic nonlinearity in Eq. (2) when considering the interaction of solitons of different polarities, that is, an attempt to describe the problem by the modified KdV equation, can give a qualitatively different result (see Fig. 3). Figure 3a presents the result of the interaction of two solitons of the Gardner equation (2) when the smaller (positive) soliton is faster (the parameters of the solitons are $\Gamma_1 = 3.8$, $\Gamma_2 = 4$, $A_1 = -4.9$, and $A_2 = 3.1$). As was explained above, the interaction produces a positive wave with the amplitude equal to the sum of those (Fig. 3a) of the interacting solitons. Figure 3b

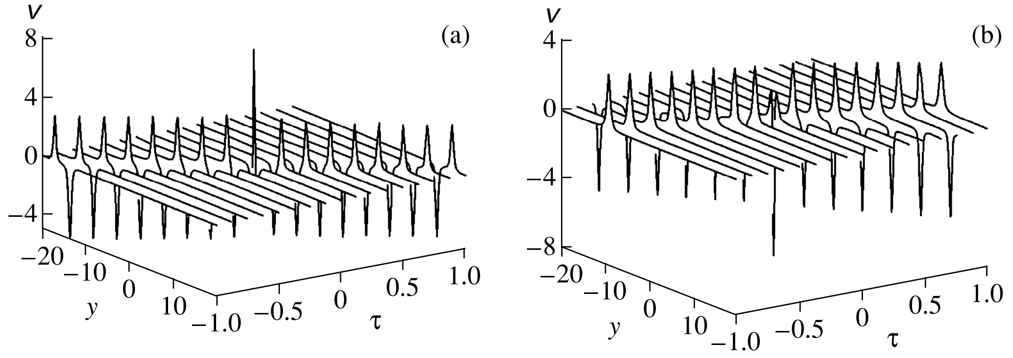

Fig. 3. Modeling the interaction of two solitons of different polarity for (a) the Gardner equation and (b) the modified KdV equation. The parameters of the solitons are $\Gamma_1 = 3.8$, $\Gamma_2 = 4$, $A_1 = -4.9$, and $A_2 = 3.1$.

demonstrates the results of modeling the same problem by the modified KdV equation (the amplitudes of the interacting solitons are the same as in the example in Fig. 3a). In this case, the amplitude of the combined wave is determined by the greater soliton, and the wave is negative.

The presence of two nonlinear terms in the Gardner equation implies interesting phenomena in the case of the interaction of slow solitons of different polarity. Since the amplitude of the positive soliton tends to zero as its speed decreases, whereas the amplitude of the negative soliton cannot be less than v_{cr}, we see that the small positive soliton can be indiscernible at the background of the negative one (Fig. 4a). However, if the positive soliton is faster, the wave sharply changes its polarity at the moment of overtaking (Fig. 4b), and then the polarity of the wave is recovered.

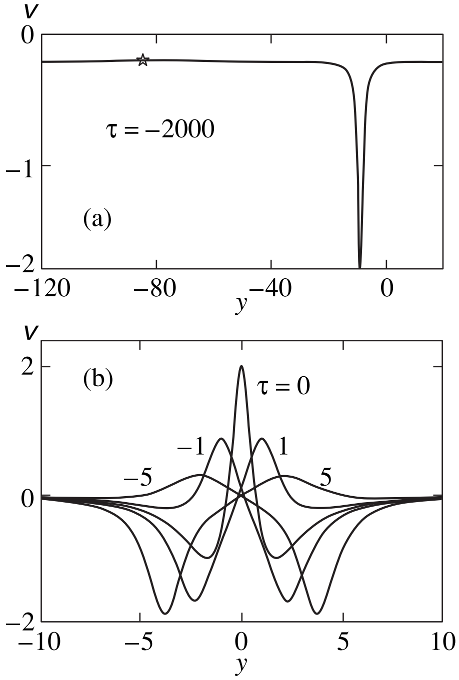

Fig. 4. Interaction of a negative soliton with a positive small-amplitude, but faster, one ("unpredictable" soliton): (a) before interaction (the positive soliton is marked by an asterisk); (b) sharp change in the wave polarity at the moment of interaction.

As a result of the interaction, the solitons acquire a coordinate (phase) shift

$$\Delta y_{1,2} = \pm\frac{2}{\Gamma_{1,2}}\ln\frac{\Gamma_2+\Gamma_1}{\Gamma_2-\Gamma_1}, \qquad (11)$$

which is the same as in the case of the KdV and modified KdV equations.

4. A NONLINEAR WAVE PACKET (BREATHER)

In addition to solitons, the Gardner equation has one more solitary solution that corresponds to the "breathing" wave packet, the so-called breather. For example, a breather can appear as a result of a soliton passing the domain where the quadratic linearity changes its sign [10], as a result of a perturbation of the algebraic soliton [16], or from a certain initial perturbation (in [24], the appearance of a breather for the modified KdV equation from an initial antisymmetric perturbation is considered). A formula for the breather of Eq. (2) was obtained in [16] by solving the inverse scattering problem. The breathing solution can be also obtained from the two-soliton solution (8). In this case, the wave packet corresponds to two coupled solitons of different polarity with the parameters

$$\Gamma_2 = a + ib, \quad \Gamma_1 = a - ib, \quad a > 0, \quad b > 0. \qquad (12)$$

In the most compact form, the breather can be written as

$$v_{br}(y,\tau) = -2\mathrm{Im}(\gamma^2) \times \mathrm{Re}\left(\frac{1}{\gamma\tanh\left[\frac{\gamma}{2}(z+\delta)\right] - \gamma^*\tanh\left[\frac{\gamma^*}{2}(z^*-\delta^*)\right]}\right), \qquad (13)$$

where

$$\delta = \frac{1}{2\gamma}\ln\frac{i+\gamma}{i-\gamma}, \quad \gamma = a + ib, \quad z = y - y_0 - \gamma^2\tau.$$

In the real-valued form, Eq. (13) can be written as

$$v_{br}(y,\tau) = 2ab\frac{\dfrac{\cosh\eta\cos\psi+\cos\theta\cosh\varphi}{a\sin\theta\cosh\varphi+b\sinh\eta\cos\psi}+\dfrac{\sinh\eta\sin\psi+\sin\theta\sinh\varphi}{a\cos\theta\sinh\varphi-b\cosh\eta\sin\psi}}{\dfrac{b\cosh\eta\sin\psi-a\cos\theta\sinh\varphi}{a\sin\theta\cosh\varphi+b\sinh\eta\cos\psi}-\dfrac{b\sinh\eta\cos\psi+a\sin\theta\cosh\varphi}{a\cos\theta\sinh\varphi-b\cosh\eta\sin\psi}}, \qquad (14)$$

where

$$\eta = a(y - V_{\rm br}\tau - y_{\rm br}), \quad \theta = b(y - \omega\tau - y_{\rm ph})$$
$$V_{\rm br} = a^2 - 3b^2, \quad \omega = 3a^2 - b^2,$$
$$\varphi = \mathrm{Re}(\gamma\delta), \quad \psi = \mathrm{Im}(\gamma\delta).$$

The breather as a whole propagates with the speed $V_{\rm br}$; the quantity ω corresponds to the rate of the change of the breather filling; and $y_{\rm br}$ and $y_{\rm ph}$ are arbitrary real constants. For $b \gg a$, the wave packet includes a large number of wave bunches (Fig. 5a). At time intervals

$$T_{\rm br} = \frac{\pi}{b(a^2+b^2)} \qquad (15)$$

the breather repeats its shape. The wave packet of the Gardner equation tends to the cubic breather of the modified KdV equation as $(a^2 + b^2)$ increases (large amplitudes or dense filling). The presence of a quadratic nonlinearity in the equation only makes the breather asymmetric with respect to the level $v = 0$ (Fig. 5).

The case $a \gg b$ is of great interest. In this case, the propagation of the breather is similar to the situation when two solitons of different polarity (Figs. 4, 5b) overtake each other in turn. Solution (14) implies that two solitons of different polarity that are parts of a breather move apart to the distance

$$L = \frac{2}{a}\ln\frac{2a}{b} \qquad (16)$$

as a result of such an oscillation.

If we consider two solitons with close parameters $\Gamma_{1,2} \approx a$ (close speeds) that differ by a small quantity b, then formula (16) yields the phase shift acquired by the solitons as a result of the interaction (cf. formula (11)). Thus, for $a \gg b$, the breather consists of two coupled solitons of different polarity with close speeds. In the process of the interaction, the solitons acquire the phase shift characteristic of overtakes; then, the roles of the solitons are interchanged. Up to the moment of being overtaken, the overtaking soliton accelerates, while the soliton being overtaken decelerates; then, the faster soliton decelerates, and the slower one accelerates as is the case in the ordinary interaction. In this interpretation, the case when one of the solitons of the wave packet is close to the algebraic one and the other is very broad and small in amplitude (a and b are small) is of interest. The amplitude of the well-distinguished negative soliton undergoes sharp periodic variations due to the poorly discernible positive soliton, much the same as in the interaction of two solitons (Figs. 4, 5b).

For the breather, the mass and energy integrals (6) have the form

$$M_{\rm br} = \int_{-\infty}^{\infty} v_{\rm br}(y,\tau)dy = -4\psi - 2\pi,$$
$$E_{\rm br} = \int_{-\infty}^{\infty} v_{\rm br}^2(y,\tau)dy = 4a - M_{\rm br}. \qquad (17)$$

The breather's energy increases with a and decreases when b is increased (i.e., when the filling of the wave packet increases). Increase of the frequency of the wave packet filling results in decreasing the mass (in absolute value), which tends to zero for large b. The breather's mass is always negative and is maximal in absolute value (2π) as a and b tend to zero.

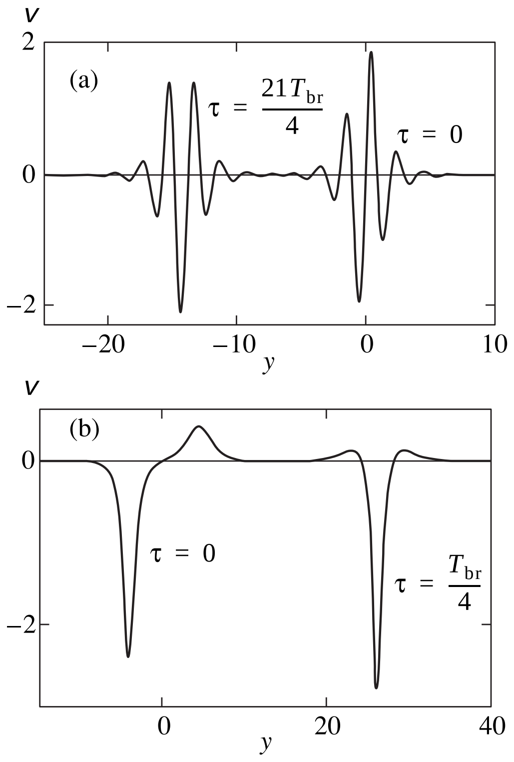

Fig. 5. Breathers of the Gardner equation: (a) a large number of wave bunches in the packet (a = 1 and b = 3); (b) two coupled solitons (a = 1 and b = 0.3).

5. CONCLUSIONS

A detailed analysis of the interaction of solitons in the framework of the Gardner equation, which is a natural generalization of the Korteweg–de Vries equation, is given. The Gardner equation involves the quadratic and positive cubic nonlinear terms. The analysis is based on the analytical two-soliton solution to this equation. It is shown that taking into account two nonlinear terms in this equation does not qualitatively change the description of the interaction dynamics of two solitons of the same polarity compared to the classical and modified Korteweg–de Vries equations; it is sufficient to allow for the dominant nonlinear term in the evolutionary equation. However, both nonlinear terms are important for the describing the interaction of two solitons of different polarity, especially slow ones. The polarity of the resultant wave is determined by the faster of the two solitons; thus, the greater soliton can sharply change its polarity under the influence of a small wave of different polarity (Fig. 4). The “breathing” wave packet (breather) becomes asymmetric if the quadratic nonlinearity is taken into account. The breather can possess a complicated behavior similar to that of two coupled solitons (Figs. 4, 5).

ACKNOWLEDGMENTS

This research was supported in part by the Russian Foundation for Basic Research, project no. 99-05-65576 and by INTAS, project no. 99-1068.

The author is grateful to E.N. Pelinovskiĭ and T.G. Talipova for the discussion of the results.

REFERENCES

1. S. Novikov, S. V. Manakov, L. P. Pitaevskiĭ, and V. E. Zakharov, *Theory of Solitons: The Inverse Scattering Method* (Nauka, Moscow, 1980; Consultants Bureau, New York, 1984).
2. M. J. Ablowitz and H. Segur, *Solitons and the Inverse Scattering Transform* (SIAM, Philadelphia, 1981).
3. G. L. Lamb, Jr., *Elements of Soliton Theory* (Wiley, New York, 1980; Mir, Moscow, 1983).
4. T. Kakutani and H. Ono, J. Phys. Soc. Jpn. **26**, 1305 (1969).
5. N. J. Zabusky, *Nonlinear Partial Differential Equations* (Academic, New York, 1967).
6. I. S. Pavlov, in *Collection of Scientific Works of Nizhni Novgorod State Technical University* (Nizhni Novgorod, 1998), p. 18.
7. R. Grimshaw, E. Pelinovsky, and T. Talipova, Nonlinear Processes Geophys. **4**, 237 (1997).
8. C. J. Knickerbocker and A. C. Newell, Phys. Lett. A **75**, 326 (1980).
9. T. G. Talipova, E. N. Pelinovskiĭ, and R. Grimshaw, Pis’ma Zh. Éksp. Teor. Fiz. **65**, 113 (1997) [JETP Lett. **65**, 120 (1997)].
10. R. Grimshaw, E. Pelinovsky, and T. Talipova, Physica D (Amsterdam) **132**, 40 (1999).
11. C. S. Gardner, J. M. Greene, M. D. Kruskal, and K. M. Miura, Phys. Rev. Lett. **19**, 1095 (1967).
12. V. E. Zakharov and A. V. Shabat, Zh. Éksp. Teor. Fiz. **61**, 118 (1971) [Sov. Phys. JETP **34**, 62 (1972)].
13. M. J. Ablowitz, D. J. Kaup, A. C. Newell, and H. Segur, Stud. Appl. Math. **53**, 249 (1974).
14. J. W. Miles, Tellus **31**, 456 (1979).
15. M. Wadati, J. Phys. Soc. Jpn. **34**, 1289 (1973).
16. D. Pelinovsky and R. Grimshaw, Phys. Lett. A **229**, 165 (1997).
17. A. S. Fokas, Physica D (Amsterdam) **87**, 145 (1995).
18. T. R. Marchant and N. F. Smyth, J. Appl. Math. **56**, 157 (1996).
19. H. Michallet and E. Barthelemy, J. Fluid Mech. **366**, 159 (1998).
20. E. N. Pelinovskiĭ and A. V. Slyunyaev, Pis’ma Zh. Éksp. Teor. Fiz. **67**, 628 (1998) [JETP Lett. **67**, 655 (1998)].
21. A. V. Slyunyaev and E. N. Pelinovskiĭ, Zh. Éksp. Teor. Fiz. **116**, 318 (1999) [JETP **89**, 173 (1999)].
22. M. Miyata, *A Note on Broad and Narrow Solitary Waves*, IPRC Report 00-01 SOEST 00-05 (Honolulu, Hawaii, 2000).
23. Y. Chen and P. L.-F. Liu, Wave Motion **24**, 169 (1996).
24. R. Grimshaw, P. Miller, E. Pelinovsky, and T. Talipova, Chaos **10**, 383 (2000).

Translated by A. Klimontovich

Journal of Experimental and Theoretical Physics, Vol. 92, No. 3, 2001, pp. 535–541.
Translated from Zhurnal Éksperimental'noĭ i Teoreticheskoĭ Fiziki, Vol. 119, No. 3, 2001, pp. 613–621.
Original Russian Text Copyright © 2001 by Skokov, Koverda, Reshetnikov.

MISCELLANEOUS

Self-Organized Criticality and 1/*f* Fluctuation under Conditions of Nonequilibrium Phase Transitions

V. N. Skokov*, V. P. Koverda, and A. V. Reshetnikov
Institute of Thermophysics, Ural Division, Russian Academy of Sciences, Yekaterinburg, 620219 Russia
**e-mail: vnskokov@itp.uran.ru*

Received July 14, 2000

Abstract—The results are given of an experimental investigation of fluctuation phenomena under conditions of electric arc discharge. Fluctuations are observed whose spectral density is inversely proportional to frequency (1/*f* noise). Power dependences are revealed of the fluctuation distribution functions. The behavior of spectral density and of distribution functions is associated with the simultaneous occurrence of various nonequilibrium phase transitions. Within the framework of the mean field theory, a mathematical model is suggested of interacting nonequilibrium phase transitions in a distributed system, which predicts the self-organization of the critical state and the generation of fluctuations with diverging spectral characteristics. An adequate agreement is observed between the suggested model and experimental data. *© 2001 MAIK “Nauka/Interperiodica”.*

1. INTRODUCTION

Fluctuation processes, whose power spectrum varies inversely proportionally to frequency (flicker or 1/*f* noise), are observed in diverse systems (electrophysical, geophysical, astrophysical, biological, environmental, etc.).

To date, various models are available in the literature, which explain the origin of flicker noise. The best known models of flicker noise in solids include the model of exponential distribution of relaxation times (see, for example, [1, 2]), as well as thermal models in which the mechanisms of thermal conductivity are taken to be responsible for flicker noise [3]. Theoretical reasoning, which points to the possibility of switching off the thermal-conductivity mechanism and to the responsibility of nonlinear interaction of the diffusion and thermal-conductivity modes in metals for $1/f^\alpha$ noise, is given in [4]. According to [5], the scale-invariant power form of the spectrum in phonon systems is associated with fluctuations of the rate of diffusion of the phase and of relaxation of the phonon modes. Klimontovich [6] treats 1/*f* noise as anomalous Brownian motion in bounded space. However, in spite of the efforts of many years, no generally accepted pattern of this phenomenon exists until now, and it is often that the mechanisms leading to fluctuations with 1/*f* spectrum are not clear. Therefore, the problems associated with the search for new systems with flicker noise and with the construction of new models of this phenomenon retain their urgency.

Interest in random processes with diverging spectral characteristics has sharply increased recently in view of the discovery of the phenomenon of self-organized criticality [7]. With self-organized criticality, a system comes to behave critically in the course of its evolution and needs no fine adjustment of controlling parameters. The concept of self-organized criticality is very general and can be used to describe the behavior of diverse dynamic systems. An important and unresolved problem of the theory of self-organized criticality is that of how a system with flicker noise comes to find itself in the critical state.

The low-frequency divergence of the spectral density of fluctuations points to the absence of a characteristic time scale of the process with flicker spectrum. This leads one to assume that the system is in the neighborhood of critical phase transition. The experiments performed in [8–10] revealed fluctuations with 1/*f* spectrum upon changeover of the modes of boiling of nitrogen on the surface of thin films of high-temperature superconductors under conditions of Joule self-heating. In this case, the superposition and interaction of two nonequilibrium phase transitions occur. In [11], thermal fluctuations with 1/*f* and $1/f^2$ spectra were observed experimentally under conditions of film boiling of water on a vertically oriented wire heater, and a similarity was observed between the investigated process and the effect of self-organized criticality. A mathematical model has been suggested [9, 10] for interpreting the experimental results that describes nonequilibrium phase transitions in a lumped nonpotential system which is a system of two nonlinear stochastic equations that transforms white noise into two stochastic processes with the values of spectral density proportional to 1/*f* and $1/f^2$. It appears of interest to find the possibility of fluctuations of order parameters with 1/*f* spectrum in spatially distributed potential systems.

The intersection and interaction of two nonequilibrium phase transitions is a phenomenon that is observed fairly frequently. For this reason, 1/*f* noise may be observed in a wide range of processes with phase transitions. A typical example of nonequilibrium phase

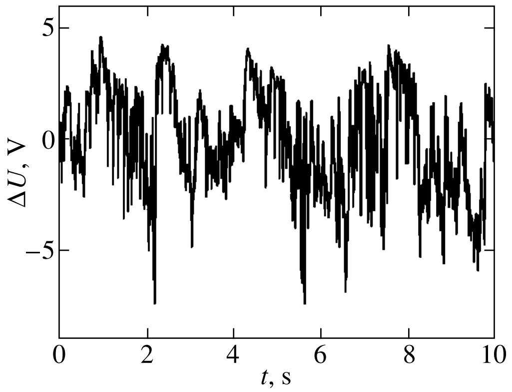

Fig. 1. An oscillogram of the voltage drop between the anode and cathode under conditions of arc discharge in water.

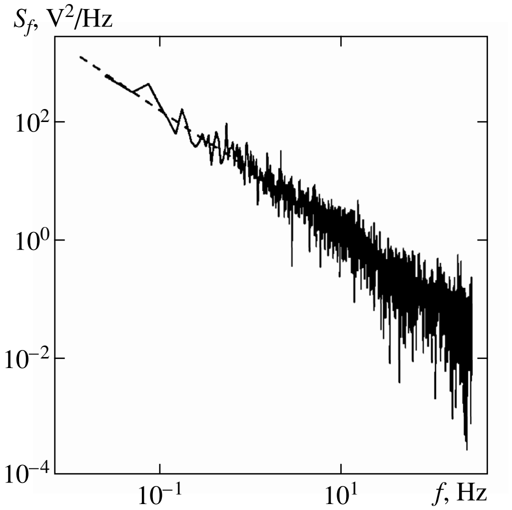

Fig. 2. The spectral density of oscillation of the voltage drop between the anode and cathode. The dashed line indicates the $S(f) \propto f^{-1}$ correlation.

transitions is provided by processes associated with electric discharge. Thus, different phase transitions may occur simultaneously and interact in the discharge plasma and in the electrode regions. For example, an arc discharge is accompanied by intensive erosion and evaporation of electrodes [12].

In this paper, the results are given of an experimental study into fluctuations of the current of a high-pressure electric arc, and a mathematical model is suggested of the emergence of fluctuations with flicker spectrum under conditions of interaction of phase transitions in a distributed system.

2. EXPERIMENT

In this study, we investigated electric fluctuations under conditions of burning arc discharge. The arc was ignited with contacting carbon electrodes moved 0.3 to 0.5 mm apart. The electrode diameter was 6 mm. The experiments were performed either in the air or with the electrodes immersed in water. In the former case, a high-pressure hot-cathode arc was realized [12], and in the latter case, a cold-cathode arc. A strong destruction of the electrodes occurred in the process of arc burning, first of all, of the anode. Therefore, in order to avoid the short-circuiting of the interelectrode gap by coal dust, the anode was located underneath the cathode. The experiments were performed at direct current.

The fluctuations of transport current and voltage drop between the anode and cathode were measured in the experiments. The method of Fourier transform was used to find the spectral density of fluctuations by the measured oscillograms. In many of the experiments performed in the air, the frequency dependence of spectral density had the $1/f$ form. The $1/f$ behavior of the spectrum was also often observed for fluctuations of the arc current (in this case, the voltage drop was tapped off a calibrated resistor). A random phase shift was observed between the electrodes and current, which was due to the reactive component of the arc conductivity.

When the electrodes were immersed in water, the arc became less stable, as manifested in a faster extinction of the arc; however, in this case, the $1/f$ behavior of spectra was observed for almost all oscillograms. In order to extend the frequency range (defined for a single oscillogram by the buffer memory of the oscilloscope, 2048 points), the measurements were performed with different time discretization. Figure 1 gives one of the oscillograms of the voltage drop between the anode and cathode. Figure 2 gives the spectral density of oscillation of the voltage drop between the anode and cathode. The broken line in Fig. 2 corresponds to the $S(f) \propto f^{-1}$ correlation. One can see in Fig. 2 that the correlation of the $1/f$ form extends over more than four decimal orders of magnitude.

A microscopic study of the electrodes after the experiments revealed traces of appreciable erosion. In experiments with a cold cathode (arc discharge in water), characteristic traces of cathode spots were clearly observed on the cathode [12]. Special experiments were performed in order to investigate the dynamics of electrode destruction; in these experiments, cylindrical carbon electrodes were arranged perpendicular to the arc column (in our case, horizontally). In the course of experiments, a moderate transport current was passed through the electrodes in the direction perpendicular to that of the arc current. Simultaneously with measuring the voltage drop between the electrodes, fluctuations of the voltage drop across the horizontal electrodes were recorded. Figure 3 gives the spectrum of fluctuations of the voltage drop on the cathode and the corresponding oscillogram (in the inset). One can see in Fig. 3 that the spectrum of fluctuations on the cathode corresponds to the white noise spectrum, and the realization consists of a sequence of random spikes. A similar pattern was observed for fluctuations of the voltage drop on the horizontal anode.

3. MATHEMATICAL MODEL

We will treat, within the framework of the phenomenological mean field theory, two simultaneous and interacting phase transitions. In this paper, we will not define the physical meaning of the order parameters concretely. We will assume that the space-time evolution of the process is described by two one-dimensional stochastic equations of the diffusion type,

$$
\begin{aligned}
\frac{\partial\phi}{\partial t} &= D_1\frac{\partial^2\phi}{\partial x^2} + Q_1(\phi,\psi) + \Gamma_1(x,t),\\
\frac{\partial\psi}{\partial t} &= D_2\frac{\partial^2\psi}{\partial x^2} + Q_2(\phi,\psi) + \Gamma_2(x,t),
\end{aligned}
\tag{1}
$$

where D_1 and D_2 are the diffusion coefficients, and $\Gamma_1(x, t)$ and $\Gamma_2(x, t)$ are δ-correlated random forces. The set of equations (1) is fairly general and describes nonequilibrium phase transitions in numerous physical and chemical systems. We will treat the case in which the characteristic space scales of variation of the order parameters differ strongly, i.e., $D_1/D_2 \gg 1$. In a particular case, this may imply a strong difference between the coefficients of thermal diffusivity and diffusion. We will approximate the source functions characterizing the interaction of the order parameters (as in [9, 10]) by the expressions

$$Q_1(\phi,\psi) = -\phi\psi^2 + \psi, \quad Q_2(\phi,\psi) = -\psi\phi^2 + \phi.$$

In this case, the set of stochastic equations takes the form

$$
\begin{aligned}
\frac{\partial\phi}{\partial t} &= D_1\frac{\partial^2\phi}{\partial x^2} - \phi\psi^2 + \psi + \Gamma_1(x,t),\\
\frac{\partial\psi}{\partial t} &= -\psi\phi^2 + \phi + \Gamma_2(x,t).
\end{aligned}
\tag{2}
$$

The set of equations (2) describes random walks in the potential

$$\Phi = \Phi_0 + \int\left[\frac{1}{2}\phi^2\psi^2 - \phi\psi + \frac{1}{2}(\nabla\phi)^2\right]dx. \tag{3}$$

The form of the potential surface is shown schematically in Fig. 4. The function $\Phi(\phi, \psi)$ has a saddle point at zero. In the absence of uniformity ($\nabla\phi = 0$), lines of stationary points are also available, which are defined by the condition $\phi\psi = 1$. When a nonuniformity of the parameter ϕ appears, the $\phi\psi = 1$ hyperbolas incline towards an increase in the parameter ψ. Figure 5 gives a phase pattern of the system, obtained by numerical integration of the set of equations (2) without random sources ($\Gamma_1 = \Gamma_2 = 0$). The broken lines in Fig. 5 indicate separatrices. This set of equations has an asymptotic solution at $t \longrightarrow \infty$ in the form of power dependences

$$\phi \longrightarrow t^{-1/4}, \quad \psi \longrightarrow t^{1/4}.$$

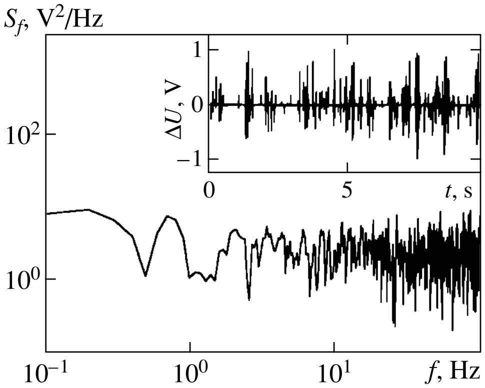

Fig. 3. The spectrum of erosion-related fluctuations of the voltage drop on the cathode. An oscillogram is given in the inset.

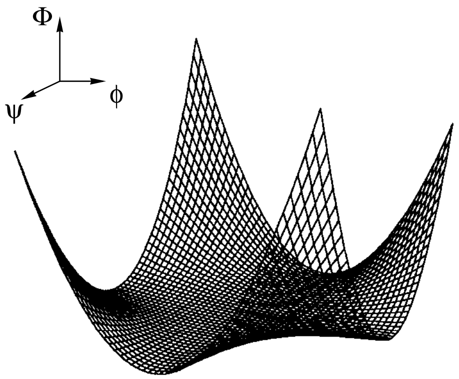

Fig. 4. The system potential defined by expression (3).

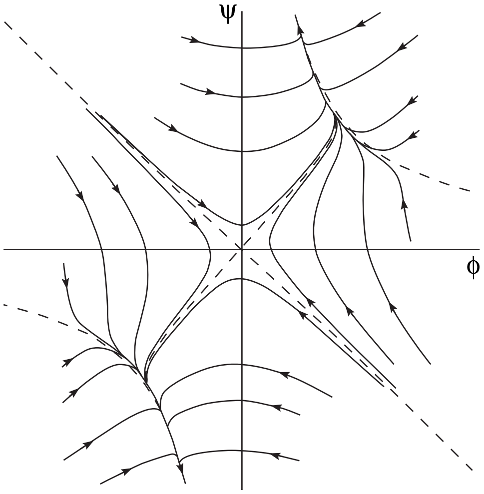

Fig. 5. A phase pattern of a dynamic system, averaged over spatial variable.

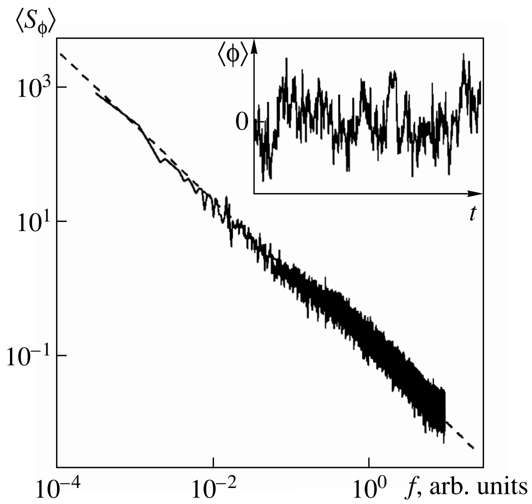

Fig. 6. The space-averaged spectral density $\langle S_\phi \rangle$ of fluctuations of the parameter ϕ, and the respective averaged realization of $\langle \phi \rangle$. Broken line indicates the $\langle S_\phi \rangle \propto 1/f^{1.09}$ correlation.

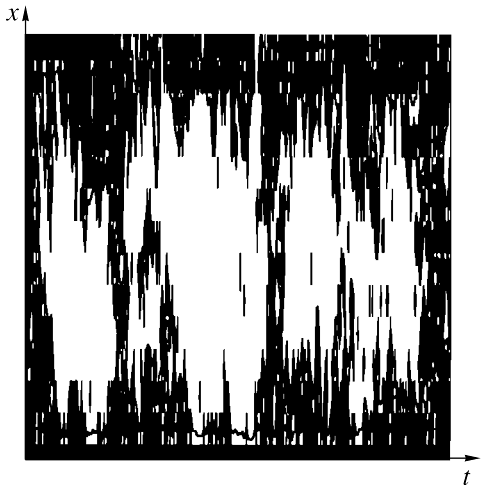

Fig. 7. A contour diagram of space-time realization of $\phi(x, t)$.

In the presence of a spatially distributed random source, an analytic investigation of the set of equations (2) presents considerable difficulties because of the presence of nonlinear terms and the absence of stationary points. The transition from stochastic equations to the respective nonlinear Fokker–Planck equation fails to solve the problem of finding spectral characteristics. Therefore, in this study we have restricted ourselves to the numerical methods of solving the set of equations (2).

The explicit integration scheme was used to derive numerical solutions. Sequences of Gaussian random numbers were taken to serve as spatially distributed white noise. The intensities of random sources and the diffusion coefficient were used as the controlling parameters. For a low intensity of noise, solutions of the set of equations (2) had the form of slightly noisy relaxation correlations $\phi(t)$ and $\psi(t)$, i.e., the system performed random walks along one of the valleys of the potential $\Phi(\phi, \psi)$ depending on the initial conditions. In so doing, the process was non-steady-state. As the intensity of random sources increased, changes from one valley to another started. The process became steady-state (at least by the first two moments of the distribution function of the parameter ϕ and during the final steps of integration). The transition to the steady-state process is due to the fact that the external random forces prevent the system from moving too far along the narrowing valleys of the potential $\Phi(\phi, \psi)$. The distribution functions of variables $\phi(t)$ and $\psi(t)$ had a symmetric cupola shape and were well approximated by Gaussian distribution.

The method of Fourier transform was used to find the spectral density of fluctuations by the calculated realizations of variables. It was found that, in fairly wide variations of the diffusion coefficient D_1 and of the intensity of random sources, the spectral density S_ϕ of fluctuations of the parameter ϕ varied in inverse proportion to frequency. At the same time, the frequency dependence of S_ψ was inversely proportional to the square of the frequency. Figure 6 gives the frequency dependence of spectral density $S_\phi(f)$ obtained by space averaging of spectra. The same drawing gives the respective space-averaged realization. The numerical data in Fig. 6 were obtained for 65 540 time integration steps and 32 space integration steps, with $dt = 0.05$, $dx = 0.8$, the intensity $\sigma = 3$, and zero initial and boundary conditions. The variation of the initial and boundary conditions had almost no effect on the results of numerical integration of the set of equations (2). One can see in Fig. 6 that the $1/f$ behavior is observed in the frequency range of over four decimal orders. One can extend this range and observe diverging low-frequency asymptotics if, as the number of integration steps is increased by a factor of n, the time integration step is reduced by a factor of $\sqrt{n}$ (with a simultaneous increase in the intensity of random sources). The spectrum of the parameter ψ is the same as in the case of Wiener's process of random walks. However, as distinct from the classical Brownian motion, no deviation of the mean value of the variable, calculated along the realization of a random process, from the value averaged over the entire realization is observed in our case in the realizations of $\psi(t)$. This indicates the stationarity of the process.

The fluctuation spectra of the variable ϕ at every space point also had the characteristic $1/f$ form. In spite of the fact that the external random forces were δ-correlated, significant space-time correlations are observed in the solutions of the system of $\phi(x, t)$ and $\psi(x, t)$. Figure 7 gives a contour diagram of the space-time distribution of the parameter $\phi(x, t)$. Light-colored in Fig. 7

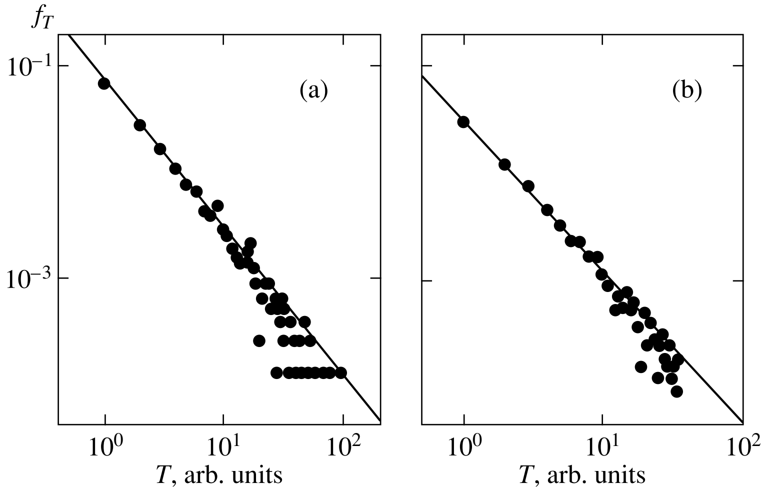

Fig. 8. The distribution functions of time intervals of passing the preassigned level: (a) experiment, (b) model.

are the regions of strong space-time correlation. Such regions may be interpreted as avalanches of sorts.

Note that the 1/*f* behavior of spectral characteristics was also retained in the case when random forces in Eq. (1) did not depend on the space coordinate, i.e., the external noise acting at every point in space was one and the same.

The above-described results correspond to the case when one of the diffusion coefficients (in this case, D_2) is zero. The results of numerical analysis have demonstrated that, as D_2 increases from zero to D_1, the $S_\phi(f)$ and $S_\psi(f)$ curves exhibit horizontal "shelves" in the low-frequency region characteristic of Lorentz spectra. In the case of equality of the diffusion coefficients, the parameters ϕ and ψ coincide, and the set of equations (2) is equivalent to the Ginzburg-Landau equation for a first-order phase transition with one order parameter.

For better understanding of the physical meaning of the set of equations (2), we will perform a linear transformation of variables in the expression for potential (3). We will introduce new variables

$$\theta = \frac{\psi - \phi}{\sqrt{2}}, \quad \eta = \frac{\phi + \psi}{\sqrt{2}}.$$

This transformation corresponds to a turn of the phase plane through angle $\pi/4$ and causes no variation of the type of potential surface. In the new variables, the expression for potential will take the form

$$\Phi(\theta, \eta) = \int\Big[\frac{1}{8}\theta^4 + \frac{1}{8}\eta^4 + \frac{1}{2}\theta^2 - \frac{1}{2}\eta^2 + \frac{1}{2}(\nabla\theta)^2 + \frac{1}{2}(\nabla\eta)^2 - \frac{1}{4}\theta^2\eta^2 - \nabla\theta\nabla\eta\Big]dx. \tag{4}$$

One can see from the structure of expression (4) that the potential $\Phi(\theta, \eta)$ corresponds to an intersection of two phase transitions with the order parameters θ and η [13]. Different signs before the squares of the order parameters imply an intersection of subcritical and supercritical phase transitions. The last two terms in Eq. (4) characterize the interaction of the order parameters. The negativity of the coefficients before the term $\theta^2\eta^2$ describing the interaction corresponds to the absence of nonzero steady-state solutions in a purely dynamic (noiseless) system.

4. DISCUSSION OF THE RESULTS

A distinguishing feature of self-organized criticality is the presence of power laws of distribution of physical quantities (which was largely the reason for the emergence of the very term "criticality"). In the papers dealing with self-organized criticality in distributed models of the "sand pile" type, power distributions of avalanches with respect to size are analyzed, as well as distributions of avalanche duration [14–16]. In the case when we have a time series of data obtained experimentally or as a result of numerical integration of equations, the concept of "avalanche" must be defined in order to obtain such distribution functions.

Assume that we have a discrete time series $x_i(t_i)$. We will select an arbitrary level, for example, $x = 0$, and designate the moments at which this level is passed as t_k. We will refer to the time interval between two successive passages of this level as the avalanche duration,

$$T_k = t_{k+1} - t_k.$$

The avalanche size will be defined (by analogy with [16]) as

$$s_k = \frac{1}{N}\sum_{t_i = t_k}^{t_{k+1}} |x_i(t_i)|. \tag{5}$$

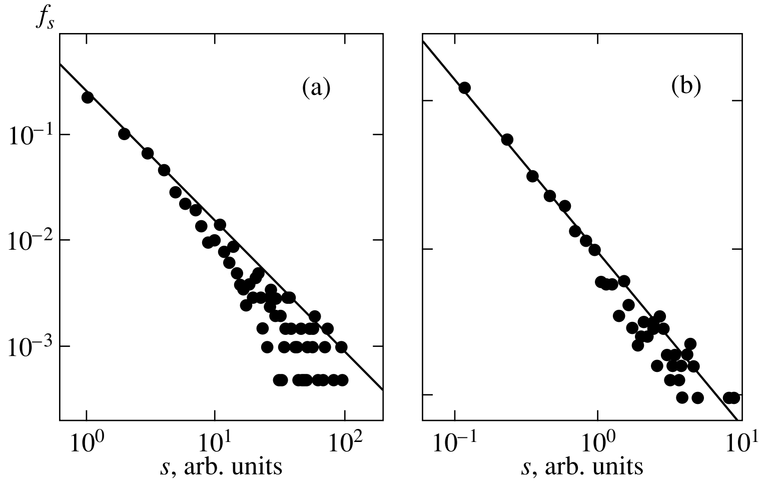

Fig. 9. The size distribution functions of avalanches: (a) experiment, (b) model.

Figure 8a gives the distribution functions of time intervals of passing zero level for experimental realization, and Fig. 8b gives the distribution functions for a numerical solution of the set of equations (2) (the variable $\langle\phi(t)\rangle$ averaged over space coordinate). Straight lines in Fig. 8 indicate the $f_T \propto T^{-1.4}$ correlation. Therefore, the distribution of time intervals (avalanche durations) both for experimental realizations and for the model is described by the power law,

$$f_T \propto T^{-\tau}, \quad \tau = 1.4. \tag{6}$$

Figure 9 gives the size distribution functions of avalanches for experimental realization (a) and for the model (b), determined in accordance with expression (5). Straight lines in Fig. 9 indicate the $f_s \propto s^{-1.2}$ correlation. In other words, the size distribution of avalanches obeys the power law,

$$f_s \propto s^{-\gamma}, \quad \gamma = 1.2. \tag{7}$$

These results are independent of the choice of the level from which the time intervals and sizes of avalanches are reckoned.

Therefore, the distributions of avalanche size and duration, determined experimentally and from model realizations, are described by the same power laws. The suggested model of emergence of fluctuations with flicker spectrum upon interaction of phase transitions in a spatially distributed potential system describes qualitatively correctly the experimentally observed results. Note that the spatial distribution of a system is not of fundamental importance from the standpoint of self-organization of the critical state of a system and generation of flicker noise. Such behavior may also be observed in point systems in the presence of external flows [9, 10]. As distinct from [9, 10], the model suggested by us is a potential one and predicts the possibility of both time and space correlations.

The model of interacting phase transitions within the mean field theory is fairly general and offers a fresh view of the cause of flicker noise and of self-organized criticality.

The divergence of the spectral characteristics of fluctuations and the power behavior of relaxation dependences are indicative of the critical behavior of a system. Such behavior is observed in a wide range of controlling parameters and does not require their fine adjustment. In this sense, one can refer to self-organization of the critical state.

ACKNOWLEDGMENTS

We are grateful to V.P. Skripov for the discussion of our results, as well as to N.B. Volkov and V.B. Priezzhev for encouraging discussions.

This study received support from the Russian Foundation for Basic Research (grants nos. 00-02-16288 and 00-15-96719).

REFERENCES

1. Sh. M. Kogan, Usp. Fiz. Nauk **145**, 285 (1985) [Sov. Phys. Usp. **28**, 170 (1985)].
2. G. P. Zhigal'skiĭ, Usp. Fiz. Nauk **167**, 623 (1997) [Phys. Usp. **40**, 599 (1997)].
3. R. F. Voss and J. Clarke, Phys. Rev. B **13**, 556 (1976).
4. R. O. Zaĭtsev, Pis'ma Zh. Éksp. Teor. Fiz. **58**, 978 (1993) [JETP Lett. **58**, 915 (1993)].
5. Yu. E. Kuzovlev, Zh. Éksp. Teor. Fiz. **111**, 2086 (1997) [JETP **84**, 1138 (1997)].
6. Yu. L. Klimontovich, Statistical Theory of Open Systems (Yanus, Moscow, 1995; Kluwer, Dordrecht, 1995).
7. P. Bak, C. Tang, and K. Wiesenfeld, Phys. Rev. A **38**, 364 (1988).

8. V. P. Koverda, V. N. Skokov, and V. P. Skripov, Pis'ma Zh. Éksp. Teor. Fiz. **63**, 739 (1996) [JETP Lett. **63**, 775 (1996)].
9. V. P. Koverda, V. N. Skokov, and V. P. Skripov, Zh. Éksp. Teor. Fiz. **113**, 1748 (1998) [JETP **86**, 953 (1998)].
10. V. P. Koverda and V. N. Skokov, Physica A (Amsterdam) **262**, 376 (1999).
11. V. N. Skokov, V. P. Koverda, and A. V. Reshetnikov, Pis'ma Zh. Éksp. Teor. Fiz. **69**, 590 (1999) [JETP Lett. **69**, 636 (1999)].
12. Yu. P. Raĭzer, *The Physics of Gas Discharge* (Nauka, Moscow, 1987).
13. I. F. Lyuksyutov, V. L. Pokrovskiĭ, and D. E. Khmel'nitskiĭ, Zh. Éksp. Teor. Fiz. **69**, 1817 (1975) [Sov. Phys. JETP **42**, 923 (1975)].
14. V. B. Priezzhev and K. Sneppen, Phys. Rev. E **58**, 6959 (1998).
15. S. Maslov, P. Rios, M. Marsili, and Y.-Ch. Zhang, Phys. Rev. E **58**, 7141 (1998).
16. F. Daerden and C. Vanderzande, Phys. Rev. E **53**, 4723 (1996).

Translated by H. Bronstein